Quantum non-Gaussianity certification in continuous-variable optics

Ganaël Roeland

Thèse de doctorat de
Sorbonne Université

présentée par

Ganaël Roeland

pour obtenir le grade de Docteur de Sorbonne Université
sur le sujet:

Quantum non-Gaussianity certification in continuous-variable optics

Laboratoire Kastler Brossel
Physique quantique et applications

Membres du jury :

Mme Rosa TUALLE-BROURI	Rapporteure
M. Matteo PARIS	Rapporteur
Mme Eleni DIAMANTI	Examinatrice
M. Jonas NEERGAARD-NIELSEN	Examinateur
Mme Valentina PARIGI	Invitée
M. Ulysse CHABAUD	Invité
M. Nicolas TREPS	Directeur de thèse

Abstract

This thesis focuses on both theoretical and experimental aspects of generating and certifying multimode quantum non-Gaussian states of light in continuous-variable optics. On the generation side, we theoretically investigated conditions for single-mode and mode-selective single-photon addition on a multimode field of light, showing in particular under which experimental conditions it is achievable. We also highlighted the unique challenges and benefits of both subtraction and addition processes. The insights obtained from this work may pave the way for experimental implementation of a single-photon addition on a multimode state of light. In the experiment, we used a synchronously pumped optical parametric oscillator (SPOPO) with an optical frequency comb to generate multimode squeezed vacuum states. We then subtracted a single photon to produce a quantum non-Gaussian state. Arises the question: How can we certify quantum non-Gaussianity? This question is particularly relevant in the context of the rapidly growing field of quantum information and of the race for building quantum computers. In collaboration with the LiP6 laboratory, we developed theoretical certification methods suitable for the states generated in our experiment. We derived an optimized fidelity estimation protocol using the double homodyne detection, allowing for the certification quantum non-Gaussianity features such as stellar rank and Wigner negativity. On the experimental side, we constructed a double homodyne detector and we made improvements to the setup, including better management of the intra-cavity dispersion of the SPOPO and the creation of an optical phase lock. These advancements enhance the multimodeness of the experiment, and allow for protocols otherwise out of reach. Bridging both theoretical and experimental works, we obtained preliminary results suggesting that we are on the brink of certifying stellar rank 1 single-mode single-photon subtracted states. The potential for future work includes the realization of a multimode double homodyne detector, the implementation of two-photon subtraction, and the certification of stellar rank 2 states.

Cette thèse se concentre sur les aspects théoriques et expérimentaux de la génération et de la certification d'états quantiques non-Gaussiens multimodes de la lumière dans l'optique à variables continues. En ce qui concerne la génération, nous avons étudié théoriquement les conditions pour une addition monomode et mode sélective de photon unique à un champ de lumière multimode, montrant en particulier sous quelles conditions expérimentales une telle addition est réalisable. Nous soulignons également les défis et les avantages uniques des processus de soustraction et d'addition de photon unique. Ce travail peut ouvrir la voie à la mise en œuvre expérimentale d'une addition de photon unique sur un état multimode de la lumière. Dans l'expérience, nous avons utilisé un oscillateur paramétrique optique pompé de manière synchrone (SPOPO) avec un peigne de fréquences optiques pour générer des états multimodes de vide comprimé. Nous

avons ensuite soustrait un photon unique pour produire un état quantique non-Gaussien. La question qui se pose est la suivante : Comment pouvons-nous certifier la non-Gaussianité quantique ? Cette question est particulièrement pertinente dans le contexte de la croissance rapide du domaine de l'information quantique et de la course à la construction d'ordinateurs quantiques. En collaboration avec le laboratoire LiP6, nous avons développé des méthodes de certification théoriques adaptées aux états générés dans notre expérience. Nous avons dérivé un protocole optimisé d'estimation de la fidélité utilisant la détection double homodyne, permettant de certifier des propriétés non-Gaussiennes quantiques telles que le rang stellaire et la négativité de la fonction de Wigner. Sur le plan expérimental, nous avons construit un détecteur double homodyne et nous avons amélioré l'expérience, notamment en améliorant la gestion de la dispersion intra-cavité du SPOPO et l'implémentation d'un asservissement de phase optique. Ces avancées renforcent le caractère multimodal de l'expérience et permettent de réaliser des protocoles autrement hors de portée. Combinant ces travaux théoriques et expérimentaux, nous avons obtenu des résultats préliminaires suggérant que nous sommes sur le point de certifier des états monomodes soustraits d'un photon unique, des états de rang stellaire 1. Le potentiel des travaux futurs comprend la réalisation d'un détecteur double homodyne multimode, la mise en œuvre d'une soustraction à deux photons et la certification d'états de rang stellaire 2.

Remerciements

Suite à la soutenance, j'aimerais, par ces quelques lignes, remercier les nombreuses personnes qui ont contribué à ce travail ou m'ont apporté leur soutien.

Merci tout d'abord à mon jury de thèse. Merci d'avoir accepté d'évaluer mon travail, et de vous être rendu en personne à Paris pour assister à ma soutenance. Merci pour vos questions qui ont donné lieu à une riche discussion et qui, à mon sens, ont montré votre intérêt pour ce travail de recherche.

First of all, I would like to thank my jury. Thank you for agreeing to assess my work, and for coming to Paris in person to attend my defence. Thank you for your questions, which gave rise to a rich discussion and, in my opinion, showed your interest in this research work.

Je souhaite remercier l'ensembles des personnes du LKB que j'ai rencontrées pendant ces quatre années de doctorat. Les personnes avec qui j'ai partagé une simple pause à la cafétéria, ainsi toute l'équipe de l'administration (spéciale dédicace à David pour son efficacité et son humeur toujours agréable), créant un environnement de travail agréable. Merci à Bérengère et aux personnes de l'atelier électronique du laboratoire, Elie, Loïc, et David, pour votre persévèrance et votre temps pour construire des détecteurs homodynes à haute perfromance, ainsi que l'amplificateur écréteur. Ce fut un plaisir de collaborer avec vous sur ces projets.

Merci en particulier à mon équipe de laboratoire, le groupe d'optique quantique multimode. Merci aux anciens de l'expérience SPOPO, Alex, Thibault, et Paul, auprès desquels j'ai beaucoup appris. Merci Thibault pour les discussions riches et intéressantes qu'on a pu avoir entre deux galères interminables de labo. Merci à mes collègues des autres projets, Tiphaine, Matthieu, Francesca, Johan, Guilherme, David F., Clémentine, Antonin, Ilya, Mathieu et Carlos. Même si vous n'avez pas choisi le bon projet, on a eu de multiples occasions d'échanger de bons moments en one-to-one ou même tous ensemble pendant les group days! Merci en particulier à mes deux voisins de labo pendant ces dernières années, Francesca et Johan, pour vos incessants enquiquinements mutuels, et votre "chill" permanent. Francesca, malgré un départ difficile, nous avons finalement réussi à accepter l'autre sans vouloir l'assassiner sournoisement (bien que seule l'une d'entre nous avait un tel désir), et découvert en l'autre un soutien précieux pendant les phases mouvementées qu'ont connues nos doctorats respectifs. Merci Francesca d'être la personne spéciale que tu es, et pour l'amitié partagée.

En parlant d'amitié, je tiens à remercier David et Niels, mes camarades d'expérience sur ces deux dernières années. David, merci pour ton grand coeur, ta générosité et l'attention que

tu portes, tel un papa, aux doctorants couvés sous ton aile de gentil post-doc. Niels, merci pour ta gaïeté quotidienne, ton enthousiasme intarissable, et ton écoute bienveillante. Je suis heureux d'avoir trouvé en toi non seulement un collègue compétant et persévérant, mais aussi une personne riche avec qui j'ai pu échanger sur mes problématiques personnelles, et écouter les siennes, avec qui j'ai tissé des liens d'amitié qu'il me "tarde" de nouer à nouveau lors de futures aventures... notamment d'escalade en falaise (merci encore à tous pour les cadeaux!) !

Enfin, je ne pourrais m'arrêter là sans remercier les "chefs", c'est-à-dire les personnes qui ont encadré, supervisé et contribué à ces travaux. Merci à toi Mattia pour nos dicsussions sur la théorie technique de ce domaine de recherche qui m'ont beaucoup inspiré. Cela a toujours été un plaisir d'être en ta compagnie, que ce soit pour boire du champagne à la célébration de ton poste permanent au CNRS, ou lorsque ton nouveau-né Chloé fait la star au laboratoire, attirant l'attention de tous ainsi qu'un mélange de désespoir et d'admiration de son papa. Merci à toi Valentina pour les divers moments qu'on a partagés, et pour ton écoute attentive et bienveillante. Merci également pour ton expertise et ton aide sur les sujets techniques et parfois insolubles qui sont venus très régulièrement égayer mes journées. Enfin, un grand merci à toi Nicolas pour tant de raisons que je ne pourrais pas en faire la liste ici. J'ai beaucoup appris à tes côtés, évidemment, et je dirais même que j'ai grandi, mûri personnellement et professionellement. Comme le montre la chronologie des faits qui mènent à ma venue dans ton équipe il y a plus de quatre ans, nous avions tous deux envie de travailler ensemble, et je pense pouvoir dire que nous avions raison d'écouter cette envie. Merci pour nos longues discussions, nos désaccords constructifs (et même ceux qui ne l'étaient absolument pas), et tout le temps partagé malgré le nombre impressionant et toujours grandissant de tes responsabilités. Ces responsabilités mêmes que tu endosses avec une compétance et une aisance que j'admire et qui m'inspirent. Merci aussi pour tout le reste.

Un court paragraphe pour remercier les nombreuses personnes avec qui j'ai partagé une danse à l'occasion d'un bal folk, pour leur soutien affectif sans mot et souvent même sans se connaître.

Je souhaite conclure en remerciant les peronnes proches qui me sont chères et qui se sont réjouies avec moi des succès de cette aventure qu'a été mon doctorat, et qui m'ont soutenu lors des difficultés inévitables qui l'accompagnent. Merci à mes amis et à ma famille. Merci Ivailo pour avoir partagé avec moi l'aventure du doctorat et bien d'autres activités dites "folles". Merci maman pour toujours avoir su être là, à me soutenir, même lorsque les épreuves que je traversais semblaient indéchiffrable.

Ces derniers mots sont dédiés à ma compagne et fiancée, Luna. Merci pour ton précieux soutien pendant la difficile période d'écriture. Merci pour les moments magiques que l'on a partagés. Merci pour m'avoir fait découvrir un amour dont l'existence même je ne croyais plus. Merci pour tout. Je t'aime.

Contents

Introduction

Light is an ubiquitous physical element of our world. Radiated from the Sun, it is our fundamental source of energy. Perceived by our eyes, it is our sense of sight enabler. Emitted from lasers, it is one of our most useful modern tools. Transmitted through optical fibers, it is our everyday mean for worldwide communication.

Light has fascinated among the most brilliant thinkers throughout history, since ancient times. The ancient Greeks, including figures like Euclid and Aristotle, already proposed initial theories on light, its properties, and how it interacts with matter. In the Islamic Golden Age, scholars like Alhazen revolutionized our understanding of light and vision, using experimental methods to refine the ideas inherited from the Greeks. This is the birth of the science of light: optics.

In the 17^{th} century, remarkable advancements in optics were made leading for instance to the design of telescopes and microscopes used to probe the world at large and small scales. Around the same time, Newton and Huygens proposed two (apparently) opposing theories on the nature of light itself. Newton viewed light as an assembly of small particles, while Huygens advocated the idea that light was a wave. Newton's corpuscle theory of light was widely accepted until the Young's and Fresnel's experiments the early 19^{th} century. Young's experiment consists in diffracting light through two slits, leading to the observation of an interference pattern, a wave-like behavior.

The nature of light as a wave was further understood in the late 19^{th} century, when Maxwell united electricity, magnetism, and light into one theory of electromagnetism. Given Maxwell's equations, light was then seen as a propagating excitation of both the electric and magnetic fields. As these excitation can occur at any frequency, this finding led to the later study and discovery of invisible light, such as radio waves, microwaves, X-rays and others.

Maxwell's theory also set the stage for some groundbreaking experiments in the early 20th century. In 1900, Planck successfully described the black-body radiation by assuming that the exchange of energy between light an matter only occurred in discrete amounts he called "quanta". In 1905, Einstein, inspired by this idea, exhibited the photoelectric effect. In 1913, Bohr showed that atoms can only emit discrete amounts of energy. These experiments clearly demonstrated the particle nature of light. To reconcile with Young's and Fresnel's wave-like experiments, the only possibility left was to consider light as neither a particle nor a wave. A conclusion that led to the current understanding of the dual nature of light: light is a quantized excitation of the electromagnetic field, in the sense that it consists of elementary excitations, or photons, behaving as particules or waves depending on the context.

These three discoveries also led to the development of quantum mechanics, and to quantum optics, the science of light at the quantum level, with in particular the invention of lasers

[Maiman 60]. The ability of the lasers to emit light that is coherent allows for a broad range of applications from precise surgical operations to advanced manufacturing. More than a technological breakthrough, lasers has become the main tool used in all modern quantum optics laboratories, greatly enhancing our capability to understand better the fascinating and often counter-intuitive quantum nature of light. In turn, this understanding has given rise to flourishing quantum technologies, with numerous application.

A striking example is vacuum fluctuations. The quantum electromagnetic field of light is null in mean, but exhibits fluctuations. These quantum fluctuations are present everywhere, in particular in what we usually refer to as vacuum. In the case of a non-zero-mean field, it is affected by the same vacuum fluctuations. This means that the physical quantities which characterize the light field, its amplitude and its phase, or field quadratures, are intrinsically noisy. The precision of their measurements are then limited by the vacuum fluctuations, a limit called standard quantum limit [Caves 81]. However, it is possible to reduce the noise on the amplitude quadrature at the expense of excess noise in the phase, or vice-versa, resulting into a state of light we call squeezed vacuum states [Slusher 85]. This reduced noise allows for enhancing the precision of measurements [Polzik 92]. For instance, this allowed for increasing the sensitivity of the gravitational wave detectors [Tse 19].

An emerging branch of quantum physics is quantum information, which consists in taking advantage of the intriguing quantum properties to convey, process, and manipulate information, asking in particular the question whether a quantum computer is feasible. The idea is then to encode information on quantum systems, resulting in quantum bits, called qubits, instead of the usual classical bits 0 and 1. For instance, one may encode the information on the absence of a photon (0) and the presence of a photon (1), relying on the discrete nature of light. Alternatively, one can encode the information on the quadratures of the field of light, with 0 for a particular probability distribution of a quadrature, and 1 for another (orthogonal). Since the field quadratures can take any real values, we refer to this domain as continuous variables quantum information [Gottesman 99, Raussendorf 01, Menicucci 06, Furusawa 11].

One of the key difference between qubits and bits is superposition, which refers to the ability of a physical system to exist in multiple states simultaneously until observed or measured. This was illustrated by the re-visited double-slit experiment, where single-photons were used instead of bright light.Classical bits may only be either in the state 0 or in the state 1, while the qubits may be in the superposition of the state 0 and the state 1. This property attains its fullest potential for encoding information when used together with quantum entanglement, another perplexing yet fascinating phenomenon. When two qubits are entangled, one cannot fully describe the state of one qubit without the knowledge of the state of the other qubit. In other words, the two qubits form an inseparable quantum state as whole. This means in particular that measuring one qubit may influence the state of the other qubit, whatever the distance between them. This is best demonstrated by the EPR Paradox, proposed by Einstein, Podolsky, and Rosen in 1935. Despite Einstein's famous phrase calling it "spooky action at a distance," subsequent experiments have confirmed that quantum entanglement is a fundamental aspect of the physical world [Freedman 72, Aspect 82, Weihs 98, Hensen 15, Aspect 15].

The information of all 2^N possible combinations of N classical bits can be encoded into the quantum state of N of maximally entangled qubits, in superposition on these 2^N possibilities. Then we can apply a quantum single operation on this superposition of 2^N states. Still, there

is a caveat: measuring the output state projects the result into a single result. Smarter algorithms have been formulated, providing up to an exponential computational speed-up with respect to their classical counterparts [Shor 94, Grover 96]. We refer to this computational speed-up as quantum advantage. For this reason, a quantum computer with a large number of entangled qubits and able to process arbitrarily long number of operations, i.e. an universal quantum computer, could bring a technological revolution, allowing for achieving tasks otherwise unfeasible in reasonable amounts of time. Although it was theoretically proven that such quantum computer can physically exist and function [Shor 96, Knill 98], many technological and conceptual challenges have to be overcome to build one [Temme 17].

Many efforts are undergoing in both the public and private research sectors to make progress towards building quantum computers, using a broad range of different physical support for encoding information, from optical to superconducting platforms. Up to now, only imperfect quantum computers, without the ability to correct computational errors, were reported [Arute 19, Zhong 20, Morvan 23], claiming a quantum advantage which raised heated debates in the community [Kalai 23]. Although these devices did not perform useful computations, some evidence for the utility of such noisy quantum computer was recently reported [Kim 23].

On the conceptual side, one of the main endeavor is to determine which resources facilitates the task of building a quantum computer. Some already identified resources are the entanglement and the highly-dimensionality of the input states of qubits. In continuous-variable (CV) quantum optics, both resources are readily available, due to the capability of on-demand generation of ever larger entangled states relying on either the light spatial degrees of freedom (spatial modes) [Su 07, Yukawa 08] or the time-frequency ones [Roslund 14, Chen 14, Cai 17, Asavanant 19, Larsen 19, Yang 21].

However, the generated states in these experiments are Gaussian states. Gaussian quantum states of light are defined as the states for which measurement statistics of the field quadratures is Gaussian. A good example is the aforementioned squeezed vacuum state. The issue with Gaussian states is that all Gaussian operations (that preserves the Gaussian character of the states) on such states can be efficiently simulated by classical computers [Bartlett 02], which hinders any quantum advantage.

Non-Gaussian states are hard to generate experimentally [Wenger 04, Ourjoumtsev 06, Parigi 07b, Takeda 13, Serikawa 18, Ra 20, Lvovsky 20, Bourassa 21] and hard to characterize theoretically [Walschaers 21]. Notably, it has been shown that not all non-Gaussian states are interesting for quantum computing, leaving us with a sub-set of non-Gaussian states, namely the quantum non-Gaussian states. Some of these states feature properties which have been shown to be necessary resources for quantum advantage [Mari 12, Chabaud 23].

Going one step further, assuming we have access to a useful quantum computer at hand, an important question is: can we prove its quantum advantage? A relevant step in this direction, owing to the above identified resources for quantum computing, consists in investigating the following question: How can we certify the non-Gaussianity of quantum states of light? This question is at the core of my PhD thesis.

The group of research I was part of during my PhD focuses on using optical frequency combs to generate multimode quantum states. The optical frequency combs are ultra-short pulses of light, which feature many degrees of freedom in the time-frequency domain. By synchronously pumping an optical parametric oscillator (SPOPO) with an optical frequency comb,

it is possible to generate a multimode entangled Gaussian state [de Valcárcel 06, Roslund 14]. The group also developed theoretically [Averchenko 14, Averchenko 16] and experimentally [Ra 17, Ra 20] the subtraction of a single photon on such multimode Gaussian state of light, resulting in a non-Gaussian state. To complement these advances, I took part in a project for developing a similar theoretical framework for the addition of a single-photon to a multimode field, a work published in [Roeland 22].

In collaboration with researchers from the Lip6 who developed a classification of the quantum non-Gaussian states, namely the stellar hierarchy [Chabaud 20c, Chabaud 20b], I worked on showing that certifying quantum non-Gaussianity was promisingly feasible using double homodyne detection with the support of simulations. This work was published in [Chabaud 21d]. Following this motivating results, I worked on designing and building a double homodyne detection on the existing experiment, and pushing towards the experimental certification of non-Gaussianity. As a first step, this detection can only measure one mode at a time, restricting to the certification of single-mode state. The challenging extension of the certification to the multimode case is planned, motivating the emphasis on the multimode aspect all along this thesis, both theoretically and experimentally. Finally, I also worked on successfully locking the optical phase at detection, which proved non-trivial owing to the spectrally broadband nature of our light.

This thesis is structured into four comprehensive chapters. In chapter 1, we focus on the description and characterization of the light field, and the Gaussian and non-Gaussian quantum states of light. In particular, we detail the notions of Wigner negativity and of stellar rank in the context of quantum information, providing theoretical tools for witnessing these properties.

Chapter 2 is dedicated to the description of the whole experiment. We focus on the description of the experimental generation of the multimode Gaussian states, and their detection using the (single) homodyne detection. In particular, the optical phase locking system is detailed, and applied to measure squeezing.

Chapter 3 provides the tools and methods used to characterize both single-photon subtraction and single-photon addition to multimode fields, with an emphasis on the theory of addition. We describe and characterize the experimental implementation of single-photon subtraction.

Finally, chapter 4 tackles the topic of certification itself, introducing this notion in the context of quantum information. We provide the working principle of the double homodyne detection, along with its experimental implementation. We detail the simulation of the certification of quantum non-Gaussianity for states as realistic as possible, close to the ones generated by our experiment. Lastly, we present our preliminary results and the progress we've achieved for implementing the certification experimentally.

Chapter 1

Gaussian and non-Gaussian quantum light

Contents

In this first chapter, we first introduce some fundamental concepts and tools of multimode quantum optics. We then focus on the multimode Gaussian and non-Gaussian quantum states of light along with their representations. In particular, we describe two quantities of interest for quantum information, namely the Wigner negativity and the stellar rank, and show how one can witness such quantum non-Gaussianity features. Presenting some results of our paper [Chabaud 21d], we establish the theoretical framework for the main goal of this work, that is, the certification of quantum non-Gaussianity.

This chapter does not contain a complete and thorough introduction to multimode quantum optics. The reader is advised to consult the books [Grynberg 10, Vogel 06, Leonhardt 95] for a full understanding of quantum optics basic concepts and beyond. Also, we recommend [Fabre 20] for a helpful and complete review of "*Modes and states in quantum optics*".

1.1 Multimode quantum light

This section gives a quantum description of the physical system this thesis is focused on — namely light. We present a functional description allowing one to grasp the multi-dimensional and quantized nature of light and what are the physical measurable quantities of interest.

1.1.1 Modal Hilbert space

Let us first consider how light is classically modeled. Light is an electromagnetic radiation that is usually described through the classical electric field $\mathbf{E}(\mathbf{r},t)$, which is a real vector field function of both space $\mathbf{r}$ and time t, where we use bold characters for vector fields as for the rest of the manuscript. More practically, we will use the analytical field $\mathbf{E}^{(+)}(\mathbf{r},t)$, a complex vector field which satisfies $\mathbf{E}(\mathbf{r},t)$ equals $\mathbf{E}^{(+)}(\mathbf{r},t)+(\mathbf{E}^{(+)}(\mathbf{r},t))^*$[1]. To take into account the high dimensionality of light, stemming from its multiple independent degrees of freedom, one can use the concept of *modes* of the electromagnetic field, $\mathbf{f}(\mathbf{r},t)$. Any such mode $\mathbf{f}(\mathbf{r},t)$ is defined as a normalized solution of Maxwell's equations in the vacuum, such that

$$\nabla^2\mathbf{f}(\mathbf{r},t)-\frac{1}{c^2}\frac{\partial^2\mathbf{f}(\mathbf{r},t)}{\partial t^2}=0, \tag{1.1}$$

and, at any time t,

$$\frac{1}{V}\int_V \mathrm{d}^3\mathbf{r}\,|\mathbf{f}(\mathbf{r},t)|^2=1 \tag{1.2}$$

where V is the large volume that contains all the physical system under consideration.

The set of all the vector fields $\{\mathbf{f}(\mathbf{r},t)\}$ that satisfy equation (1.1) forms a Hilbert space that one can call the *modal space* [Fabre 20]. We will adopt the arrow notation $\vec{\mathbf{f}}$ for the modal

[1] More precisely, it is defined as the positive frequency part of the electric field $\widetilde{\mathbf{E}^{(+)}}(\mathbf{r},\omega)=\int_0^\infty \widetilde{\mathbf{E}}(\mathbf{r},\omega)\,\mathrm{d}\omega$, where $\widetilde{\mathbf{E}}(\mathbf{r},\omega)$ (resp. $\widetilde{\mathbf{E}^{(+)}}(\mathbf{r},\omega)$) is the temporal Fourier transform of $\mathbf{E}(\mathbf{r},t)$ (resp $\mathbf{E}^{(+)}(\mathbf{r},t)$). $\mathbf{E}^{(+)}(\mathbf{r},t)$ may also be referred to as complex representation.

vectors in the modal space. The inner product $\left(.\middle|.\right)$ of any modal vectors $\vec{\mathbf{g}}$ and $\vec{\mathbf{h}}$ is defined as the spatial overlap of their corresponding vector fields $\mathbf{g}(\mathbf{r},t)$ and $\mathbf{h}(\mathbf{r},t)$, at any time t

$$\left(\vec{\mathbf{g}}\middle|\vec{\mathbf{h}}\right) = \frac{1}{V}\int_V \mathrm{d}^3\mathbf{r}\, \mathbf{g}(\mathbf{r},t)^*\, \mathbf{h}(\mathbf{r},t) \tag{1.3}$$

Let $\left\{\vec{\mathbf{f}}_m\right\}$ be an *orthonormal mode basis*. We can label it by an integer m, since the modal space has infinite but countable dimension. In practice, we restrict to a finite number N of modes $\left\{\vec{\mathbf{f}}_1, \vec{\mathbf{f}}_2, \cdots, \vec{\mathbf{f}}_N\right\}$, where N can be set arbitrarily large to fulfill one's application needs. Any mode $\vec{\mathbf{f}}_m$ satisfies equation (1.1) and the orthonormal property, at any time t

$$\left(\vec{\mathbf{f}}_m\middle|\vec{\mathbf{f}}_{m'}\right) = \frac{1}{V}\int_V \mathrm{d}^3\mathbf{r}\, \mathbf{f}_m(\mathbf{r},t)^*\, \mathbf{f}_{m'}(\mathbf{r},t) = \delta_{mm'} \tag{1.4}$$

with $\delta_{mm'}$ the Kronecker symbol. Now, one can decompose any modal vector $\vec{\mathbf{g}}$ as a column vector of complex amplitudes $(\mathcal{G}_1, \mathcal{G}_2, \ldots, \mathcal{G}_N)^\top \in \mathbb{C}^N$ over the mode basis $\left\{\vec{\mathbf{f}}_m\right\}$, where $\top$ stands for the transposition in the modal space. Decomposing two modal vectors $\vec{\mathbf{g}}$ and $\vec{\mathbf{h}}$ this way, one can then re-write their inner product defined in equation (1.3) as

$$\left(\vec{\mathbf{g}}\middle|\vec{\mathbf{h}}\right) = \sum_{m=1}^{N} \mathcal{G}_m^* \mathcal{H}_m \tag{1.5}$$

$$\text{with} \quad \vec{\mathbf{g}} = \sum_{m=1}^{N} \mathcal{G}_m \vec{\mathbf{f}}_m \quad \text{and} \quad \vec{\mathbf{h}} = \sum_{m=1}^{N} \mathcal{H}_m \vec{\mathbf{f}}_m \tag{1.6}$$

One can change from one orthonormal basis $\left\{\vec{\mathbf{f}}_m\right\}$ to another $\left\{\vec{\mathbf{g}}_n\right\}$ through a unitary matrix $\mathbf{U}$ that satisfies $\mathbf{U}^{\top *}\mathbf{U} = \mathbb{1}_N$, such that for all n

$$\mathbf{g}_n(\mathbf{r},t) = \sum_m \mathbf{U}_{nm}\, \mathbf{f}_m(\mathbf{r},t), \quad \vec{\mathbf{g}}_n = \sum_m \mathbf{U}_{nm}\, \vec{\mathbf{f}}_m \tag{1.7}$$

where we set aside the equivalent equations for the vector fields on the left and the modal vectors on the right. In particular equation (1.7) means that the choice of a mode basis boils down to the choice of a unitary matrix $\mathbf{U}$.

We now have all the mathematical tools to describe in more details the electric field $\mathbf{E}^{(+)}(\mathbf{r},t)$. It is itself a non-normalized electromagnetic mode, such that it verifies Maxwell's equations (1.1) and can be decomposed on any mode basis similarly as equation (1.6). We choose the convenient and most common basis of plane wave modes $\{\mathbf{u}_\ell(\mathbf{r},t)\}$

$$\mathbf{E}^{(+)}(\mathbf{r},t) = \sum_\ell \mathcal{A}_\ell\, \mathbf{u}_\ell(\mathbf{r},t), \quad \vec{\mathbf{E}}^{(+)} = \sum_\ell \mathcal{A}_\ell\, \vec{\mathbf{u}}_\ell \tag{1.8}$$

$$\text{with} \quad \mathbf{u}_\ell(\mathbf{r},t) = \boldsymbol{\epsilon}_\ell e^{\mathrm{i}(\mathbf{k}_\ell\cdot\mathbf{r}-\omega_\ell t)}$$

with $\mathcal{A}_\ell, \boldsymbol{\epsilon}_\ell, \mathbf{k}_\ell, \omega_\ell$ respectively the complex amplitude, the polarization vector, wave vector and frequency of the mode $\vec{\mathbf{u}}_\ell$. Note that the plane waves $\vec{\mathbf{u}}_\ell$ form an orthonormal basis and as such satisfy equations (1.1) and (1.4).

1.1.2 Quantum electric field

Let us now introduce the quantum electric field operator in the Heisenberg picture[1] $\hat{\mathbf{E}}^{(+)}(\mathbf{r},t)$ as the quantum extension of the classical electric field $\mathbf{E}^{(+)}(\mathbf{r},t)$, defined in equation (1.8). One can expand it on the plane wave mode basis as follows [Grynberg 10]

$$\hat{\mathbf{E}}^{(+)}(\mathbf{r},t) = \sum_\ell \mathcal{E}_\ell \hat{a}_\ell \mathbf{u}_\ell(\mathbf{r},t), \quad \vec{\hat{\mathbf{E}}}^{(+)} = \sum_\ell \mathcal{E}_\ell \hat{a}_\ell \vec{\mathbf{u}}_\ell \tag{1.9}$$

$$\text{with} \quad \mathbf{u}_\ell(\mathbf{r},t) = \boldsymbol{\epsilon}_\ell e^{i(\mathbf{k}_\ell\cdot\mathbf{r}-\omega_\ell t)} \quad \text{with} \quad \mathcal{E}_\ell = \sqrt{\frac{\hbar\omega_\ell}{2\varepsilon_0 V}}$$

$\vec{\hat{\mathbf{E}}}^{(+)}$ is the (analytical) quantum electric modal vector, $\hat{a}_\ell$ the quantum operator of annihilation of a photon in the plane wave mode $\vec{\mathbf{u}}_\ell$, and the annihilation operators $\{\hat{a}_\ell\}$ satisfy the following commutation rules

$$\left[\hat{a}_\ell, \hat{a}_{\ell'}^\dagger\right] = \delta_{\ell\ell'} \tag{1.10}$$

$$[\hat{a}_\ell, \hat{a}_{\ell'}] = 0 \tag{1.11}$$

The idea behind equation (1.9) is the discretization of the electromagnetic energy, which means that the energy in a given mode is not continuous, but an integer number of extremely low amounts of energy, the energy of a photon. It consists in considering each plane wave mode of frequency ω_ℓ as a quantum harmonic oscillator. Then, its Hamiltonian operator $\mathbf{H}_\ell$ is given by $\hbar\omega_\ell\left(\hat{a}_\ell^\dagger\hat{a}_\ell + \text{h.c.}\right)$, where h.c. stands for hermitian conjugate, and $\hat{a}_\ell^\dagger\hat{a}_\ell$ counts the number of photons in the mode $\vec{\mathbf{u}}_\ell$.

The amplitude coefficients $\mathcal{E}_\ell$ of the quantum electric field defined in equation (1.9) are frequency dependent in general. The fields we consider in the scope of this thesis satisfy the conditions of the *narrow-band approximation*, for which the electric field is not vacuum only for plane waves oscillating at nearby frequencies $\omega \simeq \omega_0$, or equivalently $\omega_0 \gg \Delta\omega$. Under such approximation, the amplitude coefficients $\mathcal{E}_\ell$ write

$$\mathcal{E}_\ell = \mathcal{E}_0 \quad \text{with} \quad \mathcal{E}_0 = \sqrt{\frac{\hbar\omega_0}{2\varepsilon_0 V}} \tag{1.12}$$

and the quantum electric field writes in the plane wave basis

$$\hat{\mathbf{E}}^{(+)}(\mathbf{r},t) = \mathcal{E}_0 \sum_\ell \hat{a}_\ell \mathbf{u}_\ell(\mathbf{r},t), \quad \vec{\hat{\mathbf{E}}}^{(+)} = \mathcal{E}_0 \sum_\ell \hat{a}_\ell \vec{\mathbf{u}}_\ell \tag{1.13}$$

The annihilation operators $\{\hat{a}_\ell\}$ are tightly linked to the modes $\{\vec{\mathbf{u}}_\ell\}$, and contain by themselves both the world of quantum states through the Hilbert space of quantum states and the world of electromagnetic modes through the modal Hilbert space. We steer the attention of the reader on [Fabre 20] for deep understanding of this dual structure of light. In the following we show this duality under a mode basis change.

[1] Meaning that the operators are time dependent, not the quantum states. Instead of applying the action of a given operator $\hat{A}$ on any state $|\psi\rangle$ as $|\psi\rangle \mapsto \hat{A}|\psi\rangle$, we equivalently apply its action on any operator $\hat{B}$ as $\hat{B} \mapsto \hat{A}^\dagger\hat{B}\hat{A}$.

Let us consider the change of mode basis from $\{\vec{\mathbf{u}}_\ell\}$ to a new orthonormal basis $\left\{\vec{\mathbf{g}}_n\right\}$ with a unitary matrix $\mathbf{U}$ similarly as in equation (1.7). Let $\left\{\hat{b}_n\right\}$ be annihilation operators associated with the modes $\left\{\vec{\mathbf{g}}_n\right\}$, hence the action of $\hat{b}_n$ is defined as the removal of a photon in the mode $\vec{\mathbf{g}}_n$. Their action in the plane-wave basis $\{\vec{\mathbf{u}}_\ell\}$ is given through the action of $\mathbf{U}$ as

$$\hat{b}_n^\dagger \mapsto \sum_\ell \mathbf{U}_{n\ell}\,\hat{a}_\ell^\dagger, \quad \vec{\hat{b}}^\dagger \mapsto \mathbf{U}\,\vec{\hat{a}}^\dagger \tag{1.14}$$

$$\hat{b}_n \mapsto \sum_\ell (\mathbf{U}_{n\ell})^*\,\hat{a}_\ell, \quad \vec{\hat{b}} \mapsto \mathbf{U}^*\,\vec{\hat{a}} \tag{1.15}$$

where we introduced for practical reasons $\vec{\hat{a}}$ and $\vec{\hat{b}}$ as column vectors of the operators $(\hat{a}_1, \hat{a}_2, \dots, \hat{a}_N)^\top$ and $\left(\hat{b}_1, \hat{b}_2, \dots, \hat{b}_N\right)^\top$. In other words, we can write $\hat{U}^\dagger \vec{\hat{b}}^\dagger \hat{U} = \mathbf{U}\,\vec{\hat{a}}^\dagger$ and $\hat{U}^\dagger \vec{\hat{b}}\,\hat{U} = \mathbf{U}^*\,\vec{\hat{a}}$, consistently with the Heisenberg picture, see appendix B.1 for details[1]. Equations (1.14) and (1.15) are consistent with equation (1.7) under the narrow-band approximation, see also appendix B.1.

In the new basis $\left\{\vec{\mathbf{g}}_n\right\}$, the quantum electric field operator writes

$$\hat{\mathbf{E}}^{(+)}(\mathbf{r},t) = \mathcal{E}_0 \sum_n \hat{b}_n \mathbf{g}_n(\mathbf{r},t), \quad \vec{\hat{\mathbf{E}}}^{(+)} = \mathcal{E}_0 \sum_n \hat{b}_n \vec{\mathbf{g}}_n \tag{1.16}$$
$$\text{with} \quad \vec{\mathbf{g}}_n = \sum_n \mathbf{U}_{n\ell}\vec{\mathbf{u}}_\ell$$

1.1.3 Electric field quadrature operators

The annihilation operators $\{\hat{a}_\ell\}$ in equation (1.9) are not Hermitian[2], which means they are not physically measurable operators, called *observables*. They are useful to build a mathematical functional framework as briefly depicted in the previous section, but from an experimental point of view, the operators of interest beyond the Hamiltonian are the electric field *quadrature operators*. We can define the Hermitian quadrature operators $\hat{q}_\ell$ and $\hat{p}_\ell$ in each mode $\vec{\mathbf{u}}_\ell$ as

$$\hat{q}_\ell = \sigma_0\left(\hat{a}_\ell^\dagger + \hat{a}_\ell\right) \quad \text{and} \quad \hat{p}_\ell = \mathrm{i}\sigma_0\left(\hat{a}_\ell^\dagger - \hat{a}_\ell\right) \tag{1.17}$$
$$\text{with} \quad \left[\hat{q}_\ell, \hat{p}_{\ell'}\right] = 2\mathrm{i}\sigma_0^2\delta_{\ell\ell'}$$

where σ_0 is the *standard deviation of the quantum fluctuations of the vacuum*, such that $\sigma_0^2 = \langle 0|\hat{q}_\ell^2|0\rangle = \langle 0|\hat{p}_\ell^2|0\rangle$, with $|0\rangle$ the vacuum quantum state. We choose the letter σ, as a reference to the usual symbol used in statistics for standard deviation to avoid confusion with the variance. Many conventions are used in the quantum optics community regarding the value of the vacuum standard deviation σ_0, and none makes unanimity[3]. This unfortunately leads to

[1] Usually, in most of the literature using mode basis changes, equations (1.14) and (1.15) are written as $\vec{\hat{b}}^\dagger = \mathbf{U}\,\vec{\hat{a}}^\dagger$ and $\vec{\hat{b}} = \mathbf{U}^*\,\vec{\hat{a}}$, considering the action of $\hat{U}$ implicit in the notation of the operators $\{\hat{b}_n\}$. In this manuscript, we use another formalism detailed in appendix B.1. Both approaches are equivalent, whereas they use different notations.

[2] meaning $\hat{a}_\ell$ is not equal to its Hermitian conjugate $\hat{a}_\ell^\dagger$.

[3] Often found conventions are $\sigma_0^2 = 1$, $\sigma_0^2 = 1/2$, $\sigma_0^2 = 1/4$ or even $\sigma_0^2 = \hbar/2$ with $\hbar$ the Planck constant divided by 2π.

confusions. In this manuscript, we try to explicitly keep σ_0. If not, the reader should assume that for the sake of simplicity, everything is defined with $\sigma_0 = 1$.

Note that the choice of the phase of reference may be viewed as the choice of the angle of a rotation applied on the quadrature operators. We then conveniently define the *quadrature operator at angle* θ for each mode $\vec{\mathbf{u}}_\ell$ as

$$\hat{q}_\ell^\theta = \cos(\theta)\hat{q}_\ell + \sin(\theta)\hat{p}_\ell \tag{1.18}$$

verifying similarly

$$\left[\hat{q}_\ell^\theta, \hat{q}_{\ell'}^{\theta+\pi/2}\right] = 2\mathrm{i}\sigma_0^2\delta_{\ell\ell'} \tag{1.19}$$

The quadrature operators are the operators that we can access and measure experimentally. To clearly see to what physical entity these operators refer to, let us use them to re-write the electric field real-valued operator $\hat{\mathbf{E}}(\mathbf{r}, t)$ (not the analytical one)

$$\begin{aligned}\hat{\mathbf{E}}(\mathbf{r}, t) &= \sum_\ell \mathcal{E}_\ell \boldsymbol{\epsilon}_\ell \left(\hat{a}_\ell \mathrm{e}^{-\mathrm{i}(\omega_\ell t - \mathbf{k}_\ell\cdot\mathbf{r})} + \hat{a}_\ell^\dagger \mathrm{e}^{\mathrm{i}(\omega_\ell t - \mathbf{k}_\ell\cdot\mathbf{r})}\right) \\ &= \sum_\ell \mathcal{E}_\ell \boldsymbol{\epsilon}_\ell \frac{1}{\sigma_0}\left(\hat{q}_\ell \cos(\omega_\ell t - \mathbf{k}_\ell\cdot\mathbf{r}) + \hat{p}_\ell \sin(\omega_\ell t - \mathbf{k}_\ell\cdot\mathbf{r})\right)\end{aligned} \tag{1.20}$$

One can see on equation (1.20) that the quadrature operators $\hat{q}_\ell$ and $\hat{p}_\ell$ are the cosine and sine channels of the field amplitude inthe plane wave mode $\vec{\mathbf{u}}_\ell$. They are accessed experimentally using the homodyne detection for example, see section 2.4 for more details.

1.2 Quantum state representations

In the previous section, we briefly introduced a multimode quantum description of light. We focused our attention on deriving the relevant measurable physical operators $\left\{\hat{q}_\ell\right\}$ and $\left\{\hat{p}_\ell\right\}$. In this section, we focus on the Hilbert space of quantum states, and present different state representations that contain each all the information on the state, which makes them in this sense equivalent.

1.2.1 Quantum state Hilbert space

The set of all *pure* quantum states forms the unit sphere[1] of a complex Hilbert space $\mathscr{H}$, that we will call the *state space*. To take into account the multimode nature of the system, the Hilbert space $\mathscr{H}$ is decomposed, for a given mode basis $\left\{\vec{\mathbf{f}}_m\right\}$, as a tensor product of underlying Hilbert spaces $\mathscr{H}_m$, each associated with the mode $\vec{\mathbf{f}}_m$

$$\mathscr{H} = \mathscr{H}_1 \otimes \mathscr{H}_2 \otimes \cdots \otimes \mathscr{H}_N \tag{1.21}$$

From the annihilation operator $\hat{a}_m$, we can define the Hermitian *number operator* $\hat{n}_m = \hat{a}_m^\dagger \hat{a}_m$ and its eigenstates $\{|n_m\rangle\}_{n_m\in\mathbb{N}}$. The state $|n_m\rangle$, called a *Fock state*, is a pure quantum state with

[1] as they are normalized to 1.

a fixed number of photons n_m in mode $\vec{\mathbf{f}}_m$ and the vacuum state in the other modes. The full set $\{|n_1\rangle \otimes |n_2\rangle \otimes \cdots \otimes |n_N\rangle\}$ forms an orthonormal basis of the Hilbert space $\mathscr{H}$ such that any pure multimode quantum state $|\psi\rangle$ can be written in the mode basis $\left\{\vec{\mathbf{f}}_m\right\}$, along with its normalization

$$|\psi\rangle = \sum_{n_1}\sum_{n_2}\cdots\sum_{n_N} C_{n_1,n_2,\cdots,n_N}\,|n_1\rangle \otimes |n_2\rangle \otimes \cdots \otimes |n_N\rangle \tag{1.22}$$
$$\text{with} \quad \sum_{n_1}\sum_{n_2}\cdots\sum_{n_N} \left|C_{n_1,n_2,\cdots,n_N}\right|^2 = 1$$

The Fock states are further studied in subsection 1.4.1, as they display interesting features for quantum information.

1.2.2 Density operator

A non-pure state can not be represented by a ket, contrary to pure states (e.g. the state $|\psi\rangle$ in equation (1.22)). Consider the situation where pure quantum states $|\psi_1\rangle, |\psi_2\rangle, \ldots$ are prepared with respective probabilities $p_1, p_2, \ldots$ To obtain a meaningful representation of the quantum state of this statistical ensemble, one can examine the outcomes of a measurement performed on this ensemble using a detection apparatus. We briefly describe here the detection as a projective measurement with outcome m by the application of a projector $\hat{\Pi}_m$ on the ensemble, such that the probability of obtaining measurement result m is given by [Nielsen 00]

$$\sum_j p_j \langle\psi_j|\hat{\Pi}_m|\psi_j\rangle = \mathrm{Tr}\left[\hat{\Pi}_m\left(\sum_j p_j |\psi_j\rangle\langle\psi_j|\right)\right],$$

which naturally leads us to define the *density operator*, first introduced by [VonNeumann 32], as

$$\hat{\rho} = \sum_j p_j |\psi_j\rangle\langle\psi_j| \quad \text{with} \quad \mathrm{Tr}(\hat{\rho}) = 1 \tag{1.23}$$

The density operator $\hat{\rho}$ is a positive semi-definite Hermitian operator. Its matrix representation in a given basis of the state space is referred to as the *density matrix*, a term often used interchangeably with density operator. Moreover, for any Hermitian operator $\hat{A}$, its expectation value on state $\hat{\rho}$ is given by

$$\langle\hat{A}\rangle = \sum_j p_j \langle\psi_j|\hat{A}|\psi_j\rangle = \sum_j\sum_i p_j c_i \left|\langle\phi_i|\psi_j\rangle\right|^2 = \mathrm{Tr}\left(\hat{\rho}\hat{A}\right) \tag{1.24}$$

with c_i and $|\phi_i\rangle$ the eigenvalues and eigenstates of $\hat{A}$.

Equation (1.24) shows that the density operator representation contains all the information on the quantum system, since any measurement of the system can be written in the form of the expectation value.

Finally, a key quantity associated with the density operator is the *purity* μ of a given quantum state $\hat{\rho}$, defined as

$$\mu = \mathrm{Tr}\left(\hat{\rho}^2\right) \tag{1.25}$$

The purity represents the degree of non-mixedness of a quantum state. For a pure state, the purity equals its maximal value of one. Conversely, a highly mixed state has a near-zero purity. Moreover, the concept of purity is closely related to losses in a quantum system. For example, the probabilistic loss of a photon applied on a quantum state results in the statistical sum of the state without and with the removal of a photon, in particular a mixed state.

Another key concept here is that mixed states can always be viewed as the partial trace of a pure state on a larger system, stemming from the very nature of quantum entanglement [Bassi 03]. Consider a pure entangled state on a bipartite quantum system $\mathscr{H}_1 \otimes \mathscr{H}_2$, with subsystem $\mathscr{H}_2$ being inaccessible to observation. The measured state is obtained by tracing over $\mathscr{H}_2$. As the state is entangled, part of the information regarding this state is only accessible through $\mathscr{H}_2$. This lack of information results in the state measured being mixed.

1.2.3 Wigner function

While the introduction of the density operator is necessary for describing mixed states, it is not always the most suitable representation depending on the application.

In quantum optics, the community of *Discrete Variables* (DV) usually characterizes quantum state of light using photon-counting detection schemes. For this kind of measurement, the density matrix expressed in the basis of Fock states is particularly appropriate, since truncating the Fock state basis to some suitable maximum integer leaves the matrix representation finite, yielding an easily handled representation of the full state.

On the other hand, the quantum optics community of *Continuous Variables* (CV) usually characterizes quantum states of light using electric field quadrature detection schemes, as for instance homodyne detection (detailed in section 2.4). The name "continuous variables" stems from the fact that each measurement yields real numbers from the quadrature operators. The density matrix may be infinite dimensional, making it not practical.

For a more suitable representation, one naturally consider the *phase space*, which is the space built upon the coordinates of real numbers $\{q\}$ and $\{p\}$ (we consider for now only a single mode space for simplicity). The probability of measuring q (resp. p) is given by $\mathrm{Tr}(\hat{\rho}\,|q\rangle\langle q|)$ (resp. $\mathrm{Tr}(\hat{\rho}\,|p\rangle\langle p|)$) or equivalently $\langle q|\hat{\rho}|q\rangle$ (resp. $\langle p|\hat{\rho}|p\rangle$), where the eigenstates $\{|q\rangle\}$ of $\hat{q}$ form an orthonormal and complete basis

$$\hat{q}\,|q\rangle = q\,|q\rangle \qquad (\textit{definition}) \tag{1.26}$$

$$\langle q|q'\rangle = \delta(q-q') \qquad (\textit{orthogonality}) \tag{1.27}$$

$$\int |q\rangle\langle q|\,\mathrm{d}q = \hat{\mathbb{1}} \qquad (\textit{completeness}) \tag{1.28}$$

with similar equations for $\{|p\rangle\}$. These equations can be naturally generalized to the quadrature operator $\hat{q}^\theta$ at angle θ (defined in equation (1.18)), together with its eigenstates $|q^\theta\rangle$.

The *Wigner function* $W_{\hat{\rho}}(q,p)$ of the state $\hat{\rho}$, first introduced by [Wigner 32], is a real-valued function of the phase space defined as

$$W_{\hat{\rho}}(q,p) = \frac{1}{2\pi\sigma_0^2}\int_{\mathbb{R}} \langle q-y|\hat{\rho}|q+y\rangle\, \mathrm{e}^{\mathrm{i}py/\sigma_0^2}\,\mathrm{d}y \tag{1.29}$$

While the marginals of the Wigner function are the probability distribution of the quadrature operators

$$\langle q|\hat{\rho}|q\rangle = \int_{\mathbb{R}} W_{\hat{\rho}}(q,p)\,\mathrm{d}p \tag{1.30}$$

$$\langle p|\hat{\rho}|p\rangle = \int_{\mathbb{R}} W_{\hat{\rho}}(q,p)\,\mathrm{d}q \tag{1.31}$$

and it integrates to one $\int_{R^2} W_{\hat{\rho}}(q,p)\,\mathrm{d}q\,\mathrm{d}p = \mathrm{Tr}(\hat{\rho}) = 1$, it is not the joint-probability of the probabilities $\langle q|\hat{\rho}|q\rangle$ and $\langle p|\hat{\rho}|p\rangle$. Actually, it is not a probability at all, but instead a *quasiprobability*, as it can exhibit negative values for some quantum states. This feature, known as *Wigner negativity*, is one of the key concepts for quantum information, as explained in more details in section 1.4. This feature stems from the fact that the quadrature operators $\hat{q}, \hat{p}$ do not commute and cannot be measured simultaneously.

More generally, the Wigner function can also be used to represent any operator $\hat{A}$ as

$$W_{\hat{A}}(q,p) = \frac{1}{2\pi\sigma_0^2}\int_{\mathbb{R}} \langle q-y|\hat{A}|q+y\rangle\, \mathrm{e}^{\mathrm{i}py/\sigma_0^2}\,\mathrm{d}y \tag{1.32}$$

If the operator $\hat{A}$ is Hermitian, as the density matrix, then the Wigner function is real-valued. For two Hermitian operators $\hat{A}$, $\hat{B}$ one can write their overlap as [Leonhardt 95, Wolfgang 01, Morin 13a]

$$\mathrm{Tr}\left(\hat{A}\hat{B}\right) = 4\pi\sigma_0^2\int_{\mathbb{R}^2} W_{\hat{A}}(q,p)W_{\hat{B}}(q,p)\,\mathrm{d}q\,\mathrm{d}p \tag{1.33}$$

from which we can deduce the expectation value of an Hermitian operator $\hat{A}$

$$\mathrm{Tr}\left(\hat{\rho}\hat{A}\right) = 4\pi\sigma_0^2\int_{\mathbb{R}^2} W_{\hat{\rho}}(q,p)W_{\hat{A}}(q,p)\,\mathrm{d}q\,\mathrm{d}p \tag{1.34}$$

From this property (1.34), we then deduce that the Wigner function $W_{\hat{\rho}}(q,p)$ contains all information on the state $\hat{\rho}$, similarly as its density matrix. The Wigner function is very convenient as it allows for a real-valued complete state representation on the phase space, which can be practically represented in 3D plots for single-mode states.

We can also deduce the purity μ (defined as $\mathrm{Tr}(\hat{\rho}^2)$ from equation (1.25)) as

$$\mu = 4\pi\sigma_0^2\int_{\mathbb{R}^2} W_{\hat{\rho}}^2(q,p)\,\mathrm{d}q\,\mathrm{d}p \tag{1.35}$$

Equation (1.29) is not the only formula that gives the Wigner function of a state $\hat{\rho}$. For instance, one can express the Wigner function in terms of the *parity operator* $\hat{\Pi}_{\mathrm{P}} = (-1)^{\hat{a}^\dagger\hat{a}}$ [Royer 77]

$$W_{\hat{\rho}}(\alpha) = \frac{2}{\pi}\,\mathrm{Tr}\left[\hat{D}(\alpha)\hat{\Pi}_{\mathrm{P}}\hat{D}^\dagger(\alpha)\hat{\rho}\right], \tag{1.36}$$

where $\hat{D}(\alpha) = \mathrm{e}^{\alpha\hat{a}^\dagger - \alpha^*\hat{a}}$ is the displacement operator, and $\alpha = \frac{1}{2\sigma_0^2}(q+\mathrm{i}p)$ is an equivalent complex representation of the phase space point (q,p). Using the variable α instead of the

variables (q, p) is common in the literature[1]. Except for the convention $\sigma_0^2 = 1/4$, this adds a global factor which may bring confusion. This factor can be obtained by ensuring their normalization $\int_{\mathbb{R}^2} W_{\hat{\rho}}(q,p)\,\mathrm{d}q\,\mathrm{d}p = \int_{\mathbb{R}^2} W_{\hat{\rho}}(\alpha)\,\mathrm{d}^2\alpha = 1$, with $\mathrm{d}^2\alpha = \mathrm{d}\,\mathrm{Re}(\alpha)\,\mathrm{d}\,\mathrm{Im}(a)$ and $\alpha = \frac{1}{2\sigma_0^2}(q + \mathrm{i}p)$, so that

$$W_{\hat{\rho}}(\alpha) = 4\sigma_0^2 W_{\hat{\rho}}(q,p). \tag{1.37}$$

Depending on the application, one notation or the other may drastically simplify the equations, leading to a much better readability, which is probably why both are used in the literature. Also, from equation (1.37) and equation (1.29), one can see that the notation $W_{\hat{\rho}}(\alpha)$ has the advantage of being independent of the convention σ_0.

Let us consider the multimode case. The phase space sees its dimension increased by N, the number of modes, such that it is now isomorphic to $\mathbb{R}^{2N}$. One can represent a point in the phase space by $(\vec{q}^{\top}, \vec{p}^{\top})^{\top} = (q_1, \cdots, q_N, p_1, \cdots, p_N)^{\top} \in \mathbb{R}^{2N}$ corresponding to the eigenvalues of operators $\hat{\vec{q}} = (\hat{q}_1, \cdots, \hat{q}_N)^{\top}$ and $\hat{\vec{p}} = (\hat{p}_1, \cdots, \hat{p}_N)^{\top}$, in the mode basis $\{\vec{\mathbf{u}}_\ell\}$, which is essentially a convenient way to pack together the $2N$ variables in the fromulas, along with the $\vec{\cdot}$ notation to be consistent with the modal notation of section 1.1. One can now re-write the equation (1.29) as

$$W_{\hat{\rho}}(\vec{q}, \vec{p}) = \frac{1}{(2\pi\sigma_0^2)^N} \int_{\mathbb{R}^N} \left\langle \vec{q} - \vec{y} \middle| \hat{\rho} \middle| \vec{q} + \vec{y} \right\rangle \mathrm{e}^{\mathrm{i}\vec{p}\cdot\vec{y}/\sigma_0^2}\,\mathrm{d}^N\vec{y} \tag{1.38}$$

with $|\vec{q}\rangle = |q_1\rangle \otimes \cdots \otimes |q_N\rangle$ the multimode eigenstate of $\hat{\vec{q}}$ with eigenvalues $(q_1, \cdots, q_N) \in \mathbb{R}^N$.

We will often use also the following equivalent and convenient notation of a point in the phase space: $\vec{x} = (q_1, \cdots, q_N, p_1, \cdots, p_N)^{\top} \in \mathbb{R}^{2N}$. Note the subtle different notations between $\vec{\cdot}$ for $\mathbb{R}^N$ and $\vec{\cdot}$ for $\mathbb{R}^{2N}$ vectors. We obtain for instance the generalization of equation (1.33)

$$\mathrm{Tr}\left(\hat{A}\hat{B}\right) = (4\pi\sigma_0^2)^N \int_{\mathbb{R}^{2N}} W_{\hat{A}}(\vec{x}) W_{\hat{B}}(\vec{x})\,\mathrm{d}^{2N}\vec{x} \tag{1.39}$$

with $\mathrm{d}^{2N}\vec{x} = \mathrm{d}q_1 \cdots \mathrm{d}q_N\,\mathrm{d}p_1 \cdots \mathrm{d}p_N$.

Beyond the Wigner function, there exists a continuous family of s-parametrized quasiprobability densities $W_{\hat{\rho}}^u(\vec{x})$ for $-1 \leqslant u \leqslant 1$ [Cahill 69a], that each equivalently provides a complete representation of a quantum state in the phase space. For more details, see textbooks, e.g. [Leonhardt 95, Vogel 06]. The most commonly used quasiprobabilities are the Wigner function with $u = 0$, the *Husimi function*, also referred to as the Q *function*, with $u = -1$, and the *Glauber-Sudarshan representation*, or the P *function*, with $u = 1$.

These quasiprobability densities are all interrelated through convolution by Gaussian functions of the phase space. We can relate $W_{\hat{\rho}}^u(\vec{x})$ to $W_{\hat{\rho}}^{u'}(\vec{x})$, for $u < u'$ by [Leonhardt 95]

$$W_{\hat{\rho}}^u(\vec{x}) = \left(\frac{1}{2\pi\sigma_0^2(u'-u)}\right)^N \int_{\mathbb{R}^{2N}} W_{\hat{\rho}}^{u'}(\vec{x}')\,\mathrm{e}^{-\frac{1}{2\sigma_0^2(u'-u)}\left\|\vec{x}'-\vec{x}\right\|^2}\,\mathrm{d}^{2N}\vec{x}' \tag{1.40}$$

[1]The notation $W_{\hat{\rho}}(\alpha, \alpha^*)$ may also be found. In either case, they represent the Wigner function as a function of the real parameters $(\mathrm{Re}(\alpha), \mathrm{Im}(\alpha))$.

Note that this equation is not valid for $u > u'$. While we can use equation (1.40) to directly deduce the Q function from the Wigner function for instance, the reverse is not true.

The Gaussian convolution in equation (1.40) may be interpreted as a smoothing operation on the quasiprobability $W^{u'}_{\hat{\rho}}(\vec{x})$, resulting in a "smoothed" version $W^{u}_{\hat{\rho}}(\vec{x})$, with $u < u'$. One could say that the lowest u is, the smoother the representation is, such that globally the Q function is a much "smoother" version of the Wigner function, while the P function is a much "sharper" one. These qualitative assessments show through their properties, see sections 1.2.4 and 1.2.5.

We point out that the correspondence between quadrature phase space (q, p) and complex one $(\mathrm{Re}(\alpha), \mathrm{Im}(\alpha))$ in equation (1.37) is seamlessly generalized to the multimode case, for any quasiprobability $W^u(\vec{x})$ as

$$W^u(\vec{\alpha}) = \left(4\sigma_0^2\right)^N W^u(\vec{x}) \tag{1.41}$$

with $\vec{x} = (q_1, \cdots, q_N, p_1, \cdots, p_N)^\top \in \mathbb{R}^{2N}$ and $\vec{\alpha} = (\alpha_1, \cdots, \alpha_N)^\top \in \mathbb{C}^N$.

As a side note for the sake of completeness, the quasiprobabilities may be defined from *characteristic functions*, and may be related to the ordering of annihilation and creation operators, though we choose not to follow these approaches, details can be found in [Cahill 69a, Leonhardt 95, Adesso 14].

1.2.4 Glauber-Sudarshan representation or P function

The Glauber-Sudarshan representation is a quasiprobability first introduced by [Glauber 63, Sudarshan 63]. It can be defined as the coefficients of the decomposition of the density operator over the overcomplete basis of coherent states $\{|\alpha\rangle\}_{\alpha\in\mathbb{C}}$

$$\hat{\rho} = \int_{\mathbb{R}^2} \mathrm{P}_{\hat{\rho}}(\alpha)\, |\alpha\rangle\langle\alpha|\, \mathrm{d}^2\alpha \tag{1.42}$$

where we restrict ourselves to a single mode of light for now, and $\mathrm{d}^2\alpha$ is defined as $\mathrm{d}\,\mathrm{Re}(\alpha)\,\mathrm{d}\,\mathrm{Im}(\alpha)$. See subsection 1.3.2 for details on coherent states. Similarly to the Wigner function, the P function integrates to unity $\int_{\mathbb{R}^2} \mathrm{P}_{\hat{\rho}}(\alpha)\,\mathrm{d}^2\alpha = 1$, and is real as $\hat{\rho}$ is Hermitian. Furthermore, corresponding to the parameter $u = 1$, the P function is "less smooth" than the Wigner function. Not only it may display negative values, it may also be mathematically irregular, hence again the term "quasiprobability". To get a better understanding of the P function, it may be expressed with the coefficients of the density operator $\hat{\rho}$ in the Fock basis [Sudarshan 63]

$$\mathrm{P}_{\hat{\rho}}(\alpha) = \sum_n \sum_k \langle n|\hat{\rho}|k\rangle \frac{\sqrt{n!k!}}{2\pi r(n+k)!} \mathrm{e}^{r^2 - \mathrm{i}(n-k)\theta} \left(-\frac{\partial}{\partial r}\right)^{n+k} \delta(r) \tag{1.43}$$

where r and θ are the modulus and phase of the complex number α, and δ is the Dirac delta function. In equation (1.43) appears many derivatives of Dirac delta functions, meaning that in general the P function may be very ill-behaved, and it might not even exist as a tempered distribution. No wonder why there is no known measurement apparatus that measures directly the P function of any states [Leonhardt 95]. In practice, this means that one needs to

take great care when dealing with this representation, and may require to approximate the P function with well defined functions, at the cost of precision.

Although it can be quite impractical, the Glauber-Sudarshan representation has a straight physical interpretation [Mandel 95]. Basically if there exist a classical analog to the system, then its P function is non-negative everywhere, as for instance the P function of a coherent state of complex amplitude α_0 is $\mathrm{P}_{|\alpha_0\rangle\langle\alpha_0|}(\alpha) = \delta(\alpha - \alpha_0)$ by construction (1.42). On the other hand, if there is no classical analog to the system, then its P function is negative somewhere or more singular than a Dirac delta function as illustrated in equation (1.43). For example, one can easily apply equation (1.43) to a Fock state $|1\rangle$ and obtain $\mathrm{P}_{|1\rangle\langle 1|}(\alpha) = \frac{1}{4\pi r} e^{r^2} \frac{\partial^2 \delta(r)}{\partial r^2}$. For these reasons, it may be used for defining non-classicality of a quantum system, see for instance [Usha Devi 13]. In practice, we will use other tools to define and study the quantumness of a system, see section 1.4.

The density operator is not the only operator that can be decomposed on the coherent state basis as in equation (1.42). More generally, any operator $\hat{A}$ may be represented by its Glauber-Sudarshan representation $\mathrm{P}_{\hat{A}}$ as the coefficients of its decomposition on the coherent state basis[1]

$$\hat{A} = \int_{\mathbb{R}^{2N}} \mathrm{P}_{\hat{A}}(\vec{\alpha}) \, |\vec{\alpha}\rangle\langle\vec{\alpha}| \, \mathrm{d}^{2N}\vec{\alpha} \tag{1.44}$$

with $|\vec{\alpha}\rangle = |\alpha_1\rangle \otimes \cdots \otimes |\alpha_N\rangle$ the coherent state on $\mathscr{H}$ of amplitude $\vec{\alpha} = (\alpha_1, \cdots, \alpha_N) \in \mathbb{C}^N$. Note that equation (1.44) is formally always correct, but $\mathrm{P}_{\hat{A}}(\vec{\alpha})$ may not always mathematically "exist", meaning that it has mathematical irregularities or infinities beyond the scope of distributions. As we don't elaborate on these technicalities[2], the interested reader should look at [Cahill 69b, Cahill 69a]. Equation (1.44) is in particular the multimode version of equation (1.42) for $\hat{A} = \hat{\rho}$.

1.2.5 Husimi function or Q function

The *Husimi function*, or Q *function*, was introduced by [Husimi 40]. It is defined in the multimode mode scenario as

$$\mathrm{Q}_{\hat{\rho}}(\vec{\alpha}) = \frac{1}{\pi^N} \langle\vec{\alpha}|\hat{\rho}|\vec{\alpha}\rangle \tag{1.45}$$

which is proportional to the projection of the density operator $\hat{\rho}$ on the multimode coherent state $|\vec{\alpha}\rangle$, with $\vec{\alpha} \in \mathbb{C}^N$. Contrary to the previous quasiprobabilities, the Q function is always positive everywhere on the phase space, stemming from its definition (1.45) and the Hermitianity of the density operator. Also, the Q function integrates to unity:

$$\int_{\mathbb{R}^{2N}} \mathrm{Q}_{\hat{\rho}}(\vec{\alpha}) \, \mathrm{d}^{2N}\vec{\alpha} = 1 \tag{1.46}$$

[1] Note that remarkably, if such decomposition on the coherent state basis exists, it is diagonal. This stems from the overcompleteness of the coherent state basis (see subsection 1.3.2).

[2] A sufficient condition for $\mathrm{P}_{\hat{A}}(\vec{\alpha})$ to converge is that the operator $\hat{A}$ is expressible as a power series in the creation and annihilation operators in the anti-normal order, which is always the case for the density operator $\hat{\rho}$ for instance.

owing to the overcompleteness of the coherent state basis $\int |\vec{\alpha}\rangle\langle\vec{\alpha}| \, \mathrm{d}^{2N}\vec{\alpha} = \pi^N$.

From the above properties, one might be tempted to call the Husimi function an actual probability density rather than a quasiprobability density. However, it is not, as the Husimi function does not satisfy the σ-additivity of mutually exclusive states, owing to the non-orthogonality of the coherent states (see subsection 1.3.2 for details on these states). This means in practice that we cannot define proper marginal probability densities from which the Husimi function would be the joint probability density [Mandel 95].

The Q function is directly measurable using a double homodyne detector[1], as shown in chapter 4 section 4.1. A primary focus of this manuscript is to explore this feature of the Q function, and how it can help with certifying non-Gaussianity.

Resulting from its smoothness compared to the other quasiprobability densities as shown by equation (1.40), the non-classical properties of a given state are harder to retrieve from its Q function. One would need many more measurements to get the finer details of the Q function than for sharper quasiprobabilities. In other words, the cost of its smoothness is a lesser sensitivity to state details. This topic is further elaborated in chapter 4.

Although it may require many samples to measure, the Q function contains all information on the represented quantum state. Simply put, the zeros of the Q function of a pure state allow for distinguishing classical pure states, when it has no zero, from non-classical pure states, when it has more than one zero [Lütkenhaus 95]. This property can be extended to non-pure states. We will use this to distinguish between Gaussian and non-Gaussian states (see section 1.4).

While the focus of this manuscript is on the Q function, the Wigner function is more widely used and studied in the quantum optics community. Thankfully, one can derive the expression of the Q function from the Wigner function's one from equation (1.40) with $u = -1$ and $u' = 0$, along with equation (1.41)

$$\begin{aligned} \mathrm{Q}_{\hat{\rho}}(\vec{x}) &= \left(\frac{1}{2\pi\sigma_0^2}\right)^N \int_{\mathbb{R}^{2N}} W_{\hat{\rho}}(\vec{x}') \, \mathrm{e}^{-\frac{1}{2\sigma_0^2}\|\vec{x}'-\vec{x}\|^2} \, \mathrm{d}^{2N}\vec{x}' \\ \text{with} \quad \mathrm{Q}_{\hat{\rho}}(\vec{\alpha}) &= \left(4\sigma_0^2\right)^N \mathrm{Q}_{\hat{\rho}}(\vec{x}) \end{aligned} \tag{1.47}$$

One may apply equation (1.40) with $s = -1$ and $s' = 1$ to derive the Q function from the P function, although this would prove less useful, as the P function is less studied than the Wigner function, and it features mathematical irregularities, as detailed in subsection 1.2.4.

Instead, one can derive an interesting relation involving both Q and P functions. The expectation value $\mathrm{Tr}(\hat{\rho}\hat{A})$ of a given operator $\hat{A}$ on the state $\hat{\rho}$ can be developed by replacing $\hat{A}$ by its P representation (1.44). Using the linearity of the trace to exhibit $\mathrm{Tr}(\hat{\rho}\,|\vec{\alpha}\rangle\langle\vec{\alpha}|)$ as part of the integrand, which is by definition $\pi^N \mathrm{Q}_{\hat{\rho}}(\vec{\alpha})$, we find the following expression

$$\mathrm{Tr}\left(\hat{\rho}\hat{A}\right) = \pi^N \int_{\mathbb{R}^{2N}} \mathrm{P}_{\hat{A}}\left(\vec{\alpha}\right) \mathrm{Q}_{\hat{\rho}}\left(\vec{\alpha}\right) \mathrm{d}^{2N}\vec{\alpha} \tag{1.48}$$

For reference, this equation (1.48) may also be derived as a consequence of the optical equivalence theorem in its anti-normal version [Cahill 69a].

[1] One can also use a heterodyne detector [Wai Leong 86] to measure the Q function. We won't study such detector in this manuscript.

We can obtain an expression for the fidelity of $\hat{\rho}$ to a *target state* $\hat{\rho}'$, simply substituting $\hat{A}$ with $\hat{\rho}'$ in equation (1.48)

$$\mathrm{Tr}\left(\hat{\rho}\hat{\rho}'\right) = \pi^N \int_{\mathbb{R}^{2N}} \mathrm{P}_{\hat{\rho}'}\left(\vec{\alpha}\right)\mathrm{Q}_{\hat{\rho}}\left(\vec{\alpha}\right)\mathrm{d}^{2N}\vec{\alpha} \tag{1.49}$$

This expression proves to be very useful as soon as one can measure the Q function of the experimental state, as it allows us to compute the fidelity to a chosen target state, of which we know the P function, or an approximation. The idea of fidelity estimation through equation (1.49) is at the core of the non-Gaussianity certification protocol presented in this manuscript, see chapter 4.

1.3 Gaussian states

Gaussian states play an important role in continuous-variable quantum optics, as they represent in particular nonclassical states produced deterministically through second order nonlinear optical processes. These states are also of practical significance, as they can be fully described by the first and second moments of the quadrature operators. Furthermore, Gaussian states show potential as fundamental components for quantum information [Weedbrook 12], even though practical quantum information requires to go beyond Gaussianity, see next section 1.4.

We introduce the basic notions about Gaussian states here, notably for a better understanding of the Gaussian source of the experiment described in chapter 2. Still we won't cover this topic in-depth, and we suggest the reader to have a look at the thesis [Michel 21], the paper [Adesso 14] or the book [Weedbrook 12].

1.3.1 Gaussian states and covariance matrix

A *Gaussian state* is by definition a state that is described by a Gaussian Wigner function. In particular from equation (1.47), the Q function of a Gaussian state is Gaussian, as it is given by the convolution of the Wigner function with a Gaussian function. Note that any state whose Q function is Gaussian is a Gaussian state[1], so that the Gaussianity of a quantum state may be defined by the Gaussianity of its Q function.

Since the Wigner function of a Gaussian state is a Gaussian function of the phase space, it is positive everywhere. Thus, it can be seen as an effective joint probability density of its Gaussian marginals, the quadrature probability densities defined in equations (1.30) and (1.31). Any Gaussian probability density is fully characterized by the statistics given by its first two moments. This means that a Gaussian state is fully characterized by the first two moments of both quadrature marginals, a few parameters only.

[1]Taking the Fourier transform of equation (1.47), the Fourier transform of the Wigner function is then given by the ratio of two Gaussian functions, which is a Gaussian. We used that the Fourier transform of a convolution becomes a product, and the Fourier transform of a Gaussian is Gaussian (see appendix A.3 for more on the Fourier transform). This conclude the proof, with the Wigner function being Gaussian.

The first quadrature moments $\langle\vec{\hat{q}}\rangle$ and $\langle\vec{\hat{p}}\rangle$ are represented by $\langle\vec{\hat{x}}\rangle = (\langle\hat{q}_1\rangle, \cdots, \langle\hat{q}_N\rangle, \langle\hat{p}_1\rangle, \cdots, \langle\hat{p}_N\rangle)^\top \in \mathbb{R}^{2N}$, called the *mean* or *displacement* of the Gaussian state. The second quadrature moments are represented by the *covariance matrix* $\mathbf{V}$. These moments are defined as

$$\langle\vec{\hat{x}}\rangle = \mathrm{Tr}\left(\hat{\rho}\vec{\hat{x}}\right) \tag{1.50}$$

$$\mathbf{V}_{ij} = \left\langle \tfrac{1}{2}\{\vec{\hat{x}}_i, \vec{\hat{x}}_j\} \right\rangle - \langle\vec{\hat{x}}_i\rangle \langle\vec{\hat{x}}_j\rangle \tag{1.51}$$

where we use the notations introduced in subsection 1.2.3, $\{\cdot,\cdot\}$ is the anticommutator, and the covariance matrix $\mathbf{V}$ is a real positive symmetric $2N \times 2N$ matrix.

The Wigner function of a Gaussian state $\hat{\rho}_\mathrm{G}$ is then simply given by [Weedbrook 12]

$$W_{\hat{\rho}_\mathrm{G}}(\vec{x}) = \frac{1}{(2\pi)^N \sqrt{\det \mathbf{V}}} \exp\left(-\tfrac{1}{2}(\vec{x} - \langle\vec{\hat{x}}\rangle)^\top \mathbf{V}^{-1} (\vec{x} - \langle\vec{\hat{x}}\rangle)\right) \tag{1.52}$$

where we stress that $\vec{x}$ is the phase space coordinate vector, while $\langle\vec{\hat{x}}\rangle$ is the expectation value of the quadrature operators on the Gaussian state $\hat{\rho}_\mathrm{G}$.

We can apply equation (1.35) in its multimode version to obtain the purity of a Gaussian state μ_G

$$\mu_\mathrm{G} = \frac{\sigma_0^{2N}}{\sqrt{\det \mathbf{V}}} \tag{1.53}$$

A fundamental example of a Gaussian state is *the vacuum*. The multimode vacuum $\hat{\rho}_0$ is characterized by a null mean and the identity for covariance matrix (up to the σ_0^{2N} factor). Its Gaussian Wigner function is given by

$$W_{\hat{\rho}_0}(\vec{x}) = \frac{\mathrm{e}^{-\frac{1}{2\sigma_0^2}\|\vec{x}\|^2}}{(2\pi\sigma_0^2)^N} \tag{1.54}$$

In the following two subsections, we describe two other common Gaussian states, namely the coherent states, and the squeezed vacuum states. We detail their main properties, and show their phase space representations.

1.3.2 Coherent states

Coherent states were first introduced by [Schrödinger 26], and then further studied by [Glauber 63, Sudarshan 63]. They are often used to model the output light of lasers with a well defined phase and mean-field. This doesn't take into account the classical noise stemming from the laser imperfections. Still, this model is a very good approximation for lasers far above threshold. For this reason, the coherent states are often considered as the most relevant quantum states for describing classical light.

In the single-mode scenario, the coherent states $|\alpha\rangle$ are often defined as the eigenvetors of the annihilation operator $\hat{a}$

$$\hat{a}\,|\alpha\rangle = \alpha\,|\alpha\rangle \tag{1.55}$$

with $\alpha \in \mathbb{C}$ the *amplitude* of the coherent state $|\alpha\rangle$. It is common to decompose the amplitude α into

$$\alpha = |\alpha| e^{i\theta_\alpha} \tag{1.56}$$

with θ_α the optical phase of the coherent state, and $|\alpha|^2$ the intensity of the coherent state, as it is directly the number of photons

$$|\alpha|^2 = \langle \hat{n} \rangle_{|\alpha\rangle} \tag{1.57}$$

with $\hat{n} = \hat{a}^\dagger \hat{a}$, and $\langle \hat{\cdot} \rangle_{|\alpha\rangle} = \langle \alpha | \hat{\cdot} | \alpha \rangle$.

The coherent states may also be defined from the vacuum $|0\rangle$ by a displacement operation $\hat{D}(\alpha)$ as [Leonhardt 95]

$$\hat{D}(\alpha)\,|0\rangle = |\alpha\rangle \tag{1.58}$$

$$\text{with} \quad \hat{D}(\alpha) = e^{\alpha \hat{a}^\dagger - \alpha^* \hat{a}} \tag{1.59}$$

In particular, the vacuum is the coherent state of zero amplitude. From equation (1.58), we deduce that the coherent states share the same quadrature variance with the vacuum

$$\langle \Delta^2 \hat{q} \rangle_{|\alpha\rangle} = \langle \Delta^2 \hat{p} \rangle_{|\alpha\rangle} = \sigma_0^2 \tag{1.60}$$

with $\langle \Delta^2 \hat{q} \rangle_{|\alpha\rangle} = \langle \alpha | \hat{q}^2 | \alpha \rangle - \langle \alpha | \hat{q} | \alpha \rangle^2$, and similarly for $\hat{p}$.

The parametrization shown in equation (1.56) allows for an easy phase space 2D representation of the state, see figure 1.1, where we represent the state quantum fluctuations with a disk of diameter given by its quadrature standard deviation σ_0.

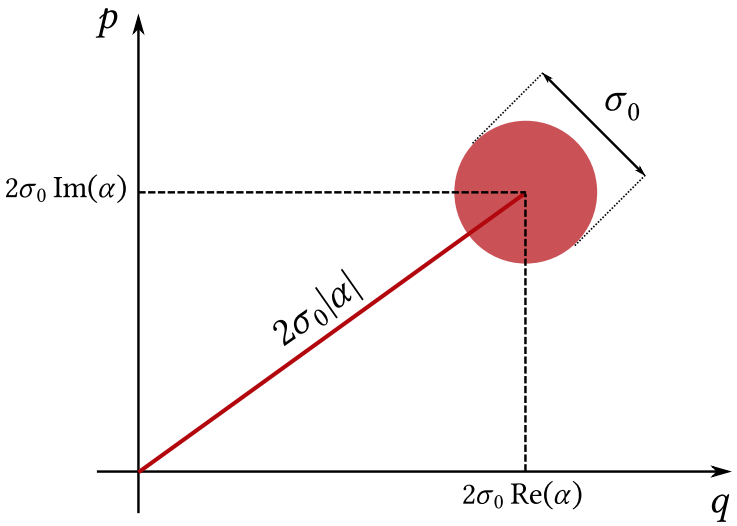

Fig. 1.1 Phase space representation of a coherent state $|\alpha\rangle$ of amplitude $\alpha \in \mathbb{C}$. The quantum fluctuations of the state are represented by a disk of diameter its quadrature standard deviation equal to vacuum's σ_0.

Equation (1.58) allows us to infer the decomposition of the coherent states on the Fock basis

$$|\alpha\rangle = \mathrm{e}^{-\frac{|\alpha|^2}{2}} \sum_{n=0}^{\infty} \frac{\alpha^n}{\sqrt{n!}} |n\rangle \tag{1.61}$$

Furthermore, the coherent states form a non-orthogonal overcomplete basis, which can be expressed as

$$\langle\beta|\alpha\rangle = \mathrm{e}^{-\frac{1}{2}(|\beta|^2+|\alpha|^2-2\beta\alpha^*)} \neq \delta(\alpha-\beta) \qquad (\textit{non-orthogonality}) \tag{1.62}$$

$$\frac{1}{\pi}\int_{\mathbb{R}^2} |\alpha\rangle\langle\alpha| \,\mathrm{d}^2\alpha = \hat{\mathbb{1}} \qquad (\textit{overcompleteness}) \tag{1.63}$$

with $\mathrm{d}^2\alpha = \mathrm{d}\,\mathrm{Re}(\alpha)\,\mathrm{d}\,\mathrm{Im}(\alpha)$.

Since a coherent state is a displaced vacuum, it shares the same covariance matrix as the vacuum, i.e. $\sigma_0^2\mathbb{1}$. Using equation (1.52), we obtain its Wigner function

$$W_{|\alpha\rangle\langle\alpha|}(q,p) = \frac{1}{2\pi\sigma_0^2} \mathrm{e}^{-\frac{1}{2\sigma_0^2}(q-\langle\hat{q}\rangle)^2 - \frac{1}{2\sigma_0^2}(p-\langle\hat{p}\rangle)^2} \tag{1.64}$$

with $\langle\hat{q}\rangle = 2\sigma_0\,\mathrm{Re}(\alpha)$ and $\langle\hat{p}\rangle = 2\sigma_0\,\mathrm{Im}(\alpha)$.

The Q function can be directly inferred from its definition (1.45) and equation (1.62)

$$\mathrm{Q}_{|\alpha\rangle\langle\alpha|}(\beta) = \frac{1}{\pi}\mathrm{e}^{-|\beta-\alpha|^2} \tag{1.65}$$

or equivalently with the correspondence (1.47)

$$\mathrm{Q}_{|\alpha\rangle\langle\alpha|}(q,p) = \frac{1}{4\pi\sigma_0^2} \mathrm{e}^{-\frac{1}{4\sigma_0^2}(q-\langle\hat{q}\rangle)^2 - \frac{1}{4\sigma_0^2}(p-\langle\hat{p}\rangle)^2} \tag{1.66}$$

with $\beta = \frac{1}{2\sigma_0}(q+\mathrm{i}p)$. We point out that the Q function is a 2-dimensional Gaussian broader than the Wigner function, stemming from the Gaussian convolution relation (1.47). Both quasiprobability representations (1.64) and (1.65) are pictured in figure 1.2. Note that the vacuum state has the same representations, but centered at the phase-space origin.

Note that any pure multimode coherent state is single mode in a well chosen basis [Treps 05]. In other words for any pure multimode coherent state of the form $|\psi\rangle = |\alpha_1\rangle \otimes \cdots \otimes |\alpha_N\rangle$, there exists a basis change to a new mode basis where the state $|\psi\rangle$ is single mode

$$|\psi\rangle = |\beta\rangle \otimes |0\rangle \otimes \cdots \otimes |0\rangle \tag{1.67}$$
$$\text{with} \quad \beta = \sum_m |\alpha_m|^2$$

see [Fabre 20] for details. Note that while this is true for pure states, it is not true in general for mixed coherent states.

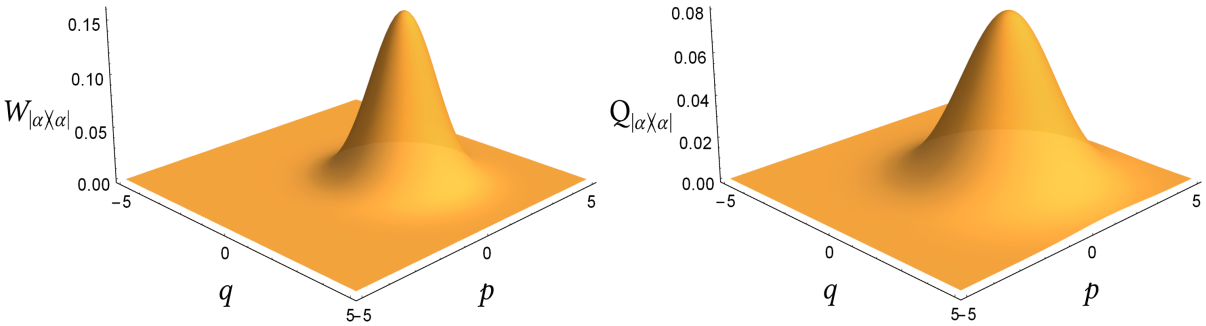

Fig. 1.2 The Wigner function (left) and the Q function (right) of a coherent state $|\alpha\rangle$ of amplitude $\alpha = 1$, with $\sigma_0^2 = 1$.

1.3.3 Squeezed vacuum states

While a coherent state features quadrature variances equal to the ones of the vacuum, a squeezed state, as the name suggests, features a lower variance on one of its quadrature at the expense of a larger one on the other one. This allows beating the "shot-noise", the quantum fluctuation noise of the vacuum, and measuring finer details on one of the observables in a metrology context. This is the reason why it is largely studied, after its introduction by [Kennard 27]. Notably, it is used to enhance the sensitivity of gravitational wave detectors, see [Tse 19].

The *squeezed vacuum states* $|\psi_\zeta\rangle$ are defined as the application of the squeezing operator $\hat{S}(\zeta)$ on the vacuum

$$|\psi_\zeta\rangle = \hat{S}(\zeta)\,|0\rangle \tag{1.68}$$

$$\text{with} \quad \hat{S}(\zeta) = \exp\left[\frac{\zeta}{2}\left(\hat{a}^2 - \hat{a}^{\dagger 2}\right)\right] \tag{1.69}$$

where $\zeta \in \mathbb{R}$ is called the *squeezing parameter*. One can derive some properties of the squeezing operator [Leonhardt 95] [1]

$$\hat{S}(\zeta)^\dagger\, \hat{a}\, \hat{S}(\zeta) = \hat{a}\cosh(\zeta) - \hat{a}^\dagger \sinh(\zeta) \tag{1.70}$$

$$\hat{S}(\zeta)^\dagger\, \hat{q}\, \hat{S}(\zeta) = \hat{q}e^{-\zeta} \quad \text{and} \quad \hat{S}(\zeta)^\dagger\, \hat{p}\, \hat{S}(\zeta) = \hat{p}e^{\zeta} \tag{1.71}$$

from which we straightforwardly deduce the variances and the mean photon number of a squeezed vacuum state $|\psi_\zeta\rangle$

$$\langle \Delta^2 \hat{q} \rangle_{|\psi_\zeta\rangle} = \sigma_0^2 s \tag{1.72}$$

$$\langle \Delta^2 \hat{p} \rangle_{|\psi_\zeta\rangle} = \sigma_0^2 s^{-1} \tag{1.73}$$

$$\langle \hat{n} \rangle_{|\psi_\zeta\rangle} = \sinh^2(\zeta) = \tfrac{1}{4}(s + s^{-1} - 2) \tag{1.74}$$

$$\text{with} \quad s = e^{-2\zeta} \tag{1.75}$$

[1] To derive these forms of operator action, one can use the Hausdorff recursion formula, see appendix A.1.

s is called the *squeezing factor*, and directly corresponds to the ratio between the quadrature variances and the vacuum variance. This property is illustrated on the phase space representation of $|\psi_\zeta\rangle$ in figure[1] 1.3. More pragmatically, the squeezing factor is often given in the base-ten logarithmic absolute scale

$$s_{\mathrm{dB}} = 10\left|\log_{10}(s)\right| = \frac{20}{\ln 10}|\zeta| \tag{1.76}$$

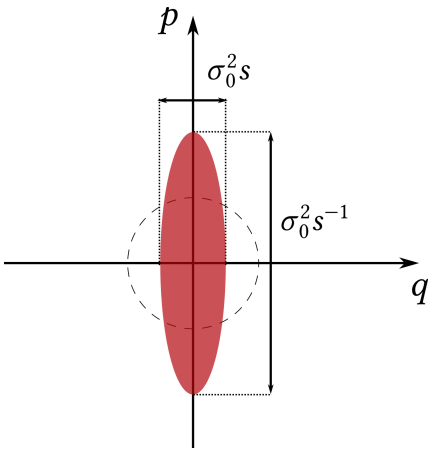

Fig. 1.3 Phase space representation of a squeezed state $|\psi_\zeta\rangle$ of squeezing parameter ζ, and squeezing factor $s = \mathrm{e}^{-2\zeta}$. The quantum fluctuations of the state are represented by an ellipse of dimensions its quadrature variances given by equations (1.72) and (1.73). For reference, a dashed circle of diameter the vacuum quadrature variance σ_0^2 is represented. The figure is to scale, with $\zeta = \ln(2)/2$, $s_{\mathrm{dB}} \simeq 3\,\mathrm{dB}$.

For $\zeta > 0$, we will refer to $\hat{q}$ as the *squeezed quadrature*, and to $\hat{p}$ as the *antisqueezed quadrature*, consistently with equation (1.72) and (1.73). We can also consider a complex squeezing operator $\zeta \in \mathbb{C}$, with $\zeta = |\zeta|\mathrm{e}^{\mathrm{i}\theta_\zeta}$ where θ_ζ defines the squeezing direction, and the squeezing operator then writes

$$\hat{S}(\zeta) = \exp\left[\frac{\zeta^*}{2}\hat{a}^2 - \frac{\zeta}{2}\hat{a}^\dagger\right] \tag{1.77}$$

In this case, the squeezed quadrature is $q^{\theta_\zeta/2}$ and the antisqueezed quadrature is $q^{\theta_\zeta/2+\pi/2}$, where the quadrature operator q^θ at angle θ is defined by equation (1.18). The factor $1/2$ in the phase is consistent with the fact that the squeezed vacuum state is invariant under π-rotations, see figure 1.3[2].

[1] We choose the variance to represent the quantum fluctuations instead of the standard deviation as squeezing factors are conventionally referring to variances. Note that this common choice is fine as the state has a null mean, and may be understood by replacing the axes (q, p) by (q^2, p^2).

[2] More precisely, the squeezing operator in (1.77) can be obtained by applying the phase-space rotation operation $\hat{R}(\theta_\zeta/2)$ of angle $\theta_\zeta/2$ on the squeezing operator in (1.69) (see next subsection 1.3.4 for the definition of $\hat{R}(\theta)$). Under its action, the squeezing operator maps as $\hat{S}(\zeta) \mapsto \hat{S}(\zeta\mathrm{e}^{\mathrm{i}\theta_\zeta})$, while the quadrature operators map as $\hat{q} \mapsto \hat{q}^{\theta_\zeta/2}$, $\hat{p} \mapsto \hat{q}^{\theta_\zeta/2+\pi/2}$, see appendix A.1 for demonstrations.

One can develop equation (1.68) (see [Ferraro 05])

$$|\psi_\zeta\rangle = \hat{S}(\zeta)\,|0\rangle = \frac{1}{\sqrt{\cosh(\zeta)}} \exp\left[-\tfrac{1}{2}\tanh(\zeta)\,\hat{a}^{\dagger 2}\right]|0\rangle \tag{1.78}$$

to derive the expression of a vacuum squeezed state on the Fock basis $\{|n\rangle\}$

$$|\psi_\zeta\rangle = \frac{1}{\sqrt{\cosh(\zeta)}} \sum_{n=0}^{\infty} \sqrt{\binom{2n}{n}} \frac{\tanh^n(\zeta)}{2^n}\,|2n\rangle \tag{1.79}$$

where one can see that all the odd number of photon terms are zero, resulting in a main contribution in the vacuum followed by only even terms. Note that this property is extremely sensitive to photon losses, since for any amount of losses odd terms appear in equation (1.79).

From equation (1.71), we deduce that the covariance matrix of a squeezed vacuum state is simply given by $\mathrm{diag}(s, s^{-1})$. Applying equation (1.52), we obtain the Wigner function of a squeezed vacuum state

$$W_{|\psi_\zeta\rangle\langle\psi_\zeta|}(q,p) = \frac{1}{2\pi\sigma_0^2} \mathrm{e}^{-\frac{1}{2\sigma_0^2 s}q^2 - \frac{1}{2\sigma_0^2/s}p^2} \tag{1.80}$$

where one can clearly see the squeezed and anti-squeezed width of the Gaussian quadrature marginals. For $s = 1$, we recover the vacuum Wigner function given in equation (1.54).

One can derive the Q function from the Wigner function with equation (1.47) and obtain

$$\mathrm{Q}_{|\psi_\zeta\rangle\langle\psi_\zeta|}(q,p) = \frac{1}{2\pi\sigma_0^2} \frac{1}{\sqrt{(1+s)(1+1/s)}} \mathrm{e}^{-\frac{1}{2\sigma_0^2(1+s)}q^2 - \frac{1}{2\sigma_0^2(1+1/s)}p^2} \tag{1.81}$$

which is still a Gaussian as expected. We note that even though its marginals are not the quadrature probability densities as discussed in subsection 1.2.5, they are "squeezed" in the expected way, similarly as the Wigner function but both broader. This can be checked by looking at the quasiprobability plots in figure 1.4.

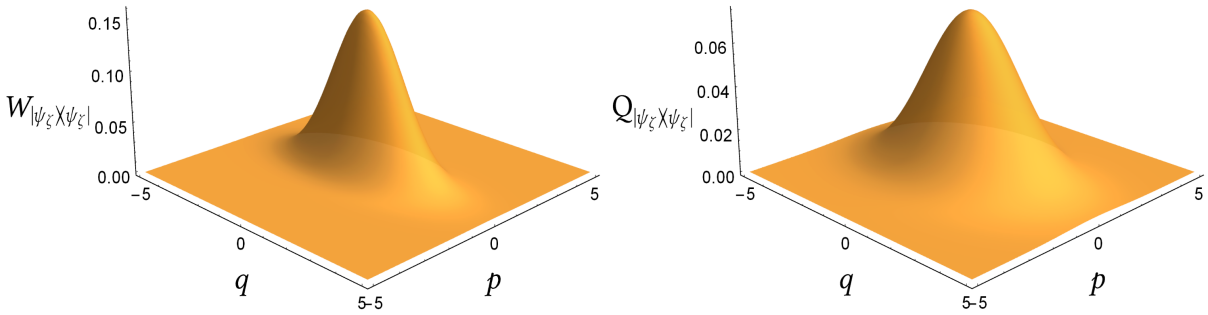

Fig. 1.4 The Wigner function (left) and the Q function (right) of a vacuum squeezed state $|\psi_\zeta\rangle$ of squeezing parameter $\zeta = \ln(2)/2$ (i.e. $s_{\mathrm{dB}} \simeq 3\,\mathrm{dB}$), with $\sigma_0^2 = 1$.

1.3.4 Gaussian operations

In the two previous examples, we saw that both coherent states and squeezed vacuum states can be defined from the action of an operator on the vacuum. Let us now generalize this remark, which will allows us to introduce powerful tools to further comprehend the Gaussian states.

Gaussian operations are the transformations that preserve Gaussianity, i.e. a Gaussian state is again a Gaussian state under such transformation. These transformations have been largely investigated in the literature, such that one can define and characterize them completely. They are useful for studying Gaussian states, seen as generated states from these operations, or non-Gaussian states, defining the boundaries one has to cross to go beyond Gaussianity. We will only give the main ideas as it is not the focus of this manuscript, referring to [Weedbrook 12, Michel 21].

By definition, a Gaussian operation is reversible, i.e. it is a unitary transformation. As it is unitary, a Gaussian transformation can not model losses[1], or a measurement. We denote the associated unitary operator $\hat{G}$[2].

To characterize a Gaussian operation we would usually describe its action on the annihilation and creation operators, as we did for the change of mode basis see equations (1.14) and (1.15). This can be conveniently reduced to the determination of a $N \times N$ unitary matrix.

Often, it is convenient to describe the action of a Gaussian operation on the quadrature operators, as we did for the squeezing operator, see equation (1.71). More generally, a Gaussian transformation is fully characterized by a *symplectic transformation* along with a phase-space *displacement* [Weedbrook 12]. The symplectic formalism is quite useful in the multimode scenario, and allows for the expression of powerful theorems, as we will see in the next subsection 1.3.5. For this reason, we focus on the symplectic representation of the Gaussian operations in the following.

The symplectic transformations form a group, called the *symplectic group*. A symplectic transformation is defined by a $2N \times 2N$ real matrix $\mathbf{S}$ which acts on the quadrature operators as $\vec{\hat{x}} \mapsto \mathbf{S}\vec{\hat{x}}$, and satisfies [Simon 88]

$$\mathbf{S}\,\mathbf{\Omega}\,\mathbf{S}^\top = \mathbf{\Omega}, \quad \text{where} \quad \mathbf{\Omega} = \begin{pmatrix} \mathbf{0} & \mathbb{1}_N \\ -\mathbb{1}_N & \mathbf{0} \end{pmatrix} \tag{1.82}$$

with $\mathbb{1}_N$ the identity matrix of size $N \times N$. In particular, their determinant is 1. Equation (1.82) means in particular that symplectic transformations preserve the quadrature commutation relations (1.17), which can be written in the multimode scenario as

$$\left[\vec{x}_i, \vec{x}_j\right] = 2\mathrm{i}\sigma_0^2 \mathbf{\Omega}_{ij} \tag{1.83}$$

A displacement on the multimode phase space can be defined as the product of single-mode displacement operators $\hat{D}(\alpha)$ defined in equation (1.59). A single-mode displacement operator

[1] While losses are indeed non-unitary operations, one can still model them by introducing extra loss channels or modes, which are not measured. Considering all implied modes, the operation is unitary. When the output state is mixed, this relates to the concept introduced with the density operator, see subsection 1.2.2.

[2] A unitary operator $\hat{G}$ satisfies $\hat{G}^\dagger\hat{G} = \hat{G}\hat{G}^\dagger = \hat{\mathbb{1}}$, with $\hat{\mathbb{1}}$ the identity operator. Note also that for a Gaussian operation, $\hat{G}$ is generated from an Hamiltonian at most quadratic in the annihilation and creation operators.

acts on the quadrature operators as [Leonhardt 95]

$$\hat{D}(\alpha)^\dagger \hat{q} \hat{D}(\alpha) = \hat{q} + q, \quad \hat{D}(\alpha)^\dagger \hat{p} \hat{D}(\alpha) = \hat{p} + p \tag{1.84}$$

with $\alpha = (q + \mathrm{i}p)/(2\sigma_0)$.

For the Wigner function, the action of any Gaussian operator $\hat{G}$ on the state $\hat{\rho}$ is equivalent to the action of the corresponding symplectic and displacements actions on the phase space [Fabre 20]

$$W_{\hat{G}\hat{\rho}\hat{G}^\dagger}\left(\vec{x}'\right) = W_{\hat{\rho}}\left(\vec{x}\right) \quad \text{with} \quad \vec{x}' = \mathrm{S}\vec{x} + \vec{d} \tag{1.85}$$

where $\vec{d}$ is a $2N$ real vector in the quadrature phase space, corresponding to displacement operations of the form (1.84) applied on each of the N modes.

Since the Gaussian states are fully characterized by their first and second moments defined in (1.50) and (1.51), the action of a Gaussian operation $(\mathrm{S}, \vec{d})$ is simply given by

$$\langle \vec{\hat{x}} \rangle \mapsto \langle \vec{\hat{x}} \rangle + \vec{d} \tag{1.86}$$

$$\mathbf{V} \mapsto \mathbf{S}\mathbf{V}\mathbf{S}^\top \tag{1.87}$$

which can be obtained by applying the transformation (1.85) in equation (1.52).

Equation (1.85) illustrates the main interest of using the symplectic representation of Gaussian transformations: a Gaussian operation may be simply viewed as a transformation of the $2N$ dimensional phase space, applied on the phase space representation of the states - here the Wigner function. These properties only partially transfer to the Q function, as we show in details in chapter 4.

Any single-mode Gaussian operation may be decomposed into the product of three elementary single-mode Gaussian operations [Weedbrook 12]:

- The displacement operation $\hat{D}(\alpha)$ defined in subsection 1.3.2, equation (1.59). Its action on the quadrature operators $\hat{q}$ and $\hat{p}$ is given by equation (1.84). On the phase space, it is a translation: $q \mapsto q + 2\sigma_0^2 \mathrm{Re}(\alpha)$ and $p \mapsto p + 2\sigma_0^2 \mathrm{Im}(\alpha)$. In the lab, it may be implemented by combining the state to displace with a bright coherent field on a highly transmitting beamsplitter. In the experiment presented in this manuscript, this operation is not needed.

- The *phase-space rotation operation* $\hat{R}(\theta)$ of angle θ, defined as generated by the number operator $\hat{n}$, i.e.

  $$\hat{R}(\theta) = \exp(-\mathrm{i}\theta\hat{n}) \tag{1.88}$$

  with $\theta \in \mathbb{R}$. Its action on the quadrature operators $\vec{\hat{x}}$ is described by the symplectic matrix $\mathbf{R}$ which writes

  $$\mathbf{R} = \begin{pmatrix} \cos(\theta) & \sin(\theta) \\ -\sin(\theta) & \cos(\theta) \end{pmatrix} \tag{1.89}$$

  On the phase space, it is simply a 2D rotation: $\vec{x} \mapsto \mathbf{R}\vec{x}$, where $\vec{x} = (q, p)^\top$. Experimentally, this operation is usually simply implemented by using piezoelectric stacks on a mirror to shift the beams by less than a wavelength.

- The squeezing operation $\hat{S}(\zeta)$ defined in subsection 1.3.3, equation (1.69). Its action on the quadrature operators $\vec{\hat{x}}$ is given by equation (1.71), or is equivalently described by the symplectic matrix $\mathbf{K}$ which writes

$$\mathbf{K} = \begin{pmatrix} e^{-\zeta} & 0 \\ 0 & e^{\zeta} \end{pmatrix} \tag{1.90}$$

  On the phase space, it is both a stretching (in the squeezed direction) and a contraction (in the antisqueezed direction): $\vec{x} \mapsto \mathbf{K}\vec{x}$. In the laboratory, it's the only Gaussian operation that requires non-linear crystals. A detailed example of implementation is given in the description of our source of Gaussian states in chapter 2.

To complete the set of all Gaussian operations, multimode and single-mode, it is enough to add 2-mode basis changes. The N-mode basis change $\hat{U}$ is characterized by its $N \times N$ unitary matrix $\mathbf{U}$ acting on the annihilation and creation operators in equation (1.14) and (1.15). Its action on the quadrature operators $\vec{\hat{x}}$ is described by a real orthogonal symplectic $2N \times 2N$ matrix $\mathbf{O}$ which is obtained from $\mathbf{U}$ as

$$\mathbf{O} = \begin{pmatrix} \mathrm{Re}(\mathbf{U}) & \mathrm{Im}(\mathbf{U}) \\ -\mathrm{Im}(\mathbf{U}) & \mathrm{Re}(\mathbf{U}) \end{pmatrix} \tag{1.91}$$
$$\text{with} \quad \mathbf{U} = \mathrm{Re}(\mathbf{U}) + i\,\mathrm{Im}(\mathbf{U})$$

1.3.5 Decompositions of Gaussian states and Gaussian operations

As is described in chapter 2, an important state preparation step is to generate multimode squeezed vacuum states, using a synchronously pumped optical parametric oscillator (SPOPO). This multimode operation, when considered lossless, can be modeled as a multimode Gaussian operation applied on the vacuum. When accounting for losses which are non-unitary operations, it is not true anymore. We then need to introduce a more advanced framework. Let us use the symplectic formalism and consider only zero-displacement Gaussian operations to express two powerful decompositions, namely the *Bloch-Messiah decomposition* and the *Williamson decomposition*. Let us first define both decompositions.

The Bloch-Messiah decomposition. First introduced by [Bloch 62], and then further applied in quantum optics by [Braunstein 05], it is stemming from the singular value decomposition. It states that any symplectic matrix $\mathbf{S}$ can be decomposed into the product of three elementary symplectic matrices

$$\mathbf{S} = \mathbf{O}_1 \mathbf{K} \mathbf{O}_2 \tag{1.92}$$

where $\mathbf{K}$ is the symplectic matrix of a multimode squeezing operation, and $\mathbf{O}_1$, $\mathbf{O}_2$ are the symplectic matrices of mode-basis changes.

The symplectic matrix $\mathbf{K}$ in equation (1.92) represents the action of a collection of independent squeezing operators, which can be written $\hat{S}_1(\zeta_1) \otimes \cdots \otimes \hat{S}_N(\zeta_N)$ with $\zeta_m \in \mathbb{R}$ the squeezing parameter of mode $\mathbf{u}_m$. It generalizes the single-mode squeezing operation represented by equation (1.90), and consistently $\mathbf{K}$ writes

$$\mathbf{K} = \mathrm{diag}(e^{-\zeta_1}, \cdots, e^{-\zeta_N}, e^{\zeta_1}, \cdots, e^{\zeta_N}) \tag{1.93}$$

The Williamson decomposition. The Williamson's theorem [Williamson 36, Ikramov 18] states that any real positive definite matrix $\mathbf{V}$ can be decomposed as

$$\mathbf{V} = \mathbf{S}\mathbf{V}_{\mathrm{W}}\mathbf{S}^{\top} \tag{1.94}$$

with $\mathbf{S}$ a symplectic matrix, $\mathbf{V}_{\mathrm{W}} = \sigma_0^2\,\mathrm{diag}(\kappa_1,\cdots,\kappa_N,\kappa_1,\cdots,\kappa_N)$, and $0 \leqslant \kappa_1 \leqslant \cdots \leqslant \kappa_N$ the Williamson eigenvalues. This theorem applied to the covariance matrix of a quantum state requires $1 \leqslant \kappa_1 \leqslant \cdots \leqslant \kappa_N$ to account for the Heisenberg inequality relations.

Interpretation and application. Let us consider a given experimental setup only consisting of zero-displacement Gaussian operations, and a zero-mean Gaussian input state, e.g. the SPOPO acting on the vacuum. To apply the two decompositions, we actually don't need to make any assumption on the input state purity, or on the losses caused by the setup. It just requires to have a Gaussian output state, which is the case we consider. We note $\mathbf{V}_{\mathrm{out}}$ the covariance matrix of the output state. Let us now apply the Williamson decomposition (1.94) on $\mathbf{V}_{\mathrm{out}}$, followed by the Bloch-Messiah decomposition (1.92) applied on the symplectic matrix $\mathbf{S}$ of (1.94). The result writes

$$\mathbf{V}_{\mathrm{out}} = \mathbf{O}_1\mathbf{K}\,\mathbf{O}_2\mathbf{V}_{\mathrm{W}}\mathbf{O}_2^{\top}\mathbf{K}\,\mathbf{O}_1^{\top} \tag{1.95}$$

Let us first assume that the output state is pure. Since the unit-determinant transformation $\mathbf{O}_1\mathbf{K}\,\mathbf{O}_2$ does not change the purity (see equation (1.53)), then $\mathbf{V}_{\mathrm{W}}$ represents a pure state, hence the Williamson eigenvalues $\{\kappa_m\}$ must all equal 1. Equation (1.95) gets simplified to

$$\mathbf{V}_{\mathrm{out}}^{\mathrm{pure}} = \sigma_0^2\,\mathbf{O}_1\mathbf{K}^2\mathbf{O}_1^{\top} \tag{1.96}$$

which is then a multimode squeezed vacuum state in the basis defined by $\mathbf{O}_1$, with squeezing parameters $\zeta_1,\cdots,\zeta_N$. The assumption that the output state is pure implies that the input state is pure (e.g. the vacuum) and that the setup do not introduce any losses on the state, which never occurs experimentally.

In general, the output state is a Gaussian mixed state described by equation (1.95). The covariance matrix $\mathbf{V}_{\mathrm{W}}$ defined in (1.94) can be interpreted as a collection of independent symmetric thermal states, or equivalently, independent modes containing classical noise. The symplectic transformation on $\mathbf{V}_{\mathrm{W}}$ is then a multiport beamsplitter $\mathbf{O}_2$, followed by an assembly of individual squeezing operators in parallel $\mathbf{K}$, and another multiport beamsplitter $\mathbf{O}_1$.

1.3.6 Two-mode squeezed vacuum states

As a final Gaussian state example, let us describe the two-mode squeezed vacuum states to illustrate some key concepts that arise from stepping into the multimode world.

The *two-mode squeezed vacuum states* are defined from the action of the two-mode squeezing operator $\hat{S}^{(2)}(\zeta)$ on the vacuum

$$\left|\mathrm{EPR}_{\zeta}\right\rangle = \hat{S}^{(2)}(\zeta)\,|0\rangle \otimes |0\rangle \tag{1.97}$$

$$\text{with}\quad \hat{S}^{(2)}(\zeta) = \exp\left(\zeta\,\hat{a}_1\hat{a}_2 - \zeta\,\hat{a}_1^{\dagger}\hat{a}_2^{\dagger}\right) \tag{1.98}$$

where ζ is a real parameter, and we use the notation $\left|\mathrm{EPR}_\zeta\right\rangle$ as it is also often called an *Einstein-Podolsky-Rosen (EPR) state* or *EPR pair* to refer to the historical debate between the named physicists [Einstein 35]. In particular, the EPR state is a maximally entangled state, and we refer to [Nielsen 00] for more details on its entanglement properties.

The EPR state on the Fock state basis is given by [Leonhardt 95]

$$\left|\mathrm{EPR}_\zeta\right\rangle = \frac{1}{\cosh(\zeta)} \sum_{n=0}^{\infty} \tanh^n(\zeta) \left|n\right\rangle \otimes \left|n\right\rangle \tag{1.99}$$

One can derive the action of the two-mode squeezing operator $\hat{S}^{(2)}(\zeta)$ on the quadrature operators [Ferraro 05]

$$\hat{S}^{(2)}(\zeta)^\dagger \, \hat{q}_1 \, \hat{S}^{(2)}(\zeta) = \hat{q}_1 \cosh(\zeta) - \hat{q}_2 \sinh(\zeta) \tag{1.100}$$

$$\hat{S}^{(2)}(\zeta)^\dagger \, \hat{p}_1 \, \hat{S}^{(2)}(\zeta) = \hat{p}_1 \cosh(\zeta) - \hat{p}_2 \sinh(\zeta) \tag{1.101}$$

and similarly for $\hat{q}_2$ and $\hat{p}_2$ by symmetry of the index roles. One can use the formulas given in appendix A.1 to derive these equations. From equations (1.100) and (1.101), we deduce the corresponding symplectic matrix $\mathbf{S}^{(2)}(\zeta)$

$$\mathbf{S}^{(2)}(\zeta) = \begin{pmatrix} \mathbf{C} & \mathbf{0} \\ \mathbf{0} & \mathbf{C} \end{pmatrix} \quad \text{with} \quad \mathbf{C} = \begin{pmatrix} \cosh(\zeta) & -\sinh(\zeta) \\ -\sinh(\zeta) & \cosh(\zeta) \end{pmatrix} \tag{1.102}$$

Using equation (1.87), we deduce the covariance matrix $\mathbf{V}_{\mathrm{EPR}_\zeta}$ by the symplectic transformation $\mathbf{S}^{(2)}(\zeta)$ on the vacuum covariance matrix $\mathbf{V}_0 = \sigma_0^2 \mathbb{1}_{2N}$

$$\mathbf{V}_{\mathrm{EPR}_\zeta} = \sigma_0^2 \begin{pmatrix} \mathbf{C}^2 & \mathbf{0} \\ \mathbf{0} & \mathbf{C}^2 \end{pmatrix} \quad \text{with} \quad \mathbf{C}^2 = \begin{pmatrix} \cosh(2\zeta) & -\sinh(2\zeta) \\ -\sinh(2\zeta) & \cosh(2\zeta) \end{pmatrix} \tag{1.103}$$

From either equation (1.85) or equation (1.52), we deduce the Wigner function of the EPR state

$$W_{\left|\mathrm{EPR}_\zeta\right\rangle\!\left\langle\mathrm{EPR}_\zeta\right|}(q_1, q_2, p_1, p_2) = \frac{1}{(2\pi\sigma_0^2)^2} \exp\left[-\frac{\cosh(2\zeta)}{2\sigma_0^2}\left(q_1^2 + q_2^2 + p_1^2 + p_2^2 + 2\tanh(2\zeta)(q_1 q_2 + p_1 p_2)\right)\right] \tag{1.104}$$

where the quadrature correlations of the EPR state appear in the quadrature cross terms, which correspond to off-diagonal terms in the covariance matrix $\mathbf{V}_{\mathrm{EPR}_\zeta}$. As mentioned when introducing the density matrix in subsection 1.2.2, the entanglement of a two-mode system implies that the partial trace over one mode yields a mixed state. We can check it with this example by tracing the EPR Wigner function $W_{\left|\mathrm{EPR}_\zeta\right\rangle\!\left\langle\mathrm{EPR}_\zeta\right|}$ over mode 2 for instance (tracing over mode 1 yields the same Wigner function by symmetry)

$$W_{\hat{\rho}_{\mathrm{EPR}}^{\mathrm{red}}}(q_1, p_1) = \frac{1}{2\pi\sigma_0^2 \cosh(2\zeta)} \exp\left[-\frac{1}{2\sigma_0^2 \cosh(2\zeta)}\left(q_1^2 + p_1^2\right)\right] \tag{1.105}$$

with $\hat{\rho}_{\mathrm{EPR}}^{\mathrm{red}}$ denoting the resulting state on the reduced 1-mode space. One can compute the purity of this Gaussian state using equation (1.53). It yields $\mu_{\mathrm{EPR}}^{\mathrm{red}} = 1/\cosh(2\zeta)$, which is always smaller than one for $\zeta \neq 0$. The Wigner function $W_{\hat{\rho}_{\mathrm{EPR}}^{\mathrm{red}}}$ in (1.105) represents then a

mixed state that is called thermal state. This comes in pair with quadrature variances both larger than the vacuum variance

$$\langle \Delta^2 \hat{q} \rangle_{\hat{\rho}_{\text{EPR}}^{\text{red}}} = \langle \Delta^2 \hat{p} \rangle_{\hat{\rho}_{\text{EPR}}^{\text{red}}} = \cosh(2\zeta)\, \sigma_0^2 > \sigma_0^2 \tag{1.106}$$

A deeply insightful property of the EPR state is that upon a well chosen change of mode basis, this state becomes a factorized state and as such "looses" all its entanglement properties. This stems from the following identity [Ferraro 05]

$$\hat{U}_{\text{BS}}^{\text{even}\dagger}\, \hat{S}^{(2)}(\zeta)\, \hat{U}_{\text{BS}}^{\text{even}} = \hat{S}(\zeta) \otimes \hat{S}(-\zeta) \tag{1.107}$$

with $\hat{U}_{\text{BS}}^{\text{even}} = \exp\left(\frac{\pi}{4}(\hat{a}_1^\dagger \hat{a}_2 - \hat{a}_1 \hat{a}_2^\dagger)\right)$ is a two-mode change basis that can be implemented with an even beamsplitter. The action of $\hat{U}_{\text{BS}}^{\text{even}}$ on the annihilation operators writes

$$\begin{aligned} \hat{a}_1 &\mapsto (\hat{a}_1 + \hat{a}_2)/\sqrt{2} \\ \hat{a}_2 &\mapsto (-\hat{a}_1 + \hat{a}_2)/\sqrt{2} \end{aligned} \tag{1.108}$$

Applying equation (1.107) on the vacuum yields the state

$$\left(\hat{S}(\zeta)\,|0\rangle\right) \otimes \left(\hat{S}(-\zeta)\,|0\rangle\right) \tag{1.109}$$

which describes two separate single-mode squeezed vacuum states with squeezing in orthogonal quadratures. This reversible transformation in equation (1.107) is illustrated by figure[1] 1.5.

This two-mode example illustrates the mode basis dependence of the separability, which is in general the ability to write a state as a statistical ensemble of factorized states [Peres 96]. It actually leads to the question of *intrinsic separability* of a given multimode state, i.e. does a mode basis in which the state is separable exist? For zero-mean pure Gaussian states, equation (1.96) shows that there always exists a mode basis in which the state is a multimode squeezed state. This means that any zero-mean pure Gaussian state is intrinsically separable. This result extends to any Gaussian states, mixed and displaced ones included, and we refer to [Walschaers 17a, Fabre 20] for a complete demonstration, essentially stemming from the Bloch-Messiah and Williamson decompositions introduced in subsection 1.3.5.

1.4 Non-Gaussian states

A non-Gaussian state is by definition a state described by a non-Gaussian Wigner function, or equivalently a non-Gaussian Q function[2]. The most straightforward example of non-Gaussian states are the Fock states, which we introduce in the first subsection 1.4.1. As one can expect from such a negative definition, it is hard to characterize non-Gaussian states. While numerous works have been carried out to give a structure to the set of non-Gaussian states, there's still much left to uncover.

[1] As in subsection 1.3.3, we represent the quantum fluctuations with the quadrature variances as each implied state has a null mean. Again, one can understand it by simply replacing the quadrature axes by their squares.

[2] As shown in section 1.3, a state is Gaussian if and only if its Q function is Gaussian.

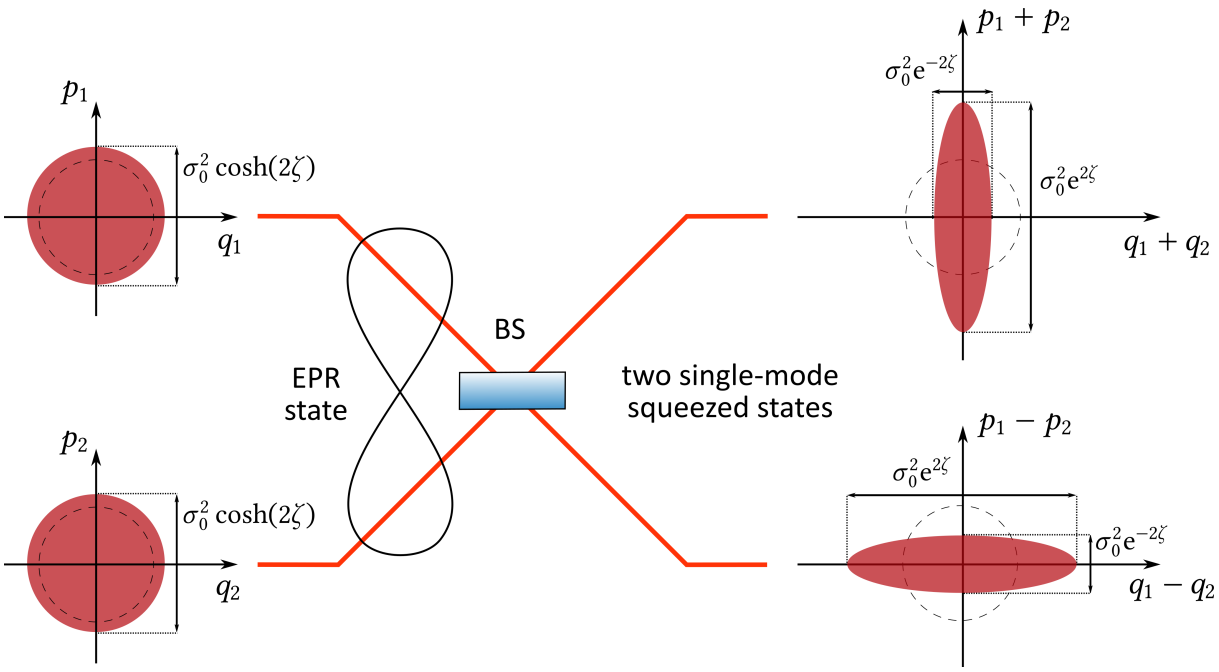

Fig. 1.5 Scheme of the change of mode basis transformation linking an EPR state $|\mathrm{EPR}_\zeta\rangle$ to two single-mode squeezed vacuum states $\left(\hat{S}(\zeta)|0\rangle\right) \otimes \left(\hat{S}(-\zeta)|0\rangle\right)$, with squeezing parameter ζ. On the left of the beamsplitter (BS), the EPR reductions on mode 1 and 2 are represented in their respective phase space. They are thermal states, see the main text. On the right of the BS, the two single-mode squeezed vacuum states are represented with alternate squeezed quadrature. For reference, a dashed circle of diameter the vacuum quadrature variance σ_0^2 is represented in each phase space. The phase space representations are to scale, with $\zeta = \ln(2)/2, s_{\mathrm{dB}} \simeq 3\,\mathrm{dB}$.

The negative formulation of the non-Gaussian state definition tends to naturally lead us to characterize these states by quantifying how much they are not Gaussian. This approach consists in using specific properties that only Gaussian states satisfy to assess how much a non-Gaussian state differ from Gaussian ones, see [Genoni 07, Genoni 08, Genoni 10].

Another approach is to look for features which are specific to non-Gaussian states. For instance, the presence of negative values in the Wigner function (or *Wigner negativity* in short) of a quantum state is of particular relevance for quantum information, as we comment in the subsection 1.4.2. More recently, numerous efforts to classify the set of non-Gaussian states have been carried out, and we will focus on the stellar hierarchy, presenting some results of our paper [Chabaud 21d] in particular in subsection 1.4.3. In the last subsection 1.4.4, we will describe in some details the non-Gaussian states we aim at producing in the laboratory, namely photon subtracted and added squeezed vacuum states[1].

We will not cover the whole topic of non-Gaussianity, and we refer to "Non-Gaussian States and Where to Find Them" [Walschaers 21] for an overview of current research on non-

[1]We don't generate photon added squeezed vacuum states in the experiment, while we present some theoretical investigation on such practical addition in chapter 3.

Gaussian states. In particular, we recommend this tutorial to readers interested in quantum correlations in non-Gaussian states, which we do not cover here.

1.4.1 Fock states

In this subsection, we describe the first non-Gaussian states that comes to mind, namely the Fock states. As seen before in subsection 1.2.1, Fock states are of particular theoretical interest as they provide a basis for the state Hilbert space. In practice, they are produced using non-linear optics. The simplest setup to produce them is using spontaneous parametric down-conversion to generate probabilistically pairs of single photons [Hong 86]. Heralding on the detection of one photon of the pair allows one to post-select on photon pair event, and recover pure single photons.

In the single-mode scenario, a *Fock state* $|n\rangle$ is defined as the eigenstate of the number operator $\hat{n}$ with photon number $n \in \mathbb{N}$ as

$$\hat{n}\,|n\rangle = n\,|n\rangle \tag{1.110}$$

In particular, the vacuum is a Fock state with photon number $n = 0$.

A Fock state $|n\rangle$ can be explicitely obtained from the vacuum $|0\rangle$ by applying multiple times the creation operator $\hat{a}^\dagger$ on the vacuum $|0\rangle$ as

$$|n\rangle = \frac{(\hat{a}^\dagger)^n}{\sqrt{n!}}\,|0\rangle \tag{1.111}$$

As mentioned in subsection 1.2.1, the set of Fock states $\{|n\rangle\}$ forms a complete orthonormal basis on any single-mode state Hilbert space, which writes

$$\langle n|n'\rangle = \delta_{n,n'} \qquad (\textit{orthonormality}) \tag{1.112}$$

$$\sum_n |n\rangle\langle n| = \hat{\mathbb{1}} \qquad (\textit{completeness}) \tag{1.113}$$

where $\delta_{n,n'}$ is the Kronecker symbol. We will refer to this basis as the *Fock basis*.

The Wigner function of a Fock state $|n\rangle$ is given by [Leonhardt 95]

$$W_{|n\rangle\langle n|}(q,p) = \frac{(-1)^n}{2\pi\sigma_0^2}\,L_n\!\left(\frac{q^2+p^2}{\sigma_0^2}\right)\mathrm{e}^{-\frac{1}{2\sigma_0^2}(q+p)^2} \tag{1.114}$$

$$\text{where}\quad L_n(x) = \sum_{k=0}^{n}\binom{n}{k}\frac{(-1)^k}{k!}x^k \tag{1.115}$$

with L_n the n-th Laguerre polynomial and x an arbitrary variable.

The Q function of a Fock state $|n\rangle$ is straightforwardly derived from both the definition (1.45) and the decomposition of coherent states on the Fock basis given in equation (1.61)

$$\mathrm{Q}_{|n\rangle\langle n|}(\alpha) = \frac{1}{\pi n!}|\alpha|^{2n}\mathrm{e}^{-|\alpha|^2} \tag{1.116}$$

or equivalently with the correspondence (1.47)

$$\mathrm{Q}_{|n\rangle\langle n|}(q,p) = \frac{1}{4\pi\sigma_0^2 n!}\left(q^2+p^2\right)^n \mathrm{e}^{-\frac{1}{4\sigma_0^2}(q^2+p^2)} \tag{1.117}$$

Both the Wigner function (1.114) and the Q function (1.117) of Fock states $|1\rangle$ and $|2\rangle$ are pictured in figure 1.6. We see that indeed, Wigner and Q functions of Fock states are not Gaussian functions, which qualifies Fock states as non-Gaussian states (for $n > 0$). Furthermore, their Wigner function features negative values and their Q function vanishes at zero, two properties we elaborate on the next two subsections.

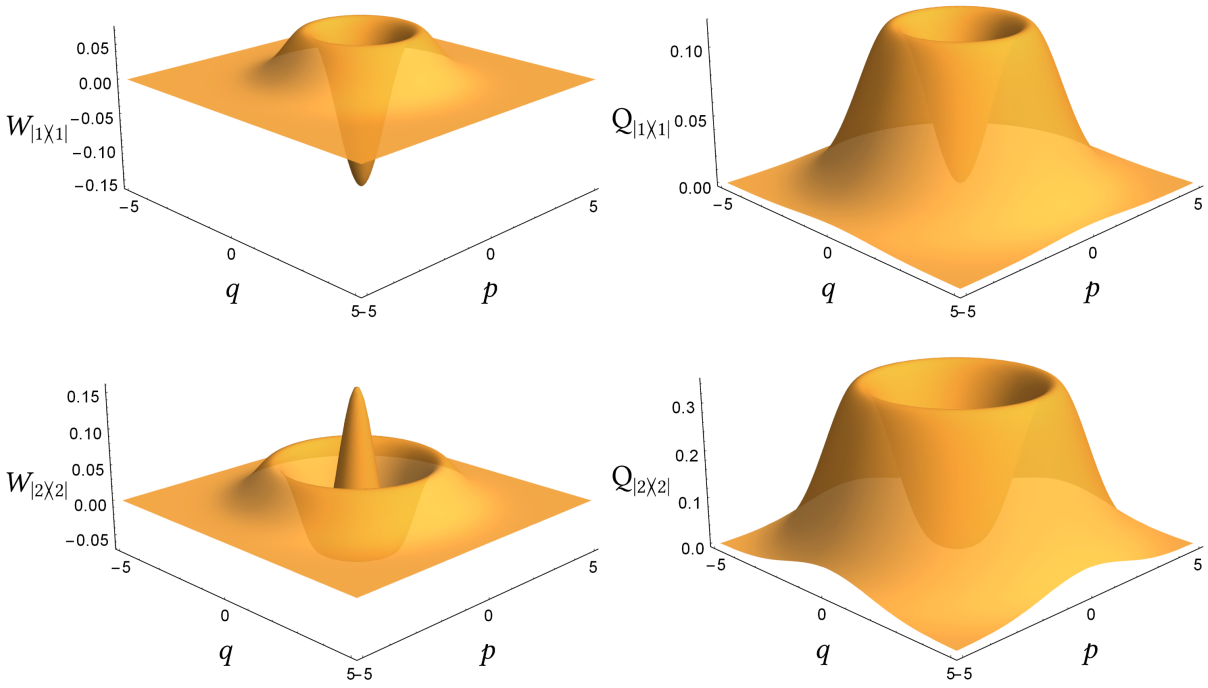

Fig. 1.6 The Wigner function (left) and Q function (right) of the Fock states $|1\rangle$ (top row) and $|2\rangle$ (bottom row).

As remarkable on the plots and equations (1.114) and (1.117), the Wigner and Q functions of any Fock state are invariant under a phase-space rotation. This property stems from their completely defined number of photons, resulting in a completely undefined phase[1].

1.4.2 Wigner negativity

Quantum advantage. It has been known for some time now that entirely Gaussian systems, i.e. for which initial states, operations and measurements are Gaussian, are easy to simulate with classical computers [Bartlett 02]. An interesting question, for both academic research

[1]The fundamental reason of this relation between phase and photon number is the fact that the phase-space operator $\hat{R}(\theta) = \mathrm{e}^{-\mathrm{i}\theta\hat{n}}$ is generated from the number operator $\hat{n}$.

and private research, is then to know what are the conditions for a non-Gaussian system to be hard to simulate with classical computers, or in other words, to reach the so-called *quantum advantage*.

As advertised in the manuscript introduction, quantum advantage could lead to building quantum simulators or quantum computers with expected large impact on both the industrial and research worlds, with numerous applications.

As it turns out, reaching quantum advantage requires more than merely non-Gaussianity. It has been shown that Wigner negativity, i.e. the presence of negative values in a state, an operation or a measurement, is a necessary requirement for implementing any type of protocol that cannot be efficiently simulated by a classical computer [Mari 12, Veitch 13, Rahimi-Keshari 16]. In other words, Wigner negativity is necessary to reach quantum advantage. In particular, this makes the search for Wigner negative states very attractive.

However, it is worth noting that Wigner negativity is not a sufficient condition. There actually exist many quantum systems involving Wigner negativity that can be efficiently simulated [García-Álvarez 20].

An interesting approach is then to look for a system that is known to lead to a quantum advantage. A fundamental example in recent research is Gaussian Boson sampling [Hamilton 17], where squeezed vacuum states are sent to a multiport interferometer and are measured by photon number resolving detectors at the output. Note that in such systems, the Wigner negativity manifests in the photon counting measurement. Despite ongoing debate in the community about the practicality of this specific circuit, Gaussian Boson sampling can be used to produce Wigner negative states when one output of the interferometer is not measured. This is actually the key Wigner negativity resource in a recent blueprint for photonic quantum computation presented in [Bourassa 21] and further improved in [Tzitrin 21].

Witnessing Wigner negativity Up to now, we presented the Fock states as examples of pure non-Gaussian states (for $n > 0$). As we have seen, they feature Wigner negativity. Hudson's theorem actually generalizes this result for pure states: a pure state has a non-negative Wigner function if and only if the state is Gaussian [Hudson 74]. In other words, all non-Gaussian pure states exhibit Wigner negativity. While this result was shown for single-mode states in [Hudson 74], it was generalized to multimode states in [Soto 83].

However, for non-pure states, there exist no such theorem, since there are many mixed non-Gaussian states which are described by a positive Wigner function. Let us take for example the mixed state

$$(1-\gamma)\,|0\rangle\langle 0| + \gamma\,|1\rangle\langle 1| \tag{1.118}$$

It is a non-Gaussian state for any $\gamma > 0$. However its Wigner function is negative only for $\gamma > 1/2$, as one can easily show by adding the Wigner function of both the vacuum and the Fock state $|1\rangle$.

This example, besides shedding light on the complexity of identifying Wigner negative states, also brings forth another idea: the construction of witnesses for Wigner negativity. For this small class of non-Gaussian states parametrized by $\gamma \in]0, 1]$, the state in equation (1.118) is Wigner negative if and only if its fidelity to Fock state $|1\rangle$ is over 0.5. Let us show that

we can derive a more general witness for Wigner negativity using the fidelity of any (mixed) experimental state $\hat{\rho}$ to the Fock state $|1\rangle$ or to a sum of odd Fock states.

Let use reproduce here the alternative expression of the Wigner function (1.36)

$$W_{\hat{\rho}}(\alpha) = \frac{2}{\pi} \mathrm{Tr}\left[\hat{D}(\alpha)\hat{\Pi}_{\mathrm{P}}\hat{D}^{\dagger}(\alpha)\hat{\rho}\right] \tag{1.119}$$

where $\hat{\Pi}_{\mathrm{P}} = \sum_{k\geq 0}(-1)^k |k\rangle\langle k|$ is the parity operator.

The parity operator may be re-written as

$$\hat{\Pi}_{\mathrm{P}} = \hat{\mathbb{1}} - 2\sum_{k\geq 0} |2k+1\rangle\langle 2k+1| \tag{1.120}$$

so that we can obtain the following inequality from equation (1.119) by truncating the series of odd term in equation (1.120) to an arbitrary integer $n > 0$

$$W_{\hat{\rho}}(\alpha) \leq \frac{2}{\pi}\left[1 - 2\sum_{k=0}^{L-1} \langle 2k+1|\hat{D}^{\dagger}(\alpha)\hat{\rho}\hat{D}(\alpha)|2k+1\rangle\right] \tag{1.121}$$

where we used the positive semi-definite property of $\hat{\rho}$.

Let us then define the witnesses of Wigner negativity $\omega_{\hat{\rho}}(\alpha, L)$ as

$$\omega_{\hat{\rho}}(\alpha, L) = \sum_{k=0}^{L-1} \langle 2k+1|\hat{D}^{\dagger}(\alpha)\hat{\rho}\hat{D}(\alpha)|2k+1\rangle \tag{1.122}$$

From equation (1.121), we deduce the following witness property of the quantities $\omega_{\hat{\rho}}(\alpha, L)$

$$\omega_{\hat{\rho}}(\alpha, L) > 0.5 \implies W_{\hat{\rho}}(\alpha) < 0 \tag{1.123}$$

holding true for any $L > 0$ arbitrarily chosen. Textually, if $\omega_{\hat{\rho}}(\alpha, L) > 0.5$ for any $L > 0$ then the Wigner function of the state $\hat{\rho}$ is negative at α.

At any point $\alpha \in \mathbb{C}$ in the phase space, the Wigner negativity at this point can be probed using the witnesses $\{\omega_{\hat{\rho}}(\alpha, L)\}$. Also, inequality (1.121) becomes an identity at large L. We then deduce that for any (mixed) state described by a negative Wigner function, at least one of the quantities $\omega_{\hat{\rho}}(\alpha, L)$ witnesses its negativity. In this sense, these witnesses go beyond other Wigner negativity witnesses introduced in [Mari 11, Fiurášek 13].

These witnesses have been improved recently in [Chabaud 21a] to offer tighter bounds, using semi-definite algorithms.

Let us now consider the witness at $L = 1$ and $\alpha = 0$. This witness $\omega_{\hat{\rho}}(0, 1)$ is directly equal to the fidelity to the Fock state $|1\rangle$, i.e. $\langle 1|\hat{\rho}|1\rangle$. Equation (1.123) then reads: if the fidelity of any state $\hat{\rho}$ to the Fock state $|1\rangle$ is greater than 0.5, then the Wigner function of $\hat{\rho}$ is negative at the origin of the phase space. For instance, we find back that the states $(1-\gamma)|0\rangle\langle 0| + \gamma|1\rangle\langle 1|$ are Wigner negative for $\gamma > 0.5$.

Let us generalize this idea in the context of certification, which will be further introduced in chapter 4. Consider we want to certify a specific property of the experimental state $\hat{\rho}$, and we can estimate a quantity which witnesses this property when above a certain value. We then refer to this value as *witness threshold*: certifying the witness is above its witness threshold certifies the property of the state $\hat{\rho}$.

Wigner negativity volume As a side note, there exists several measure of Wigner negativity. Using the lowest value of the Wigner function as a measure for Winger negativity is inadequate to classify non-Gaussian states, as it yields counter-intuitive results. For instance, the Fock state $|1\rangle$ would be more Wigner negative than Fock state $|2\rangle$, as can be seen on the plots 1.6. A more appropriate measure is the *negativity volume* introduced in [Kenfack 04], defined as

$$\mathrm{N}_{\mathrm{vol}}(\hat{\rho}) = \int \mathrm{d}\vec{x} \left| W_{\hat{\rho}}(\vec{x}) \right| - 1 \tag{1.124}$$

Form the normalization of the Wigner function, the negativity volume $\mathrm{N}_{\mathrm{vol}}(\hat{\rho})$ is negative if and only if the Wigner function is negative. From Liouville's theorem, the negativity volume is unchanged under any Gaussian unitary operation [Walschaers 21].

While the negativity volume is a theoretical interesting tool for classifying states, it has proven hard to witness or measure experimentally. In the next section, we describe more practical non-Gaussian hierarchies. In particular, we introduce the stellar rank which, with the Wigner negativity, are the key features which we aim at certifying in this work.

1.4.3 Stellar rank and quantum non-Gaussianity

In this subsection, we focus on classifying the non-Gaussian states, which leads us to describing the stellar hierarchy introduced in [Chabaud 20c]. In particular, we present some results of our paper [Chabaud 21d] in the subparts 1.4.3.5 and 1.4.3.6. For clarity purposes, most demonstrations are not reported here.

As mentioned before, when considering non-pure states, Hudson's theorem does not apply, leaving us with a large and wild set of non-Gaussian states. In addition to mixed non-Gaussian states of the form of equation (1.118), another striking example is simply the sum of two Gaussian states, which results in a non-Gaussian one. For instance the sum of two coherent states of opposite amplitude $\alpha \neq 0$

$$\tfrac{1}{2}(|\alpha\rangle\langle\alpha| + |-\alpha\rangle\langle-\alpha|) \tag{1.125}$$

The Wigner function of the state (1.125) is simply the sum of the Wigner function of each coherent states $|\alpha\rangle$ and $|-\alpha\rangle$, which is positive but not a Gaussian function.

Following [Walschaers 21], we generalize the example of equation (1.125) by considering any convex combinations of Gaussian states, which form the set

$$\mathscr{G} = \left\{ \hat{\rho} \text{ such that } \hat{\rho} = \sum_i p_i \, |\psi_{\mathrm{G},i}\rangle\langle\psi_{\mathrm{G},i}| \right\} \tag{1.126}$$

where $|\psi_{\mathrm{G},i}\rangle\langle\psi_{\mathrm{G},i}|$ are pure Gaussian states labeled by i and p_i is a probability distribution on these labels i.

Since any state in the set $\mathscr{G}$ has a positive Wigner function, these states are of limited interest for quantum information. On the other hand, the states that lie outside the set $\mathscr{G}$ are named *quantum non-Gaussian states* [Genoni 13]. However, there still exist quantum non-Gaussian states which have a positive Wigner function, as we show below.

Quantum non-Gaussianity has been studied using photon counting statistics [Filip 11, Straka 14, Straka 18]. This research resulted in a complete hierarchy of "genuine n-photon quantum non-Gaussian" states [Lachman 19].

Let us present a generalization and formalization of these ideas introducing the *stellar rank* [Chabaud 20c]. Note that the resulting *stellar hierarchy* matches the genuine n-photon hierarchy of [Lachman 19].

Our goal in this subsection is two-fold. We want to introduce the notion of stellar rank, and shed light on its properties. We also want to lay out the framework for the certification of this property. As we will see, the witnesses of stellar rank rely on well chosen target pure states, which we will usually denote $|\psi\rangle$. Hence the relevance of spending time on the stellar rank of pure states.

In the following, we first define the stellar rank for single-mode pure states and show that the induced stellar hierarchy is robust. Then we define the stellar rank for single-mode non-pure states, and show that the stellar robustness can be used as a tool for certification. Lastly, we discuss the generalization of the stellar hierarchy to multimode states, and the link between stellar rank and quantum advantage.

1.4.3.1 Stellar hierarchy of single-mode pure states

As mentioned before, a pure state is non-Gaussian if and only if its Wigner function is negative, which is equivalent to its Q function having zeros.

Following this lead, it was shown that the zeros of the Q function form a discrete set. Moreover, the Q function of a single-mode pure state is completely determined by the distribution of its zeros in the phase space [Chabaud 20c] up to Gaussian operations.

This motivates the definition of the *stellar rank* $r^\star(|\psi\rangle)$ of a pure state $|\psi\rangle$ as the number of zeros of its Q function counted with multiplicity, divided by two[1]. In particular, the stellar rank is invariant under Gaussian operations.

Since any pure state is non-Gaussian if and only if its Q function has zeros, the pure Gaussian states are the pure states with stellar rank 0. For instance, the coherent states have a null stellar rank as can be checked with the expression (1.65) of their Q function.

Let us consider the Fock states described in subsection 1.4.1. From equation (1.116), the Q function of a Fock state $|n\rangle$ has $2n$ zeros, leading to a stellar rank

$$r^\star(|n\rangle) = n \tag{1.127}$$

Note that the stellar rank may be infinite, as states may be described by a Q function with an (discrete) infinite number of zeros. Notable examples are the Schrödinger cat states [Yurke 86], and the Gottesman-Kitaev-Preskill (GKP) states [Gottesman 01]. While these non-Gaussian states carry much attention in modern research, they are not the focus of this PhD work.

More generally, as mentioned before the Q function of a single-mode pure state is completely determined by the distribution of its zeros in the phase space up to a Gaussian oper-

[1] We use the same notation as introduced in [Chabaud 20c] with the star $\cdot^\star$, which is not the same notation as for the complex conjugation which writes $\cdot^*$.

ation. For finite stellar rank pure states $|\psi\rangle$, this stems formally from the following unique[1] decomposition [Chabaud 20c]

$$|\psi\rangle = \frac{1}{\mathcal{N}} \left[\prod_{i=1}^{r^\star(|\psi\rangle)} \hat{D}(\alpha_i)\, \hat{a}^\dagger\, \hat{D}(\alpha_i)^\dagger \right] |G_\psi\rangle \tag{1.128}$$

where $\{\alpha_i\}$ are the zeros of the Q function counted with half multiplicity, $\{\hat{D}(\alpha_i)\}$ are the corresponding displacement operators, $|G_\psi\rangle$ is a Gaussian state, and $\mathcal{N}$ is a normalization constant.

In particular, the decomposition (1.128) shows that the stellar rank can be interpreted as the minimal number of photon additions (i.e. application of the creation operator $\hat{a}^\dagger$) needed to engineer the state from the vacuum, together with Gaussian operations. In [Chabaud 21d], we further show that a single-photon subtraction may only increase the stellar rank by at most 1. Putting these results together, we can assert that any pure state of finite stellar rank n cannot be engineered with less than n single-photon additions and/or subtractions, together with Gaussian operations.

Let us now classify the single-mode pure states using their stellar rank. We define the sets R_n of states with stellar rank equal to n, which writes

$$R_n = \{|\psi\rangle \in \mathscr{H}_1 \text{ such that } r^\star(|\psi\rangle) = n\} \tag{1.129}$$

where $\mathscr{H}_1$ is a single-mode state Hilbert space, and n may be infinite.

The sets $\{R_n\}$ form then the *stellar hierarchy*. Note that the sets R_n form a well defined partition over the whole considered single-mode state Hilbert space. Figure 1.7 illustrates the *stellar hierarchy*, showing at least one representative of each set R_n, using the provided examples. The interpretation of the stellar rank as the minimal number of photon additions is also pictured.

1.4.3.2 Stellar robustness

A key property of the stellar hierarchy is the *stellar robustness*. In simple words, any pure states of finite stellar rank is robust in the sense that it is only surrounded by states of equal or higher stellar rank.

To formalize this idea, [Chabaud 20c] defined the *stellar robustness* $R^\star(|\psi\rangle)$ of a pure state $|\psi\rangle$ as the trace distance between this state and the nearest possible pure state of lower stellar rank as

$$R^\star(|\psi\rangle) = \inf_{r^\star(|\phi\rangle)<r^\star(|\psi\rangle)} D(|\phi\rangle, |\psi\rangle) \tag{1.130}$$
$$\text{with} \quad D(|\phi\rangle, |\psi\rangle) = \sqrt{1 - |\langle\phi|\psi\rangle|^2}$$

where $D(|\phi\rangle, |\psi\rangle)$ is the *trace distance* between the states $|\phi\rangle$ and $|\psi\rangle$[2].

[1] Up to reordering the factors in the product of over the zeros of the Q function.

[2] The name "trace distance" stems from the identity $|\langle\phi|\psi\rangle|^2 = \mathrm{Tr}[|\phi\rangle\langle\phi|\,|\psi\rangle\langle\psi|]$, and the fact that it defines a proper distance over the state Hilbert space.

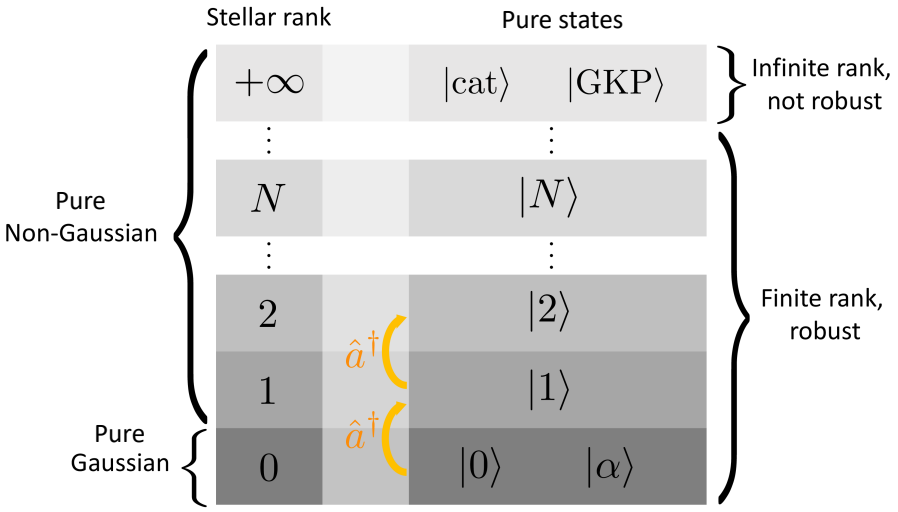

Fig. 1.7 Stellar hierarchy. The right column gives examples of pure states of each stellar rank, which corresponds to the minimal number of photon additions $\hat{a}^\dagger$ necessary to obtain the state from the vacuum. All states of finite stellar rank are robust, i.e., they only have states of equal or higher stellar rank in their close vicinity.

Formally, any state $|\psi\rangle$ of finite stellar rank is *stellar robust*, which writes $R^\star(|\psi\rangle) > 0$ [Chabaud 20c]. This means that the trace distance between $|\psi\rangle$ and any other state of lower rank is non-zero. In other words, there exists a ball of non-zero radius around $|\psi\rangle$ in the state Hilbert space which only contains states of equal or higher stellar rank.

Note that infinite stellar rank states are not stellar robust, i.e. their stellar robustness is zero. More precisely, they are not isolated from lower stellar rank states. This means that any state of infinite stellar rank can be approximated arbitrarily well by finite rank states. However the required finite stellar rank has to go arbitrarily high as you get close. The finiteness of the robustness of some pure states is given in figure 1.7.

1.4.3.3 Stellar hierarchy of single-mode non-pure states

We can naturally extend the definition of the *stellar rank* to a general mixed state $\hat{\rho}$ via a convex roof construction as

$$r^\star(\hat{\rho}) = \inf_{\substack{p_i,|\psi_i\rangle \text{ s.t.} \\ \hat{\rho}=\sum_i p_i|\psi_i\rangle\langle\psi_i|}} \sup_i r^\star(|\psi_i\rangle) \tag{1.131}$$

In other words, we minimize over all possible decompositions of $\hat{\rho}$ in pure states, where we take the highest stellar rank in each decomposition.

Previously, we saw that the pure Gaussian states are the pure states of stellar rank zero. From equation (1.131), we deduce then that a mixed state has a zero stellar rank if and only if

it can be expressed as a mixture of pure Gaussian states. This writes formally

$$r^\star(\hat{\rho}) = 0 \iff \hat{\rho} \in \mathscr{G} \tag{1.132}$$

where $\mathscr{G}$ is the set of convex combinations of Gaussian states defined in equation (1.126). Equivalently, any state $\hat{\rho}$ of non-zero stellar rank is a quantum non-Gaussian state.

We understand then that the stellar hierarchy provides a classification of the set of quantum non-Gaussian states. The definition (1.131) seems formal, in the way that it seems unclear how to rank experimental (mixed) states in practice. It turns out that it allows for certifying its their stellar rank, using the stellar robustness of pure states.

1.4.3.4 Witnessing the stellar rank using the stellar robustness

As we saw in 1.4.3.2, the pure states of finite stellar rank are stellar robust, in the sense that if another pure state is close enough, it shares the same stellar rank or higher. While not a priori obvious, this is also true for another mixed state.

The stellar robustness $R^\star(|\psi\rangle)$ of a pure state $|\psi\rangle$, defined in equation (1.130), can be shown equal to the infinimum of $\sqrt{1-\mathrm{Tr}[\hat{\rho}\,|\psi\rangle\langle\psi|]}$ over (mixed) states $\hat{\rho}$ of stellar rank lower than $r^\star(|\psi\rangle)$, i.e. [Chabaud 20c]

$$R^\star(|\psi\rangle) = \inf_{r^\star(\hat{\rho})<r^\star(|\psi\rangle)} \sqrt{1-\mathrm{Tr}[\hat{\rho}\,|\psi\rangle\langle\psi|]} \tag{1.133}$$

where $\hat{\rho}$ is a pure or mixed quantum state. This extension essentially stems from the convex roof construction of the stellar rank $r^\star(\hat{\rho})$ of the state $\hat{\rho}$ given by equation (1.131).

Let us re-write this result (1.133) by identifying the quantity $\mathrm{Tr}[\hat{\rho}\,|\psi\rangle\langle\psi|]$ with the fidelity of the state $\hat{\rho}$ to the pure state $|\psi\rangle$. In general, for two arbitrary states $\hat{\rho}_1$ and $\hat{\rho}_2$ the fidelity $F(\hat{\rho}_1,\hat{\rho}_2)$ is defined as

$$F(\hat{\rho}_1,\hat{\rho}_2) = \left(\mathrm{Tr}\left[\sqrt{\sqrt{\hat{\rho}_2}\hat{\rho}_1\sqrt{\hat{\rho}_2}}\right]\right)^2 \tag{1.134}$$

where, for each semi-definite operator $\hat{\rho}_i$, $\sqrt{\hat{\rho}_i}$ is its unique positive square root which verifies $\sqrt{\hat{\rho}_i}^\dagger\sqrt{\hat{\rho}_i} = \hat{\rho}_i$.

In our case, we consider the fidelity $F(\hat{\rho},|\psi\rangle)$ of the experimental (mixed) state $\hat{\rho}$ to the pure state $|\psi\rangle$, referred to as target state. In this case, $\hat{\rho}_2 = |\psi\rangle\langle\psi|$ is pure in equation (1.134), which implies $\hat{\rho}_2^2 = \hat{\rho}_2$, i.e. $\sqrt{\hat{\rho}_2} = \hat{\rho}_2$. We then obtain

$$\begin{aligned} F(\hat{\rho},|\psi\rangle) &= \left(\mathrm{Tr}\left[\sqrt{|\psi\rangle\langle\psi|\,\hat{\rho}\,|\psi\rangle\langle\psi|}\right]\right)^2 \\ &= \langle\psi|\hat{\rho}|\psi\rangle\left(\mathrm{Tr}\left[\sqrt{|\psi\rangle\langle\psi|}\right]\right)^2 \\ &= \langle\psi|\hat{\rho}|\psi\rangle \end{aligned} \tag{1.135}$$

where we used the linearity of the trace in the second line, and the purity of $|\psi\rangle\langle\psi|$ in the last one. We deduce the simpler expression of the fidelity for a pure target state

$$F(\hat{\rho},|\psi\rangle) = \mathrm{Tr}[\hat{\rho}\,|\psi\rangle\langle\psi|] \tag{1.136}$$

Using equation (1.136), we can re-write equation (1.133) as

$$R^\star(|\psi\rangle) = \inf_{r^\star(\hat{\rho})<r^\star(|\psi\rangle)} \sqrt{1 - F(\hat{\rho}, |\psi\rangle)} \tag{1.137}$$

The fidelity is a common tool to measure the closeness between two states. Similarly as in 1.4.3.2, we can interpret equation (1.137) as an infinimum of a distance over (mixed) states $\hat{\rho}$ of stellar rank lower than $r^\star(|\psi\rangle)$, with $|\psi\rangle$ pure. We deduce that upon choosing a pure state $|\psi\rangle$ of finite stellar rank, if we can show that the state $\hat{\rho}$ is close enough to $|\psi\rangle$ in fidelity, then we show that the state $\hat{\rho}$ has stellar rank $r^\star(|\psi\rangle)$ or higher.

Let us interpret this result in the spirit of witnessing stellar rank. We re-write equation (1.137) as

$$\sup_{r^\star(\hat{\rho})<r^\star(|\psi\rangle)} F(\hat{\rho}, |\psi\rangle) = 1 - [R^\star(|\psi\rangle)]^2 \tag{1.138}$$

In simple words, equation (1.138) means that the maximum fidelity $F(\hat{\rho}, |\psi\rangle)$ achievable with the states $\hat{\rho}$ of stellar rank lower than $r^\star(|\psi\rangle)$ is equal to $1 - [R^\star(|\psi\rangle)]^2$.

We can interpret equation (1.138) as: given a pure target state $|\psi\rangle$, if the experimental (mixed) state $\hat{\rho}$ satisfies

$$F(\hat{\rho}, |\psi\rangle) > 1 - [R^\star(|\psi\rangle)]^2 \tag{1.139}$$

then it has a stellar rank greater or equal to the stellar rank of $|\psi\rangle$.

We deduce that the fidelity $F(\hat{\rho}, |\psi\rangle)$ to a pure target state $|\psi\rangle$ is a witness for the stellar rank $r^\star(|\psi\rangle)$, with witness threshold equal to $1 - [R^\star(|\psi\rangle)]^2$[1]. In other words, certifying an experimental state $\hat{\rho}$ has a fidelity greater than $1-[R^\star(|\psi\rangle)]^2$ to the pure target state $|\psi\rangle$ certifies in turn that the state $\hat{\rho}$ has a stellar rank greater or equal to $r^\star(|\psi\rangle)$.

Note that for pure states of infinite stellar rank, the corresponding witness threshold is 1, making infinite stellar rank certification impossible with such witnesses.

One question left unanswered if how can we obtain the value of these witness thresholds, i.e. the value of the stellar robustness $R^\star(|\psi\rangle)$. In our paper [Chabaud 21d], this question is answered and the stellar rank witnesses extended, as we present in the following.

1.4.3.5 Extension to k-robustness and robustness computation

We generalize the notion of stellar robustness by defining the *k-robustness* $R^\star_k(|\psi\rangle)$ of a pure state $|\psi\rangle$ as

$$R^\star_k(|\psi\rangle) = \inf_{r^\star(|\phi\rangle)<k} D(|\phi\rangle, |\psi\rangle) \tag{1.140}$$

where the infimum is over all pure states of stellar rank lower than k, and k may be infinite. Note that from its definition, the k-robustness is invariant under any Gaussian operation on the target state $|\psi\rangle$.

[1]For reference, since the witness threshold $1 - [R^\star(|\psi\rangle)]^2$ is equal to the supremum of equation (1.138), it is referred to in [Chabaud 21d] as "achievable fidelity".

The k-robustness $R_k^\star(|\psi\rangle)$ quantifies how much one has to deviate in trace distance from $|\psi\rangle$ to find another quantum state, which has a stellar rank between 0 and $k-1$. For $k = r^\star(|\psi\rangle)$, we recover the stellar robustness defined in equation (1.130).

Consistently, we also define the *robustness profile* of a pure state $|\psi\rangle$ as the set of its k-robustnesses, i.e. the set $\{R_k^\star(|\psi\rangle)\}$.

Similarly as before, the k-robustness also writes

$$R_k^\star(|\psi\rangle) = \inf_{r^\star(\hat{\rho})<k} \sqrt{1 - \mathrm{Tr}[\hat{\rho}\,|\psi\rangle\langle\psi|]} \tag{1.141}$$

from which we obtain

$$\sup_{r^\star(\hat{\rho})<k} F(\hat{\rho}, |\psi\rangle) = 1 - \left[R_k^\star(|\psi\rangle)\right]^2 \tag{1.142}$$

We deduce that given a pure target state $|\psi\rangle$, if the experimental (mixed) state $\hat{\rho}$ satisfies

$$F(\hat{\rho}, |\psi\rangle) > 1 - \left[R_k^\star(|\psi\rangle)\right]^2 \tag{1.143}$$

where $R_k^\star(|\psi\rangle)$ is the k-robustness of the state $|\psi\rangle$, then it has a stellar rank greater or equal to k.

In other words, the fidelity $F(\hat{\rho}, |\psi\rangle)$ to a pure target state $|\psi\rangle$ is a witness for the stellar rank k, with witness threshold equal to $1 - \left[R_k^\star(|\psi\rangle)\right]^2$. We can then deduce a similar statement as before: certifying that an experimental state $\hat{\rho}$ has a fidelity greater than $1 - \left[R_k^\star(|\psi\rangle)\right]^2$ with the pure target state $|\psi\rangle$ certifies in turn that the state $\hat{\rho}$ has a stellar rank greater or equal to k.

An advantage of such extension is that the fidelity to a given target pure state $|\psi\rangle$ may serve as a witness for any lower stellar ranks than its rank, i.e. all stellar ranks $0, \dots, r^\star(|\psi\rangle)$. To benefit from this, we need to derive the value of the corresponding witness thresholds, i.e. the robustness profile of $|\psi\rangle$: $\{R_k^\star(|\psi\rangle)\}$.

In [Chabaud 21d], we show

$$R_k^\star(|\psi\rangle) = \inf_{\hat{G}} \sqrt{1 - \mathrm{Tr}\left[\hat{\Pi}_{k-1}\hat{G}\,|\psi\rangle\langle\psi|\,\hat{G}^\dagger\right]} \tag{1.144}$$

$$\text{with} \quad \hat{\Pi}_k = \sum_{n\geq 0}^{k} |n\rangle\langle n|$$

where the supremum is over the Gaussian unitary operations $\hat{G}$, and $\hat{\Pi}_k$ is the projector onto the subspace spanned by the Fock states $|0\rangle, \dots, |k\rangle$.

Briefly, the demonstration of equation (1.144) consists in noticing that the pure states $|\phi\rangle$ of stellar rank lower than k may be decomposed in the form given by equation (1.128). These states may be viewed as a Gaussian operation $\hat{G}$ applied on a state $|C\rangle$ such that the decomposition of $|C\rangle$ over the Fock basis does not contain terms with higher photon number than $k-1$. In other words, they are left unchanged under the action of the projector $\hat{\Pi}_{k-1}$, i.e. $|C\rangle = \hat{\Pi}_{k-1}|C\rangle$. The fidelity of any pure state $|\psi\rangle$ to the state $|\phi\rangle$ is then bounded by $\mathrm{Tr}\left[\hat{\Pi}_{k-1}\hat{G}^\dagger\,|\psi\rangle\langle\psi|\,\hat{G}\right]$ using the Cauchy-Schwarz inequality. The proof is concluded using this result in the definition (1.140) of the k-robustness $R_k^\star(|\psi\rangle)$. Details are given in appendix D of [Chabaud 21d].

Since single-mode Gaussian operations can be decomposed as a squeezing and a displacement operations[1], the infinimum in equation (1.144) is equivalently run over only two complex parameters. This allows for numerically computing the k-robustness $R_k^\star(|\psi\rangle)$ upon minimizing these two complex parameters.

In figure 1.8, we provide the witness thresholds $1 - \left[R_k^\star(|\psi\rangle)\right]^2$ along the axis of the fidelity to the state $|\psi\rangle$, where $|\psi\rangle$ is the Fock states $|1\rangle, |2\rangle, |3\rangle$, and $|4\rangle$. We can interpret these plots using equation (1.143). For instance, if we show that an experimental state has a fidelity to the target Fock state $|2\rangle$ equal to 0.4, then it has a stellar rank greater or equal to 1. Still this fidelity measurement is not enough to certify it has a stellar rank greater or equal to 2. It would as soon as the fidelity is higher than $1 - \left[R_2^\star(|2\rangle)\right]^2 \simeq 0.557$.

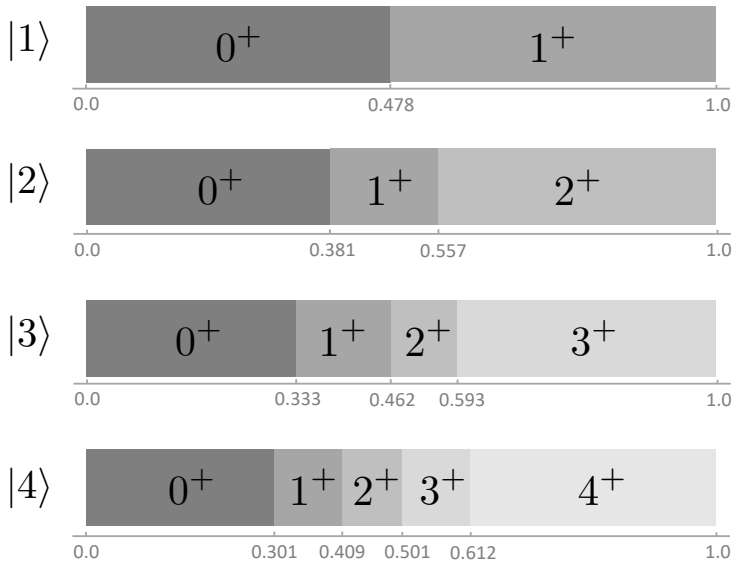

Fig. 1.8 Stellar-rank witness thresholds with target Fock states $|1\rangle$, $|2\rangle$, $|3\rangle$ and $|4\rangle$. For each Fock state $|n\rangle$, the axis of fidelity $F(\hat{\rho}, |n\rangle)$ is drawn along with ticks at the different witness threshold values $\{1 - \left[R_k^\star(|n\rangle)\right]^2\}$, where $\hat{\rho}$ is any state and $k \leq n$. In each fidelity region, the number indicates the minimal stellar rank of the states $\hat{\rho}$ achieving these fidelities.

Let us pay a particular attention on the single-photon Fock state $|1\rangle$. The witness threshold of the Fock state $|1\rangle$ for stellar rank 1 is $3\sqrt{3}/(4e) \simeq 0.478$. This means in particular, coming back to the family of states defined in equation (1.118), that the states $(1-\gamma)\,|0\rangle\langle 0| + \gamma\,|1\rangle\langle 1|$ are quantum non-Gaussian when $\gamma > 0.478$, while their Wigner function is still positive when $\gamma < 0.5$. Thus this provides examples of quantum non-Gaussian states with positive Wigner function.

It is worth noting that the single-photon Fock state $|1\rangle$ is the most robust pure state among all states of stellar rank 1 [Chabaud 21d]. In other words, it is the pure state of stellar rank 1

[1]Indeed in section 1.3, we mentioned that the elementary Gaussian operations are the displacement, squeezing and phase-space rotation operations. Using a general squeezing operator with a complex squeezing parameter allows to take directly into account the phase operation.

with the biggest robustness ball with states of stellar rank 1 or higher. Equivalently, it is the pure state of stellar rank 1 with the lowest witness threshold for certifying stellar rank 1 or higher. This result is true for all the pure states of the form $\hat{G}|1\rangle$ with $\hat{G}$ a Gaussian operation, since the robustness is invariant under Gaussian operations. In particular, it is true for pure single-photon subtracted squeezed vacuum states $\hat{a}\,\hat{S}(\zeta)|0\rangle$, owing to the following identity

$$\hat{a}\,\hat{S}(\zeta)|0\rangle = -\sinh(\zeta)\,\hat{S}(\zeta)|1\rangle \tag{1.145}$$

where we used the property (1.70) of the squeezing operator $\hat{S}(\zeta)$ defined in subsection 1.3.3.

In particular, the stellar rank of pure single-photon subtracted squeezed vacuum states is 1. Experimentally generated (mixed) such states are the states we want to certify, and are described in more details in subsection 1.4.4.

In chapter 4, we explicit a fidelity estimation protocol using the double homodyne detection, which allows for the certification of both stellar rank and Wigner negativity of single-mode states using the witnesses we provided above.

1.4.3.6 Towards witnessing the stellar-rank of multimode states

In order to give the theoretical foundations for multimode certification, we extend some of the previous results in this part.

Let us first point out that the notion of stellar rank can not be naturally generalized to the multimode states. Indeed, the multimode Q function admits either no zeros, or an uncountable infinite number of zeros [Chabaud 21b, Soto 83]. In particular, this means that some results cannot be generalized, such as decomposition (1.128) [Chabaud 21b].

Still, [Chabaud 21b] generalizes the stellar rank to multimode states as follows. Let us consider the states of the form

$$\hat{G}|C\rangle \tag{1.146}$$

where $\hat{G}$ is a Gaussian operation and $|C\rangle$ is a pure state with bounded support over the multimode Fock basis[1].

Any pure state which admits the decomposition (1.146) has a finite stellar rank, defined as the highest sum of the Fock numbers of the decomposition of $|C\rangle$ in the Fock basis. In other words, the stellar rank of the state $\hat{G}|C\rangle$ is the highest possible photon number of $|C\rangle$.

On the other hand, any state that does not admit the decomposition (1.146) has an infinite stellar rank.

For instance, the multimode state

$$\tfrac{1}{\sqrt{2}}(|1\rangle\otimes|2\rangle\otimes|3\rangle\otimes|0\rangle + |0\rangle\otimes|0\rangle\otimes|0\rangle\otimes|4\rangle) \tag{1.147}$$

has two terms in its decomposition, for which the sum of Fock numbers are 6 and 4. Also, the highest possible photon number is 6. Thus the stellar rank of this state is equal to 6. This multimode generalization of the stellar rank is consistent, as it matches with the single-mode stellar rank for single-mode states.

[1] This means that its decomposition over the Fock basis, given generally by equation (1.22), contains a finite number of terms.

Note that the set of states which admit the decomposition (1.146) is dense in the Hilbert space of pure states, and that the multimode stellar rank is still invariant under Gaussian operations [Chabaud 21b]. As shown in the same reference, the induced multimode stellar hierarchy is robust with respect to the trace distance.

In [Chabaud 21d], we extended the definition of the multimode stellar rank to non-pure states, naturally with the same convex roof construction as in equation (1.131). We also show that the identity (1.144) naturally generalizes to the multimode case, considering general multimode Gaussian operations and projectors on the subspace of multimode states with less than k photons. We refer to our paper for a thorough demonstration. This result allows one to numerically compute the robustness profile of the N-mode target pure states.

For example, we computed the 1 and 2-robustness for the two-mode Fock state $|1\rangle \otimes |1\rangle$. We can then deduce two thresholds for the stellar-rank witness $F(\hat{\rho}, |1\rangle \otimes |1\rangle)$: 0.250 for stellar rank 1 or higher, and 0.478 for stellar rank 2 and higher[1].

In other words, certifying that a two-mode experimental (mixed) state $\hat{\rho}$ has a fidelity to the target state $|1\rangle \otimes |1\rangle$ higher than 0.250 allows us to assert that the state $\hat{\rho}$ is at least of stellar rank 1, and at least stellar rank 2 with a fidelity higher than 0.478.

As is mentioned in chapter 4, [Chabaud 21c] naturally extends the fidelity estimation protocol to multimode states using a multimode version of the double homodyne detection. This opens the path to the stellar-rank certification of multimode states.

1.4.3.7 Stellar rank and quantum advantage

We saw in subsection 1.4.2 that Wigner negativity is a necessary resource in a given quantum system for reaching quantum advantage, i.e. such that the quantum system is hard to simulate with classical computers.

While the stellar rank allows for an insightful classification of the quantum non-Gaussian states, is it also a necessary resource for quantum advantage?

We saw that the stellar rank matches the minimal number of photon additions needed to engineer single-mode pure states of this rank from the vacuum, together with Gaussian unitary operations. Intuitively, the complexity of the generated states should play a role in the hardness to classically simulate a quantum system, and thus the stellar rank too.

[Chabaud 23] answers the previous question by providing an algorithm to classically simulate any quantum system, with a complexity in time which scales exponentially with the stellar rank of the input state and of the measurement. The latter is defined from the stellar rank of the eigenstates of the measurement observables, see the paper for details. More precisely, the scaling is in $r^3 2^r$ in the stellar rank r of the system and polynomial in the other parameters.

This result is then two fold. First, if the stellar rank of a quantum system is null, then this algorithm can efficiently (polynomially) simulate the system. In other words, the stellar rank of a quantum system is a necessary resource for achieving quantum advantage. Second, the exponential scaling of time complexity of the algorithm with the stellar rank shows that the higher the stellar rank, the harder it is for this algorithm to simulate the system. In other words, "the more the merrier". Although, there may be more efficient classical algorithms for

[1] Note that in our paper [Chabaud 21d], the displayed bounds are incorrect in appendix F.3.

specific tasks, this praises for viewing the stellar rank as a potential measure of the hardness to classically simulate a quantum system.

1.4.4 Single-photon subtracted and added squeezed vacuum states

As final examples of non-Gaussian states, we describe here the single-photon subtracted and added squeezed vacuum states. As shown in the next chapter 2, we generate single-photon subtracted squeezed vacuum states in the experiment. In chapter 3, we detail how the subtraction is controlled to subtract a single-photon in an arbitrarily chosen single-mode from a multimode source of light. We also report a theoretical investigation to show similar results for single-photon addition. This motivates the description of such states, and the discussion of their properties in the light of the aforementioned developed tools, namely the Wigner negativity and the stellar rank.

Considering single-mode and pure states, we define single-photon subtracted (resp. added) squeezed state $\left|\psi_\zeta^-\right\rangle$ (resp. $\left|\psi_\zeta^+\right\rangle$) as

$$\begin{cases} \left|\psi_\zeta^-\right\rangle = \dfrac{1}{\sinh(\zeta)} \hat{a}\, \hat{S}(\zeta) \left|0\right\rangle \\ \left|\psi_\zeta^+\right\rangle = \dfrac{1}{\cosh(\zeta)} \hat{a}^\dagger \hat{S}(\zeta) \left|0\right\rangle \end{cases} \tag{1.148}$$

where $\hat{a}$ is the annihilation operator in the considered mode, and $\hat{S}(\zeta)$ is the squeezing operator as defined in subsection 1.3.3, with $\zeta \in \mathbb{R}$.

Using the property (1.70) of the squeezing operator $\hat{S}(\zeta)$, one can straightforwardly show that both $\left|\psi_\zeta^-\right\rangle$ and $\left|\psi_\zeta^+\right\rangle$ are proportional to the pure squeezed single-photon state $\hat{S}(\zeta)\,\hat{a}^\dagger \left|0\right\rangle$. Since they are normalized states, we then deduce that

$$\left|\psi_\zeta^-\right\rangle = \left|\psi_\zeta^+\right\rangle \tag{1.149}$$

We can then assert that both single-mode single-photon subtraction and addition operations result in the same state when applied on a single-mode pure squeezed vacuum state. To observe a difference between the two operations, it is necessary to consider non-pure states or non-single-mode subtraction/addition processes with multimode states. The last of those two cases is developed in depth in chapter 3. In the following, we thus only consider single-mode subtraction/addition operations.

Let us consider experimental (mixed) a multimode null-mean Gaussian state $\hat{\rho}_\mathrm{G}$ on which we apply a single-photon subtraction or addition in a specific single-mode $\vec{\mathbf{g}}$. The density operator of the resulting subtracted state $\hat{\rho}^-$ (resp. added state $\hat{\rho}^+$) writes

$$\begin{cases} \hat{\rho}^- = \dfrac{\hat{a}_{\vec{\mathbf{g}}} \hat{\rho}_\mathrm{G} \hat{a}_{\vec{\mathbf{g}}}^\dagger}{\mathrm{Tr}\left[\hat{a}_{\vec{\mathbf{g}}} \hat{\rho}_\mathrm{G} \hat{a}_{\vec{\mathbf{g}}}^\dagger\right]} \\ \hat{\rho}^+ = \dfrac{\hat{a}_{\vec{\mathbf{g}}}^\dagger \hat{\rho}_\mathrm{G} \hat{a}_{\vec{\mathbf{g}}}}{\mathrm{Tr}\left[\hat{a}_{\vec{\mathbf{g}}}^\dagger \hat{\rho}_\mathrm{G} \hat{a}_{\vec{\mathbf{g}}}\right]} \end{cases} \tag{1.150}$$

$\hat{a}_{\vec{g}}$ is the annihilation operator associated with the subtraction/addition mode $\vec{g}$. Note that the denominators ensure both density operators $\hat{\rho}^{\pm}$ trace to unity, and correspond to the probability of the subtraction/addition.

Since the state $\hat{\rho}_G$ is a null-mean Gaussian state, it is completely characterized by its covariance matrix $\mathbf{V}$, or equivalently by its Gaussian Wigner function given by equation (1.52) which we reproduce here

$$W_{\hat{\rho}_G}(\vec{x}) = \frac{e^{-\frac{1}{2}\vec{x}^\top \mathbf{V}^{-1}\vec{x}}}{(2\pi\sigma_0^2)^N \sqrt{\det \mathbf{V}}} \tag{1.151}$$

While we keep this state $\hat{\rho}_G$ general here, we have in mind a multimode squeezed vacuum state which underwent losses, which models well the Gaussian source of our experiment (see next chapter 2).

During the 5 last years, the group developed a general multimode framework for computing the Wigner function of the states $\hat{\rho}^{\pm}$ given by equation (1.150). In particular, we will us the following expression to compute the Q functions that suit our needs in the rest of the manuscript. We refer to [Walschaers 17a, Walschaers 17b] for the demonstration. The Wigner function of the states $\hat{\rho}^{\pm}$ is given by

$$W_{\hat{\rho}^{\pm}}(\vec{x}) = \frac{1}{2}\left[\vec{x}^\top \mathbf{V}^{-1}\mathbf{A}^{\pm}(\mathbf{V},\vec{g})\mathbf{V}^{-1}\vec{x} - \mathrm{Tr}\left[\mathbf{V}^{-1}\mathbf{A}^{\pm}(\mathbf{V},\vec{g})\right] + 2\right] W_{\hat{\rho}_G}(\vec{x}) \tag{1.152}$$

$$\text{and} \quad \mathbf{A}^{\pm}(\mathbf{V},\vec{g}) = 2\frac{(\mathbf{V} \pm \sigma_0^2\mathbb{1})\mathbf{\Pi}_{\vec{g}}(\mathbf{V} \pm \sigma_0^2\mathbb{1})}{\mathrm{Tr}\left[(\mathbf{V} \pm \sigma_0^2\mathbb{1})\mathbf{\Pi}_{\vec{g}}\right]} \tag{1.153}$$

where the Gaussian Wigner function $W_{\hat{\rho}_G}(\vec{x})$ is given in equation (1.151), $\mathbf{\Pi}_{\vec{g}}$ is the matrix of the projector on the two-dimensional phase space associated with the mode $\vec{g}$ in which the photon was subtracted/added.

While equation (1.152) seems complex at first glance, it mainly is a convenient way of writing the Wigner function in terms of the covariance matrix $\mathbf{V}$ of the initial state $\hat{\rho}_G$. In the single-mode scenario, the Wigner function $W_{\hat{\rho}^{\pm}}(\vec{x})$ in equation (1.152) can be simply written as the product of a second-order polynomial with a Gaussian function

$$W_{\hat{\rho}^{\pm}}(q,p) = \left(d_1^{\pm}\frac{q^2}{\sigma_0^2} + d_2^{\pm}\frac{p^2}{\sigma_0^2} + d_3^{\pm}\right)\exp\left[d_4^{\pm}\frac{q^2}{\sigma_0^2} + d_5^{\pm}\frac{p^2}{\sigma_0^2}\right] \tag{1.154}$$

where $\{d_i^{\pm}\}$ are real coefficients which depend on the matrix elements of the 2×2 covariance matrix $\mathbf{V}$. Similarly, in the multimode scenario, the Wigner function is then the product of a second-order $2N$-variable polynomial with a $2N$-variable Gaussian function.

Note that the single-mode subtraction/addition assumption shows itself in the expression of the matrix $\mathbf{A}^{\pm}(\mathbf{V},\vec{g})$. For general multimode subtraction/addition processes which we describe in more details in later chapter 3, the projector matrix $\mathbf{\Pi}_{\vec{g}}$ is replaced with a weighted sum over all the modes in which the single-photon subtraction/addition may occur (see [Walschaers 17b] for details). In particular, the coefficients $\{d_i^{\pm}\}$ in equation (1.154) would then depend on the probabilities to subtract in the different modes.

The Wigner negativity of the states $\hat{\rho}^{\pm}$ was studied in [Walschaers 17a, Walschaers 17b]. They concluded that the Wigner function of a single-photon added state is always negative,

while for single-photon subtracted state it is true if and only if

$$\mathrm{Tr}\left[\mathbf{V}^{-1}\mathbf{\Pi}_{\vec{\mathbf{g}}}\right] > 2 \tag{1.155}$$

which is convenient as it only depends on the covariance matrix $\mathbf{V}$ of the initial state $\hat{\rho}_{\mathrm{G}}$.

Using the convolution (1.47), we can derive the Q function of the states $\hat{\rho}^{\pm}$ from their Wigner function given in equation (1.152). The derivation is provided in appendix B.2. We find

$$\mathrm{Q}_{\hat{\rho}^{\pm}}(\vec{x}) = \tfrac{1}{2}\left[\vec{x}^{\top}(\mathbf{V}+\sigma_0^2\mathbb{1})^{-1}\mathbf{A}^{\pm}(\mathbf{V},\vec{\mathbf{g}})(\mathbf{V}+\sigma_0^2\mathbb{1})^{-1}\vec{x} - \mathrm{Tr}\left[(\mathbf{V}+\sigma_0^2\mathbb{1})^{-1}\mathbf{A}^{\pm}(\mathbf{V},\vec{\mathbf{g}})\right] + 2\right]\mathrm{Q}_{\hat{\rho}}(\vec{x}) \tag{1.156}$$

$$\text{with} \quad \mathrm{Q}_{\hat{\rho}_{\mathrm{G}}}(\vec{x}) = \frac{\mathrm{e}^{-\frac{1}{2}\vec{x}^{\top}(\mathbf{V}+\sigma_0^2\mathbb{1})^{-1}\vec{x}}}{(2\pi\sigma_0^2)^N\sqrt{\det(\mathbf{V}+\sigma_0^2\mathbb{1})}} \tag{1.157}$$

One can see that expression equation (1.156) is very analogue to equation (1.152), replacing $\mathbf{V}$ by $(\mathbf{V}+\sigma_0^2\mathbb{1})$, except in $\mathbf{A}^{\pm}(\mathbf{V},\vec{\mathbf{g}})$. This can be understood considering the Q function is the convolution of the Wigner function of the subtracted state (1.152) with the Wigner function of the vacuum of covariance matrix $\sigma_0^2\mathbb{1}$, according to equation (1.47).

Note that the expression of $\mathrm{Q}_{\hat{\rho}_{\mathrm{G}}}(\vec{x})$ in equation (1.157) in particular provides the general expression of the Q function of any Gaussian state $\hat{\rho}_{\mathrm{G}}$.

Similarly as for the Wigner function, in the single-mode scenario, the Q function $\mathrm{Q}_{\hat{\rho}^{\pm}}(\vec{x})$ in equation (1.156) can be simply written as the product of a second-order polynomial with a Gaussian function

$$\mathrm{Q}_{\hat{\rho}^{\pm}}(q,p) = \left(c_1^{\pm}\frac{q^2}{\sigma_0^2} + c_2^{\pm}\frac{p^2}{\sigma_0^2} + c_3^{\pm}\right)\exp\left[c_4^{\pm}\frac{q^2}{\sigma_0^2} + c_5^{\pm}\frac{p^2}{\sigma_0^2}\right] \tag{1.158}$$

where $\{c_i^{\pm}\}$ are real coefficients which depend on the matrix elements of the 2×2 covariance matrix $\mathbf{V}$. In the multimode scenario, the Q function is then the product of a second-order $2N$-variable polynomial with a $2N$-variable Gaussian function.

In appendix B.2.2, we verify that the derived Q functions $\mathrm{Q}_{\hat{\rho}^{\pm}}(\vec{x})$ are positive everywhere on the phase space, as they should. In particular, we show

$$\mathrm{Tr}\left[(\mathbf{V}+\sigma_0^2\mathbb{1})^{-1}\mathbf{A}^{\pm}(\mathbf{V},\vec{\mathbf{g}})\right] \leq 2 \tag{1.159}$$

This inequality (1.159) is always saturated for any single-photon added states, pure or non-pure. From equation (1.156), we deduce that the Q function $\mathrm{Q}_{\hat{\rho}^{+}}(\vec{x})$ is zero at $\vec{x}=0$ with multiplicity 2. In other words, the single-mode addition of a photon to a (mixed) experimental Gaussian state $\hat{\rho}$ always lead to a stellar rank 1 state[1].

For single-photon subtracted states, a similar statement applies only for pure states. For any non-pure initial state $\hat{\rho}_{\mathrm{G}}$, the resulting Q function $\mathrm{Q}_{\hat{\rho}^{-}}(\vec{x})$ does not vanish. Determining the resulting stellar rank of such non-pure state is then non-trivial, as it requires to look at all

[1]For multimode states, the stellar rank can be derived as the sum-degree of the polynomial multiplying the exponential in the explicit expression of the Q function in equation (1.156). This definition is equivalent to the one introduced in subsection 1.4.3, see [Chabaud 21b].

possible pure-state decomposition of the density operator $\hat{\rho}$, as required by equation (1.131) (which naturally generalizes to multimode states).

Thanks to the general form of the Q function given in equation (1.156), we are able in chapter 4 to precisely describe the states generated in our experiment. Together with the certification tools developed in the previous subsection, this allows for the simulating the fidelity estimation of our experimental states, and simulate a certification of their stellar rank 1.

For illustration purposes, we compute the Wigner and Q functions of the pure single-mode photon subtracted/added squeezed vacuum state $\left|\psi_\zeta^\pm\right\rangle$, using equations (1.152) and (1.156) simplified to the single-mode pure case, yielding

$$W_{\left|\psi_\zeta^\pm\right\rangle}(q,p) = \left(\frac{1}{\sigma_0^2 s}q^2 + \frac{s}{\sigma_0^2}p^2 - 1\right) W_{\left|\psi_\zeta\right\rangle}(q,p) \tag{1.160}$$

$$\mathrm{Q}_{\left|\psi_\zeta^\pm\right\rangle}(q,p) = \frac{1}{(1+s)(1+1/s)\sigma_0^2}\left(q^2+p^2\right)\mathrm{Q}_{\left|\psi_\zeta\right\rangle}(q,p) \tag{1.161}$$

where the Wigner function $W_{\left|\psi_\zeta\right\rangle}(q,p)$ and Q function $\mathrm{Q}_{\left|\psi_\zeta\right\rangle}(q,p)$ of a pure squeezed vacuum state is given in equations (1.80) and (1.81), and $s = \mathrm{e}^{-2\zeta}$.

The functions $W_{\left|\psi_\zeta^\pm\right\rangle}(q,p)$ and $\mathrm{Q}_{\left|\psi_\zeta^\pm\right\rangle}(q,p)$ are given in figure 1.9. One can see that the Wigner function corresponds to the Wigner function of the Fock state $|1\rangle$ given in figure 1.6 upon which is applied stretching and contraction. This is in agreement with the fact that the state $\left|\psi_\zeta^\pm\right\rangle$ is proportional to the squeezed single-photon state $\hat{S}(\zeta)|1\rangle$, and that the fact that applying a squeezing operation on the state or on the phase space is equivalent for the Wigner function. This last property is not in general true for the Q function. The shape of the Q function in figure 1.9 is in particular not the Q function of the Fock state $|1\rangle$ upon which a squeezing operation is applied. As we will see in chapter 4, the squeezing operation is the only Gaussian operation which does not translate to an equivalent phase-space transformation of the Q function.

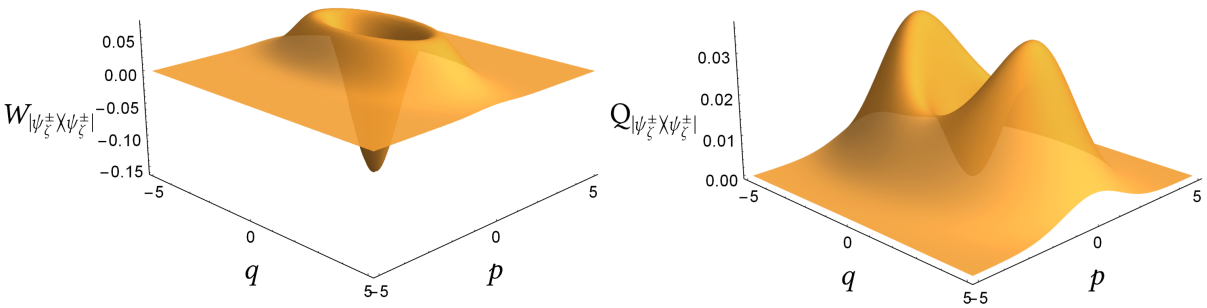

Fig. 1.9 The Wigner function (left) and Q function (right) of the subtracted/added squeezed vacuum state $\left|\psi_\zeta^\pm\right\rangle$, with squeezing parameter $\zeta = \ln(2)/2$ (i.e. $s_{\mathrm{dB}} \simeq 3\,\mathrm{dB}$) and $\sigma_0^2 = 1$.

Chapter 2

Experimental generation and detection of spectrally multimode quantum states

Contents

In this chapter, we describe the experiment used in this work. In the first section, we explain concisely yet completely how the experiment sub-parts work all together, allowing the reader to acquire a clear and global understanding of how the experiment works. Most sub-parts are then described in the subsequent sections. As part of the main results of this thesis, the non-Gaussian operation and the detection sub-parts are detailed in-depth in the later chapters 3 and 4 respectively.

As a consequence of this structure, the reader who seeks only a global understanding of the experiment may only read the first section. Note yet that sections 2.3 and 2.5 describe two significant improvements of the current experiment, as part of this thesis' work.

A note on the multimode aspect of the experiment design. This PhD thesis is part of an ambitious experimental project, which goes beyond this thesis' work. It aims at both generating and certifying *multimode* non-Gaussian states of light. While the generation of non-Gaussian multimode states was done prior to this PhD work as highlighted in the manuscript introduction, the single-mode non-Gaussian certification is the central goal of this work, with the ambition of implementing multimode non-Gaussian certification in the future. Consistently the experiment is designed to be fully multimode (where only the newly developed double homodyne detector remains currently single-mode).

2.1 Experiment design

In this section, we take the reader for a "virtual lab tour", and explain the whole experiment design, see figure 2.1. The experiment is decomposed into numbered modules, each having a specific role. The section is organized according to figure 2.1, describing each main experiment parts defined as the ultrafast pulsed laser **0)** (subsection 2.1.0), the multimode Gaussian state generation **1)** (subsection 2.1.1), the non-Gaussian operation **2)** (subsection 2.1.2), and the detection **3)** (subsection 2.1.3). The extra modules **1.b)** and **3.a)**, delimited by dashed lines in figure 2.1, are described in section 2.6. While these extra modules were not used in the scope of this thesis' work, they show potential for the multimode extension of this work.

2.1.0 Ultrafast pulsed laser

The mode-locked ultrafast pulsed laser **0)** in figure 2.1 is the light source for the whole experiment. As described with more details in subsection 2.2.1, it is a titanium-sapphire laser that relies on a passive Kerr-lens mode-locking operation to generate pulsed light at its output, at a repetition rate of 76 MHz.

As described in the subsection 2.2.2, the successive output pulses form what is called an optical frequency comb (OFC). In a nutshell, an optical frequency comb is the product of an evenly frequency spaced array of Dirac functions with a Gaussian envelope.

In the time domain, the output pulses are ultrashort with a time bandwidth of 90 fs. In the frequency domain, the Gaussian envelope is characterized by 10.3 nm full width half maximum (in intensity) and a central wavelength of 795 nm. Featuring a large spectrum, this light can be viewed as multimode in its frequency-time dimension, in the sense that different parts (or modes) of its spectrum are separately measurable by a detector with a resolution given by

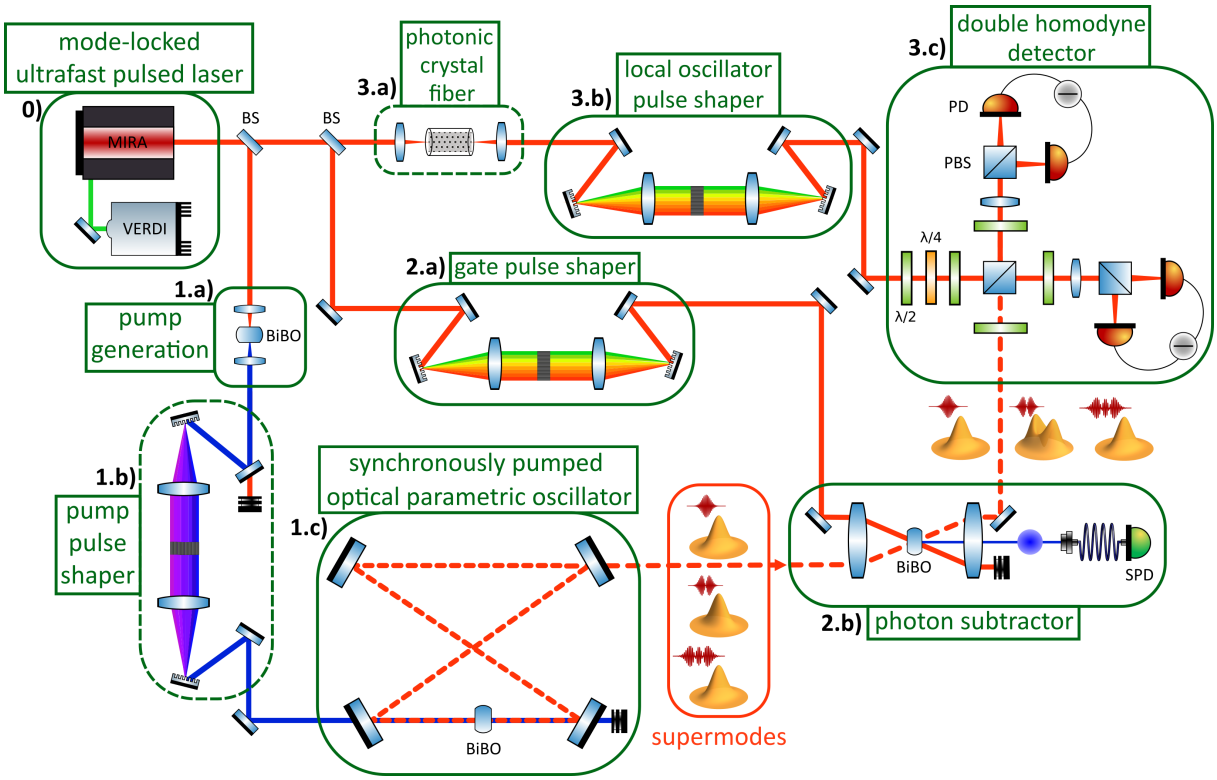

Fig. 2.1 Experiment scheme. The laser source **0)** produces a beam made of a train of femtosecond pulses, which splits into three beams. One beam is up-converted via second-harmonic generation in a BiBO non-linear crystal. The resulting beam is fed to the pulse shaper **1.b)** which shapes its time-frequency mode, and then used as a pump for the parametric down-conversion process that occurs in **1.c)**. A synchronously pumped optical parametric oscillator (SPOPO) **1.c)** amplifies the process, which generates squeezed vacuum states (dashed beam) in well-defined time-frequency modes called "supermodes". The Q functions of the first modes are pictured. Another beam sees its time-frequency mode engineered by another pulse shaper **2.a)**, and is used as a gate for the photon subtraction in **2.b)** applied on the supermodes. A possible outcome is pictured, when the gate mode matches the second supermode. The last beam is time-frequency-engineered with both the photonic crystal fiber **3.a)** and the pulse shaper **3.b)**. It is used as the local oscillator for the double homodyne detector **3.c)**. The measurement in **3.c)** is post-selected on the single-photon detector (SPD) counts of the photon subtractor **2.b)**. The dashed modules **1.b)** and **3.a)** are available but not used in this thesis' work. BS: beamsplitter; PBS: polarizing beamsplitter; $\lambda/2$: half-wave plate; $\lambda/4$: quarter-wave plate. See the main text for details.

current technology. This is where resides the multimode resource used in the experiment. Note that in the spatial domain, we will only consider Gaussian profiles, so that we will often dismiss any spatial field dependency in the remaining of the manuscript.

2.1.1 Multimode Gaussian state generation

The first beam from the laser source **0)** is used to produce Gaussian multimode light through the use of the modules **1.a)**, **1.b)** and **1.c)**, see figure 2.1. In module **1.a)**, the beam is first up-converted in a BiBO crystal via second-harmonic generation, as described in subsection 2.3.1. The resulting 397.5 nm centered spectrum beam is called the *pump* beam. It is then down-converted back to 795 nm via parametric down-conversion in the BiBO crystal in module **1.c)**. In module **1.c)**, a cavity encloses the non-linear BiBO crystal to amplify the process. Its length matches the distance between two pulses, so that each pulse completes one round trip before the next comes in, resulting in a synchronous amplification. The ensemble formed by this cavity and the crystal it houses is then called a synchronously pumped optical parametric oscillator (SPOPO), see subsection 2.3.2.

The second order non-linear process occurring in the BiBO crystal in the SPOPO **1.c)** generates squeezed vacuum states in time-frequency eigenmodes, which we refer to as *supermodes*. The supermode basis is well approximated by the Hermite-Gaussian mode basis. The *Hermite-Gaussian mode n* is a mode (as defined in section 1.1), denoted HG_n, whose spectrum is the n-th-order Hermite-Gaussian function of the frequency space, defined in appendix A.2. Note that the index n starts at 0, with the first Hermite-Gaussian mode HG_0 being a Gaussian function.

As our pulsed light is broadband, the pulses in the cavity experience losses which are not uniform over their whole spectrum. A phenomenon we try to minimize using negative-dispersion mirrors, see subsection 2.3.6. Assuming the intra-cavity losses are spectrally uniform, the output state of the SPOPO, which we refer to as the *signal* state, is a factorized multimode vacuum squeezed state in the supermode basis. In figure 2.1, the Q function of each squeezed vacuum state in the three first supermodes is pictured, at the output of module **1.c)**.

The pulse shaper **1.b)** is not used in the scope of this thesis' work. Its potential role in the multimode certification future project along with the works of [Michel 21] and [Arzani 18] are briefly described in subsection 2.6.1. In short, it can be used to engineer the squeezing distribution of the SPOPO output supermodes.

2.1.2 Non-Gaussian operation

The second beam from the laser source **0)**, called the *gate* beam, is used to perform a non-Gaussian operation on the signal multimode squeezed state in the photon subtractor **2.b)**, see figure 2.1. This operation, named *photon subtraction*, is the topic of chapter 3, along with the photon addition. In particular, details on the experimental realization can be found in section 3.4. In a nutshell, the photon subtraction relies on a non-linear process in another BiBO crystal where the gate beam interacts with the signal beam. As a result two photons,

one from each input beam, are up-converted to a photon which is detected on a single-photon detector. Upon detection, a photon is effectively removed from the signal state.

As explained in chapter 3, the mode in which the photon subtraction occurs is directly given by the time-frequency mode of the gate. For this reason, we use the pulse shaper **2.a)** to engineer the gate time-frequency mode. The ultrafast pulse shaping concept is described in the section 2.2.4. In a nutshell, both amplitude and phase of each frequency band of the gate spectrum can be engineered using the pulse shaper. For example, one can choose the second supermode for the gate mode, which yields a subtracted state in the second supermode. To illustrate this example, the resulting Q functions of the first three supermodes are displayed on the figure 2.1 after **2.b)**. The Q function of the second supermode is not Gaussian anymore, and represents a single-photon subtracted squeezed vacuum state as described in more detail in section 1.4.

2.1.3 Detection

The last and third beam from the laser source **0)**, called the *local oscillator* beam, is used as a reference beam for the double homodyne detector **3.c)**, see figure 2.1. The double homodyne detection is detailed in-depth in chapter 4 section 4.1. In a nutshell, the signal beam is split and measured on two different homodyne detections, whose principle is described in section 2.4. As a result, the double homodyne detection is effectively sampling the Q function of the signal state, which then gives access to all the information on the signal state.

While an ongoing project aims at building a multimode double homodyne detector, the detector **3.c)** is currently designed to measure one mode at a time. This mode is given by the local oscillator time-frequency mode, property which is naturally inherited from the working principle of the homodyne detection, as described in subsection 2.4.2. The mode of the local oscillator can be chosen using another pulse shaper **3.b)**, allowing us to choose the mode on which the measurement is performed.

In the experiment, the double homodyne detection is used to certify the non-Gaussianity of the signal state in the measured mode. Taking for example the pictured state at the output of the photon subtractor **2.b)** in figure 2.1 as the signal state, the goal would be to certify that the signal state is indeed non-Gaussian in the second supermode. Instead of performing a full tomography of the signal state, we use an optimized protocol for this specific task, protocol which is detailed in chapter 4.

The photonic crystal fiber **3.a)** is not used in the scope of this thesis' work. Its potential role in the multimode certification future project along with the work of [Renault 22] are briefly described in subsection 2.6.2. In short, it can be used to broaden the spectrum of the local oscillator beam before its pulse shaper **3.b)** so as to cope with a limitation of the experiment design, inhibiting the efficient measurement of high order modes.

Note that another part of the experiment, the optical phase locking system, is not shown in figure 2.1. The optical relative phase between the signal field and the local oscillator field is locked using a feedback system. The working principle is described in detail in section 2.5. It was implemented during this thesis' work to improve the overall stability, and to significantly simplify the measurement protocol. This improvement is illustrated in subsection 2.5.3, where we show both squeezing measurement protocols, with and without the optical phase lock.

2.2 Ultrafast light

In this section, we first detail the characteristics of our femtosecond laser. We then describe the frequency-temporal structure of the laser output, namely an optical frequency comb. Finally, we explain the working principle of a pulse shaper, used to engineer the time-frequency mode of multiple beams as presented in section 2.1.

2.2.1 Our laser source

The laser used in the experiment belongs to the class of ultrafast pulsed lasers, characterized by the coherent excitation of a substantial number of longitudinal modes within the laser cavity. This broadband excitation, in conjunction with a high degree of coherence, facilitates the generation of ultra-short pulses, reaching temporal durations as brief as the picosecond, femtosecond regimes. The pulsed lasers industry has continuously improved over the years. In recent developments, attosecond pulses (with durations of 10^{-18} seconds) have been successfully measured, providing valuable insight into the dynamics of atomic and molecular in chemical reactions [Krausz 09, Duris 20]. The term “ultrafast" is used to denote the necessity for an exceedingly fast response from a detector in order to temporally resolve such ultra-short pulses.

Our femtosecond laser is a titanium-sapphire ($Ti:Al_2O_3$) MIRA-900-F laser pumped by a continuous-wave beam at 532 nm produced by a VERDI G-15 laser. The gain of the Ti:Sapph crystal is broadband, enabling numerous longitudinal modes within the cavity to see higher gain than losses and oscillate (see figure 2.2, graph (a)). The MIRA laser cavity of approximately 3.92 meters in length, houses a pulse compressor [Fork 84] and a Lyot filter [Lyot 33]. The pulse compressor serves to compensate intra-cavity dispersion, while the Lyot filter facilitates tuning of the pulse central frequency. Passive *mode-locking*, or the coherent oscillation of all longitudinal modes exceeding the laser threshold, is achieved thanks to the Kerr lensing effect within the crystal. This uses a non-linear optical process, the optical Kerr effect, which results in high-intensity light being more focused than low-intensity light (see [Kerr 75b, Kerr 75a, Brabec 92]). A slit tweaking the aperture at the output allows us to add losses to the less focused continuous wave mode, at the advantage of the pulsed modes, which then oscillate.

As a result the laser outputs a 76 MHz repetition rate train of pulses centered at 795 nm, with a 10.3 nm full width half maximum (FWHM)[1] envelope well approximated by a Gaussian function, see graph 2.2 (b). The available average power is around 2.1 W (with ~ MW peak power), while the Verdi pump power is at 13 W. The output pulse is close to be Fourier-transform-limited, with a bandwidth of 90 fs. For a more detailed description of the laser source and beam preparation in our setup see the theses [Pinel 10, de Araujo 12] (in French) or [Cai 15] (in English but less thorough).

[1] In this manuscript, we always consider the full width half maximum in intensity, and should be considered as is if not mentioned.

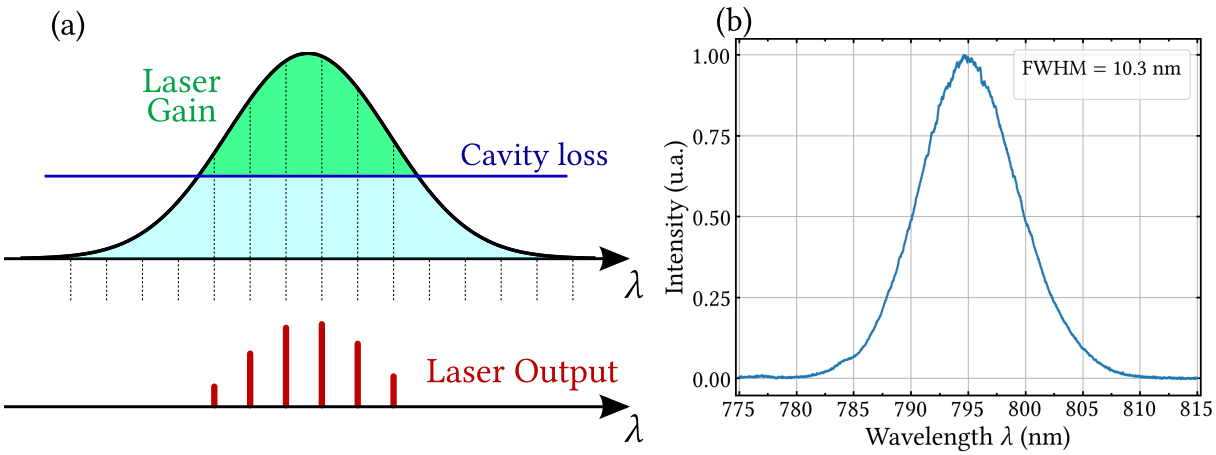

Fig. 2.2 (a): Principle of mode-locking for ultrafast lasers. The large bandwidth of the crystal gain covers many cavity longitudinal modes (represented by the dotted line). Consequently, numerous longitudinal modes have the ability to lase (oscillate). When these modes function collectively and in phase, the laser produces a train of extremely brief pulses, which is known as mode-locked operation. Figure from [Thiel 15]. (b): Measured intensity spectrum of the normalized envelope of the laser output. A Gaussian fit yields a FWHM of 10.3 nm.

2.2.2 Optical frequency combs

The output train of pulses forms what is called an *optical frequency comb* (OFC). Optical frequency combs were initially developed as tools for measuring the cycles of atomic optical clocks. The remarkable phase stability between the "teeth" of the comb allows for the achievement of unparalleled precision in time and frequency measurements. Subsequently, OFC have been employed in a diverse range of applications, as well as fundamental research in metrology, spectroscopy, and studies of optical, atomic, molecular, and solid-state systems [Hall 00, Udem 02, Diddams 10, Fortier 19]. In recognition to their lifelong contributions to the field of precision optical frequency metrology, as well as their technical vision and expertise that culminated in the realization of the OFC, John Hall and Theodor Hänsch were awarded the Nobel Prize in 2005 [Hall 06, Hänsch 06].

Let us now model an OFC. For a detailed description of ultrafast light, we recommend the book [Weiner 11a]. Since our focus is on the modes of light, we can restrict ourselves to the modal description of the classical electric field $\mathbf{E}^{(+)}(\mathbf{r},t)$ of equation (1.8), leaving the quantum operator aspect of equation (1.9) apart. Within this thesis, our interest lies solely in the time-frequency modes of light, hence we drop any spatial dependency of the fields and their spatial mode is considered Gaussian. We write $\mathbf{E}^{(+)}(\mathbf{r},t)$ as $\mathbf{E}^{(+)}(t)$.

The laser output can be described in the time domain as a succession of pulses at regular repetition interval T_r, as represented in figure 2.3. This ensemble of pulses is called a *train of pulses*. A single pulse can be simply modeled under the narrow-band approximation (see subsection 1.1.2) as the product of a plane wave $\mathrm{e}^{-\mathrm{i}\omega_0 t}$ at frequency ω_0, called the *carrier frequency*,

with a Gaussian envelope, denoted $\mathbf{h}(t)$

$$\mathbf{E}^{(+)}_{\text{pulse}}(t) = \mathcal{A}\,\mathbf{h}(t)\,\mathrm{e}^{-\mathrm{i}\omega_0 t} \tag{2.1}$$

with $\mathcal{A}$ the amplitude of the field.

To describe the train of pulses, we would then simply sum the pulses of the form given by equation (2.1) at different times kT_r, with $k \in \mathbb{Z}$ (as the train is spread on an infinite time dimension). However, from one pulse to the next one, the carrier plane wave and envelope are dephased by the quantity $\Delta\phi_{\text{CEP}}$, called the *carrier to envelope phase* (CEP), as shown in figure 2.3. The electric field at the output of the laser is then

$$\mathbf{E}^{(+)}(t) = \mathcal{A}\sum_{k\in\mathbb{Z}} \mathbf{h}(t-kT_\mathrm{r})\,\mathrm{e}^{-\mathrm{i}\omega_0(t-kT_\mathrm{r})}\mathrm{e}^{-\mathrm{i}k\Delta\phi_{\text{CEP}}} \tag{2.2}$$

This accumulating dephasing $\Delta\phi_{\text{CEP}}$ from pulse to pulse is due to the linear dispersion in the cavity of the laser. Let us derive $\Delta\phi_{\text{CEP}}$ using the phase ϕ accumulated in a cavity round-trip by a single pulse, which is given by

$$\phi(\omega) = \frac{L}{c}\omega\, n(\omega) \tag{2.3}$$

where $n(\omega)$ is the effective refractive index[1] inside the cavity of length L. Assuming the intra-cavity dispersion is at most linear[2], we can develop ϕ to the first order around ω_0

$$\begin{aligned} &\phi(\omega) = \phi^{(0)} + (\omega-\omega_0)\phi^{(1)} \\ &\text{with}\quad \phi^{(0)} = \frac{L}{c}\omega_0 n(\omega_0) \\ &\text{and}\quad \phi^{(1)} = \frac{L}{c}\left(n(\omega_0) + \omega_0 \left.\frac{\partial n}{\partial\omega}\right|_{\omega_0}\right) \end{aligned} \tag{2.4}$$

which allows us to re-write equation (2.3) as

$$\begin{aligned} &\phi(\omega) = \frac{\omega L}{v_g} + \omega_0 L\left(\frac{1}{v_\varphi} - \frac{1}{v_g}\right) \\ &\text{with}\quad v_\varphi = \frac{c}{n_0}\quad\text{and}\quad v_g = c\left(n_0 + \omega_0\left.\frac{\partial n}{\partial\omega}\right|_{\omega_0}\right)^{-1} \end{aligned} \tag{2.5}$$

where the phase velocity v_φ corresponds to the speed of the plane wave $\mathrm{e}^{-\mathrm{i}\omega_0 t}$ whereas the group velocity v_g corresponds to the speed of the envelope $\mathbf{h}(t)$. In equation (2.5), we then understand that at each round trip, the pulse phase accumulates a constant term, which we recognize as the carrier to envelope phase $\Delta\phi_{\text{CEP}}$

$$\Delta\phi_{\text{CEP}} = \omega_0 L\left(\frac{1}{v_\varphi} - \frac{1}{v_g}\right) \tag{2.6}$$

[1] When the cavity contains media of different index (air and cavity crystal), $n(\omega)$ is the mean index over the cavity length.

[2] In practice femtosecond lasers are so broadband that non-linear dispersion needs to be compensated.

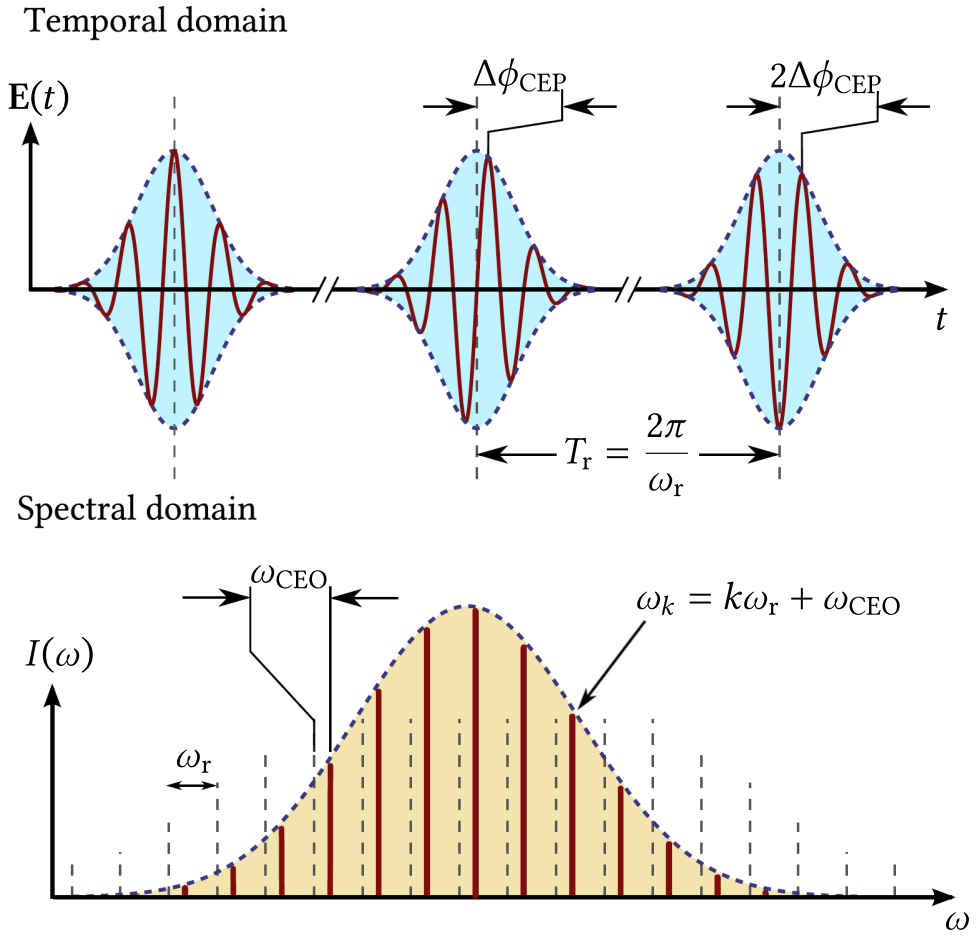

Fig. 2.3 An optical frequency comb (OFC), in the temporal (top) and spectral (bottom) domains. (top): The real electric field $\mathbf{E}(t) = \mathbf{E}^{(+)}(t) + \mathbf{E}^{(-)}(t)$ is a train of single pulses, with accumulating phase $\Delta\phi_{\text{CEP}}$ from pulse to pulse. (bottom): The spectral intensity $I(\omega) = \left|\mathscr{F}\left[\mathbf{E}^{(+)}\right](\omega)\right|^2$ is an evenly-spaced series of Dirac function peaks, modulated by a Gaussian envelope. Figures from [Thiel 15], with adapted notations.

which then arises from the difference of speed between the carrier plane wave and the envelope.

Let us consider the frequency representation of the pulse of train $\mathbf{E}^{(+)}(t)$. As we show in appendix A.3, taking the Fourier transform of equation (2.2) yields

$$\mathscr{F}\left[\mathbf{E}^{(+)}\right](\omega) = \omega_{\mathrm{r}}\mathcal{A}\,\widetilde{\mathbf{h}}(\omega-\omega_0)\sum_{k\in\mathbb{Z}}\delta(\omega-k\omega_{\mathrm{r}}-\omega_{\mathrm{CEO}}) \tag{2.7}$$
$$\text{where}\quad \omega_{\mathrm{CEO}} = \frac{\Delta\phi_{\mathrm{CEP}}}{T_{\mathrm{r}}},\quad \omega_{\mathrm{r}} = \frac{2\pi}{T_{\mathrm{r}}}$$

and both $\mathscr{F}[\cdot]$ and $\widetilde{\cdot}$ represent the Fourier transform defined in appendix A.3.

The time-frequency representation of the laser output is then an *optical frequency comb* (OFC) described by equation (2.7). An OFC is the product of the Gaussian function[1] $\widetilde{\mathbf{h}}(\omega-\omega_0)$ with a series of delta Dirac functions evenly spaced by ω_{r} with an offset ω_{CEO} called the *carrier to envelope offset* (CEO), illustrated by figure 2.3.

Each "tooth" of the OFC is a resonant longitudinal mode of the cavity, with frequency

$$\omega_k = k\omega_{\mathrm{r}} + \omega_{\mathrm{CEO}} \tag{2.8}$$

By resonance in the cavity, each longitudinal mode k has a spectral phase satisfying $\phi(\omega_k) = 2\pi k$. In particular, this resonance condition straightforwardly yields $T_{\mathrm{r}} = L/v_g$, using the expression (2.5) of $\phi(\omega)$.

With a repetition rate of $f_{\mathrm{r}} = 76\,\mathrm{MHz}$, with $f_{\mathrm{r}} = 1/T_{\mathrm{r}}$, the total number of "teeth" is estimated to 10^5 within the envelope FWHM of 10.3 nm[2]. Most optics then see a continuous spectrum profile given by the Gaussian envelope $\widetilde{\mathbf{h}}(\omega-\omega_0)$. In the following, we will refer specifically to the comb structure of our light when necessary.

2.2.3 Group delay dispersion

After the laser cavity, an output pulse may encounter dispersive media with a refractive index that varies with frequency. The larger its spectrum, the most sensitive it will be to these index variations. These effects are then important to consider when working with ultrafast lasers. Let us go one step further than in equation (2.4) in the development of the spectral phase around ω_0 and write

$$\phi(\omega) = \phi^{(0)} + (\omega-\omega_0)\,\phi^{(1)} + \tfrac{1}{2}(\omega-\omega_0)^2\phi^{(2)} + \mathcal{O}((\omega-\omega_0)^3) \tag{2.9}$$

The zero-order $\phi^{(0)}$ and first-order $\phi^{(1)}$ terms represents respectively a relative phase and a temporal delay with respect to the original pulse as detailed for the laser output in subsection 2.2.2. The second-order term $\phi^{(2)}$ is called *group delay dispersion* (GDD), *group velocity dispersion* (GVD), or simply *chirp*. The GDD of a material leads to the time broadening of any incoming pulse. We write the normalized Gaussian envelope of a pulse with zero GDD as

$$\mathbf{h}(t) = \frac{1}{(2\pi\Delta t^2)^{1/4}}\mathrm{e}^{-\frac{t^2}{4\Delta t^2}} \tag{2.10}$$

[1] The Fourier transform of a Gaussian function is again a Gaussian function.

[2] The estimation is equal to $cT_{\mathrm{r}}\mathrm{FWHM}/\lambda_0^2$, with $\lambda_0 = 795\,\mathrm{nm}$ and c the speed of light.

The broadening due to the GDD $\phi^{(2)}$ leads then to a new Gaussian envelope given, up to a phase factor, by [Michel 21]

$$\mathbf{h}'(t) = \frac{1}{(2\pi\Delta t'^2)^{1/4}} \mathrm{e}^{-\frac{t^2}{4\Delta t'^2}} \mathrm{e}^{\mathrm{i}\frac{t^2\phi^{(2)}}{8\Delta t'^4}} \tag{2.11}$$

$$\text{with} \quad \Delta t' = \Delta t \sqrt{1 + \left(\frac{\phi^{(2)}}{2\Delta t^2}\right)^2} \tag{2.12}$$

When there is no GDD, $\Delta t'$ reachs its minimum value Δt and we say the pulse is *Fourier-limited*, and its envelope is given by equation (2.10). Equation (2.12) shows that the shorter the initial pulse is, the broader the resulting pulse will be when going through dispersive media. To give some insights to the reader, a Gaussian Fourier-limited pulse of duration $\Delta t = 90\,\mathrm{fs}$ (as our laser outputs) will see its duration increased to $\Delta t' = 143\,\mathrm{fs}$ with a $\phi^{(2)} = 20\,000\,\mathrm{fs}^2$ GDD, while a Fourier-limited pulse of duration $\Delta t = 180\,\mathrm{fs}$ will see its duration increased to only $\Delta t' = 189\,\mathrm{fs}$ with the same GDD.

Another effect of the GDD stems from the quadratic temporal phase $t^2\phi^{(2)}/(8\Delta t'^4)$ in equation (2.11). This term represents a linear change in the frequency of the carrier from the beginning to the end of the pulse[1].

In the laboratory, we need to avoid or compensate such broadening of the pulses, as it may be detrimental to, for instance, the efficiency of the interference between two beams of different GDD. Any common optical elements in the lab induce more or less positive group delay dispersion $\phi^{(2)}$, such as lenses, beamsplitters, mirrors, etc... To cope with this, we usually use low GDD materials, such as N-BK7. However, this is often not enough to limit the GDD, and another solution is to opt for compensation tools which features negative GDD. For instance, we use a prism compressor at the output of the laser to compensate most of the dispersion induced by the laser cavity, see the thesis [Pinel 10]. A less cumbersome and more local solution consists in using mirrors with negative GDD coatings, a solution we adopt for compensating the dispersion in the SPOPO cavity as described in later subsection 2.3.6. Yet another possibility is to use a pulse shaper, and engineer a negative quadratic phase on the light. See next subsection 2.2.4 for details on pulse shaping.

Another practical matter is the distance between two pulses. Each pair of pulses is spatially separated by the length of the laser cavity, i.e. about 3.92 m. Any time we need to make two beams interfere, we then need to match the path of the two beams by a multiple of 3.92 m, with a precision given by a fraction of the spatial spread of the pulse, of the order of 10 µm. This is achieved using µm precision delay lines, which translates mirrors.

2.2.4 Ultrafast pulse shaping

As we saw in section 2.1, we need to be able to choose the time-frequency mode of our light for the generation of multimode states and its detection, so as to exploit in a controlled manner the large spectrum resource of our pulsed light (see subsection 2.2.1). Femtosecond pulses are extremely short, so that there exist no acousto-optic or electro-optic devices to directly engineer the temporal properties of light. Instead, we can rely on using a *pulse shaper*, which

[1] The instantaneous frequency can be defined as the time derivative of the phase.

is a device that can manipulate the temporal amplitude and phase of a pulse of light. Pulse shaping techniques were originally proposed for pico-second pulses [Heritage 85] and applied later to femto-second pulses [Weiner 88]. The technique we use was further elaborated in [Monmayrant 05, Monmayrant 10, Weiner 11b].

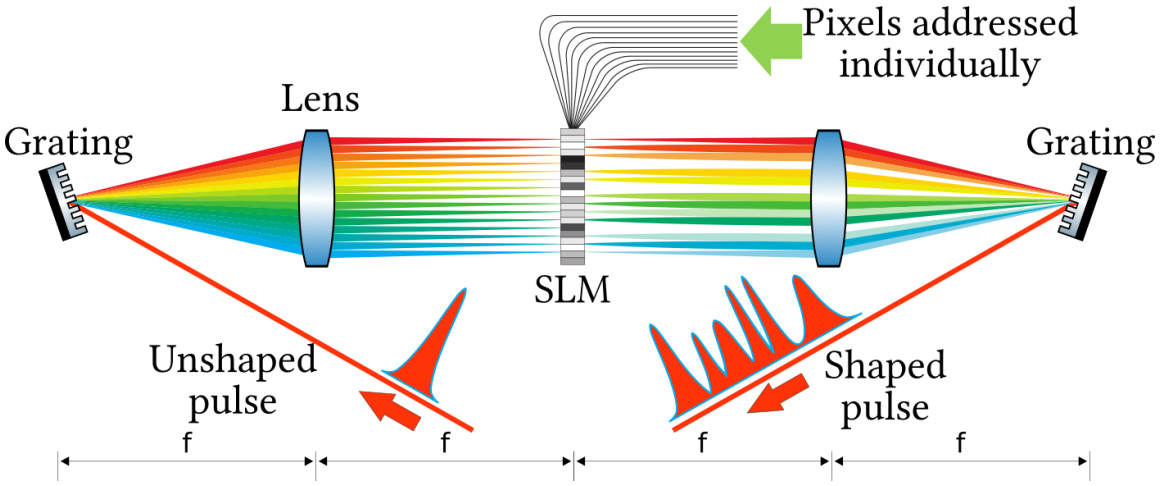

Fig. 2.4 Scheme of a pulse shaper. The spectral components of the incoming pulse are spatially separated with a grating and imaged onto an spatial light modulator (SLM) which imprints a tunable phase shift on each of them. The spectral components are then recombined in a symmetric way. The amplitude of each spectral component is also engineered, see the main text.

Working principle. Figure 2.4 shows the general principle of a pulse shaper. It is composed of two gratings, two lenses and one spatial light modulator (SLM), arranged in a 4-f line, with f the focal length of the lenses. The incoming pulse sees its frequency components spatially spread by the first grating. The result can then be thought as multiple beams, each associated to a frequency, with a propagation direction angle which depends on the frequency. These beams are then imaged onto the SLM by a lens positioned such that the grating and the SLM are at the Fourier plans. Each frequency beam is then focused onto a spatial region of the SLM "screen". In other words, the frequency components of the input light are mapped to spatial coordinates on the SLM screen.

The *SLM screen* is a 2D array of liquid crystals, called pixels, which apply a voltage-controlled phase shift on the incident light. Up to the resolution of the SLM, the phase of each frequency beam may then be chosen, after what the light undergoes the same transformations to recombine into a pulse with an altered spectral phase.

Shaping the spectral amplitude. More than just the phase, we can engineer the amplitude of each frequency beam impinging the SLM screen. Since we can apply any spectral phase pattern on the SLM, called *SLM mask*, we can in particular apply a pattern that mimics the one of a grating. A grating relies on a repetitive phase pattern which results in a diffracted beam due to interference patterns.

We use the second dimension of the 2D SLM mask to imprint such grating (this spatial dimension is then orthogonal to the figure 2.4 plan). The diffractive SLM mask we use is a "saw-tooth" mask, pictured in figure 2.5 (left). The diffracted intensity at the output of such mask depends on its optical depth d_{opt}, as shown in figure 2.5 (right). For details on the properties of this mask, see [Vaughan 05] or [Jacquard 17].

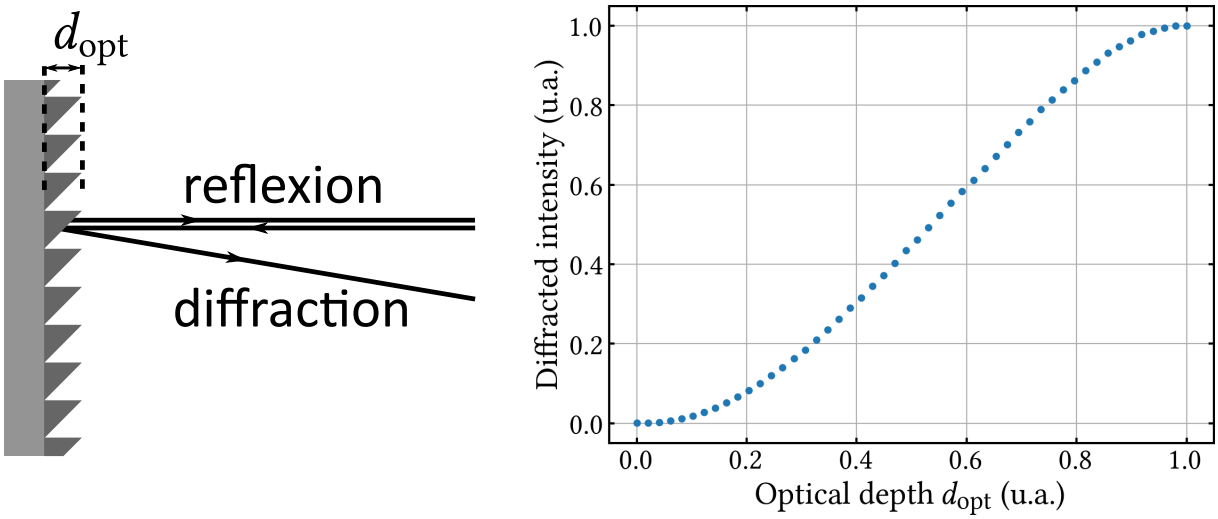

Fig. 2.5 Left: Cut of the SLM in the orthogonal direction with respect to figure 2.4. The saw-tooth mask is pictured, and the optical depth d_{opt} is defined. The mask diffracts partially any incoming beam with an angle that depends on the saw-tooth mask period. Right: Measured intensity of the diffracted beam as a function of the saw-tooth mask optical depth d_{opt}.

A saw-tooth mask is applied on each pixel column. Engineering the optical depth of each column saw-tooth mask allows us to control the amplitude of each frequency beam impinging the SLM. In figure 2.4, the different degrees of gray on the SLM screen illustrate the optical depth applied on each local pixel column, resulting in different amplitude frequency beams at the output.

Note that the output diffracted and non-diffracted beams come out with a different angle (which depends on the common period of the saw-tooth masks), as pictured on figure 2.5. This is used to dump the non-diffracted beam at the output of the pulse shaper by using a pinhole.

Pulse shaper resolution. To resume, a pulse shaper allows one to engineer the time-frequency amplitude and phase of ultrafast light, up to its resolution. To characterize the resolution of a pulse shaper, we use the *complexity*, which can be interpreted as the number of degrees of freedom available to manipulate the input spectrum. We consider two complexities, the pixel complexity and the optical complexity, such that the actual complexity of the pulse shaper is equal to the minimum between those two complexities. While we won't get into the details and refer to [Michel 21] for a detailed complexity analysis, we will give some insights.

The *pixel complexity* is defined as the number of accessible frequency components taking into account the number of pixels on the SLM screen and the spread of the spectral components

on the screen. Given an SLM with a fixed number of pixel, the pixel complexity is maximized when one manages to spread the input spectrum on the whole screen, choosing wisely the focal length of the lens and the number of grooves of the grating.

Due to the optics of spatial Gaussian beams, the larger the input waist the smaller each frequency beam is focused onto the SLM, as depicted in figure 2.4. A single frequency component beam may then spread on several pixels on the SLM and smear the shaping, regardless of the pixel complexity. We refer to this resolution limit as the *optical complexity*. A larger beam then allows for a higher complexity, while being limited by the size of the optic elements or the size of the SLM screen.

Setup technical details. In our setup the SLM is reflective, so that the 4-f line is folded onto itself. This allows the use of the same lens and the same grating twice. Instead of a lens, we use a cylindrical mirror, which acts as a reflective lens on the relevant plane. For insights on how to properly align a pulse shaper, see the theses [Michel 21, Renault 22].

As shown in the section 2.1, three pulse shapers are used in the experiment. Table 2.1 shows the estimated complexity of each pulse shapers. During this PhD, the former gate SLM broke. We replaced it with the former local oscillator (LO) SLM. A new SLM was installed on the LO pulse shaper setup, with upgraded number of pixels, hence the higher pixel complexity. Note though that the optical complexity remains the limiting factor, meaning that we should be able to imprint up to 60 "features" in the LO spectrum.

	Pixel complexity	Optical complexity	SLM reference
LO pulse shaper	218	60	LCOS-SLM X15213-02
Gate pulse shaper	136	60	LCOS-SLM X10468-02
Pump pulse shaper	44	42	LCOS-SLM X10468-05

Table 2.1: Complexities and reference of each pulse shaper used in the experiment pictured in figure 2.1. All the SLM are from Hamamatsu. LO: local oscillator.

2.3 Generation of spectrally multimode squeezed vacuum states

In this section, we describe the source of Gaussian multimode states of the experiment, whose design is represented in figure 2.1. The key concept of our source is the fact that parametric down-conversion (PDC) process acts as a vacuum squeezer. To pump the crystal in which occurs the PDC, we need a new field of carrier frequency $2\omega_0$ where ω_0 is the carrier frequency of our laser source. In our experiment, we do not use a second laser to generate such *pump* field, as it would add the challenge of stabilizing it to a common reference with our main laser. Instead, we use another non-linear process, namely second-harmonic generation (SHG), which is described in subsection 2.3.1. In the subsection 2.3.2, we describe how we enhance the PDC process using a cavity surrounding it, forming a synchronously pumped optical parametric oscillator (SPOPO).

While we detail the non-linear process used for the photon subtraction and addition operations in later chapter 3, in this section we won't get into the details of the SHG and PDC processes that both occur in the BiBO crystal and refer the reader to [Ghotbi 04] for a complete analysis of the BiBO optical properties, along with [Ghotbi 05] for SHG and [Ghotbi 06] for PDC.

2.3.1 Pump generation

In order to bring energy to the squeezing process of our SPOPO, we generate the pump beam by second-harmonic generation (SHG) of our laser source in the BiBO crystal of module **1.a)** in figure 2.1. See [Ghotbi 05] for technical details on the phase-matching conditions of SHG in BiBO.

As we saw in section 2.2, our laser output is an optical frequency comb which contains many frequency components $\omega_k = \omega_{\text{CEO}} + k\,\omega_{\text{r}}$. In the SHG process, each frequency component ω_k of the input comb interacts with any other $\omega_{k'}$ of the same input comb, generating the sum frequency component $\omega_k + \omega_{k'}$ in the output comb . We deduce from the regular structure of the comb that the frequency components of the newly generated comb are $\omega_k = 2\omega_{\text{CEO}} + k\,\omega_{\text{r}}$ with $k \in \mathbb{Z}$, while the new carrier frequency is $2\omega_0$. In particular, the generated frequency comb has the same repetition rate as the input comb.

Let us now consider the envelope of the generated pump field in the frequency domain $\widetilde{\mathbf{h}}_{\text{p}}(\omega)$. The expected spectral profile of the pump envelope is given by

$$\widetilde{\mathbf{h}}_{\text{p}}(\omega) \propto \int_0^\infty \mathrm{d}\omega'\, \widetilde{\mathbf{h}}(\omega')\, \widetilde{\mathbf{h}}(\omega - \omega') \Phi_{\text{SHG}}(\omega, \omega') \tag{2.13}$$

where $\widetilde{\mathbf{h}}(\omega)$ is the envelope of the laser field, and $\Phi_{\text{SHG}}(\omega, \omega')$ is the phase-matching function of the SHG process. In our experiment, the input spectrum has a 10.3 nm full width half maximum (FWHM), and we use a 0.3 mm long BiBO crystal. A Gaussian fit of the measured pump spectrum shown on figure 2.6 yields a FWHM of 3.0 nm. If the phase-matching function $\Phi_{\text{SHG}}(\omega, \omega')$ was sufficiently broad, the pump envelope $\widetilde{\mathbf{h}}_{\text{p}}(\omega)$ would be then proportional to the self-convolution of the input envelope $\int_0^\infty \mathrm{d}\omega'\, \widetilde{\mathbf{h}}(\omega')\, \widetilde{\mathbf{h}}(\omega - \omega')$. The resulting Gaussian would have a FWHM given by the one of the input divided by $2\sqrt{2}$, hence 3.64 nm. The discrepancy with the measured FWHM indicates that the phase-matching function is too narrow and acts as a spectral filter. While the bandwidth of the phase-matching function $\Phi_{\text{SHG}}(\omega, \omega')$ may be increased by reducing the crystal's length, it would decrease the output power. The crystal length of 0.3 mm is a good trade-off between power and bandwidth [Michel 21, de Araujo 12].

2.3.2 Synchronously pumped optical parametric oscillator

We now describe the generation of a spectrally multimode Gaussian state in the module **1.c)** in figure 2.1. A photo of the actual setup is given in figure 2.7 (a), along with a principle scheme in figure 2.7 (b). In this subsection, we give first a brief description of the setup, while in the subsequent subsections we characterizing the output states.

In figure 2.7 (b), the cavity along with the non-linear crystal forms an ensemble called an *optical parametric oscillator* (OPO). In the BiBO crystal, the pump at carrier frequency $2\omega_0$

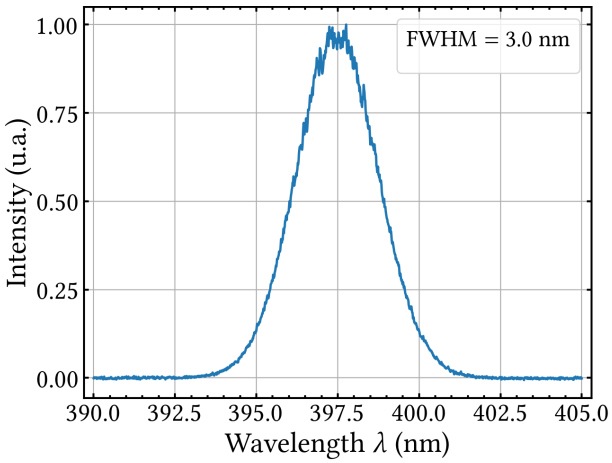

Fig. 2.6 The measured intensity spectrum of the normalized pump envelope $\left|\widetilde{\mathbf{h}}_{\mathrm{p}}(\omega)\right|^2$, with respect to the wavelength $\lambda = 2\pi c/\omega$. A Gaussian fit yields a FWHM of 3.0 nm.

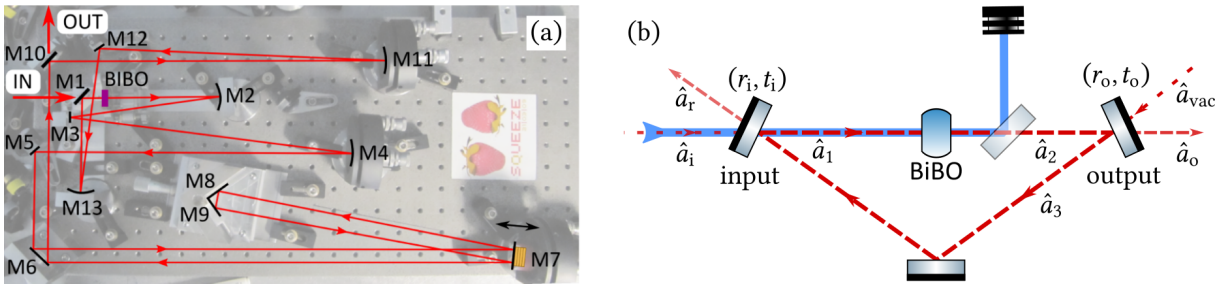

Fig. 2.7 (a) Photo of the synchronously pumped optical parametric oscillator (SPOPO) of the experiment. The mirrors are labeled from M1 to M13, see the text for a description of their roles. (b) Principle scheme of the SPOPO with an input coupler, an output coupler and a BiBO non-linear crystal. The pump beam (in blue) powers the crystal, generating resonant squeezed vacuum (in dashed red) in the cavity. The annihilation operators of the electric field at different positions are represented. The subscripts i, o, L, and vac stand respectively for input, output, losses, and vacuum. The subscripts 1, 2, 3 denote useful other positions in the cavity for the computation in subsection 2.3.4. Note that the pump beam is going through the mirror M2 in the real setup (a).

and the input vacuum at ω_0 interact through parametric down-conversion (PDC), resulting in a squeezed vacuum state at ω_0. The OPO is chosen to enhance the squeezed vacuum in the cavity by matching the mirrors' broadband operating frequency range around ω_0. As the squeezed vacuum inherits the spectral comb structure from the pump, we set the cavity length to match the train of pulses repetition rate $f_r = 1/T_r$. It then takes one cavity round-trip to a newly generated squeezed vacuum pulse before another one is generated by the next pump pulse. All generated pulses are then temporally overlapping, resulting in enhancing the squeezing strength. For this timely reason, the resulting system is called *synchronously pumped optical parametric oscillator* (SPOPO).

Matching the cavity length to the repetition rate $f_r = 76\,\text{MHz}$ means building a cavity of 3.92 m length, the length of the MIRA laser cavity. In practice, we fold the cavity on itself for better compaction of the available optical table space, resulting in using 13 mirrors, see figure 2.7 (a). Some of these mirrors have other roles than simply reflecting the resonant beam:

- M1 is the input coupler with a reflectivity of $r_i^2 = 99.85\%$.
- M10 is the output coupler, with available reflectivity $r_o^2 = 80\%, 70\%$, or 50%, depending on the optics we want to use.
- M2 and M13 are concave spherical mirrors with a curvature radius of 250 mm. M4 and M11 are also concave spherical mirrors but with a larger curvature radius of 6 m. They are used to focus the resonant beam in the 2 mm long BiBO crystal to enhance the non-linear effect. The pump is also focused with a matching waist using lenses before the cavity, not shown in the figure.
- M3 and M7 compensate 150 fs^2 group delay dispersion thanks to their coating. For more on intra-cavity dispersion compensation, see 2.3.6.

To guarantee that the SPOPO cavity is resonant with the central wavelength of the Mira laser, a counter-propagating beam, not depicted in figure 2.7, is measured to supply feedback to a locking system based on the Pound-Drever-Hall (PDH) technique [Drever 83]. The piezo-electric mirror M7 allows then to lock the cavity length in real time. For more details on the PDH technique applied on the SPOPO, see [Renault 22]. For details on the effect of cavity length mismatch on the output intensity, taking into account the comb structure of the light, see [Michel 21].

The general description of the SPOPO provided above does not shed light on the features of the output states. In the subsequent subsections, we start from a simple model without cavity nor losses. Then, we refine the model to take into account the cavity, the losses and finally intra-cavity dispersion (defined in subsection 2.2.3), progressively delving deeper into the physics that shape the SPOPO output states.

2.3.3 Parametric down-conversion as a multimode squeezing operation

We describe here the single-pass parametric down-conversion (PDC) process, without a cavity surrounding it. The PDC occurs in a non-linear BiBO crystal (see [Ghotbi 06] for non-linear

optical properties of BiBO for PDC). The crystal is pumped by an optical frequency comb with "teeth" at frequencies $\omega_{\mathrm{p},k} = 2\omega_{\mathrm{CEO}} + k\,\omega_{\mathrm{r}}$ and carrier frequency $2\omega_0$ (see the description of the pump generation in subsection 2.3.1).

At the photon level, each pump photon of frequency $\omega_{\mathrm{p},k}$ may convert into two correlated photons at lower frequencies $\omega_{\mathrm{s},n}$ and $\omega_{\mathrm{s},m}$ such that $\omega_{\mathrm{p},k} = \omega_{\mathrm{s},n} + \omega_{\mathrm{s},m}$. Taking into account the comb structure of the pump $\omega_{\mathrm{p},k} = 2\omega_{\mathrm{CEO}} + k\,\omega_{\mathrm{r}}$, the down-converted frequencies also follow a comb structure with $\omega_{\mathrm{s},n} = \omega_{\mathrm{CEO}} + n\,\omega_{\mathrm{r}}$ and $\omega_{\mathrm{s},m} = \omega_{\mathrm{CEO}} + m\,\omega_{\mathrm{r}}$. The energy conservation equation $\omega_{\mathrm{p},k} = \omega_{\mathrm{s},n} + \omega_{\mathrm{s},m}$ can then be re-written $k = n + m$. The comb conversion is illustrated in figure 2.8. The generated pulsed light is referred to as the *signal*.

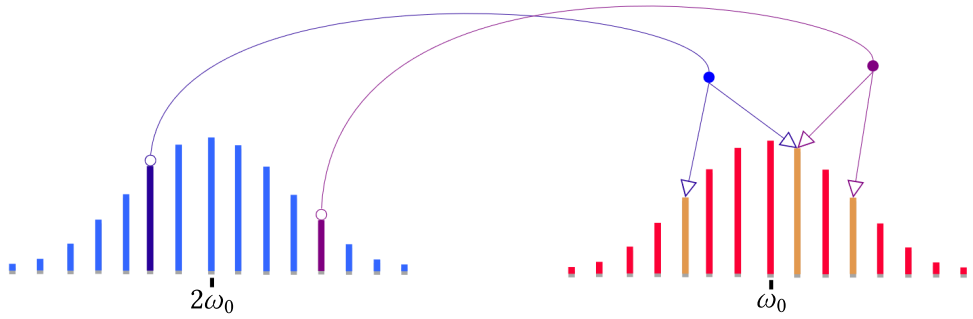

Fig. 2.8 Principle scheme of the parametric down conversion of a frequency comb with carrier frequency $2\omega_0$. A photon from a given "tooth" of the comb probabilistically down-converts to a pair of entangled photons, conserving energy. The teeth of the resulting down-converted comb are then highly entangled. Figure from [Dufour 18] with suitable notations.

Let us write the Hamiltonian $\hat{H}_{\mathrm{PDC}}$ of the PDC process. We describe the pump field in the classical form of equation (2.7), denoting $\widetilde{\mathbf{h}}_{\mathrm{p}}(\omega)$ its spectral envelope. We assume that there are no losses for both the pump and the signal. Assuming that the depletion of the pump is negligible, the Hamiltonian writes

$$\hat{H}_{\mathrm{PDC}} \propto \mathrm{i} \sum_{n,m} J_{nm}(\omega_{\mathrm{s},n}, \omega_{\mathrm{s},m})\, \hat{a}_n^\dagger \hat{a}_m^\dagger + \mathrm{h.c.} \tag{2.14}$$

$$\text{with} \quad J_{nm}(\omega_{\mathrm{s},n}, \omega_{\mathrm{s},m}) = \widetilde{\mathbf{h}}_{\mathrm{p}}(\omega_{\mathrm{s},n} + \omega_{\mathrm{s},m})\, \Phi_{\mathrm{PDC}}(\omega_{\mathrm{s},n}, \omega_{\mathrm{s},m})$$

where Φ_{PDC} is the PDC phase-matching function, $\hat{a}_n^\dagger$ and $\hat{a}_n^\dagger$ are the creation operators associated to the signal frequencies $\omega_{\mathrm{s},n}$ and $\omega_{\mathrm{s},m}$, and h.c. stands for Hermitian conjugate. The function $J_{nm}(\omega_{\mathrm{s},n}, \omega_{\mathrm{s},m})$ is called the *joint spectral amplitude* (JSA) [Grice 01, Mosley 08]. It is possible to perform an eigendecomposition of the JSA using Mercer's theorem (see [Eckstein 12, de Araujo 12]), as $J_{nm}(\omega_{\mathrm{s},n}, \omega_{\mathrm{s},m})$ is real and symmetric. Let Λ_n be the n-th eigenvalue associated with the eigenmode $\vec{\mathbf{v}}_n$ and the annihilation operator $\hat{s}_n$. The eigendecomposition of the JSA allows us to write the Hamiltonian as

$$\hat{H}_{\mathrm{PDC}} \propto \mathrm{i} \sum_{n} \Lambda_n\, \hat{s}_n^{\dagger 2} + \mathrm{h.c.} \tag{2.15}$$

The eigenmodes $\{\vec{\mathbf{v}}_n\}$ are called the *supermodes* [de Araujo 12]. From equation (2.15), we can deduce the evolution operator of the PDC process using $\hat{U}_{\text{PDC}} = \exp\left(-\mathrm{i}\hat{H}_{\text{PDC}}/(2\sigma_0^2)\right)$[1]. Since the Hamiltonian is written as a sum of operators that commute between each other, we can write

$$\hat{U}_{\text{PDC}} = \hat{S}_1(\kappa\Lambda_1) \otimes \cdots \otimes \hat{S}_N(\kappa\Lambda_N) \quad \text{with} \quad \hat{S}_n(\kappa\Lambda_n) = \mathrm{e}^{\kappa\Lambda_n(\hat{s}_n^2 - \hat{s}_n^{\dagger 2})/2} \tag{2.16}$$

where κ is a quantity which depends on the crystal length and non-linearity and on the pump power (see [Michel 21] for an explicit expression of κ), and we recognize each $\hat{S}_n(\kappa\Lambda_n)$ as a squeezing operator with squeezing parameter $\kappa\Lambda_n$ as defined in subsection 1.3.3. Equation (2.16) shows that the PDC process is equivalent to the action of independent squeezing operators in the supermode basis. Since the input state at the signal frequencies is the vacuum state, the output state is then a multimode squeezed vacuum state in the supermode basis.

In subsection 1.3.6, we studied in detail the two-mode squeezed vacuum states. In particular, it was shown that a two-mode squeezed vacuum state becomes a two-mode entangled state upon well chosen change of mode basis. Similarly, the change of mode basis from the supermode basis to the plane wave mode basis allows us to see this state as a highly multipartite entangled state, as shown in [Patera 08]. This stems from the PDC process itself, as described in figure 2.8. Other changes of mode basis can be engineered to partially transfer squeezing resources to entanglement resources, resulting in an engineered graph structure with custom entanglement links between the modes, as shown in [Cai 17]. In this manuscript, we won't get into the details of the multimode entanglement properties of our Gaussian source.

Consistently the associated covariance matrix is given by the pure version of the Bloch-Messiah-Williamson decomposition, see equation (1.96). The change of mode basis $\mathbf{O}_1$ then defines the supermode basis, such that the covariance matrix is simply given in the supermode basis by

$$\mathbf{V}_{\text{PDC}} = \sigma_0^2\, \mathbf{K}_{\text{PDC}}^2 \tag{2.17}$$

with $\mathbf{K}_{\text{PDC}}$ the symplectic matrix representing $\hat{U}_{\text{PDC}}$, defined by

$$\mathbf{K}_{\text{PDC}} = \exp[\text{diag}(-\kappa\Lambda_1, \cdots, -\kappa\Lambda_N, \kappa\Lambda_1, \cdots, \kappa\Lambda_N)] \tag{2.18}$$

The eigenvalues and first supermodes of the decomposition of the JSA corresponding to our experimental parameters are shown in figure 2.9. On the graph (b), the sign of the eigenvalues alternates between positive-valued and negative-valued, meaning that each operator $\hat{S}_n(\kappa\Lambda_n)$ associated to an even-numbered (resp. odd-numbered) supermode $\vec{\mathbf{v}}_n$ squeezes the quadrature $\hat{q}_n$ (resp. $\hat{p}_n$). The distribution of the eigenvalues $\{\Lambda_n\}$ is very broad, meaning that the process is very multimode. A convenient quantity to compute is the *Schmidt number* K, which yields the effective number of modes of the process [Ekert 95]. K is defined as

$$K = \frac{\left(\sum_n \Lambda_n\right)^2}{\sum_n \Lambda_n^2} \tag{2.19}$$

[1] The Hamiltonian $\hat{H}_{\text{PDC}}$ is a dimensionless effective Hamiltonian which takes into account the physical properties of the crystal such as its length.

The Schmidt number of the PDC process is equal to 95 in our experiment. This makes it a significantly large multimode resource. However, using this process as a single pass, i.e. without cavity, would yield low squeezing values. An estimation the constant κ allows us to estimate the squeezing factors to values lower than 0.3 dB. Such squeezing factors are too low for our desired application, as shown in later chapter 4.

On the graph 2.9 (b), the shape of each supermode $\vec{\mathbf{v}}_n$ is close to the shape of the Hermite-Gaussian mode HG_n defined in appendix A.2. A Gaussian fit of the first supermode yields a FWHM of 4.14 nm.

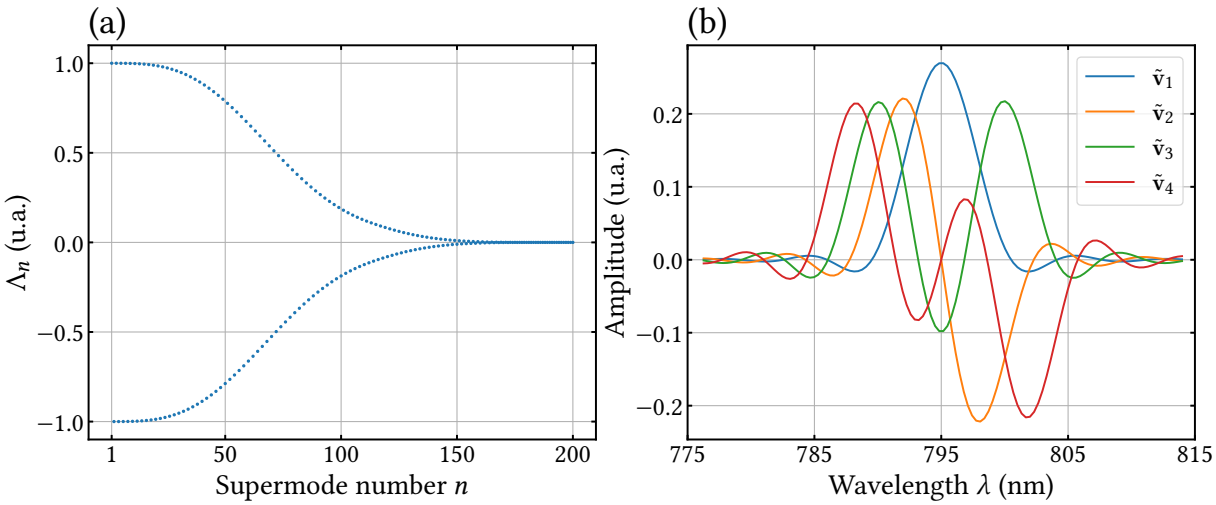

Fig. 2.9 Simulation of the PDC process in a a 2 mm long BiBO crystal, with a pump envelope of 3.0 nm FWHM. (a): Eigenvalues Λ_n for the first 200 supermodes. (b): Amplitude of the first four normalized supermodes $\widetilde{\mathbf{v}}_n(\omega)$ against $\lambda = 2\pi c/\omega$. The first supermode features a FWHM of 4.14 nm.

2.3.4 Single-mode optical parametric oscillator

We now consider the crystal and the cavity around it, i.e. the SPOPO, taking into account intra-cavity losses but assuming no intra-cavity dispersion. This model was thoroughly studied in [Jiang 12, de Araujo 12, Patera 10], in particular using the symplectic formalism. Here we adopt a pragmatic approach which allows us to study the effect of intra-cavity losses, and discuss the purity of the output state. For a more detailed analysis, we thus refer to the mentioned article and theses.

Assuming no intra-cavity dispersion means frequency independent intra-cavity losses, which apply equally on every parts of the spectrum of the resonant light. In particular, this means that the supermodes are still the eigenmodes of the Hamiltonian of this SPOPO model, while the eigenvalues do change, or equivalently the squeezing factors do change (see equation (2.16)).

As we expect an equivalent effect on each supermode, let us consider a single-mode optical parametric oscillator (OPO). We then model the PDC process as a single-mode squeezing operation $\hat{S}(\zeta)$. We derive the input-output relations for the annihilation operators of the field

at play in figure 2.7 (b), using the beamsplitter and squeezing operations in the Heisenberg picture. We have the following (using in particular equation (1.70)):

$$\begin{cases} \hat{a}_1 = t_\mathrm{i}\hat{a}_\mathrm{i} + r_\mathrm{i}\hat{a}_3 \\ \hat{a}_\mathrm{L} = t_\mathrm{i}\hat{a}_3 - r_\mathrm{i}\hat{a}_\mathrm{i} \\ \hat{a}_2 = \cosh(\zeta)\,\hat{a}_1 - \sinh(\zeta)\,\hat{a}_1^\dagger \\ \hat{a}_\mathrm{o} = t_\mathrm{o}\hat{a}_2 - r_\mathrm{o}\hat{a}_\mathrm{vac} \\ \hat{a}_3 = t_\mathrm{o}\hat{a}_\mathrm{vac} + r_\mathrm{o}\hat{a}_2 \end{cases} \tag{2.20}$$

We then deduce the expressions of the output quadrature operators $\hat{q}_\mathrm{o}$ and $\hat{p}_\mathrm{o}$ as

$$\begin{cases} \hat{q}_\mathrm{o} = \dfrac{t_\mathrm{i}t_\mathrm{o}\mathrm{e}^{-\zeta}\hat{q}_\mathrm{i} + \left(r_\mathrm{i}\mathrm{e}^{-\zeta} - r_\mathrm{o}\right)\hat{q}_\mathrm{vac}}{1 - r_\mathrm{i}r_\mathrm{o}\mathrm{e}^{-\zeta}} \\ \hat{p}_\mathrm{o} = \dfrac{t_\mathrm{i}t_\mathrm{o}\mathrm{e}^{\zeta}\hat{p}_\mathrm{i} + \left(r_\mathrm{i}\mathrm{e}^{\zeta} - r_\mathrm{o}\right)\hat{p}_\mathrm{vac}}{1 - r_\mathrm{i}r_\mathrm{o}\mathrm{e}^{\zeta}} \end{cases} \tag{2.21}$$

Considering the input fields $\hat{a}_\mathrm{i}$ and $\hat{a}_\mathrm{vac}$ to be in the vacuum state, the quadrature means $\langle\hat{q}_\mathrm{o}\rangle$ and $\langle\hat{p}_\mathrm{o}\rangle$ are then null from equation (2.21). Since there are no correlations between the two vacuum inputs, we obtain the output quadrature variances:

$$\begin{cases} \langle\Delta^2\hat{q}_\mathrm{o}\rangle = \sigma_0^2\,\dfrac{t_\mathrm{i}^2t_\mathrm{o}^2\mathrm{e}^{-2\zeta} + \left(r_\mathrm{i}\mathrm{e}^{-\zeta} - r_\mathrm{o}\right)^2}{\left(1 - r_\mathrm{i}r_\mathrm{o}\mathrm{e}^{-\zeta}\right)^2} \\ \langle\Delta^2\hat{p}_\mathrm{o}\rangle = \sigma_0^2\,\dfrac{t_\mathrm{i}^2t_\mathrm{o}^2\mathrm{e}^{2\zeta} + \left(r_\mathrm{i}\mathrm{e}^{\zeta} - r_\mathrm{o}\right)^2}{\left(1 - r_\mathrm{i}r_\mathrm{o}\mathrm{e}^{\zeta}\right)^2} \end{cases} \tag{2.22}$$

We define the cavity threshold ζ_th as the squeezing parameter for which the variance $\langle\Delta^2\hat{p}_\mathrm{o}\rangle$ diverges in equation (2.22). This yields

$$\zeta_\mathrm{th} = \ln\left(\frac{1}{r_\mathrm{i}r_\mathrm{o}}\right) \tag{2.23}$$

Physically, the gain of the non-linear medium equals the losses when the threshold ζ_th is reached, meaning that the OPO oscillates and lases. In this work, we are only interested in the below-threshold regime $\zeta < \zeta_\mathrm{th}$, where the OPO acts as an enhanced squeezer[1]. The squared squeezing parameter ζ^2 is proportional to the pump power $\mathcal{P}_\mathrm{p} = \left|\mathcal{A}_\mathrm{p}\right|^2$ (see e.g. [Michel 21]). We can then conveniently express the ratio $\zeta^2/\zeta_\mathrm{th}^2$ as

$$\frac{\zeta^2}{\zeta_\mathrm{th}^2} = \frac{\mathcal{P}_\mathrm{p}}{\mathcal{P}_\mathrm{p,th}} \tag{2.24}$$

In practice, the squeezing parameter of the OPO is then experimentally controlled by setting the pump power.

[1]Strictly speaking, since the cavity operates below-threshold and does not oscillate, the cavity is then called *optical parametric amplifier* (OPA) in the literature. To avoid confusion with previous works, we will maintain the wording optical parametric oscillator (OPO) in this manuscript.

In equations (2.21), a small amount of losses is already part of the model, from the non-unity input reflectivity $r_i^2 = 99.85\%$, leading to a non-vacuum loss field $\hat{a}_L$. We can further add losses to the model by taking a value of r_i^2 smaller than 99.85%. Using the notation ν for the additional intra-cavity losses, we write the input reflectivity $r_i^2 = 0.9985 - \nu$.

The output of the single-mode OPO is a lossy squeezed vacuum state, with asymmetric squeezing of the quadrature distributions as shown in the result (2.22). We define the effective squeezing factor s^- and antisqueezing factor s^+, along with their decibel version, as

$$\begin{aligned} s^- &= \langle \Delta^2 \hat{q}_o \rangle / \sigma_0^2 \quad \text{and} \quad s^+ = \langle \Delta^2 \hat{p}_o \rangle / \sigma_0^2 \\ s^\pm_{dB} &= 10 \log_{10}(s^\pm) \end{aligned} \tag{2.25}$$

Since the output lossy squeezed state is a Gaussian state, we can also directly deduce the output purity from equation (1.53):

$$\mu_o = \frac{1}{\sqrt{s^- s^+}} \tag{2.26}$$

In figure 2.10, we show the squeezing factors in (a) and the output purity in (b) against the power ratio $\mathcal{P}_p/\mathcal{P}_{p,th}$, for the output coupler of reflectivity $r_o^2 = 80\%$. We chose the intra-cavity loss ν values 0%, 3%, 10% as the usual measured losses in our cavity are around 3%.

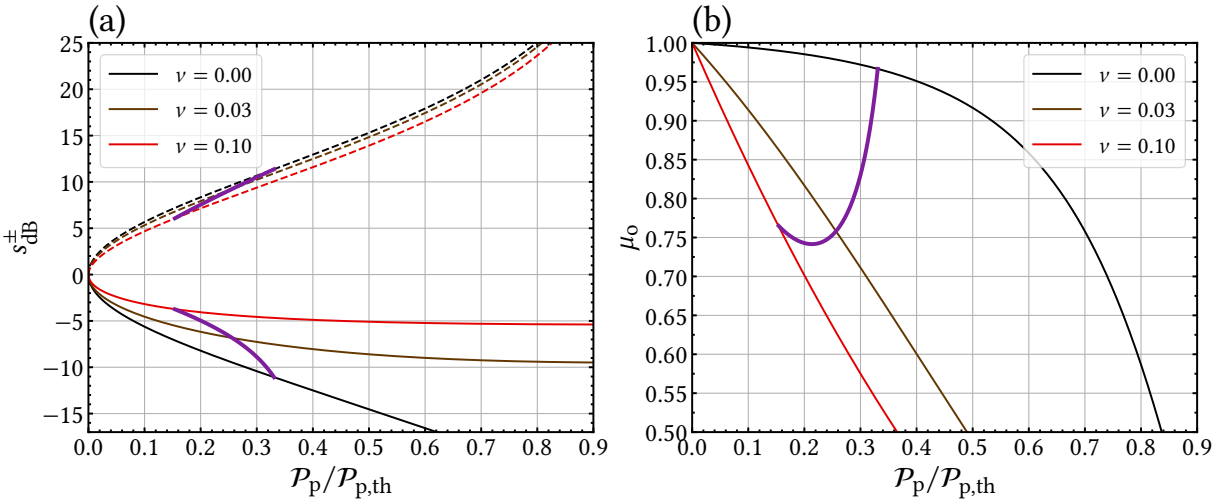

Fig. 2.10 Simulation of a single-mode OPO, at $r_o^2 = 80\%$, for three intra-cavity additional loss ν values: 0% (black), 3% (black), and 10% (red). The total intra-cavity losses are $0.0015 + \nu$. (a): the squeezing factor s^-_{dB} (solid lines) and the antisqueezing factor s^+_{dB} (dashed lines) against the normalized to threshold pump power $\mathcal{P}_p/\mathcal{P}_{p,th}$. The three dashed lines diverge at the threshold, while the solid black curve converges to -22 dB. (b): the output purity μ_o against $\mathcal{P}_p/\mathcal{P}_{p,th}$. The purple bold curves corresponds to the purple curves in figure 2.11.

In graph 2.10 (a), above $\mathcal{P}_p/\mathcal{P}_{p,th} = 0.5$, there is not much to gain, as the squeezing factor s^-_{dB} saturates. At $\nu = 3\%$, we can see that this saturation is almost -10 dB, which is high, considering the record is -15 dB [Vahlbruch 16]. However, we can see on graph 2.10 (b) that the purity

drops quickly with the pump power, which is coherent with the fact that the antisqueezing is diverging while the squeezing is saturating on graph (a). As we will see in chapter 4, high output purity plays a major role in the success of non-Gaussian certification.

Let us study the model at fixed pump power $\mathcal{P}_\mathrm{p}$. Fixing the pump power allows us to better understand the influence of the other parameters in the model. We measured $\mathcal{P}_\mathrm{p,th} = 156\,\mathrm{mW}$ for a reflectivity of $r_\mathrm{o}^2 = 80\%$ and a measured intra-cavity loss of 3%. Let us choose a reasonable pump power of $\mathcal{P}_\mathrm{p} = 40.0\,\mathrm{mW}$. We can then use these measurements to deduce the corresponding squeezing parameter ζ. Using equations (2.23) and (2.24), we obtain $\zeta \simeq 6.46 \times 10^{-2}$. Using the model (2.22), we can then compute the purity μ_o and squeezing factors $s^{\pm}_\mathrm{dB}$ for different losses ν at fixed pump power.

Let us come back to figure 2.10. The pump ratio is then $\mathcal{P}_\mathrm{p}/\mathcal{P}_\mathrm{p,th} = 0.256$ at $\nu = 3\%$, for which we can read an expected squeezing factor s^{-}_dB of about $-7\,\mathrm{dB}$ on graph 2.10 (a), and a purity μ_o of about 0.76, on graph 2.10 (b). Now, if we change the loss parameter ν, the pump threshold power $\mathcal{P}_\mathrm{p,th}$ is modified accordingly to equation (2.23). At fixed pump power $\mathcal{P}_\mathrm{p}$, the ratio $\mathcal{P}_\mathrm{p}/\mathcal{P}_\mathrm{p,th}$ is then varying with the loss parameter ν. The resulting curve is plotted in purple on both graphs in figure 2.10. For comparison, we performed the same simulation for reflecitvities $r_\mathrm{o}^2 = 70\%$ and $r_\mathrm{o}^2 = 50\%$, see respectively figure D.1 and figure D.2 in appendix D.1. For an easier graph reading, we reproduce the curves of fixed pump power against the losses in figure 2.11 for all considered reflectivities.

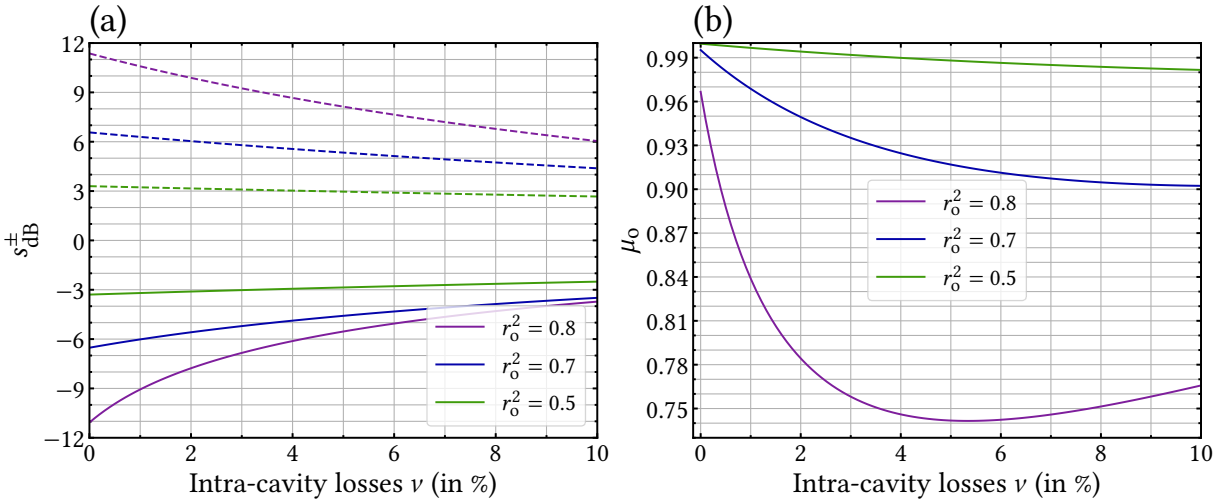

Fig. 2.11 Simulation of a single-mode OPO at fixed pump power $\mathcal{P}_\mathrm{p} = 40\,\mathrm{mW}$, with three available output reflectivities r_o^2: 80% (purple), 70% (blue), and 50% (green). (a): the squeezing factor s^{-}_dB (solid lines) and the antisqueezing factor s^{+}_dB (dashed lines) against the additional losses ν. (b): the output purity μ_o against the additional losses ν. Note that the total intra-cavity losses are $0.0015 + \nu$.

In graph 2.11 (b), the output purity curves are always higher than 0.74, and feature a non-trivial shape, owing to the aforementioned dependency of the pump threshold with losses[1]. In

[1]For losses higher than 6% at $r_\mathrm{o}^2 = 80\%$ for example, the decrease in purity due to losses is lower than the increase of purity due to the pump threshold increasing with losses. The purity goes indeed to 1 for a pump threshold going to zero, see graph 2.10 (a).

graph 2.11 (a), the absolute squeezing $|s^{\pm}_{\mathrm{dB}}|$ remains lower than 12 dB. Increasing the reflectivity r_{o}^2 reduces the squeezing $|s^{-}_{\mathrm{dB}}|$ but improves the purity μ_{o} and its resilience to intra-cavity additional losses ν. As we prioritize purity for this thesis' experiment, we will therefore choose the $r_{\mathrm{o}}^2 = 50\%$ output coupler[1]. Reading the green curve at $\nu = 3\%$, we can remember from this analysis that we can theoretically expect at the output of our single-mode OPO a squeezing factor of about -3 dB with a purity above 0.99, in our experimental conditions.

2.3.5 Spectrally multimode optical parametric oscillator

Let us briefly summarize the previous results. The lossless PDC process is by itself a multimode squeezing operation in the supermode basis. Modeling the SPOPO without intra-cavity dispersion allows us to describe the addition of a cavity around the PDC crystal as a squeezing factor enhancement for each supermode independently. We refined the model by adding intra-cavity losses, so that the output state is then understood as a lossy multimode squeezed state. In other words, the SPOPO is a collection of single-mode lossy OPO (studied in the previous subsection) each acting on a different supermode, or equivalently a spectrally multimode OPO.

The output state is now well described by the non-pure Bloch-Messiah-Williamson decomposition (1.95) of its covariance matrix. Representing the output covariance matrix $\mathbf{V}_{\mathrm{SPOPO}}$ in the supermode basis yields

$$\mathbf{V}_{\mathrm{SPOPO}} = \mathbf{K}_{\mathrm{PDC}}\, \mathbf{O}_2 \mathbf{V}_{\mathrm{W}} \mathbf{O}_2^{\top} \mathbf{K}_{\mathrm{PDC}} \tag{2.27}$$

where $\mathbf{K}_{\mathrm{PDC}}$ is defined in equation (2.17), $\mathbf{O}_2$ is a change of mode basis and $\mathbf{V}_{\mathrm{W}}$ is the Williamson covariance matrix. The losses modeled in the previous section can be seen as independent lossy channels, resulting in the collection of independent thermal states represented by $\mathbf{V}_{\mathrm{W}}$. These channels are not necessarily independent from one mode to another as we assumed. Up to now, we then only considered the trivial change of basis $\mathbf{O}_2 = \mathbb{1}_{2N}$, assuming frequency-independent losses, so that equation (2.27) writes

$$\mathbf{V}^{\mathrm{nodisp}}_{\mathrm{SPOPO}} = \mathbf{K}_{\mathrm{PDC}}\, \mathbf{V}_{\mathrm{W}} \mathbf{K}_{\mathrm{PDC}} \tag{2.28}$$

where the superscript $^{\mathrm{nodisp}}$ means no dispersion. Equation (2.28) provides the output state of the SPOPO when considered as a lossy spectrally multimode OPO.

It is worth noting that $\mathbf{V}_{\mathrm{W}}$ is not proportional to the identity matrix in equation (2.28). First, each supermode associated squeezing factor is $\kappa\Lambda_n$ from equation (2.16). This squeezing factor is then proportional to the pump power, and can be related to the normalized pump power in figure 2.10 (b). We deduce that two different supermodes with eigenvalues $\Lambda_n \neq \Lambda_m$ have then different output purities, and thus different Williamson eigenvalues in $\mathbf{V}_{\mathrm{W}}$ for the same intra-cavity losses.

When taking into account the intra-cavity dispersion, the SPOPO covariance matrix is in general given by equation (2.27), and more work needs to be done to get more insight on the effects of the dispersion. Simulations were run taking into account the dispersion in [Michel 21], see figure 2.12. These simulations rely on the symplectic model of the SPOPO from [Jiang 12], taking the general symplectic transformation including dispersion and performing

[1] Since the cavity alignment is easier at $r_{\mathrm{o}} = 80\%$, most of our calibration measurements are done at $r_{\mathrm{o}} = 80\%$.

its Bloch-Messiah decomposition, which we don't reproduce here. Interestingly, one can see in figure 2.12 that the dominant effects of intra-cavity dispersion is spectrally filtering the supermodes, and lowering the associated squeezing factors.

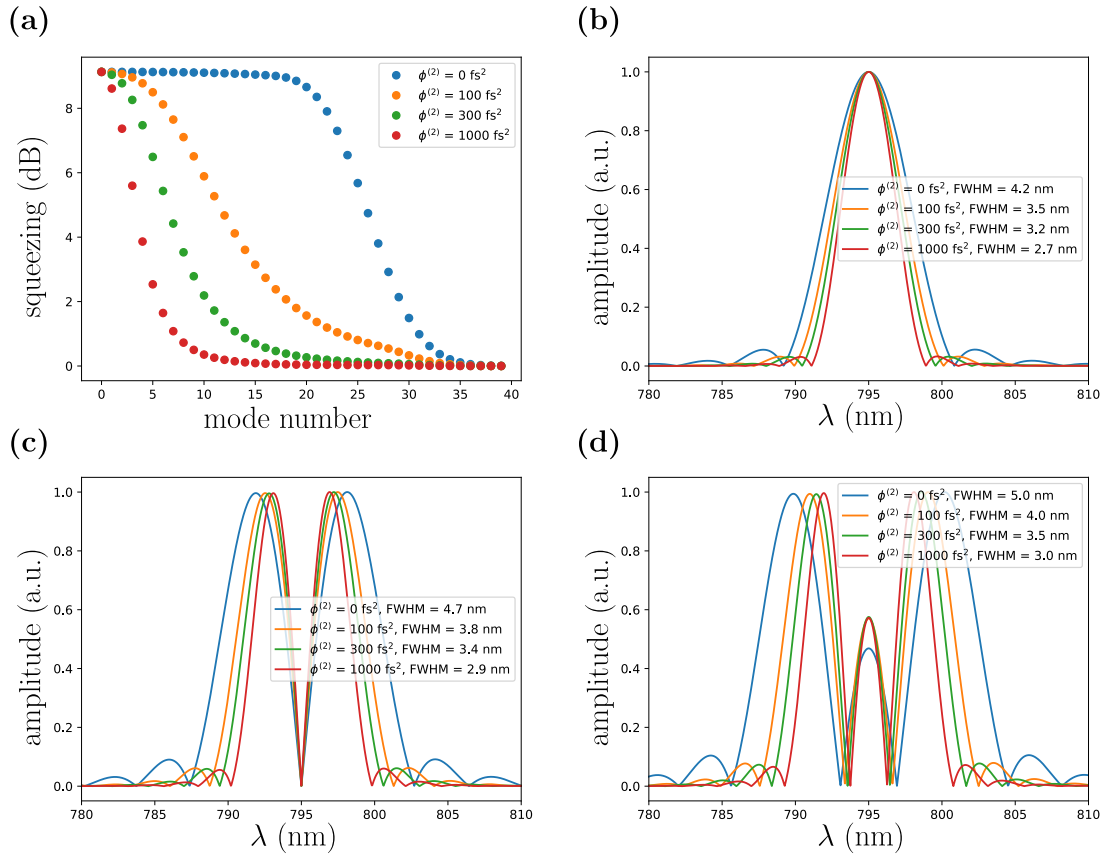

Fig. 2.12 Simulation of the SPOPO output squeezing factors (a) and the absolute amplitude of the first supermodes (b-d) with intra-cavity dispersion for $r_o^2 = 80\%$, a 2.8 nm FWHM Gaussian pump, and a 2 mm long BiBO crystal. The displayed FWHM values are in intensity. Figure from [Michel 21].

In our setup, a resonant pulse goes through about 417 fs^2 group delay dispersion (GDD) in one cavity round-trip: 83 fs^2 from the air, 334 fs^2 from the 2 mm long BiBO crystal, while all the mirrors of the cavity induce negligible dispersion. As one can see from figure 2.12, the 417 fs^2 intra-cavity dispersion is expected to drastically reduce the number of supermodes the SPOPO which can be generated with squeezing factors significantly higher than zero. There is then a high motivation to try and compensate this intra-cavity dispersion. In practice, we use negative GDD mirrors to compensate the dispersion as mentioned in subsection 2.2.3. In the next subsection, we model the compensation of negative GDD mirrors, and show how we can improve the SPOPO output eigenvalue distribution using well-suited compensation.

2.3.6 Intra-cavity dispersion compensation

At the beginning of my PhD, the dispersion was compensated using a negative group delay dispersion (GDD) coating on both mirrors M3 and M7, see figure 2.7. We refer to this coating 115065 from Layertech by the name "C80", as it features a mean compensation of about $-80\,\mathrm{fs}^2$ GDD over our bandwidth. With three cumulative reflections per round-trip (one on M3 and two on M7), the total mean GDD compensation is about $-320\,\mathrm{fs}^2$. For limitations that we show below, we turned to another coating of the same constructor (but not referenced online[1]), which we refer to as "C200" (with similar meaning). With two reflections, we show that the coating C200 further improves the GDD compensation of the SPOPO.

Using the mean GDD value of the coatings would be a poor approximation, since the coatings induce non-negligible higher order spectral phase terms than $\phi^{(2)}$ in equation (2.9). In figure 2.13 (a), the second derivative of the spectral phase $\frac{\partial^2\phi}{\partial\omega^2}$ of the mirrors is plotted. The data was measured by the constructor on our batch for coating C200, while for C50 we used the typical GDD also provided by the constructor. For reference, we plot the constant $-417\,\mathrm{fs}^2$ GDD that would be required for ideal compensation. Note that we used a larger wavelength range than in the plot 2.9 where the first four supermodes are displayed. We indeed aim for a compensation bandwidth of around 30 nm to host tens of supermodes (whose width increases with the mode number n, see appendix A.2).

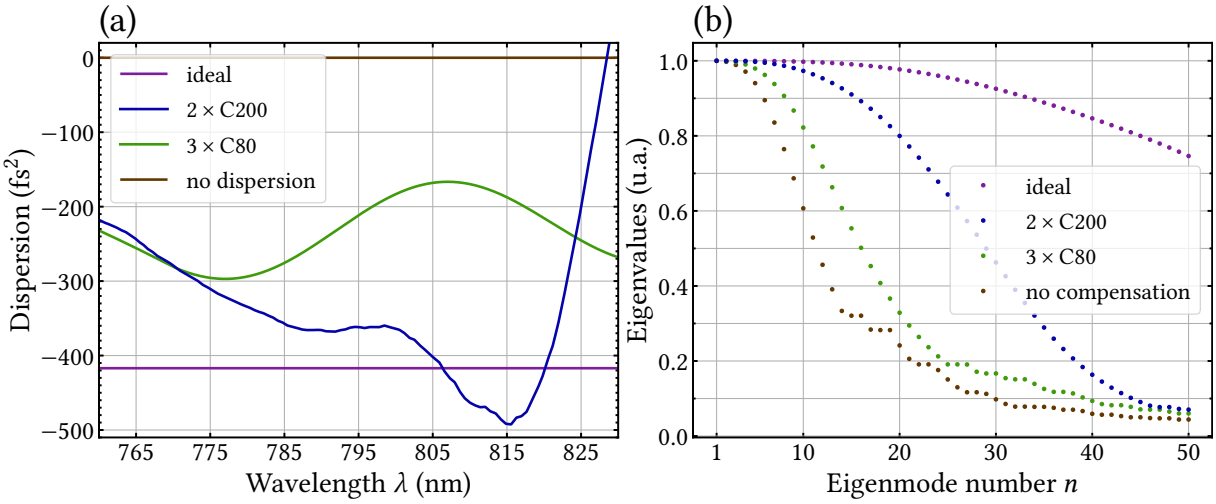

Fig. 2.13 (a) Group delay dispersion (GDD) of both coatings C80 (green) and C200 (blue) with respectively three reflections and two reflections. The second derivative of the spectral phase $\frac{\partial^2\phi}{\partial\omega^2}$ is plotted against the wavelength $\lambda = 2\pi c/\omega$. The horizontal lines represent the ideal dispersion case (purple) at $-417\,\mathrm{fs}^2$ and the no-dispersion case (brown) at $0\,\mathrm{fs}^2$. (b) Eigenvalues from the simulation of the SPOPO taking into account intra-cavity dispersion, with a reflectivity of $r_o^2 = 50\%$ and no losses. The dispersion is compensated using the different profiles given in graph (a).

To compare the compensation of these coatings, we perform the simulation of the SPOPO

[1]For reference, it's the batch numbered "C116I009".

with a dispersion given by:

$$\frac{\partial^2\phi}{\partial\omega^2} = \phi^{(2)}_{\text{air}} + \phi^{(2)}_{\text{crystal}} + \frac{\partial^2\phi_{\text{CX}}}{\partial\omega^2} \qquad (2.29)$$
$$\text{with} \quad \phi^{(2)}_{\text{air}} = 83.3\,\text{fs}^2 \quad \text{and} \quad \phi^{(2)}_{\text{crystal}} = 333.8\,\text{fs}^2$$

and $\phi_{\text{CX}}(\omega)$ the spectral phase of either coating C80 or C200, containing also the negligible spectral phase induced by the low-GDD mirrors of the cavity. In the simulation, we integrate twice equation (2.29), arbitrarily choosing the integration constants. The results are shown in figure 2.13 (b). Note that we chose an output coupler reflectivity of $r_o^2 = 50\%$, which differs from the simulation in figure 2.12. For comparison purposes, we added two simulations: one without compensating coating, and another with ideal compensation. One can see that the eigenvalue distribution using coating C200 is significantly broader than the one using C80. A more quantitative assessment is done computing the Schmidt number K (defined in equation (2.19)) for each compensation case, with results displayed in table 2.2. From both the graph and the table, we see a clear improvement in the Schmidt number from using the coating C200 instead of the coating C80.

GDD compensation	None	3× C80	2× C200	Ideal
Schmidt number K	27	31	40	72

Table 2.2: Schmidt number for different compensation scenarios pictured in figure 2.13.

The coating C80 doesn't perform much better than the no-compensation case. We deduce that the improvement from compensation is quite sensitive to the closeness of the GDD compensation to the ideal constant compensation in figure 2.13 (a).

One might argue that we could have simply stacked more reflections of the coating C80, so as to reach a mean value close to the target $-417\,\text{fs}^2$. Indeed with 5 reflections of C80, the mean GDD is then of about $-383\,\text{fs}^2$. A simulation with such compensation yields a Schmidt number of 41, similar to the case of C200. However, stacking more reflections increases the intra-cavity losses, as compensating coatings are slightly less reflective than standard ones, further optimized for high reflectivity. For this reason, using two reflections on coating C200 is our best option.

It is worth noting that one can deduce from the eigenvalue distribution in graph 2.13 (b) the expected squeezing using figure 2.10. The expected squeezing factor of the first eigenmode reads with the measured pump power ratio $\mathcal{P}_{\text{p}}/\mathcal{P}_{\text{p,th}}$ as the abscissa, while the expected squeezing factor of subsequent supermodes reads with the abscissa $\Lambda_n \times \mathcal{P}_{\text{p}}/\mathcal{P}_{\text{p,th}}$ with Λ_n the n-th eigenvalue, where we use the fact that the eigenvalues are proportional to the squeezing parameters from equation (2.16) and the pump power ratio equal to the squeezing parameter ratio from equation (2.24).

Note, however, that one needs to take into account any subsequent losses on the path to detection to infer the actual measured value in the lab (see subsection 2.5.3 for a measurement example). Also, measuring higher order mode than the first mode is challenging as the modes increase in width with the mode number: see subsection 2.6.2 for more on how to cope with this limitation.

As of writing this thesis, we replaced the mirror M3 by a non-compensating mirror, and the mirror M7 by a C200 coated mirror, resulting in total in two C200 reflections. We measured the output spectrum of the SPOPO just after threshold before and after the change, see figure 2.14. From theory, only the first SPOPO mode oscillates above threshold [Chalopin 10]. Gaussian fits of the spectrums in figure 2.14 yield 8.5 nm FWHM before the change and 15 nm after. We deduce then that the FWHM of the first supermode increased indeed significantly.

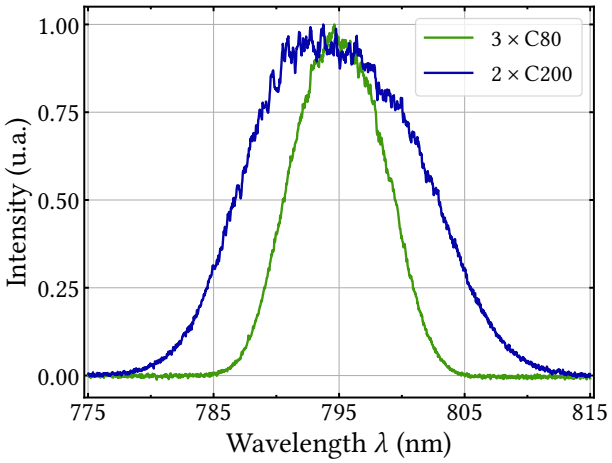

Fig. 2.14 Measured spectrums of the output light of the SPOPO, right above threshold, for compensation from coatings C80 (green) and C200 (blue) with respectively three reflections and two reflections. The spectral intensity is plotted against the wavelength $\lambda = 2\pi c/\omega$. The output coupler reflectivity is 80%.

Note the discrepancy between the measured 15 nm FWHM of the first supermode above threshold in figure 2.14 compared with the expected 4.2 nm FWHM from the simulations, in either graph 2.9 (b) or graph 2.12 (b). A more advanced model may result in a better match between theory and observations. Potential improvements include taking into account a spatial mismatch between the cavity mode and the mode of the squeezed vacuum, and the effect of walk-off angle in the PDC process. The larger effective FWHM is expected to result in an effective significantly reduced Schmidt number, since larger modes are more sensible to dispersion.

For further prospects on the intra-cavity dispersion compensation, we would suggest for example to model more precisely the dispersion induced by the air and the crystal, to take into account higher order dispersion terms than only $\phi^{(2)}$. Note that another potential improvement of the SPOPO is to enclose it under vacuum, removing the air induced dispersion along with a better overall stability. It is indeed easier to find commercial compensating coatings at lower values of GDD than the current 417 fs^2, or requires less reflections. However, going to vacuum requires many efforts at start, and again for any subsequent change of the cavity.

2.4 Homodyne detection

In figure 2.1, the double homodyne detector **3.c)** is composed of two homodyne detectors. Each homodyne detector measures one of the two beams the input signal is split into. For

this reason, the double homodyne detection inherits most of the properties of the homodyne detection. As shown in later chapter 4, the double homodyne detector can be configured to act as a single homodyne detector, property that we use for the measurements shown in later subsection 2.5.3.

In this section, we describe the homodyne detection. We additionally show that the signal mode measured by the homodyne detection is given by the local oscillator mode, which we can engineer with its pulse shaper **3.b)**. Lastly, we investigate the various sources of losses in the homodyne detection scheme.

2.4.1 Working principle

The *homodyne detection* is a common technique used to measure the quantum fluctuations of a field of light which we will refer to as the *signal*. It was first introduced by [Yuen 83, Abbas 83]. It consists in interfering on a balanced beamsplitter the signal field with a bright field called the *local oscillator* (LO), see figure 2.15.

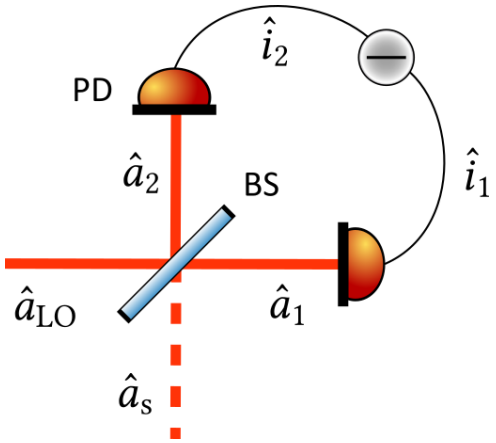

Fig. 2.15 Scheme of the homodyne detection. The annihilation operator of the different fields at play are represented. The local oscillator (subscript LO) and the signal (s) interfere on a balanced beamsplitter (BS), resulting in fields 1 and 2. There fields are measured on photodiodes (PD), resulting in currents 1 and 2 (see the text).

We first consider that the time-frequency modes of the input fields are matched. It is then enough to only consider the transformation of the annihilation operator of the input fields, defined in figure 2.15, in the Heisenberg picture. The beamsplitter transformation writes

$$\begin{cases} \hat{a}_1 = \frac{1}{\sqrt{2}}(\hat{a}_{\mathrm{LO}} + \hat{a}_{\mathrm{s}}) \\ \hat{a}_2 = \frac{1}{\sqrt{2}}(\hat{a}_{\mathrm{LO}} - \hat{a}_{\mathrm{s}}) \end{cases} \tag{2.30}$$

The two output beams are then each measured on a photodiode. The photodiodes produce the currents $\hat{i}_1$ and $\hat{i}_2$ which are proportional to the light intensity, or more pragmatically to

the photon numbers $\hat{n}_1$ and $\hat{n}_2$. We can then write

$$\begin{cases} \hat{i}_1 \propto \hat{n}_1 = \frac{1}{2}(\hat{a}_{\mathrm{LO}}^\dagger \hat{a}_{\mathrm{LO}} + \hat{a}_{\mathrm{LO}}^\dagger \hat{a}_{\mathrm{s}} + \hat{a}_{\mathrm{s}}^\dagger \hat{a}_{\mathrm{LO}} + \hat{a}_{\mathrm{s}}^\dagger \hat{a}_{\mathrm{s}}) \\ \hat{i}_2 \propto \hat{n}_2 = \frac{1}{2}(\hat{a}_{\mathrm{LO}}^\dagger \hat{a}_{\mathrm{LO}} - \hat{a}_{\mathrm{LO}}^\dagger \hat{a}_{\mathrm{s}} - \hat{a}_{\mathrm{s}}^\dagger \hat{a}_{\mathrm{LO}} + \hat{a}_{\mathrm{s}}^\dagger \hat{a}_{\mathrm{s}}) \end{cases} \tag{2.31}$$

from which we deduce the difference of currents $\hat{i}_{\mathrm{d}} = \hat{i}_1 - \hat{i}_2$

$$\hat{i}_{\mathrm{d}} \propto \hat{a}_{\mathrm{LO}}^\dagger \hat{a}_{\mathrm{s}} + \hat{a}_{\mathrm{s}}^\dagger \hat{a}_{\mathrm{LO}} \tag{2.32}$$

Since the local oscillator is a bright field (i.e. $\langle \hat{n}_{\mathrm{LO}} \rangle \gg \langle \hat{n}_{\mathrm{s}} \rangle$), we can write $\hat{a}_{\mathrm{LO}} = \alpha_{\mathrm{LO}} + \delta\hat{a}_{\mathrm{LO}}$ where $\langle \delta\hat{a}_{\mathrm{LO}} \rangle = 0$. Keeping the dominant term in the LO amplitude $\alpha_{\mathrm{LO}} = |\alpha_{\mathrm{LO}}| e^{i\theta}$ we obtain from equation (2.32)

$$\begin{aligned} &\hat{i}_{\mathrm{d}} \propto |\alpha_{\mathrm{LO}}|\, \hat{q}_{\mathrm{s}}^\theta \\ &\text{with} \quad \hat{q}_{\mathrm{s}}^\theta = \sigma_0 \hat{a}^\dagger e^{i\theta} + \sigma_0 \hat{a} e^{-i\theta} \end{aligned} \tag{2.33}$$

where $\theta \in \mathbb{R}$ is understood as the optical phase between the signal and the local oscillator, and $\hat{q}_{\mathrm{s}}^\theta$ is the signal quadrature operator at angle θ defined in equation (1.18). Note that this phase can be changed experimentally by using a piezoelectric mirror.

Equation (2.33) shows that the homodyne detection allows us to directly measure the distribution of the quadrature $\hat{q}_{\mathrm{s}}^\theta$ of the signal. In particular, we can directly access the variance $\langle \Delta^2 \hat{q}_{\mathrm{s}}^\theta \rangle$ of the signal, by first measuring the current variance of vacuum $\langle 0|\Delta^2 \hat{i}_{\mathrm{d}}|0\rangle$, and then deduce

$$\langle \Delta^2 \hat{q}_{\mathrm{s}}^\theta \rangle = \sigma_0^2 \frac{\langle \Delta^2 \hat{i}_{\mathrm{d}} \rangle}{\langle 0|\Delta^2 \hat{i}_{\mathrm{d}}|0\rangle} \tag{2.34}$$

This can then be directly applied for example to measure the squeezing factor of a squeezed vacuum state (see section 1.3.3 for details on these states).

Up to now, we derived an operational description of the homodyne detection. Let us now use the Positive Operator-Valued Measure (POVM) formalism to describe the homodyne detection. For homodyne detection, only orthogonal projectors are necessary, but this formalism is useful for the rest of the manuscript. We briefly introduce this formalism (see [Nielsen 00] for more details). A POVM is a set of positive Hermitian operators $\{\hat{\Pi}_m\}$ defined as

$$\hat{\Pi}_m = \hat{M}_m^\dagger \hat{M}_m \tag{2.35}$$

$$\text{with} \quad \sum_m \hat{\Pi}_m = \hat{\mathbb{1}} \tag{2.36}$$

where the measurement operators $\{\hat{M}_m\}$ are not assumed neither Hermitian, nor orthogonal. This allows for a more general description of a measurement scheme.

The probability of measuring the signal state $\hat{\rho}_{\mathrm{s}}$ with outcome m is given by

$$\mathrm{Tr}\left[\hat{\rho}_{\mathrm{s}} \hat{\Pi}_m\right] \tag{2.37}$$

and the state after the measurement $\hat{\rho}_{\mathrm{s}}^{\mathrm{out}}$ is given by

$$\hat{\rho}_{\mathrm{s}}^{\mathrm{out}} = \frac{\hat{M}_m \, \hat{\rho}_{\mathrm{s}} \, \hat{M}_m^\dagger}{\mathrm{Tr}\left[\hat{\rho}_{\mathrm{s}} \hat{\Pi}_m\right]} \tag{2.38}$$

The POVM of the homodyne detection is given by the eigenstates of the quadrature $\hat{q}_{\mathrm{s}}^\theta$ (see [Tyc 04] for a thorough demonstration). At fixed phase θ, the homodyne POVM then writes

$$\hat{\Pi}_{\mathrm{HD}}(q_{\mathrm{s}}^\theta) = |q_{\mathrm{s}}^\theta\rangle\langle q_{\mathrm{s}}^\theta| \tag{2.39}$$

where the projectors $|q_{\mathrm{s}}^\theta\rangle\langle q_{\mathrm{s}}^\theta|$ indeed satisfy the aforementioned properties, see equation (1.28). Applying equation (2.37), we consistently find that the probability of measuring outcome q_{s}^θ is given by $\langle q_{\mathrm{s}}^\theta|\hat{\rho}_{\mathrm{s}}|q_{\mathrm{s}}^\theta\rangle$ the marginal of the quadrature $\hat{q}_{\mathrm{s}}^\theta$. From equation (2.38), the homodyne detection projects the signal onto an infinitely squeezed state $\hat{\rho}_{\mathrm{s}}^{\mathrm{out}} = |q_{\mathrm{s}}^\theta\rangle\langle q_{\mathrm{s}}^\theta|$, even though this state is not physical.

2.4.2 A modal projective measurement

In the previous subsection, we assumed that the signal and local oscillator (LO) fields were mode-matched in time-frequency. Let us now consider multimode fields and show that the homodyne detection projects the signal on the LO mode. We decompose the LO field over an arbitrary mode basis in the form of equation (1.16) with LO-specific notations, and the signal field over the supermode basis (introduced in section 2.3.2)

$$\begin{cases} \hat{\mathbf{E}}_{\mathrm{LO}}^{(+)}(t) = \mathcal{E}_0 \sum_m \hat{a}_{\mathrm{LO},m} \mathbf{f}_{\mathrm{LO},m}(t) \\ \hat{\mathbf{E}}_{\mathrm{s}}^{(+)}(t) = \mathcal{E}_0 \sum_n \hat{s}_n \mathbf{v}_n(t) \end{cases} \tag{2.40}$$

where the signal and LO modes $\mathbf{f}_{\mathrm{LO},m}(t)$ and $\mathbf{v}_n(t)$ are single-pulse envelopes as defined in equation (2.1). The extension of the following derivation to a train of pulses is immediate by linearity.

Let us choose the LO mode basis such that the mean value of the field is non-zero only in the first mode, a mode basis we call *mean-field mode basis*. In this basis,

$$\mathcal{E}_0 \langle \hat{a}_{\mathrm{LO},m} \rangle = \alpha_{\mathrm{LO}} \delta_{m,1} \tag{2.41}$$

so that the LO field writes

$$\hat{\mathbf{E}}_{\mathrm{LO}}^{(+)}(t) = \alpha_{\mathrm{LO}} \mathbf{f}_{\mathrm{LO}}(t) + \mathcal{E}_0 \sum_m \delta\hat{a}_{\mathrm{LO},m} \mathbf{f}_{\mathrm{LO},m}(t) \tag{2.42}$$

$$\text{with} \quad \delta\hat{a}_{\mathrm{LO},m} = \hat{a}_{\mathrm{LO},m} - \langle \hat{a}_{\mathrm{LO},m} \rangle \quad \text{and} \quad \mathbf{f}_{\mathrm{LO}}(t) = \mathbf{f}_{\mathrm{LO},1}(t)$$

Since the operators $\delta\hat{a}_{\mathrm{LO},m}$ are zero-mean, we can write the LO field in the dominant term in α_{LO} as simply

$$\hat{\mathbf{E}}_{\mathrm{LO}}^{(+)}(t) = \alpha_{\mathrm{LO}} \mathbf{f}_{\mathrm{LO}}(t) \tag{2.43}$$

where we keep the hat notation for the field operator $\hat{\mathbf{E}}^{(+)}_{\mathrm{LO}}(t)$ with the meaning that the right hand expression is a development in α_{LO} with implicit terms containing the null-mean operators $\delta\hat{a}_{\mathrm{LO},m}$.

The current operator must now take into account the time dependency of the fields. We thus introduce the (real) temporal response function $r(t)$ of the detector. The time dependent current operator $\hat{i}(t)$ is then given by the temporal convolution of the detector response with the incoming light intensity as [Loudon 00]

$$\begin{aligned} \hat{i}(t) &\propto \int \mathrm{d}\tau\, r(\tau)\hat{\mathbf{E}}^{(+)}(t-\tau)\hat{\mathbf{E}}^{(-)}(t-\tau) + \mathrm{h.c.} \\ \text{with} \quad \hat{\mathbf{E}}^{(-)}(t-\tau) &= \left(\hat{\mathbf{E}}^{(+)}(t-\tau)\right)^{\dagger} \end{aligned} \tag{2.44}$$

where h.c. means Hermitian conjugate.

We assume that the response of the detector is given by a "gate" function, such that

$$r(\tau) = \begin{cases} 1 & \text{for } \tau \in \left[-\frac{T_{\mathrm{d}}}{2}, \frac{T_{\mathrm{d}}}{2}\right] \\ 0 & \text{elsewhere} \end{cases} \tag{2.45}$$

where T_{d} is the time response of the detector. This response time T_{d} is typically larger than 10 ns, which is much larger than the temporal duration of our ultrasfast pulses, i.e. 100 fs. We can then re-write equation (2.44) as

$$\hat{i} \propto \int \mathrm{d}t\, \hat{\mathbf{E}}^{(+)}(t)\hat{\mathbf{E}}^{(-)}(t) + \mathrm{h.c.} \tag{2.46}$$

where the integral bounds are sent to $\pm\infty$.

Applying equation (2.46) with $\hat{\mathbf{E}}^{(+)}(t) = \hat{\mathbf{E}}^{(+)}_{\mathrm{LO}}(t) + \hat{\mathbf{E}}^{(+)}_{\mathrm{s}}(t)$, the difference of currents $\hat{i}_{\mathrm{d}}$ writes

$$\hat{i}_{\mathrm{d}} \propto \int \mathrm{d}t\, \hat{\mathbf{E}}^{(+)}_{\mathrm{s}}(t)\hat{\mathbf{E}}^{(-)}_{\mathrm{LO}}(t) + \mathrm{h.c.} \tag{2.47}$$

Using the fields expression in equations (2.40) and (2.43), we obtain

$$\hat{i}_{\mathrm{d}} \propto \alpha^*_{\mathrm{LO}} \sum_n \hat{s}_n \int \mathrm{d}t\, \mathbf{f}^*_{\mathrm{LO}}(t)\mathbf{v}_n(t) + \mathrm{h.c.} \tag{2.48}$$

Assuming that each mode overlap $\int \mathrm{d}t\, \mathbf{f}^*_{\mathrm{LO}}(t)\mathbf{v}_n(t)$ is real valued, which is always possible by multiplying $\mathbf{v}_n(t)$ by a constant phase, we find the elegant expression

$$\begin{aligned} \hat{i}_{\mathrm{d}} &\propto |\alpha_{\mathrm{LO}}| \sum_n \hat{q}^{\theta}_n \int \mathrm{d}t\, \mathbf{f}^*_{\mathrm{LO}}(t)\mathbf{v}_n(t) \\ \text{with} \quad \hat{q}^{\theta}_n &= \sigma_0 \hat{s}^{\dagger}_n \mathrm{e}^{\mathrm{i}\theta} + \sigma_0 \hat{s}_n \mathrm{e}^{-\mathrm{i}\theta} = \cos(\theta)\hat{q}_n + \sin(\theta)\hat{p}_n \end{aligned} \tag{2.49}$$

where $\hat{q}_n$ and $\hat{p}_n$ are the supermode quadratures.

Equation (2.49) shows that the quadratures $\hat{q}^{\theta}_n$ which do not contribute to the current are the ones for which the LO mode is orthogonal with the corresponding supermode, in the

sense that their temporal overlap $\int \mathrm{d}t\, \mathbf{f}_{\mathrm{LO}}^{*}(t)\mathbf{v}_n(t)$ is zero. For instance, if the LO mode $\mathbf{f}_{\mathrm{LO}}(t)$ is equal to the first supermode $\mathbf{v}_1(t)$, then the homodyne detector measures the quadrature $\hat{q}_0^\theta$ as all the other contributions vanish in equation (2.49). For a general LO mode $\mathbf{f}_{\mathrm{LO}}(t)$ seen as a combinations of supermodes, the homodyne detector measures the corresponding weighted sum of quadratures given in equation (2.49). Consistently, this combination of quadratures is the quadrature of the signal in the LO mode. In other words, decomposing the signal field in a mode basis with first mode $\mathbf{f}_{\mathrm{LO}}(t)$ and subsequently completed, one can write

$$\hat{i}_{\mathrm{d}} \propto |\alpha_{\mathrm{LO}}|\, \hat{q}^{\theta}_{\mathrm{s},\mathbf{f}_{\mathrm{LO}}} \tag{2.50}$$

where $\hat{q}^{\theta}_{\mathrm{s},\mathbf{f}_{\mathrm{LO}}}$ is the signal quadrature operator of angle θ associated with the mode $\mathbf{f}_{\mathrm{LO}}(t)$.

We refer to this feature as the homodyne detection acting as a *modal projection*: it projects the signal field on the LO mode and measures the signal quadrature in this mode. Since we can engineer the time-frequency mode $\mathbf{f}_{\mathrm{LO}}(t)$ of the LO using our LO pulse shaper (up to the limitations discussed in subsection 2.2.4), we can therefore fully exploit this projective feature, and choose the mode in which we want to measure the signal to be measured.

It is worth noting that we can obtain similar results in the frequency domain, by simply pointing out that the temporal integral of the fields in equation (2.46) may be written

$$\int \mathrm{d}t\, \hat{\mathbf{E}}^{(+)}(t)\hat{\mathbf{E}}^{(-)}(t) = \int \frac{\mathrm{d}\omega}{\sqrt{2\pi}}\frac{\mathrm{d}\omega'}{\sqrt{2\pi}}\mathscr{F}[\hat{\mathbf{E}}^{(+)}](\omega)\mathscr{F}[\hat{\mathbf{E}}^{(-)}](\omega')\underbrace{\int \mathrm{d}t\, \mathrm{e}^{\mathrm{i}(\omega'-\omega)t}}_{2\pi\delta(\omega'-\omega)} \tag{2.51}$$

from which we deduce

$$\hat{i} \propto \int \mathrm{d}\omega\, \mathscr{F}[\hat{\mathbf{E}}^{(+)}](\omega)\mathscr{F}[\hat{\mathbf{E}}^{(-)}](\omega) + \mathrm{h.c.} \tag{2.52}$$

where we used the definition of the Fourier transform $\mathscr{F}$, see appendix A.3.

Applying equation (2.52) in the previous derivation, we obtain a similar expression as equation (2.49) with overlaps of the Fourier transformed signal and LO modes instead of their temporal ones. Similarly, deriving the analysis considering spatial modes yields an analogue equation, with overlaps of spatial modes.

2.4.3 Experimental imperfections in a homodyne detection scheme

Equation (2.33) models an ideal homodyne detection. In practice, many experimental imperfections introduce losses to the measured state. These imperfections can be modeled using a fictitious beamsplitter of transmission η_{HD} equal to one minus the losses. η_{HD} is the *efficiency* of the homodyne detection. A non ideal homodyne detection is then equivalent to such beamsplitter followed by an ideal homodyne detection. The beamsplitter operation on the signal operator field $\hat{\mathbf{E}}_{\mathrm{s}}^{(+)}$ can be expressed as

$$\hat{\mathbf{E}}_{\mathrm{s}}^{(+)} \mapsto \sqrt{\eta_{\mathrm{HD}}}\,\hat{\mathbf{E}}_{\mathrm{s}}^{(+)} + \sqrt{1-\eta_{\mathrm{HD}}}\,\hat{\mathbf{E}}_{\mathrm{vac}}^{(+)} \tag{2.53}$$

where $\hat{\mathbf{E}}_{\mathrm{vac}}^{(+)}$ is the vacuum field.

Let us list the different sources of loss that may occur between the experimental part that generates the signal field (from module **2.b)** in figure 2.1) and the ideal detection. For each source of loss, we estimate the corresponding efficiency, which results in the total detection losses. Note that we consider module **3.c)** as a single homodyne detection as mentioned before.

Optical elements. Any optical element in the path of the signal beam is imperfect and absorbs part of the light, e.g. lenses, mirrors, etc... We denote by η_{optical} the total optical efficiency. We can assess these losses by measuring the light intensity before I_{in} and after I_{out} the optical element. The optical efficiency then writes

$$\eta_{\text{optical}} = \frac{I_{\text{out}}}{I_{\text{in}}} \tag{2.54}$$

and we measured

$$\eta_{\text{optical}} \simeq 96\% \tag{2.55}$$

LO mode mismatch. In the previous subsection 2.4.2, we showed that the homodyne detection is a measurement of a weighted sum of signal quadratures with weights given by overlaps between the LO mode and the signal modes. See equation (2.49) for the time-frequency version.

Let us consider the spatial overlaps. The signal spatial mode is defined by the cavity of the SPOPO, which is spatially single-mode. This means that any non-zero overlap between the LO mode and any other mode than the cavity mode contributes as a quadrature measurement of the vacuum. This results then in effective losses, which can be modeled with equation (2.53), denoting η_{overlap} the spatial mode matching efficiency. Note that such model of the losses induced by a mode mismatch was shown in [Grosshans 01] for time-frequency modes.

To estimate the spatial overlap in practice, we measure the visibility V_{interf} of the interference between the LO beam and a classical beam which went through the SPOPO cavity, inheriting the spatial mode of the signal. The visibility V_{interf} is given by the spatial overlap of the two fields. As mentioned before, the difference of current is proportional to the spatial overlap. Since it is also linear in the signal field $\hat{\mathbf{E}}_{\text{s}}^{(+)}$, we can then model the effect of the spatial mode mismatch as in equation (2.53), with an efficiency given by

$$\eta_{\text{overlap}} = V_{\text{interf}}^2 \tag{2.56}$$

where V_{interf} is the visibility of the mentioned interferences.

We usually measure a spatial visibility of about 95%, resulting in

$$\eta_{\text{overlap}} \simeq 90\% \tag{2.57}$$

Concerning time-frequency overlaps, since we can engineer the LO pusle shaper mode, we can then match the LO mode to the mode we want to measure, up to the precision of the pulse shaping discussed in subsection 2.2.4. A mode mismatch with the target mode, e.g. the first supermode $\mathbf{v}_1(t)$, may result in a non-zero overlap with other modes in which the signal state is not vacuum, e.g. other squeezed supermode with non-zero squeezing parameter. Technically, this can not be modeled by equation (2.53). For these reasons, we won't take into account any time-frequency mode mismatch in the loss estimation.

Photodiode imperfections. The photodiodes are not unit-efficient contrary to what we assumed up to now. This means that for N_{ph} photon number impeding a photodiode, only a fraction of this number $N_{\text{e}^-} < N_{\text{ph}}$ is converted to electrons, such that the photodiode efficiency η_{PD} simply writes

$$\eta_{\text{PD}} = \frac{N_{\text{e}^-}}{N_{\text{ph}}} \tag{2.58}$$

The manufacturer (Hamamatsu) provides us with photodiodes (S3883-02) operating at our wavelength range with an efficiency

$$\eta_{\text{PD}} \simeq 95.5\% \tag{2.59}$$

Imperfect electronic response. From equation (2.44), any imperfection in the detector response $r(\tau)$ results in a non-ideal detection. This stems from imperfections of the electronic circuit that treat the electronic signals of the photodiodes. First, the response may be too loose, i.e. its bandwidth is too narrow to resolve the light we are measuring. In our case, the cavity acts as an optical low-pass filter of bandwidth 8 MHz. Our detection bandwidth of 40 MHz is large enough so that this is not a limitation. Second, over its bandwidth, the detector efficiency may not be one due to electronic noise. Electronic noise stems from photodiodes dark currents and the intrinsic noise of the amplifiers on the electronic circuit. The effect of this noise is to add a random quantity $\hat{i}_{\text{elec}}$ to the measured current $\hat{i}_{\text{d}}$. The equivalent efficiency η_{elec} is given by [Appel 07]

$$\eta_{\text{elec}} = 1 - \frac{\langle 0|\Delta^2 \hat{i}_{\text{elec}}|0\rangle}{\langle 0|\Delta^2 \hat{i}_{\text{d}}|0\rangle} \tag{2.60}$$

In practice, we use a spectrum analyzer which gives access to the electronic spectral density of the homodyne detection output current. Let us introduce here this quantity. First, the auto-correlation function $C_{\text{d}}(t,t')$ of the output current of the homodyne detection $\hat{i}_{\text{d}}$ is defined as

$$C_{\text{d}}(t,t') = \langle \hat{i}_{\text{d}}(t)\hat{i}_{\text{d}}(t')\rangle - \langle \hat{i}_{\text{d}}(t)\rangle \langle \hat{i}_{\text{d}}(t')\rangle \tag{2.61}$$

In the stationary regime, $C_{\text{d}}(t,t')$ depends only on the variable $\tau = t - t'$ [Reynaud 97], and may be written

$$C_{\text{d}}(\tau) = \langle \hat{i}_{\text{d}}(\tau)\hat{i}_{\text{d}}(0)\rangle - \langle \hat{i}_{\text{d}}(\tau)\rangle \langle \hat{i}_{\text{d}}(0)\rangle \tag{2.62}$$

The spectral density $S_{\text{d}}(f)$ associated to the current $\hat{i}_{\text{d}}$ is then defined as the Fourier transform of the auto-correlation function $C_{\text{d}}(\tau)$

$$S_{\text{d}}(f) = \tfrac{1}{\sqrt{2\pi}} \int \mathrm{d}\tau\, C_{\text{d}}(\tau) \mathrm{e}^{2\mathrm{i}\pi f \tau} \tag{2.63}$$

where f is the frequency (in Hz) at which the noise is measured. We similarly define also the spectral density $S_{\text{elec}}(f)$ associated to the current $\hat{i}_{\text{elec}}$.

From equation (2.62),

$$\langle \Delta^2 \hat{i}_{\mathrm{d}} \rangle = C_{\mathrm{d}}(\tau = 0)$$

which allows us to write

$$\langle \Delta^2 \hat{i}_{\mathrm{d}} \rangle = \tfrac{1}{\sqrt{2\pi}} \int \mathrm{d}f \, S_{\mathrm{d}}(f) \tag{2.64}$$

and similarly for $\hat{i}_{\mathrm{elec}}$. Equation (2.64) allows then to express equation (2.60) in terms of the spectral densities $S_{\mathrm{d}}(f)$ and $S_{\mathrm{elec}}(f)$, accessible to the measurement[1]. In other words, the electronic losses $1-\eta_{\mathrm{elec}}$ is then given by the ratio of the electronic and signal integrated spectral densities, considering vacuum as input. A result shown in [Kumar 12].

It is common to use the clearance $C_{\mathrm{dB}} = -10\log_{10}(1-\eta_{\mathrm{elec}})$ expressed in dB to quantify the electronic efficiency. We characterized our newest homodyne detectors and obtained a clearance of $C_{\mathrm{dB}} = 17$ dB over a large bandwidth of 40 MHz, see appendix C.1 where we included their electronic scheme. We then deduce the electronic efficiency

$$\eta_{\mathrm{elec}} \simeq 98\% \tag{2.65}$$

Homodyne detection efficiency. The total efficiency of the homodyne detection η_{HD} is then given by the product of the above efficiencies

$$\eta_{\mathrm{HD}} = \eta_{\mathrm{optical}}\, \eta_{\mathrm{overlap}}\, \eta_{\mathrm{PD}}\, \eta_{\mathrm{elec}} \tag{2.66}$$

and yields

$$\eta_{\mathrm{HD}} \simeq 81\% \tag{2.67}$$

In later subsection 2.5.3, we illustrate the effect of such losses on the measurement of squeezing factors of squeezed vacuum states.

2.5 Optical phase locking

As shown in the section 2.4, the homodyne detection directly measures the quadrature of the signal in the local oscillator (LO) mode $\mathbf{f}_{\mathrm{LO}}$

$$\hat{q}^{\theta}_{\mathrm{s},\mathbf{f}_{\mathrm{LO}}} = \cos(\theta)\hat{q}_{\mathrm{s},\mathbf{f}_{\mathrm{LO}}} + \sin(\theta)\hat{p}_{\mathrm{s},\mathbf{f}_{\mathrm{LO}}} \tag{2.68}$$

which corresponds to the signal quadrature in the LO mode $\hat{q}_{\mathrm{s},\mathbf{f}_{\mathrm{LO}}}$ upon which is applied a rotation of angle given by the relative optical phase θ between the LO and the signal. While it is a great advantage to have access to different quadratures with the same device, it also adds the parameter θ to be controlled experimentally.

[1] We actually make the ergodic assumption here, assuming that the state averages $\langle\cdot\rangle$ are equal to the temporal averages $\int \mathrm{d}\tau$, allowing us to measure them.

In this section, we describe the optical phase locking system, which allows us to lock the relative phase between the LO and the signal, while still allowing the measurement of the quantum signal field. Conceiving and building this system is part of this thesis' work. This improvement, while usually common in optical setups, proved to be challenging in our setup, as we observe significant pointing noise in our beams up to about a few kHz and we need to manage the dispersion effects on our broadband optical pulses. This noise is likely to stem from the long distances the beams propagate over on our setup. As our ultrafast light takes the form of trains of pulses, it is indeed required to match the trains anywhere in the experiment where we make the beams interact or interfere. As the pulses are separated by about 4 m, the total optical path length tends to quickly increase.

As an initial step, we demonstrate the ability to lock the phase θ in the first subsection. In the subsequent subsection, we show the ability to measure while still maintaining a constant phase θ. In the final subsection, we show measurements of a squeezed vacuum state to illustrate the advantages of the locking system.

2.5.1 Double optical phase locking

To build the locking system, we need a detection which is sensible to the LO-signal phase θ. For reasons that are illustrated in the later subsection 2.5.3, we want to avoid using the LO-signal homodyne detection for both the measurement and the lock. Instead, we use a classical control beam, which we refer to as the *seed* beam, produced by partially splitting our laser source. The general idea is that the seed beam takes the role of the signal beam, allowing us to make this bright beam interact with both the pump beam (defined in subsection 2.3.1) and the LO beam. The relative phase of each pair of bright beams (seed-pump and LO-seed) can then be locked using a control scheme. Since the signal itself is generated from the pump, their phases are intrinsically related. Under locking operation, the three relative phases (seed-pump, LO-seed, and pump-signal) are then fixed, so that the LO-signal phase θ is constant over time. Let us show it in detail.

We use the scheme of the locking system in figure 2.16 as a graphical support. Figure 2.16 contains the modules SPOPO **1.c)**, photon subtraction **2.b)** and detection **3.c)** from figure 2.1, with some technical changes we detail below. We consider that the double homodyne detection **3.c)** is used as a single homodyne detection, in the whole section.

Seed-pump lock. Let us first focus on the non-linear interaction between the seed beam and the pump beam, which occurs in the BiBO crystal of the SPOPO, see figure 2.16 (b). With a non-zero-mean field as input, the parametric down-conversion process acts as a phase-sensitive amplifier, see e.g. [Loudon 00]. For these two classical beams, it can be seen as a phase-sensitive energy exchange between the pump and the seed, and we will refer to this process as *seed amplification-deamplification*. The intensity of the pump field, measured on a photodiode, is then sensitive to the seed-pump relative phase. Following standard loop control schemes, an electronic device called the "seed-pump lock" uses this electronic signal to lock the seed-pump relative phase using the piezoelectric mirror pictured in figure 2.16 (b).

Let us derive the electronic signal used in the control scheme. Assuming that the pump variations remain small, the seed intensity I_{seed} at the output of the crystal is given by [Collett 87,

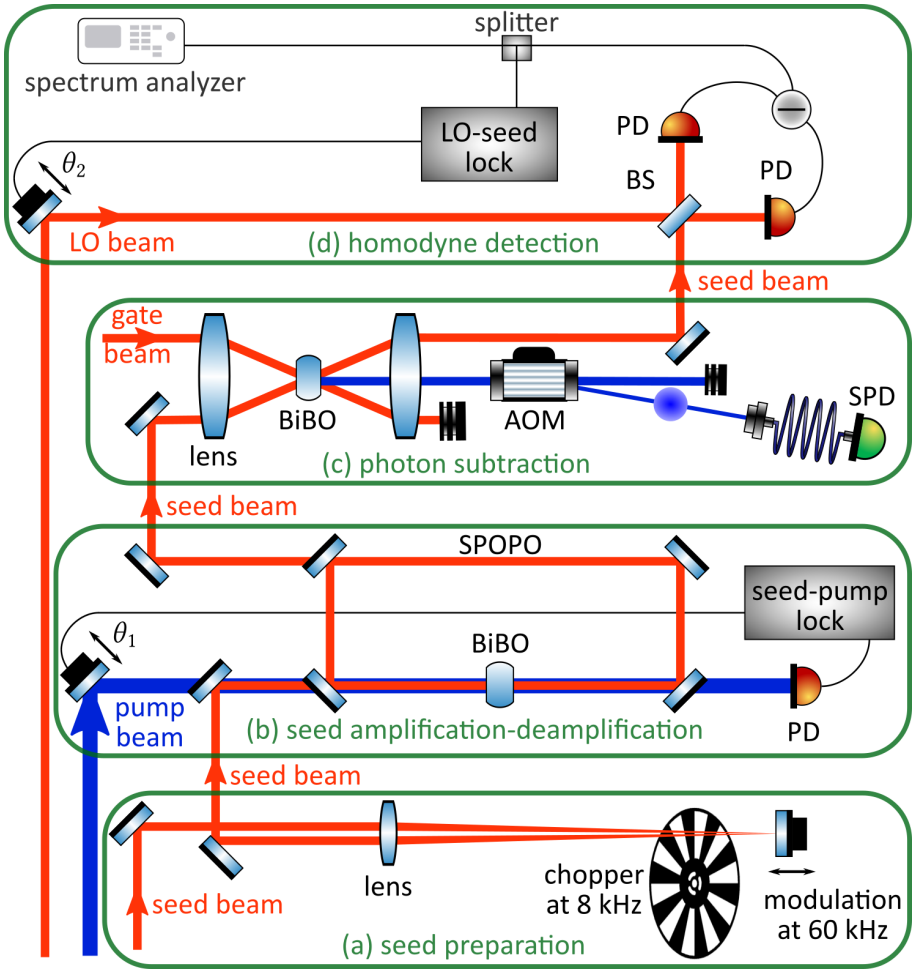

Fig. 2.16 Scheme of the optical phase locking system. (a): The bright seed beam is modulated at $f_{\text{mod}} = 60\,\text{kHz}$ and chopped at 8 kHz. (b): The seed and pump beams undergo parametric down-conversion through the BiBO crystal of the SPOPO. The seed-pump phase θ_1 is locked by measuring the intensity of the pump. Following the chopping cycle, the SPOPO outputs either the signal multimode squeezed vacuum beam (not represented) or the amplified seed beam. (c): The seed (resp. signal) and gate beams undergo sum-frequency generation through the BiBO crystal, and produce a bright (resp. few-photon) beam which is dumped (resp. diffracted by an acousto-optic modulator (AOM) to a single photon detector (SPD)). (d): The LO-seed phase θ_2 is locked by measuring the intensity of the interfering seed and LO fields. Alternatively, the signal field is measured in a homodyne detection configuration, using a spectrum analyzer. BS: beamsplitter; PD: photodiode; LO: local oscillator. See the main text for details.

Loudon 00]

$$I_{\text{seed}} = I_{\text{seed}}^{in}\left[\cosh(2r) - \sinh(2r)\cos\left(2\theta_{\text{seed}}^{\text{in}} - \theta_{\text{pump}}\right)\right] \tag{2.69}$$

where I_{seed}^{in} is the input intensity of the seed, r is the *gain parameter* of the (single-pass) PDC process, and we define generically the optical phase of a non-zero-mean field along with its intensity as (taking the pump field as example)

$$\langle\hat{\mathbf{E}}_{\text{pump}}^{(+)}\rangle = \left|\langle\hat{\mathbf{E}}_{\text{pump}}^{(+)}\rangle\right| e^{i\theta_{\text{pump}}} \tag{2.70}$$

$$I_{\text{pump}} = \left|\langle\hat{\mathbf{E}}_{\text{pump}}^{(+)}\rangle\right|^2 \tag{2.71}$$

In equation (2.69), the pump phase θ_{pump} is defined at the output of the crystal, and the seed phase $\theta_{\text{seed}}^{\text{in}}$ is defined at the input of the crystal. The seed phase θ_{seed}, defined at the output of the crystal, is given by

$$\theta_{\text{seed}} - \tfrac{1}{2}\theta_{\text{pump}} = \arctan\left(e^{2r}\tan\left(\theta_{\text{seed}}^{\text{in}} - \tfrac{1}{2}\theta_{\text{pump}}\right)\right) \tag{2.72}$$

By energy conservation, any variation in the seed intensity results in the opposite variation in the pump intensity, which we write as

$$I_{\text{pump}} - I_{\text{pump}}^{in} = -(I_{\text{seed}} - I_{\text{seed}}^{in}) \tag{2.73}$$

where I_{pump}^{in} is the input pump intensity and I_{pump} the output pump intensity. The photodiode outputs a current i_{PD} proportional to the pump intensity. Using equations (2.69) and equation (2.73), we deduce the expression

$$i_{\text{PD}} \propto c_0 + \cos\left(2\theta_{\text{seed}}^{\text{in}} - \theta_{\text{pump}}\right) \tag{2.74}$$

where c_0 is a constant.

Before describing how the "seed-pump lock" processes the current i_{PD}, note that a phase modulation is applied on the seed beam using a piezoelectric mirror, see figure 2.16 (a) where we consider not using the pictured chopper for now. This modulation is used to effectively filter the electronic signal at $f_{\text{mod}} = 60\,\text{kHz}$ with a bandwidth of 15 kHz, using a demodulation scheme. For more technical details on the electronic scheme, see the appendix C.2[1]. This allows us to isolate the electronic signal from any source of low frequency noise, such as mechanical vibrations, air fluctuations, laser power fluctuations, etc... With a modulation frequency $f_{\text{mod}} = 60\,\text{kHz}$, we are far from these low frequency noises, typically occurring below the kHz range.

The modulation of the seed phase writes

$$\theta_{\text{seed}}^{\text{in}} \mapsto \theta_{\text{seed}}^{\text{in}} + A\sin(2\pi f_{\text{mod}} t) \tag{2.75}$$

where A is the amplitude of the modulation. Taking A very small compared to π, we develop equation (2.74) to the first order which yields

$$i_{\text{PD}}(t) \propto c_0 + \cos\left(2\theta_{\text{seed}}^{\text{in}} - \theta_{\text{pump}}\right) - 2A\sin\left(2\theta_{\text{seed}}^{\text{in}} - \theta_{\text{pump}}\right)\sin(2\pi f_{\text{mod}} t) + \mathcal{O}(A) \tag{2.76}$$

[1]We recommend the reader to first read subsections 2.5.1 and 2.5.2 before reading the appendix.

In practice, the demodulation is the multiplication of the current $i_{\mathrm{PD}}(t)$ by an electronic local oscillator (eLO) oscillating of the form $\cos(2\pi f_{\mathrm{mod}} t + \phi_1)$, with ϕ_1 the phase of the eLO (relative to the modulation phase). The resulting signal is then filtered by a 15 kHz low pass-filter (LPF), which we can model as an integration over the inverse of the LPF frequency. Assuming the phase noises occur at much lower frequency than the modulation frequency f_{mod}, we find the resulting electronic signal u_1^{err} by performing such integration on equation (2.76)

$$\begin{aligned} u_1^{\mathrm{err}} &\propto \sin(\theta_1)\sin(\phi_1) \\ \text{with} \quad \theta_1 &= 2\theta_{\mathrm{seed}}^{\mathrm{in}} - \theta_{\mathrm{pump}} \end{aligned} \tag{2.77}$$

The electronic signal u_1^{err}, referred to as the *error signal*, is then fed to a Red Pitaya used as a proportional–integral–derivative (PID) controller. In a nutshell, the PID controller makes the error signal u_1^{err} go to zero by correcting the seed-pump phase θ_1 in a feedback loop scheme. The parameter ϕ_1 is set to maximize the amplitude of the error signal, at $\phi_1 = \pm\pi/2$.

From equation (2.77), locking the error signal u_1^{err} to zero implies then that θ_1 is locked at zero modulo π. This means

$$\theta_{\mathrm{seed}}^{\mathrm{in}} = \tfrac{1}{2}\theta_{\mathrm{pump}} \quad \text{or} \quad \theta_{\mathrm{seed}}^{\mathrm{in}} = \tfrac{1}{2}\theta_{\mathrm{pump}} + \frac{\pi}{2} \tag{2.78}$$

As we will see below, the relevant optical phase for our problem is the output seed phase θ_{seed}, which is related to the input seed phase $\theta_{\mathrm{seed}}^{\mathrm{in}}$ by equation (2.72). Note that for this equation only, the gain to consider is the single-pass gain of the crystal, not the gain enhanced by the SPOPO cavity. Reasoning in the stationary regime, the (single-pass) operation of the crystal applies on the stationary field in the cavity, relating the phases at its input and output by equation (2.72) with the single-pass gain. By resonance, the cavity only adds multiples of 2π on the phase of the field.

In our configuration, we expect the single-pass gain to be small, as we rely on the SPOPO cavity for obtain significant squeezing factors. In the thesis [Thiel 15], the single-pass gain is estimated at 1 dB in our usual configuration, i.e. $\mathrm{e}^{2r} \simeq 1.3$. To see the effect of equation (2.72), the output seed intensity and phase are plotted in figure 2.17.

The blue curve corresponds to our 1 dB single-pass gain, the red curve corresponds to a 3 dB gain and the black one serves as reference. On the graph 2.17 (a), at relative phase $\theta_{\mathrm{seed}}^{\mathrm{in}} - \frac{1}{2}\theta_{\mathrm{pump}} = 0$ the seed intensity is maximally deamplified, while at $\theta_{\mathrm{seed}}^{\mathrm{in}} - \frac{1}{2}\theta_{\mathrm{pump}} = \pi/2$ the seed intensity is maximally amplified. We will consistently refer to these two situations as respectively *seed deamplification* and *seed amplification*. Note that for the blue curve shows the seed intensity after a single pass through the crystal. The expected intensity at the output of the cavity follows the cavity gain, estimated at about 4 dB, i.e. $\mathrm{e}^{2r_{\mathrm{cav}}} = 2.5$[1].

On the graph 2.17 (b), we notice that at both seed amplification and deamplification, the abscissas and ordinates coincide, i.e. $\theta_{\mathrm{seed}} = \theta_{\mathrm{seed}}^{\mathrm{in}}$. Whatever the gain, we can then re-write the seed-pump phase locking relation of equation (2.78) as

$$\theta_{\mathrm{seed}} = \tfrac{1}{2}\theta_{\mathrm{pump}} \quad \text{or} \quad \theta_{\mathrm{seed}} = \tfrac{1}{2}\theta_{\mathrm{pump}} + \frac{\pi}{2} \tag{2.79}$$

[1]For reference, this gain correspond to a contrast $C_{\text{amp-deamp}}$ of 75%, where the contrast is defined as $C_{\text{amp-deamp}} = (I_{\mathrm{seed}}^{\max} - I_{\mathrm{seed}}^{\min})/(I_{\mathrm{seed}}^{\max} + I_{\mathrm{seed}}^{\min})$, measured at the output of the SPOPO, and is related to the gain parameter by $C_{\text{amp-deamp}} = \tanh(2r)$.

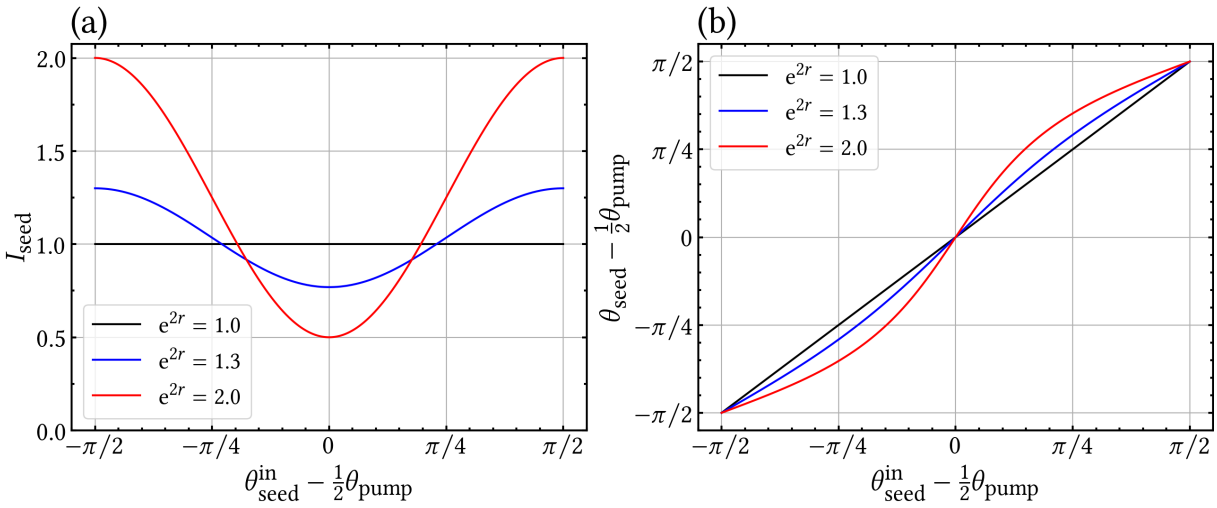

Fig. 2.17 Seed amplification-deamplification effects on (a) the output relative phase $\theta_{\text{seed}} - \frac{1}{2}\theta_{\text{pump}}$ and (b) the output seed intensity I_{seed} versus the input relative phase $\theta^{\text{in}}_{\text{seed}} - \frac{1}{2}\theta_{\text{pump}}$ for different values of the gain e^{2r}.

It is worth noting that these two locking points are not equivalent in terms of sensitivity to locking error. In graph 2.17 (b), the derivative is significantly higher at seed deamplification than at seed amplification. Using equation (2.72), we find that the ratio between the two derivatives equals e^{4r}, hence 1.7 for a gain of $e^{2r} = 1.3$. In other words, a locking error on the input seed phase yields an error on the output seed phase 1.7 times higher in deamplification than in amplification, an qualitative effect experimentally observed. Although our single-pass gain is small, this effect is not negligible and allows for some improvement of the lock stability. Note that for other configurations, which rely more on the single-pass gain of the PDC, this effect may play a significant role in the locking success.

Experimentally, we can switch between the two seed-pump locking points defined in equation (2.79) by switching the sign of the parameter $\phi_1 = \pm\pi/2$. Looking at the seed intensity while locking, we can then deduce whether the seed is amplified or deamplified. Depending on the application, we need either both locking points or only one. In the latter case, we thus preferentially set ourselves at seed amplification, to benefit from a decreased locking error.

Up to now, we showed that the seed-pump lock relates the output seed phase θ_{seed} (which we now refer to as simply the seed phase) and the pump phase θ_{pump} by equation (2.79). Let us now relate the pump phase with the signal phase.

Signal-pump phase relation. We cannot define the signal phase θ_s the same way we defined the pump phase θ_{pump} in equation (2.70): for quantum states that feature a null-mean field, there is no generic way of defining an optical phase. For example, a thermal state (or the vacuum) is perfectly symmetric in the phase space, so that its phase is non-definite. The phase of squeezed vacuum states is commonly defined such that the corresponding quadrature is the squeezed quadrature (defined in subsection 1.3.3).

Since the signal is generated from the parametric down-conversion (PDC) of the pump beam, we can define θ_s following the same idea. Assuming first that the signal state is a

single-mode squeezed vacuum state, the PDC operation writes when taking into account the phase of the pump [Loudon 00]

$$\hat{S}(\zeta) = \exp\left[\tfrac{1}{2}(-re^{-i\theta_{\text{pump}}}\hat{a}^2 + re^{i\theta_{\text{pump}}}\hat{a}^{\dagger 2})\right] \tag{2.80}$$

where $\hat{S}(\zeta)$ is the squeezing operator defined in equation (1.77) subsection 1.3.3 with complex squeezing parameter $\zeta = -re^{i\theta_{\text{pump}}}$[1], with $r > 0$.

The corresponding squeezed quadrature is the quadrature operator $\hat{q}^{\theta_{\text{pump}}/2}$ at angle $\theta_{\text{pump}}/2$. We then define the signal phase θ_s as

$$\theta_s = \tfrac{1}{2}\theta_{\text{pump}} \tag{2.81}$$

Note that with such definition, the phase θ_s is defined modulo π since the pump phase is defined modulo 2π. For a general multimode signal state, we keep defining the optical phase of the signal θ_s from the optical phase of the pump as in equation (2.81).

Using both equations (2.78) and (2.81), we can relate the seed phase with the signal phase at the output of the BiBO crystal (under locking operation) as

$$\theta_{\text{seed}} = \theta_s \quad \text{or} \quad \theta_{\text{seed}} = \theta_s + \frac{\pi}{2} \tag{2.82}$$

LO-seed lock. Since the seed beam takes the role of the vacuum in the parametric down-conversion process in the SPOPO, the signal and seed optical paths coincide exactly. Since they also share the same polarization, spatial mode and central wavelength, any phase shift experienced by the seed beam is equally experienced by the signal beam. The relation between the seed and signal phases at the output of the crystal in equation (2.82) holds then true at any point in the common path of the beams, in particular up to the homodyne detection. We thus keep the notations θ_{seed} and θ_s for the seed and signal phases at the homodyne detection.

We can now define the LO-signal relative phase θ at the homodyne detection as

$$\theta = \theta_{\text{LO}} - \theta_s \tag{2.83}$$

where θ_{LO} is defined similarly as θ_{pump} in equation (2.70). Let us now relate the LO phase θ_{LO} and the seed phase θ_{seed} at the homodyne detection.

As mentioned, the seed beam follows the same optical path as the signal pictured in figure 2.1 of the complete experience. After going through the photon subtraction setup (which we discuss later), the seed beam reaches the homodyne detection where it can interfere with the LO beam, see figure 2.16 (d) (where we ignore the spectrum analyzer for now). The classical interference of the two fields results then in a phase-sensitive electronic signal. Using a similar setup as before, the "LO-seed lock" locks the LO-seed relative phase through demodulation, filtering and another (Red Pitaya) PID controller (see appendix C.2 for the detailed electronic circuit).

[1] We chose $\zeta = -re^{i\theta_{\text{pump}}}$ instead of $\zeta = -re^{i\theta_{\text{pump}}}$ for better readability in the following. Note that this choice is a matter of convention or more generally a matter of pump phase reference.

From equation (2.47) applied for the seed and LO fields assumed mode-matched, the homodyne detection output current $i_d = \langle \hat{i}_d \rangle$ writes

$$i_d = 2\,\mathrm{Re}\left(\langle \hat{\mathbf{E}}_{LO}^{(+)} \rangle \, \langle \hat{\mathbf{E}}_{seed}^{(-)} \rangle \right) \tag{2.84}$$

which yields

$$i_d \propto \cos(\theta_{LO} - \theta_{seed}) \tag{2.85}$$

Experimentally, we expect to measure a null difference of current on the homodyne detection when the intensity on each arm of the homodyne detection (defined as arms 1 and 2 on figure 2.15) are equal. This happens when the LO and seed fields are in phase quadrature, i.e. at $\theta_{LO} - \theta_{seed} = \pi/2$. At this relative phase value, the current i_d vanishes in expression (2.85), as expected.

Taking into account the modulation of the seed beam and the demodulation in the "LO-seed lock" device, we derive the LO-seed error signal u_2^{err} following the same steps as before. We find

$$\begin{aligned} u_2^{err} &\propto \sin(\theta_2)\sin(\phi_2) \\ \text{with} \quad \theta_2 &= \theta_{LO} - \theta_{seed} \end{aligned} \tag{2.86}$$

with ϕ_2 the phase of the demodulating eLO. The parameter ϕ_2 is set to maximize the error signal amplitude, at $\pm\pi/2$, and do not play any role on the locked phase this time. Minimizing equation (2.86) results in θ_2 equaling zero modulo π. Together with equation (2.82) which relates θ_{seed} and θ_s, we can write under locking operation

$$\theta_{LO} = \theta_s \quad \text{or} \quad \theta_{LO} = \theta_s + \frac{\pi}{2} \tag{2.87}$$

which rewrites using equation (2.83) as

$$\theta = 0 \quad \text{or} \quad \theta = \frac{\pi}{2} \tag{2.88}$$

We can thus lock the LO-signal phase θ to either zero or $\pi/2$ through the interaction of the seed beam with both the LO and pump beam.

Note that, according to our phase definitions, the case $\theta = 0$ corresponds to both locking on the deamplification of the seed and on the squeezed quadrature of the signal, when the LO mode is the first supermode (or any odd-numbered supermode). We then expect to measure a variance below the vacuum variance at $\theta = 0$, and above at $\theta = \pi/2$.

Choosing the value of the locked phase θ. For numerous applications, such as to perform the tomography of a quantum state with a single homodyne detection, it is interesting to be able to arbitrarily control the value of the phase θ. Up to now, we showed that we can lock on two locking points, $\theta = 0$ and $\theta = \pi/2$.

In general, one can change the value at which a PID locks, moving from 0 to a desired value, which we refer to as *setting point*. Changing the setpoint of a lock comes at the cost

of increased error and instability. Considering the non-linear relation between the input seed phase and the output seed phase plotted in graph 2.17 (b), we expect the seed-pump lock to be less stable than the LO-seed lock.

Note yet that we can switch easily between $\theta = 0$ and $\theta = \pi/2$ with the seed-pump lock. To cover a complete π range θ phases, it is then enough to change the setting point of the LO-seed lock such that the phase θ varies in the range $[-\pi/4, \pi/4]$. This is half the maximal range of the seed-LO setting point range. As I am writing these lines, the lock has not been tested yet outside of the two locking phases $\theta = 0$ and $\theta = \pi/2$, and the question whether the LO-seed lock remain stable enough to cover this range is open to investigation.

2.5.2 Measuring while locking

In practice, we need the phase θ to be locked while we are measuring the signal quadrature $\hat{q}_s^\theta$ in the homodyne detection. Since the seed beam is taking the exact same path as the signal beam, with the same spatial mode, the same polarization, and the same central wavelength at 795 nm, there is no way to physically distinguish them (especially without adding losses to the signal). Even worse, we measure them both on the same device, the homodyne detection. Thus, we can not measure them both at the same time.

We therefore use a common trick which consists in blocking periodically the seed beam. The resulting periodic cycle allows us to alternatively lock the phase θ or measure the signal beam.

Chopping the seed beam. To periodically block the seed beam, we use a MC2000B Thorlabs optical chopper, pictured in the figure 2.16 (a). We chose a mechanical chopper as the light is completely absorbed in the blocking configuration. If it was not the case, even if a few photons were going through, the measurement would be not reliable anymore. The signal beam indeed only contains in average about 1 photon per supermode.

Running the motor at 80% of its maximal speed, i.e. turning at 80 Hz, allows for low amplitude induced vibrations and a chopping rate of 8 kHz using a blade of 100 slots. Measuring the seed intensity after the chopper yields a 135 us period cycle, shown in figure 2.18. The chopping rate is then effectively smaller, at about 7.3 kHz. When the seed beam is completely going through, both seed-pump and LO-seed lock devices are enabled, corresponding to the "Lock" time slots in figure 2.18. For the rest of the time, the lock devices are deactivated yet maintain a constant control signal, which corresponds to the final value of the locking control signal. The corresponding time slot is "Hold" in figure 2.18. When the seed beam is completely blocked by the chopper, we can measure the signal beam on the homodyne detection, corresponding to the "Measure" time slot in figure 2.18. The rising and lowering times of the chopper only partially absorbs the light, and cannot be used for neither the measurement nor the lock. Furthermore, we need some additional dead time before and after measurement in order to safely protect the single-photon detector of the experiment, as we explain below. As a result, in the configuration of figure 2.18, we can measure on 35 us over each cycle of 135 us, corresponding to a duty cycle of 26%.

One of the critical parameters for a functional lock is a high chopping rate with respect to the typical LO-signal phase θ fluctuations. A high chopping rate indeed allows for short

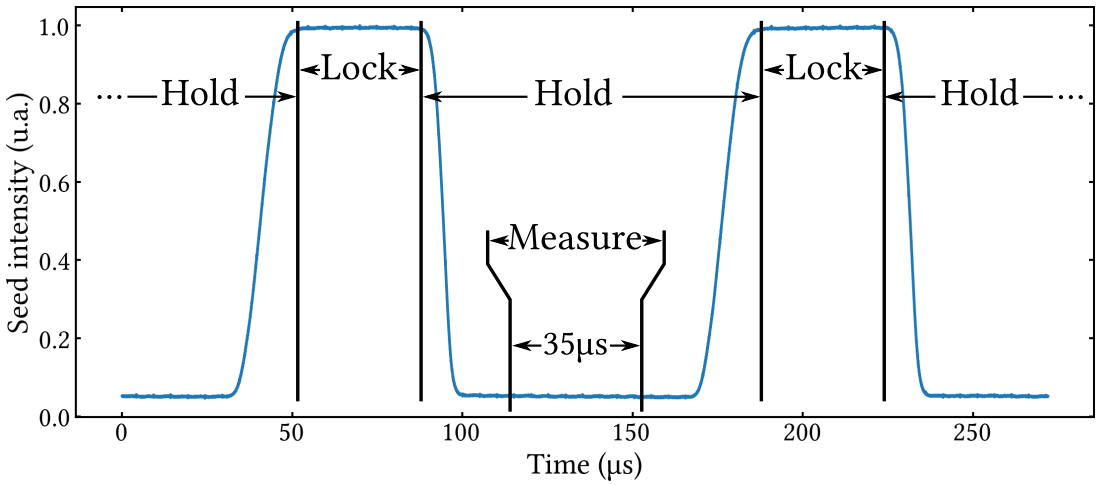

Fig. 2.18 Intensity of the seed beam measured after the optical chopper, whose the blades regularly absorb the light. The resulting pattern is partitioned in "Lock" and "Hold" times slots, referring to the operation of the locking devices. The actual measurement is done during the "Measure" time slot. The synchronization between the optical chopper, the lock devices and the AOM is done using a TTL generator.

"Hold" time slots, during which the phase may drift. If the drift is too large during this time slot, then the lock devices cannot follow and fail to properly lock. As mentioned, we observe phase noise up to a few kHz. The chopping rate of 7.3 kHz proved to be high enough for the lock devices to function properly. This is among the highest rates available in the commercial market for mechanical choppers.

It is worth noting that our second-best choice is using an acousto-optic modulator in a double path configuration, see for instance [Donley 05]. While it permits an equivalent mechanical chopping at MHz range rates, it adds the challenge of introducing significant amounts of dispersion to the seed beam, leading to a decreased interaction efficiency with the LO and pump beams.

Setup constraints. Let us focus on the details of the setup pictured in figure 2.16 (a). To fit the space constraints on our optical table, we chose to implement both the beam chopping and the phase modulation in a folded 2-f configuration. The seed beam is focused on a zero-degree piezoelectric mirror positioned at the Fourier plan of the lens, and goes through the same lens on its way back. This compact setup allows us to

- set the blades of the optical chopper close to the minimal waist of the focused beam. This decreases the rising and lowering times shown in figure 2.18.
- use a zero-degree mirror for a lower induced misalignment of the focused beam compared to a 90° configuration[1].

Note that if we had more space, the optical chopper could be built on a non-folded 2-f configuration. This would result in further decreased rising and lowering times as the chopper could

[1] In principle, this effect is negligible for typical small piezoelectric translation of about 1 µm.

be precisely positioned at the minimal waist. It would also avoid the seed beam to pass twice the chopper, which may result in an effective larger beam. This effect was minimized in our setup by aligning the back and forth beams with the motor axis on the same plane.

Preventing killing the single photon detector. When not absorbed by the chopper blade, the seed beam follows the optical path taken by the signal, and in particular goes through the photon subtraction, see figure 2.16 (c). As mentioned in section 2.1, the signal beam interacts with a classical beam, called the gate beam, in the BiBO crystal through sum-frequency generation. This non-linear process generates single photons centered at 397.5 nm. These single photons are collected by a fiber and detected by a single photon detector.

This detector can not sustain bright fields, due to its single-photon sensitivity. Its power threshold before damage can be estimated at a few millions of photons per second at this wavelength. When the bright seed beam goes through the crystal, it generates a bright beam at more than 100 nW power, which is very large compared to the detector power threshold, as it corresponds to about 10^{11} photons per second. This forbids then any solution with partial power deflection, such as Pockel's cells which feature an extinction ratio of up to 10^3.

Instead, we use an acousto-optic modulator (AOM) to protect the single photon detector. It is an AOM MQ110-A3-UV from AA Opto-Electronic. The AOM uses a piezoelectric transducer to produce standing sound waves in a transparent material, in which the incoming light sees a periodic modulation of the index of refraction. The incoming light is then mostly diffracted with a small angle of a few degrees. For our AOM, about 90% of the light is diffracted.

The AOM is set such that the transmitted light is dumped, while the diffracted light is detected on the single photon detector as pictured in figure 2.16 (c). Consistently, it is only enabled when the seed is completely blocked by the chopper blade, during the "Measure" time slots pictured in the figure 2.18. Only the signal beam is sent by the AOM to the detector, protecting the precious detector from any damage.

Note that the diffracted light sees its frequency shifted by about 100 MHz, which is negligible compared to the carrier frequency of the light, around 10^{16} Hz. It then has no consequence in the measurement.

Induced square signal. By cutting the seed beam, the wheel is modulating the intensity, resulting in a seed intensity of the form of a square function with respect to time as shown in figure 2.18. Since both lock systems described in subsection 2.5.1 rely on measuring seed-intensity dependent signals, we have to cope with a square electronic signal. In appendix C.2, we explain how we cope with it using filters to avoid saturating the electronics. Furthermore, as we alternatively measure the seed and signal fields at the detection, the measurement signal also features extremely sharp behavior at transitions between "Lock" times and "Hold" times. Simply filtering does not solve this issue and a more elaborate solution is required, as explained in later chapter 4, section 4.4.

2.5.3 Application: measuring squeezing

In the previous subsections, we showed that using an optical chopper and an acousto-optic modulator, we can lock the LO-signal phase θ in a periodic cycle given by figure 2.18. During

the "Measure" time slots, the signal beam is then measured by the homodyne detection (d) in figure 2.16. In this subsection, we show how we use the homodyne detection to characterize the signal squeezed vacuum, and then discuss the advantage of locking the optical phase θ.

Measuring squeezed vacuum states. To characterize squeezed vacuum states, we only need to measure their squeezing and antisqueezing quadrature variances, as they are zero-mean Gaussian states, see subsection 1.3.3 for details on these states.

While we could directly gather the measurement outcomes of the homodyne detection, which follow the probability distribution of the quadrature $\hat{q}_s^\theta$, we use an alternative measurement method to avoid the low frequency noise in the measurements. We feed the output homodyne detection current to a MXA N9020A spectrum analyzer (20 Hz- 2.6 GHz) as pictured in figure 2.16 (d). As explained in details in subsection 2.4.3, a spectrum analyzer measures the spectral density $S_d(f)$ of the output current of the homodyne detection. From equation (2.64), the spectral density $S_d(f)$ integrated over the bandwidth of the detector yields the variance of the output current $\langle \Delta^2 \hat{i}_d \rangle$. Normalizing to the measured variance of the vacuum as in equation (2.34), we can deduce the variance $\langle \Delta^2 \hat{q}_s^\theta \rangle / \sigma_0^2$ of the signal quadrature.

To avoid low frequency noise, we usually choose to integrate the spectral density $S_d(f)$ over a limited bandwidth of 100 kHz at central frequency $f_0 = 1$ MHz. Technically, we are then measuring the variance of the quadrature associated to the signal side-band modes at this frequency f_0. We won't enter into the details, and refer to [Michel 21] for more on the side-band modes. Note that the squeezing factors in the side-band modes are expected to be close to constant over the cavity bandwidth of the SPOPO, which is of the order of a few MHz. We are then correctly estimating the signal variance when measuring the side-band mode at 1 MHz. We will keep denoting by $\langle \Delta^2 \hat{q}_s^\theta \rangle / \sigma_0^2$ the measured quantity on the spectrum analyzer. Let us now discuss the measurement methods, both prior and after the implementation of the optical phase locking system.

Measuring while scanning the LO phase. When the locking system was not set up yet, the optical LO-signal phase θ was freely drifting while measuring squeezed signal field in the homodyne detection. To retrieve a phase reference, the phase of the LO beam was scanned by feeding a periodic signal to a piezoelectric mirror on the LO optical path. An example of such measurement is shown in figure 2.19. The measured variance of the signal quadrature $\langle \Delta^2 \hat{q}_s^\theta \rangle / \sigma_0^2$ is then varying with θ from the variance of the squeezed quadrature (low) to the variance of the antisqueezed quadrature (high). By convention, we assign the phase $\theta = 0$ to the most squeezed quadrature, hence $\hat{q}_s$. The antisqueezed quadrature is then $\hat{p}_s$ at $\theta = \pi/2$. Fitting the resulting curve with a cosine allows to retrieve the phase θ and therefore infer the measured quadrature $\hat{q}_s^\theta$ at any time. In the provided example, the measured mean variance of the squeezed quadrature $\langle \Delta^2 \hat{q}_s \rangle / \sigma_0^2$ is estimated to about -2 dB, while for the antisqueezed quadrature, its variance $\langle \Delta^2 \hat{p}_s \rangle / \sigma_0^2$ is estimated to about 3.5 dB, for a pump power of $\mathcal{P}_p = 20$ mW.

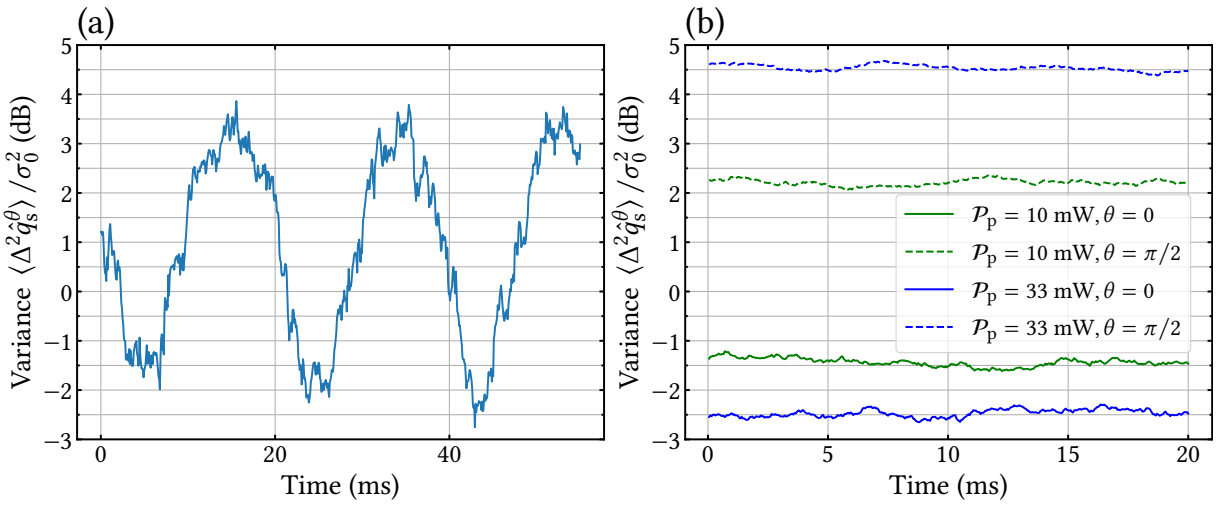

Fig. 2.19 Squeezing measurement on a spectrum analyzer. The measured variance of the signal quadrature $\langle \Delta^2 \hat{q}_s^\theta \rangle / \sigma_0^2$ (normalized to the vacuum variance) against the time is plotted for different phases θ depending on the method. (a): The phase θ is scanned over time at pump power $\mathcal{P}_p = 20\,\text{mW}$. (b): The phase θ is locked at either 0 (solid lines) or $\pi/2$ (dashed lines), for different pump powers $\mathcal{P}_p$. The output reflectivity is $r_o^2 = 80\%$.

Measuring while locking the LO-signal phase. Using the optical phase locking system, the LO-signal phase θ is locked at either $\theta = 0$ or $\theta = \pi/2$[1]. We give for example some measurements in figure 2.19 (b). We concatenate the measurements of each locking cycle by suitably triggering the spectrum analyzer (using its "gate" function). The traces are averaged 10 times over.

Let us denote the signal squeezing factors as $s^- = \langle \Delta^2 \hat{q}_s \rangle / \sigma_0^2$ and $s^+ = \langle \Delta^2 \hat{p}_s \rangle / \sigma_0^2$ (with their dB versions $s^\pm_{\text{dB}}$), and the resulting signal purity $\mu_s = 1/\sqrt{s^+ s^-}$. Their averaged values are displayed in the table 2.3. As expected, the squeezing factors increase with the pump power, at the cost of a lower purity.

$\mathcal{P}_p$	s^-_{dB}	s^+_{dB}	μ_s
10 mW	−1.43 dB	2.21 dB	0.914
33 mW	−2.47 dB	4.54 dB	0.788

Table 2.3: Averaged signal squeezing factors $s^\pm_{\text{dB}}$ and purity μ_s for different pump power $\mathcal{P}_p$ values.

We can estimate the squeezing factors at the output of the SPOPO by correcting the losses of the homodyne detection. The homodyne efficiency η_{HD} was estimated to 81% in subsection 2.4.3. We can then apply the model described by equation (2.53) to infer the corrected

[1]For this set of measurements, the double homodyne was used, locking at $\theta = 0$ on one homodyne detection, which implies measuring at $\theta = \pi/2$ on the other homodyne detection. The measurements were rescaled to take into account the inherent mixing with the vacuum, due to the double homodyne configuration. See chapter 4 for more details on the double homodyne.

squeezing factors as

$$s^{\pm}_{\mathrm{dB}} \mapsto \frac{s^{\pm}_{\mathrm{dB}}}{\eta_{\mathrm{HD}}} + \frac{1-\eta_{\mathrm{HD}}}{\eta_{\mathrm{HD}}} \tag{2.89}$$

The corrected values are shown in table 2.4. We can see that the change on the signal purity μ_{s} is lower for already highly pure states. Comparing with the figure 2.10, we measure lower squeezing factors than expected. The discrepancy may stem from inaccuracy in the SPOPO model, an underestimation of the losses, an inaccurate phase locking, or other non-considered errors in the measurement.

$\mathcal{P}_{\mathrm{p}}$	s^{-}_{dB}	s^{+}_{dB}	μ_{s}
10 mW	−1.85 dB	2.60 dB	0.917
33 mW	−3.33 dB	5.15 dB	0.811

Table 2.4: Loss-corrected averaged signal squeezing factors $s^{\pm}_{\mathrm{dB}}$ and purity μ_{s} for different pump power $\mathcal{P}_{\mathrm{p}}$ values.

One of the main advantage of locking the phase θ is to drastically simplify the data analysis, as we directly measure the quantity of interest. A simple averaging is enough. Previously, fitting the traces to recover the phase often proved to be hard for technical reasons. For instance, the number of accurate enough oscillations in one trace is limited to a few, and it is not possible to average over multiple traces before recovering the phase θ. Such reduction of data analysis complexity opens the path to more complex measurements than squeezing measurements, otherwise considered unfeasible. In particular, locking (or knowing) the phase θ is necessary for the certification protocol presented in chapter 4.

Towards multimode optical phase locking. Up to now, the LO-signal phase θ was successfully locked only when the LO time-frequency mode is the first supermode, i.e. when the LO spectrum is Gaussian. As the seed inherits the laser source properties, it also has a Gaussian spectrum, which allows for the aforementioned LO-seed interference. If we choose to shape the LO time-frequency in another supermode, then the seed and LO modes would be orthogonal, resulting in a null-interference term. The LO-seed locking would then be impossible.

As the LO-seed feedback signal is not required to have a high amplitude for the lock to function properly, a possible solution would be to slightly shift the central frequency of either spectrums in order to recover non-orthogonal time-frequency modes.

2.6 Extra experimental tools for a multimode extension

In this section, we briefly describe the additional experimental modules displayed in figure 2.1 in section 2.1, namely the pump blue pulse shaper (module **1.b)**) and the photonic cristal fiber (module **3.a)**). These additional modules, while not used in the context of this thesis, offer potential for the multimode development of this work.

2.6.1 Engineering the supermodes squeezing

Introduced in section 2.3, the Hamiltonian of the parametric down-conversion occurring in the SPOPO is given by the joint spectral amplitude which is the product of the pump spectrum $\widetilde{\mathbf{h}}_{\mathrm{p}}$ and the phase-matching function Φ_{PDC}, see equation (2.14). The phase-matching function depends on the crystal attributes that are fixed upon choosing and engineering the crystal. However, the pump spectrum may be engineered using the pump pulse shaper **1.b)**, see figure 2.1. As detailed in subsection 2.2.4, the pulse shaper allows us to engineer the amplitude and phase of the pump spectrum $\widetilde{\mathbf{h}}_{\mathrm{p}}$.

By engineering the time-frequency mode of the pump, we can thus engineer the Hamiltonian of the process. This in turn results in a new eigenvalue distribution, or equivalently to new squeezing factors in the supermodes.

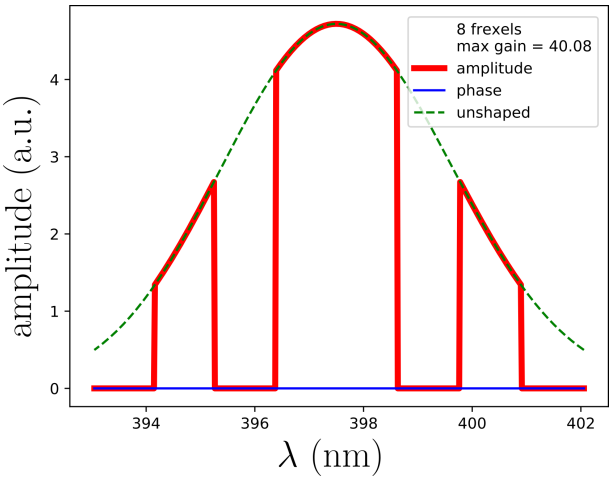

Fig. 2.20 Pump spectrum which optimized the squeezing factor in the first supermode, resulting from the neural network algorithm. Figure from [Michel 21].

This potential re-distribution of the squeezing at the output of the SPOPO has been studied by F. Arzani and T. Michel. F. Arzani studied how to improve output states by using a genetic algorithm which mimics Darwinian evolution to explore the different input parameters [Arzani 18]. To extend these results T. Michel used a reinforcement algorithm based on projective simulation method and a deep learning one based on neural network [Michel 21]. These algorithms searched for the pump spectrum that best optimize a chosen squeezing distribution. For instance, the resulting pump spectrum which optimize the squeezing in the first supermode (at the expanse of the squeezing in the other supermodes) is shown in figure 2.20. Another example is to flatten the squeezing factor distribution, which may prove useful for measurement based quantum computing, as the output state can be used to construct a good approximation of a cluster state [Michel 21].

The pump pulse shaper definitely holds interest for a future extension of the current work, as a tool to engineer the source of multimode Gaussian states of the experiment.

2.6.2 Broadening the local oscillator spectrum

The global experiment design pictured in figure 2.1 has a flaw, which stems from using the same laser source **0)** for both the multimode squeezing generation **1)** and the detection **2)**[1]. Since the local oscillator pulse shaper **3.b)** is composed of only passive elements, it may only carve in the spectrum, as it can not add energy. The input spectrum from **0)** is thus the given available spectral energy distribution used to shape the modes. However, the supermodes are approximately Hermite-Gaussian modes whose spectral full width half maximums grow with n the mode number, see appendix A.2. These modes may then be much larger than the Gaussian spectrum of the laser source. Measuring such modes demands for shaping spectral regions with near-zero energy, which is physically inhibited.

To cope with this pulse shaper limitation, we can further engineer the time-frequency mode of the local oscillator using the photonic crystal fiber **3.a)** before the pulse shaper **3.b)**. This device broadens the input spectrum by about twice its full width half maximum, as shown in figure 2.21. The broadening of the spectrum is due to a non-linear phase self-modulation effect, stemming from the third order non-linear Kerr effect [Dudley 10, Hammer 16]. The photonic crystal fiber has been designed and fabricated by Nicolas Joly and his team from the Max Planck Institute based in Erlangen for our purpose [Joly 12, Hammer 16]. The fiber was shown to increase the efficiency to measure an increased number of supermodes in our setup without adding additional noise, see [Renault 22].

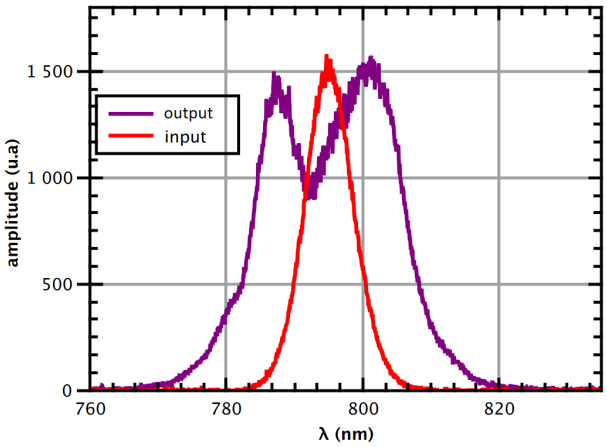

Fig. 2.21 Output spectrum of the photonic crystal fiber (in purple), for an input power of 110 mW and Gaussian input spectrum (in red). Figure from [Renault 22].

In the scope of this thesis' experimental project, we used the local oscillator pulse shaper **3.b)** to shape a mode that didn't require a large spectral distribution, and as such we did not use the photonic crystal fiber. We expect it to prove useful to extend the current work to multimode certification in this setup.

[1]Note that using just one laser offers benefits over multiple lasers in terms of cost, space requirements, and the need for mode matching between lasers.

Chapter 3

Non-Gaussian operations using non-linear optics

Contents

The states of light whose quantum non-Gaussianity we aim at certifying in this thesis are the single-photon subtracted and added squeezed vacuum states described in subsection 1.4.4. These states are generically produced by heralding on the subtraction or addition of a single photon from a squeezed vacuum state. In chapter 2, we elaborated in particular on the experimental generation of multimode squeezed vacuum states. In this chapter, we focus on the non-Gaussian single-photon addition or subtraction applied on such Gaussian multimode states.

Both operations have been largely investigated acting on single-mode fields [Lvovsky 20], where photon-subtraction can be implemented via a low-reflectivity beam-splitter [Ourjoumtsev 06] and single-photon addition on coherent states via a parametric amplifier with a strongly filtered heralding field [**?**]. These operations are not suitable in the context of a spectrally multimode light, since the spectral mode in which the single photon is added or subtracted cannot be controlled in these setups. Such operation may then result in a statistical mixture of single-photon subtracted or added states.

To circumvent this issue, a general theoretical framework for the mode-selective single-photon subtraction and the investigation on its application via sum-frequency generation in non-linear crystals were developed in [Averchenko 14, Averchenko 16]. Differently from the low-reflectivity beam-splitter, the non-linear process allows for the subtraction of a single photon from a selected time-frequency mode of a multimode input field. Single-photon addition has been recently implemented in delocalized temporal modes [Biagi 21] but spectral mode selectivity was still missing.

In the first three sections of this chapter, we report on the development of a complete theoretical framework to generate non-Gaussian quantum states of light by performing the addition of a single photon to multimode light fields, following our work [Roeland 22]. We both analytically and numerically investigate under which conditions and experimental configurations it is possible to achieve single-mode and mode-selective single-photon addition. We analyze configurations of parametric down-conversion processes in non-linear bulk crystals both at near infrared and telecommunication wavelength, and discuss the effect of filtering.

While this recent theoretical investigation opens the way to an experimental implementation of single-photon addition for spectrally multimode sates, in the experimental work of this thesis we use a single-photon subtraction setup. In our group, the mode-selective single-photon subtraction theoretically developed in [Averchenko 14, Averchenko 16] was experimentally demonstrated via sum-frequency generation in non-linear crystals in [Ra 17, Ra 20]. In a subsequent section, we describe how we implement such subtraction in the laboratory, and report on the current performance.

In the last section of this chapter, we open the discussion to potential developments towards experimental multiple-photon subtraction.

3.1 Theoretical framework for multimode single-photon addition

In this section, we study general models, abstracted from a specific physical implementation, for the single-mode and multimode single-photon addition. The single-mode model is an ideal approach, requiring the underlying physical implementation to perfectly add a single-photon in only one mode. We show in particular that an imperfect addition process, in the sense that it is multimode, results necessarily in a non-pure output state.

3.1.1 Single-mode single-photon addition

Let us consider a general single-mode single-photon addition process. We consider a general heralding addition process illustrated in figure 3.1, similarly to parametric down-conversion occurring in a non-linear crystal. At the input, we consider two modes, the *signal* mode containing the quantum state $\hat{\rho}_s^{in}$ to be photon-added, and the *idler* mode, which is in the vacuum state initially. The process itself is modeled by the evolution operator $\hat{U}$, which generates one photon in both the signal and idler modes. We note $\hat{\rho}_s^+$ the signal single-photon added state conditioned by the detection of a photon in the idler output.

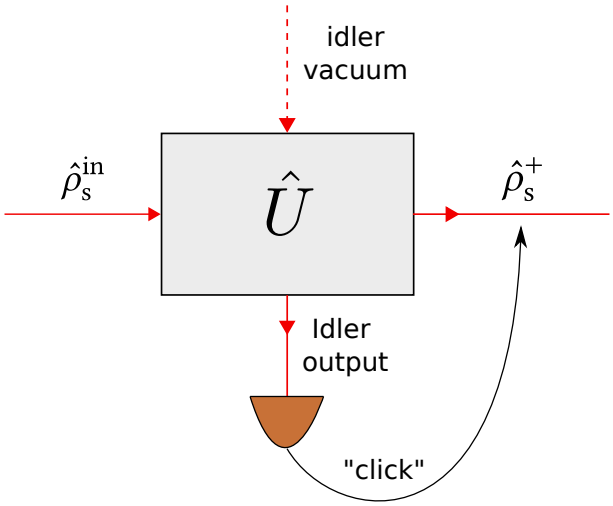

Fig. 3.1 Scheme of conditional single-photon addition. The state $\hat{\rho}_s^{in}$ in the signal mode and the vacuum in the idler mode undergo the process operation $\hat{U}$. At the output, the single-photon added state $\hat{\rho}_s^+$ is conditioned on the detection of a single photon at the idler output.

The unitary evolution operator $\hat{U}$ may be modeled as

$$\hat{U} = \exp\left(ig(\hat{a}_s\hat{a}_i + \hat{a}_s^\dagger\hat{a}_i^\dagger)\right) \tag{3.1}$$

where $g > 0$ is the strength of the parametric generation taking into account the power of the non-depleted classical gate, $\hat{a}_s$ is the annihilation operator associated to the signal mode, and $\hat{a}_i$ is the annihilation operator associated to the idler mode.

The detection on the idler mode after the evolution $\hat{U}$ is not assumed to be photon-number resolving. Such detection may be efficiently implemented with avalanche photodiodes for instance. This detection may be modeled by the positive operator-valued measure (POVM) $\{|0\rangle\langle 0|_i, \hat{\Pi}_i\}$ with $\hat{\Pi}_i = \hat{\mathbb{1}}_i - |0\rangle\langle 0|_i$ (see section 2.4 for details on POVMs).

The output density operator in the signal mode $\hat{\rho}_s^+$ conditioned to the measurement of a photon in the idler mode is then formally given by

$$\hat{\rho}_s^+ = \frac{1}{P^+}\,\mathrm{Tr}_i\left[\hat{\Pi}_i\,\hat{U}\hat{\rho}^{in}\hat{U}^\dagger\right] \tag{3.2}$$
$$\text{with} \quad P^+ = \mathrm{Tr}\left[\hat{\Pi}_i\,\hat{U}\hat{\rho}^{in}\hat{U}^\dagger\right]$$

where $\hat{\rho}^{\text{in}} = \hat{\rho}_{\text{s}}^{\text{in}} \otimes |0\rangle\langle 0|_{\text{i}}$ is the complete two-mode input state, the normalization constant P^+ is the probability to successfully detect a photon in the idler mode. This result was already shown in [Zavatta 07]. We point out that the probability P^+ to detect a photon depends linearly on $1+\bar{n}_{\text{s}}$, which corresponds to the fact that parametric down-conversion behaves as an amplifier. Indeed, for an amplifier the output power is proportional to the input one, and thus the number of generated photons in both idler and signal modes increases with the signal input power. In other words, the more photons are in the input state, the more likely it is to add a photon to the signal.

Since we look for single-photon addition, we restrict ourselves to the weak-coupling regime, i.e. $g \ll 1$. In this regime, we can develop equation (3.1) to the second order in g as

$$\hat{U} = \hat{\mathbb{1}} + \mathrm{i}g(\hat{a}_{\text{s}}\hat{a}_{\text{i}} + \hat{a}_{\text{s}}^\dagger\hat{a}_{\text{i}}^\dagger) - \frac{g^2}{2}(\hat{a}_{\text{s}}^2\hat{a}_{\text{i}}^2 + \hat{a}_{\text{s}}^{\dagger 2}\hat{a}_{\text{i}}^{\dagger 2} + \hat{a}_{\text{s}}\hat{a}_{\text{s}}^\dagger\hat{a}_{\text{i}}\hat{a}_{\text{i}}^\dagger + \hat{a}_{\text{s}}^\dagger\hat{a}_{\text{s}}\hat{a}_{\text{i}}^\dagger\hat{a}_{\text{i}}) + \mathcal{O}(g^3) \tag{3.3}$$

In equation (3.2), the only relevant terms to keep in $\hat{U}\hat{\rho}^{\text{in}}\hat{U}^\dagger$ are the terms of the form $|n\rangle\langle n|_{\text{i}}$ in the idler mode with $n \geq 1$, considering the partial trace $\mathrm{Tr}_{\text{i}}[\cdot] = \sum_n \langle n|\cdot|n\rangle_{\text{i}}$ and the projector $\hat{\Pi}_{\text{i}} = \hat{\mathbb{1}}_{\text{i}} - |0\rangle\langle 0|_{\text{i}}$. Computing $\mathrm{Tr}_{\text{i}}[\hat{\Pi}_{\text{i}}\hat{U}\hat{\rho}^{\text{in}}\hat{U}^\dagger]$, the only non-zero term at second order in g is the term $g^2\hat{a}_{\text{s}}^\dagger\hat{a}_{\text{i}}^\dagger\hat{\rho}^{\text{in}}\hat{a}_{\text{s}}\hat{a}_{\text{i}}$. We deduce that the signal single-photon added state $\hat{\rho}_{\text{s}}^+$ writes

$$\hat{\rho}_{\text{s}}^+ = \frac{\hat{a}_{\text{s}}^\dagger\hat{\rho}_{\text{s}}^{\text{in}}\hat{a}_{\text{s}}}{1+\bar{n}_{\text{s}}} \tag{3.4}$$

and that the success probability P^+ defined in equation (3.2) is given by

$$\begin{aligned} P^+ &= g^2(1+\bar{n}_{\text{s}}) \\ \text{with} \quad \bar{n}_{\text{s}} &= \mathrm{Tr}(\hat{a}_{\text{s}}^\dagger\hat{a}_{\text{s}}\hat{\rho}_{\text{s}}^{\text{in}}) \end{aligned} \tag{3.5}$$

where $\bar{n}_{\text{s}}$ is the mean number of photons in the input state.

The output signal state in equation (3.4) is of the form one would expect, i.e. equal to the input state on which is added a single photon by applying $\hat{a}_{\text{s}}^\dagger$.

3.1.2 Multimode single-photon addition

In this section, we extend the simple previous theory to the multimode case. We consider that the signal and idler lights are multimode, keeping the modes nature abstract (e.g. time-frequency modes, spatial modes, etc...). figure 3.1 still describes the general setting of the process, considering the density operators $\hat{\rho}_{\text{s}}^{\text{in}}$ and $\hat{\rho}_{\text{s}}^+$ multimode.

We thus consider the multimode version of the evolution operator in equation (3.1), which writes

$$\hat{U} = \exp\left(\mathrm{i}\sum_{n,m} g_{n,m}\hat{a}_{\text{s},n}^\dagger\hat{a}_{\text{i},m}^\dagger + \text{h.c.}\right) \tag{3.6}$$

where the annihilation operators $\{\hat{a}_{\text{s},n}\}$ are associated to the signal modes $\{\vec{\mathbf{f}}_{\text{s},n}\}$, the annihilation operators $\{\hat{a}_{\text{i},m}\}$ are associated to the idler modes $\{\vec{\mathbf{f}}_{\text{i},m}\}$, each coefficient $g_{n,m} > 0$ is the strength

of the process for the modes $(\vec{\mathbf{f}}_{s,n}, \vec{\mathbf{f}}_{i,m})$, and h.c. stands for Hermitian conjugate. Note that the expression (3.6) of the unitary operator $\hat{U}$ can be derived from a Hamiltonian approach [Grynberg 10, Parigi 07a].

Following a similar approach as in the previous subsection, we compute the output signal state $\hat{\rho}_s^+$ conditioned on the detection of a photon in the idler mode. Its expression takes again the general form of equation (3.2).

In general, the efficiency of the detector on the idler modes is not uniform in time-frequency, polarization, and space. One can model a detector with a set of eigenmodes $\{\vec{\mathbf{r}}_d\}$ with $d \in \mathbb{N}$, with associated detection efficiencies $\{\gamma_d\}$ and associated annihilation operators $\{\hat{a}_{i,\vec{\mathbf{r}}_d}\}$. In this case, the projector $\hat{\Pi}_i$ in the POVM $\{|0\rangle\langle 0|_i, \hat{\Pi}_i\}$ is defined as[1]

$$\hat{\Pi}_i = \sum_d \gamma_d \hat{\Pi}_{i,\vec{\mathbf{r}}_d} \tag{3.7}$$
$$\text{with} \quad \hat{\Pi}_{i,\vec{\mathbf{r}}_d} = \hat{\mathbb{1}}_{i,\vec{\mathbf{r}}_d} - |0\rangle\langle 0|_{i,\vec{\mathbf{r}}_d}$$

where each $\hat{\Pi}_{i,\vec{\mathbf{r}}_d}$ is the measure operator for the idler detection mode $\vec{\mathbf{r}}_d$, and where the operators act as the identity on any mode unreferenced in their expression.

In the following, we assume for simplicity that the detector efficiencies $\{\gamma_d\}$ are one over the idler modes where the idler output state is not vacuum. For time-frequency modes, this assumption requires that the detector is broadband in frequency with respect to the non-vacuum frequency output idler modes. Under this assumption, we write can simply write

$$\hat{\Pi}_i = \hat{\mathbb{1}}_i - |0\rangle\langle 0|_i \tag{3.8}$$

In equation (3.2), the combined effect of the detection operator $\hat{\Pi}_i$ in the simplified form (3.8) together with the partial trace $\mathrm{Tr}_i[\cdot]$ can be viewed again as taking the trace over the idler subspace of more than one photon, which writes

$$\mathrm{Tr}_i\left[\hat{\Pi}_i \hat{U} \hat{\rho}^{\mathrm{in}} \hat{U}^\dagger\right] = \sum_{k\geq 1} \sum_\ell \langle k|_{i,\ell} (\hat{U} \hat{\rho}_s^{\mathrm{in}} \otimes |0\rangle\langle 0|_i \ \hat{U}^\dagger) |k\rangle_{i,\ell} \tag{3.9}$$

where $|k\rangle_{i,\ell}$ is the Fock state of k photons in the idler mode $\vec{\mathbf{f}}_{i,\ell}$. Similarly as before, in the weak coupling regime $g_{n,m} \ll 1$ the only relevant dominant term in $\hat{U}\hat{\rho}^{\mathrm{in}}\hat{U}^\dagger$ contains at most a single photon in the idler modes. In particular, the terms for $k > 1$ in equation (3.9) are negligible. We then find

$$\hat{\rho}_s^+ = \frac{1}{P^+} \sum_\ell \sum_{n,m} \sum_{n',m'} g_{n,m} g_{n',m'} \langle 1|_{i,\ell} \hat{a}_{s,n}^\dagger \hat{a}_{i,m}^\dagger \hat{\rho}_s^{\mathrm{in}} \otimes |0\rangle\langle 0|_i \ \hat{a}_{s,n'} \hat{a}_{i,m'} |1\rangle_{i,\ell} \tag{3.10}$$

In equation (3.10), we can compute separately in the idler modes the scalar products $\langle 0|_{i,\ell} \ \hat{a}_{i,m'} |1\rangle_{i,\ell}$ and $\langle 1|_{i,\ell} \ \hat{a}_{i,m}^\dagger |0\rangle_{i,\ell}$ which evaluate to $\delta_{\ell,m}\delta_{\ell,m'}$, so that we obtain

$$\hat{\rho}_s^+ = \frac{1}{P^+} \sum_{n,n'} \mathbf{A}_{nn'}^+ \hat{a}_{s,n}^\dagger \hat{\rho}_s^{\mathrm{in}} \hat{a}_{s,n'} \tag{3.11}$$

$$\mathbf{A}_{nn'}^+ = \sum_m g_{n,m} g_{n',m} \tag{3.12}$$

[1] We assume that the efficiency is the same whatever the input quantum state, which is not true in general. In our case, it's valid as we are in the low-photon number regime.

where the coefficients $\mathbf{A}^+_{nn'}$ form the matrix $\mathbf{A}^+$ referred to as the *addition matrix*. The behaviour of the multimode single-photon addition process is completely governed by the matrix $\mathbf{A}^+$. Note that the addition matrix is Hermitian and semi-positive by definition (3.12). The diagonalization of the addition matrix gives access to the eigenvalues $\lambda_1 \geq \cdots \geq \lambda_n \geq 0$ and the eigenmodes $\{\vec{\mathbf{e}}_n\}$ associated to the annihilation operators $\{\hat{e}_n\}$. We obtain

$$\hat{\rho}_s^+ = \frac{1}{P^+} \sum_n \lambda_n \hat{e}_n^\dagger \hat{\rho}_s^{\text{in}} \hat{e}_n \tag{3.13}$$

$$\text{where} \quad P^+ = \sum_n \lambda_n (1 + \bar{n}_n) \tag{3.14}$$

and $\bar{n}_n = \text{Tr}[\hat{e}_n^\dagger \hat{e}_n \hat{\rho}_s^{\text{in}}]$ is the photon number of the input signal in the addition eigenmode $\vec{\mathbf{e}}_n$. The single-photon added state $\hat{\rho}_s^+$ in equation (3.13) is understood as the mixed state resulting from a probabilistic single-photon addition on the eigenmodes $\{\vec{\mathbf{e}}_n\}$, each corresponding addition occurring with the probability $\lambda_n(1 + \bar{n}_n)/P^+$.

In the general case, the single-photon addition process is *multimode*, i.e. more than one eigenvalue λ_n is non-zero. To quantify the number of effective number of modes of the process, we can use the Schmidt number K introduced in chapter 2, equation (2.19). With the eigendecomposition (3.13), the Schmidt number K writes

$$K = \frac{(\sum_n \lambda_n)^2}{\sum_n \lambda_n^2} \tag{3.15}$$

The single-photon addition process is *single-mode* when $K = 1$.

We will now discuss in detail both the single-mode and multimode cases, and look for their link with the purity of the single-photon added state. Intuitively, the purity of the output state decreases as the total number of modes involved in the process increases, since the single photon can be added into more eigenmodes, following equation (3.13).

3.1.3 Single-photon added state purity

In this section, we assume that the (multimode) input signal is pure, i.e. $\hat{\rho}_s^{\text{in}} = |\phi\rangle\langle\phi|_s$, and we study the purity of the single-photon added state $\hat{\rho}_s^+$.

Single-mode case. If both the single-photon addition process and the input state $|\phi\rangle\langle\phi|_s$ are in the same single-mode, then equation (3.13) simply re-writes as

$$\hat{\rho}_s^+ \propto \hat{e}_1^\dagger \hat{\rho}_s^{\text{in}} \hat{e}_1 \tag{3.16}$$

We deduce that the signal output state is pure: $\hat{\rho}_s^+ = |\psi\rangle\langle\psi|_s$, with $|\psi\rangle_s \propto \hat{e}_1^\dagger |\phi\rangle_s$. A photon has been properly added to the eigenmode. This is the ideal single-mode single-photon addition process, at $K = 1$.

Multimode case. For multimode single-photon addition process, i.e. $K > 1$, we show that the single-photon added state is always mixed once the addition process is multimode.

For simplicity, we first assume that only two eigenvalues are non-zero. Then, equations (3.13) and (3.14) rewrite

$$\hat{\rho}_s^+ = \frac{1}{P^+}\left(\lambda_1 \hat{e}_1^\dagger \hat{\rho}_s^{in} \hat{e}_1 + \lambda_2 \hat{e}_2^\dagger \hat{\rho}_s^{in} \hat{e}_2\right) \tag{3.17}$$

$$\text{with} \quad \lambda_1(1+\bar{n}_1) + \lambda_2(1+\bar{n}_2) = P^+ \tag{3.18}$$

As $\hat{\rho}_s^{in}$ is pure, we find, using trace properties, that the purity of the single-photon added state writes

$$\mathrm{Tr}\left[(\hat{\rho}_s^+)^2\right] = \frac{1}{P^{+2}}\left(\lambda_1^2(1+\bar{n}_1)^2 + \lambda_2^2(1+\bar{n}_2)^2 + 2\lambda_1\lambda_2 |\langle\phi|\hat{e}_1\hat{e}_2^\dagger|\phi\rangle_s|^2\right) \tag{3.19}$$

We apply the Cauchy-Schwarz inequality

$$|\langle\phi|\hat{e}_1\hat{e}_2^\dagger|\phi\rangle_s|^2 \leq \langle\phi|\hat{e}_1\hat{e}_1^\dagger|\phi\rangle_s \langle\phi|\hat{e}_2\hat{e}_2^\dagger|\phi\rangle_s = (1+\bar{n}_1)(1+\bar{n}_2) \tag{3.20}$$

which allows us to write

$$\mathrm{Tr}\left[(\hat{\rho}_s^+)^2\right] \leq \frac{1}{P^{+2}}(\lambda_1(1+\bar{n}_1) + \lambda_2(1+\bar{n}_2))^2 = 1 \tag{3.21}$$

where we used the normalization equation (3.18). The Cauchy-Schwarz inequality (3.21) is saturated if and only if $\hat{e}_1^\dagger|\phi\rangle_s \propto \hat{e}_2^\dagger|\phi\rangle_s$, which is not possible (see formal proof in appendix B.3). So the purity of the signal single-photon added state is strictly lower than 1, meaning that the single-photon added state is mixed.

This result can be generalized to more than two non-zero eigenvalues, without any additional steps, as we show in appendix B.4. Therefore, we have shown that for a multimode addition process ($K \neq 1$), for any input signal state, the signal single-photon added state is not pure.

Purity of the single-photon added state for a single-mode input. Let us quantitatively study the dependence of the purity of the single-photon added state on some relevant input states.

In this section, to simplify the discussion, we consider that the process is mainly determined by two eigenmodes, so that the single-photon added state is given by equation (3.17).

We consider the situation where the input signal is a pure single-mode state:

$$\hat{\rho}_s^{in} = |\phi\rangle\langle\phi|_s, \quad |\phi\rangle_s = |\chi\rangle_1 \otimes |0\rangle_2 \tag{3.22}$$

where in the eigenmode $\vec{\mathbf{e}}_1$, the state $|\chi\rangle_1$ has $\bar{n}_1$ mean number of photons, and in the eigenmode $\vec{\mathbf{e}}_2$ the state is the vacuum. Using the fact that the scalar product $\langle\phi|\hat{e}_1\hat{e}_2^\dagger|\phi\rangle_s$ vanishes and $\bar{n}_2 = 0$ in equations (3.18) and (3.19), we obtain

$$\mathrm{Tr}\left[(\hat{\rho}_s^+)^2\right] = \frac{1 + (\lambda_1/\lambda_2)^2(1+\bar{n}_1)^2}{[1 + (\lambda_1/\lambda_2)(1+\bar{n}_1)]^2} \tag{3.23}$$

We show in figure 3.2 the purity of the single-photon added state as a function of the Schmidt number $K = (1 + \lambda_1/\lambda_2)^2/(1 + (\lambda_1/\lambda_2)^2)$, and mean number of photons $\bar{n}_1$. The figure illustrates the competition between the multimodality and the amplification effect of the process. We point out that for a Schmidt number smaller or equal to 1.1, the purity is always above about 0.90. The usual candidate for single-photon addition are coherent, thermal and squeezed vacuum states. We show on a secondary axis the squeezing parameter ζ, related to the mean number of photons by $\bar{n}_1 = \sinh^2(\zeta)$ for single-mode squeezed vacuum states (see subsection 1.3.3).

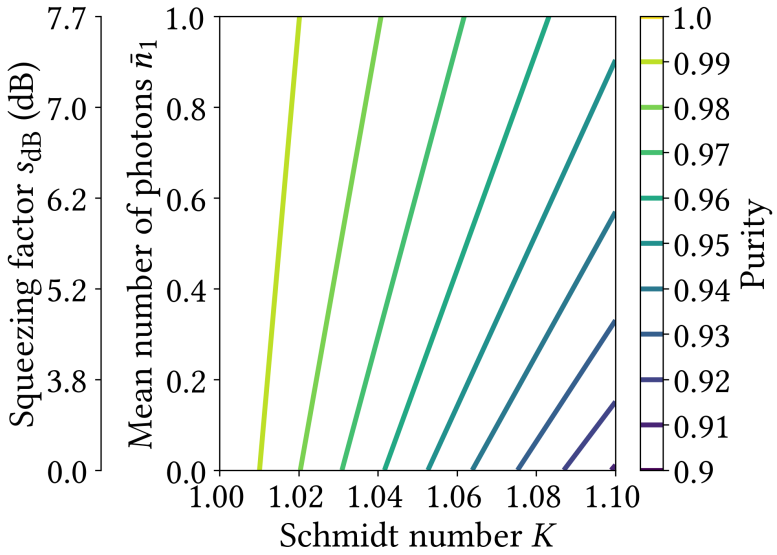

Fig. 3.2 Purity of the single-photon added state for a single-mode input state. At $K = 1$, the process is single-mode, which leads to a purity equal to 1. Below, the purity drops with K, and increases with $\bar{n}_1$. The squeezing factor axis is non linear, and is derived from $\bar{n}_1 = \sinh^2(\zeta)$, with $s_{\mathrm{dB}} = 20\,\zeta/\ln(10)$.

The fact that a non-pure state can emerge from single-photon addition on a pure single-mode state essentially comes from the non-zero probability of adding a photon to the vacuum. In comparison, in the photon subtraction process [Averchenko 16], the single-photon added state is always pure if the input signal is pure and single-mode, as subtracting from the vacuum is impossible.

Purity of the single-photon added state for a two-mode input. We now consider the input state as a two-mode squeezed vacuum state, separable over the two eigenmodes of the addition process, which writes

$$|\phi\rangle_{\mathrm{s}} = \hat{S}(\zeta_1)\,|0\rangle \otimes \hat{S}(\zeta_2)\,|0\rangle \tag{3.24}$$

where ζ_1 (resp. ζ_2) is the squeezing parameter in mode $\vec{\mathbf{e}}_1$ (resp. $\vec{\mathbf{e}}_2$), and $\hat{S}(\zeta_1), \hat{S}(\zeta_2)$ are the corresponding squeezing operators. We define $\bar{n}_1 = \sinh^2(\zeta_1)$ and $\bar{n}_2 = \sinh^2(\zeta_2)$ the mean number of photon in each mode. Note that since we chose the ordering $\lambda_1 \geq \lambda_2$, the addition

process favors one mode over the other and the probability to add a photon in mode 1 is higher. So for clarity purposes, the eigenmode $\vec{\mathbf{e}}_1$ is called dominant mode while the eigenmode $\vec{\mathbf{e}}_2$ is called the weak mode.

The purity of the single-photon added state re-writes

$$\mathrm{Tr}\left[(\hat{\rho}_s^+)^2\right] = \frac{(1+\bar{n}_2)^2 + (\lambda_1/\lambda_2)^2(1+\bar{n}_1)^2}{[(1+\bar{n}_2) + (\lambda_1/\lambda_2)(1+\bar{n}_1)]^2} \tag{3.25}$$

We represent the purity of the single-photon added state from equation (3.25) in figure 3.3, fixing the Schmidt number at $K = 1.2$. First, we can see that the presence of a squeezed vacuum state in the weak mode 2 with a small squeezing parameter ζ_2, results in a decreased purity with respect to a null squeezing parameter ζ_2, i.e. when the mode 2 is vacuum.

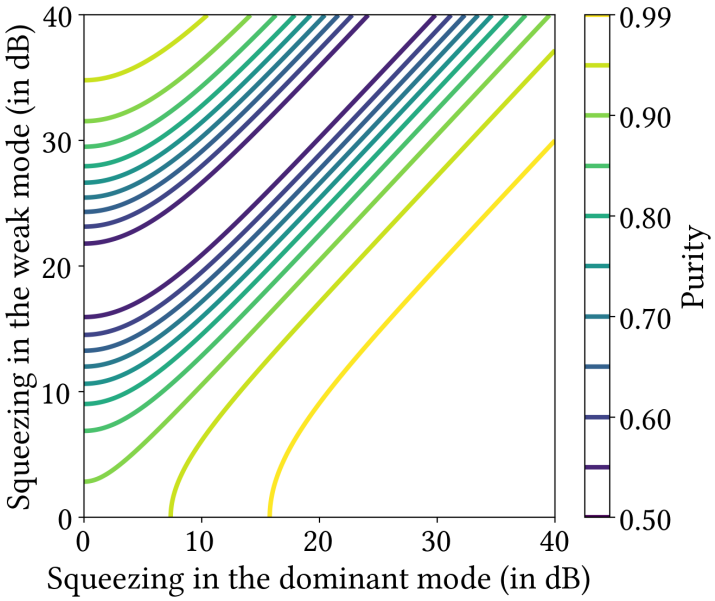

Fig. 3.3 Purity of the single-photon added state for a two-mode squeezed vacuum input state, at fixed Schmidt number $K = 1.2$. For more details, see the text.

We chose to look at squeezing up to 40 dB in order to show the competition between the three parameters: both squeezing parameters ζ_1 and ζ_2 (which directly affects the number of photon in each mode) and the Schmidt number K of the process. Each of these parameters affects the probability to add a single photon in one or the other mode. Since the Schmidt number is fixed at $K = 1.2$, the addition process favor the mode 1 with an eigenvalue λ_1 10 times larger than the eigenvalue λ_2. The parametric amplifier effect is visible at larger squeezing, since the probability to add a photon in mode n scales with $1 + \sinh^2(\zeta_n)$. At a given squeezing in the dominant mode, the state purity first decreases with the squeezing in the weak mode. When the squeezing in the weak mode is large enough to compensate the unbalanced addition process than in the dominant mode (e.g. at (1,40) dB in figure 3.3), we can see that the single-photon added state is almost pure, with a single-photon addition almost certainly in the weak mode.

3.2 Mode-selective single-photon addition in collinear type-II parametric down-conversion

In this section, we develop an experimental model of the addition matrix $\mathbf{A}^{+}_{n,n'}$, and diagonalize it both analytically and numerically. The goal is to find:

- under which conditions the process can be *single-mode*, meaning that the effective number of modes in which it adds a single photon is reduced to one (i.e. $K = 1$).
- under which conditions the process can be *mode-selective*, meaning that one can choose in which mode the single photon is added[1].

While the general principle of the process remains the same as described in figure 3.1, we now consider parametric down-conversion (PDC) in a non-linear crystal and the light to be in the pulsed regime. The modes at play are frequency modes of the large spectrum pulses. We refer to the *gate* beam as the classical beam that feeds the non-linear crystal at the input, and is part of the process described by $\hat{U}$.

In this section, we focus on collinear type-II parametric down-conversion, see figure 3.4. Collinear means that input and output fields are all propagating in the same direction (on figure 3.4 they are not collinear for clarity purposes). Being type-II means that the signal and idler output fields have orthogonal polarizations. This allows for separating the output beams in practice. In section 3.3, we will investigate non-collinear parametric down-conversion configurations.

For non-linear processes, the Hamiltonian operator is given by the interaction of the input electric field $\hat{E}_{in}$ with the induced non-linear polarization $\hat{\mathbf{P}}_{\mathrm{NL}}(\mathbf{r},t)$ and generally writes [Loudon 00]

$$\hat{\mathbf{H}}(t) = \int_V \mathrm{d}\mathbf{r}\, \hat{\mathbf{P}}_{\mathrm{NL}}(\mathbf{r},t)\hat{\mathbf{E}}_{\mathrm{g}}(\mathbf{r},t) \tag{3.26}$$

where V is the volume of the non-linear crystal, $\hat{\mathbf{E}}_{\mathrm{g}}(\mathbf{r},t)$ is the gate quantum electric field operator. Keeping only the second order non-linear polarization effect, the non-linear polarization $\hat{\mathbf{P}}_{\mathrm{NL}}(\mathbf{r},t)$ writes

$$\hat{\mathbf{P}}_{\mathrm{NL}}(\mathbf{r},t) = \varepsilon_0 \chi^{(2)} \left(\hat{\mathbf{E}}_{\mathrm{s}}(\mathbf{r},t) + \hat{\mathbf{E}}_{\mathrm{i}}(\mathbf{r},t)\right)\left(\hat{\mathbf{E}}_{\mathrm{s}}(\mathbf{r},t) + \hat{\mathbf{E}}_{\mathrm{i}}(\mathbf{r},t)\right) \tag{3.27}$$

where $\chi^{(2)}$ is the effective second order non-linear susceptibility[2], and $\hat{\mathbf{E}}_{\mathrm{s}}(\mathbf{r},t)$ (resp. $\hat{\mathbf{E}}_{\mathrm{i}}(\mathbf{r},t)$)) is the *signal* (resp. *idler*) quantum electric field operator. The signal and idler fields are the two fields induced by the polarization of the non-linear medium through the interaction with the gate field.

[1] Note that the mode in which the single photon is added may be an eigenmode of the addition process or any combination of eigenmodes.

[2] Note that in general $\chi^{(2)}$ is a tensor to take into account all the possible polarization. We consider using the relevant tensor element for simplicity.

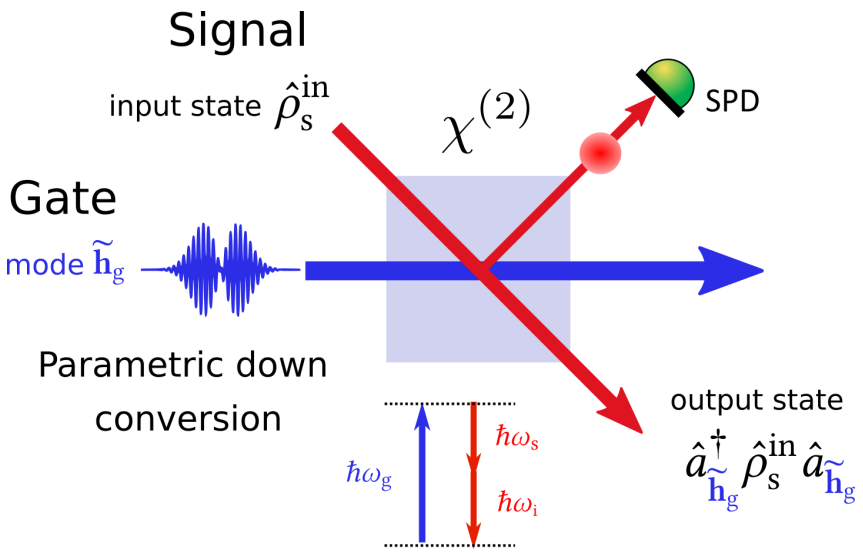

Fig. 3.4 Scheme of mode-selective single-photon addition through collinear parametric down-conversion in a non-linear crystal (for clarity, the beams are pictured not collinear). Each gate photon is probabilistically down-converted into one photon added to the signal field and one idler photon detected for heralding purposes. Single-photon addition occurs in the spectral mode $\widetilde{h}_g$ of the gate. SPD: single-photon detector.

Developing equation (3.26) yields many terms, which correspond to second-harmonic generation (SHG), sum-frequency generation (SFG), parametric down-conversion (PDC), and optical rectification (see e.g. [Boyd 13]). Here, we consider that only the PDC process is phase-matched, and as such, dominant. Assuming the transverse spatial modes of the fields are matched, equation (3.26) then re-writes

$$\hat{H}(t) = \int_{-L/2}^{L/2} \mathrm{d}z\, \varepsilon_0 \chi^{(2)} \hat{E}_s^{(-)}(z,t) \hat{E}_i^{(-)}(z,t) \hat{E}_g^{(+)}(z,t) + \mathrm{h.c.} \tag{3.28}$$

where we have taken the origin at the middle of the crystal of total length L.

We write the quantum electric field operators in the plane wave basis under the narrow-band approximation $\omega_0 >> \Delta\omega$ (1.13). Let us describe this decomposition in a continuous format, whose correspondence generically writes

$$\begin{aligned} \sum_\ell \Delta\omega &\mapsto \int \mathrm{d}\omega \\ \frac{\hat{a}_\ell}{\Delta\omega} &\mapsto \hat{a}(\omega) \\ \mathbf{u}_\ell &\mapsto \mathrm{e}^{\mathrm{i}k(\omega)z - \mathrm{i}\omega t} \end{aligned} \tag{3.29}$$

where the operators $\{\hat{a}(\omega)\}$ obey the commutation relations

$$[\hat{a}(\omega), \hat{a}^\dagger(\omega')] = \delta(\omega - \omega') \tag{3.30}$$

Using equation (1.13) and the correspondence (3.29), we can write the signal and idler field operators as

$$\hat{\mathbf{E}}_{\mathrm{s}}^{(-)}(z,t) = \mathcal{E}_0 \int \mathrm{d}\omega_{\mathrm{s}}\, \hat{a}_{\mathrm{s}}^{\dagger}(\omega_{\mathrm{s}}) \exp(-ik_{\mathrm{s}}(\omega_{\mathrm{s}})z + i\omega_{\mathrm{s}}t) \tag{3.31}$$

$$\hat{\mathbf{E}}_{\mathrm{i}}^{(-)}(z,t) = \mathcal{E}_0 \int \mathrm{d}\omega_{\mathrm{i}}\, \hat{a}_{\mathrm{i}}^{\dagger}(\omega_{\mathrm{i}}) \exp(-ik_{\mathrm{i}}(\omega_{\mathrm{i}})z + i\omega_{\mathrm{i}}t) \tag{3.32}$$

Since the gate beam is an intense pulsed classical beam, its field $\hat{\mathbf{E}}_{\mathrm{g}}^{(+)}(z,t)$ can be approximated[1] as

$$\hat{\mathbf{E}}_{\mathrm{g}}^{(+)}(z,t) = \mathcal{E}_0 \int \mathrm{d}\omega_{\mathrm{g}}\, \widetilde{\mathbf{h}}_{\mathrm{g}}(\omega_{\mathrm{g}}) \exp\left(ik_{\mathrm{g}}(\omega_{\mathrm{g}})z - i\omega_{\mathrm{g}}t\right) \tag{3.33}$$

where $\widetilde{\mathbf{h}}_{\mathrm{g}}(\omega_{\mathrm{g}})$ is the spectral envelope profile of the gate field, normalized as $\int d\omega_{\mathrm{g}} |\widetilde{\mathbf{h}}_{\mathrm{g}}(\omega_{\mathrm{g}})|^2 = 1$.

Injecting the field decompositions (3.31), (3.32) and (3.33) into equation (3.28), we perform the integration over the length of the crystal, and obtain

$$\hat{H}(t) \propto \int \mathrm{d}\omega_{\mathrm{s}}\, \mathrm{d}\omega_{\mathrm{i}}\, \mathrm{d}\omega_{\mathrm{g}}\, \widetilde{\mathbf{h}}_{\mathrm{g}}(\omega_{\mathrm{g}})\, \hat{a}_{\mathrm{s}}^{\dagger}(\omega_{\mathrm{s}})\, \hat{a}_{\mathrm{i}}^{\dagger}(\omega_{\mathrm{i}})\, \phi_{\mathrm{PM}}(\omega_{\mathrm{s}},\omega_{\mathrm{i}},\omega_{\mathrm{g}})\, \mathrm{e}^{-i(\omega_{\mathrm{g}}-\omega_{\mathrm{s}}-\omega_{\mathrm{i}})t} + \mathrm{h.c.} \tag{3.34}$$

$$\text{with} \quad \phi_{\mathrm{PM}}(\omega_{\mathrm{s}},\omega_{\mathrm{i}},\omega_{\mathrm{g}}) = \mathrm{sinc}\left(\frac{\Delta k(\omega_{\mathrm{s}},\omega_{\mathrm{i}},\omega_{\mathrm{g}})\, L}{2}\right)$$

$$\text{and} \quad \Delta k(\omega_{\mathrm{s}},\omega_{\mathrm{i}},\omega_{\mathrm{g}}) = k_{\mathrm{g}}(\omega_{\mathrm{g}}) - k_{\mathrm{s}}(\omega_{\mathrm{s}}) - k_{\mathrm{i}}(\omega_{\mathrm{i}})$$

where $\phi_{\mathrm{PM}}(\omega_{\mathrm{s}},\omega_{\mathrm{i}},\omega_{\mathrm{g}})$ is called the *phase-matching function*, and Δk the *phase mismatch*. Taking into account the temporal dependency of the Hamiltonian, the evolution operator $\hat{U}(t)$ generally writes

$$\hat{U}(t) = \hat{\mathcal{T}} \exp\left[-\frac{i}{\hbar}\int_0^t \mathrm{d}t'\, \hat{H}(t')\right] \tag{3.35}$$

where $\hat{\mathcal{T}}$ is the time ordering operator. In usual experimental conditions, the time ordering operator may be neglected, in agreement with [Christ 13, Brecht 14]. As the gate temporal mode has a finite temporal length and that we do not consider any other interaction, we can extend both temporal integral boundaries to infinity. Performing the temporal integration in equation (3.35) consists in computing $\int_{-\infty}^{+\infty} dt \mathrm{e}^{-i(\omega_{\mathrm{g}}-\omega_{\mathrm{s}}-\omega_{\mathrm{i}})t} = 2\pi\delta(\omega_{\mathrm{g}}-\omega_{\mathrm{s}}-\omega_{\mathrm{i}})$. Integrating over ω_{g} reduces then to the energy conservation equation

$$\omega_{\mathrm{g}} = \omega_{\mathrm{s}} + \omega_{\mathrm{i}} \tag{3.36}$$

The evolution operator $\hat{U}$ then writes

$$\hat{U} = \exp\left[\mathrm{i}\int \mathrm{d}\omega_{\mathrm{s}}\, \mathrm{d}\omega_{\mathrm{i}}\, J(\omega_{\mathrm{s}},\omega_{\mathrm{i}})\, \hat{a}_{\mathrm{s}}^{\dagger}(\omega_{\mathrm{s}})\hat{a}_{\mathrm{i}}^{\dagger}(\omega_{\mathrm{i}}) + \mathrm{h.c.}\right] \tag{3.37}$$

$$\text{with} \quad J(\omega_{\mathrm{s}},\omega_{\mathrm{i}}) \propto \widetilde{\mathbf{h}}_{\mathrm{g}}(\omega_{\mathrm{s}}+\omega_{\mathrm{i}})\, \phi_{\mathrm{PM}}(\omega_{\mathrm{s}},\omega_{\mathrm{i}}) \tag{3.38}$$

[1] Similarly as in section 2.4, we keep the operator notation for the field, in the sense that this is implicitly a development at first order, where in the higher order the quantum fluctuations appear with null-mean operators.

where $J(\omega_s, \omega_i)$, referred to as the *joint spectral amplitude* (JSA) function, is the product of the spectral profile of the gate with the phase-matching function. Since the evolution operator has a similar form as in equation (3.6), we follow similar steps and find

$$\hat{\rho}_s^+ = \frac{1}{P^+} \int \mathrm{d}\omega_s \, \mathrm{d}\omega_s' \, A(\omega_s, \omega_s') \hat{a}_s^\dagger(\omega_s) \hat{\rho}_s^{\mathrm{in}} \hat{a}_s(\omega_s') \tag{3.39}$$

$$\text{with} \quad A(\omega_s, \omega_s') = \int \mathrm{d}\omega_i \, J(\omega_s, \omega_i) J(\omega_s', \omega_i)^* \tag{3.40}$$

where P^+ is the probability that a single-photon addition occurs, and that ensures the normalization $\mathrm{Tr}[\hat{\rho}_s^+] = 1$. Again, we can diagonalize $A(\omega_s, \omega_s')$, as it is an Hermitian function. Its eigendecomposition yields

$$\begin{cases} A(\omega_s, \omega_s') = \sum_{n \geq 1} \lambda_n \widetilde{\mathbf{e}}_{s,n}(\omega_s) \widetilde{\mathbf{e}}_{s,n}^*(\omega_s') \\ \hat{e}_n^\dagger = \int d\omega_s \widetilde{\mathbf{e}}_{s,n}(\omega_s) \hat{a}_s^\dagger(\omega_s) \end{cases} \tag{3.41}$$

where $\widetilde{\cdot}$ is the Fourier transform. The eigenmodes $\{\mathbf{e}_n(t)\}$ form a time-frequency mode basis for the signal electric field, and the operators $\hat{e}_n$ are their associated annihilation operators.

Combining equations (3.39) and (3.41), we obtain back the expression (3.13) of the signal single-photon added state

$$\hat{\rho}_s^+ = \frac{1}{P^+} \sum_n \lambda_n \hat{e}_n^\dagger \hat{\rho}_s^{\mathrm{in}} \hat{e}_n \tag{3.42}$$

with P^+ given by equation (3.14). In particular, the results of the discussion on the purity of the single-photon added state in subsection 3.1.3 apply.

3.2.1 Mode selectivity

Let us now show that under some approximation we can analytically compute the Schmidt number K, defined in equation (3.15). This computation allows us to derive conditions for the addition process to be single mode (i.e. $K = 1$). We also show that under such conditions, the process is mode selective.

We first assume that both the phase-matching function and the gate spectral profile are Gaussian functions, which we write

$$\phi_{\mathrm{PM}}(\omega_s, \omega_i) \approx \exp\left[-\gamma \left(\frac{\Delta k(\omega_s, \omega_i) L}{2}\right)^2\right] \tag{3.43}$$

$$\widetilde{\mathbf{h}}_g(\omega_s + \omega_i) \propto \exp\left[-\frac{\left(\underline{\omega}_s + \underline{\omega}_i\right)^2}{2\Delta\omega_g^2}\right] \tag{3.44}$$

where $\gamma \simeq 0.193$ is defined such that the functions $\mathrm{sinc}(x)$ and $\mathrm{e}^{-\gamma x^2}$ have the same full width at half maximum (FWHM), $\Delta\omega_g$ is the gate spectral width, and we define the centered frequencies $\underline{\omega}_j = \omega_j - \omega_{j,0}$ with the central frequency $\omega_{j,0}$ for both signal (j = s) and idler (j = i) fields.

Developing the phase mismatch $\Delta k(\omega_s, \omega_i)$, we keep up to the first order in $\underline{\omega}_s$ and $\underline{\omega}_i$, allowing us to write

$$\Delta k(\omega_s, \omega_i) = (k'_g - k'_s)\underline{\omega}_s + (k'_g - k'_i)\underline{\omega}_i \tag{3.45}$$

where $k'_j \equiv \frac{\partial k_j}{\partial \omega_j}|_{\omega_{j,0}}$ are the inverse of the field group velocities and where we have assumed perfect phase matching at the central frequencies, i.e. $\Delta k(\omega_{s,0}, \omega_{i,0}) = 0$.

Substituting equations (3.43), (3.44) and (3.45) into the JSA function (3.38) leads to:

$$J(\omega_s, \omega_i) \propto \exp\left(-\frac{(\underline{\omega}_s + \underline{\omega}_i)^2}{2\Delta\omega_g^2} - \frac{\gamma L^2}{4}\left((k'_g - k'_s)\underline{\omega}_s + (k'_g - k'_i)\underline{\omega}_i\right)^2\right) \tag{3.46}$$

Under these Gaussian approximations, K has an explicit analytical form (see Appendix B.5 for a detailed proof)

$$K = \sqrt{\frac{(1 + r_s^2)(1 + r_i^2)}{(r_s - r_i)^2}} \tag{3.47}$$
$$\text{with} \quad r_j = \Delta\omega_g L \sqrt{\frac{\gamma}{2}} \left|k'_g - k'_j\right| \quad \text{for} \quad j = i, s$$

where the adimensional r_j coefficients contain all the key parameters of the problem. Expression (3.47) allows for quantifying the number of effective modes of the addition process. In particular, the process is single-mode when $K = 1$. To obtain $K = 1$ from equation (3.47), one of the r_j coefficients must vanish. Since we are interested in the selectivity over the signal mode, we choose $r_s = 0$ similarly to [Mosley 08]. This leads to the *group velocity matching condition* (GVM condition) which writes

$$k'_g = k'_s \tag{3.48}$$

This condition can be achieved in some common crystals, as discussed in the next subsection 3.2.2. Under this condition, K goes to one for large r_i , i.e.

$$K = \sqrt{1 + \frac{1}{r_i^2}} \approx 1 \quad \text{if} \quad r_i^2 \gg 1 \tag{3.49}$$

The condition $r_i^2 \gg 1$ writes

$$\Delta\omega_g^2 \gg \frac{1}{\gamma L^2 (k'_g - k'_i)^2/2} \tag{3.50}$$

This condition (3.50) can be physically seen as a long enough crystal condition or equivalently as a broad enough gate spectrum. We have shown that the single-photon addition process is single-mode under conditions (3.50) and (3.48).

For the process to be mode-selective, the output signal mode should be controllable by an experimental parameter. Let us show that under the same conditions this parameter is

the gate spectral profile $\widetilde{\mathbf{h}}_{\mathrm{g}}(\omega_{\mathrm{g}})$, which is then not assumed to be Gaussian anymore. Under condition (3.48), we can rewrite equation (3.46) as

$$J(\omega_{\mathrm{s}},\omega_{\mathrm{i}}) \propto \widetilde{\mathbf{h}}_{\mathrm{g}}(\omega_{\mathrm{s}}+\omega_{\mathrm{i}}) \exp\left(-\frac{\gamma L^2}{4}(k'_{\mathrm{g}}-k'_{\mathrm{i}})^2\underline{\omega}_{\mathrm{i}}^2\right) \tag{3.51}$$

Under condition (3.50), the spectral width of the gate is large compared to the one of the phase-matching function, and it can thus be considered constant with respect to the variable ω_{i}. We can then write $\widetilde{\mathbf{h}}_{\mathrm{g}}(\omega_{\mathrm{s}}+\omega_{\mathrm{i}}) \approx \widetilde{\mathbf{h}}_{\mathrm{g}}(\omega_{\mathrm{s}}+\omega_{\mathrm{i},0})$ in equation (3.51). Now, the JSA function can be written in a factorized from, in the sense that the variables ω_{s} and ω_{i} are separable as a product, as

$$J(\omega_{\mathrm{s}},\omega_{\mathrm{i}}) \propto \widetilde{\mathbf{h}}_{\mathrm{g}}(\omega_{\mathrm{s}}+\omega_{\mathrm{i},0}) \exp\left(-\frac{\gamma L^2}{4}(k'_{\mathrm{g}}-k'_{\mathrm{i}})^2\underline{\omega}_{\mathrm{i}}^2\right) \tag{3.52}$$

Replacing the JSA function $J(\omega_{\mathrm{s}},\omega_{\mathrm{i}})$ in the expression (3.39) of the single-photon added state with its factorized form (3.52), the resulting function $A(\omega_{\mathrm{s}},\omega'_{\mathrm{s}})$ writes directly in the diagonal form of equation (3.41) with only one term in the sum

$$A(\omega_{\mathrm{s}},\omega'_{\mathrm{s}}) \propto \widetilde{\mathbf{h}}_{\mathrm{g}}(\omega_{\mathrm{s}}+\omega_{\mathrm{i},0})\widetilde{\mathbf{h}}_{\mathrm{g}}(\omega'_{\mathrm{s}}+\omega_{\mathrm{i},0})^* \tag{3.53}$$

We then deduce that the single-photon addition process is single-mode and the signal eigenmode $\widetilde{\mathbf{e}}_{\mathrm{s}}(\omega_{\mathrm{s}})$ is given by the spectral shape $\widetilde{\mathbf{h}}_{\mathrm{g}}(\omega_{\mathrm{g}})$ of the gate, i.e. $\widetilde{\mathbf{e}}_{\mathrm{s}} = \widetilde{\mathbf{h}}_{\mathrm{g}}$. In other words, the photon is added to the mode of the signal that has the same spectral shape as the gate. The mode selectivity of the addition process is pictured in figure 3.4. In practice, the mode of the gate can then be tailored via ultra-fast shaping in order to choose the addition mode for the signal, see section 2.2.4 for detail on pulse shaping techniques.

We conclude from these analytical considerations that the collinear PDC addition process is single-mode and mode-selective under Gaussian phase-matching approximation, group velocity matching condition (3.48) and broad enough gate spectrum or equivalently long enough crystal condition (3.50). Note that this model neglects the additional oscillations around the main peak of the phase-matching function, that may have a small contribution to the Schmidt number. Illustrations of this effect are shown in the simulations of the next section.

3.2.2 Simulations

In this subsection, we consider collinear type-II PDC in non-linear bulk crystals and show that the single-mode and mode-selective conditions derived in subsection 3.2.1 can be achieved with realistic parameters with the support of simulations.

In type-II PDC, for uniaxial bulk crystals, phase matching at signal and idler's central frequencies (i.e. $\Delta k(\omega_{\mathrm{s},0},\omega_{\mathrm{i},0}) = 0$) is achieved when

$$2n_{\mathrm{e}}(\lambda_{\mathrm{g},0},\theta_{\mathrm{c}}) = n_{\mathrm{e}}(\lambda_{\mathrm{i},0},\theta_{\mathrm{c}}) + n_o(\lambda_{\mathrm{s},0}) \tag{3.54}$$

where θ_{c} is the *crystal cut angle* defined as the angle between the gate propagation direction and the optical axis of the crystal, n_{o} is the ordinary refractive index and n_{e} the extraordinary

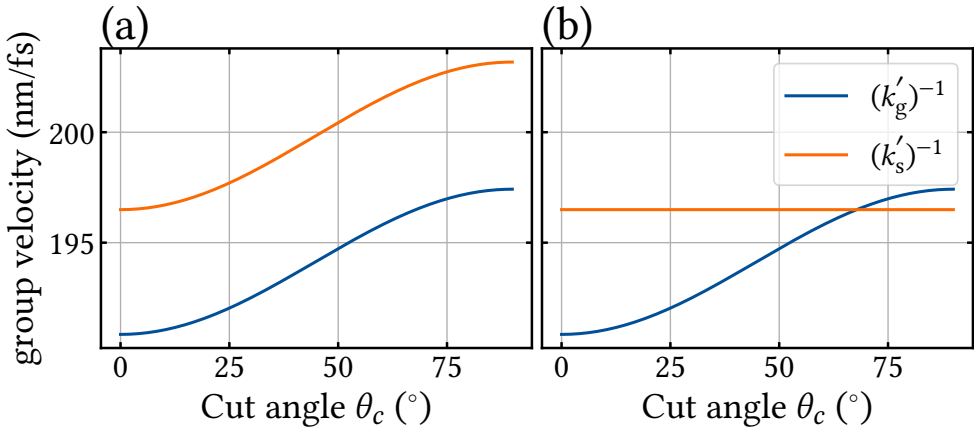

Fig. 3.5 Group velocity curves of the gate and signal fields for degenerate type-II PDC in KDP. The gate is extraordinarily polarized in both graphs. The signal is (a) extraordinarily polarized, or (b) ordinarily polarized.

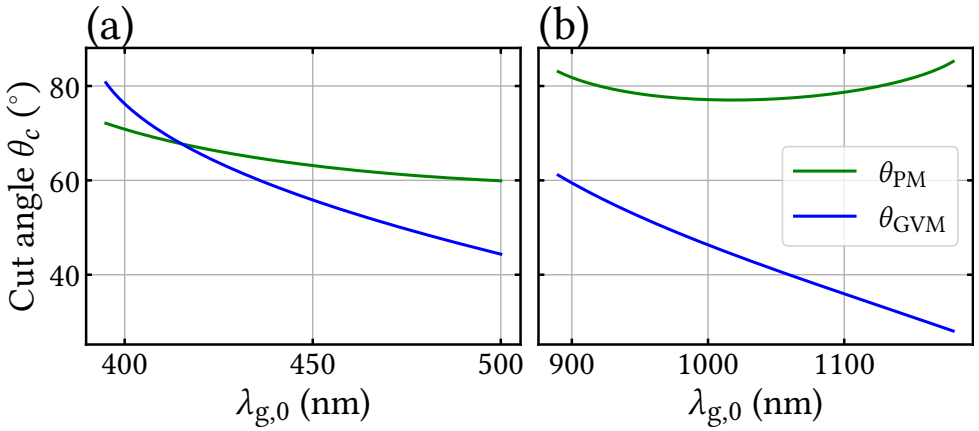

Fig. 3.6 Group velocity matching and phase-matching curves for different gate central wavelengths $\lambda_{g,0}$, for (a) KDP and (b) LN crystals. For LN, there is no solution to Eqs. (3.55).

one, associated to their respective field polarizations. At given wavelengths, this condition is satisfied if the crystal is cut at a specific angle called the *phase-matching angle*, $\theta_c = \theta_{PM}$.

As discussed earlier, the GVM condition (3.48) is satisfied if $k_g' = k_s'$. For uniaxial crystals, the signal field can be chosen as ordinary or extraordinarily polarized. For KDP crystal, it is not possible to achieve the GVM condition for an extraordinarily polarized signal field, see figure 3.5. When the signal field is ordinarily polarized, however, the group velocities of the gate and the signal match for a particular cut angle $\theta_c = \theta_{GVM}$, which we refer to as the *group velocity matching angle* (GVM angle).

For a given central gate wavelength $\lambda_{g,0}$, to achieve both the phase-matching condition (3.54)

and the GVM condition (3.48), it requires that

$$\begin{cases} \theta_c = \theta_{PM} \\ \theta_c = \theta_{GVM} \end{cases} \tag{3.55}$$

This condition cannot be achieved for an arbitrary gate central wavelength, which constitutes a limitation for single-photon addition in bulk crystals. We call this particular gate central wavelength the GVM wavelength, λ_{GVM}, satisfying equations (3.55), at which in particular $\theta_{PM} = \theta_{GVM}$.

As shown in figure 3.6, for the KDP crystal, the GVM and phase-matching conditions are achieved for $\lambda_{g,0} = 415$ nm and $\theta_{GVM} = \theta_{PM} = 67.74^\circ$, while for LN, no gate central wavelength satisfies Eqs. (3.55). Table 3.1 shows the different combinations of λ_{GVM} and θ_{GVM} for four non-linear crystals typically used in quantum optics experiments.

Crystal	λ_{GVM} (nm)	θ_{GVM} ($^\circ$)
KDP	415	67.74
BBO	585	30.96
LN	-	-
BiBO	647	24.12
KTP	711	46.84

Table 3.1: Group velocity matching wavelengths λ_{GVM} and angles θ_{GVM} for different non-linear crystals in collinear degenerate type-II PDC.

As seen in the previous section, the GVM condition is necessary but not sufficient for achieving $K = 1$, as we should also have a phase-matching bandwidth much smaller than the gate bandwidth, see condition (3.50). This condition can be satisfied by setting appropriately the crystal length L or the gate width $\Delta\omega_g$.

For the KDP crystal, the results are displayed on figure 3.7, with a Gaussian gate envelope. The crystal length is set to $L = 5$ mm, the gate bandwidth is $\Delta\omega_g = 3$ nm, the gate central wavelength is $\lambda_{g,0} = 415$ nm, and $\theta_{GVM} = 67.74^\circ$ in this simulation.

The singular value decomposition of the JSA is numerically performed, yielding a Schmidt number $K = 1.08$. For this set of parameters, the analytical expression (3.47) obtained under Gaussian approximations estimates $K = 1.02$. The quantity $\Delta\omega_g^2 \gamma L^2 (k_g' - k_i')^2/2$ is computed to be around 10, which makes the condition on the gate and phase-matching function of equation (3.50) valid.

From the previous discussion, since those conditions are satisfied, we expect to have a nearly single-mode single-photon added state ($K \approx 1$), and to be able to select the signal output mode. On figure 3.7 (b), the signal spectral dominant eigenmode is a Gaussian like the gate spectral mode.

To further check the modes selectivity, we also compute the JSA function for a first order Hermite-Gaussian function as gate spectral envelope, see figure 3.8 (a). Again, the dominant signal eigenmode has approximately the same spectral shape as the gate in figure 3.8 (b). Hence, shaping the gate allows for selecting the signal mode to which the photon is added.

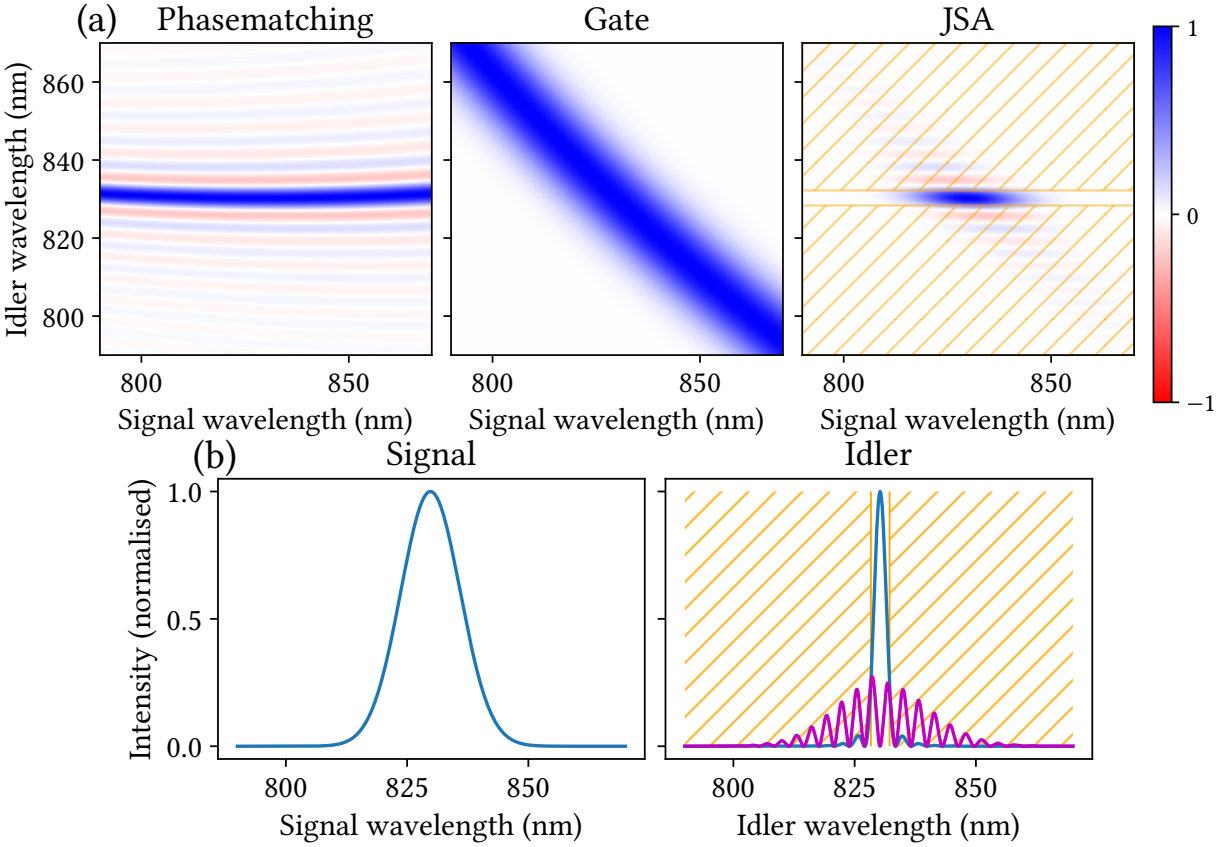

Fig. 3.7 Simulations for collinear type-II PDC in KDP with a Gaussian gate spectral envelope. (a) JSA as the product of the phase-matching function and the gate spectral envelope. (b) In blue: first normalized signal (left) and idler (right) eigenmodes of the JSA. In magenta: the second idler eigenmode. The orange dashed area represents a 4 nm wide spectral filtering applied on the idler field. For more details, see the main text.

Here we obtain $K = 1.17$, meaning that changing the gate spectrum comes at a cost on the Schmidt number of the process, which affects the purity of the single-photon added state.

To summarize, the numerical simulations show a realistic configuration for mode-selective single-photon addition in a KDP crystal through collinear type-II PDC. Similar results are obtained for BBO, BiBO, and KTP crystals, in which the GVM condition of equation (3.55) can also be satisfied.

3.2.3 Filtering

In order to obtain a Schmidt number K closer to 1, one may filter the idler field spectrally just before its detection. Detecting a single photon in a given idler eigenmode heralds the single-photon addition in the corresponding signal eigenmode. When two idler eigenmodes are spectrally easily separable with a small spectral overlap, filtering allows then to drastically reduce the detection probability of one with respect to the other. We investigate the effect of

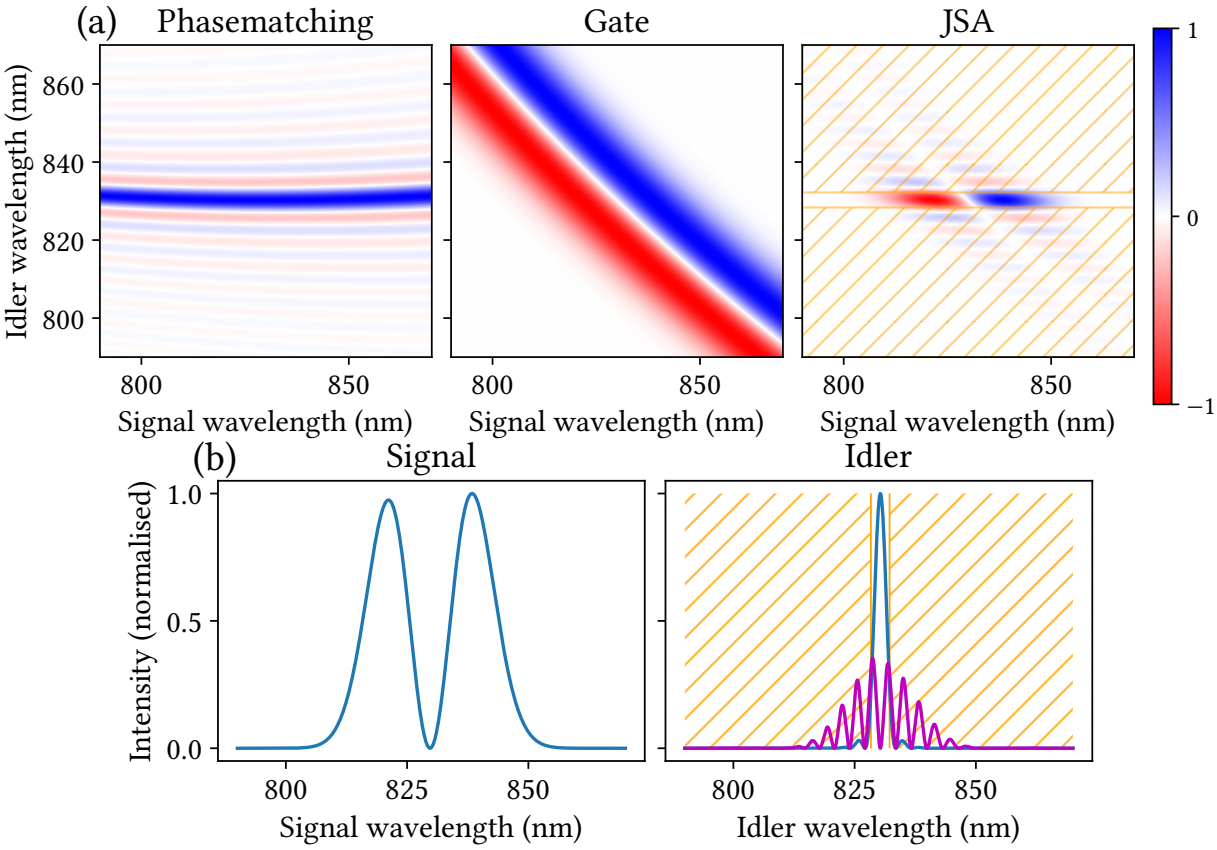

Fig. 3.8 Simulations for collinear type-II PDC in KDP with a first order Hermite-Gaussian gate spectral envelope. (a) JSA as the product of the phase-matching function and the gate spectral envelope. (b) In blue: first normalized signal (left) and idler (right) eigenmodes of the JSA. In magenta: the second idler eigenmode. The orange dashed area represents a 4 nm wide spectral filtering applied on the idler field.

filtering in the previous simulation, and show where it is easily implementable for reducing the Schmidt number closer to 1.

The idler spectral filtering with transmission $F(\omega_\mathrm{i})$ can be implemented by multiplying it with the JSA in equation (3.37), i.e. $J(\omega_\mathrm{s}, \omega_\mathrm{i}) \mapsto J(\omega_\mathrm{s}, \omega_\mathrm{i})F(\omega_\mathrm{i})$. Such substitution is not unitary. Since we only consider the situation where the output state is conditioned upon the successful idler photon detection, we do not need the substitution to be unitary. In the simulations, we use a "gate" filtering function $F(\omega_\mathrm{i})$ which writes

$$F(\omega_\mathrm{i}) = \begin{cases} 1 & \text{for } \omega_\mathrm{i} \in \left[\omega_{\mathrm{i},0} - \Delta\omega_F/2, \omega_{\mathrm{i},0} + \Delta\omega_F/2\right] \\ 0 & \text{elsewhere} \end{cases} \tag{3.56}$$

where $\Delta\omega_F$ is the spectral width of the filter. In the following, we use the related wavelength version $\Delta\lambda_F$, with $\Delta\omega_F = \Delta\lambda_F 2\pi c/\lambda_{\mathrm{i},0}^2$.

We apply the idler spectral filter in the simulation for collinear type-II PDC in KDP for both a HG_0 gate (figure 3.7) and a HG_1 gate (figure 3.8). The effect of the filter translates into making the corresponding JSA part vanish, as represented by the dashed regions on JSA graphs 3.7 (a) and 3.8 (a) (with $\Delta\lambda_F = 4\,\mathrm{nm}$). This effect is also represented with a dashed region on the idler eigenmodes in graphs 3.7 (b) and 3.8 (b), where one can see that most of the second eigenmode is filtered. This means that the probability of adding a photon to the first eigenmode is relatively increased, increasing the single-mode character of the addition process. The simulation results are given in table 3.2 for $\Delta\lambda_F = 4\,\mathrm{nm}$ and $\Delta\lambda_F = 2\,\mathrm{nm}$ wide filters. One can see that filtering can indeed significantly reduce the Schmidt number towards 1.

	K	filter losses
HG_0, $\Delta\lambda_F = \infty$	1.08	0%
HG_0, $\Delta\lambda_F = 4\,\mathrm{nm}$	1.01	17%
HG_0, $\Delta\lambda_F = 2\,\mathrm{nm}$	1.00	45%
HG_1, $\Delta\lambda_F = \infty$	1.17	0%
HG_1, $\Delta\lambda_F = 4\,\mathrm{nm}$	1.04	15%
HG_1, $\Delta\lambda_F = 2\,\mathrm{nm}$	1.01	44%

Table 3.2: Schmidt numbers K and idler first eigenmode filtering losses for idler $\Delta\lambda_F$ wide filters applied for collinear type-II PDC in KDP with both HG_0 and HG_1 gate spectral profiles. $\Delta\lambda_F = \infty$ corresponds to applying no filter. (For HG_0, $\Delta\lambda_F = 2\,\mathrm{nm}$, $K = 1.004$).

On the other hand, filtering induces the downside to reduce the idler detection probability. For K close to 1, most of the idler energy is contained in the first eigenmode. For this reason, we estimate the losses by computing the overlap of this mode before and after filtering. The assessed losses are given in table 3.2.

Spectrally filtering the idler beam prior detection is then a significantly helpful tool for improving the single-mode character of the addition process in collinear type-II PDC in KDP, as soon as one allows for a certain decrease of single-photon detection events rate. In particular, the detrimental increase of the Schmidt number when changing the gate envelope spectral shape may be limited using idler spectral filtering, improving of the mode selectivity of the addition process.

3.3 Single-mode single-photon addition via non-collinear parametric down-conversion

Up to now, we discussed collinear configurations for which it is often hard to separate the signal and idler beams experimentally. As we show numerically in this section, single-mode single-photon addition can be also achieved in non-collinear configurations, for which the difficulty of separating the signal and idler beams is directly solved. However, we don't have an analytical derivation as for the collinear case. In particular, we don't find configurations where practical mode selectivity is similarly feasible.

On the other hand, in the non-collinear case, the non-collinear angle is a new degree of freedom that can be exploited to achieve the GVM condition at an arbitrary gate central wavelength. This removes the unpractical condition of restricting to a particular gate central wavelength for any given crystal as shown in the previous section.

3.3.1 Type-II

The phase-matching conditions for type-II non-collinear PDC are [Boeuf 00]

$$\begin{cases} 2n_{\mathrm{e}}(\lambda_{\mathrm{g},0},\theta_c) = n_o(\lambda_{\mathrm{s},0})\cos(\theta_{\mathrm{s}}) + n_{\mathrm{e}}(\lambda_{\mathrm{i},0},\theta_c,\theta_{\mathrm{s}},\phi_{\mathrm{s}})\cos(\theta_{\mathrm{i}}) \\ n_o(\lambda_{\mathrm{s},0})\sin(\theta_{\mathrm{s}}) = n_{\mathrm{e}}(\lambda_{\mathrm{i},0},\theta_c,\theta_{\mathrm{s}},\varphi_{\mathrm{s}})\sin(\theta_{\mathrm{i}}) \end{cases} \tag{3.57}$$

where θ_{s} (resp. θ_{i}) is the (non-collinear) angle of the signal (resp. idler) field with respect to the gate field with in particular $\theta_{\mathrm{i}} = -\theta_{\mathrm{s}}$, and where φ_{s} is the azimuthal angle of the signal propagation direction with respect to the optical axis. The introduction of the angle φ_{s} is necessary to take into account the eventual biaxial nature of the crystals. Note that equations (3.57) generalize the collinear case given by equation (3.54), which is consistently deduced with $\theta_{\mathrm{s}} = \theta_{\mathrm{i}} = \varphi_{\mathrm{s}} = 0$. Solving the system (3.57) yields the phase-matching angle $\theta_{\mathrm{c}} = \theta_{\mathrm{PM}}$.

For a given non-collinear angle θ_{s}, the refractive index matching curve and the group velocity matching curve intersect exactly at an unique gate central wavelength λ_{GVM}, similarly as in the collinear case. Figure 3.9 shows for each non-collinear angle θ_{s} the corresponding GVM gate central wavelength λ_{GVM} and GVM cut angle θ_{GVM} for KDP, for which both phase-matching conditions (3.57) and group velocity matching (3.48) are achieved. As one can see, a non negligible range of gate central wavelengths is available for small non-collinear angle θ_{s}. Similar results are obtained for BBO, BiBO and KTP.

In this non-collinear configuration, the longitudinal wave vector mismatch $\Delta k_z(\omega_{\mathrm{s}},\omega_{\mathrm{i}})$ and transverse wave vector mismatch $\Delta k_\perp(\omega_{\mathrm{s}},\omega_{\mathrm{i}})$ are given by

$$\begin{cases} \Delta k_z(\omega_{\mathrm{s}},\omega_{\mathrm{i}}) = k_{\mathrm{g}}(\omega_{\mathrm{s}}+\omega_{\mathrm{i}}) - (k_{\mathrm{s}}(\omega_{\mathrm{s}}) + k_{\mathrm{i}}(\omega_{\mathrm{i}}))\cos\theta_{\mathrm{s}} \\ \Delta k_\perp(\omega_{\mathrm{s}},\omega_{\mathrm{i}}) = (k_{\mathrm{i}}(\omega_{\mathrm{i}}) - k_{\mathrm{s}}(\omega_{\mathrm{s}}))\sin\theta_{\mathrm{s}} \end{cases} \tag{3.58}$$

The first order Taylor expansion of the wave vector mismatch around the central frequencies yields

$$\begin{cases} \Delta k_z(\omega_{\mathrm{s}},\omega_{\mathrm{i}}) = \Delta k_z(\omega_{\mathrm{s},0},\omega_{\mathrm{i},0}) + (k'_{\mathrm{g}} - k'_{\mathrm{s}}\cos\theta_{\mathrm{s}})\underline{\omega}_{\mathrm{s}} + (k'_{\mathrm{g}} - k'_{\mathrm{i}}\cos\theta_{\mathrm{s}})\underline{\omega}_{\mathrm{i}} \\ \Delta k_\perp(\omega_{\mathrm{s}},\omega_{\mathrm{i}}) = \Delta k_\perp(\omega_{\mathrm{s},0},\omega_{\mathrm{i},0}) - (k'_{\mathrm{s}}\underline{\omega}_{\mathrm{s}} - k'_{\mathrm{i}}\underline{\omega}_{\mathrm{i}})\sin\theta_{\mathrm{s}} \end{cases} \tag{3.59}$$

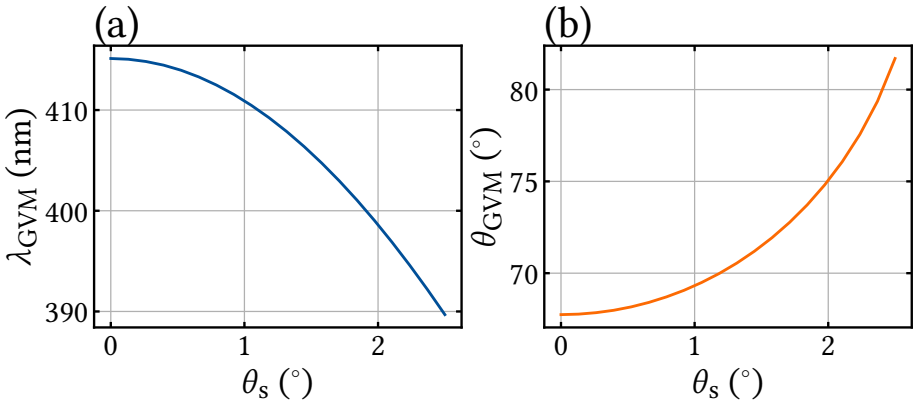

Fig. 3.9 Group velocity matching wavelengths λ_{GVM}, and angles θ_{GVM}, computed for different non-collinear angles θ_s, for KDP in degenerate type-II PDC.

where the wave vector derivatives k'_j, the centered frequencies $\underline{\omega}_j$ and the central frequencies $\omega_{s,0}$ for $j = i, s$ are defined in equation (3.45).

At central frequencies and for a given θ_s, both the transverse wave vector mismatch $\Delta k_z(\omega_{s,0}, \omega_{i,0})$ and the longitudinal wave vector mismatch $\Delta k_\perp(\omega_{s,0}, \omega_{i,0})$ are expected to vanish for perfect phase matching, i.e. when equations (3.57) are satisfied. In type-II PDC, the signal and idler fields have orthogonal polarizations, therefore in practice their refractive indices are not equal. This makes it impossible to have both $\Delta k_\perp(\omega_{s,0}, \omega_{i,0})$ and $\Delta k_z(\omega_{s,0}, \omega_{i,0})$ equal to zero. Thus, only approximate phase-matching may be achieved.

In order to have a full description of the phase-matching function in the non-collinear case, we should take into account the spatial dependency of the gate beam. From [U'Ren 03], the phase-matching function is given by

$$\phi_{PM}(\omega_s, \omega_i) \propto \exp\left(-\frac{(\Delta k_\perp(\omega_s, \omega_i))^2 w_0^2}{4}\right) \operatorname{sinc}\left[\left(\frac{(\Delta k_\perp(\omega_s, \omega_i))^2}{4k_g(\omega_s + \omega_i)} - \frac{\Delta k_z(\omega_s, \omega_i)}{2}\right) L\right] \tag{3.60}$$

where w_0 is the beam diameter at the beam waist of the gate Gaussian beam. Following [U'Ren 03], for large enough gate waist w_0 the phase-matching function can be factorized into a product of its longitudinal and transverse parts as

$$\phi_{PM}(\omega_s, \omega_i) \propto \phi_z(\omega_s, \omega_i)\phi_\perp(\omega_s, \omega_i) \tag{3.61}$$

$$\text{with} \quad \begin{cases} \phi_z(\omega_s, \omega_i) = \operatorname{sinc}\left(\dfrac{\Delta k_z(\omega_s, \omega_i)}{2} L\right) \\ \phi_\perp(\omega_s, \omega_i) = \exp\left(-\dfrac{(\Delta k_\perp(\omega_s, \omega_i))^2 w_0^2}{4}\right) \end{cases} \tag{3.62}$$

The condition writes more precisely $w_0/L \gg \sin^2(\theta_s)$. In the simulations, we make sure to always remain in these conditions.

In the frequency space (ω_s, ω_i), the longitudinal phase-matching function depends on the sum of signal and idler frequencies $\omega_s + \omega_i$ and its width depends on the length of the crystal L. Similarly, the transverse phase-matching function depends on the frequency difference $\omega_s - \omega_i$ and its width depends on the gate waist w_0.

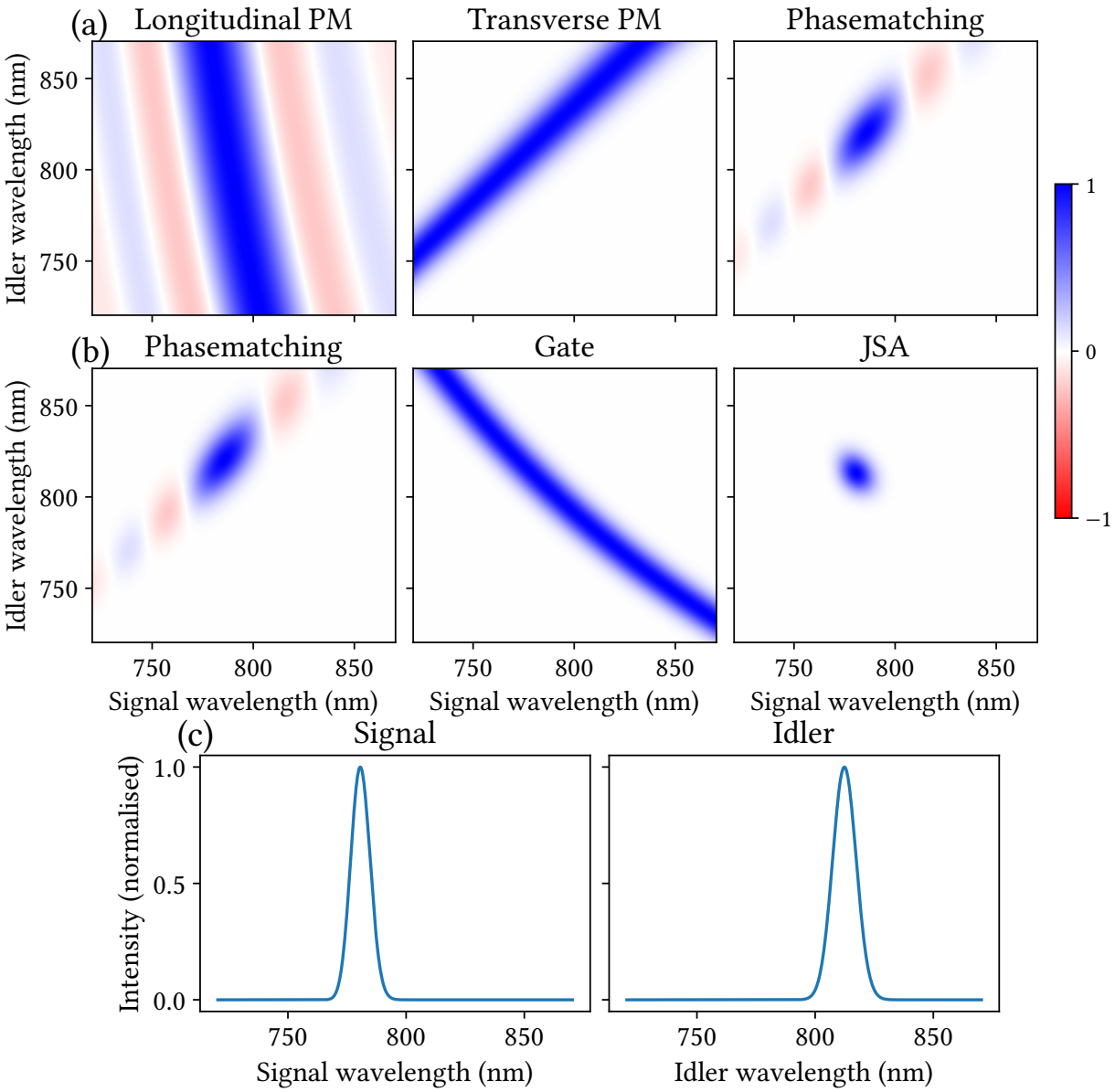

Fig. 3.10 Simulations for non-collinear type-II PDC in BBO. (a) Phase-matching function as the product of the longitudinal and transverse phase-matching functions. (b) JSA as the product of the phase-matching function with the Gaussian gate psectral envelope. (c) First normalized signal (left) and idler (right) eigenmodes of the JSA. PM: phase-matching function.

After fixing the gate central wavelength and the cut angle to best satisfy the phase matching, the remaining experimentally tunable parameters are the gate spectral width $\Delta\omega_g$, the crystal length L and the beam waist w_0.

The results are shown in figure 3.10 for BBO in the type-II non-collinear configuration. The gate spectral envelope is set as a Gaussian of width $\Delta\lambda_g = 5$ nm[1]. For a non-collinear angle of $\theta_s = 5.325^\circ$, we obtain $\lambda_{GVM} = 398$ nm and $\theta_{GVM} = 49.1^\circ$. The crystal length of $L = 0.3$ mm and a beam waist of $w_0 = 85$ μm ensures the condition $w_0/L \gg \sin^2(\theta_s)$ is valid. The first signal and idler eigenmodes are given in the bottom of figure 3.10. We obtain the Schmidt number $K = 1.04$. Applying a 15 mn wide filter, the Schmidt number can be further reduced to $K = 1.02$, at the cost of 15% losses on the idler first eigenmode.

In figure 3.10, one can see that the transverse phase-matching function is not centered around the desired central frequencies. As mentioned earlier in this section, this effect is due to the non-vanishing component of the transverse wave vector mismatch, which results in shifting the total phase-matching function. As a result, the idler and signal fields do not have the same central frequency, which can be a limitation depending on the application.

3.3.2 Type-I

Finally, we treat the case of single-photon addition in degenerate type-I non-collinear PDC. In this case, we can have perfect phasetmatching ($\Delta k_\perp(\omega_{s,0}, \omega_{i,0}) = \Delta k_z(\omega_{s,0}, \omega_{i,0}) = 0$ in equation (3.59)).

The phase-matching condition for the degenerate type-I PDC process is given by

$$n_e(\omega_g, \theta_c) = n_o(\omega_s)\cos\theta_s \tag{3.63}$$

where all the quantities involved have been defined before. Table 3.3 shows λ_{GVM} and θ_{GVM} for different non-linear crystals for degenerate type-I PDC at $\theta_s = 0^\circ$.

Crystal	λ_{GVM} (nm)	θ_{GVM} ($^\circ$)
KDP	517	41.15
BBO	771	19.83
LN	1012	44.95
KTP	919	24.98

Table 3.3: Group velocity matching wavelengths λ_{GVM} and angles θ_{GVM} for different non-linear crystals for degenerate type-I PDC at $\theta_s = 0^\circ$.

In the case of the BBO crystal, we show in figure 3.11 the variation of λ_{GVM} and θ_{GVM} with respect to non-collinear angles θ_s. In the case of the BiBO, the BiBO crystal only fulfills the conditions from $\theta_s = 5^\circ$. In other words, there are no group velocity matching for non-collinear angles θ_s below 5° for the BiBo crystal.

[1]The gate spectral width $\Delta\omega_g$ is related to $\Delta\lambda_g$ to $\Delta\lambda_g$ by $\Delta\omega_g = \Delta\lambda_g 2\pi c/\lambda_{g,0}^2$

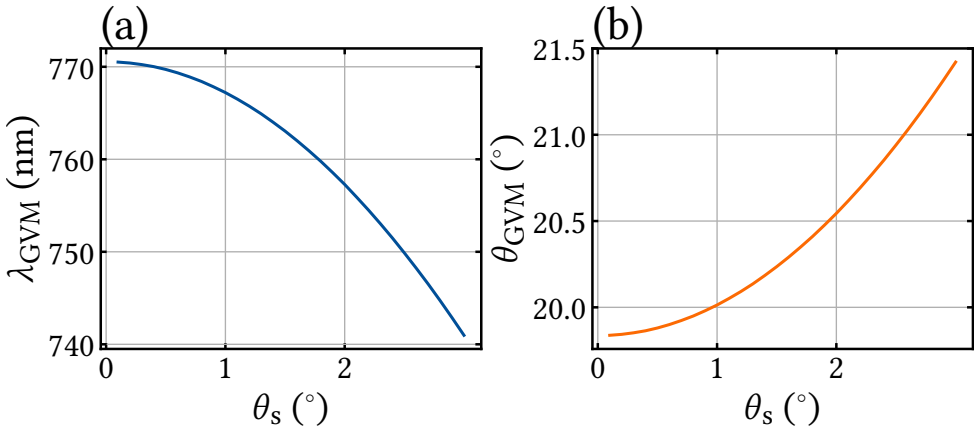

Fig. 3.11 Group velocity matching wavelengths λ_{GVM}, and angles θ_{GVM}, computed for different non-collinear angles θ_s, for type-I PDC in BBO.

In type-I, $k'_s = k'_i$ and therefore equation (3.59) re-writes as (with $\Delta k_\perp(\omega_{s,0}, \omega_{i,0}) = \Delta k_z(\omega_{s,0}, \omega_{i,0}) = 0$)

$$\begin{cases} \Delta k_z = (k'_g - k'_s \cos\theta)(\underline{\omega}_s + \underline{\omega}_i) \\ \Delta k_\perp = -k'_s \sin\theta(\underline{\omega}_s - \underline{\omega}_i) \end{cases} \tag{3.64}$$

Numerical simulations are carried out for the uniaxial crystals KDP, BBO and LN as well as for biaxial crystals BiBO and KTP. We choose to present the simulation of the BiBO crystal, as it is notably the crystal we have at hand in the laboratory. Figure 3.12 shows the phase-matching function and JSA for the BiBO crystal in the type-I non-collinear configuration. The gate spectral envelope is set as a Gaussian of width $\Delta\lambda_g = 6\,\text{nm}$[1]. For a non-collinear angle of $\theta_s = 5°$, we obtain $\lambda_{GVM} = 708\,\text{nm}$ and $\theta_{GVM} = 8.02°$. The central wavelengths are $\lambda_{s,0} = \lambda_{i,0} = 1416\,\text{nm}$. The crystal length of $L = 1\,\text{mm}$ and a beam waist of $w_0 = 225\,\mu\text{m}$ ensures the condition $w_0/L \gg \sin^2(\theta_s)$ is valid. The first signal and idler eigenmodes are displayed on figure 3.12. As expected, the shift of the phase-matching function observed in type-II non-collinear PDC is not present here in figure 3.12 for type-I non-collinear PDC.

We obtain the Schmidt number $K = 1.00$ ($K = 1.0005$). As the Schmidt number is very close to 1, spectrally filtering the idler eigenmodes was not investigated. This result shows that there are non-collinear configurations which allow for a highly single-mode single-photon addition process.

For both type-I and type-II non-collinear PDC, mode selectivity does not seem to be achievable from our studies. Indeed, increasing the order of the gate Hermite-Gauss mode by 1 increases the Schmidt number to more than 2, resulting in non single-mode single-photon addition.

Although filtering helps improving the single-mode character of the process, it does not clearly improve its mode selectivity in the non-collinear configurations. Indeed, the success of filtering relies on the spectral distinguishability between the first idler eigenmode and the higher order ones. For non-collinear type-I PDC in BiBO, with a first order Hermite-Gauss

[1]The gate spectral width $\Delta\omega_g$ is related to $\Delta\lambda_g$ by $\Delta\omega_g = \Delta\lambda_g 2\pi c/\lambda^2_{g,0}$

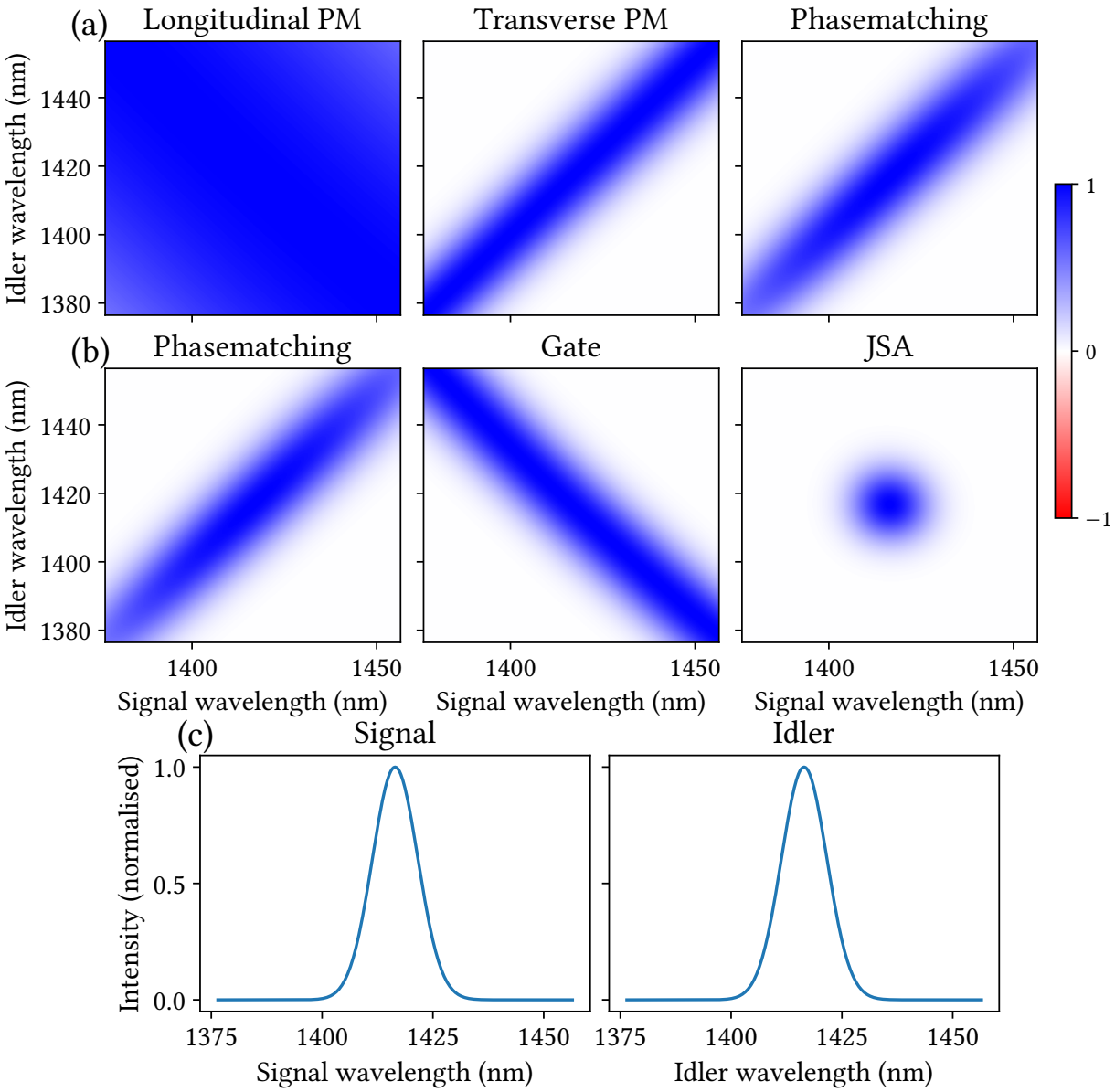

Fig. 3.12 Simulations for non-collinear type-I PDC in BiBO. (a) Phase-matching function as the product of the longitudinal and transverse phase-matching functions. (b) JSA as the product of the phase-matching function with the Gaussian gate spectral envelope. (c) First normalized signal (left) and idler (right) eigenmodes of the JSA. PM: phase-matching function.

gate, $K = 2$ and the first idler eigenmode highly overlaps with the second, which means spectral filtering is not helpful.

3.3.3 Conclusion of the single-photon addition investigation

In the current and two previous sections, we developed a theoretical framework for the addition of a single photon to multimode light fields in order to generate non-Gaussian quantum states [Roeland 22]. We showed that multimode single-photon added states cannot be pure, although numerical simulations show that very high purity states are achievable in realistic experimental conditions. We have investigated different PDC configurations that support single-photon addition, with uniaxial and biaxial crystals (KDP, BBO, LN, BiBO, KTP).

For collinear type-II PDC, mode-selective photon addition is shown to be achievable both analytically and numerically under group velocity matching and long enough crystal conditions. We prove that one can arbitrarily choose the unique mode in which the single photon is added. Moreover, spectrally filtering the idler field can be used to improve both the single-mode and the mode-selectivity characters of the addition process.

For non-collinear PDC, we extended the group velocity matching condition for both type-I and type-II processes, and shown numerically that single-mode single-photon addition is achievable.

As a possible future development of this work, other materials than raw bulk crystals may be considered in order to achieve better results exploiting extra degrees of freedom, such as periodically or aperiodically poled crystals.

3.4 Experimental single-photon subtraction via sum-frequency generation

From the previous sections, single-photon addition is a promising operation to generate non-Gaussian multimode states. Practically implementing single-photon addition may be thought a priori more challenging than single-photon subtraction, because it is always possible to add a photon to the vacuum. If a gate non-vacuum mode have a non-zero overlap with a signal vacuum mode, photons are added to an irrelevant mode with a non-zero probability. For instance, a spatial mode mismatch due to a broader gate beam than the signal beam results in photon addition in vacuum modes[1]. Subtraction processes are free from such effects, since a photon can not be removed from the vacuum. This big picture observation does not tell the whole story. In the first subsection, we describe the single-photon subtraction process we use in this thesis, and further discuss the pros and cons of both addition and subtraction processes.

For the experimental project of this thesis, we use the single-photon subtraction implementation developed in the theses [Jacquard 17] (English) [Dufour 18] (French, though more advanced). In a subsequent subsection, we describe the technical aspects and challenges of the setup, and assess the current performance of the subtractor. The single-photon subtractor

[1]In this example, this effect can in particular be coped with the homodyne or double homodyne detection, using the LO mode as a spatial filter with a beam waist matching the signal beam waist.

corresponds to the module **2.b)** in figure 2.1, briefly presented in chapter 2 among the rest of the complete experiment.

3.4.1 Mode-selective single-photon subtraction via type-I non-collinear sum-frequency generation

In this subsection, we briefly give the framework of multimode single-photon subtraction, for which the main concepts already elaborated in the previous sections are applied here to the subtraction case. We then specify the physical system to type-I non-collinear sum-frequency generation for which mode selectivity is achievable. We also discuss some applications of such non-Gaussian mode-selective subtraction operation. We compare the properties of single-photon subtraction with the ones of single-photon addition when relevant.

The principle scheme of the single-photon subtraction is pictured by figure 3.13.

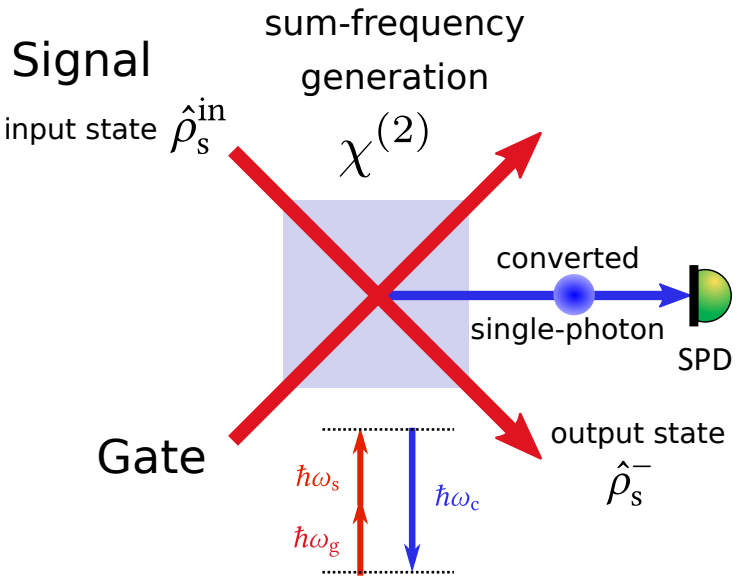

Fig. 3.13 Scheme of single-photon subtraction through non-collinear sum-frequency generation in a non-linear crystal. Each gate photon and signal photon are probabilistically up-converted into a single photon detected for heralding purposes. SPD: single-photon detector.

Multimode single-photon subtraction. The theoretical framework for multimode single-photon subtraction was developed in [Averchenko 16]. This framework is similar as in the addition case developed in section 3.1. It boils down to replace $\hat{a}_{s,n}^\dagger$ by $\hat{a}_{s,n}$ in expression (3.6) of the evolution operator $\hat{U}$.

Following the same steps, we obtain the output subtracted state $\hat{\rho}_s^-$ conditioned to the detection of an up-converted photon

$$\hat{\rho}_s^- = \frac{1}{P^-} \sum_{n,n'} \mathbf{A}_{nn'}^- \hat{a}_{s,n} \hat{\rho}_s^{in} \hat{a}_{s,n'}^\dagger \tag{3.65}$$

where the coefficients $\mathbf{A}^-_{nn'}$ form the matrix $\mathbf{A}^-$ referred to as the *subtraction matrix* and P^- is the detection success probability.

Upon diagonalizing the subtraction matrix $\mathbf{A}^-$, we find similarly

$$\hat{\rho}_s^- = \frac{1}{P^-} \sum_n \lambda_n \hat{e}_n \hat{\rho}_s^{\text{in}} \hat{e}_n^\dagger \tag{3.66}$$

$$\text{where} \quad P^- = \sum_n \lambda_n \bar{n}_n \tag{3.67}$$

where we kept the notations for the eigenvalues $\{\lambda_n\}$ and eigenmodes $\{\vec{\mathbf{e}}_n\}$ associated to the annihilation operators $\{\hat{e}_n\}$, and $\bar{n}_n = \text{Tr}[\hat{e}_n^\dagger \hat{e}_n \hat{\rho}_s^{\text{in}}]$ is the photon number of the input signal in the eigenmode $\vec{\mathbf{e}}_n$.

Note that for $\bar{n}_n < 1$, the subtraction probability $\lambda_n \bar{n}_n / P^-$ in a given eigenmode is a priori significantly smaller than the analogue addition probability $\lambda_n(1 + \bar{n}_n)/P^+$ assuming equal eigenvalues, and similar gate power.

With respect to subsection 3.1.3, the results on the output state purity differ for subtraction because the probability to subtract in a vacuum mode is zero. Indeed, the probability $\lambda_n \bar{n}_n / P^-$ to subtract in eigenmode $\vec{\mathbf{e}}_n$ goes to zero when the quantum state in $\vec{\mathbf{e}}_n$ is the vacuum (i.e. $\bar{n}_n = 0$)[1].

In particular, the subtracted state purity is always equal to 1 for any Schmidt number K, provided the input state is a pure single-mode state. For this reason, the subtracted state purity is always higher in a subtraction process compare to an addition process, provided the input state is a pure approximately single-mode state.

Let us consider a two-mode squeezed vacuum input state, similarly as in subsection 3.1.3. Contrary to the addition case (see equation (3.25)), the subtraction purity for a two-mode input state writes

$$\text{Tr}\left[(\hat{\rho}_s^-)^2\right] = \frac{\bar{n}_2^2 + (\lambda_1/\lambda_2)^2 \bar{n}_1^2}{[\bar{n}_2 + (\lambda_1/\lambda_2)\bar{n}_1]^2} \tag{3.68}$$

Note that for equation (3.68) to be valid, we do not require the subtraction process to be limited to the two first eigenmodes, only the input state, contrary to the addition case.

The subtracted state purity is shown in figure 3.14, to be compared with the added state purity in figure 3.3. There are parameter regions where the added state purity is higher than the subtracted state purity, and vice-versa. This depends on the relative squeezing between the two modes. In particular, the subtracted state purity goes to 1 when the number of photons, or equivalently the squeezing factor, in one of the two modes goes to zero. This behavior differs in the addition case, for which the purity in this case is given by the lines of abscissa 0 dB and of ordinate 0 dB in figure 3.3.

Mode selectivity in type-I non-collinear sum-frequency generation. As shown in [Averchenko 14], single-photon subtraction can be implemented in type-I non-collinear sum-frequency generation. In particular they show that mode selectivity, i.e. the ability to control the mode in which the single-photon is subtracted, can be achieved in such physical system.

[1] This property generalizes naturally to any vacuum mode and is not specific to the eigenmodes.

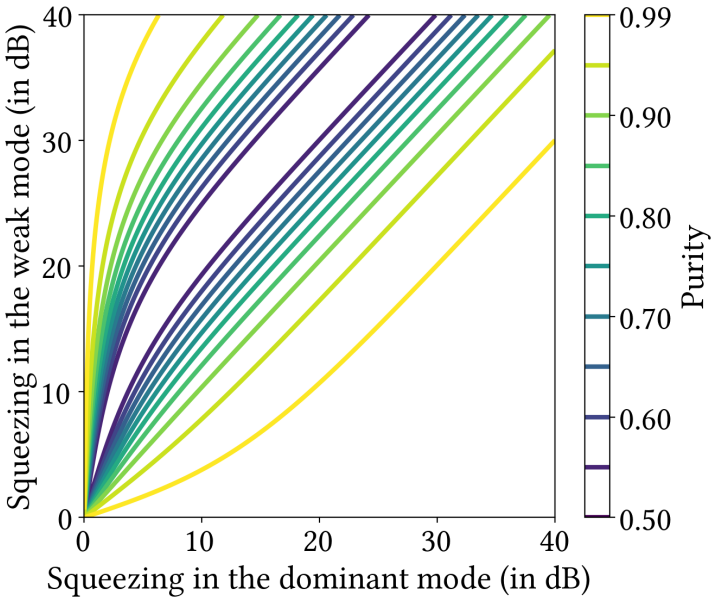

Fig. 3.14 Output subtracted state purity for a two mode squeezed vacuum input state, at fixed Schmidt number $K = 1.2$.

For sum-frequency generation (SFG), the corresponding phasematched term in the Hamiltonain integral equation (3.26) is $2\varepsilon_0\chi^{(2)}\hat{\mathbf{E}}_{\mathrm{s}}^{(+)}(z,t)\hat{\mathbf{E}}_{\mathrm{c}}^{(-)}(z,t)\hat{\mathbf{E}}_{\mathrm{g}}^{(+)}(z,t)$ + h.c. [Boyd 13], using the subscript c for the up-converted field. We consider the type-I process with both signal and gate field in the ordinary polarization and the up-converted field in the extraordinary polarization[1]. With this term in the Hamiltonian, a single-photon is removed from both the gate field and the signal field, down-converting them into an up-converted single-photon. The single-photon subtraction is illustrated in figure 3.15. In terms of energy conservation, it writes

$$\omega_{\mathrm{g}} = \omega_{\mathrm{c}} - \omega_{\mathrm{s}} \tag{3.69}$$

We refer the reader to [Averchenko 14] for the demonstration that such subtraction process becomes single-mode under group velocity matching condition $k'_{\mathrm{g}} = k'_{\mathrm{s}}$ and long enough crystal conditions. Similarly, it is also shown that under such conditions, the signal mode in which occurs the subtraction is given by the gate spectral mode $\widetilde{\mathbf{h}}_{\mathrm{g}}$. In other words, the subtraction process is then mode selective.

As explained in chapter 2, this mode-selectivity property can be exploited using the gate pulse shaper **2.a)** in figure 2.1, which engineer the gate time-frequency mode $\widetilde{\mathbf{h}}_{\mathrm{g}}$ (see subsection 2.2.4 on pulse shaping techniques).

The single-mode property and mode selectivity of this single-photon subtractor allows for the investigation of non-Gaussianity in both the single-mode case and the multimode entangled case. We briefly describe two applications of the single-photon subtractor in the following.

[1]Technically, this set of polarizations is referred to type-VI in the literature, while the type-I is usually restricted to the case where the gate field is extraordinarily polarized and the signal and up-converted fields are ordinarily polarized.

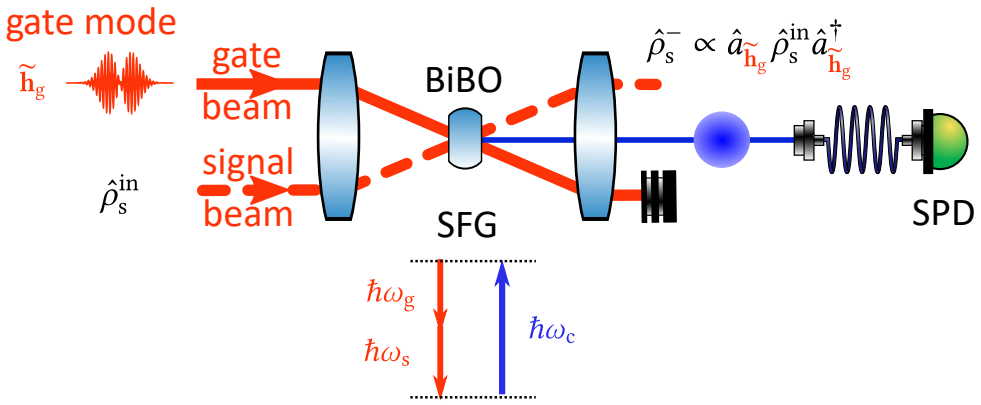

Fig. 3.15 Scheme of mode-selective single-photon subtraction via sum-frequency generation (SFG) in a BiBO crystal. A single photon form both gate and signal fields are probabilistically converted into an up-converted single photon detected for heralding purposes. Single-photon subtraction occurs in the gate spectral mode $\widetilde{\mathbf{h}}_\mathrm{g}$. SPD: single-photon detector.

Wigner negativity induced by single-photon subtraction. As shown in subsection 1.4.4, the single-photon subtraction operation applied to a squeezed vacuum input state may result in a quantum state which has a negative Wigner function. The condition for Wigner negativity upon subtraction is given by inequality (1.155), which writes $\mathrm{Tr}\left[\mathbf{V}^{-1}\mathbf{\Pi}_{\vec{\mathrm{g}}}\right] > 2$ with $\mathbf{V}$ the covariance matrix of the squeezed vacuum input state and $\mathbf{\Pi}_{\vec{\mathrm{g}}}$ the projector on the two-dimensional phase space associated with subtraction mode $\vec{\mathrm{g}}$. This result is valid for a single-mode subtraction process, with Schmidt number $K = 1$. For a multimode subtraction process described by equation (3.66), the results of subsection 1.4.4 are directly generalized upon replacing the projector $\mathbf{\Pi}_{\vec{\mathrm{g}}}$ with

$$\mathbf{\Pi}_{\vec{\mathrm{g}}} \mapsto \frac{1}{P^-} \sum_n \lambda_n \bar{n}_n \mathbf{\Pi}_{\vec{\mathrm{e}}_n} \tag{3.70}$$

where P^- is defined by equation (3.67), $\mathbf{\Pi}_{\vec{\mathrm{e}}_n}$ is the projector on the two-dimensional phase space associated with subtraction eigenmode $\vec{\mathrm{e}}_n$, and $\bar{n}_n$ the number of input photons in this eigenmode. In particular, this generalizes inequality (1.155), which is expected to be harder to beat when the Schmidt number K is higher than 1.

For comparison, single-photon added states always satisfy their analogue inequality $\mathrm{Tr}\left[\mathbf{V}^{-1}\mathbf{\Pi}_{\vec{\mathrm{g}}}\right] > -2$ and yield a negative Wigner function. This last statement holds true for non-pure input states and multimode single-photon addition [Walschaers 17b], for which the projector $\mathbf{\Pi}_{\vec{\mathrm{g}}}$ is replaced according to

$$\mathbf{\Pi}_{\vec{\mathrm{g}}} \mapsto \frac{1}{P^+} \sum_n \lambda_n (1 + \bar{n}_n) \mathbf{\Pi}_{\vec{\mathrm{e}}_n} \tag{3.71}$$

with similar notation as for equation (3.70).

In [Walschaers 17a, Walschaers 17b], they study of output state purity versus input state purity for both single-photon subtraction and addition processes. In the simulations, at a given

purity of the input state and for single-mode processes, the purity of the single-photon added state is always higher than the purity of the subtracted state. This suggests that the purity of the added state is more robust to the input state purity, with respect to the purity of the subtracted state.

The two above remarks show a clear advantage of addition over subtraction. Considering also the previous discussions on the subtraction/addition success probabilities (where addition may win) and on the output state purity with respect to the Schmidt number of the process (where subtraction wins over addition for some interesting cases), it is unclear theoretically which one of the two operations is the most suitable for generating non-Gaussian multimode states. A choice between them depends on the application in terms of input state purity, output state purity requirements, output non-Gaussianity "amount" requirements[1], along with the experiment constraints.

Generating a subtracted squeezed vacuum state pure enough to be Wigner negative may then be challenging experimentally. [Ra 20] demonstrates such successful application by performing a tomography of the subtracted state using an homodyne detection. As explained in section 2.4, the homodyne detection measures the quadrature of the signal $\hat{q}_s^\theta$ at a controllable angle θ given by the optical phase between the local oscillator field and the signal field. All the information on the experimental state is contained in the set of all the quadrature distributions $\{\mathrm{Tr}[\hat{\rho}\hat{q}_s^\theta]\}$ for all angles θ. Since these distributions are all the marginals of the Wigner function, measuring their set allows one to rebuild the Wigner function of the measured state, i.e. performing its tomography. Since θ is a real parameter, one can only measure a discrete subset in practice. To cope with this lack of information, one can use the maximum likelihood algorithm [Lvovsky 04]. The iterative algorithm yields the most likely quantum state to correspond to the measurements, provided some assumptions on the measured state such as finite density matrix, and reasonable amount of losses[2]. Using these methods and the subtractor aforementioned, [Ra 20] obtained the Wigner function of experimental single-photon subtracted squeezed vacuum states with sufficiently high purity to demonstrate their Wigner negativity.

Wigner negativity induced by single-photon subtraction in a multimode entangled state. Along with these results, the group studied the effect of the entanglement structure between different modes when subtracting in one of the modes in [Ra 20].

In the supermode basis, the output state of the SPOPO is a separable multimode squeezed vacuum state (see section 2.3). It was shown in subsection 1.3.6 that a two-mode squeezed vacuum state becomes a two-mode entangled state upon a change of mode basis. The subtraction mode may be chosen as a supermode, as well as a mode of a mode basis in which the SPOPO output state is entangled. The effect of subtraction on this resulting state has been studied in [Walschaers 19], where it is in particular shown that the resulting state may not feature non-Gaussianity in modes distant from the subtraction mode by more than two entanglement links. In [Ra 20], they experimentally show that subtracting in a mode form a square-like entanglement structured state yields a Wigner function with maximal negativity in the furthest

[1] See section 1.4 for more details on non-Gaussianity properties, Wigner negativity and stellar rank, and how to witness them.

[2] These assumptions allows one to search the state in a subset of the very large state Hilbert space.

mode, two steps away. This particular result was predicted in [Walschaers 18].

The two aforementioned applications demonstrate the capabilities of the single-photon subtractor for the study of non-Gaussianity in multimode fields.

3.4.2 Experimental realization

The single-photon subtractor used in [Ra 20] and developed in the theses [Jacquard 17, Dufour 18] is the same one we use in this thesis work. Due to a recent replacement of the optical table for a bigger one, the subtraction setup has been rebuilt with minor changes. After describing the subtractor, we show that we recover similar performances as before, using the method developed in [Ra 17].

3.4.2.1 Technical description and challenges

Description. A photo of the single-photon subtraction setup is given in figure 3.16. The type-I sum-frequency generation occurs in a 2.5 mm long BiBO crystal. Both the gate and signal beams are vertically polarized, with spectrums centered at 795 nm. With a beam diameter of 1.6 mm, both beams are collimated and parallel prior entering a 200 mm focal lens. Symmetrically with respect to the lens optical axis, the distance between both beams is horizontally 10 mm and vertically 7.5 mm, where the horizontal plan is the optical table. From this geometry, we deduce that the non-collinear angle[1] θ_s is equal to 3.58°.

After the lens, the beams focus at the same position in the lens focal plan, where the crystal is then placed. After the crystal both gate and signal beams encounter a lens with the same focal length, such that they have the same spatial properties as at the entrance of the subtractor, with switched positions. The signal is later sent to the homodyne or double homodyne setup, while the gate beam is dumped.

SFG beam and SFG counts. The sum-frequency generated (SFG) beam (i.e. up-converted beam), whose spectrum is centered at 397.5 nm, outputs the second lens before being coupled to a monomode fiber, with 65% coupling efficiency. The up-converted photons are then measured by a Hamamatsu C13001-01 single-photon detector (SPD), with 40% efficiency at this wavelength. We estimated the optical losses from the crystal to the SPD to 70%, resulting in a total loss of 90% (taking into account a spectral filter whose role we explain later). We denote the corresponding efficiency η_c (10%). With coherent bright signal and gate beams, we can estimate the proportion of power which is up-converted with respect to the input signal power, at a given gate power. We usually use 1 mW gate power for both alignment and measurements. At this gate power, the up-conversion efficiency η_{SFG} is about 0.16%. We can then deduce a simple estimation of the expected number of detector counts per second due to SFG c_{SFG} as

$$c_{SFG} = \frac{\bar{n}_{s,\vec{g}}}{T_{cav}} \eta_{SFG} \eta_c \tag{3.72}$$

[1] We keep the same definition given for equation (3.57), i.e. θ_s is the angle between the signal and gate beams.

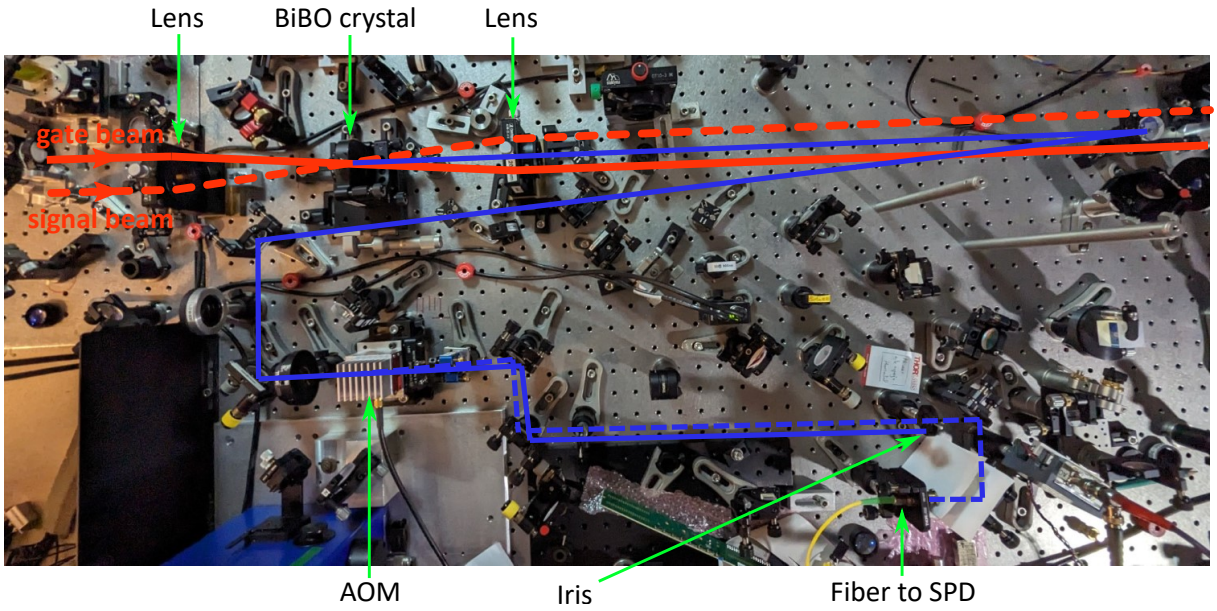

Fig. 3.16 Photo of the current single-photon subtraction setup on the optical table. After the subtraction, the signal beam is sent to the detection (not shown) and the gate beam is later dumped. The up-converted beam is diffracted by an acousto-optic modulator (AOM) when single photons are generated (dashed-blue beam), which are sent to a single-photon detector (SPD) via a fiber.

where $\bar{n}_{s,\vec{g}}$ is the number of signal photons in the subtraction mode $\vec{g}$, T_{cav} is the SPOPO cavity mode temporal duration. Since the signal pulses make several round trips in the SPOPO cavity prior significantly loose energy, the relevant signal temporal duration is the inverse of the SPOPO cavity bandwidth. The cavity bandwidth can be estimated as the product of the pulse repetition rate 76 MHz divided by the cavity finesse, 28 for an output coupler of reflectivity $r_o^2 = 80\%$. From these estimations, we can expect $c_{SFG} = 55$ counts per second on the SPD from the SFG, assuming the signal state is a 3 dB squeezed state in the mode $\vec{g}$. For a lower squeezing factor s_{dB} of 2 dB, we obtain $c_{SFG} = 24$ counts per second. For higher reflectivity of the output coupler, the finesse decreases, and we expect higher count rates. For instance, at $r_o^2 = 50\%$, the finesse is about 9 and we obtain higher count rates of $c_{SFG} = 170$ for $s_{dB} = 3$ dB, and $c_{SFG} = 74$ for $s_{dB} = 2$ dB. We refer to these detector counts as *SFG counts*. Note that equation (3.72) is valid under the assumption that the probability of having SFG double-photon events is negligible.

Dark counts. Imperfections of both the SPD and the setup leads to other sources of recorded counts on the detector. These counts are not coming from actual signal photon subtractions, and lead to a loss of purity of the signal output state conditioned on all the detector counts. The imperfection the SPD itself produces *dark counts*, i.e. counts that occur in the absence of input light. The detector is an avalanche photodiode (APD) working at room temperature, with usually very low dark counts. We measured a typical dark count rate of 12 counts per second. To further reduce this rate, we use a taggering electronic device. Taking advantage from the pulsed nature of our light, this device allows for selecting a 1 ns time windows when

light actually impinge the detector. As a result, we obtain a dark count rate c_{dark} of less than 1 count per second.

Gate SHG counts. On top of the dark counts, we observe a significant amount of detector counts from a side effect of the physics of our subtractor. Even though it is not phasematched for this process, the 1 mW bright gate beam produces a second-harmonic generated (SHG) beam of about 1 uW, corresponding to about 10^{12} photons per second. The gate SHG photons are diffracted by the crystal defects, so that a fraction get coupled into the fiber, up to the detector. We observe typically thousands of counts per second. We refer to these counts as *gate SHG counts*.

Note that it was observed in [Dufour 18] that such defects are produced when the gate power reaches 10 mW when used alone, or when both signal and gate beams are used as 1 mW bright beams for alignment purposes.

To cope with this limitation, [Dufour 18] increased the non-collinear angle θ_s to the current 3.58° so as to reduce the gate diffusion coupling into the fiber, and thus the gate SHG counts. Since the subtraction mode selectivity is conditioned to small non-collinear angles θ_s [Averchenko 14], further increasing θ_s may risk the loss of this essential property. To further reduce the gate SHG counts, we use a 0.35 nm wide spectral filter on the path to the detector to get rid of the gate SHG photons that lie outside this range. The remaining gate SHG photons can not be distinguished from the SFG photons, with the same spatial modes, time-frequency modes and polarizations. Yet, the crystal is rotated in order to minimize the SHG phase matching, while maintaining a good SFG phase matching. We also scan the crystal transverse position to find seldom spots where the crystal diffracts significantly less. For instance, we measured a gate SHG count rate c_{SHG} of 2 counts per second for which we recorded $c_{\text{SFG}} = 23$ counts per second for an estimated 2 dB squeezed state and a reflectivity $r_o^2 = 80\%$, with the usual dark rate $c_{\text{dark}} = 1$ count per second. This measurement is consistent with the estimation given in equation (3.72).

3.4.2.2 Single-photon subtraction tomography

In this subsection, we follow the method used in [Jacquard 17] and further developed in [Ra 17] to assess the performance of our subtractor. The method is based on quantum process tomography using coherent states [Lobino 08, Fedorov 15]. The subtraction process, as any quantum process, can be completely characterized sending only coherent states as input, and measuring both the output states and corresponding success probabilities. In the case of single-photon subtraction, the tomography is drastically simplified as a single-photon subtracted coherent state is again a coherent state (as $\hat{a}\,|\alpha\rangle = \alpha\,|\alpha\rangle \propto |\alpha\rangle$). It is then only required to measure the success probabilities.

Let us consider a multimode coherent state $|\vec{\alpha}\rangle$ which we write in the eigenmode basis of the subtraction process $\{\vec{\mathbf{f}}_n\}$

$$|\vec{\alpha}\rangle = |\alpha_1\rangle \otimes \cdots \otimes |\alpha_N\rangle \tag{3.73}$$

with total number of photons $\left\|\vec{\alpha}\right\|^2 = \sum_n |\alpha_n|^2$.

From equation (3.65), the output subtracted state is again $|\vec{\alpha}\rangle$, with subtraction success probability $P^-_{|\vec{\alpha}\rangle\langle\vec{\alpha}|}$

$$P^-_{|\vec{\alpha}\rangle\langle\vec{\alpha}|} = \sum_{n,n'} \mathbf{A}^-_{n,n'} \alpha_n \alpha^*_{n'} \tag{3.74}$$

Measuring the success probability of equation (3.74) with a finite number of well chosen coherent states allows one to retrieve the subtraction matrix $\mathbf{A}^-$. The diagonal term $\mathbf{A}^-_{n,n}$ is obtained using a coherent state with an arbitrary amplitude β in mode $\vec{\mathbf{f}}_n$, and vacuum in the other modes. The off-diagonal term $\mathbf{A}^-_{n,n'}$ is obtained using two coherent states with amplitudes $(\frac{1}{\sqrt{2}}\beta, \frac{1}{\sqrt{2}}\beta)$ and $(\frac{1}{\sqrt{2}}\beta, \frac{-\mathrm{i}}{\sqrt{2}}\beta)$ in the modes $(\vec{\mathbf{f}}_n, \vec{\mathbf{f}}_{n'})$, and vacuum in the other modes. The mean number of photons $|\beta|^2$ is arbitrary and is not required to be varied since the subtraction matrix is independent of the input state.

This subtraction tomography was performed in [Ra 17] for the subtractor prior the optical table replacement. To check the current performance, we perform the tomography of our subtractor using bright coherent input fields in the Hermite-Gaussian mode basis (whose modes are defined in appendix A.2), restricting to the first six HG modes. We use the local oscillator (LO) beam for this task, as we can set its time-frequency mode using the LO pulse shaper (module **3.b)** in figure 2.1). The temporary additional optical path used to feed the crystal with the LO beam is not shown.

We use alignment power levels, around 1 mW. It has been checked in [Ra 17] that probing with 1 photon per pulse fields or bright fields yield the same results, as expected by theory. The gate spectral mode is set to the HG_0 mode[1], corresponding to the mode in which we expect the highest squeezing (see section 2.3). The measured subtraction matrix is given in figure 3.17.

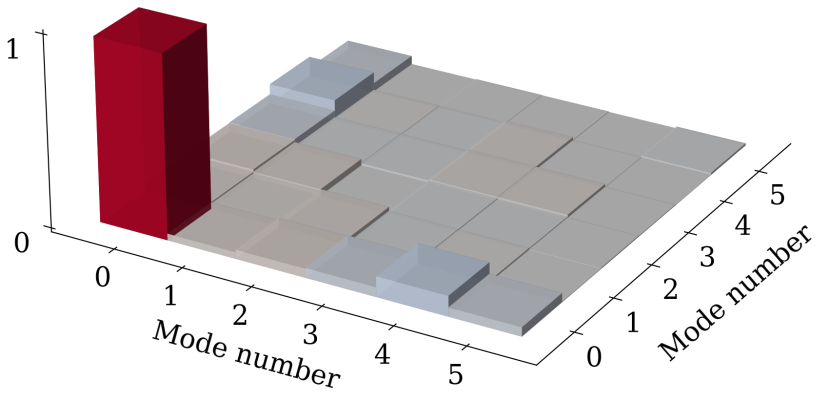

Fig. 3.17 Measured subtraction matrix $\mathbf{A}^-$ in the Hermite-Gaussian mode basis, restricted to the first six modes. The mode of local oscillator field used to probe the subtraction process is engineered as combinations of the Hermite-Gaussian modes, as described in the text. The mode of the gate field is set to the first Hermite-Gaussian mode. The subtraction matrix is normalized to satisfy $\mathrm{Tr}[\mathbf{A}^-] = 1$.

[1]We used HG modes of 11 nm FWHM.

Diagonalizing the measured subtraction matrix gives us access to the Schmidt number K of the single-photon subtraction process, which is equal to 1.03. The probability to subtract in the gate spectral mode, the HG_0 mode, is equal to 0.98. Form the previous discussions, we expect highly pure output subtracted states, provided the input states are highly pure. Note that these subtraction tomography results are very similar to the ones shown in [Ra 17], which confirms that the performance of the subtractor has been restored.

3.5 Towards multiple-photon subtraction

In the future, extending our subtraction setup to multiple-photon subtraction would allow us to generate and measure a broader class of non-Gaussian states, in particular states of stellar rank 2 or higher[1].

A potential approach to achieving this goal involves substituting the existing single-photon detector with an efficient photon number resolving detector, such as a transition-edge sensors (TES). The idea is then to post-select data on the specific multiple-photon events of interest. This post-selection eliminates the purity cost associated with blindly taking into account other photon events. This could also bring the advantage to pumping the subtraction harder with a higher gate power, boosting the subtraction event rate without other-photon-event purity loss. However, pumping harder would increase the gate SHG counts. Given that the number of gate SHG counts is already almost maximal before significantly reducing the output state purity, the subtraction rate can not be increased with the current scheme. Since the two-photon subtraction probability is approximately the square of the single-photon one, practical measurements with this approach may require better coping with the gate SHG counts.

Another potential approach would be to purposely set the current single-photon subtractor in a spectrally multimode configuration instead of the current single-mode one (to $K > 2$ for instance). The subtractor would then statistically subtract in several modes. Pumping it harder again (with the same to-be-addressed limitations) would give raise to multiple-photon events with a reasonable success probability. Among these subtraction events, some occur for instance in two photons, one from each of two different modes. We then need to post-select on these events, or in other words, we need a detection that can distinguish between these two modes. For instance, one could use a grating on the path of SFG beam to spread its spectrum prior coupling it into an array of single-photon detectors, such as avalanche photodiodes (APDs). Taking the modes HG_0 and HG_1 as examples, distinguishing between them would be done by detecting a single photon on the edge of the spectrum or in the middle. Taking into account any overlapping regions between the modes adds the challenge to decrease the output purity, as we don't know in which mode the subtraction occurred in these regions. Spectrally selecting small regions can lower this effect, at the expense to even lower efficiency. This scheme has the advantage to use APDs which offer high quantum efficiency, speed, and work at ambient temperature, avoiding the hassle of cooling down the detector at cryogenic temperatures, compared to TESs.

Yet another approach is to chain single-photon subtractors. Already limiting to two sub-

[1]For instance a state of stellar rank 2 may indeed not be engineered with less than 2 single-photon subtractions, see subsection 1.4.3

tractors has the large drawback to potentially double the cost in space and setup complexity. While using two gate pulse shapers provides the great advantage to subtract in two controlled modes, it would be challenging to build another one. One could relieve such cost by using the same gate pulse shaper for both subtractors, limiting us to subtracting two photons in the same mode. Another possibility is to split the gate SLM screen into two parts (a priori vertically to keep the number of spectral degrees of freedom), independently engineering the time-frequency mode of both gate beams. This trick was implemented previously to shape both the local oscillator (LO) and the gate beam in [Jacquard 17], using a 512×512 resolution SLM screen. With the recent upgrade of the gate SLM to a 792×600 screen mentioned in subsection 2.2.4, we can expect such implementation to be less of a challenge. While still costy, this approach has the advantage not to require additional care for the gate SHG photons. Such double-subtractor setup allows then for two-photon success probabilities as high as current probabilities for single-photon events with one single-photon subtractor, with similar expected output state purity. Yet, it suffers from poor scalability.

Chapter 4

Certifying quantum non-Gaussianity using double homodyne detection

Contents

In this final chapter, we tackle the main topic of this PhD work, namely certification. We aim at certifying the quantum non-Gaussianity of single-photon subtracted squeezed vacuum states, both property and states which are described theoretically in chapter 1. In chapter 2, we described how to experimentally generate such non-Gaussian states using continous-variable optics. In chapter 3, we elaborated in particular on the single-photon subtraction operation, shedding more light on the experimentally generated states.

To certify the quantum non-Gaussianity of these states, an appropriate resource-efficient

detection scheme is required. In the first section 4.1, we describe the double homodyne detection, its properties and its experimental implementation. Owing to its ability to directly retrieve all information on the input state, the double homodyne detection allows for a reliable certification protocol, which was introduced by [Chabaud 20b, Chabaud 21c].

In section 4.2, we introduce and motivate certification in the context of quantum information. We argue in particular that current methods using homodyne detection are not suitable for state certification, making the choice of the double homodyne detection relevant. We then discuss the potential of the aforementioned certification protocol for state tomography and state certification. In particular for the latter, the protocol relies on the estimation of the fidelity of the experimental state to a chosen target state. In the subsequent section 4.3, we specify this fidelity estimation protocol to certify the stellar rank and Wigner negativity of single-photon subtracted squeezed vacuum states, a work we published in [Chabaud 21d]. Modeling the states and detection in realistic experimental conditions, we show simulation of certification results we expect. In particular, we extend the simulation performed in [Chabaud 21d] by accounting for detection losses. We also show one can enhance the certifiability of our states using an unbalanced double homodyne detection.

In the last section 4.4, we elaborate on the experimental challenges measuring with the double homodyne detection, and report on our most recent experimental results.

4.1 Double homodyne detection

In this section, we describe the working principle, properties and experimental setup of the double homodyne detection [Ferraro 05] (sometimes referred to as eight-port homodyne detection). Its principle scheme is given in figure 4.1.

As its name suggests, the double homodyne detection consists in measuring the input signal state using two homodyne detections. As shown in section 2.4, each homodyne detection outputs a difference current proportional to the signal quadrature $\hat{q}_{\mathrm{s}}^{\theta} = \cos(\theta)\hat{q}_{\mathrm{s}} + \sin(\theta)\hat{p}_{\mathrm{s}}$ at angle θ given by the optical relative phase between the signal beam and a local oscillator (LO) beam. The idea of double homodyne detection is to simultaneously measure one quadrature $\hat{q}_{\mathrm{s}}^{\theta}$ on one homodyne and the orthogonal quadrature $\hat{q}_{\mathrm{s}}^{\theta+\pi/2}$ on the second homodyne.

As pictured in figure 4.1, this is achieved by splitting the signal beam on a beamsplitter into two arms, both sent to one homodyne detection fed with a common LO beam. It is then enough to ensure that the relative phases between the signal and both LO are θ and $\theta + \pi/2$ at the homodynes. This is pictured with a $\pi/2$-phase-shifter prism in the scheme 4.1 where we took $\theta = 0$ for simplicity. Both orthogonal quadratures are then simultaneously sampled.

Note that simultaneously measuring two orthogonal quadratures can not be achieved with arbitrary precision, owing to the Heisenberg relations for non-commutative observables. In the given scheme 4.1, the precision on both signal quadratures is indeed limited to the vacuum noise, due to the vacuum injection into the signal at the first beamsplitter BS*.

As we show in the first subsection 4.1.1, this simultaneous sampling is equivalent to the direct sampling of the Q function of the signal state $\hat{\rho}_{\mathrm{s}}$, independently of the value of θ. As explained in section 1.2.5, the Q function contains all the information on the quantum state, similarly as the Wigner function. The Q function is positive everywhere in the phase space,

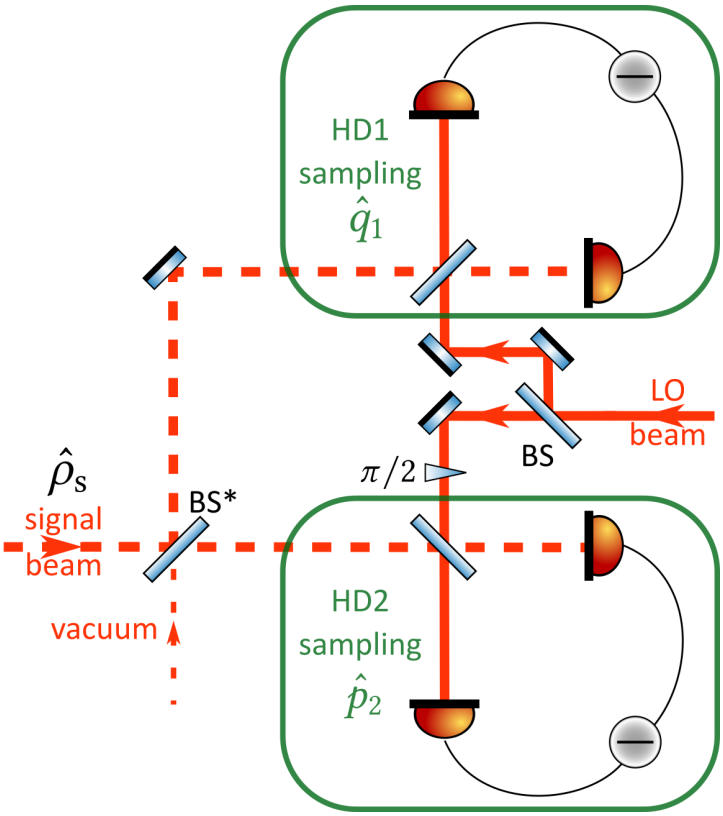

Fig. 4.1 Principle scheme of the double homodyne detection. The signal beam is first split into two beams, mixing the signal with the vacuum on beamsplitter BS* which may be unbalanced. The two beams are measured using homodyne detections (HDs), which are fed with two local oscillator (LO) beams with relative phase of $\pi/2$. The two homodyne detections HD1 and HD2 then sample orthogonal signal quadratures $\hat{q}_1$ and $\hat{p}_2$ from the signal state $\hat{\rho}_s$.

which is then consistent with the existence of a detection which directly samples the Q function, hence considered as a probability distribution. The double homodyne detection then allows for the direct retrieval of all information on the input state. A result we also show for multimode input states, using several double homodyne detections in parallel.

For comparison, the (single) homodyne detection only samples the quadrature $\hat{q}_s^\theta$ or equivalently a marginal of the Wigner function, which by itself (at a given θ) does not contain all information on the signal state. Still sampling the marginals for many different measurement settings, one for each value of θ, allows for the reconstruction of the Wigner function using maximum-likelihood algorithms [Lvovsky 04, Lvovsky 09][1]. For a two-mode state, for each mode 1 sampling at angle θ_1, the quadratures of mode 2 should be sampled for all angles θ_2. This means that for multimode states the number of required quadrature-sampling measurements grows exponentially with the number of modes.

While being experimentally slightly more complex to build, the double homodyne detection thus only requires one same measurement setting to retrieve all information on the signal state. This means that for multimode states the required number of measurement settings does not grow exponentially with the number of modes. Note that the total number of measurements may still grow exponentially, which is the case in the double homodyne tomography protocol developed in the later section 4.2. Interestingly, the certification protocol we use in this thesis can be generalized to the multimode case, for which the number of measurements only grows polynomially with the number of modes, see section 4.3.

The double homodyne detection features some striking properties which prove useful in a certification scenario. In the first subsection 4.1.1, we show that unbalancing the first beamsplitter (BS* in figure 4.1) is equivalent to applying a squeezing operation on the input state prior to a balanced measurement. In the subsequent subsection 4.1.2, we show that both single-mode displacements and mode basis changes prior measurement may be engineered by applying simple transformations on the measurement outcomes in post-processing.

While these properties can be extended to the multimode scenario, the current experimental implementation, described in subsection 4.1.3, is a single-mode double homodyne detection. In the last subsection 4.1.4, we discuss the challenges to build a spectrally multimode double homodyne detection.

4.1.1 A Q function sampler

In this subsection, we prove that the double homodyne detection directly samples the Q function of the input state. More precisely, we show that the POVM of this detection is the set of projectors on squeezed displaced states, following the demonstration given in the appendix of [Chabaud 17] which we extend later to the multimode scenario. In other words, we want to show that the double homodyne detection projects the single-mode input signal state $\hat{\rho}_s$ onto states of the form

$$\left|\psi_{\zeta,\alpha}\right\rangle = \hat{S}(\zeta)\hat{D}(\alpha)\left|0\right\rangle \tag{4.1}$$

where $\hat{S}(\zeta)$ is the squeezing operator (defined in subsection 1.3.3) with squeezing parameter $\zeta \in \mathbb{R}$, and $\hat{D}(\alpha)$ is the displacement operator (defined in subsection 1.3.2) with $\alpha \in \mathbb{C}$.

[1] An application example of such homodyne tomography is given in subsection 3.4.1.

POVM proof. To describe the detection scheme given in figure 4.1, the projectors must model the action of the (unbalanced) beamsplitter BS* on both the signal and the vacuum, along with the action of both homodyne detections at the output. The beamsplitter operation $\hat{U}_{\text{BS}}$ is generally speaking a spatial two-mode basis change. It describes the transformation from the signal and vacuum input modes $(\vec{\mathbf{f}}_{\text{s}}, \vec{\mathbf{f}}_{\text{vac}})$ to the output modes $(\vec{\mathbf{g}}_1, \vec{\mathbf{g}}_2)$ following equation (1.7). The corresponding unitary matrix $\mathbf{U}_{\text{BS}}$ writes[1]

$$\mathbf{U}_{\text{BS}} = \begin{pmatrix} t & -r \\ r & t \end{pmatrix} \tag{4.2}$$

where r^2 (resp. t^2) is the reflectivity (resp. transmissivity) of the beamsplitter.

As shown in section 2.4, the POVM of the homodyne detection is the set of projectors on the eigenstates of the quadrature operator. The measurement of both homodyne detections on the output modes $(\vec{\mathbf{g}}_1, \vec{\mathbf{g}}_2)$ with outcomes (q_1, p_2) is then the projection on the eigenstates $|q_1\rangle_1 \otimes |p_2\rangle_2$ satisfying

$$\hat{q}_1 |q_1\rangle_1 \otimes |p_2\rangle_2 = q_1 |q_1\rangle_1 \otimes |p_2\rangle_2 \tag{4.3}$$
$$\hat{p}_2 |q_1\rangle_1 \otimes |p_2\rangle_2 = p_2 |q_1\rangle_1 \otimes |p_2\rangle_2 \tag{4.4}$$

where $\hat{q}_1$ (resp. $\hat{p}_2$) is the amplitude (resp. phase) quadrature associated with mode $\vec{\mathbf{g}}_1$ (resp. $\vec{\mathbf{g}}_2$).

The measurement with outcome (q_1, p_2) can thus be described by the projection onto the single-mode state[2]

$$|\psi_{q_1,p_2}\rangle_{\text{s}} = \frac{1}{\mathcal{N}} \langle 0|_{\text{vac}} \hat{U}_{\text{BS}}^{\dagger} |q_1\rangle_1 \otimes |p_2\rangle_2 \tag{4.5}$$

where $\mathcal{N}$ is a normalization constant, and where we explicitly indicate the modes for each state with the corresponding subscripts, e.g. state $|\psi_{q_1,p_2}\rangle_{\text{s}}$ is in mode $\vec{\mathbf{f}}_{\text{s}}$.

The POVM elements $\{\hat{\Pi}_{\text{DHD}}(q_1, p_2)\}$ of the double homodyne detection are then of the form

$$\hat{\Pi}_{\text{DHD}}(q_1, p_2) = \frac{1}{c} |\psi_{q_1,p_2}\rangle\langle\psi_{q_1,p_2}|_{\text{s}} \tag{4.6}$$

with c a constant such that the POVM sums up to the identity operator (see the end of subsection 2.4.1 for the definition of POVMs).

Let us show that each state $|\psi_{q_1,p_2}\rangle_{\text{s}}$ is a squeezed displaced state of the form $|\psi_{\zeta,\alpha}\rangle_{\text{s}}$ given by equation (4.1).

We first write

$$|q_1\rangle_1 \otimes |p_2\rangle_2 = \frac{1}{4\pi\sigma_0^2} \int \mathrm{d}q_2 \exp\left(\frac{\mathrm{i}p_2 q_2}{2\sigma_0^2}\right) |q_1\rangle_1 \otimes |q_2\rangle_2 \tag{4.7}$$

[1] We choose a unusual sign convention for this unitary matrix so as to obtain more natural equations. Note that the inverse transformation $\hat{U}_{\text{BS}}^{\dagger}$ swaps the sign in front of r.

[2] The state $|q_1\rangle_1 \otimes |p_2\rangle_2$ is written in the mode basis $(\vec{\mathbf{g}}_1, \vec{\mathbf{g}}_2)$, so we want the action of the inverse beasmplitter operation on it, i.e. the action of $\hat{U}_{\text{BS}}^{\dagger}$ on the state $|q_1\rangle_1 \otimes |p_2\rangle_2$, which writes $\hat{U}_{\text{BS}}^{\dagger} |q_1\rangle_1 \otimes |p_2\rangle_2$.

which is the Fourier transformation of the ket $|p_2\rangle_2$, and can be shown using the completness identity (1.28).

The action of the beamsplitter $\hat{U}_{\text{BS}}$ on the quadrature operator column vector $(\hat{q}_1, \hat{q}_2, \hat{p}_1, \hat{p}_2)^\top$ is given by its symplectic matrix $\mathbf{O}_{\text{BS}}$, which is derived from equation (1.91) as

$$\mathbf{O}_{\text{BS}} = \begin{pmatrix} \mathbf{U}_{\text{BS}} & \mathbf{0} \\ \mathbf{0} & \mathbf{U}_{\text{BS}} \end{pmatrix} \tag{4.8}$$

with $\mathbf{U}_{\text{BS}}$ is the real matrix given in equation (4.2), and the action of the inverse transformation $\hat{U}_{\text{BS}}^\dagger$ is given by $\mathbf{O}_{\text{BS}}^\top$[1].

The state $\hat{U}_{\text{BS}}^\dagger |q_1\rangle_1 \otimes |q_2\rangle_2$ is an eigenstate of $\hat{q}_{\text{s}}$ (resp. $\hat{q}_{\text{vac}}$) with eigenvalue $tq_1 + rq_2$ (resp. $-rq_1 + tq_2$)[2]

$$\hat{U}_{\text{BS}}^\dagger |q_1\rangle_1 \otimes |q_2\rangle_2 = |tq_1 + rq_2\rangle_{\text{s}} \otimes |-rq_1 + tq_2\rangle_{\text{vac}} \tag{4.9}$$

Projecting equation (4.9) onto the vacuum $\langle 0|_{\text{vac}}$ yields

$$\langle 0|_{\text{vac}} \hat{U}_{\text{BS}}^\dagger |q_1\rangle_1 \otimes |q_2\rangle_2 = \frac{1}{(2\pi\sigma_0^2)^{1/4}} \exp\left(-\frac{1}{4\sigma_0^2}(-rq_1 + tq_2)^2\right) |tq_1 + rq_2\rangle_{\text{s}} \tag{4.10}$$

where we used

$$\langle q|0\rangle = \frac{1}{(2\pi\sigma_0^2)^{1/4}} \exp\left(-\frac{1}{4\sigma_0^2} q^2\right) \tag{4.11}$$

which can be shown by computing the p-marginal of the vacuum Wigner function given in equation (1.54).

Using both equations (4.7) and (4.10), the state $|\psi_{q_1,p_2}\rangle_{\text{s}}$ defined by (4.5) rewrites

$$|\psi_{q_1,p_2}\rangle_{\text{s}} = \frac{1}{\mathcal{N}} \int \mathrm{d}q_2 \exp\left(-\frac{1}{4\sigma_0^2}(-rq_1 + tq_2)^2\right) \exp\left(\mathrm{i}\frac{1}{2\sigma_0^2} p_2 q_2\right) |tq_1 + rq_2\rangle_{\text{s}} \tag{4.12}$$

where we absorbed the constant $2(2\pi\sigma_0^2)^{5/4}$ into $\mathcal{N}$.

We change variables in equation (4.12) with

$$\frac{t}{r} q = -rq_1 + tq_2 \tag{4.13}$$

which implies $tq_1 + rq_2 = q + q_1/t$ (from $r^2 + t^2 = 1$), and $\mathrm{i}p_2 q_2 = +\mathrm{i}\frac{r}{t} p_2 q_1 + \mathrm{i}\frac{p_2}{r} q$. We obtain

$$|\psi_{q_1,p_2}\rangle_{\text{s}} = \frac{\mathrm{e}^{\mathrm{i}\frac{r}{2t\sigma_0^2} p_2 q_1}}{\mathcal{N}} \int \mathrm{d}q \exp\left(-\frac{1}{4\sigma_0^2}\left(\frac{t}{r}\right)^2 q^2\right) \exp\left(\mathrm{i}\frac{p_2}{2r\sigma_0^2} q\right) |q + q_1/t\rangle_{\text{s}} \tag{4.14}$$

[1]Nota bene: The operator $\hat{U}_{\text{BS}}$ maps the operators $\vec{\hat{x}}_{1,2} = (\hat{q}_1, \hat{q}_2, \hat{p}_1, \hat{p}_2)^\top$ to the operators $\vec{\hat{x}}_{\text{s,vac}} = (\hat{q}_{\text{s}}, \hat{q}_{\text{vac}}, \hat{p}_{\text{s}}, \hat{p}_{\text{vac}})^\top$ through $\hat{U}_{\text{BS}}^\dagger \vec{\hat{x}}_{1,2} \hat{U}_{\text{BS}} = \mathbf{O}_{\text{BS}} \vec{\hat{x}}_{\text{s,vac}}$. This is consistent with the mode basis change from $(\vec{\mathbf{f}}_{\text{s}}, \vec{\mathbf{f}}_{\text{vac}})$ to $(\vec{\mathbf{g}}_1, \vec{\mathbf{g}}_2)$ in the Heisenberg picture, see appendix B.1 for details.

[2]For instance, we have $\hat{q}_{\text{s}}\big(\hat{U}_{\text{BS}}^\dagger |q_1\rangle_1 \otimes |q_2\rangle_2\big) = \hat{U}_{\text{BS}}^\dagger\big(\hat{U}_{\text{BS}} \hat{q}_{\text{s}} \hat{U}_{\text{BS}}^\dagger\big) |q_1\rangle_1 \otimes |q_2\rangle_2 = \hat{U}_{\text{BS}}^\dagger\big(t\hat{q}_1 + r\hat{q}_2\big) |q_1\rangle_1 \otimes |q_2\rangle_2 = (tq_1 + rq_2)\big(\hat{U}_{\text{BS}}^\dagger |q_1\rangle_1 \otimes |q_2\rangle_2\big)$, using the inverse beamsplitter transformation on $\hat{q}_{\text{s}}$ via $\mathbf{O}_{\text{BS}}^\top$.

In equation (4.14), let us exhibit a displacement operation. The displacement operator $\hat{D}(\alpha)$ writes with the quadrature operators $\hat{q}_s$ and $\hat{p}_s$ in the signal mode $\vec{\mathbf{f}}_s$

$$\hat{D}(\alpha) = \exp\left[\frac{1}{2\sigma_0^2}\left(\mathrm{i}p_\alpha\hat{q}_s - \mathrm{i}q_\alpha\hat{p}_s\right)\right] \tag{4.15}$$

$$\hat{D}(\alpha) = \exp\left(-\frac{1}{2\sigma_0^2}\mathrm{i}p_\alpha q_\alpha\right)\exp\left(\frac{1}{2\sigma_0^2}\mathrm{i}p_\alpha\hat{q}_s\right)\exp\left(-\frac{1}{2\sigma_0^2}\mathrm{i}q_\alpha\hat{p}_s\right) \tag{4.16}$$

$$\text{with}\quad \alpha = \frac{1}{2\sigma_0}(q_\alpha + \mathrm{i}p_\alpha)$$

where we used the Baker-Hausdorff formula [Leonhardt 95] for the second line.

We can use the eigenstate property to exhibit a displacement operation (with $q_\alpha = 0$) in equation (4.14)

$$\exp\left(\mathrm{i}\frac{p_2}{2r\sigma_0^2}q\right)|q + q_1/t\rangle_s = \exp\left(-\mathrm{i}\frac{p_2q_1}{2rt\sigma_0^2}\right)\exp\left(\mathrm{i}\frac{p_2}{2r\sigma_0^2}\hat{q}_s\right)|q + q_1/t\rangle_s \tag{4.17}$$

Using equation (1.84) and a similar reasoning on the eigenstates of $\hat{q}_s$ as for showing equation (4.9), we can find the action of a displacement operation (with $p_\alpha = 0$) on the state $|q\rangle_s$

$$|q + q_1/t\rangle_s = \exp\left(-\mathrm{i}\frac{q_1}{2t\sigma_0^2}\hat{p}_s\right)|q\rangle_s \tag{4.18}$$

Combining both equations (4.17) and (4.18), we recognize the displacement operation form equation (4.16), and deduce up to a constant phase factor

$$\exp\left(\mathrm{i}\frac{p_2}{2r\sigma_0^2}q\right)|q + q_1/t\rangle_s \propto \hat{D}(\alpha)|q\rangle_s \tag{4.19}$$

$$\text{with}\quad \alpha = \frac{1}{2\sigma_0}\left(\frac{q_1}{t} + \mathrm{i}\frac{p_2}{r}\right)$$

Since α is independent of the integration variable q, we can re-write equation (4.14) up to a multiplicative constant

$$|\psi_{q_1,p_2}\rangle_s \propto \hat{D}(\alpha)\int \mathrm{d}q\,\exp\left(-\frac{1}{4\sigma_0^2}\left(\frac{t}{r}\right)^2 q^2\right)|q\rangle_s \tag{4.20}$$

The right hand side integral can be intuitively viewed as a squeezed vacuum state, as it exhibits a Gaussian quadrature distribution with variance which depends on t and r. Let us show this using first the completness of the quadrature eigenstates (1.28) to write

$$\hat{S}(\zeta)|0\rangle_s = \int \mathrm{d}q\,\hat{S}(\zeta)|q\rangle_s\langle q|0\rangle_s \tag{4.21}$$

From the squeezing operator action (1.71) on the quadrature operator $\hat{q}_s$ and a reasoning on eigenstates, we find $\hat{S}(\zeta)|q\rangle_s = \left|\mathrm{e}^{-\zeta}q\right\rangle_s$. Combining this result with the expression (4.11) of $\langle q|0\rangle$, equation (4.21) writes

$$\hat{S}(\zeta)|0\rangle_s = \frac{1}{(2\pi\sigma_0^2)^{1/4}}\int \mathrm{d}q\,\exp\left(-\frac{1}{4\sigma_0^2}q^2\right)|\mathrm{e}^{-\zeta}q\rangle_s \tag{4.22}$$

Using the change of variables $e^{-\zeta}q \mapsto q$ in equation (4.22), we identify in equation (4.20) $e^{-2\zeta} = (t/r)^2$, and obtain

$$|\psi_{q_1,p_2}\rangle_s \propto \hat{D}(\alpha)\hat{S}(\zeta)\,|0\rangle_s \tag{4.23}$$

with $\alpha = \frac{1}{2\sigma_0}(q_1/t + ip_2/r)$ and $\zeta = \ln(r/t)$.

Inverting the displacement and squeezing operations in equation (4.23) would result in the wanted state form of equation (4.1). While these operators do not commute, they are linked by a simple formula [Nieto 97]

$$\begin{aligned} &\hat{D}(\alpha)\hat{S}(\zeta) = \hat{S}(\zeta)\hat{D}(\alpha') \\ &\text{with} \quad \alpha' = \alpha\cosh(\zeta) + \alpha^*\sinh(\zeta) \end{aligned} \tag{4.24}$$

Applying equation (4.24) to equation (4.23) concludes the proof, i.e. $|\psi_{q_1,p_2}\rangle_s$ is a squeezed coherent state $|\psi_{\zeta,\alpha'}\rangle_s$. In other words, we have shown that the double homodyne detection with measurement outcomes q and p from the two homodynes can be modeled with the POVM elements which write (renaming the variable α' by α for convenience purposes)

$$\hat{\Pi}_{\mathrm{DHD}_\zeta}(\alpha) = \frac{1}{\pi}\hat{S}(\zeta)\hat{D}(\alpha)\,|0\rangle\langle 0|\,\hat{D}(\alpha)^\dagger\hat{S}(\zeta)^\dagger \tag{4.25}$$

$$\text{where} \quad \alpha = \frac{1}{2\sigma_0}\left(\frac{q}{r} + i\frac{p}{t}\right) \tag{4.26}$$

$$\text{and} \quad \zeta = \ln(r/t) \tag{4.27}$$

Q function sampling. In particular, we deduce from this result (4.25) and equation (2.37) that the probability $P_{\mathrm{DHD}_\zeta}(\alpha)$ of measuring the signal state $\hat{\rho}_s$ with outcome α is given by

$$\begin{aligned} P_{\mathrm{DHD}_\zeta}(\alpha) &= \mathrm{Tr}\left[\hat{\rho}_s\hat{\Pi}_{\mathrm{DHD}_\zeta}(\alpha)\right] \\ P_{\mathrm{DHD}_\zeta}(\alpha) &= \frac{1}{\pi}\,\langle 0|\,\hat{D}(\alpha)^\dagger\hat{S}(\zeta)^\dagger\hat{\rho}_s\,\hat{S}(\zeta)\hat{D}(\alpha)\,|0\rangle \\ P_{\mathrm{DHD}_\zeta}(\alpha) &= Q_{\hat{S}(-\zeta)\hat{\rho}_s\hat{S}(-\zeta)^\dagger}(\alpha) \end{aligned} \tag{4.28}$$

where we recognize the Q function of the state $\hat{\rho}_s$ on which is applied the squeezing operation $\hat{S}(-\zeta) = \hat{S}(\zeta)^\dagger$, with ζ given in equations (4.27).

In practice, collecting the samples $\{q_i\}$ and $\{p_i\}$ from the two homodyne detections, the Q function of the state $\hat{S}(\ln(t/r))\hat{\rho}_s\hat{S}(\ln(t/r))^\dagger$ is obtained by building the histogram in the phase space from the complex samples $\{\alpha_i\}$, with $\alpha_i = (q_i/r + ip_i/t)/(2\sigma_0)$. These samples are referred to as *double homodyne samples*.

Note that with a balanced beamsplitter ($r = t$), the squeezing operation reduces to the identity, i.e. $\zeta = 0$. In other words, the balanced double homodyne detection is directly sampling the Q function of the input state. The unbalanced ($r \neq t$) double homodyne detection is formally equivalent to a squeezing operation followed by a balanced double homodyne detection.

The squeezing factor in decibels s_{dB} of the equivalent squeezing operation $\hat{S}(-\zeta)$ is

$$s_{\mathrm{dB}} = 10\log_{10}\left(\frac{t^2}{r^2}\right) \tag{4.29}$$

Around the balanced configuration at transmissivity $t^2 = 0.5$, s_{dB} is approximately linear around 0 dB, with an increase of 1.7 dB for an increase of 0.1 in t^2. When r or t tends to 1, the squeezing parameter $|\zeta|$ becomes infinite. In particular, if one can experimentally set any value of the beamsplitter transmissivity t^2, then any squeezing factor value may be reached. Taking the limit $r \to 1$ in equation (4.25), we deduce that the double homodyne detection POVM reduces to the POVM of a single homodyne detection, i.e. a set of projectors on infinitely squeezed states.

LO-signal relative phase. In the proof, we considered for simplicity that the quadratures $\hat{q}_1$ and $\hat{p}_2$ were measured instead of the more general quadratures $\hat{q}_1^{\theta}$ and $\hat{q}_2^{\theta+\pi/2}$, with θ the signal-LO relative phase. We can take into account this phase by applying a global phase-space rotation $\hat{R}(\theta) = \exp(-\mathrm{i}\theta\hat{n}_{\mathrm{s}})$ on the POVM elements of equation (4.25), with $\hat{n}_{\mathrm{s}}$ the number operator on the signal mode. Inserting $\hat{\mathbb{1}} = \hat{R}(\theta)\hat{R}(\theta)^{\dagger}$ between each operators allows us to apply the phase-space rotation to each operator in order to compute the action of $\hat{R}(\theta)$ on the POVM element $\hat{\Pi}_{\mathrm{DHD}_{\zeta}}(\alpha)$ (in the Heisenberg picture). The action of the phase-space rotation on the involved operators is

$$|0\rangle\langle 0| \mapsto |0\rangle\langle 0| \tag{4.30}$$

$$\hat{D}(\alpha) \mapsto \hat{D}(\alpha \mathrm{e}^{\mathrm{i}\theta}) \tag{4.31}$$

$$\hat{S}(\zeta) \mapsto \hat{S}(\zeta \mathrm{e}^{2\mathrm{i}\theta}) \tag{4.32}$$

where we used the fact that the vacuum is invariant under phase-space rotations, and we used appendix A.1. Since the POVM is the same set under $\alpha \mapsto \alpha \mathrm{e}^{\mathrm{i}\theta}$, equation (4.31) is transparent. In equation (4.32), we use the definition equation (1.77) of the squeezing operator for a complex parameter. Thus, the action of $\hat{R}(\theta)$ on the POVM element $\hat{\Pi}_{\mathrm{DHD}_{\zeta}}(\alpha)$ is simply mapping the squeezing parameter ζ to $\zeta \mathrm{e}^{2\mathrm{i}\theta}$.

In other words, the complete POVM of the double homodyne detection $\hat{\Pi}_{\mathrm{DHD}_{\zeta}}(\alpha)$ is given by equation (4.25), when considering $\zeta \in \mathbb{C}$ with modulus $|\zeta| = \ln(r/t)$ and with phase controlled by the LO-signal phase. As states are determined up to a global phase factor, the phase of the squeezing parameter is irrelevant in the single-mode scenario.

Multimode double homodyne detection. Let us now consider N parallel double homodyne detections each measuring one of the orthogonal modes $\{\vec{\mathbf{f}}_m\}$. In this case, taking into account the signal-LO phase of each double homodyne detection becomes relevant. The POVM of such N-mode double homodyne detection writes

$$\hat{\Pi}_{\mathrm{DHD}_{\vec{\zeta}}}(\vec{\alpha}) = \bigotimes_{m=1}^{N} \hat{\Pi}_{\mathrm{DHD}_{\zeta_m}}(\alpha_m) \tag{4.33}$$

where $\hat{\Pi}_{\mathrm{DHD}_{\zeta_m}}(\alpha_m)$ is given by equation (4.25) with $\zeta_m \in \mathbb{C}$ and $\alpha_m \in \mathbb{C}$.

Following the same steps as before and using the multimode definition (1.45) of the Q function, the probability $P_{\mathrm{DHD}_{\vec{\zeta}}}(\vec{\alpha})$ of measuring the signal multimode state $\hat{\rho}_{\mathrm{s}}$ with outcome $\vec{\alpha}$

is given by

$$P_{\mathrm{DHD}_{\vec{\zeta}}}(\vec{\alpha}) = \mathrm{Q}_{\hat{S}^{\otimes N}(-\vec{\zeta})\hat{\rho}_{\mathrm{s}}\,\hat{S}^{\otimes N}(-\vec{\zeta})^{\dagger}}(\vec{\alpha}) \tag{4.34}$$
$$\text{where} \quad \hat{S}^{\otimes N}(\vec{\zeta}) = \bigotimes_{m=1}^{N} \hat{S}(\zeta_m)$$

Using N parallel double homodyne detections allows one then to sample the Q function of any experimental N-mode quantum state $\hat{\rho}_{\mathrm{s}}$, upon which is optionally applied single-mode squeezing operations, in a single measurement setting. Each squeezing parameter ζ_m is experimentally controlled in absolute value by unbalancing the m-th double homodyne detection, and in phase by setting the LO-signal relative phase.

4.1.2 Post-processing single-mode displacements and mode-basis changes

In the previous subsection, we have shown in particular that the double homodyne detection is a Q function sampler, and that an equivalent squeezing operation prior Q function sampling can be implemented by experimentally controlling the beamsplitter (BS*) reflectivity. In this subsection, we show that if one has access to the Q function of a state, then one also has access to the Q function of this state on which is applied single-mode displacements or mode basis changes, upon applying simple transformations on the double homodyne samples in post-processing.

Single-mode displacements. The displacement operator $\hat{D}(\alpha)$ defined in equation (1.59) satisfy the simple product following formula

$$\hat{D}(\alpha)\hat{D}(\beta) = \mathrm{e}^{(\alpha\beta^{*}-\alpha^{*}\beta)/2}\hat{D}(\alpha+\beta) \tag{4.35}$$

which can be shown using the Baker-Campbell-Hausdorff formula.

Let us consider that we have access to the Q function of the state $\hat{\rho}$ using the double homodyne detection (considered single-mode). From the definition (1.45), the Q function of the displaced state $\hat{D}(\beta)\hat{\rho}\,\hat{D}(\beta)^{\dagger}$ is given by

$$\mathrm{Q}_{\hat{D}(\beta)\hat{\rho}\,\hat{D}(\beta)^{\dagger}}(\alpha) = \frac{1}{\pi}\langle\alpha|\hat{D}(\beta)\hat{\rho}\,\hat{D}(\beta)^{\dagger}|\alpha\rangle \tag{4.36}$$

From equation (4.35), the displaced coherent state $\hat{D}(\beta)^{\dagger}|\alpha\rangle = \hat{D}(-\beta)\hat{D}(\alpha)|0\rangle$ writes

$$\hat{D}(\beta)^{\dagger}|\alpha\rangle = \mathrm{e}^{(\beta^{*}\alpha-\beta\alpha^{*})/2}|\alpha-\beta\rangle \tag{4.37}$$

where the global phase factor is irrelevant, and is in particular exactly compensated by its dagger in equation (4.36).

We deduce that the Q function of a displaced state is given by the displaced Q function of the initial state, i.e.

$$\mathrm{Q}_{\hat{D}(\beta)\hat{\rho}\,\hat{D}(\beta)^{\dagger}}(\alpha) = \mathrm{Q}_{\hat{\rho}}(\alpha-\beta) \tag{4.38}$$

Once one sampled the Q function $\mathrm{Q}_{\hat{\rho}}(\alpha)$ using the double homodyne detection, one can easily translate the histogram by translating the samples after measurement, and obtain the Q function given in equation (4.38). In other words, applying the translation $\alpha \mapsto \alpha - \beta$ on the double homodyne samples in post-processing gives access to the Q function of the displaced state $\hat{D}(\beta)\hat{\rho}\,\hat{D}(\beta)^\dagger$, for any $\beta \in \mathbb{C}$.

Equation (4.38) can be generalized to the multimode scenario. We consider measuring the N-mode state $\hat{\rho}$ using N double homodyne detections. We are then sampling the multimode Q function $\mathrm{Q}_{\hat{\rho}}\left(\vec{\alpha}\right)$ with $\vec{\alpha} \in \mathbb{C}^N$. We consider the product of single-mode displacement operations $\hat{D}^{\otimes N}(\vec{\alpha})$ defined as

$$\hat{D}^{\otimes N}\left(\vec{\alpha}\right) = \bigotimes_{m=1}^{N} \hat{D}(\alpha_m) \tag{4.39}$$

where $\vec{\alpha} = (\alpha_1, \cdots, \alpha_N)^\top$.

Following the same steps, we straightforwardly obtain

$$\mathrm{Q}_{\hat{D}^{\otimes N}(\vec{\beta})\hat{\rho}\,\hat{D}^{\otimes N}(\vec{\beta})^\dagger}\left(\vec{\alpha}\right) = \mathrm{Q}_{\hat{\rho}}\left(\vec{\alpha} - \vec{\beta}\right) \tag{4.40}$$

since the multimode Q function is defined (1.45) as the projection of $\hat{\rho}$ on the separable coherent states $\left|\vec{\alpha}\right\rangle = |\alpha_1\rangle \otimes \cdots \otimes |\alpha_N\rangle$.

We conclude that sampling the Q function of a N-mode state $\hat{\rho}$ using N double homodyne detections gives access to the Q function of the state $\hat{D}^{\otimes N}(\vec{\beta})\hat{\rho}\,\hat{D}^{\otimes N}(\vec{\beta})^\dagger$ upon applying the translation $\vec{\alpha} \mapsto \vec{\alpha} - \vec{\beta}$ on the samples in post-processing.

Mode basis changes. We consider sampling the Q function of a multimode state $\hat{\rho}$ by measuring N modes simultaneously using N double homodyne detections. Denoting $\{\vec{\mathbf{f}}_m\}$ the mode basis in which is written the state $\hat{\rho}$, we want to compute the Q function of the same state in the mode basis $\{\vec{\mathbf{g}}_m\}$ defined by the change of mode basis (1.7). We note $\mathbf{U}$ the unitary matrix of the corresponding change of mode basis operator $\hat{U}$. The Q function in the new basis writes

$$\mathrm{Q}_{\hat{U}\hat{\rho}\hat{U}^\dagger}\left(\vec{\alpha}\right) = \frac{1}{\pi^N}\left\langle \vec{\alpha}\middle|\hat{U}\hat{\rho}\,\hat{U}^\dagger\middle|\vec{\alpha}\right\rangle_{\{\vec{\mathbf{g}}_m\}} \tag{4.41}$$

where we explicitly write in subscript the mode basis for the multimode coherent state, i.e. $\left|\vec{\alpha}\right\rangle_{\{\vec{\mathbf{g}}_m\}} = |\alpha_1\rangle_{\vec{\mathbf{g}}_1} \otimes \cdots \otimes |\alpha_N\rangle_{\vec{\mathbf{g}}_N}$.

A multimode coherent state is again a coherent state under a change of mode basis. Let us show in the following this property which then allows us to obtain a similar statement as before from equation (4.41).

We show that $\hat{U}^\dagger \left|\vec{\alpha}\right\rangle_{\{\vec{\mathbf{g}}_m\}}$ is an eigenstate of each annihilation operator $\hat{a}_i$ associated with the mode $\vec{\mathbf{f}}_i$, i.e. a coherent state in the mode basis $\{\vec{\mathbf{f}}_m\}$ with amplitudes we compute. We have

$$\hat{a}_i\left(\hat{U}^\dagger \left|\vec{\alpha}\right\rangle_{\{\vec{\mathbf{g}}_m\}}\right) = \hat{U}^\dagger\left(\hat{U}\hat{a}_i\hat{U}^\dagger\right)\left|\vec{\alpha}\right\rangle_{\{\vec{\mathbf{g}}_m\}} \tag{4.42}$$

$$= \hat{U}^\dagger\left(\sum_\ell \left(\mathbf{U}^{-1}_{i\ell}\right)^* \hat{b}_\ell\right)\left|\vec{\alpha}\right\rangle_{\{\vec{\mathbf{g}}_m\}} \tag{4.43}$$

$$= \left(\sum_\ell \mathbf{U}^\top_{i\ell}\alpha_\ell\right)\left(\hat{U}^\dagger \left|\vec{\alpha}\right\rangle_{\{\vec{\mathbf{g}}_m\}}\right) \tag{4.44}$$

where $\{\hat{b}_m\}$ are the annihilation operators associated with the modes $\{\vec{\mathbf{g}_m}\}$, in the second line we use the inverse action mode basis change on the operator $\hat{a}_i$ (cf. equation (1.15)), and in the last line we used the unitary relation $\mathbf{U}^{-1} = \mathbf{U}^{\top *}$. Since $\sum_\ell \mathbf{U}^\top_{i\ell}\alpha_\ell$ is the i-th component of the amplitude vector $\mathbf{U}^\top\vec{\alpha}$, we deduce

$$\hat{U}^\dagger \left|\vec{\alpha}\right\rangle_{\{\vec{\mathbf{g}}_m\}} = \left|\mathbf{U}^\top\vec{\alpha}\right\rangle_{\{\vec{\mathbf{f}}_m\}} \tag{4.45}$$

From equations (4.41) and (4.45) We then obtain

$$\mathrm{Q}_{\hat{U}\hat{\rho}\hat{U}^\dagger}\left(\vec{\alpha}\right) = \mathrm{Q}_{\hat{\rho}}\left(\mathbf{U}^\top\vec{\alpha}\right) \tag{4.46}$$

We conclude that sampling the Q function of a N-mode state $\hat{\rho}$ using N double homodyne detections gives access to the Q function of the state $\hat{U}\hat{\rho}\hat{U}^\dagger$ upon applying the unitary transformation $\vec{\alpha} \mapsto \mathbf{U}^\top\vec{\alpha}$ on the samples in post-processing.

Post-processing and unbalancing equivalent operations. Here we consider sampling the Q function of a N-mode state with N parallel double homodyne detections. From the previous results, unbalancing the double homodyne detections, setting the LO-signal relative phases (see subsection 4.1.1), and translating the output samples is equivalent to applying any single-mode Gaussian operation on the input state on any measured mode. A single-mode Gaussian operation can indeed be decomposed as the product of a displacement operation, a squeezing operation and a rotation operation (see subsection 1.3.4). One can also apply a mode basis change on top by applying it on the samples as in equation (4.46).

Putting these pieces together, controlling experimental parameters (prior measurement) and applying transformations on samples (in post-processing), one can equivalently apply on the input state any Gaussian operation of the following form

$$\hat{U}\left(\bigotimes_{i=1}^{N}\hat{G}_i\right) \tag{4.47}$$

where $\hat{U}$ is a N-mode basis change, and $\hat{G}_i$ are single-mode Gaussian operations.

Note that while a squeezing operation can be "swapped" with a displacement operation using equation (4.24), there is no general analogue relation for swapping it with a mode basis change[1]. For this reason, we cannot swap the two factors in equation (4.47) in general.

Note that the single-mode phase-space rotations may not only be controlled experimentally but also via post-processing. Indeed, the action of the phase-space rotation operation $\hat{R}(\theta)^\dagger$ on a coherent state $|\alpha\rangle$ yields the coherent state $|\alpha e^{-i\theta}\rangle$. We deduce, similarly as before, that the Q function of the state $\hat{R}(\theta)\hat{\rho}\,\hat{R}(\theta)^\dagger$ at α is the Q function of the state $\hat{\rho}$ at $\alpha e^{-i\theta}$. The transformation $\alpha \mapsto \alpha e^{-i\theta}$ should be performed on each mode prior applying $\hat{U}$ in equation (4.47). Such lessening of experimental parameter control requirements is always welcomed.

[1] In the particular case where the squeezing parameters all have the same phase and the mode basis change $\hat{U}$ is orthogonal, then it is possible to swap them.

4.1.3 Polarization based double homodyne detection setup

In this subsection, we focus on the experimental implementation of the double homodyne detection.

Implementing the fixed $\pi/2$ phase shift between the two homodyne detections in the scheme 4.1 may be a challenging task, as it would require us to lock the optical phase between the two LO beams. It would cost space on the table, and may introduce errors in the Q function sampling if the lock is not stable or efficient enough. Moreover, as we already implement a lock for the relative phase between the LO and the signal (see section 2.5), this would increase the complexity of the global locking system, which may lead to additional locking error or decreased stability.

It turns out that we can avoid such optical lock implementation by relying on the polarization degrees of freedom of the fields at play, as we show in the following. For this reason, we chose to replace the beamsplitters with waveplates and polarizing beamsplitters (PBS). The experimental setup is pictured in figure 4.2.

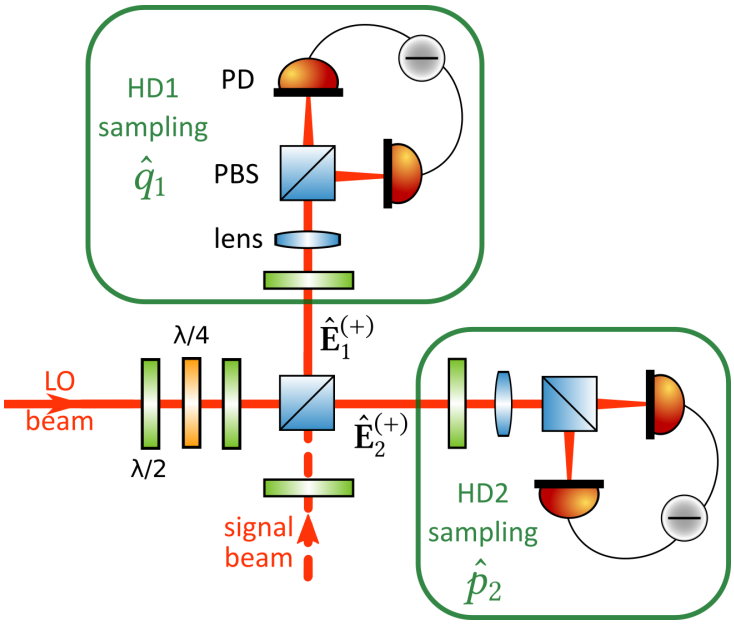

Fig. 4.2 Scheme of the experimental double homodyne detection setup. Corresponds to module **3.c)** of figure 2.1. Polarization-based scheme equivalent to the non-polarization-based scheme 4.1: the $\pi/2$ phase is implemented using a circularly polarized local oscillator (LO) beam and the unbalancing is implemented by turning the linear polarization of the signal beam. $\hat{\mathbf{E}}_1^{(+)}$ (resp. $\hat{\mathbf{E}}_2^{(+)}$) denotes the field in the arm 1(resp. 2) measured by the homodyne detection 1 (resp. 2). HD: homodyne detection. PBS: polarizing beamsplitter; $\lambda/2$: half-wave plate; $\lambda/4$: quarter-wave plate.

Schemes equivalence. In the scheme 4.2, the first PBS together with the waveplates that precedes it play the role of the beamsplitters "BS*" and "BS" in the scheme 4.1, and the role of the $\pi/2$ phase shifter. Each of the two spatial outputs of the PBS, referred to as *arms*,

encounter a half-wave plate and a second PBS which play the role of the even beamsplitter of the corresponding homodyne detection. Let us give more details, considering lossless optical elements.

The LO field $\hat{\mathbf{E}}^{(+)}_{\mathrm{LO}}$ is prepared before the first PBS as a circularly polarized field using the combination of a half-wave plate, quarter-wave plate and half-wave plate[1] as

$$\hat{\mathbf{E}}^{(+)}_{\mathrm{LO}} = \left(\hat{\mathbf{E}}^{(+)}_{\mathrm{LO,H}} + \mathrm{i}\hat{\mathbf{E}}^{(+)}_{\mathrm{LO,V}}\right)/\sqrt{2} \tag{4.48}$$

where the $\hat{\mathbf{E}}^{(+)}_{\mathrm{LO,H}}$ (resp. $\hat{\mathbf{E}}^{(+)}_{\mathrm{LO,V}}$) is the horizontally (resp. vertically) polarized component of the LO field, considering the PBS transmits/reflects in the horizontal/vertical polarization mode basis.

The initially linearly polarized signal field $\hat{\mathbf{E}}^{(+)}_{\mathrm{s}}$ is prepared in the following polarization before the second input of the first PBS using a half-wave plate

$$\hat{\mathbf{E}}^{(+)}_{\mathrm{s}} = t\hat{\mathbf{E}}^{(+)}_{\mathrm{s,H}} + r\hat{\mathbf{E}}^{(+)}_{\mathrm{s,V}} \tag{4.49}$$

Since the PBS action is a four-port unitary operation, we need to consider the orthogonally polarized vacuum field for both inputs. The only vacuum field which plays a role is the one in the spatial mode of the signal, which we denote $\hat{\mathbf{E}}^{(+)}_{\mathrm{vac}}$. It is in the orthogonal polarization[2] to the signal field before the PBS

$$\hat{\mathbf{E}}^{(+)}_{\mathrm{vac}} = -r\hat{\mathbf{E}}^{(+)}_{\mathrm{vac,H}} + t\hat{\mathbf{E}}^{(+)}_{\mathrm{vac,V}} \tag{4.50}$$

The PBS transmits horizontally polarized light, and reflects vertically polarized light. Denoting by $\hat{\mathbf{E}}^{(+)}_1$ and $\hat{\mathbf{E}}^{(+)}_2$ the output fields in each of the output spatial modes (or arms) that lead to the respective homodyne detections, we can write

$$\hat{\mathbf{E}}^{(+)}_1 = \frac{\mathrm{i}}{\sqrt{2}}\hat{\mathbf{E}}^{(+)}_{\mathrm{LO,V}} + t\hat{\mathbf{E}}^{(+)}_{\mathrm{s,H}} - r\hat{\mathbf{E}}^{(+)}_{\mathrm{vac,H}} \tag{4.51}$$

$$\hat{\mathbf{E}}^{(+)}_2 = \frac{1}{\sqrt{2}}\hat{\mathbf{E}}^{(+)}_{\mathrm{LO,H}} + r\hat{\mathbf{E}}^{(+)}_{\mathrm{s,V}} + t\hat{\mathbf{E}}^{(+)}_{\mathrm{vac,V}} \tag{4.52}$$

In each of the arms 1 and 2, the two orthogonal polarization modes H and V can be thought as independent channels. For the LO beam, the PBS effectively splits in half its power, with a $\pi/2$ phase shift between the two arms. Independently, the PBS acts exactly as the beamsplitter transformation given by the matrix $\mathbf{U}_{\mathrm{BS}}$ in equation (4.2), on the signal and vacuum input fields.

Finally, for the arm 1 (resp. arm 2), the corresponding second PBS acts as an even beamsplitter for both the horizontal and vertical polarization modes of the field $\hat{\mathbf{E}}^{(+)}_1$ (resp. $\hat{\mathbf{E}}^{(+)}_2$), when the half-wave plate turns their polarization by 45° before entering the PBS. Note that the second spatial input of this PBS plays no role, as it leads at the output to vacuum fields which are orthogonally polarized to the non-vacuum fields.

This concludes the equivalence between the schemes 4.1 and 4.2. The main advantage of the chosen scheme is the fact that the $\pi/2$ relative phase between the arms is implemented via

[1] This combination allows one to transform any polarization to any other polarization.

[2] This orthogonal polarization is unique up to a global phase factor.

waveplates. Since the waveplates are mechanically fixed, this parameter is then very stable over time and do not require regular alignment in practice.

Another advantage is the ability to change the coefficient r and t by simply turning the half-wave plate on the signal path before the first PBS. In particular, we can then switch efficiently from a single homodyne setup ($r = 1$ or $t = 1$) to a double homodyne setup. Also, since any value of r and t can be easily chosen, any equivalent squeezing operation prior measurement may be engineered (see subsection 4.1.1).

Optical phase lock and arms phase noise. In chapter 2, we mostly considered the double homodyne detection as a single homodyne detection. In particular, we described the optical phase lock in this configuration in section 2.5. In practice, we can lock the phase between the LO and the signal fields for both homodynes by applying the lock on only one homodyne detection, without any additional locking error.

This result stems from yet another advantage of using the scheme 4.2. For each arm after the first PBS, both the LO and the signal fields are together in the same spatial mode. In particular, any phase noise in each arm is then equally experienced for both LO and signal beams. In other words, the angle θ of the measured quadrature $\hat{q}^\theta$ at the homodyne detection is independent of the phase noise after the first PBS. In particular, the $\pi/2$ relative phase between the two homodyne detections is preserved under such noise.

The signal-LO phase lock relies on the interference between the LO and signal fields when the latter is replaced by a bright field (the seed field). Since the LO-seed interference depends also directly on θ, it is also independent on the phase noise after the first PBS on both homodyne detection. Thus, locking the relative signal-LO phase on only one homodyne detection using a piezoelectric mirror on the common LO beam prior the first PBS allows us to lock both homodyne detection on the quadratures $\hat{q}_1^\theta$ and $\hat{q}_2^{\theta+\pi/2}$.

A modal projective measurement. The double homodyne detection naturally inherits the modal projective measurement property of the homodyne detection shown in section 2.4. The mode in which the Q function of the signal is measured is then given by the mode of the LO field. The spectral LO mode is engineered using the LO pulse shaper, module **3.b)** in figure 2.1. Note that the current scheme can only measure one time-frequency mode at a time. To probe a multimode Q function, it requires to change the setup, see next subsection 4.1.4.

Double homodyne detection losses. In section 2.4, we assessed the losses of the detection in the whole experiment 2.1, considering a single homodyne detection. In practice, the losses were effectively estimated with the double homodyne detection scheme 4.2 in the single homodyne detection configuration.

Since we used the same high quality optical elements and detectors on both arms of the double homodyne detection, we obtain similar losses for both configurations $r = 1$ or $t = 1$. The losses for the whole double homodyne detection are then the same as for one arm. The double homodyne detection features the same optical, overlap, photodiode and electronic efficiencies as the ones defined and estimated in details in subsection 2.4.3. We deduce the

double homodyne detection efficiency η_{DHD}

$$\eta_{\mathrm{DHD}} = \eta_{\mathrm{HD}} \tag{4.53}$$

where η_{HD} is given in equation (2.66). From the estimation (2.67), we deduce $\eta_{\mathrm{DHD}} \simeq 81\%$.

As we will show using simulations in section 4.3, the detection losses are detrimental to the success of certification. For this reason, we take particular care in choosing very high quality optical elements prior building the double homodyne detection.

The optical losses to take into account in the scheme 4.2, which are part of the losses in $1 - \eta_{\mathrm{DHD}}$, are the ones induced by the optics on the signal path. The signal field encounters two half-wave plates and two PBSs:

- For the PBSs, we chose the 780 nm Laser Line Polarizing Cube Beamsplitter #47-048 from Edmund Optics. They feature a very broadband high transmission (higher than 99%) with very low transmission of the wrong polarization, see figure C.8 in appendix C.3.1. Such low-loss PBS are hard to find in the current optics market. It is common to find 10%-loss PBS, which would be prohibitive. We experimentally checked that the chosen PBS features less than 1% losses.

- We chose the CVI Laser Optics QWPO-800-05-2-R10 half-wave plates. With 0.2% losses per surface and two surfaces, they are among the best commercially available half-wave plates in terms of losses. As zero-order waveplates, their retardance is not as flat as achromatic waveplates. In appendix C.3.2, we compare with the Edmund Optics 700-1000 nm $\lambda/2$ Achromatic Waveplate #46-561. We expect the retardance lack of flatness to have a negligible effect, allowing us to avoid the heavy 2.4% loss cost of the achromatic waveplates.

- Finally, the choice of the waveplates mounts is also of particular relevance as a poor control on the rotation of the waveplates may lead to losses. Indeed, to ensure that the homodyne detections work properly, the LO mean-field contribution to the difference of currents should vanish. Since the LO power is orders of magnitude higher than the quantum noise level we aim at measuring, a precise control over the beamsplitter transmission is required. Since the second PBS of each arm and the corresponding half-wave plate play the role of the homodyne detection beamsplitter, we use a high precision Thorlabs mount PRM1/M. Such precision mount proved useful for setting the $\pi/2$ relative phase between the two arms, using it with the quarter-wave plate on the LO path. In appendix C.3.3, a simple estimation allows us to dismiss the need for such precision on the reflectivity r experienced by the signal field at the first PBS.

Note that as losses are less relevant for the LO beam, we use an achromatic quarter-wave plate for its very broadband retardance. This allows for minimizing the spectral deformation of the LO mode, along with the LO-signal overlap induced losses (see section 2.4).

Note also that we use lenses before the second PBS in each arm to focus the light onto the photodiodes, see scheme 4.2. Due to the high sensitivity of the homodyne detections, we observed that a tight focus is required to increase the stability over time.

4.1.4 Towards spectrally multimode double homodyne detection

The current double homodyne detection setup is limited to single-mode measurements. While we may measure any mode of a given multimode input state[1], we can not yet measure two modes simultaneously. This means in particular that we can not sample the Q function of a multimode state, nor certify the non-Gaussianity of a multimode state. Even more, going multimode may open the path to entanglement certification, another valuable resource for quantum information.

In practice, as we are dealing with spectrally multimode fields, we can extend the scheme 4.2 by replacing the two homodyne detections with multipixel homodyne detections. The latter consists in using gratings to open the spectrum of the output fields of the beamsplitter where the LO and signal fields interfere. N_{frex} portions of the spectrum, called *frexels*, are focused to an array of N_{frex} photodiodes using an array of micro-lenses. Collecting the N_{frex} difference of currents results in the simultaneous homodyne detection of the N_{frex} frexel modes of the signal. See [Michel 21] for a detailed description.

Building such multipixel double homodyne detection would allow us then to measure the Q function of the multimode signal state in the frexel mode basis. Applying a change of mode basis on the data would then allow us to get access to its Q function in any other mode basis, from the results in subsection 4.1.2.

Although we expect the number of samples which are required for a decent precision to increase with the number of modes N_{frex}, a N_{frex}-pixel double homodyne detection is sampling with a N_{frex}-fold increase in speed. We saw that the scaling of the sample number with respect to the number of modes is not expected to be exponential. In section 4.3, we show a polynomial scaling for the certification protocol we will use.

A drawback of such implementation is the inability to unbalance the beamsplitter BS* for each frexel mode individually and independently. The setup only allows for a global unbalancing for all frexel modes. Improving this setup to permit such individual control seems challenging as it would require somehow a wavelength-dependent beamsplitter, or a wavelength-dependent half-wave plate when using a PBS. As we will see, we use the unbalancing in the protocol to revert the squeezing of the experimentally generated squeezed vacuum states. In the frexel mode basis, we expect the output of the SPOPO to be highly entangled (see section 2.3), which implies low or no squeezing in each frexel mode (see subsection 1.3.6). For this reason, such challenging extension do not seem to be a priority.

Building an efficient multipixel homodyne detection has been a long term project in the team since [Cai 15]. Several challenges impede its development. The first prototype has a low efficiency, with a photodiode efficiency of 80% and a low clearance between 10 dB and 5 dB [Michel 21]. Several attempts to build a more efficient version encountered challenges in the electronic implementation of the detector [Dufour 18, Michel 21], in particular managing the crosstalks at high frequency ($> 10 - 100$ MHz).

Out-sourcing the electronic conceptualization and fabrication to specialized private companies is one of our best path to obtain efficient multipixel homodyne detections. A promising design is currently under development.

[1] As for now, we didn't try to measure another mode than the first supermode. Measuring another mode would first require to make the optical lock work with other than a Gaussian LO mode, see section 2.5

4.2 Certification via double homodyne detection

In the previous section, we have seen in particular that double homodyne detection gives access to the Q function of the input state. However in practice, we can not retrieve the exact Q function, as we are sampling with a finite number of points, from which arises naturally statistical errors. This rises the following questions. Can we guarantee that the state represented by the sampled Q function is the actual measured state? If not, how close is it? Can we ascertain the quantum non-Gaussian nature of the measured state from its sampled Q function with limited number of samples? If so, can we provide the probability that the statement is true?

These questions lie in the more general topic of certification. We first briefly introduce certification in the context of quantum information and provide insights on its relevance in the field in the first subsection 4.2.1.

In the subsequent subsection 4.2.2, we argue the non-suitability of homodyne detection for state certification with current available methods. On the other hand, we show that double homodyne detection allows for a reliable state certification.

4.2.1 Certification concept and motivation

Let me first quote an expert colleague on the topic: "Quantum certification denotes the methods seeking to verify the correct functioning of a quantum machine", Ulysse Chabaud, from [Chabaud 20a].

This is in essence the main topic we tackle in this thesis work. Let us first take a step back to better comprehend certification in the blooming context of quantum information. *Delegated quantum computing* refers to relying on an hybrid quantum network where classical computers (clients) are sending requests to centralized quantum computers. Viewed as the most likely emerging platform, delegated quantum computing requires a way for the clients to be ensured of the correct functioning of the quantum computers and that the network is secure. In particular, the former is a priori not trivial, since the clients can not directly check the received results using their classical computer at hand. By definition, a quantum computer may perform tasks which are not simulable using a classical computer.

In this context, *verification* is needed. A verification task aims at ensuring the proper behavior of the quantum machine, or that the quantum computation aborts securely in case of an adversarial attack, without trusting the quantum computer node.

For instance, a recent startup (VeriQloud) launched on the idea of sending many requests whose answers are already known, together with few actual queries [Fitzsimons 17]. Based on the randomness of this request distribution, this verification protocol manages to ensure security over the network relying on the matching rate of the received results with the known answers.

In the context of verifying the correct functioning of an experiment in a lab or of an industrial quantum device, we refer to *certification*. In this sense, certification may be viewed as both an essential development towards delegate quantum computing and a method to guarantee the quantum advantage of a given quantum device. Given the rapid development of quantum technologies recently, increasing demands for a reliable certification for quantum

advantage arise, along with concomitant efforts in this field see e.g. the review [Eisert 20]. In the following, we focus on certification[1].

4.2.2 State tomography and expectation-value estimation protocol

Given an experimental source of quantum states, the purpose of *state certification* protocols is then to check whether its output state is close to a given target state or far from it[2]. To implement such certification, quantum state tomography [D'Ariano 03] is a relevant candidate method. It aims at reconstructing a good approximation of the output state of a quantum device by performing the measurement of many copies of said output state. A natural question which arises is: can we perform a sufficiently reliable state tomography so as to certify a given quantum machine?

The most used continuous variable state tomography method relies on using the homodyne detection. Such *homodyne tomography* is typically based on maximum-likelihood algorithm which we briefly presented in page 132. In a nutshell, homodyne detection samples the distribution of the signal quadrature $\hat{q}_{\mathrm{s}}^{\theta}$ at angle θ. Repeating many measurement for many angles θ yields a set of sampled quadrature distributions, which allows for the reconstruction of the Wigner function of the maximum-likely state.

Homodyne tomography is not reliable in the sense of [Christandl 12], because errors coming from the reconstruction procedure itself are indistinguishable from errors coming from the data. In other words, error bars are hard to extract from maximum-likelihood tomography [Blume-Kohout 10, Faist 16, Silva 17]. Without reliable error bars, one can not claim a legitimate Wigner negativity of the experimental state from the reconstruction of the tomography. Consequently, current methods using homodyne detection do not allow for state certification, as one cannot reliably provide a precision or a confidence degree on the certification claim.

The double homodyne detection was shown to be a promising tomographic tool in [Paris 96]. [Chabaud 20b] recently extended these results, and shown *double homodyne tomography* with reliable error bars is achievable, allowing for state certification. This state tomography is based on the *double homodyne expectation-value estimation protocol*, which was later improved in [Chabaud 21c]. Let us give some insights on this protocol for single-mode states here, before specifying it for our goals in the next section 4.3.

Double homodyne expectation-value estimation protocol. The idea of the protocol is to estimate the expectation value $\mathrm{Tr}(\hat{\rho}\hat{A})$ of the state $\hat{\rho}$ with any operator $\hat{A}$ with a bounded support over the Fock basis[3]. Since the double homodyne detection allows for sampling the Q function, we naturally want to compute $\mathrm{Tr}(\hat{\rho}\hat{A})$ using equation (1.48), which we reproduce

[1] For verification protocols using double homodyne detection based on the same principles described later in this section, we refer to [Chabaud 20b, Chabaud 20a]

[2] In this context, the question whether we assume that the states are independently and identically distributed (i.i.d.) arises. While we will restrict to this assumption, we refer to [Chabaud 20b, Chabaud 20a] for a version of the certification protocol presented in this section without the i.i.d. assumption (requiring much larger number of state copies).

[3] This means that its decomposition on the Fock basis $\hat{A} = \sum_{k,k'} \mathbf{A}_{kk'} |k\rangle\langle k'|$ only contains a finite number of non-zero terms.

here in the single-mode version

$$\mathrm{Tr}\left(\hat{\rho}\hat{A}\right) = \pi \int_{\mathbb{R}^2} \mathrm{P}_{\hat{A}}(\alpha)\mathrm{Q}_{\hat{\rho}}(\alpha)\,\mathrm{d}^2\alpha \tag{4.54}$$

where $\mathrm{P}_{\hat{A}}(\alpha)$ is the P function of the operator $\hat{A}$.

As explained in subsection 1.2.4, the P function is often an ill-behaved mathematical object, which makes the direct computation of $\mathrm{Tr}(\hat{\rho}\hat{A})$ in equation (4.54) impractical. To circumvent this issue, [Chabaud 20b, Chabaud 21c] introduced a set of parametrized functions which approximate $\mathrm{P}_{\hat{A}}(\alpha)$ efficiently enough to provide a certification statement.

Let us define here these functions. If one wonders how one could guess such ansatz, some inspiration can be retrieved from the Wigner function of Fock states, see equation (1.114). Let us introduce the polynomials

$$\mathcal{L}_{k,k'}(\alpha) = \sum_{\ell=0}^{\min(k,k')} \frac{\sqrt{k!}\sqrt{k'!}(-1)^\ell}{\ell!(k-\ell)!(k'-\ell)!}\alpha^{k'-\ell}\alpha^{*k-\ell} \tag{4.55}$$

for $\alpha \in \mathbb{C}$, which are the 2D Laguerre polynomials up to a normalization factor. For all $k, k' \in \mathbb{N}$, we define with these polynomials the functions

$$f^{(\gamma)}_{k,k'}(\alpha) = \frac{1}{\gamma^{1+\frac{k+k'}{2}}} e^{\left(1-\frac{1}{\gamma}\right)\alpha\alpha^*}\mathcal{L}_{k',k}\left(\frac{\alpha}{\sqrt{\gamma}}\right) \tag{4.56}$$

where γ is a parameter satisfying $0 < \gamma < 1$.

The functions $f^{(\gamma)}_{k,k'}(\alpha)$ are meant to approximate $\mathrm{P}_{|k\rangle\langle k'|}(\alpha)$. To approximate $\mathrm{P}_{\hat{A}}(\alpha)$, we use instead $f^{(\gamma)}_{\hat{A}}(\alpha)$ defined as

$$f^{(\gamma)}_{\hat{A}}(\alpha) = \sum_{k,k'} \mathbf{A}_{kk'}\, f^{(\gamma)}_{k,k'}(\alpha) \tag{4.57}$$

where $\mathbf{A}_{kk'}$ are the matrix coefficients of the operator $\hat{A}$ in the Fock basis, with $\hat{A} = \sum_{k,k'} \mathbf{A}_{kk'}\,|k\rangle\langle k'|$ where only a finite number of terms are non-zero.

[Chabaud 21c] improved these functions by defining

$$g^{(m,\gamma)}_{k,k'}(\alpha) = \sum_{j=0}^{m-1} (-1)^j f^{(\gamma)}_{k+j,k'+j}(\alpha)\,\gamma^j \sqrt{\binom{k+j}{k}\binom{k'+j}{k'}} \tag{4.58}$$

$$g^{(m,\gamma)}_{\hat{A}}(\alpha) = \sum_{k,k'} \mathbf{A}_{kk'}\, g^{(m,\gamma)}_{k,k'}(\alpha) \tag{4.59}$$

where m is a non-zero natural integer parameter. Note that at $m = 1$, $g^{(1,\gamma)}_{k,k'}(\alpha) = f^{(\gamma)}_{k,k'}(\alpha)$. Compared with the $f^{(\gamma)}_{k,k'}(\alpha)$ functions, the $g^{(m,\gamma)}_{k,k'}(\alpha)$ ones are more efficient at estimating $\mathrm{Tr}(\hat{\rho}\hat{A})$.

Let us consider that we obtained the double homodyne samples $\alpha_1, \cdots, \alpha_M$. From section 4.1, these samples follow the probability distribution $\mathrm{Q}_{\hat{\rho}}(\alpha)$. The expression (4.54) of $\mathrm{Tr}(\hat{\rho}\hat{A})$ can then be seen as the expectation value of the P function $\mathrm{P}_{\hat{A}}(\alpha)$ for the probability distribution

$Q_{\hat{\rho}}(\alpha)$, when $P_{\hat{A}}(\alpha)$ is a well-defined function. The mean value of $P_{\hat{A}}(\alpha)$ over the detection samples $\{\alpha_i\}$ then tends to $\mathrm{Tr}(\hat{\rho}\hat{A})$ when the number of samples M tends to ∞, which writes

$$\frac{\pi}{M}\sum_{i=1}^{M} P_{\hat{A}}(\alpha_i) \xrightarrow[M\to\infty]{} \mathrm{Tr}\left(\hat{\rho}\hat{A}\right) \tag{4.60}$$

When the P function is ill-behaved, we then recourse to the approximations $\{g_{\hat{A}}^{(m,\gamma)}(\alpha)\}$. We then define the *expectation-value estimator* $E_{\hat{A}}^{(m,\gamma)}$, meant to estimate $\mathrm{Tr}(\hat{\rho}\hat{A})$, as

$$E_{\hat{A}}^{(m,\gamma)}(\alpha_1,\dots,\alpha_M) = \frac{1}{M}\sum_{i=1}^{M} g_{\hat{A}}^{(m,\gamma)}(\alpha_i) \tag{4.61}$$

Without getting into the details, [Chabaud 21c] showed that the expectation-value estimator in equation (4.61) can be chosen as close to $\mathrm{Tr}(\hat{\rho}\hat{A})$ as one asks with sufficiently high number of samples M which depends on the choice of parameters γ and m. More precisely, one can ask for any precision $\epsilon > 0$ together with any certification degree of confidence $1-\delta$ with $\delta > 0$. This means asking for

$$\left|E_{\hat{A}}^{(m,\gamma)}(\alpha_1,\dots,\alpha_M) - \mathrm{Tr}\left(\hat{\rho}\hat{A}\right)\right| \leq \epsilon \tag{4.62}$$

with a probability greater than $1-\delta$. They proved that such statement is achievable with a number of samples M which scales as

$$M = \mathcal{O}\left(\frac{1}{\epsilon^{2+t}}\log\left(\frac{1}{\delta}\right)\right) \tag{4.63}$$

where $t > 0$ is a free parameter which depends on the choice of γ and m. Note that this scaling is at most polynomial in (ϵ, δ). We don't give here the explicit rates of convergence with respect to the parameters γ and m and the choice of the operator $\hat{A}$, and refer to [Chabaud 21c] for details. In the next subsection, we explicit them for the protocol we use in this work.

Double homodyne tomography. Continuous variable quantum state tomography methods usually assume that the measured state has a bounded support over the Fock basis [Lvovsky 09]. Under this assumption and noting B this bound, we can then simply apply the result (4.62) with $\hat{A} = |k\rangle\langle k'|$ for all k, k' smaller than B and with the samples $\{\alpha_i\}$. This yields the estimates of each density matrix non-zero element, along with their precisions and degrees of confidence. Contrary to homodyne tomography, no additional reconstruction procedure is required, and the samples are acquired with a single measurement setting, and the number of required measurement settings does not grow exponentially with the number of the input state modes (as argued in section 4.1, page 142). In other words, this protocol provides a reliable quantum state tomography using the double homodyne detection with the advantage of providing analytical error bars together with a confidence degree.

However, requiring the state to have a bounded support on the Fock basis, quantum state tomography may be inappropriate for state certification in continuous variables. Indeed, truncating the Fock decomposition of the Gaussian coherent state $|\alpha\rangle$ with $\alpha \neq 0$ for instance yields

the non-Gaussian state $\propto \sum_{n=0}^{B} \alpha^n / \sqrt{n!}\,|n\rangle$ for any truncating integer $B \neq 0$. How to quantify in general the error made by the truncation? This may be hard to estimate, and is an essential question in the context of certification.

Moreover, while the number of measurement settings does not grow exponentially with the number of modes of the input state, the number of measurements does scale exponentially using the expectation-value protocol for double homodyne tomography. We will see in the following that considering certification from another perspective allows us to circumvent both the bounded support assumption and exponential scaling caveats.

4.2.3 State certification via fidelity estimation

As argued before, quantum state tomography may not be suitable for state certification. If the goal of the certification task is to guarantee the quantum advantage of a given state, we may better rephrase the problem and answer it with another tool. Instead of trying to reconstruct completely the state, we may want to guarantee that the experimental state is close to a *target state*. This target state can be arbitrarily chosen. In particular, choosing a target state which has a bounded support on the Fock basis allows us to remove this assumption on the experimental state. Note that the closeness of the experimental state with the target state depends then on the choice of the target state, while the certification precision may be arbitrarily high independently of this choice.

We need a tool to estimate the closeness of the experimental state to the target state. We can apply the double homodyne expectation-value protocol given in subsection 4.2.2 with operator $\hat{A} = \hat{\rho}_{\text{target}}$, where $\hat{\rho}_{\text{target}}$ is the density operator of the target state. The protocol yields then an estimation of $\text{Tr}(\hat{\rho}\hat{\rho}_{\text{target}})$. However, this quantity is not a good measure of the closeness of $\hat{\rho}$ to $\hat{\rho}_{\text{target}}$, since when $\hat{\rho} = \hat{\rho}_{\text{target}}$, $\text{Tr}(\hat{\rho}\hat{\rho}_{\text{target}}) = \text{Tr}(\hat{\rho}^2)$ which is smaller than 1 for a mixed state.

A more suitable quantity is the fidelity $F(\hat{\rho}, \hat{\rho}_{\text{target}})$ of the state $\hat{\rho}$ to the target state $\hat{\rho}_{\text{target}}$ defined in equation (1.134). In subsection 1.4.3, we showed that the fidelity $F(\hat{\rho}, \hat{\rho}_{\text{target}})$ reduces to $\text{Tr}(\hat{\rho}\hat{\rho}_{\text{target}})$ when $\hat{\rho}_{\text{target}}$ is pure.

We can then apply the expectation-value protocol with $\hat{A} = |\psi\rangle\langle\psi|$ to estimate $F(\hat{\rho}, |\psi\rangle)$, with a precision ϵ and a confidence degree $1 - \delta$. This more specific protocol, referred to as *double homodyne fidelity estimation protocol*, provides then a reliable method for state certification by assessing the closeness of the states via a fidelity estimation, without any assumption on the input state[1].

Choice of the target state. Since the fidelity estimation protocol relies on approximating the P function of the target state $|\psi\rangle$, we expect the simpler the target state the easier the approximation of its P function. In other words, the efficiency of the certification in terms of the number of required samples depends on the complexity of the target state $|\psi\rangle$. Note that due to the usually singular nature of the P function (cf. subsection 1.2.4), one can expect this criterion to be critical for the feasibility of the protocol.

[1]Except the independently and identically distributed assumption, which can be removed at the cost of additional samples, unpractical for current implementations.

Choosing the target state should then result from a trade-off between the closeness to the experimental state $\hat{\rho}$ and the simplicity of the target state. A good a priori knowledge of the state $\hat{\rho}$ helps for making this choice. Note that this is not strictly speaking necessary, as in practice one can try multiple target states on the same data to improve the results. This however is quickly limited resource-wise by the infinite dimension of the state space.

We can use the properties of the double homodyne detection shown in section 4.1 at our advantage in the search for a suitable target state. Upon unbalancing and post-processing, we can equivalently sample the Q function of $\hat{G}\hat{\rho}\,\hat{G}^\dagger$ instead of the one of $\hat{\rho}$, with $\hat{G}$ a Gaussian operation given by equation (4.47). Noting $|\psi\rangle$ the target state we initially have in mind for $\hat{\rho}$, we now consider applying the protocol with the Q function $\mathrm{Q}_{\hat{G}\hat{\rho}\,\hat{G}^\dagger}$ with a new target state $|\psi'\rangle$ equal to $\hat{G}\,|\psi\rangle\langle\psi|\,\hat{G}^\dagger$. Interestingly, the estimated fidelity $F(\hat{G}\hat{\rho}\,\hat{G}^\dagger, |\psi'\rangle)$ re-writes

$$\mathrm{Tr}\left(\hat{G}\hat{\rho}\,\hat{G}^\dagger\,|\psi'\rangle\langle\psi'|\right) = \mathrm{Tr}\left(\hat{\rho}\,\hat{G}^\dagger\,|\psi'\rangle\langle\psi'|\,\hat{G}\right) = F(\hat{\rho}, |\psi\rangle) \tag{4.64}$$

Equation (4.64) means that certifying the closeness of state $\hat{G}\hat{\rho}\,\hat{G}^\dagger$ with $\hat{G}\,|\psi\rangle\langle\psi|\,\hat{G}^\dagger$ yields the same certification statement for the closeness of state $\hat{\rho}$ with $|\psi\rangle$, as one could expect. We deduce that instead of looking for a target state $|\psi\rangle$ close to the state $\hat{\rho}$, we can look for a target state $|\psi'\rangle$ close to the state $\hat{G}\hat{\rho}\,\hat{G}^\dagger$. In particular, if we know that the initial target state $|\psi\rangle$ is built from Gaussian operations applied on a simple state, i.e. $|\psi\rangle\langle\psi| = \hat{G}^\dagger\,|\psi'\rangle\langle\psi'|\,\hat{G}$, we may use this trick to choose instead this simple state $|\psi'\rangle$ as target state, providing the Gaussian operations $\hat{G}$ are of the form given by equation (4.47).

4.3 Quantum non-Gaussianity certification and fidelity estimation protocol

In this section, we simplify the double homodyne fidelity protocol by specifying it for our goal. First, we want to certify the quantum non-Gaussian nature of the experimental state, instead of trying to certify the state is as close as possible to a target state. This allows for simplifying the target state as we show in the first subsection 4.3.1. In particular, we explain the reasons for which we choose the Fock state $|1\rangle$ as target state.

This choice brings us naturally to specify and optimize the fidelity estimation protocol to the case of target Fock states in subsection 4.3.2. In the next subsection 4.3.3, we show that this protocol allows for the efficient quantum non-Gaussianity certification of simulated single-photon subtracted squeezed vacuum states. The protocol optimization together with the simulation are part of the main results of our paper [Chabaud 21d].

In the remaining of the section, we extend the simulation by accounting for detection losses, and show we can enhance the certifiability of our states using an unbalanced double homodyne detection. We also provide some perspectives as extension of the simulation.

4.3.1 Quantum non-Gaussianity certification and choice of target state

Instead of choosing a target state $|\psi\rangle$ as close as possible to the state $\hat{\rho}$, one may choose a simpler target state close enough to certify a specific property on the experimental state, for instance the necessary resources for reaching quantum computational advantage.

A first step towards certifying a quantum advantage is to certify the quantum non-Gaussianity of the output states. As we discussed in section 1.4, Wigner negativity is a necessary resource for quantum advantage. In particular, if a proclaimed quantum computer does not generate Wigner negative states, then it can be simulated classically, provided all claimed quantum advantage resources are in the generated states (not at the measurement stage[1]).

In subsection 1.4.2, we showed that if the state $\hat{\rho}$ satisfies

$$\omega_{\hat{\rho}}(\alpha, L) > 0.5 \tag{4.65}$$

then its Wigner function $W_{\hat{\rho}}$ is negative at α, for any $L \in \mathbb{N}^*$ and any $\alpha \in \mathbb{C}$, where the witnesses $\omega_{\hat{\rho}}(\alpha, L)$ are defined in equation (1.122) which we reproduce here

$$\omega_{\hat{\rho}}(\alpha, L) = \sum_{k=0}^{L-1} \langle 2k+1|\hat{D}^\dagger(\alpha)\hat{\rho}\hat{D}(\alpha)|2k+1\rangle \tag{4.66}$$

The witnesses $\omega_{\hat{\rho}}(\alpha, L)$ in equation (4.66) may be viewed as $\mathrm{Tr}(\hat{A}\,\hat{D}^\dagger(\alpha)\hat{\rho}\hat{D}(\alpha))$ with

$$\hat{A} = \sum_{k=0}^{L-1} |2k+1\rangle\langle 2k+1| \tag{4.67}$$

which has a bounded support on the Fock basis.

From subsection 4.1.2, sampling the Q function of the state $\hat{\rho}$ with the double homodyne detection is equivalent to sampling the displaced state $\hat{D}^\dagger(\alpha)\hat{\rho}\hat{D}(\alpha)$ upon applying a translation on the data in post-processing. We may thus apply the expectation-value protocol described in subsection 4.2.2 with the operator $\hat{A}$ given by equation (4.67).

Let us consider the case $L = 1$. From equation (4.66), the witnesses $\omega_{\hat{\rho}}(\alpha, 1)$ may be viewed as the fidelities

$$\omega_{\hat{\rho}}(\alpha, 1) = F\left(\hat{D}^\dagger(\alpha)\hat{\rho}\hat{D}(\alpha), |1\rangle\right) \tag{4.68}$$

for $\alpha \in \mathbb{C}$.

Using the same trick as before, we can then sample states $\hat{D}^\dagger(\alpha)\hat{\rho}\hat{D}(\alpha)$ upon data translation, and apply the fidelity estimation protocol with target state $|1\rangle$. Taking into account the precision in the protocol, we can then certify the negativity of the Wigner function of the probed state $\hat{\rho}$ at α up to a given degree of confidence, upon beating the threshold $\omega_{\hat{\rho}}(\alpha, 1) > 0.5$.[2]

On the other hand, the stellar rank is another feature of interest, which classifies the quantum non-Gaussian states. We recall from section 1.4 that the stellar rank of a single-mode pure state corresponds to the minimal number of photon additions/subtractions necessary to engineer the state from the vacuum, together with Gaussian unitary operations. Furthermore, we

[1] Else, one would need to proceed to another type of certification than state certification, which goes beyond the scope of this thesis.

[2] One could apply the same idea, noticing $\omega_{\hat{\rho}}(\alpha, L) = \sum_{k=0}^{L-1} F\left(\hat{D}^\dagger(\alpha)\hat{\rho}\hat{D}(\alpha), |2k+1\rangle\right)$. One could then try and certify Wigner negativity with the witness $\omega_{\hat{\rho}}(\alpha, L)$ with $L > 1$ using the fidelity estimation protocol several times to estimates the fidelities $F\left(\hat{D}^\dagger(\alpha)\hat{\rho}\hat{D}(\alpha), |2k+1\rangle\right)$ separately with precision ϵ each and deduce a statement on the witness $\omega_{\hat{\rho}}(\alpha, L)$ with worsen precision $L\epsilon$.

saw in 1.4.3.7 that the stellar rank is a necessary resource for achieving quantum advantage [Chabaud 23], hence the interest to certify stellar rank in this context.

In subsection 1.4.3, we showed that given a pure target state $|\psi\rangle$, if the experimental (mixed) state $\hat{\rho}$ satisfies

$$F(\hat{\rho}, |\psi\rangle) > 1 - \left[R_k^\star(|\psi\rangle)\right]^2 \tag{4.69}$$

where $R_k^\star(|\psi\rangle)$ is the k-robustness of the state $|\psi\rangle$, then it has a stellar rank greater or equal to k. We also showed that the robustness profile $\{R_k^\star(|\psi\rangle)\}$, or equivalently the fidelity thresholds $\{1 - \left[R_k^\star(|\psi\rangle)\right]^2\}$, can be computed using an explicit optimization method.

Similarly as above, we can then apply the fidelity estimation protocol to obtain the fidelity $F(\hat{\rho}, |\psi\rangle)$ of the experimental state $\hat{\rho}$ to the target state $|\psi\rangle$. Upon beating the k-th fidelity threshold $F(\hat{\rho}, |\psi\rangle) > 1 - \left[R_k^\star(|\psi\rangle)\right]^2$, this allows us to certify that the state $\hat{\rho}$ has stellar rank k or higher, taking into account the precision and degree of confidence of the protocol.

To summarize, the Wigner negativity and stellar rank witnesses both rely on the fidelity to target pure states. As such, they are then suitable tools for certifying their related properties using the double homodyne fidelity estimation protocol.

Choice of the target state for our experiment. As argued before, the required number of samples to perform the certification strongly depends on the complexity of the target state. It is then critical to choose the target state wisely.

The states we generate in the lab are squeezed single-photon subtracted states. A natural pure target state to choose is then a pure squeezed single-photon subtracted state $|\psi_\zeta^-\rangle$. From section 1.4, this state is also a squeezed Fock state 1, i.e. $|\psi_\zeta^-\rangle \propto \hat{S}(\zeta)|1\rangle$ with ζ a squeezing parameter.

As we explained in subsection 4.2.3, any Gaussian operation of the form $\hat{G}^\dagger$ in the expression of the target state may be reverted upon unbalancing and post-processing, provided $\hat{G}$ is of the form of equation (4.47). We can then apply this property on the target state $\hat{S}(\zeta)|1\rangle$, reverting the squeezing operation $\hat{S}(\zeta)$ by unbalancing the double homodyne detection, while allowing for the same certification claim. Relying on this trick, we then choose the target state $|1\rangle$. Since the P function of the Fock state $|1\rangle$ is much simpler than the one of $\hat{S}(\zeta)|1\rangle$, the fidelity estimation protocol is expected to feature a higher efficiency.

4.3.2 Fidelity estimation protocol for target Fock states

For the aforementioned reasons, we optimized the fidelity estimation protocol in our paper [Chabaud 21d] for Fock states $|n\rangle$ as target states. We give in the following the main results, and refer to the appendix A.2 of the paper for details[1].

[1]For better clarity, we changed the notations with respect to the paper. The correspondence, from the notations used here to the notations used in the paper are $M \mapsto N$, $m \mapsto p$, $\gamma \mapsto \eta$, $p_n^{(m,\gamma)} \mapsto p_n$, $\epsilon' \mapsto \lambda$, $\delta \mapsto P_{n,\mathrm{CLT}}^{\mathrm{IID}}$, $f_{k,l}^{(\gamma)}(\alpha) \mapsto f_{k,l}(\alpha,\eta)$, $g_{k,l}^{(m,\gamma)}(\alpha) \mapsto g_{k,l}^{(p)}(\alpha,\eta)$, $h_n^{(m,\gamma)}(\alpha) \mapsto h_n^{(p)}(\alpha,\eta)$, $E_n^{(m,\gamma)} \mapsto F_n$

Double homodyne fidelity estimation protocol applied to target Fock states. From the expectation-value protocol, see subsection 4.2.2, the appropriate estimator for the target state $|n\rangle$ (i.e. $\hat{A} = |n\rangle\langle n|$) writes

$$E^{(m,\gamma)}_{|n\rangle\langle n|}(\alpha_1, \dots, \alpha_M) = \frac{1}{M}\sum_{i=1}^{M} g^{(m,\gamma)}_{n,n}(\alpha_i) \tag{4.70}$$

where $\{\alpha_i\}$ are the double homodyne samples, $m \geq 1$ and $0 < \gamma < 1$ are parameters, and the functions $g^{(m,\gamma)}_{n,n}(\alpha)$ is defined in equation (4.58)[1].

Note that for Fock states, their P function is singular: $\mathrm{P}_{|n\rangle\langle n|}(\alpha)$ is the sum of even derivatives of the Dirac delta function, see subsection 1.2.4, equation (1.43) applied to $\hat{\rho} = |n\rangle\langle n|$.

While we didn't elaborate this detail in subsection 4.2.2, the fact that the functions $g^{(m,\gamma)}_{n,n}(\alpha)$ are approximations of the P function $\mathrm{P}_{|n\rangle\langle n|}(\alpha)$ comes naturally with an *approximation error*, and can be seen as the non-zero bias of the estimator given in equation (4.70). A biased estimator does not converge to the true value of the quantity it estimates. In our case, considering the number of samples M following the Q function distribution goes to infinity, the limit of the estimator, written $E^{(m,\gamma)}_{|n\rangle\langle n|}(\alpha_\infty)$, satisfies

$$\left| E^{(m,\gamma)}_{|n\rangle\langle n|}(\alpha_\infty) - F(\hat{\rho}, |n\rangle) \right| \leq E^{(m,\gamma)}_{|n\rangle\langle n|,\mathrm{bias}} \tag{4.72}$$

$$\text{with} \quad E^{(m,\gamma)}_{|n\rangle\langle n|,\mathrm{bias}} = \gamma^{p^{(m,\gamma)}_n} \binom{p^{(m,\gamma)}_n - 1}{m-1} \binom{n + p^{(m,\gamma)}_n}{n} \tag{4.73}$$

where $p^{(m,\gamma)}_n$ is the integer defined as

$$p^{(m,\gamma)}_n = \min_{\ell \in \mathbb{N}^*} \left\{ \ell \geq m, \text{ such that } \left(1 - \frac{m-1}{\ell}\right)\left(1 - \frac{n}{n+\ell+1}\right) \geq \gamma \right\} \tag{4.74}$$

Note that the integer $p^{(m,\gamma)}_n$ and the bias $E^{(m,\gamma)}_{|n\rangle\langle n|,\mathrm{bias}}$ are fully determined by the parameters n, m, and γ.

In particular for this Fock state estimator, we observed that for m odd,

$$E^{(m,\gamma)}_{|n\rangle\langle n|}(\alpha_\infty) \geq F(\hat{\rho}, |n\rangle) \tag{4.75}$$

i.e., $g^{(m,\gamma)}_{n,n}(\alpha)$ overestimates $F(\hat{\rho}, |n\rangle)$, while for m even,

$$E^{(m,\gamma)}_{|n\rangle\langle n|}(\alpha_\infty) \leq F(\hat{\rho}, |n\rangle) \tag{4.76}$$

[1]For pragmatic purposes, we write here the explicit simplified form of the $\{g^{(m,\gamma)}_{n,n}(\alpha)\}$ functions

$$\gamma^{n+1} g^{(m,\gamma)}_{n,n}(\alpha) = (-1)^n \mathrm{e}^{-(1-\gamma)\frac{|\alpha|^2}{\gamma}} \sum_{j=0}^{m-1} \binom{n+j}{n} \mathrm{L}_{n+j}\left(\frac{|\alpha|^2}{\gamma}\right) \tag{4.71}$$

$$\text{with} \quad \mathrm{L}_n(x) = \sum_{i=0}^{n} \binom{n}{i} \frac{(-1)^i x^i}{i!}, \quad \text{for} \quad x \in \mathbb{R}$$

i.e., $g_{n,n}^{(m,\gamma)}(\alpha)$ underestimates $F(\hat{\rho}, |n\rangle)$.

This observation allowed us to reduce the bias of the estimator by introducing the approximation functions $h_n^{(m,\gamma)}(\alpha)$ defined as

$$h_n^{(m,\gamma)}(\alpha) = g_{n,n}^{(m,\gamma)}(\alpha) + \frac{1}{2}(-1)^m \gamma^{p_n^{(m,\gamma)}} \binom{p_n^{(m,\gamma)} - 1}{m-1} \binom{n + p_n^{(m,\gamma)}}{n} \tag{4.77}$$

Note that the functions $h_n^{(m,\gamma)}(\alpha)$ and $g_{n,n}^{(m,\gamma)}(\alpha)$ differ only by the constant $\frac{1}{2}(-1)^m E_{|n\rangle\langle n|,\text{bias}}^{(m,\gamma)}$. The associated fidelity estimator $E_n^{(m,\gamma)}$ is consistently defined as the mean of the estimates $h_n^{(m,\gamma)}(\alpha)$ as

$$E_n^{(m,\gamma)}(\alpha_1, \dots, \alpha_M) = \frac{1}{M} \sum_{i=1}^{M} h_n^{(m,\gamma)}(\alpha_i) \tag{4.78}$$

and statisfies [Chabaud 21d]

$$\left| E_n^{(m,\gamma)}(\alpha_\infty) - F(\hat{\rho}, |n\rangle) \right| \leq E_{n,\text{bias}}^{(m,\gamma)} \tag{4.79}$$

$$\text{with} \quad E_{n,\text{bias}}^{(m,\gamma)} = \frac{1}{2} \gamma^{p_n^{(m,\gamma)}} \binom{p_n^{(m,\gamma)} - 1}{m-1} \binom{n + p_n^{(m,\gamma)}}{n} \tag{4.80}$$

$r_{m,n}$ is defined in equation (4.74). This remark and redefinition saves us a factor of $1/2$ on the estimation bias, since $E_{n,\text{bias}}^{(m,\gamma)} = \frac{1}{2} E_{|n\rangle\langle n|,\text{bias}}^{(m,\gamma)}$.

We now give the fidelity estimation statement using the estimator defined in equation (4.78), taking into account its bias, resulting from optimizing the parameters for its particular shape. Given the samples $\alpha_1, \dots, \alpha_M$ from the double homodyne detection, for arbitrary precision $\epsilon > 0$,

$$\left| E_n^{(m,\gamma)}(\alpha_1, \dots, \alpha_M) - F(\hat{\rho}, |n\rangle) \right| \leq \epsilon \tag{4.81}$$

with probability higher than $1 - \delta$, where

$$1 - \delta = \text{erf}\left(\epsilon' \sqrt{\frac{M}{2\sigma^2}} \right) \tag{4.82}$$

$$\epsilon' = \max\left\{ \epsilon - E_{n,\text{bias}}^{(m,\gamma)}, 0 \right\} \tag{4.83}$$

$E_{n,\text{bias}}^{(m,\gamma)}$ is defined in equation (4.80), σ is the standard deviation of the sampled estimations $h_n^{(m,\gamma)}(\alpha_i)$, and erf is the error function defined as

$$\text{erf}(x) = \frac{2}{\sqrt{\pi}} \int_0^x \mathrm{e}^{-y^2} \, \mathrm{d}y \tag{4.84}$$

Equation (4.82) derives the confidence degree $1-\delta$ from the application of the central limit theorem on the distribution of the $\{h_n^{(m,\gamma)}(\alpha_i)\}$[1]. The central limit theorem ensures that the

[1]We also derived analytical bounds independent of the state to probe using the Hoeffding inequality [Hoeffding 63], cf. [Chabaud 21d] for details.

distribution of the means converges towards a Gaussian distribution, provided the variance of the distribution is finite, which is the case for physical states.

For a Gaussian distribution of mean $\bar{x}_{\mathrm{G}}$ and deviation σ_{G}, the probability to draw within the interval $[\bar{x}_{\mathrm{G}} - d; \bar{x}_{\mathrm{G}} + d]$ is equal to

$$\mathrm{erf}\left(\frac{d}{\sqrt{2}\sigma_{\mathrm{G}}}\right) \tag{4.85}$$

We can apply equation (4.85) to the Gaussian distribution of the means provided by the central limit theorem, with mean $\bar{x}_{\mathrm{G}} = E_n^{(m,\gamma)}(\alpha_1, \ldots, \alpha_M)$ and standard deviation $\sigma_{\mathrm{G}} = \sigma/\sqrt{M}$. We recover then equation (4.82), where the width $d = \epsilon'$ of the interval is given by equation (4.83). Note that ϵ' takes into account the estimator bias (4.79), and allows us to give the statement in any case (when $\epsilon' = 0$, the confidence degree is then 0[1]).

To apply the protocol, one fixes the precision ϵ, the target state number n and the number of samples M. Then, the failure probability δ depends on the remaining free parameters m and γ. The procedure for optimizing the efficiency of the protocol consists then in minimizing δ over the choice of m, γ: for increasing values of the integer m, starting from $m = 1$, the minimum failure probability δ is computed by optimizing over the value of γ; then, we pick the value of m which minimizes δ. This conclude the optimization of the fidelity estimation protocol.

Note that this optimization can not be easily simplified, as it results from a trade off between the statistical error and the approximation error (coming from the estimator bias). Decreasing the systematic error at fixed number of samples may indeed induce an increase of the statistical error. This can be understood as it implies using better P-function approximations $\{h_n^{(m,\gamma)}(\alpha_i)\}$, making their distribution further ill-behaved.

The number of samples required for a precision ϵ and confidence $1 - \delta$ scales as

$$M = \mathcal{O}\left(\frac{1}{\epsilon^{2+\frac{2n}{m}}} \log\left(\frac{1}{\delta}\right)\right) \tag{4.86}$$

where the constant pre-factor (which may be large) depends on the choice of the free parameters m and γ. One can immediately see that the scaling is better when $m \geq 2$, an enhancement due to the introduction of the functions $\{g_{n,n}^{(m,\gamma)}(\alpha)\}$ (the previous functions $\{f_{n,n}^{(\gamma)}(\alpha)\}$ correspond to the new function for $m = 1$).

Application of the fidelity estimation protocol to quantum non-Gaussianity certification. Let us consider now the target state we use for our experiment, i.e. the Fock state $|1\rangle$. From equations (4.66) and (4.69), the fidelity $F(\hat{\rho}, |1\rangle)$ is a witness for both Wigner negativity at the origin and stellar rank 1 or higher for the state $\hat{\rho}$. The associated fidelity thresholds are respectively 0.478 (see subsection 1.4.3) and 0.5.

Let us assume we perform the fidelity estimation protocol on the experimental state $\hat{\rho}$ with target state $|1\rangle$, asking for a precision ϵ. Stating $\left|E_1^{(m,\gamma)}(\alpha_1, \ldots, \alpha_M) - F(\hat{\rho}, |1\rangle)\right| \leq \epsilon$ is

[1]Note that from equation (4.83), it is always possible to obtain ϵ' not equal to zero with the free parameters γ and m, with potential heavy cost in samples.

true with probability higher than $1-\delta$ is equivalent to provide the *interval of confidence* $[E_1^{(m,\gamma)}(\alpha_1,\dots,\alpha_M)-\epsilon; E_1^{(m,\gamma)}(\alpha_1,\dots,\alpha_M)+\epsilon]$ with confidence $1-\delta$ for the estimation of $F(\hat{\rho},|1\rangle)$. The latter means that the true fidelity $F(\hat{\rho},|1\rangle)$ lies within the interval of confidence with the associated confidence degree. Provided the lower bound of the interval of confidence is higher than one of the two mentioned fidelity thresholds, we then have certified that the state $\hat{\rho}$ has the corresponding property (Wigner negativity at the origin or stellar rank 1 or higher) with $1-\frac{\delta}{2}$ confidence[1].

In figure 4.3, we illustrate and summarize the protocol, drawing the resulting interval of confidence on the right. To illustrate the central limit theorem, the histogram of the Gaussian distribution of the means is given, whereas it is not computed in practice. On the plot, we also draw a red line at 0.5, the fidelity threshold for the Wigner negativity witness at the origin. Graphically, when the whole interval of confidence is above the threshold, the property is certified with the confidence $1-\frac{\delta}{2}$.

In subsection 4.3.3, we will apply this protocol to certify the stellar rank and Wigner negativity of states close to the experimentally generated ones, using simulated Q-function samples.

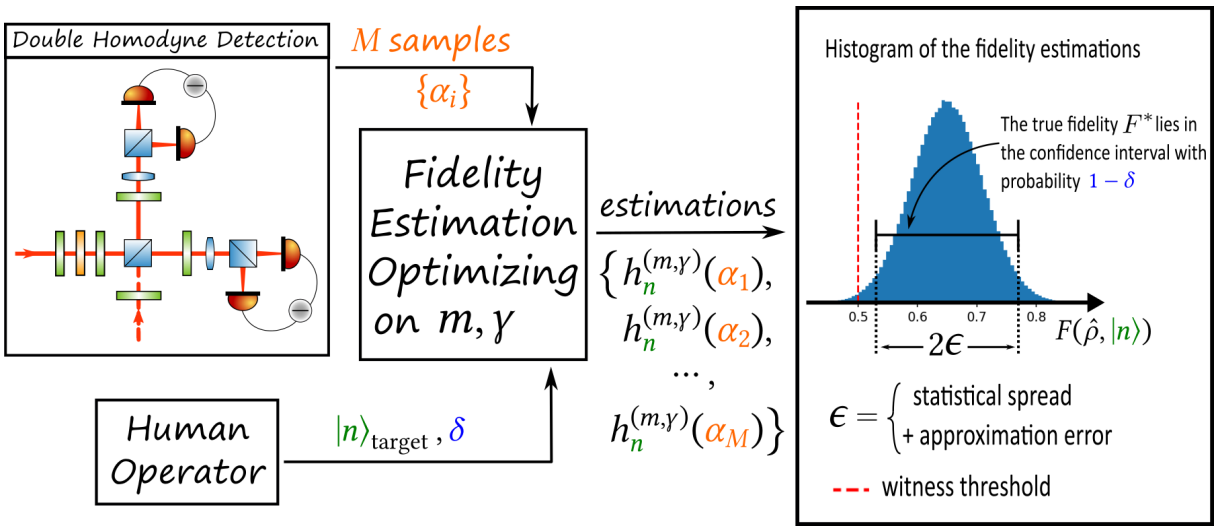

Fig. 4.3 Certification protocol using fidelity estimations and the double homodyne detection. The input parameters the M samples, the Fock number n, and the confidence interval δ are colored for clarity purposes.

Note on using homodyne detection for certification. We argued before that homodyne detection is not suitable for certification, because of intractable errors in the tomography reconstruction procedure of the Wigner function. To complete this discussion, let us consider other methods than tomography using homodyne detection to infer Wigner negativity.

[1]The factor $1/2$ applied on the failure probability δ comes from the fact that the true fidelity is above the top bound of the interval with probability $\delta/2$. The probability that the true fidelity is above the threshold is then given by $(1-\delta)+\frac{\delta}{2}=1-\frac{\delta}{2}$.

Machine learning methods have successfully been applied to benchmark the Wigner negativity of highly multimode states [Cimini 20], but these methods are most fruitful when good training data are available. In other words, a machine learning algorithm can only recognize the features of a state when it has seen many similar states before. Also, it is unclear how to extract error bars, preventing from yielding certification statements on the claimed Wigner negativity.

Another method was proposed in [Mari 11], and estimates the Fourier transform of the Wigner function[1] on arbitrary points in the phase space. Relying on Bolchner's theorems [Bochner 33], they can certify the Wigner negativity of a state $\hat{\rho}$ using the sampled distributions of at least two orthogonal quadrature operators. The main difference between their method and the protocols we presented is that their algorithm doesn't ensure the ability to find a witness which can certify the Wigner negativity, given a state with a negative Wigner function. This is because their algorithm relies on points in the phase space which should be chosen arbitrarily, without an algorithm to determine which ones to pick to find negativity. Therefore, to provide such a guarantee with their method, it would be necessary to run the algorithm on the entire phase space.

On the other hand, the double homodyne fidelity estimation protocol provides such guarantee using the Wigner negativity witness $\omega_{\hat{\rho}}(\alpha, M)$ given in equation (4.66). Indeed, for any state $\hat{\rho}$ described by a negative Wigner function, at least one of them witnesses the Wigner negativity of $\hat{\rho}$. Picking α where one expects to see negativity allows one to efficiently pick the correct witness. [Chabaud 21a] elaborates this idea and provides witnesses optimized to the target states, and compatible with our protocols. That being said, it is unclear which method is the most efficient for certifying Wigner negativity, in particular in the multimode scenario for which the authors didn't provide insight on the scaling of their method.

All in all, the double homodyne protocols are promising in the generality they provide, allowing for state certification in particular.

Certification of multimode states. As we saw in section 4.1, the double homodyne detection is a promising tool to directly sample the Q function of N-mode states. For this purpose, N parallel double homodyne detections are required.

Applying the above fidelity estimation protocol on each double homodyne detection would then yield N fidelity estimates. As we optimized the efficiency of the protocol for target Fock states, a natural choice for the N-mode target state $|\psi\rangle_{\text{target}}$ would then be a N-mode separable state, with a Fock state in each mode

$$|\psi\rangle_{\text{target}} = |n_1\rangle \otimes \cdots \otimes |n_N\rangle \tag{4.87}$$

with $\{n_i\}$ the Fock numbers. Using the N fidelity estimates, one can then use their mean as a measure of the closeness between the measured state and the target state. Unfortunately, only a limited class of states $\hat{\rho}$ would be close to the state $|\psi\rangle_{\text{target}}$ in equation (4.87), which in particular doesn't allow for much entanglement in $\hat{\rho}$. Still, to enlarge this limited class of certifiable states $\hat{\rho}$, we can use the properties of the double homodyne detection.

[1] It corresponds to the characteristic function associated to the Wigner function, see e.g. [Leonhardt 95].

The closeness of the experimental state $\hat{\rho}$ to the states of the form

$$\left(\bigotimes_{i=1}^{N} \hat{G}_i\right)\hat{U}\,|n_1\rangle \otimes \cdots \otimes |n_N\rangle \tag{4.88}$$

can be certified using the N-fidelity estimation protocol with target states given by equation (4.87), where $\hat{U}$ is a N mode basis change, and $\{\hat{G}_i\}$ are single-mode Gaussian operations.

Indeed, using the unbalancing and post-processing properties of the double homodyne detection from subsection 4.1.2, one can apply operations that undo the single mode operations $\hat{G}_i$ and the mode basis change $\hat{U}$[1]. As a result, the double homodyne detection is equivalently sampling the Q function of the state $|n_1\rangle \otimes \cdots \otimes |n_N\rangle$, allowing the certification of the states of equation (4.88). One can also apply the discussion of subsection 4.2.3 to obtain this same result.

[Chabaud 21c] formally proved the certifiability of this class of N-mode states, showing that the closeness of $\hat{\rho}$ to the target state (4.87) can be derived from the single-mode fidelities $F(\hat{\rho}_i, |n_i\rangle)$, which in turn can be estimated with the fidelity estimation protocol applied on the samples of each of the N double homodyne detections. For this protocol, the number M of measured copies of the N-mode state $\hat{\rho}$ scales in particular as N to the power $2 + 2n_{i_0}/m_{i_0}$, where the Fock number n_{i_0} and parameter m_{i_0} correspond to one of the N applied fidelity protocols[2]. This additional scaling factor makes it quickly harder to certify multimode states, while it still remains polynomial. For comparison, all other existing methods with Gaussian measurements scale exponentially with the number of modes.

Note that picking a larger class of states (as we mentioned in 1.4.3.6) implies choosing a more complex state than a Fock state on each of the N modes of the target states, for which the fidelity protocol has not been optimized up to now.

4.3.3 Simulation for the certification of single-photon subtracted squeezed vacuum states

In this subsection, we simulate the fidelity estimation protocol derived in the previous subsection 4.3.2. We show Wigner negativity and stellar rank certification of single-photon subtracted squeezed vacuum states $\hat{\rho}^-$ can be achieved efficiently in terms of the required number of samples. These results were published in [Chabaud 21d].

From the previous discussions, we choose the Fock state $|1\rangle$ as a target state for the protocol. To simulate the double homodyne detection of the state $\hat{\rho}^-$, we numerically sample its Q function, and thus compute its analytical expression.

We consider the single-photon subtraction to be single-mode in mode $\vec{\mathbf{g}}$. The double homodyne detection is assumed to measure in this same mode (engineering the correct local oscillator mode). Under these considerations, the other modes than mode $\vec{\mathbf{g}}$ do not intervene, so we consider only the states in this mode. The Q function of the Gaussian state $\hat{\rho}_{\mathrm{G}}$ (in mode

[1]The reversion is done by the operator $\hat{U}^\dagger\left(\bigotimes_{i=1}^{N} \hat{G}_i^\dagger\right)$ which is indeed of the form of the operators (4.47).

[2]More precisely, the scaling is the maximum scaling spanning over all N fidelity protocol parameters, see [Chabaud 21c] for details.

$\vec{g}$) at the output of the SPOPO writes generally

$$\mathrm{Q}_{\hat{\rho}_\mathrm{G}}(\vec{x}) = \frac{\mathrm{e}^{-\frac{1}{2}\vec{x}^\top(\mathbf{V}+\sigma_0^2\mathbb{1})^{-1}\vec{x}}}{2\pi\sigma_0^2\sqrt{\det(\mathbf{V}+\sigma_0^2\mathbb{1})}} \tag{4.89}$$

where $\mathbf{V}$ is the 2×2 covariance matrix of state $\hat{\rho}_\mathrm{G}$, and $\vec{x} = (q,p)^\top$ (linked to α by $\alpha = (q + \mathrm{i}p)/(2\sigma_0)$).

Without loss of generality[1], the state $\hat{\rho}_\mathrm{G}$ is a single-mode mixed vacuum squeezed state, which we can model with the covariance matrix[2]

$$\mathbf{V} = \frac{\sigma_0^2}{\mu_\mathrm{G}}\begin{pmatrix} s & 0 \\ 0 & s^{-1}\end{pmatrix} \tag{4.90}$$

where μ_G is the purity of $\hat{\rho}_\mathrm{G}$, and s is the squeezing factor.

Upon successful single-mode single-photon subtraction, the resulting state $\hat{\rho}^-$ is represented by the Q function (from equation (1.156))

$$\mathrm{Q}_{\hat{\rho}^-}(\vec{x}) = \tfrac{1}{2}\left[\vec{x}^\top(\mathbf{V}+\sigma_0^2\mathbb{1})^{-1}\mathbf{A}^-(\mathbf{V})(\mathbf{V}+\sigma_0^2\mathbb{1})^{-1}\vec{x} - \mathrm{Tr}\left[(\mathbf{V}+\sigma_0^2\mathbb{1})^{-1}\mathbf{A}^-(\mathbf{V})\right] + 2\right]\mathrm{Q}_{\hat{\rho}_\mathrm{G}}(\vec{x}) \tag{4.91}$$

$$\text{with}\quad \mathbf{A}^-(\mathbf{V}) = 2\frac{(\mathbf{V}-\sigma_0^2\mathbb{1})^2}{\mathrm{Tr}\left[\mathbf{V}-\sigma_0^2\mathbb{1}\right]} \tag{4.92}$$

where $\mathrm{Q}_{\hat{\rho}_\mathrm{G}}(\vec{x})$ is given in equation (4.89), or equivalently from equation (1.158)

$$\mathrm{Q}_{\hat{\rho}^-}(q,p) = \left(c_1\frac{q^2}{\sigma_0^2} + c_2\frac{p^2}{\sigma_0^2} + c_3\right)\exp\left[-c_4\frac{q^2}{\sigma_0^2} - c_5\frac{p^2}{\sigma_0^2}\right] \tag{4.93}$$

where the $\{c_i\}$ only depends on the fixed parameters s and μ_G.

In this subsection, we choose a non-unit purity μ_G to take into account the losses experienced by the squeezed vacuum state before the single-photon subtraction. Note that even though the subtraction is single-mode, the output subtracted state $\hat{\rho}^-$ has a lower purity than μ_G[3]. The detection is considered ideal. In the next subsection, we will consider a non-ideal detection.

In the simulation, in order to efficiently retrieve samples drawn from the 2D probability distribution given by $\mathrm{Q}_{\hat{\rho}^-}(\vec{x})$, we use a rejection sampling algorithm. This algorithm consists in performing a uniformly random sampling of a 3D box containing most of the Q function graph, and keep only the points in the 3D region under the graph of the Q function.

[1] We indeed only generate zero-mean states in the experiment, so a squeezing operation at an arbitrary angle (not relevant) is enough to model a Gaussian pure state.

[2] This model is equivalent to the one we used in e.g. equation (2.25): with the covariance matrix $\mathbf{V} = \mathrm{diag}(s^-, s^+)$, with two different squeezing and antisqueezing factors. At a given purity μ_G, knowing s^- determines $s^+ = \frac{\sigma_0^4}{\mu_\mathrm{G}^2}\frac{1}{s^-}$ from $\mu_\mathrm{G} = \sigma_0^2/\sqrt{\det(\mathbf{V})}$. Setting $s^+ = cs$ and $s^- = c/s$ yields $c = \sigma_0^2/\mu_\mathrm{G}$.

[3] While we didn't study this particular case in chapter 3, the behavior of the output subtracted state purity against the input state purity is analyzed in [Walschaers 17a, Walschaers 17b].

Simulation technical details. Let us summarize the algorithm of the fidelity estimation protocol, for target state $|1\rangle$ and a precision ϵ. First, we obtain M samples $\alpha_1, \cdots, \alpha_M$ from the rejection sampling of $Q_{\hat{\rho}^-}$. The failure probability δ is deduced from the standard deviation of the distribution $\{h_1^{(m,\gamma)}(\alpha_i)\}$ with equation (4.82). For each increasing integers $m \geq 1$, we minimize δ over $0 < \gamma < 1$. Then we choose the minimal δ with respect to the integers m. Note that the certification statement is valid for any parameters m, γ. This means that if we don't manage to find the exact minimal δ, the certification remains safely true for a larger than optimal confidence degree.

Fortunately, δ quickly reaches its minimum with respect to m before drastically soaring, allowing us to only probe a few steps in $m \geq 1$. The brute-force optimization over $0 < \gamma < 1$ is efficient enough, up to the precision where we don't gain much on the minimization of δ. In practice, for efficiency reasons, the expression of the failure probability δ used in the minimization is derived from the Hoeffding inequality (see appendix A.2 of our paper [Chabaud 21d] for such expression of δ). It overestimates δ with the advantage to be independent of the standard deviation of the distributions $\{h_1^{(m,\gamma)}(\alpha_i)\}$, by computing the range of the functions $\{\alpha \mapsto h_1^{(m,\gamma)}(\alpha)\}$ instead. Upon minimizing this overestimation of δ, the actual δ is finally computed with the minimization parameters m and γ. This procedure relies on the fact that minimizing δ using the overestimating expression or equation (4.82) yields the same optimized parameters, which was consistently checked.

To drastically reduce the computation time, the precise approximation of the functions $\{h_n^{(m,\gamma)}(\alpha)\}$ is pre-computed for large spans of parameters m and γ. The approximations are linear interpolations, following an algorithm which ensures the interpolation error remains bellow a customized value (the lowest this value the largest the memory cost). As the $\{h_n^{(m,\gamma)}(\alpha)\}$ may have extremely sharp behaviors in certain regions, this enhancement proved not to be straightforward and required a good analysis of this behavior to minimize the number of interpolation points.

As it is written, the simulation algorithm minimizes over δ for a given number M of samples and ϵ precision. In practice, we don't have prior knowledge on the precision we can reasonably ask for a given number of samples M (which we can expect to be up to 1×10^6 from the experiment), but we do know the degree of confidence we want (for instance $1 - \delta = 95\%$). To circumvent this caveat, we can use the fact that ϵ scales as a power of M (see equation (4.86)), which is verified empirically. In particular, this implies $\ln(\epsilon) \propto \ln(M)$. Running the complete optimization algorithm for two reasonably chosen precisions, one can then use a linear fit of $\ln(\epsilon)$ and deduce the approximate ϵ for which the optimized protocol yields a confidence degree $1 - \delta$ for M samples.

Certifying the Wigner negativity of state $\hat{\rho}^-$. From previous discussions, upon translating the samples by $\alpha \in \mathbb{C}$, the protocol estimates the fidelity $F\left(\hat{D}^\dagger(\alpha)\hat{\rho}^-\hat{D}(\alpha), |1\rangle\right)$, which is equal to the witness $\omega_{\hat{\rho}^-}(\alpha, 1)$, see equation (4.68). If $\omega_{\hat{\rho}^-}(\alpha, 1) > 0.5$, then the Wigner function of the state $\hat{\rho}^-$ is negative at α.

For each α, applying the protocol yields then a fidelity estimate, at fixed precision $\epsilon = 0.1$, at fixed number of samples $M = 5.5 \times 10^5$. We made sure that for all α, the confidence degree $1 - \delta$ is 95% or higher. If the fidelity estimate for a given α is greater than $\frac{1}{2} + \epsilon$, we can assert that the Wigner function of the state $\hat{\rho}^-$ is negative at α, i.e. $W_{\hat{\rho}^-}(\alpha) < 0$, with probability

greater than $1 - \frac{\delta}{2} = 97.5\%$.

In figure 4.4, we report such simulated Wigner negativity certification, translating the data for many $\alpha \in \mathbb{C}$. The red region shows all the α at which the Wigner negativity is certified with 97.5% confidence.

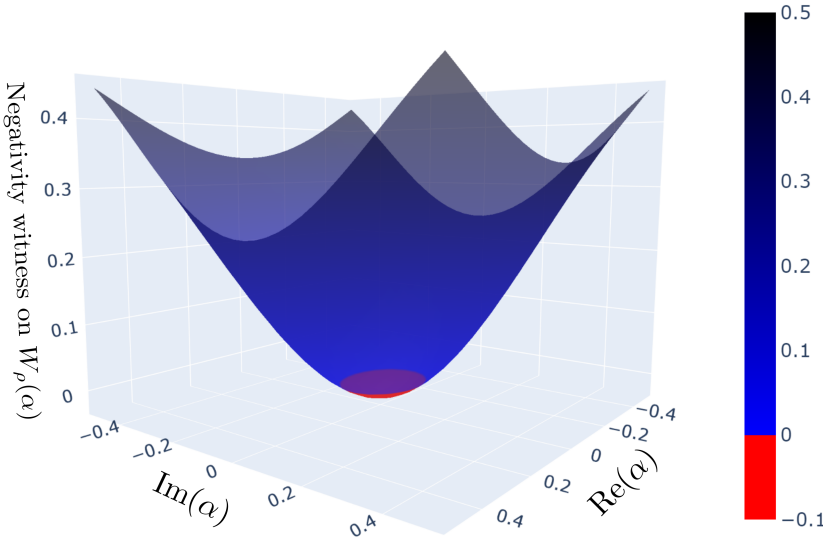

Fig. 4.4 Negativity witness estimates for a single-photon subtracted squeezed vacuum state with squeezing factor $s_{\text{dB}} = 3\,\text{dB}$ and purity before subtraction $\mu_{\text{G}} = 0.95$. Using simulated samples from double homodyne detection, the witnesses $\omega_{\hat{\rho}^-}(\alpha, 1)$ have been estimated for a thousand values of the displacement amplitude α, which have been interpolated for clarity, with a fixed precision $\epsilon = 0.1$ and a fixed number of samples $M = 5.5 \times 10^5$. The curve has been shifted upwards by the value of ϵ, and the red points witness the negativity of the state with at least 97.5% confidence.

Certifying the stellar rank 1 or higher of state $\hat{\rho}^-$. As discussed before, if the fidelity $F(\hat{\rho}^-, |1\rangle)$ of $\hat{\rho}^-$ to the target state $|1\rangle$ is higher than the threshold 0.478, then the state $\hat{\rho}^-$ has a stellar rank greater or equal to 1. As $F(\hat{\rho}^-, |1\rangle)$ is equal to $\omega_{\hat{\rho}^-}(0, 1)$, estimating $F(\hat{\rho}^-, |1\rangle)$ may allow us to certify both stellar rank 1 or higher and Wigner negativity at the origin.

Using the protocol, we estimate $F(\hat{\rho}^-, |1\rangle)$ for $s_{\text{dB}} = 3\,\text{dB}$ and different values of μ_{G}, for $M = 1 \times 10^6$ samples and $1 - \delta = 95\%$. The resulting interval of confidence are displayed on graph 4.5 (a)[1], and can be interpreted similarly as in figure 4.3 (right). In particular, we see that at $\mu_{\text{G}} = 0.90$, the lower bound of the interval of confidence is higher than the stellar rank 1 threshold and lower than the Wigner negativity threshold. The corresponding state is then certified to have a stellar rank greater or equal to 1 with confidence $1 - \frac{\delta}{2} = 97.5\%$, while no

[1]Statistical fluctuations are expected from one run to another, as the interval of confidence are centered around the fidelity mean estimations.

statement is made on its negativity at the origin. If this was a measurement result, we would require more samples to improve the precision ϵ of the estimation, or allow for reducing the confidence degree, to eventually obtain a Wigner negativity certification[1].

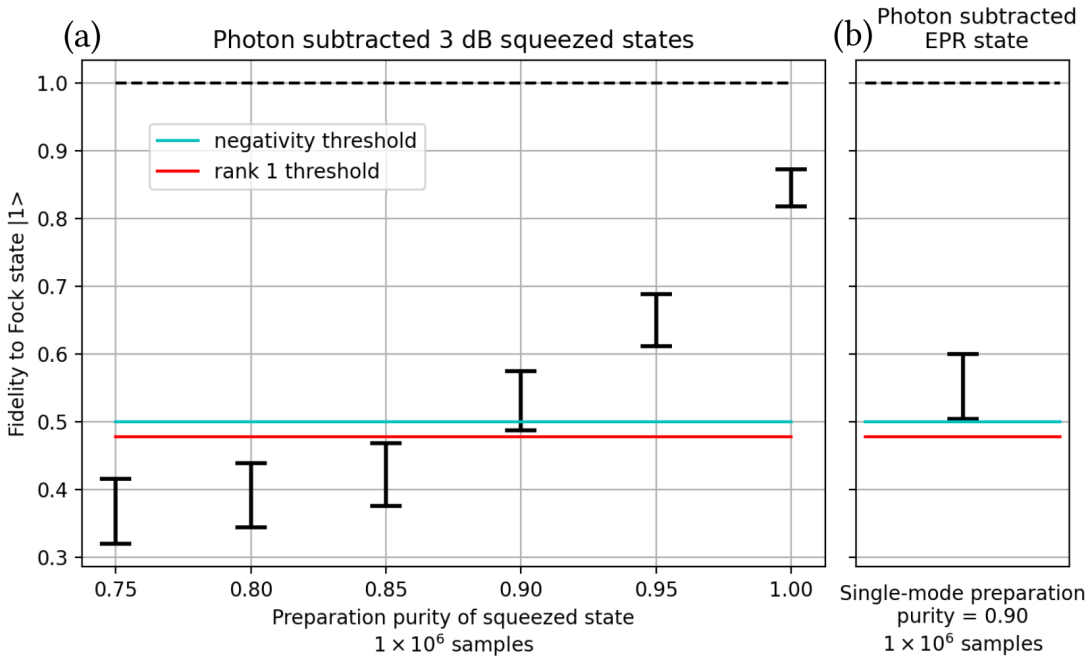

Fig. 4.5 Estimates of the fidelity to Fock state $|1\rangle$ for various states using $M = 10^6$ simulated samples from double homodyne detection. We display the stellar rank 1 threshold (red horizontal line) and the Wigner negativity (at origin) witness threshold (cyan horizontal line). When the lowest point of an interval of confidence is higher than a threshold value, the property corresponding to this threshold value is certified with more than 97.5% confidence. (a) Single-photon subtracted squeezed vacuum states with $s_{\text{dB}} = 3$ dB of squeezing, for several values of the purity before subtraction μ_{G}. (b) A photon subtracted two-mode EPR state with experimental covariance matrix taken from [Ra 20]. Simulated photon subtraction is done on the first mode and double homodyne measurement on the second mode of the EPR state.

These results show that stellar rank and Wigner negativity certification are expected to be achievable in realistic experimental conditions, close to the ones we expect to achieve in the laboratory. Note yet that for figure 4.5, the detection is supposed ideal. Taking into account the detection losses in the next subsection, bring us closer to our experimental conditions, we discuss there experimental implications.

Certifying a single-photon subtracted EPR state. Let us consider a 2-mode EPR state now, prior to single-photon subtraction. To build this Gaussian state whose Q function is

[1]Note that we may never be able to achieve better if the true fidelity is actually in between the two thresholds, for which case the state is of stellar rank 1 (or higher) but not Wigner negative (at zero), see subsection 1.4.2 for discussion of such states.

described by equation (4.89) with a 4×4 covariance matrix this time, we choose to use experimental data from the Extended Data Figure 4 of [Ra 20]. This is a 4-mode covariance matrix of separable squeezed state. We select modes 0 and 2 to obtain a 2-mode squeezed state covariance matrix. We then numerically apply a beamsplitter on this covariance matrix to obtain a 2-mode EPR state covariance matrix $\mathbf{V}_{\text{EPR}}$ (see subsection 1.3.6 for details on these maximally entangled states). We denote $(\vec{\mathbf{f}}_1, \vec{\mathbf{f}}_2)$ the EPR modes.

We consider a single-mode single-photon subtraction applied on the mode $\vec{\mathbf{f}}_1$, and measuring on mode $\vec{\mathbf{f}}_2$. The Q function of the state $\hat{\rho}^-_{\text{EPR}}$ after subtraction on mode $\vec{\mathbf{f}}_1$ is given by equation (1.156), with the covariance matrix $\mathbf{V}_{\text{EPR}}$, the subtraction mode $\vec{\mathbf{g}} = \vec{\mathbf{f}}_1$. The measured state $\hat{\rho}^-_{\text{EPR},2}$ is obtained upon tracing the Q function over mode $\vec{\mathbf{f}}_2$ (i.e. integrating over q_2, p_2).

From this single-mode Q function, we can then apply the same fidelity estimation protocol as before, with the result on graph 4.5 (b). The simulation certifies Wigner negativity with $M = 1\times10^6$ samples with 97.5% confidence. Note that this is not an actual certification of an experimental state. It is a simulation conditioned with experimental data for realistic purposes. Note that in [Ra 20], they experimentally exhibit Wigner negativity of such a state, using homodyne tomography techniques (which do not allow for a certification statement as argued before).

4.3.4 Simulation extension: accounting for detection losses

Since the publication of [Chabaud 21d], we improved the simulation by taking into account the losses experienced by the state from the subtraction to the ideal detection. These losses were estimated in section 2.4, with equivalent efficiency $\eta_{DHD} = \eta_{HD} \simeq 81\%$.

A N-mode quantum state $\hat{\rho}$ which experiences the losses $1-\eta$ sees its Q function $Q_{\hat{\rho}}(\vec{x})$ smoothed by a Gaussian function, such that the Q function of the resulting lossy state $\hat{\rho}_\eta$ writes [Leonhardt 95]

$$Q_{\hat{\rho}_\eta}(\vec{x}) = \frac{1}{\eta^N} W^u_{\hat{\rho}}(\vec{x}/\sqrt{\eta}) \tag{4.94}$$

where $W^u_{\hat{\rho}}(\vec{x})$ is given in equation (1.40) and $u = 1 - \frac{2}{\eta}$ (e.g. $u=-1$ for $\eta=1$ and $u<-1$ for $\eta<1$).

We can then derive the Q function of the single-photon subtracted state $\hat{\rho}^-_\eta$ which underwent $1-\eta$ losses after subtraction by applying equation (4.94) to the Q function of the state $\hat{\rho}^-$ which is given generally by equation (1.156). We perform the computation in appendix B.2 in the multimode scenario, and obtain in particular for a single-mode state

$$\mathrm{Q}_{\hat{\rho}^-_\eta}(\vec{x}) = \begin{cases} \left[\frac{1}{\eta}\vec{x}^\top(\mathbf{V}-u\sigma_0^2\mathbb{1})^{-1}\mathbf{A}^-(\mathbf{V})(\mathbf{V}-u\sigma_0^2\mathbb{1})^{-1}\vec{x} - \mathrm{Tr}\left[(\mathbf{V}-u\sigma_0^2\mathbb{1})^{-1}\mathbf{A}^-(\mathbf{V})\right] + 2\right] \\ \times \dfrac{\mathrm{e}^{-\frac{1}{2\eta}\vec{x}^\top(\mathbf{V}-u\sigma_0^2\mathbb{1})^{-1}\vec{x}}}{4\eta\pi\sigma_0^2\sqrt{\det(\mathbf{V}-u\sigma_0^2\mathbb{1})}} \end{cases} \tag{4.95}$$

where $\mathbf{A}^-(\mathbf{V})$ is the matrix defined in equation (4.92), $\mathbf{V}$ is again the 2×2 covariance matrix of equation (4.90), and $u = 1-\frac{2}{\eta}$. Remarkably, one can see that equation (4.95) can be obtained

from equation (4.91) upon transforming $\mathbf{V} + \sigma_0^2 \mathbb{1} \mapsto \mathbf{V} - u\sigma_0^2 \mathbb{1}$ (except in $\mathbf{A}^-(\mathbf{V})$) and $\vec{x} \mapsto \vec{x}/\sqrt{\eta}$ (up to a normalization factor). Again, the Q function $\mathrm{Q}_{\hat{\rho}_\eta^-}(q,p)$ may be viewed in the simple form given by equation (4.91), with other coefficients $\{c_i\}$ which depends on the fixed parameters u, μ_G, and η.

We run the same simulation as before, except we sample now the Q function $\mathrm{Q}_{\hat{\rho}_\eta^-}$ of the lossy single-photon subtracted squeezed vacuum state $\hat{\rho}_\eta^-$ for η equal to 1, 0.9 and 0.8, with the results in figure 4.6.

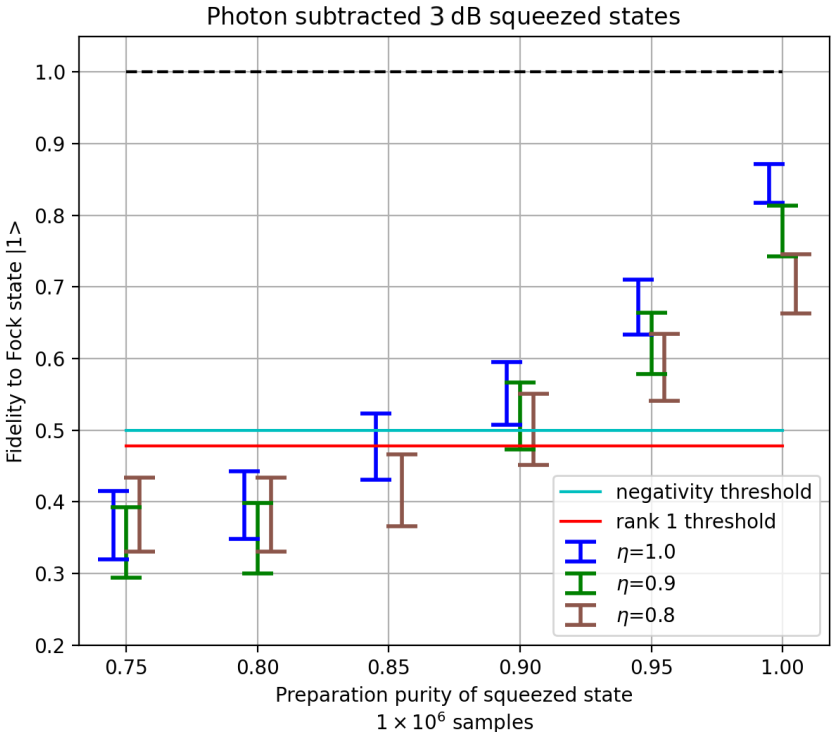

Fig. 4.6 Estimates of the fidelity to Fock state $|1\rangle$ for various lossy single-photon subtracted squeezed vacuum states $\hat{\rho}_\eta^-$ using $M = 10^6$ simulated samples from double homodyne detection. For the efficiency $\eta = 1.0$ (blue), the plot is the same as graph 4.5 (a). For lower efficiencies $\eta = 0.9$ (green) and $\eta = 0.8$ (brown), the estimations drop. For visibility, the blue and brown intervals were right and left shifted while still corresponding to the same purity μ_G as the central green interval of confidence.

As we estimated $\eta_\mathrm{DHD} \simeq 81\%$, we expect the brown interval of confidence (for $\eta = 0.8$) to accurately simulate the result of the protocol on actual experimental data from our experiment. The drop in fidelity compared to the case $\eta = 1.0$ is reasonable and is more significative for states with a high purity μ_G before subtraction.

At $\mu_\mathrm{G} = 1$ and $\eta = 1$, the state $\hat{\rho}_\eta^-$ is a pure single-photon subtracted state, and writes $|\psi_\zeta^-\rangle = \sinh(\zeta)^{-1}\hat{a}\hat{S}(\zeta)|0\rangle$ with $\zeta = s_\mathrm{dB}\ln(10)/20$. In this case, we can deduce the fidelity $F(|\psi_\zeta^-\rangle, |1\rangle) = |\langle 1|\psi_\zeta^-\rangle|^2$ from the decomposition of a squeezed state $\hat{S}(\zeta)|0\rangle$ on the Fock basis, see equation (1.79). We obtain $F(|\psi_\zeta^-\rangle, |1\rangle) = \cosh(\zeta)^{-3}$. At $s_\mathrm{dB} = 3\,\mathrm{dB}$, $F(|\psi_\zeta^-\rangle, |1\rangle) \simeq 0.84\%$,

which is coherent with figure 4.6.

We chose $s_{\mathrm{dB}} = 3$ dB for best results. At high squeezing, we expect poor fidelity estimations, as the pure subtracted state $|\psi_\zeta^-\rangle$ gets further away from the Fock state $|1\rangle$ as s_{dB} increases (and similarly for mixed states). At low squeezing, the fidelity is expected to increase for the pure subtracted state. For mixed states though, it is expected to drop, because the purity of the state after subtraction drops with the squeezing factor, an observation made in [Walschaers 17a, Walschaers 17b]. We give in the appendix D.2.1 the results of the simulation for other values of the squeezing factor s_{dB}, confirming these expectations.

We can see that at $\eta = 0.8$, we may not expect anymore to certify our states if the purity before subtraction μ_{G} is lower or equal to 0.9, with 10^6 samples. At $\mu_{\mathrm{G}} = 0.95$ and above, certification is achievable although it puts significative constraints on the experiment. The main concern is about the number of samples. From chapter 3, the expected number of single-photon events per second is about 55. This means that it would require to steadily acquire for about 5 hours to gather 10^6 samples. While achievable, this long acquisition can induce challenges of experience stability for instance. It is then a priority to reduce the number of required samples, or to improve the efficiency of the single-photon detection. However, reducing the number of samples from 10^6 to 10^5 may come approximately to the cost of a three-fold[1] increase in the size of the interval of confidence in figure 4.6. There is not enough room left on the other parameters to compensate such an increase. In the next subsection, we show how to partially relieve these constraints.

4.3.5 Certifiabilty enhancement using unbalancing

As shown in section 4.1, the double homodyne detection allows us to equivalently apply a squeezing operation on the state prior measurement via unbalancing a beamsplitter, achieving arbitrary squeezing operation $\hat{S}(\zeta')$ with squeezing parameter ζ'. We want to use this property to improve the fidelity estimation simulation presented before.

We expect the unbalancing to improve the sensitivity of the certification protocol for our states. Consider a pure single-photon subtracted state $|\psi_\zeta^-\rangle$. It may be viewed as a squeezed Fock state 1 as $|\psi_\zeta^-\rangle \propto \hat{S}(\zeta)|1\rangle$. Applying the squeezing operation $\hat{S}(\zeta')$ with $\zeta' = \zeta$ on $|\psi_\zeta^-\rangle$ via unbalancing results then in sampling the Q function of the Fock state $|1\rangle$ with the double homodyne detection. This mean that we expect to estimate $F(\hat{S}(\zeta')\hat{\rho}^-\hat{S}(\zeta')^\dagger, |1\rangle) = 1$ in the case where $\hat{\rho}^-$ is pure with the appropriate unbalancing.

To simulate the certification protocol including the equivalent squeezing operation, we compute the Q function of the resulting state $\hat{\rho}^-_{\zeta',\eta}$. The derivation is given in the appendix B.2

[1] This is an approximation taking into account only the statistical error ($\sqrt{10} \simeq 3.16$). The behavior of the bias contribution in the precision ϵ is not predictable, while other simulation run shows it behaves approximately similarly.

in the multimode scenario, and we obtain in the single-mode scenario

$$\mathrm{Q}_{\hat{\rho}^{-}_{\zeta',\eta}}(\vec{x}) = \begin{cases} \left[\frac{1}{\eta}\vec{x}^{\top}(\mathbf{V}' - u\sigma_0^2\mathbb{1})^{-1}\mathbf{A}^{-\prime}(\mathbf{V})(\mathbf{V}' - u\sigma_0^2\mathbb{1})^{-1}\vec{x} - \mathrm{Tr}\left[(\mathbf{V}' - u\sigma_0^2\mathbb{1})^{-1}\mathbf{A}^{-\prime}(\mathbf{V})\right] + 2\right] \\ \times \dfrac{\mathrm{e}^{-\frac{1}{2\eta}\vec{x}^{\top}(\mathbf{V}'-u\sigma_0^2\mathbb{1})^{-1}\vec{x}}}{4\eta\pi\sigma_0^2\sqrt{\det(\mathbf{V}' - u\sigma_0^2\mathbb{1})}} \end{cases} \tag{4.96}$$

$$\text{with} \quad \mathbf{A}^{-\prime}(\mathbf{V}) = \mathbf{K}\,\mathbf{A}^{-}(\mathbf{V})\,\mathbf{K} \quad \text{and} \quad \mathbf{V}' = \mathbf{K}\,\mathbf{V}\,\mathbf{K}$$

where $\mathbf{K}$ is the symplectic matrix representing the action of the operator $\hat{S}(\zeta')$, $\mathbf{A}^{-}(\mathbf{V})$ is the matrix defined in equation (4.92), $\mathbf{V}$ is the 2×2 covariance matrix of equation (4.90), and $u = 1 - \frac{2}{\eta}$. One can see that equation (4.96) can be obtained from equation (4.95) upon the transformations $\mathbf{A}^{-}(\mathbf{V}) \mapsto \mathbf{K}\,\mathbf{A}^{-}(\mathbf{V})\,\mathbf{K}$ and $\mathbf{V} \mapsto \mathbf{K}\,\mathbf{V}\,\mathbf{K}$ (except in $\mathbf{A}^{-}(\mathbf{V})$). Again, the Q function $\mathrm{Q}_{\hat{\rho}^{-}_{\zeta',\eta}}(q,p)$ may be viewed in the form given by equation (4.91), with other coefficients $\{c_i\}$ which depends on the fixed parameters s_{dB}, μ_{G}, η, and ζ'.

We run the same simulation as above, except we sample now the Q function of the state $\hat{\rho}^{-}_{\zeta',\eta}$ for an unbalancing parameter ζ' which exactly compensates for the preparation squeezing factor s_{dB}, i.e. $\zeta' = s_{\mathrm{dB}}\ln(10)/20$. The simulation results are given in figure 4.7.

This time, at $\mu_{\mathrm{G}} = 1$, we can see on figure 4.7 that the fidelity estimate is indeed around 1 for $\eta = 1$, as expected from the above discussion. Similarly, all other interval of confidence on figure 4.7 got lift up compared to figure 4.6, by about 5% to 15%. In particular at $\mu_{\mathrm{G}} = 0.9$, the quantum non-Gaussianity properties are certified for $\eta \geq 0.8$ which was not the case without unbalancing.

We still have the same limitation as before at low squeezing because of how subtraction behaves. On the other hand, at high squeezing, the effect of squeezing is compensated by the unbalancing, removing any limit. We then expect the fidelities to increase with the squeezing (always matched by the unbalancing). This behavior can be checked on the additional simulation results with different squeezing factors s_{dB} in the appendix D.2.2. We also estimated the sensibility of the estimated fidelity with respect to the unbalancing parameter, and found that it is quite robust for an unbalancing in the range [2 dB, 4 dB] for a 3 dB squeezed state, see appendix D.2.3.

While it might be appealing to look for preparing highly squeezed states, it remains an experimental challenge. From chapter 2 discussions, we expect $s_{\mathrm{dB}} = 3$ dB squeezing factor to be a good prediction for the first supermode of the SPOPO, with high purity. Assuming we can produce such state at purity $\mu_{\mathrm{G}} = 0.95$, then the estimated fidelity would be largely above certification thresholds, allowing for a significative decrease in terms of required number of samples. We thus expect from figure 4.7 to achieve quantum non-Gaussianity certification of our experimentally generated states in realistic conditions.

4.3.6 Simulation: perspectives

In the previous two subsections, we were considering that any detection imperfection were mapped to optical losses applied on the input state, prior measurement with an ideal detection.

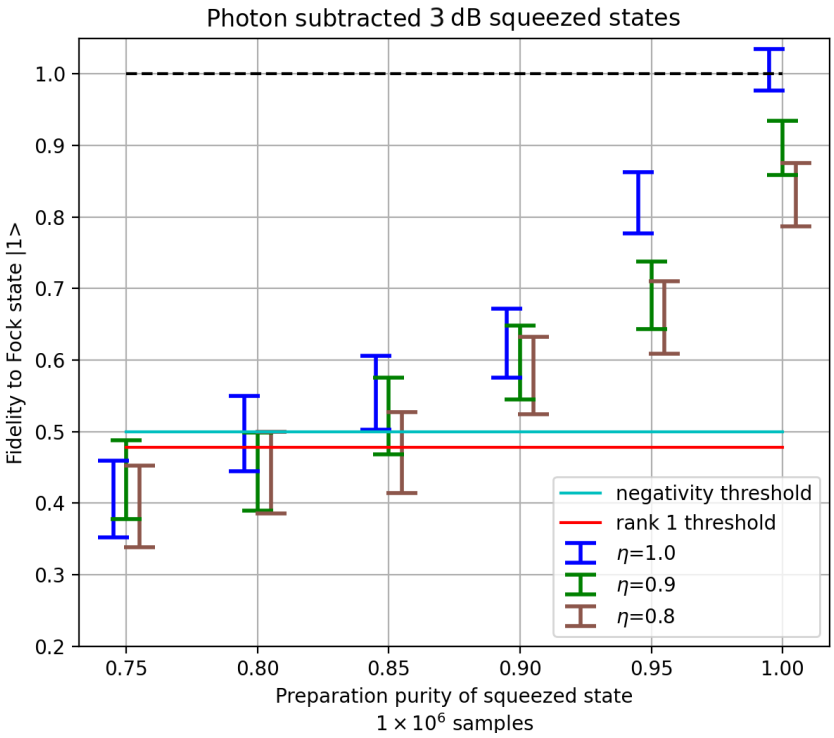

Fig. 4.7 Estimates of the fidelity to Fock state $|1\rangle$ for various lossy single-photon subtracted squeezed vacuum states with $s_{\mathrm{dB}} = 3\,\mathrm{dB}$ using $M = 10^6$ simulated samples from an unbalanced double homodyne detection. The unbalancing applies a squeezing operation with squeezing parameter exactly opposite to the squeezing parameter necessary to produce the initial squeezed vacuum states in the preparation. Same plot as figure 4.6, except for the unbalancing.

This means that the certification is not trusting the detection, as it does not correct for the losses, which allows for stronger certification claims in the opposite scenario.

A possible alternative approach consists then in taking into account the losses in the fidelity estimation protocol itself, at the cost of trusting the detection (still not the state generation). This means that the protocol would rely on the knowledge of these detection losses. It also means that we would then certify the state before the detection losses, or corrected by these losses. Some progress has been done into this direction, extending the double homodyne fidelity estimation protocol considering a noisy detector. The simulations were still not conclusive. In particular, the cost in number of samples is expected to be higher than in the previous protocol with equivalent losses, as the assumed sampled probability distributions is now a smoothed version of the Q function. From the first trials, the number of required samples seems not realistic.

Another possible extension of the simulation consist in taking into account the multimodeness of the single-photon subtraction (i.e. the fact that the Schmidt number of the subtraction process is not equal to 1). We do not expect significant changes in the simulation results since the measured Schmidt number $K = 1.03$ of our subtractor is very close to 1, see the subtraction tomography in 3.4.2.2.

To implement this extension, one would consider a multimode Gaussain squeezed state, before subtraction, with a realistic squeezing distribution. One could either use the theoretically derived distribution of the SPOPO given in chapter 2, or use actual experimentally measured squeezing distribution in the supermode basis. The Q function of the multimode state after subtraction is then given by equation (1.156), with the subtraction projector $\mathbf{\Pi}_{\vec{\mathbf{g}}}$ given by equation (3.70) with a subtraction probability distribution given by the diagonal form of the measured subtraction matrix given in figure 3.17. The subtraction mode $\vec{\mathbf{g}}$ is chosen as the mode of the gate in the subtraction tomography, i.e. the Hermite-Gaussian 0 mode. Finally, the mode of the LO is also chosen as the Hermite-Gaussian 0 mode, i.e. the measurement at the double homodyne detection is performed in this mode. In the simulation, we would then trace out the Q function on all other modes prior sampling and applying the fidelity estimation protocol. While it constitutes an interesting extension, we don't expect major changes.

4.4 Experimental quantum non-Gaussianity certification

In the previous section, we explained in particular how to apply the fidelity estimation protocol on simulated data from double homodyne detection to certify stellar rank or Wigner negativity. In this section, we present the experimental advances made for measuring the generated single-photon squeezed vacuum states using the double homodyne detection described in section 4.1.

In subsection 4.4.1, we detail the protocol for acquiring the experimental data from the double homodyne detection, notably post-selecting on the single-photon subtraction events. We also elaborate on the challenges we faced to properly isolate the data signal from the noise and from the square-like signal induced by the optical locking system.

In subsection 4.4.2, we report and discuss preliminary results.

4.4.1 Measurement technical details and challenges

Experimental protocol and cavity temporal mode. Let us describe the experimental protocol devised for sampling the Q function of the generated single-photon squeezed vacuum states. The double homodyne detection allows for measuring the two orthogonal quadratures $\hat{q}^{\theta}$ and $\hat{q}^{\theta+\pi/2}$, where θ is the LO-signal optical phase which is locked over time. The output voltage of both homodyne detections is acquired over time using a scope. To save memory and time, the scope is triggered to measure only on relevant time periods. To determine them, two main aspects have to be considered: the locking of the LO-signal phase, and the single-photon subtraction events.

As explained in section 2.5, the measurement time over a locking cycle is limited by the action of the accousto-optic modulator (AOM) which only sends the light to the single-photon detector (SPD) when safe. The first trigger on the scope is then set to match the one of the AOM. An AND gate is then applied on this trigger together with the trigger built from the clicks of the SPD, each signaling a detection occurred. In other words, the scope is only measuring data when the AOM diffracts light to the SPD and when the SPD clicks.

Yet, it is not enough to simply retrieve the couple of homodyne quadrature measurements $q(t_i)$ and $p(t_i)$ when the scope is triggered at time t_i, because the single-photon subtraction mode is given by the SPOPO cavity [Morin 13b, Ra 20]. The typical length in time of this mode is given by the inverse of the cavity bandwidth, hence of the order of a few 100 ns, which is much longer than the integrating time of the detectors. Thus, when the scope is triggered at time t_i, one has to weight the homodyne signals $q(t)$ and $p(t)$ by a temporal mode $\mathbf{f}(t)$ such that the retrieved quadrature measurements $q_{\tilde{\mathbf{f}}}(t_i)$ and $p_{\tilde{\mathbf{f}}}(t_i)$ are given by

$$\begin{cases} q_{\tilde{\mathbf{f}}}(t_i) = \int \mathbf{f}(t-t_i) q(t)\,\mathrm{d}t \\ p_{\tilde{\mathbf{f}}}(t_i) = \int \mathbf{f}(t-t_i) p(t)\,\mathrm{d}t \end{cases} \tag{4.97}$$

where $\mathbf{f}(t-t_i)$ is centered at time t_i. The amount of data kept around time t_i is determined from the temporal width of the mode $\mathbf{f}(t)$.

It was shown that the temporal mode associated to a state generated from a cavity has theoretically the shape of a decreasing exponential $\exp(-|t|)$ in first order [Nielsen 07, Morin 13a]. To experimentally retrieve the actual temporal mode $\mathbf{f}(t)$, one can compute the temporal autocorrelation of an homodyne signal, and retrieve its main eigenmode. This analysis of the temporal mode of the SPOPO cavity was performed in [Dufour 18], with the results shown in figure 4.8. The non-trivial shape of the temporal eigenmode stems from the electronic response of the detectors. In practice, an approximation (red in the figure) is used as $\mathbf{f}(t)$ and applied on the data following equations (4.97).

Finally, after having collected enough data points $\{q_{\tilde{\mathbf{f}}}(t_i)\}$ and $\{p_{\tilde{\mathbf{f}}}(t_i)\}$, the double homodyne samples are deduced as $\alpha_i = (q_{\tilde{\mathbf{f}}}(t_i)/r + \mathrm{i}p_{\tilde{\mathbf{f}}}(t_i)/t)/(2\sigma_0)$, with r^2 and t^2 the reflectivity and transmissivity of the beamsplitter of the double homodyne detection. Building the histogram from the samples $\{\alpha_i\}$ results in the sampled Q function of the state $\hat{S}(\ln(t/r))\hat{\rho}\hat{S}(\ln(t/r))^{\dagger}$, where $\hat{\rho}$ is the experimental state. One can then apply the fidelity estimation protocol on the samples $\{\alpha_i\}$ with target state $|1\rangle$ to obtain a certification statement on the stellar rank 1

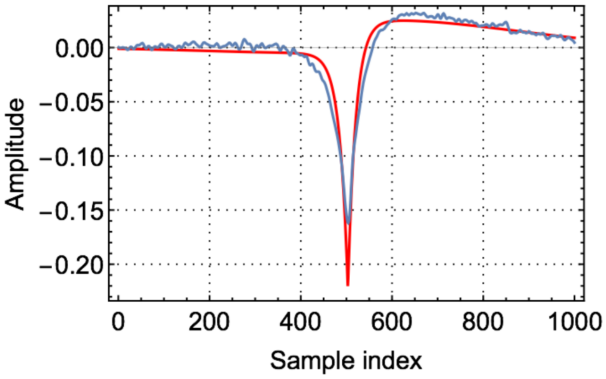

Fig. 4.8 Measured temporal eigenmode of the SPOPO cavity (in blue), and approximated mode $\mathbf{f}(t)$ used in practice (in red). The samples indices in the horizontal axis are multiples of 2 ns. From [Dufour 18].

and Wigner negativity of the state $\hat{\rho}$. The unbalancing of the double homodyne detection is experimentally chosen to maximize this fidelity.

Dependency on the optical phase lock. Is the lock necessary to perform the protocol described above? It depends on the application. If one wants to reconstruct the histogram of the Q function of the state $\hat{S}(\ln(t/r))\hat{\rho}\hat{S}(\ln(t/r))^\dagger$, then knowing the phase is necessary (except if the state $\hat{S}(\ln(t/r))\hat{\rho}\hat{S}(\ln(t/r))^\dagger$ is invariant under phase-space rotations).

If one only seeks to certify the fidelity to the target Fock state $|1\rangle$, one can notice that the Fock state $|1\rangle$ is invariant under phase space rotation. We then expect that it is the case of its P function also, along with the approximation of the P function of the protocol. One can indeed check that the functions $\{h_n^{(m,\gamma)}(\alpha)\}$ do not depend on the phase of the sample α, see equation (4.77) and equation (4.71). Since the fidelity estimator is given by their sum, it does not depend on the phase of the measurement samples $\alpha_1, \cdots, \alpha_M$.

However, this property can only be applied for a balanced homodyne detection. Indeed, for an unbalanced homodyne detection, the phase of the squeezing parameter ζ of the POVM is 2θ with θ the LO-signal phase. This means that for each different value of θ, the double homodyne detection is sampling the Q function of the state $\hat{S}(\ln(t/r)e^{i2\theta})\hat{\rho}\hat{S}(\ln(t/r)e^{i2\theta})^\dagger$. Taking a squeezed vacuum state for $\hat{\rho}$, one can see that the states $\hat{S}(\ln(t/r)e^{i2\theta})\hat{\rho}\hat{S}(\ln(t/r)e^{i2\theta})^\dagger$ do not have the same fidelity to Fock state $|1\rangle$. For instance, assuming the squeezed quadrature of $\hat{\rho}$ is $\hat{q}$ (i.e. $\theta_s = 0$), the sampled state at $\theta = 0$ is a squeezed state with squeezing factor enhanced by $\ln(t/r)$ (with $t > r$), while the sampled state at $\theta = \pi/2$ is a squeezed state with squeezing factor reduced by $\ln(t/r)$. As the fidelity to Fock state $|1\rangle$ for these squeezed states is given by $\cosh(\zeta')^{-3}$ with ζ' the new squeezing parameter, they indeed do not yield the same fidelity, which is also true for the intermediate states. A similar reasoning apply for a subtracted state as input.

To summarize, locking the LO-signal phase (or knowing it) is necessary when using an unbalanced double homodyne detection. As we saw in the previous section, unbalancing the double homodyne detection facilitates significantly the certification protocol.

In the following, we describe some challenges (among others) related to the measurement

using the double homodyne detection, and the methods used to cope with them.

Challenge: noise from the electric installation. We characterized the homodyne detectors, with results given in appendix C.1. We noticed that the clearance of the homodyne detectors at frequencies below 10 MHz was low, which can be spotted on the figures C.2 and C.4. Investigating more closely, we observed multiple peaks on the dark noise of the detectors, with an amplitude of up to 10 dB.

After a thorough search of the noise source in the lab, we understood that the electric installation of the building itself was causing this noise, spreading it in the electric ground to all devices of the experiment. Locally isolating the homodyne detectors was not enough to circumvent this issue, since there is an electric path connecting any two devices of the experiment. We then opted for a complete isolation of all devices by setting up power-inverters between the building power source (wall plugs) and the devices. These power-inverters are said on-line, in the sense that they convert the input AC power to a DC power, using batteries, and then convert it back to AC power to feed the devices. This process ensures that any noise from the building's electrical installation is effectively filtered out, providing clean and stable power to all experimental devices. The previously observed peaks were indeed removed, resulting in a flat clearance at low frequency.

Challenge: locking induced square-like signal. We faced another challenge at the measurement stage stemming from the phase optical lock working principle. During the measurement, the seed bright beam is alternatively blocked and not blocked. When it is not blocked, it interferes with the LO beam at homodyne detection, resulting into a signal with mean value proportional to both the LO and the seed field amplitudes. The measured electric signal is then alternatively a high voltage signal, and a zero-mean signal: a square signal. On figure 4.9, blue curve, we show the raw acquisition of the output of an homodyne detector without applying any filter or amplifier. Note that for simplicity, here the LO beam is blocked, and we measure the seed beam intensity on one homodyne photodiode, with the chopper on. The discussed effects are similar in the measurement configuration.

The signal of interest is the zero-mean signal, whose fluctuations are quadrature measurements of the input state. The variance of this signal is so low that we need to amplify them by at about 60 dB in power to correctly measure them on the scope. The issue is that an amplifier would also greatly increase the non-zero-mean part of the signal, which would saturate the amplifier. For this reason, we need to filter this part of the signal prior amplification using an high-pass filter (HPF), which is actually what commercial amplifiers inherently do.

As we want to keep most of the detection bandwidth, we are limited to low cut-off frequencies, of the order of 100 kHz. When fed with a sharp square signal, filters need a certain duration to react, leading to a step response with few oscillations at the period of the inverse cut-off frequency of the filter. This is what we observed in our setup, see figure 4.9 curves orange and green. We use third order butterworth 90 kHz HPFs. The higher the order of the filter, the higher its suppressing power, but the longer its step response. A similar effect occurs when multiple filters are arranged in a series, see figure 4.9. Due to the large amplification needed, we would require the strength of two of these HPFs. As one can see, the oscillations

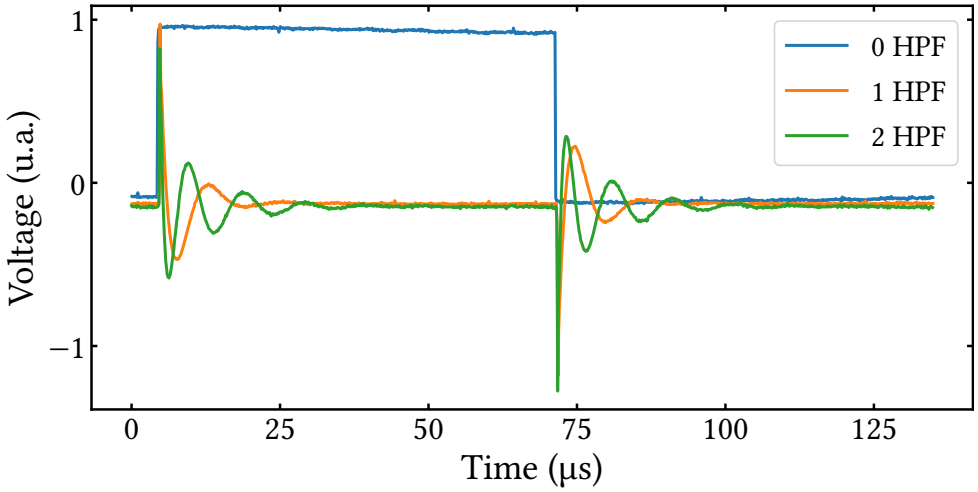

Fig. 4.9 Raw acquisition of the output signal of one homodyne detection over a complete locking cycle (of 135 µs), for 0, 1 and 2 high-pass filters (HPF) of 90 kHz cut-off frequency. The blue curve serves as a reference to distinguish when the seed beam is measured (high voltage) from when it is blocked (low voltage). The curves have been rescaled arbitrarily and individually to exhibit their step-responses.

spread over a consequent portion of the measurement time window at each locking cycle, significantly reducing the duty cycle.

To cope with this issue, we built an electronic device, called clipper-amplifier, whose electronic scheme is given in appendix C.4. The idea is to use diodes to clip both the bottom and the top of the signal[1], such that the amplitude of the signal is low enough not to saturate the following amplifier. These two operations, clipping and amplifying, are repeated four times to reach the required amplification level, which can be manually modified. Using diodes instead of HPFs, no step-response were observed, solving the above mentioned issue.

We also investigated another alternative design, which consists in using (commercial) fast electronic switches, synchronized with the locking cycles, prior amplifying the relevant signal at one of the output of the switch. We observed large peaks appearing at switch events, which also triggers a step response of the filters of the (commercial) amplifiers. For this reason, we opted for using two clipper-amplifiers, one for each homodyne detection.

Invisible in figure 4.9, there is a comparatively low amplitude step response induced by the internal HPF at the AC output in the homodyne detectors themselves (see electronic scheme in appendix C.1). The low order of this HPF filter (a first order RC filter) results in a lower amplitude and smaller spread than the ones shown in figure 4.9, while still deteriorating the signal. To mitigate this effect, we changed the capacitance of the filter from 33 nF to 10 nF, resulting in a cut-off frequency of 160 kHz. This higher cut-off frequency reduces the oscillation period of the step response, and its effect on the signal.

Lastly, we initially splitted the AC signal of one of the homodyne to feed the LO-seed

[1] In locking configuration contrary to figure 4.9, the seed interferes with the LO beam and is phase-modulated at 60 kHz for the lock to function. Thus, the signal (at locking times) is then large oscillations that still trigger the step response of filters as in figure 4.9. They need to be clipped at negative and positive voltages.

locking device, for higher efficiency. However, we observed noise of very-low frequency on the measurement channel of the splitter, which was likely due to electronic reflections. We then removed the splitter, and are now locking on the DC channel, removing the fluctuations.

Challenge: subtraction counts. As we have seen in the last sections, the number of subtraction counts per second is a critical parameter, as it increases the required acquisition length to measure relevant number of samples for the certification. In chapter 3, we estimated the subtraction counts to about 55 counts per second, without taking into account the locking cycle. With a duty cycle of 26% at a chopping rate of 8 kHz, the estimation drops down to 14 counts per second.

To mitigate this issue, we decreased the chopping frequency to 5 kHz, corresponding to a cycle length of 235 µs effectively. We then have been able to increase the duty cycle to 41%, resulting in an estimation of 22 subtraction counts per second.

However, this estimation assumes that the quantum state before subtraction is a pure squeezed vacuum state of 3 dB. From recent measurement, we are currently estimating a squeezing factor s^-_{dB} of -1.85 dB for a high purity of 0.917 at the output of the SPOPO (see squeezing measurements in subsection 2.5.3). As the state is not pure, with an excess of antisqueezing, the effective number of photons in this state is slightly higher, such that we can round the estimation to 2 dB[1]. At this level of squeezing, we estimate 10 subtraction counts per second, taking into account the 41% duty cycle. This number is consistent with the 23 counts per second that we measured without the lock. Note that up to now, we used the $r_{\mathrm{o}}^2 = 80\%$ output coupler of the SPOPO cavity. Switching to $r_{\mathrm{o}}^2 = 50\%$ may allows us to reach a more relevant regime of purity and squeezing level for certification.

Generally speaking, a trade-off between high purity with low squeezing and low purity with high squeezing becomes relevant for the certification. To summarize, at high purity and relatively low squeezing (2 dB), the number of subtraction counts per second is lower but the fidelity to Fock state $|1\rangle$ is higher, so that the certification require less samples to beat the stellar rank threshold. Inversely, at lower purity and higher squeezing (e.g. 3 dB), the number of subtraction counts per second is higher but the number of required samples is a priori higher.

4.4.2 Preliminary results

After implementing the aforementioned changes, the output signal of the double homodyne detection is "cleaner" and sufficiently amplified to adequately retrieve the quadrature measurements from each homodyne. We give few locking cycles of raw acquisition in figure 4.10, for one homodyne detection (the output of the second one is similar). One can see that the locking cycle is clearly recognizable with a bipartite pattern: scattered points, the quadrature measurements, and oscillations of the LO-seed interference at the frequency of 60 kHz which corresponds to the modulation frequency of the seed beam.

[1] Writing the state as a mixture of a pure squeezed vacuum with vacuum, $a\,|\psi_\xi\rangle\langle\psi_\xi| + b\,|0\rangle\langle 0|$, the quadrature variances write $s^+_{\mathrm{dB}} = as + b$ and $s^-_{\mathrm{dB}} = a/s + b$, with $a + b = 1$ and $s = \mathrm{e}^{-2\zeta}$. We then deduce that the number of photons in this state is 0.5, close to the number of photons 0.54 in a 2 dB squeezed state.

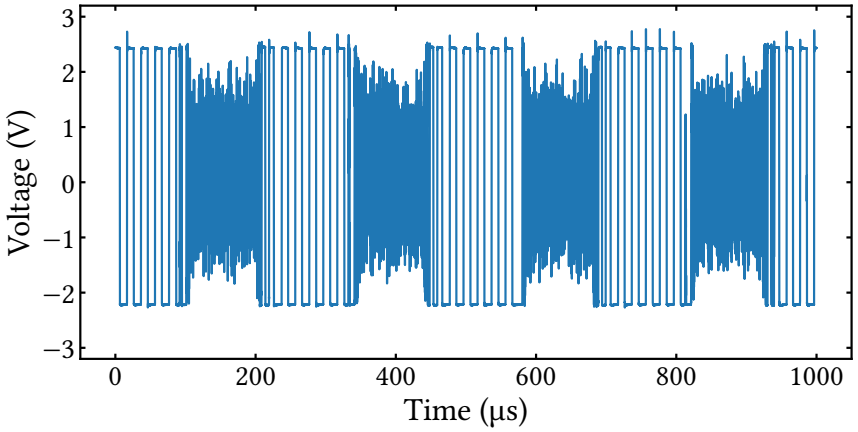

Fig. 4.10 Raw acquisition of the output signal of one homodyne detection for a squeezed vacuum state, during lock operation and using the clipper-amplifiers described in subsection 4.4.1.

Note that the trace given in figure 4.10 was taken without single-photon subtractions. In fact, we wouldn't be able to see the difference on the raw trace considering the low probability of the subtraction events (0.1%) and the non-trivial shape of the cavity temporal mode.

To retrieve a relevant Q function sampling from the completed set of data of figure 4.10, we first remove the data corresponding to the time slots where the LO-seed interference is measured. We are left with parts of data which we refer to as *data chunks*. Then, as we acquire over time, it contains all possible time-frequency modes within the detector bandwidth. As we saw in the previous subsection, the relevant temporal mode for a subtracted state is the cavity mode $\vec{\mathbf{f}}$ given by figure 4.8. We expect it to be also true for a squeezed vacuum state, as they both are generated initially from the SPOPO cavity. We then used the same idea to retrieve the cavity temporal mode: we compute the auto-correlation of the quadrature measurements $\overline{q(t_i)q(t_j)}$ for each pair t_i, t_j in the same data chunk, where $\bar{\cdot}$ denote the statistical average over all data chunks[1]. We then diagonalize the resulting auto-correlation matrix.

We also compute the auto-correlation matrix of using shot-noise measurements (with vacuum as input state). In the diagonal basis of the signal auto-correlation matrix, the diagonal of the vacuum auto-correlation matrix are then the vacuum variances in this basis, or shot-noise levels. We then rescale the diagonal signal matrix by these shot-noise levels. Finally, we determine the eigenmode of the signal matrix with the lowest eigenvalue (corresponding to the highest absolute squeezing factor).

We apply this temporal eigenmode on the initial data chunks, resulting in one quadrature measurement per chunk. Note that as we measure squeezed vacuum states, we do not have the constraint to select data at subtraction events, allowing for acquiring 1.6×10^6 quadrature measurements in about 3 seconds. Following the protocol given above in subsection 4.4.1, we can then build the histogram of the corresponding Q function. Preliminary results are given in figure 4.11, where we built the histogram of the sampled Q function of squeezed vacuum,

[1]In practice, we compute the auto-correlation over smaller chunks, with a temporal size ($\sim 1\,\mu s$) closer to the one of the expected temporal mode

using a balanced double homodyne detection.

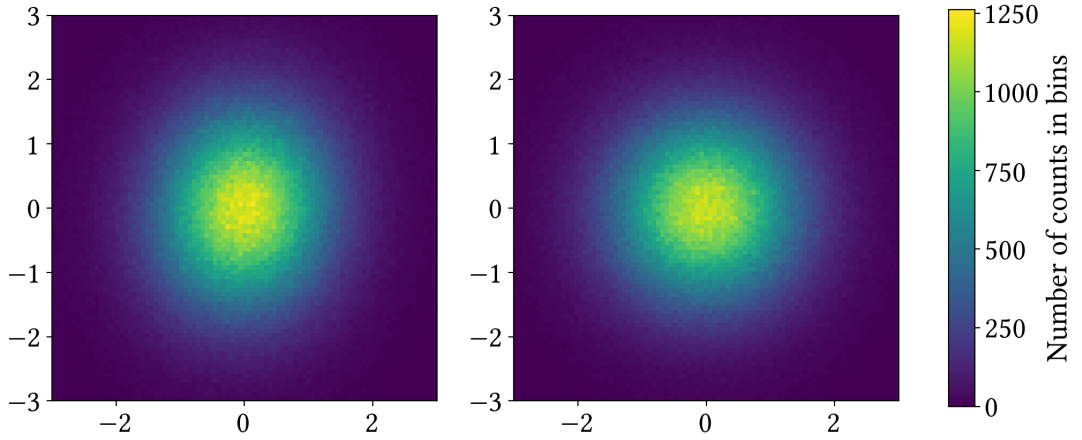

Fig. 4.11 2D histograms of the sampled Q function for squeezed vacuum (left) and vacuum (right) as input states, with $M = 1.6 \times 10^6$ samples. The pump power $\mathcal{P}_\mathrm{p}$ is set at 30 mW, and the SPOPO output reflectivity is $r_\mathrm{o}^2 = 80\%$. The inferred squeezing factor is 1.2 dB. These are preliminary results.

As I am writing these lines, we are still making progress for harnessing the double homodyne detection, coping with some random burst of electronic noise we observe in the data, and improving the stability of the optical lock. We estimate a squeezing factor of about 1.2 dB. This value is lower than what we would expect, at least 2 dB, from the measurements performed in subsection 2.5.3 while locking. This discrepancy suggests some noise is present in the electronic devices used for the measurement of figure 4.11 (in subsection 2.5.3, we were using a spectrum analyzer measuring at 1 MHz).

As soon as the issues left at hand are solved, we will be able to reliably sample the Q function of the generated states at subtraction events. We are then confident that certifying the quantum non-Gaussianity of the generated single-photon subtracted states is reachable in the short term.

Conclusion and outlook

Throughout the course of my doctorate, I worked with my research team on both theoretical and experimental fronts, each complementing the other, deepening our collective understanding of the central themes of our research.

In the purely theoretical side, we investigated the conditions for single-mode and mode-selective single-photon addition on a multimode field of light. This brought to light the nuances between photon addition and subtraction, further building upon the theoretical work already done within our group on both operations. Our findings suggest that the choice between subtraction or addition hinges significantly on the application at hand, given that each approach presents advantages and challenges. This relates to aspects like the Wigner negativity of the output state, or the purity of the output state with respect to the input state structure, number of photons, and purity. Our work opens up avenues for the experimental implementation of a single-photon addition on a multimode squeezed vacuum state. A promising extension of this work involves probing the conditions for single-mode and mode-selective addition in waveguides, such as lithium niobate ($LiNbO_3$) or potassium titanyl phosphate (KTP) waveguides.

I also had the opportunity to collaborate with researchers from the LiP6 laboratory, bridging their theoretical expertise with the experimental expertise of my group at LKB. Starting with the theoretical developments derived by Ulysse Chabaud on the stellar rank, the stellar hierarchy, and on continuous variable certification, we developed methods for certifying the generated states in our experiment. We derived an optimized fidelity estimation protocol with Fock target states, and exhibited the multiple benefits of using the double homodyne detection as a Q function sampler. This allowed us to bring the theory closer to experimental conditions, showing its feasibility in modern quantum optics laboratories with the support of realistic simulations.

Developing certification tools in our experimental group is interesting for two reasons. Firstly, it allows for reliable and legitimate claims on the properties of interest of the states we generate. Secondly, it positions our group more firmly within the quantum information field, equipping us better to respond to the burgeoning demand for certification in the context of the international race for building quantum computers.

Much of my doctoral journey was spent honing our experimental setup. For instance, we improved the multimode Gaussian state generation by better coping with the intra-cavity dispersion of the SPOPO, minimizing frequency-dependent losses in the cavity. We expect that this improvement will yield a broader distribution of supermodes with notable squeezing, thereby enhancing the overall multimodeness of the experiment.

We also built an optical phase lock and a double homodyne detection. The optical phase

lock fixes the phase between the reference beam and the signal beam at the detection, simplifying experimental protocols and facilitating data analysis. Furthermore, it opens up possibilities for new experimental protocols otherwise inaccessible, such as sampling the Q function of an asymmetric quantum state using double homodyne detection or applying the estimation protocol using an unbalanced double homodyne detection. To this end, we developed a double homodyne detection based on polarizing beam splitters, which guarantees the orthogonality of the two measured quadratures with high temporal stability. Preliminary results suggest that we are on the brink of certifying single-mode single-photon subtracted states.

Looking ahead, there are exciting opportunities to further extend this work. For instance, extending the functionality of the lock to arbitrary time-frequency modes could allow us to assess the squeezing distribution of the SPOPO under locking operation and prepare us for the certification of multimode states. This necessitates the evolution of our current single-mode double homodyne detector to a multimode variant. A promising candidate for initial multimode state certification could be a two-mode squeezed vacuum state conditioned on single-photon subtraction on one mode. When measured in a different mode basis than the one of the subtraction mode, this state transforms into a non-trivial entangled state with stellar rank 1. Lastly, promoting the single-photon subtraction to a two-photon subtraction would open up possibilities for the certification of stellar rank 2 states. If the two subtractions occur in the same mode for instance, then one would apply the estimation fidelity protocol with a Fock state $|2\rangle$. Else, if the two subtractions occur in different modes, the relevant target state is $|1\rangle \otimes |1\rangle$. In both cases, the protocol can certify the stellar rank 2 of the generated states, provided a high enough fidelity. This represents a significant milestone, whose achievement will further enrich our exploration and understanding of this fascinating field.

Appendices

Appendix A

Some mathematical tools

A.1 Hausdorff formula

In the manuscript, we often encounter operators $\hat{O}$ which writes in an exponential form as

$$\hat{O} = \exp\left(-c\hat{A}\right) \tag{A.1}$$

Its action on another operator $\hat{B}$ in the Heisenberg picture writes as

$$\hat{O}^\dagger \hat{B} \hat{O} = \mathrm{e}^{c\hat{A}} \hat{B} \mathrm{e}^{-c\hat{A}} \tag{A.2}$$

We can derive such action using the Hausdorff recursion formula [Fröhlich 77]

$$\mathrm{e}^{c\hat{A}} \hat{B} \mathrm{e}^{-c\hat{A}} = \hat{B} + c\left[\hat{A}, \hat{B}\right] + \frac{c^2}{2!}\left[\hat{A}, \left[\hat{A}, \hat{B}\right]\right] + \frac{c^3}{3!}\left[\hat{A}, \left[\hat{A}, \left[\hat{A}, \hat{B}\right]\right]\right] + \cdots \tag{A.3}$$

$$= \sum_{k=0}^{\infty} \frac{c^k}{k!} \{\{\hat{A}^k, \hat{B}\}\} \tag{A.4}$$

$$= \hat{B}_c \tag{A.5}$$

where $\{\{\hat{A}, \hat{B}\}\} = \left[\hat{A}, \hat{B}\right]$ and $\{\{\hat{A}^k, \hat{B}\}\} = \left[\hat{A}, \{\{\hat{A}^{k-1}, \hat{B}\}\}\right]$, and where we defined $\hat{B}_c$ the operator resulting from the action of $\mathrm{e}^{-c\hat{A}}$ on $\hat{B}$.

Computing $\hat{B}_c$ allows directly to infer the action on $\hat{B}^k$ with $k \in \mathbb{N}$ as

$$\mathrm{e}^{c\hat{A}} \hat{B}^k \mathrm{e}^{-c\hat{A}} = \hat{B}_c^k \tag{A.6}$$

from which we deduce the action on the operator $\exp\left(\hat{B}\right)$

$$\mathrm{e}^{c\hat{A}} \mathrm{e}^{\hat{B}} \mathrm{e}^{-c\hat{A}} = \mathrm{e}^{\hat{B}_c} \tag{A.7}$$

Interesting particular cases:

- If $\left[\hat{A}, \hat{B}\right] = K_1 \hat{B}$ with K_1 a scalar constant, then $\{\{\hat{A}^k, \hat{B}\}\} = K_1^k \hat{B}$ and

$$\mathrm{e}^{c\hat{A}} \hat{B} \mathrm{e}^{-c\hat{A}} = \mathrm{e}^{cK_1} \hat{B} \tag{A.8}$$

$$\mathrm{e}^{c\hat{A}} \mathrm{e}^{\hat{B}} \mathrm{e}^{-c\hat{A}} = \mathrm{e}^{\mathrm{e}^{cK_1} \hat{B}} \tag{A.9}$$

- If $\left[\hat{A},\hat{B}\right] = K_2\hat{\mathbb{1}}$ with K_2 a scalar constant, then $\{\{\hat{A}^k,\hat{B}\}\} = 0$ for $k \geq 2$ and

$$e^{c\hat{A}}\hat{B}e^{-c\hat{A}} = \hat{B} + cK_2\hat{\mathbb{1}} \tag{A.10}$$
$$e^{c\hat{A}}e^{\hat{B}}e^{-c\hat{A}} = e^{cK_2\hat{\mathbb{1}}}e^{\hat{B}} \tag{A.11}$$

  In particular, for $K_2 = 0$ and $c = 1$, we have that if $\left[\hat{A},\hat{B}\right] = 0$

$$e^{\hat{A}}e^{\hat{B}} = e^{\hat{B}}e^{\hat{A}} = e^{\hat{A}+\hat{B}} \tag{A.12}$$

Example: Let us consider the phase-space rotation operator $\hat{R}(\theta) = \exp\left(-i\theta\hat{a}^\dagger\hat{a}\right)$ defined in subsection 1.3.4.

Using $\left[\hat{a}^\dagger\hat{a},\hat{a}\right] = -\hat{a}$ and equation (A.8), we deduce

$$\hat{R}(\theta)^\dagger\hat{a}\hat{R}(\theta) = e^{-i\theta}\hat{a} \tag{A.13}$$
$$\hat{R}(\theta)^\dagger\hat{a}^\dagger\hat{R}(\theta) = e^{i\theta}\hat{a}^\dagger \tag{A.14}$$

from which we obtain

$$\hat{R}(\theta)^\dagger\hat{q}^{\theta_0}\hat{R}(\theta) = \hat{q}^{\theta_0+\theta} \tag{A.15}$$
$$\text{with} \quad \hat{q}^{\theta_0} = \sigma_0\hat{a}^\dagger e^{i\theta} + \sigma_0\hat{a}e^{-i\theta} \tag{A.16}$$

We can also straightforwardly obtain the action of $\hat{R}(\theta)$ on the displacement operator $\hat{D}(\alpha) = \exp\left(\alpha\hat{a}^\dagger - \alpha^*\hat{a}\right)$ as

$$\hat{R}(\theta)^\dagger\hat{D}(\alpha)\hat{R}(\theta) = \hat{D}(\alpha e^{i\theta}) \tag{A.17}$$

and on the squeezing operator $\hat{S}(\zeta) = \exp\left[\zeta^*\hat{a}^2/2 - \zeta\hat{a}^{\dagger 2}/2\right]$ with $\zeta \in \mathbb{C}$ as

$$\hat{R}(\theta)^\dagger\hat{S}(\zeta)\hat{R}(\theta) = \hat{S}(\zeta e^{2i\theta}) \tag{A.18}$$

A.2 Hermite-Gaussian functions

In the manuscript, we often encounter the "Hermite-Gaussian" functions. Let us give here their definition, and some interesting properties which makes them a well-defined time-frequency mode basis

First, we use the "physicist's" definition of the *Hermite polynomial* n, denoted $H_n(t)$, as

$$H_n(t) = (-1)^n e^{t^2}\frac{d^n}{dt^n}e^{-t^2} \tag{A.19}$$

for $n \in \mathbb{N}$.

In particular, the Hermite polynomial n is a polynomial of degree n, with leading coefficient 2^n, for $n \geq 0$.

The *Hermite-Gaussian function n*, denoted $\mathrm{HG}_n(t)$, is defined as the product of a Gaussian with the Hermite polynomial n, i.e.

$$\mathrm{HG}_n(t) = \left(2^n n! \sqrt{\pi}\right)^{-\frac{1}{2}} e^{-\frac{t^2}{2}} H_n(t) \tag{A.20}$$

for $n \in \mathbb{N}$.

The Hermite-Gaussian functions form an orthonormal basis of the square-integrable real functions, satisfying

$$\int_{-\infty}^{\infty} \mathrm{HG}_n(t)\mathrm{HG}_m(t) = \delta_{nm} \tag{A.21}$$

Furthermore, they are a set of eigenfunctions of the continuous Fourier transform $\mathscr{F}$, defined in the next appendix A.3, which writes

$$\mathscr{F}[\mathrm{HG}_n(t)](\omega) = (-\mathrm{i})^n \mathrm{HG}_n(\omega) \tag{A.22}$$

When we consider the Hermite-Gaussian functions $\mathrm{HG}_n(t)$ as time modes, the eigenvalue $(-\mathrm{i})^n$ doesn't play any role. In other words, the Fourier transform of the Hermite-Gaussian n time mode is the Hermite-Gaussian n frequency mode.

A.3 Fourier transform definition and properties

In the scope of this manuscript, we define the *Fourier transform* $\mathscr{F}$ with the following conventions

$$\mathscr{F}[f](\omega) = \int_{\mathbb{R}} \frac{\mathrm{d}t}{\sqrt{2\pi}} f(t)\mathrm{e}^{\mathrm{i}\omega t} \tag{A.23}$$

$$\mathscr{F}^{-1}[\tilde{f}](t) = \int_{\mathbb{R}} \frac{\mathrm{d}\omega}{\sqrt{2\pi}} \tilde{f}(\omega)\mathrm{e}^{-\mathrm{i}\omega t} \tag{A.24}$$

$$\text{with} \quad \tilde{f}(\omega) = \mathscr{F}[f](\omega) \quad \text{and} \quad f(t) = \mathscr{F}^{-1}[\tilde{f}](t)$$

Note the sign in the exponential is opposite to the most standard convention, this is to be consistent with the definition of the analytical field of chapter 1 in which the positive frequency components oscillate with a $\mathrm{e}^{-\mathrm{i}\omega t}$ factor.

Useful properties of the Fourier transform are given in table A.1, where $\cdot \otimes \cdot$ denotes the convolution, defined for any two functions f and g as

$$f \otimes g(x) = \int_{\mathbb{R}} f(x' - x)g(x)\,\mathrm{d}x' = \int_{\mathbb{R}} f(x')g(x - x')\,\mathrm{d}x' \tag{A.25}$$

Some typical example of Fourier transform results are given in table A.2,
with the following definition of the Dirac comb Ш

$$\text{Ш}_X(x) = \sum_{k=-\infty}^{+\infty} \delta(x - kX) \tag{A.26}$$

$$
\begin{array}{c}
\mathscr{F}[f^*](\omega) = (\mathscr{F}[f](-\omega))^* \\
\mathscr{F}[f(t-t_0)](\omega) = \mathrm{e}^{\mathrm{i}\omega t_0}\tilde{f}(\omega) \\
\mathscr{F}^{-1}[\tilde{f}(\omega-\omega_0)](t) = \mathrm{e}^{-\mathrm{i}\omega_0 t} f(t) \\
\mathscr{F}[f(t)\mathrm{e}^{-\mathrm{i}\omega_0 t}](\omega) = \tilde{f}(\omega-\omega_0) \\
\mathscr{F}^{-1}[\tilde{f}(\omega)\mathrm{e}^{-\mathrm{i}\omega t_0}](t) = f(t+t_0) \\
\mathscr{F}[f\times g] = \frac{1}{\sqrt{2\pi}}\mathscr{F}[f]\otimes\mathscr{F}[g] \\
\mathscr{F}[f\otimes g] = \sqrt{2\pi}\mathscr{F}[f]\times\mathscr{F}[g]
\end{array}
$$

Table A.1: Fourier transform properties.

$$
\begin{array}{c}
\mathscr{F}[1](\omega) = \sqrt{2\pi}\delta(\omega) \\
\mathscr{F}[\mathrm{e}^{-\mathrm{i}\omega_0 t}](\omega) = \sqrt{2\pi}\delta(\omega-\omega_0) \\
\mathscr{F}[\text{Ш}_T(t)](\omega) = \frac{\sqrt{2\pi}}{T}\,\text{Ш}_{\frac{2\pi}{T}}(\omega)
\end{array}
$$

Table A.2: Fourier transform examples.

or equivalently

$$
\text{Ш}_X(x) = \frac{1}{X}\sum_{k=-\infty}^{+\infty} \mathrm{e}^{\mathrm{i}2\pi kx/X} \tag{A.27}
$$

As an illustrative application, we prove that the Fourier transform of the train of pulses given in equation (2.2) yields the frequency comb given in equation (2.7).

$$
\mathscr{F}\left[\mathbf{E}^{(+)}(t)\right](\omega) = \mathscr{F}\left[\mathcal{A}\sum_{k\in\mathbb{Z}}\mathbf{h}(t-kT_\mathrm{r})\,\mathrm{e}^{-\mathrm{i}\omega_0(t-kT_\mathrm{r})}\mathrm{e}^{-\mathrm{i}k\Delta\phi_\mathrm{CEP}}\right](\omega) \tag{A.28}
$$

$$
= \frac{\mathcal{A}}{\sqrt{2\pi}}\sum_k \mathrm{e}^{-\mathrm{i}k\Delta\phi_\mathrm{CEP}}\left(\underbrace{\mathscr{F}[\mathbf{h}(t-kT_\mathrm{r})]}_{\widetilde{\mathbf{h}}(\omega)\mathrm{e}^{\mathrm{i}\omega kT_\mathrm{r}}}\right)\otimes\left(\underbrace{\mathscr{F}[\mathrm{e}^{-\mathrm{i}\omega_0(t-kT_\mathrm{r})}]}_{\sqrt{2\pi}\delta(\omega-\omega_0)\mathrm{e}^{\mathrm{i}\omega kT_\mathrm{r}}}\right)(\omega) \tag{A.29}
$$

$$
= \mathcal{A}\sum_k \mathrm{e}^{-\mathrm{i}k\Delta\phi_\mathrm{CEP}}\int \mathrm{d}\omega'\,\widetilde{\mathbf{h}}(\omega-\omega')\mathrm{e}^{\mathrm{i}(\omega-\omega')kT_\mathrm{r}}\delta(\omega'-\omega_0)\mathrm{e}^{\mathrm{i}\omega' kT_\mathrm{r}} \tag{A.30}
$$

$$
= \mathcal{A}\,\widetilde{\mathbf{h}}(\omega-\omega_0)\sum_k \mathrm{e}^{-\mathrm{i}k\Delta\phi_\mathrm{CEP}}\mathrm{e}^{\mathrm{i}\omega' kT_\mathrm{r}} \tag{A.31}
$$

where we used the linearity of $\mathscr{F}$ and tables A.1 and A.2 in the second line, and formula (A.25) in the third line.

Writing $\omega_\mathrm{CEO} = \Delta\phi_\mathrm{CEP}/T_\mathrm{r}$, we re-write equation (A.31) as

$$
\mathscr{F}\left[\mathbf{E}^{(+)}\right](\omega) = \mathcal{A}\widetilde{\mathbf{h}}(\omega-\omega_0)\sum_k \mathrm{e}^{\mathrm{i}kT_\mathrm{r}(\omega-\omega_\mathrm{CEO})} \tag{A.32}
$$

where we recognize up to a factor the Dirac comb formula (A.27) with parameter $X = \frac{2\pi}{T_\mathrm{r}}$ and argument $x = \omega - \omega_\mathrm{CEO}$.

We then obtain

$$\mathscr{F}\left[\mathbf{E}^{(+)}\right](\omega) = \frac{2\pi}{T_\mathrm{r}} \mathcal{A}\widetilde{\mathbf{h}}(\omega - \omega_0)\, \text{Ш}_{\frac{2\pi}{T_\mathrm{r}}}(\omega - \omega_{\mathrm{CEO}}) \tag{A.33}$$

which equivalently writes, using equation (A.26), as

$$\mathscr{F}\left[\mathbf{E}^{(+)}\right](\omega) = \omega_\mathrm{r} \mathcal{A}\, \widetilde{\mathbf{h}}(\omega - \omega_0) \sum_{k\in\mathbb{Z}} \delta(\omega - k\omega_\mathrm{r} - \omega_{\mathrm{CEO}}) \tag{A.34}$$

with $\omega_\mathrm{r} = \frac{2\pi}{T_\mathrm{r}}$, which concludes the proof.

Appendix B

Proofs

B.1 Basis change operation consistency

In this appendix, we show the consistency of the definition (1.7) of the mode basis change with its action (1.14) on the operators, together with the Heisenberg picture.

In the plane wave basis, the quantum electric field operator writes

$$\hat{\vec{\mathbf{E}}}^{(+)} = \mathcal{E}_0 \sum_\ell \hat{a}_\ell \vec{\mathbf{u}}_\ell \tag{B.1}$$

where $\{\hat{a}_\ell\}$ are the annihilation operators associated to the modes $\{\vec{\mathbf{u}}_\ell\}$.

We consider the change of mode basis $\hat{U}$ from $\{\vec{\mathbf{u}}_\ell\}$ to $\{\vec{\mathbf{g}}_n\}$, defined as

$$\vec{\mathbf{g}}_n = \sum_n \mathbf{U}_{n\ell} \vec{\mathbf{u}}_\ell \tag{B.2}$$

with $\mathbf{U}$ the unitary matrix associated to $\hat{U}$.

We want to find the unitary operator $\hat{A}$ whose action maps any operator from the mode basis $\{\vec{\mathbf{u}}_\ell\}$ to the new mode basis $\{\vec{\mathbf{g}}_n\}$. In the Heisenberg picture, the action of $\hat{A}$ maps the operators $\{\hat{a}_\ell\}$ to the operators $\{\hat{b}_n\}$ associated to the modes $\{\vec{\mathbf{g}}_n\}$ as

$$\begin{aligned} \hat{A}^\dagger \hat{\vec{a}}^\dagger \hat{A} &= \mathbf{A}\, \hat{\vec{b}}^\dagger \\ \hat{A}^\dagger \hat{\vec{a}} \hat{A} &= \mathbf{A}^* \hat{\vec{b}} \end{aligned} \tag{B.3}$$

where $\mathbf{A}$ is the unitary matrix representing $\hat{A}$. The left-hand side of equation (B.3) is a column vector of i-th component $\hat{A}^\dagger \hat{a}_i^\dagger \hat{A}$.

We compute the quantum electric field operator in the new basis as

$$\hat{A}^\dagger \vec{\hat{\mathbf{E}}}^{(+)} \hat{A} = \mathcal{E}_0 \sum_\ell \hat{A}^\dagger \hat{a}_\ell \hat{A} \vec{\mathbf{u}}_\ell \tag{B.4}$$

$$= \mathcal{E}_0 \sum_\ell \left(\sum_n \mathbf{A}^*_{\ell n} \hat{b}_n \right) \vec{\mathbf{u}}_\ell \tag{B.5}$$

$$= \mathcal{E}_0 \sum_n \hat{b}_n \left(\sum_\ell \mathbf{A}^*_{\ell n} \vec{\mathbf{u}}_\ell \right) \tag{B.6}$$

$\left\{ \sum_\ell \mathbf{A}^*_{\ell n} \vec{\mathbf{u}}_\ell \right\}$ defines an orthonormal mode basis. To be consistent with the definition of the operators $\{\hat{b}_n\}$ as associated to the modes $\{\vec{\mathbf{g}}_n\}$, we deduce that for all n

$$\sum_\ell \mathbf{A}^*_{\ell n} \vec{\mathbf{u}}_\ell = \vec{\mathbf{g}}_n \tag{B.7}$$

From equation (B.2), this implies

$$\sum_\ell \mathbf{A}^*_{\ell n} \vec{\mathbf{u}}_\ell = \sum_n \mathbf{U}_{n\ell} \vec{\mathbf{u}}_\ell \tag{B.8}$$

i.e. $\mathbf{A} = \mathbf{U}^{-1}$ $(= \mathbf{U}^{*\top})$.

We deduce that the operator $\hat{U}^\dagger$ maps the operators from the mode basis $\{\vec{\mathbf{u}}_\ell\}$ to the mode basis $\{\vec{\mathbf{g}}_n\}$, while the operator $\hat{U}$ maps the quantum states from $\{\vec{\mathbf{u}}_\ell\}$ to $\{\vec{\mathbf{g}}_n\}$.

We then have

$$\hat{U} \vec{\hat{a}}^\dagger \hat{U}^\dagger = \mathbf{U}^{-1} \vec{\hat{b}}^\dagger \tag{B.9}$$

$$\hat{U}^\dagger \vec{\hat{b}}^\dagger \hat{U} = \mathbf{U} \vec{\hat{a}}^\dagger \tag{B.10}$$

and for any multimode quantum state $|\psi\rangle$ (see section 1.2 for their definition)

$$\hat{U} |\psi\rangle_{\{\vec{\mathbf{u}}_\ell\}} = |\psi'\rangle_{\{\vec{\mathbf{g}}_n\}} \tag{B.11}$$

where we explicitly write in which basis the states are written.

From equation (B.6), we obtain the quantum electric field written in the new mode basis[1]

$$\vec{\hat{\mathbf{E}}}^{(+)} = \mathcal{E}_0 \sum_n \hat{b}_n \vec{\mathbf{g}}_n \tag{B.12}$$

Note that are consistent with the Heisenberg picture. In the Heisenberg picture, the action of an operator $\hat{U}$ on the state $|\psi(0)\rangle$ as

$$\hat{U} |\psi(0)\rangle = |\psi(t)\rangle \tag{B.13}$$

[1]For simplicity, we keep the same symbol $\vec{\hat{\mathbf{E}}}^{(+)}$ to represent the quantum electric field in the new basis, as we always specify in which basis it is written.

is mapped on the action of $\hat{U}$ on any operator $\hat{B}$ as

$$\hat{B}(t) = \hat{U}^\dagger \hat{B} \hat{U} \tag{B.14}$$

since both actions conserves any expectation-value

$$\langle\psi(t)| \hat{B}(t) |\psi(t)\rangle = \langle\psi(0)| \hat{U}^\dagger \hat{B} \hat{U} |\psi(0)\rangle \tag{B.15}$$

For the mode basis change $\hat{U}$ from $\{\vec{\mathbf{u}}_\ell\}$ to $\{\vec{\mathbf{g}}_n\}$

$$|\psi(0)\rangle = |\psi\rangle_{\{\vec{\mathbf{u}}_\ell\}} \tag{B.16}$$
$$|\psi(t)\rangle = |\psi'\rangle_{\{\vec{\mathbf{g}}_n\}} \tag{B.17}$$

consistently with equation (B.11). As the operators $\{\hat{b}_n^\dagger\}$ are associated to the modes $\{\vec{\mathbf{g}}_n\}$, they act on the states $|\psi\rangle_{\{\vec{\mathbf{g}}_n\}}$. So we have

$$\langle\psi(t)| \vec{\hat{b}}^\dagger |\psi(t)\rangle = \langle\psi(0)| \hat{U}^\dagger \vec{\hat{b}}^\dagger \hat{U} |\psi(0)\rangle \tag{B.18}$$

using equation (B.13). From the action (B.10) of $\hat{U}$ on $\vec{\hat{b}}^\dagger$, we find

$$\langle\psi(t)| \vec{\hat{b}}^\dagger |\psi(t)\rangle = \langle\psi(0)| \mathbf{U} \vec{\hat{a}}^\dagger |\psi(0)\rangle \tag{B.19}$$

which is consistent with the operators $\{\hat{a}_\ell^\dagger\}$ being associated to the modes $\{\vec{\mathbf{u}}_\ell\}$, as they act on the state $|\psi(0)\rangle = |\psi\rangle_{\{\vec{\mathbf{u}}_\ell\}}$.

To conclude, we then have shown the consistency of the above defined mode basis change $\hat{U}$ between its action on the states, its action on the operators, and its action on the modes themselves.

B.2 Single-photon subtracted and added squeezed vacuum states Q function

In this appendix, we derive the Q function of a single-photon subtracted and added squeezed vacuum state in the multimode and potentially mixed state, see appendix B.2.1. We then generalize this derivation to model additional losses (such as detection losses) and a squeezing operation applied on a single-photon subtracted and added squeezed vacuum state. These generalized Q functions are used in the simulation of chapter 4, section 4.3. Finally, we check they are positive in appendix B.2.2, showing in particular some relevant inequalities used in subsection 1.4.4 to discuss the zeros of the Q functions.

B.2.1 Derivation

We derive the Q function of a single-photon subtracted and added squeezed vacuum state in the multimode and potentially mixed state, from the Wigner function of these states given in

equation (1.152), and reproduce here

$$W_{\hat{\rho}^{\pm}}(\vec{x}) = \frac{1}{2}\left[\vec{x}^{\top}\mathbf{V}^{-1}\mathbf{A}^{\pm}(\mathbf{V},\vec{\mathbf{g}})\mathbf{V}^{-1}\vec{x} - \mathrm{Tr}\left[\mathbf{V}^{-1}\mathbf{A}^{\pm}(\mathbf{V},\vec{\mathbf{g}})\right] + 2\right]\frac{\mathrm{e}^{-\frac{1}{2}\vec{x}^{\top}\mathbf{V}^{-1}\vec{x}}}{(2\pi\sigma_0^2)^N\sqrt{\det\mathbf{V}}} \tag{B.20}$$

$$\text{and}\quad \mathbf{A}^{\pm}(\mathbf{V},\vec{\mathbf{g}}) = 2\frac{(\mathbf{V}\pm\sigma_0^2\mathbb{1})\mathbf{\Pi}_{\vec{\mathbf{g}}}(\mathbf{V}\pm\sigma_0^2\mathbb{1})}{\mathrm{Tr}\left[(\mathbf{V}\pm\sigma_0^2\mathbb{1})\mathbf{\Pi}_{\vec{\mathbf{g}}}\right]} \tag{B.21}$$

where $\hat{\rho}$ is a zero-mean Gaussian state and $\mathbf{\Pi}_{\vec{\mathbf{g}}}$ is the matrix of the projector on the two-dimensional phase space associated with the mode $\vec{\mathbf{g}}$ in which the photon was subtracted/added.

Note that when the single-photon subtraction/addition is not single mode, then the projector $\mathbf{\Pi}_{\vec{\mathbf{g}}}$ is replaced by a sum of projector on the possible subtraction/addition modes, weighted by their respective probability, see chapter 3, equations (3.70) and (3.71).

We use equation (1.47) to deduce the corresponding Q function $\mathrm{Q}_{\hat{\rho}^{\pm}}(\vec{x})$, which then writes

$$\mathrm{Q}_{\hat{\rho}^{\pm}}(\vec{x}) = \frac{1}{(2\pi\sigma_0^2)^N}\int_{\mathbb{R}^{2N}} W_{\hat{\rho}^{\pm}}(\vec{x}')\,\mathrm{e}^{-\frac{1}{2\sigma_0^2}\|\vec{x}'-\vec{x}\|^2}\,\mathrm{d}^{2N}\vec{x}' \tag{B.22}$$

$$= \frac{1}{c}\int_{\mathbb{R}^{2N}}\left[\vec{x}^{\top\prime}\mathbf{V}^{-1}\mathbf{A}^{\pm}(\mathbf{V},\vec{\mathbf{g}})\mathbf{V}^{-1}\vec{x}' - \mathrm{Tr}\left[\mathbf{V}^{-1}\mathbf{A}^{\pm}(\mathbf{V},\vec{\mathbf{g}})\right] + 2\right]\mathrm{e}^{-\frac{1}{2}\vec{x}^{\top\prime}\mathbf{V}^{-1}\vec{x}'-\frac{1}{2\sigma_0^2}\|\vec{x}'-\vec{x}\|^2}\,\mathrm{d}^{2N}\vec{x}' \tag{B.23}$$

where the constant c is equal to $2(2\pi\sigma_0^2)^{2N}\sqrt{\det\mathbf{V}}$.

Computing equation (B.23) boils down to integrate a second order polynomial multiplied by a $2N$-variable Gaussian function. Generally speaking, the integration of a $2N$-variable Gaussian function alone writes

$$\int_{\mathbb{R}^{2N}}\mathrm{e}^{-\frac{1}{2}(\vec{x}'-\vec{\delta})^{\top}\Sigma^{-1}(\vec{x}'-\vec{\delta})}\,\mathrm{d}^{2N}\vec{x}' = (2\pi)^N\sqrt{\det(\Sigma)} \tag{B.24}$$

where $\vec{\delta}$ is a constant $2N$-real vector, and Σ is a $2N\times 2N$ real matrix.

More generally, the integration of the product of a squared term $(\vec{x}^{\top}\mathbf{M}\vec{x})$ with a $2N$-variable Gaussian function, where $\mathbf{M}$ is a general $2N\times 2N$ real matrix, writes

$$\int_{\mathbb{R}^{2N}}\vec{x}'^{\top}\mathbf{M}\,\vec{x}'\,\mathrm{e}^{-\frac{1}{2}(\vec{x}'-\vec{\delta})^{\top}\Sigma^{-1}(\vec{x}'-\vec{\delta})}\,\mathrm{d}^{2N}\vec{x}' = (2\pi)^N\sqrt{\det(\Sigma)}\left(\mathrm{Tr}[\mathbf{M}\Sigma] + \vec{\delta}^{\top}\mathbf{M}\,\vec{\delta}\right) \tag{B.25}$$

We then re-write the argument of the $2N$-variable Gaussian so as to accommodate both equations as

$$-\frac{1}{2}\left\{\left[\vec{x}' - \tfrac{1}{\sigma_0^2}(\mathbf{V}^{-1}+\tfrac{1}{\sigma_0^2}\mathbb{1})^{-1}\vec{x}\right]^{\top}(\mathbf{V}^{-1}+\tfrac{1}{\sigma_0^2}\mathbb{1})\left[\vec{x}' - \tfrac{1}{\sigma_0^2}(\mathbf{V}^{-1}+\tfrac{1}{\sigma_0^2}\mathbb{1})^{-1}\vec{x}\right] + \vec{x}^{\top}(\mathbf{V}+\sigma_0^2\mathbb{1})^{-1}\vec{x}\right\} \tag{B.26}$$

where in particular we computed $\frac{1}{\sigma_0^2}\mathbb{1} - \frac{1}{\sigma_0^4}(\mathbf{V}^{-1}+\frac{1}{\sigma_0^2}\mathbb{1})^{-1} = (\mathbf{V}+\sigma_0^2\mathbb{1})^{-1}$.

First, the right-most term in the argument (B.26) is independent of the integration variable $\vec{x}'$, allowing us to put its exponential outside of the integral. Then the remaining term in equation (B.26) is of the form

$$-\frac{1}{2}(\vec{x}'-\vec{\delta})^{\top}\Sigma^{-1}(\vec{x}'-\vec{\delta}) \tag{B.27}$$

$$\text{with}\quad \vec{\delta} = \tfrac{1}{\sigma_0^2}(\mathbf{V}^{-1}+\tfrac{1}{\sigma_0^2}\mathbb{1})^{-1}\vec{x}\quad\text{and}\quad \Sigma = (\mathbf{V}^{-1}+\tfrac{1}{\sigma_0^2}\mathbb{1})^{-1}$$

With this expression, we can already deduce the integral of the $2N$-variable Gaussian function which multiplies a constant in equation (B.23), using equation (B.24). Finally, identifying the squared term $\vec{x}^\top \mathbf{M}\vec{x}$ with $\mathbf{M} = \mathbf{V}^{-1}\mathbf{A}^{\pm}(\mathbf{V},\vec{\mathbf{g}})\mathbf{V}^{-1}$, we can also apply equation (B.25). After some calculus, I obtain

$$\mathrm{Q}_{\hat{\rho}^{\pm}}(\vec{x}) = \begin{cases} \left[\vec{x}^\top(\mathbf{V}+\sigma_0^2\mathbb{1})^{-1}\mathbf{A}^{\pm}(\mathbf{V},\vec{\mathbf{g}})(\mathbf{V}+\sigma_0^2\mathbb{1})^{-1}\vec{x} - \mathrm{Tr}\left[(\mathbf{V}+\sigma_0^2\mathbb{1})^{-1}\mathbf{A}^{\pm}(\mathbf{V},\vec{\mathbf{g}})\right] + 2\right] \\ \times \dfrac{\mathrm{e}^{-\frac{1}{2}\vec{x}^\top(\mathbf{V}+\sigma_0^2\mathbb{1})^{-1}\vec{x}}}{2(2\pi\sigma_0^2)^N\sqrt{\det(\mathbf{V}+\sigma_0^2\mathbb{1})}} \end{cases} \tag{B.28}$$

Noting that equation (B.20) gives the Wigner function of the Gaussian state $\hat{\rho}$ when replacing $\mathbf{A}^{\pm}(\mathbf{V},\vec{\mathbf{g}})$ by the null matrix $\mathbf{0}$, we deduce that we can straightforwardly obtain the Q function of a general Gaussian state following the same steps. We then rewrite equation (B.28) as

$$\mathrm{Q}_{\hat{\rho}^{\pm}}(\vec{x}) = \tfrac{1}{2}\left[\vec{x}^\top(\mathbf{V}+\sigma_0^2\mathbb{1})^{-1}\mathbf{A}^{\pm}(\mathbf{V},\vec{\mathbf{g}})(\mathbf{V}+\sigma_0^2\mathbb{1})^{-1}\vec{x} - \mathrm{Tr}\left[(\mathbf{V}+\sigma_0^2\mathbb{1})^{-1}\mathbf{A}^{\pm}(\mathbf{V},\vec{\mathbf{g}})\right] + 2\right]\mathrm{Q}_{\hat{\rho}}(\vec{x}) \tag{B.29}$$

$$\text{with} \quad \mathrm{Q}_{\hat{\rho}}(\vec{x}) = \frac{\mathrm{e}^{-\frac{1}{2}\vec{x}^\top(\mathbf{V}+\sigma_0^2\mathbb{1})^{-1}\vec{x}}}{(2\pi\sigma_0^2)^N\sqrt{\det(\mathbf{V}+\sigma_0^2\mathbb{1})}} \tag{B.30}$$

where equation (B.30) provides with the general formula for the Q function of a Gaussian state.

Extension to additional losses. In chapter 4, section 4.3, the Q function $\mathrm{Q}_{\hat{\rho}^{\pm}}(\vec{x})$ of equation (B.29) models the generated state just after single-photon subtraction. In order to model a lossy double homodyne detector, we take into account the detection losses $1-\eta$ that occur after subtraction. We use equation (4.94), which we reproduce here

$$Q_{\hat{\rho}_\eta^{\pm}}(\vec{x}) = \frac{1}{\eta^N} W^u_{\hat{\rho}^{\pm}}(\vec{x}/\sqrt{\eta}) \tag{B.31}$$

where $u = 1 - \frac{2}{\eta} \leq 1$, and $W^u_{\hat{\rho}^{\pm}}(\vec{x})$ is given by

$$W^u_{\hat{\rho}^{\pm}}(\vec{x}) = \left(\frac{-1}{2\pi\sigma_0^2 u}\right)^N \int_{\mathbb{R}^{2N}} W_{\hat{\rho}^{\pm}}(\vec{x}')\,\mathrm{e}^{\frac{1}{2\sigma_0^2 u}\left\|\vec{x}'-\vec{x}\right\|^2}\,\mathrm{d}^{2N}\vec{x}' \tag{B.32}$$

which is equation (1.40) applied for $u' = 0$, which satisfies $u \leq u'$. We made this choice to make the Wigner function $W_{\hat{\rho}^{\pm}}(\vec{x}')$ appear, and to quickly resume to the same calculus as before.

Injecting the expression of $W_{\hat{\rho}^{\pm}}(\vec{x}')$ in equation (B.32) results in a similar expression as in equation (B.23), i.e. the integral of the product of second order $2N$-variable polynomial with a $2N$-variable Gaussian function. We can then apply the same methodology[1], and, upon

[1]Note to the reader who would like to check the computation, I re-named the variables as $r = -1/u$ ($r > 0 \forall \eta$), $\vec{y} = \sqrt{r}\vec{x}$, $\mathbf{V}' = r\mathbf{V}$, and made the change of variable $\vec{y}' = \sqrt{r}\vec{x}'$. The derivation is then very similar as before, using equations (B.24) and (B.25).

applying the rescaling of equation (B.31), I obtain

$$\mathrm{Q}_{\hat{\rho}_\eta^\pm}(\vec{x}) = \begin{cases} \left[\frac{1}{\eta}\vec{x}^\top(\mathbf{V}-u\sigma_0^2\mathbb{1})^{-1}\mathbf{A}^\pm(\mathbf{V},\vec{\mathbf{g}})(\mathbf{V}-u\sigma_0^2\mathbb{1})^{-1}\vec{x} - \mathrm{Tr}\left[(\mathbf{V}-u\sigma_0^2\mathbb{1})^{-1}\mathbf{A}^\pm(\mathbf{V},\vec{\mathbf{g}})\right] + 2\right] \\ \times \dfrac{\mathrm{e}^{-\frac{1}{2\eta}\vec{x}^\top(\mathbf{V}-u\sigma_0^2\mathbb{1})^{-1}\vec{x}}}{4\eta\pi\sigma_0^2\sqrt{\det(\mathbf{V}-u\sigma_0^2\mathbb{1})}} \end{cases} \tag{B.33}$$

Extension to squeezing operation. In chapter 4, section 4.3, we also want to model the effect of unbalancing in the double homodyne detection. This unbalancing is equivalent to apply a action of the squeezing operator $\hat{S}^{\otimes N}(\vec{\zeta})$ on the state $\hat{\rho}^\pm$ before sampling its Q function with a lossy double homodyne detector, where

$$\hat{S}^{\otimes N}(\vec{\zeta}) = \bigotimes_{i=1}^{N} \hat{S}(\zeta_i) \tag{B.34}$$

We denote by $\hat{\rho}^\pm_{\vec{\zeta},\eta}$ the resulting state. Taking into account the losses $1-\eta$ similarly as before, the Q function we want to compute here is then given by

$$\mathrm{Q}_{\hat{\rho}^\pm_{\vec{\zeta},\eta}}(\vec{x}) = \frac{1}{\eta^N} W^u_{\hat{S}^{\otimes N}(\vec{\zeta})\hat{\rho}^\pm\hat{S}^{\otimes N}(\vec{\zeta})}(\vec{x}/\sqrt{\eta}) \tag{B.35}$$

$$W^u_{\hat{S}^{\otimes N}(\vec{\zeta})\hat{\rho}^\pm\hat{S}^{\otimes N}(\vec{\zeta})}(\vec{x}) = \left(\frac{-1}{2\pi\sigma_0^2 u}\right)^N \int_{\mathbb{R}^{2N}} W_{\hat{S}^{\otimes N}(\vec{\zeta})\hat{\rho}^\pm\hat{S}^{\otimes N}(\vec{\zeta})}(\vec{x}')\, \mathrm{e}^{\frac{1}{2\sigma_0^2 u}\left\|\vec{x}'-\vec{x}\right\|^2} \mathrm{d}^{2N}\vec{x}' \tag{B.36}$$

where $u = 1 - \frac{2}{\eta} \leq 1$.

To compute the Wigner function $W_{\hat{S}^{\otimes N}(\vec{\zeta})\hat{\rho}^\pm\hat{S}^{\otimes N}(\vec{\zeta})}(\vec{x}')$, we use at our advantage the fact that in general for the Wigner function, the action of the Gaussian operator $\hat{S}^{\otimes N}(\vec{\zeta})$ on the state $\hat{\rho}^\pm$ is equivalent to the symplectic stretching/contraction on the $2N$ phase space, stemming from equation (1.85). Denoting $\mathbf{K}$ the symplectic matrix of $\hat{S}^{\otimes N}(\vec{\zeta})$ (given in equation (1.93)), we obtain

$$W_{\hat{S}^{\otimes N}(\vec{\zeta})\hat{\rho}^\pm\hat{S}^{\otimes N}(\vec{\zeta})^\dagger}(\vec{x}') = W_{\hat{\rho}^\pm}(\mathbf{K}^{-1}\vec{x}') \tag{B.37}$$

Using the expression (B.37) in equation (B.36), we then proceed to the same derivation as before. To make it straightforward, one can notice that the terms that changed compared to before can be written as follow

$$(\mathbf{K}^{-1}\vec{x}')^\top\mathbf{V}^{-1}\mathbf{A}^\pm(\mathbf{V},\vec{\mathbf{g}})\mathbf{V}^{-1}\mathbf{K}^{-1}\vec{x}' = \vec{x}^{\top\prime}\mathbf{V}'^{-1}\mathbf{A}^{\pm\prime}(\mathbf{V},\vec{\mathbf{g}})\mathbf{V}'^{-1}\vec{x}' \tag{B.38}$$

$$\exp\left(-\frac{1}{2}(\mathbf{K}^{-1}\vec{x}')^\top\mathbf{V}^{-1}\mathbf{K}^{-1}\vec{x}'\right) = \exp\left(-\frac{1}{2}\vec{x}^{\top\prime}\mathbf{V}'^{-1}\vec{x}'\right) \tag{B.39}$$

$$\mathrm{Tr}\left[\mathbf{V}^{-1}\mathbf{A}^\pm(\mathbf{V},\vec{\mathbf{g}})\right] = \mathrm{Tr}\left[\mathbf{V}'^{-1}\mathbf{A}^{\pm\prime}(\mathbf{V},\vec{\mathbf{g}})\right] \tag{B.40}$$

$$\text{with} \quad \mathbf{A}^{\pm\prime}(\mathbf{V},\vec{\mathbf{g}}) = \mathbf{K}\,\mathbf{A}^\pm(\mathbf{V},\vec{\mathbf{g}})\,\mathbf{K} \quad \text{and} \quad \mathbf{V}' = \mathbf{K}\,\mathbf{V}\,\mathbf{K}$$

This means in particular that the calculus is exactly upon replacing the covariance matrix $\mathbf{V}$ by $\mathbf{V}' = \mathbf{K}\,\mathbf{V}\,\mathbf{K}$ and the matrix $\mathbf{A}^{\pm}(\mathbf{V},\vec{\mathbf{g}})$ by $\mathbf{A}^{\pm\prime}(\mathbf{V},\vec{\mathbf{g}}) = \mathbf{K}\,\mathbf{A}^{\pm}(\mathbf{V},\vec{\mathbf{g}})\,\mathbf{K}$. We then directly deduce

$$\mathrm{Q}_{\hat{\rho}^{\pm}_{\vec{\zeta},\eta}}(\vec{x}) = \begin{cases} \left[\dfrac{1}{\eta}\vec{x}^{\top}(\mathbf{V}'-u\sigma_0^2\mathbb{1})^{-1}\mathbf{A}^{\pm\prime}(\mathbf{V},\vec{\mathbf{g}})(\mathbf{V}'-u\sigma_0^2\mathbb{1})^{-1}\vec{x} - \mathrm{Tr}\left[(\mathbf{V}'-u\sigma_0^2\mathbb{1})^{-1}\mathbf{A}^{\pm\prime}(\mathbf{V},\vec{\mathbf{g}})\right] + 2\right] \\ \times \dfrac{\mathrm{e}^{-\frac{1}{2\eta}\vec{x}^{\top}(\mathbf{V}'-u\sigma_0^2\mathbb{1})^{-1}\vec{x}}}{4\eta\pi\sigma_0^2\sqrt{\det(\mathbf{V}'-u\sigma_0^2\mathbb{1})}} \end{cases} \tag{B.41}$$

$$\text{with} \quad \mathbf{A}^{\pm\prime}(\mathbf{V},\vec{\mathbf{g}}) = \mathbf{K}\,\mathbf{A}^{\pm}(\mathbf{V},\vec{\mathbf{g}})\,\mathbf{K} \quad \text{and} \quad \mathbf{V}' = \mathbf{K}\,\mathbf{V}\,\mathbf{K}$$

B.2.2 Positivity

In this appendix, we prove that the Q function of single-photon subtracted and added squeezed vacuum states introduced in subsection 1.4.4 is positive.

By definition from equation (1.45), the Q function is positive over the phase space, as $\hat{\rho}$ is semi-positive. We check that $\mathrm{Q}^{\pm}_{\hat{\rho}}$ in equation (1.156) is indeed positive, deriving in particular an interesting inequality for the discussion of the zeros of $\mathrm{Q}^{\pm}_{\hat{\rho}}$.

A necessary and sufficient condition is

$$\mathrm{Tr}\left[(\mathbf{V}+\sigma_0^2\mathbb{1})^{-1}\mathbf{A}^{\pm}(\mathbf{V},\vec{\mathbf{g}})\right] \leq 2 + \vec{x}^{\top}(\mathbf{V}+\sigma_0^2\mathbb{1})^{-1}\mathbf{A}^{\pm}(\mathbf{V},\vec{\mathbf{g}})(\mathbf{V}+\sigma_0^2\mathbb{1})^{-1}\vec{x} \tag{B.42}$$

where $\mathbf{A}^{\pm}(\mathbf{V},\vec{\mathbf{g}})$ is given by equation (1.153).

Let us investigate first the right-most term and show that it is positive. We develop

$$(\mathbf{V}+\sigma_0^2\mathbb{1})^{-1}\mathbf{A}^{\pm}(\mathbf{V},\vec{\mathbf{g}})(\mathbf{V}+\sigma_0^2\mathbb{1})^{-1} = 2\frac{(\mathbf{V}+\sigma_0^2\mathbb{1})^{-1}(\mathbf{V}\pm\sigma_0^2\mathbb{1})\mathbf{\Pi}_{\vec{\mathbf{g}}}(\mathbf{V}\pm\sigma_0^2\mathbb{1})(\mathbf{V}+\sigma_0^2\mathbb{1})^{-1}}{\mathrm{Tr}\left[(\mathbf{V}\pm\sigma_0^2\mathbb{1})\mathbf{\Pi}_{\vec{\mathbf{g}}}\right]} \tag{B.43}$$

For photon addition (+ case), this matrix is obviously semi-positive, as $\mathbf{V}$ is. For photon subtraction (− case), only the denominator may be negative. Let us show that it is positive.

From the Wiliamson decomposition (see subsection 1.3.5), one can write

$$\mathbf{V} = \mathbf{S}\mathbf{V}_{\mathrm{W}}\mathbf{S}^{\top} \tag{B.44}$$

with $\mathbf{S}$ a symplectic matrix, $\mathbf{V}_{\mathrm{W}} = \sigma_0^2\,\mathrm{diag}(\kappa_1,\cdots,\kappa_N,\kappa_1^{-1},\cdots,\kappa_N^{-1})$ with $1 \leqslant \kappa_1 \leqslant \cdots \leqslant \kappa_N$, and N is the number of modes.

So $\mathrm{Tr}\left[\mathbf{V}\mathbf{\Pi}_{\vec{\mathbf{g}}}\right] \geq \mathrm{Tr}\left[\sigma_0^2\mathbf{S}\mathbf{S}^{\top}\mathbf{\Pi}_{\vec{\mathbf{g}}}\right] = \mathrm{Tr}\left[\mathbf{V}_{\mathrm{pure}}\mathbf{\Pi}_{\vec{\mathbf{g}}}\right]$ where $\mathbf{V}_{\mathrm{pure}} = \sigma_0^2\mathbf{S}\mathbf{S}^{\top}$ may be viewed as the covariance matrix of a pure state[1]. The projector $\mathbf{\Pi}_{\vec{\mathbf{g}}}$ projects on the two phase space dimensions associated to the mode $\vec{\mathbf{g}}$. Using the matrix $\mathbf{\Omega}$ defined in subsection 1.3.4, we can then write

$$\mathrm{Tr}\left[\mathbf{V}_{\mathrm{pure}}\mathbf{\Pi}_{\vec{\mathbf{g}}}\right] = \vec{g}^{\top}\mathbf{V}_{\mathrm{pure}}\vec{g} + (\mathbf{\Omega}\vec{g})^{\top}\mathbf{V}_{\mathrm{pure}}(\mathbf{\Omega}\vec{g}) = \vec{g}^{\top}\left[\mathbf{V}_{\mathrm{pure}} + \mathbf{\Omega}^{\top}\mathbf{V}_{\mathrm{pure}}\mathbf{\Omega}\right]\vec{g} = \vec{g}^{\top}\left[\mathbf{V}_{\mathrm{pure}} + \mathbf{V}_{\mathrm{pure}}^{-1}\right]\vec{g} \tag{B.45}$$

where $\vec{g}$ is the $2N$ modal vector of the form $(\vec{\mathbf{g}},0,\cdots,0)^{\top}$ so that $\mathbf{\Omega}\vec{g} = (0,\cdots,0,\vec{\mathbf{g}})^{\top}$, and where in the last equality we applied the property (1.82) of the matrix $\mathbf{\Omega}$, since $\mathbf{S}\mathbf{S}^{\top}$ is the product of two symplectic matrices, hence symplectic.

[1] Indeed, $\kappa_1,\ldots,\kappa_N = 1$ implies that the purity is 1, using its expression $\sigma_0^2/\sqrt{\det(V)}$ for Gaussian states.

One can see that $\mathbf{S}\mathbf{S}^\top + (\mathbf{S}\mathbf{S}^\top)^{-1} - 2\mathbb{1}$ is semi-positive. Indeed, its eigenvalues $\lambda + 1/\lambda - 2 = (1-\lambda)^2/\lambda$ are positive because $\mathbf{S}\mathbf{S}^\top$ is semi-positive (i.e. $\lambda > 0$). This result combined with equation (B.45), allows us to write $\mathrm{Tr}\left[\mathbf{V}\mathbf{\Pi}_{\vec{\mathbf{g}}}\right] - 2\sigma_0^2 \geq \mathrm{Tr}\left[\mathbf{V}_{\mathrm{pure}}\mathbf{\Pi}_{\vec{\mathbf{g}}}\right] - 2\sigma_0^2 \geq 0$. Using $\mathrm{Tr}\left[\mathbf{\Pi}_{\vec{\mathbf{g}}}\right] = 2$, we then deduce that $\mathrm{Tr}\left[(\mathbf{V} - \sigma_0^2\mathbb{1})\mathbf{\Pi}_{\vec{\mathbf{g}}}\right] \geq 0$ and that the quantity in equation (B.43) is positive.

So far we have shown that equation (B.42) reduces to

$$\mathrm{Tr}\left[(\mathbf{V} + \sigma_0^2\mathbb{1})^{-1}\mathbf{A}^{\pm}(\mathbf{V}, \vec{\mathbf{g}})\right] \leq 2 \tag{B.46}$$

For photon addition, this inequality is always satisfied and saturated as one can directly compute

$$\mathrm{Tr}\left[(\mathbf{V} + \sigma_0^2\mathbb{1})^{-1}\mathbf{A}^{+}(\mathbf{V}, \vec{\mathbf{g}})\right] = 2 \tag{B.47}$$

For photon subtraction:

$$\begin{aligned}
&\mathrm{Tr}\left[(\mathbf{V} + \sigma_0^2\mathbb{1})^{-1}\mathbf{A}^{-}(\mathbf{V}, \vec{\mathbf{g}})\right] \leq 2 \\
\iff\ &\mathrm{Tr}\left[(\mathbf{V} + \sigma_0^2\mathbb{1})^{-1}(\mathbf{V}\,(+\sigma_0^2\mathbb{1} - \sigma_0^2\mathbb{1}) - \sigma_0^2\mathbb{1})\mathbf{\Pi}_{\vec{\mathbf{g}}}(\mathbf{V} - \sigma_0^2\mathbb{1})\right] \leq \mathrm{Tr}\left[(\mathbf{V} - \sigma_0^2\mathbb{1})\mathbf{\Pi}_{\vec{\mathbf{g}}}\right] \\
\iff\ &\mathrm{Tr}\left[(\mathbf{V} + \sigma_0^2\mathbb{1})^{-1}\mathbf{\Pi}_{\vec{\mathbf{g}}}(\mathbf{V}\,(+\sigma_0^2\mathbb{1} - \sigma_0^2\mathbb{1}) - \sigma_0^2\mathbb{1})\right] \geq 0 \\
\iff\ &\mathrm{Tr}\left[(\mathbf{V} + \sigma_0^2\mathbb{1})^{-1}\mathbf{\Pi}_{\vec{\mathbf{g}}}\right] \leq 1
\end{aligned}$$

where we used for the last line $\mathrm{Tr}\left[\mathbf{\Pi}_{\vec{\mathbf{g}}}\right] = 2$.

Now we proceed the same way as before, using $(\mathbf{V} + \sigma_0^2\mathbb{1})^{-1} \leq (\mathbf{V}_{\mathrm{pure}} + \sigma_0^2\mathbb{1})^{-1}$, with $\mathbf{V}_{\mathrm{pure}} = \sigma_0^2\mathbf{S}^\top\mathbf{S}$. Indeed, for $\mathbf{A}, \mathbf{B}$ positive matrices, $\mathbf{A} \geq \mathbf{B} \Rightarrow \mathbf{A}^{-1} \leq \mathbf{B}^{-1}$. One also have $\mathbf{\Omega}^\top(\mathbf{V}_{\mathrm{pure}} + \sigma_0^2\mathbb{1})^{-1}\mathbf{\Omega} = (\mathbf{\Omega}^\top\mathbf{V}_{\mathrm{pure}}\mathbf{\Omega} + \sigma_0^2\mathbb{1})^{-1} = (\mathbf{V}_{\mathrm{pure}}^{-1} + \sigma_0^2\mathbb{1})^{-1}$, since $\mathbf{\Omega}^{-1} = \mathbf{\Omega}^\top = -\mathbf{\Omega}$. Similarly as in equation (B.45), we obtain

$$\mathrm{Tr}\left[(\mathbf{V}_{\mathrm{pure}}^{-1} + \sigma_0^2\mathbb{1})^{-1}\mathbf{\Pi}_{\vec{\mathbf{g}}}\right] = \vec{g}^\top\left[(\mathbf{V}_{\mathrm{pure}} + \sigma_0^2\mathbb{1})^{-1} + (\mathbf{V}_{\mathrm{pure}}^{-1} + \sigma_0^2\mathbb{1})^{-1}\right]\vec{g} \tag{B.48}$$

Finally,

$$\begin{aligned}
(\mathbf{V}_{\mathrm{pure}} + \sigma_0^2\mathbb{1})^{-1} + (\mathbf{V}_{\mathrm{pure}}^{-1} + \sigma_0^2\mathbb{1})^{-1} &= (\mathbf{V}_{\mathrm{pure}} + \sigma_0^2\mathbb{1})^{-1} + \mathbf{V}_{\mathrm{pure}}(\sigma_0^2\mathbb{1} + \mathbf{V}_{\mathrm{pure}})^{-1} \\
&= (\mathbf{V}_{\mathrm{pure}} + \sigma_0^2\mathbb{1})(\mathbf{V}_{\mathrm{pure}} + \sigma_0^2\mathbb{1})^{-1} \\
&= \mathbb{1}
\end{aligned}$$

allows us to write

$$\mathrm{Tr}\left[(\mathbf{V} + \sigma_0^2\mathbb{1})^{-1}\mathbf{\Pi}_{\vec{\mathbf{g}}}\right] \leq \mathrm{Tr}\left[(\mathbf{V}_{\mathrm{pure}} + \sigma_0^2\mathbb{1})^{-1}\mathbf{\Pi}_{\vec{\mathbf{g}}}\right] = 1 \tag{B.49}$$

We then conclude that $Q_{\hat{\rho}}^{\pm} \geq 0$.

In particular, we have shown that inequality (B.46) is saturated for any photon added state (equation (B.47)) and any pure photon subtracted state (equation (B.49) for $\mathbf{V} = \mathbf{V}_{\mathrm{pure}}$). For non-pure photon subtracted states, equation (B.46) remains an inequality, as shown by equation (B.49). We use these results to discuss the zeros of $Q_{\hat{\rho}}^{\pm}$ in subsection 1.4.4.

B.3 The Cauchy Schwarz inequality (3.20) cannot be saturated

In subsection 3.1.3, we obtained from Cauchy Schwarz inequality equation (3.20):

$$|\langle\phi|\,\hat{e}_1\hat{e}_2^\dagger\,|\phi\rangle|^2 \leq \langle\phi|\,\hat{e}_1\hat{e}_1^\dagger\,|\phi\rangle\,\langle\phi|\,\hat{e}_2\hat{e}_2^\dagger\,|\phi\rangle = (1+\bar{n}_1)(1+\bar{n}_2) \tag{B.50}$$

where $|\phi\rangle = |\phi\rangle_s$ is the signal pure input state. This inequality is saturated if and only if $\hat{e}_1^\dagger|\phi\rangle \propto \hat{e}_2^\dagger|\phi\rangle$.

Let us write $|\phi\rangle$ over the Fock basis of the two addition eigenmodes[1]:

$$|\phi\rangle = \sum_{n_1\geq 0}\sum_{n_2\geq 0} C_{n_1,n_2}\,|n_1\rangle\otimes|n_2\rangle \tag{B.51}$$

where the complex coefficients C_{n_1,n_2} ensure the normalization.

So, the saturation condition $\hat{e}_1^\dagger|\phi\rangle \propto \hat{e}_2^\dagger|\phi\rangle$ re-writes:

$$\begin{cases} C_{n_1-1,n_2}\sqrt{n_1} \propto C_{n_1,n_2-1}\sqrt{n_2} & \forall\, n_1\geq 1, n_2\geq 1 \\ C_{n_1-1,0} = 0 & \forall\, n_1\geq 1 \\ C_{0,n_2-1} = 0 & \forall\, n_2\geq 1 \end{cases} \tag{B.52}$$

From this set of equations, it is easy to show recursively that:

$$\forall p\geq 0,\quad \begin{cases} C_{n_1-1,p} = 0 & \forall\, n_1\geq 1 \\ C_{p,n_2-1} = 0 & \forall\, n_2\geq 1 \end{cases} \tag{B.53}$$

This means that all coefficients C_{n_1,n_2} must be zero, which is incompatible with the normalization of $|\phi\rangle$. We conclude that equation (B.50) cannot be saturated.

B.4 Output state purity of multimode addition processes (general case)

Following our developments in subsection 3.1.3, let us show that the output is not pure for multimode addition processes (i.e. $K\neq 1$) generally, when one do not assume that only two eigenvalues are non-zero.
In this case, we have:

$$\hat{\rho}_s^+ = \sum_n \underline{\lambda}_n \hat{e}_n^\dagger \hat{\rho}_s^{in}\,\hat{e}_n \tag{B.54}$$
$$\text{where}\quad \underline{\lambda}_n = \lambda_n/P^+$$

The input $\hat{\rho}_s^{in} = |\phi\rangle\langle\phi|$ is still assumed pure. We find, using trace properties, that the output state purity writes:

$$\mathrm{Tr}\left[(\hat{\rho}_s^+)^2\right] = \sum_k \underline{\lambda}_k^2(1+\bar{n}_k)^2 + 2\sum_{k>l}\underline{\lambda}_k\underline{\lambda}_l\left|\langle\phi|\,\hat{e}_k\hat{e}_l^\dagger\,|\phi\rangle\right|^2 \tag{B.55}$$

[1]The other modes do not intervene in the computation.

We apply the Cauchy-Schwarz inequality on the vector states $\hat{e}_k^\dagger |\phi\rangle$ and $\hat{e}_l^\dagger |\phi\rangle$, as $\left|\langle\phi| \hat{e}_k \hat{e}_l^\dagger |\phi\rangle\right|^2 \leq (1+\bar{n}_k)(1+\bar{n}_l)$.
We obtain:

$$\mathrm{Tr}\left[(\hat{\rho}_s^+)^2\right] \leq \sum_k \underline{\lambda}_k^2 (1+\bar{n}_k)^2 + 2\sum_{k>\ell} \underline{\lambda}_k \underline{\lambda}_\ell (1+\bar{n}_k)(1+\bar{n}_\ell) = \left(\sum_k \underline{\lambda}_k (1+\bar{n}_k)\right)^2 = 1 \tag{B.56}$$

where we used the fact that taking the trace of equation (B.54) yields 1.
Again, looking at the saturation of the Cauchy-Schwarz inequality leads to a similar set of equations as in equation (B.52) for k and ℓ fixed (except that the state $|\phi\rangle$ is decomposed over the full Fock space). Solving the recurrence equations for a given k, ℓ, shows that the saturation condition can't be satisfied. Thus, the purity of the output density matrix is strictly lower than 1, meaning that the output state is not pure.

B.5 Derivation of the analytical form of the Schmidt number K for collinear type-II parametric down-conversion addition process

In this section, we show the analytical expression (3.47) of the Schmidt number K.

The definition of the Schmidt number K is recalled

$$K = \frac{(\sum_n \lambda_n)^2}{\sum_n \lambda_n^2} \tag{B.57}$$

From equation (3.46), the JSA function can conveniently expressed in the Gaussian form

$$J(\omega_s, \omega_i) = D \exp\left[-\frac{1}{2}\vec{\omega}^\top \mathbf{X} \vec{\omega}\right] \tag{B.58}$$

where $\vec{\omega}^\top = (\omega_s, \omega_i)$, $\mathbf{X}$ is a real 2x2 matrix, and D is a proportionality coefficient.

The eigendecomposition of the JSA function into signal and idler frequency eigenmodes is expressed as [Eckstein 12]

$$J(\omega_s, \omega_i) = \sum_{n\geq 1} \sqrt{\lambda_n} \widetilde{\mathbf{e}}_{s,n}(\omega_s) \widetilde{\mathbf{e}}_{i,n}(\omega_i) \tag{B.59}$$

where $\{\mathbf{e}_{s,n}(t)\}$ (resp. $\{\mathbf{e}_{i,n}\}$) form the signal (resp. idler) eigenmode basis.

Using equations (B.58) and (B.59), we obtain two expressions of the integral of the JSA

$$\sum_n \lambda_n = \int d\omega_s d\omega_i |J(\omega_s, \omega_i)|^2 = D^2 \frac{2\pi}{\sqrt{\det(2\mathbf{X})}} \tag{B.60}$$

where we used the orthonormal properties of the eigenmodes for the left-most member, and we performed the integrals using the following general expression for Gaussian integrals to get the right-most member

$$\int \cdots \int \exp\left[-\frac{1}{2}\vec{y}^\top \mathbf{M} \vec{y}\right] \mathrm{d}y_1 \ldots \mathrm{d}y_n = \frac{(2\pi)^{n/2}}{\sqrt{\det(\mathbf{M})}} \tag{B.61}$$

for $\mathbf{M}$ a general $n \times n$ real matrix, and $\vec{y}^\top = (y_1, \cdots, y_n)$ a general n-real vector.

We find similar equations for the function $A(\omega_s, \omega_s')$ defined in equation (3.40) from the JSA. We have

$$\sum_n \lambda_n^2 = \int d\omega_s d\omega_s' |A(\omega_s, \omega_s')|^2 = D^4 \frac{(2\pi)^2}{\sqrt{\det(\mathbf{W})}} \tag{B.62}$$

where $\mathbf{W}$ is defined as a real 4×4 matrix such that

$$J(\omega_s, \omega_i) J^*(\omega_s', \omega_i) J^*(\omega_s, \omega_i') J(\omega_s', \omega_i') = D^4 \exp\left[-\frac{1}{2}(\vec{\omega}^\top, \vec{\omega}'^\top)^\top \mathbf{W} (\vec{\omega}^\top, \vec{\omega}'^\top)\right] \tag{B.63}$$

with $(\vec{\omega}^\top, \vec{\omega}'^\top)^\top = (\omega_s, \omega_i, \omega_s', \omega_i')$.

Now, substituting equations (B.60) and (B.62) into the definition (B.57), we obtain the expression of the Schmidt number K through the matrices defined above as

$$K = \frac{\sqrt{\det(\mathbf{W})}}{4 \det(\mathbf{X})} \tag{B.64}$$

Let us now specify the expression of K to this problem. $\mathbf{X}$ can be deduced from the JSA expression (3.46)

$$\mathbf{X} = \frac{1}{\Delta\omega_g^2} \begin{pmatrix} 1 + r_s^2 & 1 + r_s r_i \\ 1 + r_s r_i & 1 + r_i^2 \end{pmatrix} \tag{B.65}$$

$$\text{with} \quad r_j = \Delta\omega_g L \sqrt{\frac{\gamma}{2}} \left| k_g' - k_j' \right| \quad \text{for} \quad j = i, s \tag{B.66}$$

where the r_j coefficients are the adimensional parameters of the problem. The definition (B.63) of $\mathbf{W}$ leads to

$$\mathbf{W} = \frac{1}{\Delta\omega_g^2} \begin{pmatrix} 2(1 + r_s^2) & 1 + r_s r_i & 0 & 1 + r_s r_i \\ 1 + r_s r_i & 2(1 + r_i^2) & 1 + r_s r_i & 0 \\ 0 & 1 + r_s r_i & 2(1 + r_s^2) & 1 + r_s r_i \\ 1 + r_s r_i & 0 & 1 + r_s r_i & 2(1 + r_i^2) \end{pmatrix} \tag{B.67}$$

Computing the determinant of matrices (B.65) and (B.67), and substituting them into equation (B.64), we end up with an analytical expression for K under Gaussian approximations

$$K = \sqrt{\frac{(1 + r_s^2)(1 + r_i^2)}{(r_s - r_i)^2}} \tag{B.68}$$

$$\text{with} \quad r_j = \Delta\omega_g L \sqrt{\frac{\gamma}{2}} \left| k_g' - k_j' \right| \quad \text{for} \quad j = i, s$$

Appendix C

Experimental additional technical details

C.1 Homodyne detectors characterization and electronical scheme

In this appendix, we explain and show the characterization of the homodyne detectors used in the experiment, to complement their analysis given in subsection 2.4.3. Note that we use two of these homodyne detectors in the double homodyne detector experimental scheme, see section 4.1.

These detectors were developed recently in our group to host faster photodiodes (S38883-02) compared to before. With these photodiodes, [Kouadou 21] built homodyne detections fast enough to resolve pulse by pulse squeezed light (with a 150 MHz-repetition-rate laser source). For our use case, we aimed at 40 MHz of detection bandwidth, much larger than the cavity bandwidth, below 10 MHz. The electronic scheme of our homodyne detectors is given in figure C.1, and described in the figure caption.

After proper alignment with a local oscillator beam, we characterize the response of a given detector using a spectrum analyzer. As explained in subsection 2.4.3, the measured spectral densities gives us access to both the bandwidth and the clearance of the detector. The raw measurements and the inferred clearances are given in figure C.2 for different LO powers, for the detector referenced " OPA856_C2_05".

In the raw measurements, the spectrum analyzer noise trace shows that its contribution to the measurements is negligible. Noting $S_{\text{dark,BW}}$ (resp. $S_{\text{LO,BW}}$) the spectral density measured when the LO beam is blocked (resp. not blocked), integrated over the bandwidth BW, the clearance $C_{\text{dB, BW}}$ at the bandwidth BW then writes

$$C_{\text{dB, BW}} = 10 \log_{10} \left(\frac{S_{\text{LO,BW}}}{S_{\text{dark,BW}}} \right) \tag{C.1}$$

The *detector bandwidth* refers to the region where the clearance is mostly flat. And the *detector clearance* C_{dB} is the clearance integrated over the detector bandwidth.

As these two properties depends on the local oscillator optical power, we perform multiple measurements, doubling the LO power at each new measurement until saturation of the

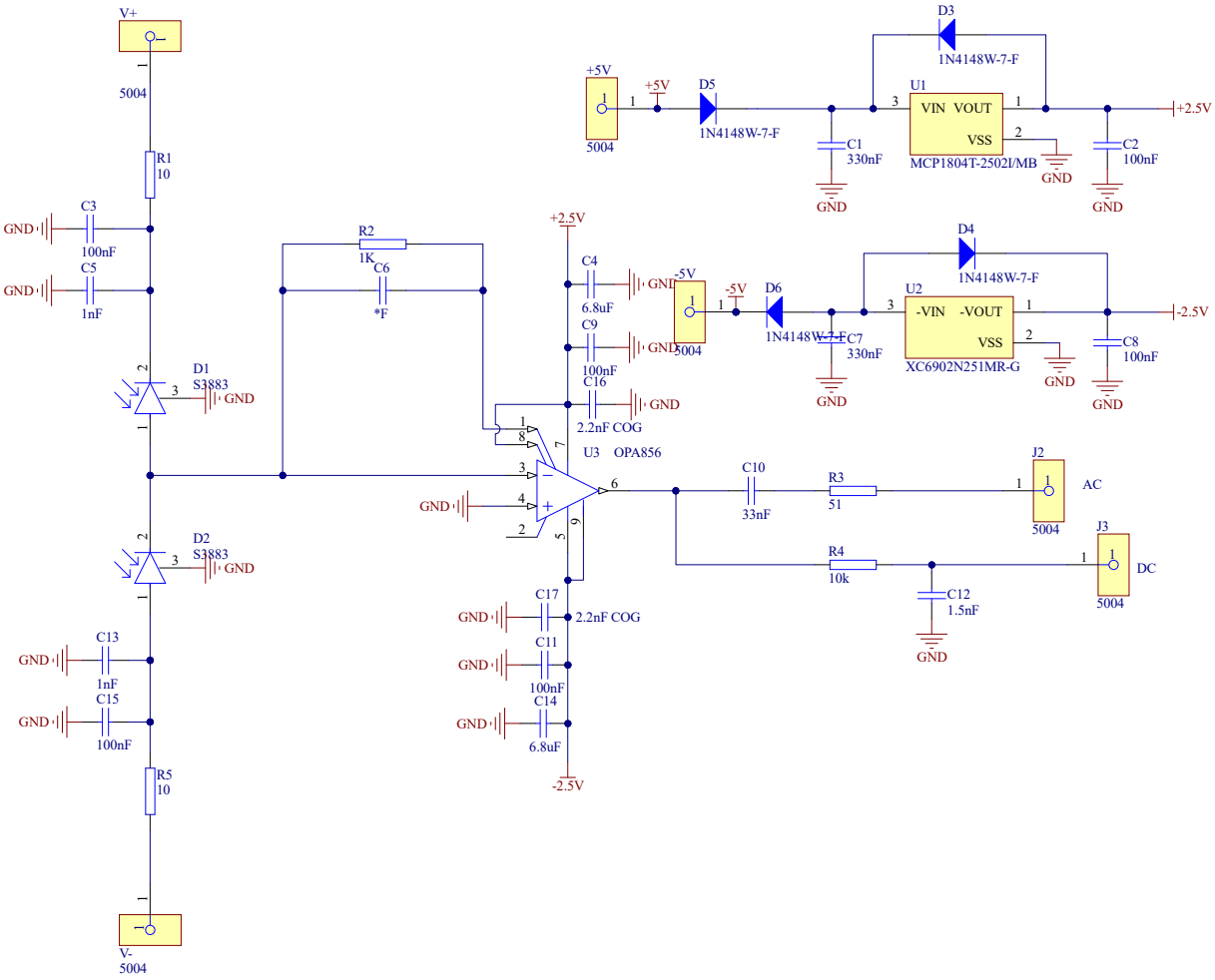

Fig. C.1 Electronic scheme of our homodyne detectors. The photodiodes S3883 (left) difference of currents is amplified with an OPA856 amplifier whose output is splitted into AC and DC outputs using passive filters. This amplifier requires ±2.5 V of input power which is provided by transforming and filtering an external power source of ±5 V (see U1 and U2). Another external power source feeds the photodiodes to provide the bias V± (usually ±15 V to ±30 V). Note that since then, the capacity C10 was replaced by a capacity of 10 nF, near the AC output.

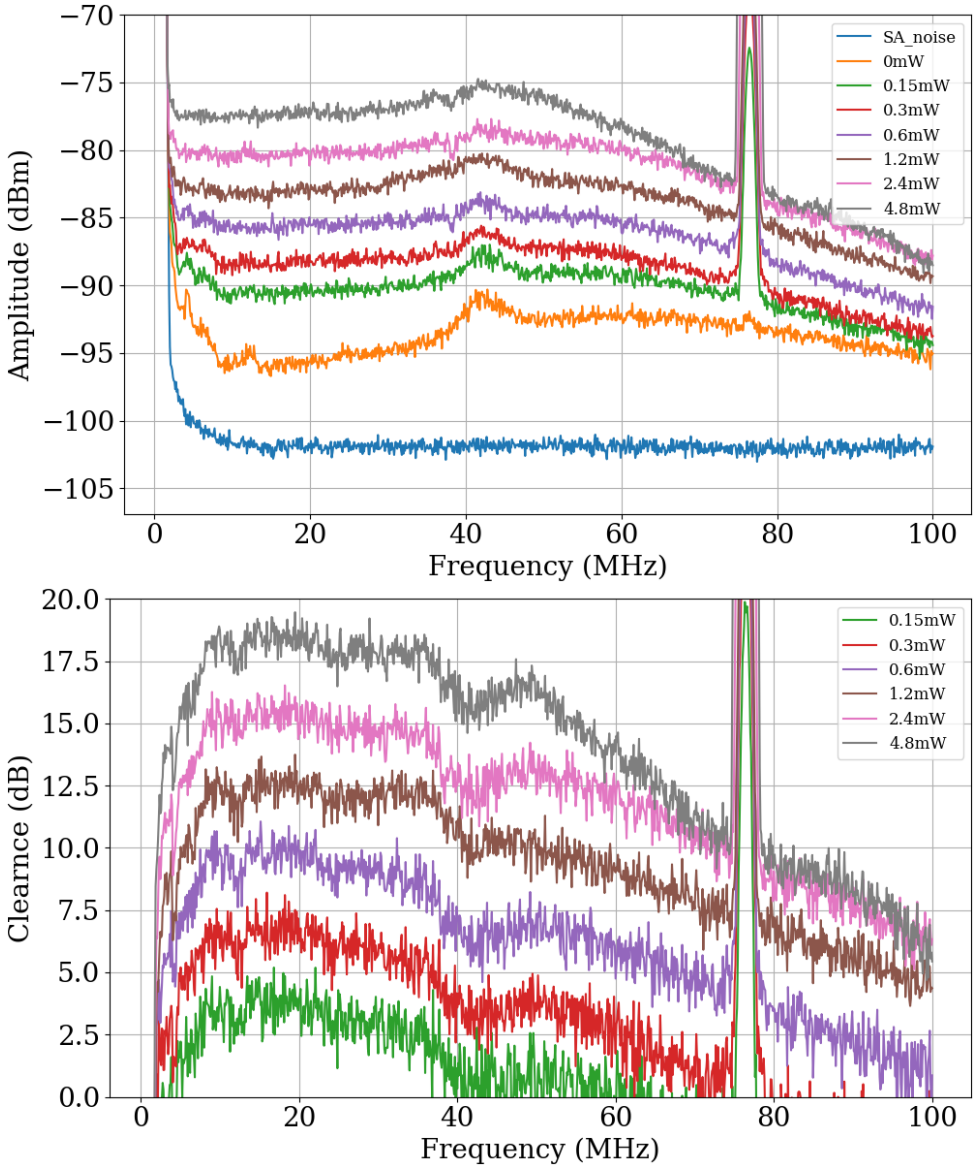

Fig. C.2 Characterization curves of the homodyne detector OPA856_C2_05 using a spectrum analyzer. The resolution bandwidth of the spectrum analyzer is set at 100 kHz. (Top): Raw measurements for different LO power values given in the legend (and for the noise of the spectrum analyzer itself). (Bottom): Deduced clearance for different LO power values given in the legend.

detector (above 4.8 mW, the saturation was clear and is not recorded). To check we are indeed below saturation, the clearance should increase by additive steps of 3 dB before saturation. The data satisfies this law as shown in figure C.3.

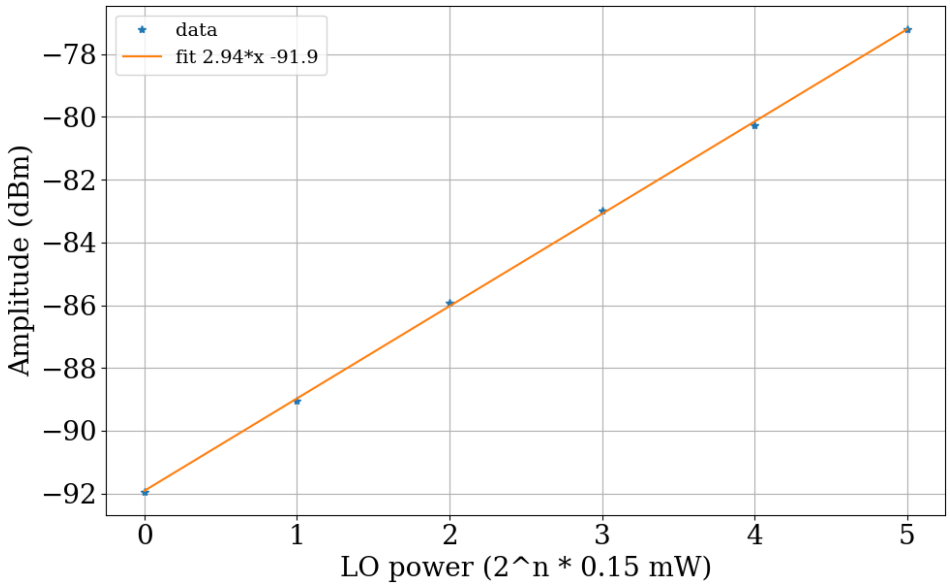

Fig. C.3 Measured spectral density integrated over a bandwidth BW of 36 MHz at central frequency 20 MHz, for each curve of figure C.2 (top) with a non-zero LO power.

The same characterization was performed for the second detector used in the double homodyne detection, referenced as "OPA856_C2_06", see figure C.4 and figure C.5. We deduce the detector bandwidth and detector clearance before saturation, estimated at about BW = 40 MHz and $C_{\mathrm{dB}} > 17$ dB for both detectors OPA856_C2_05 and OPA856_C2_06. Note that the noise at frequencies below 10 MHz was coming from the lack of isolation of the detectors from large noise in the electric installation of the building. This problem was solved by plugging all devices on filtering power inverters, resulting in a flat clearance at low frequency.

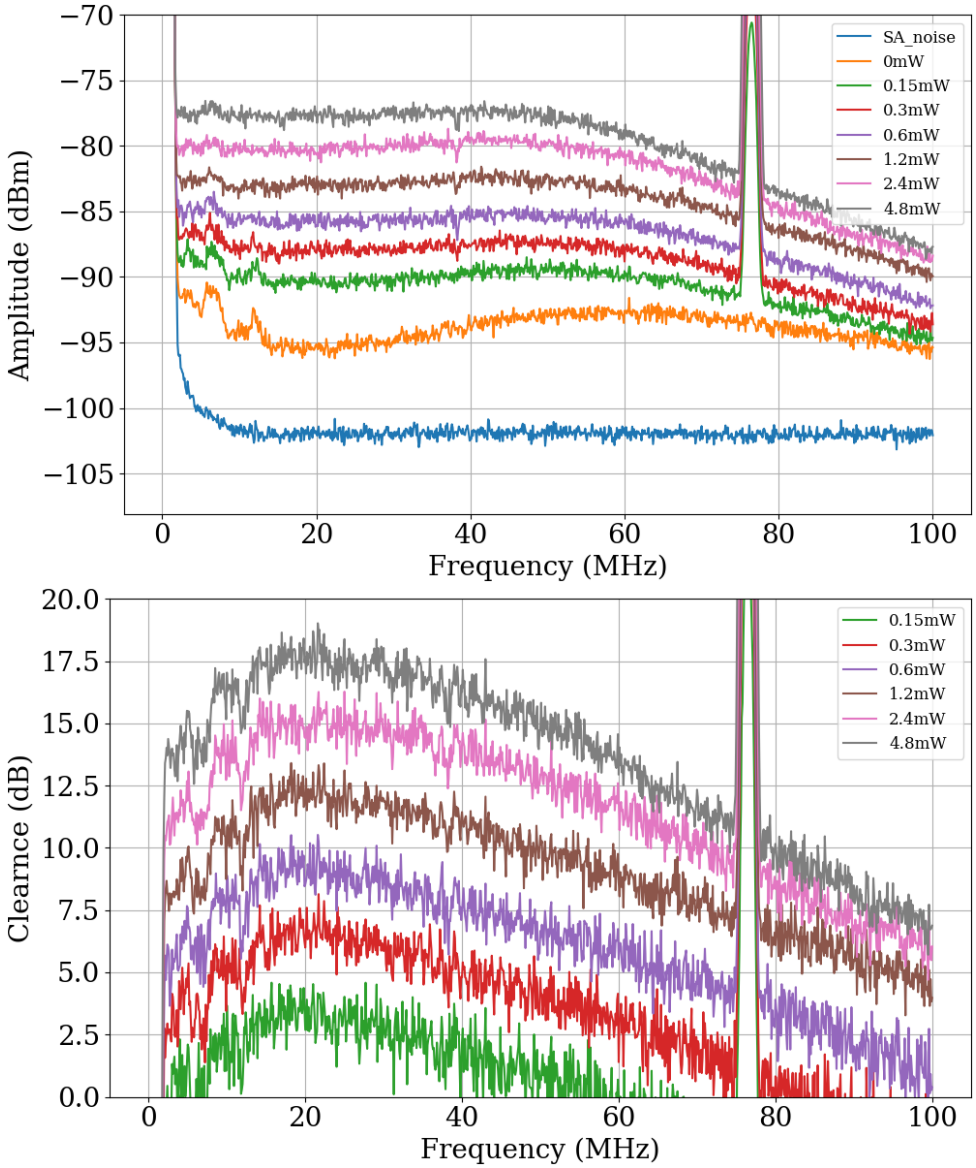

Fig. C.4 Characterization curves of the homodyne detector OPA856_C2_06 using a spectrum analyzer. The resolution bandwidth of the spectrum analyzer is set at 100 kHz. (Top): Raw measurements for different LO power values given in the legend (and for the noise of the spectrum analyzer itself). (Bottom): Deduced clearance for different LO power values given in the legend.

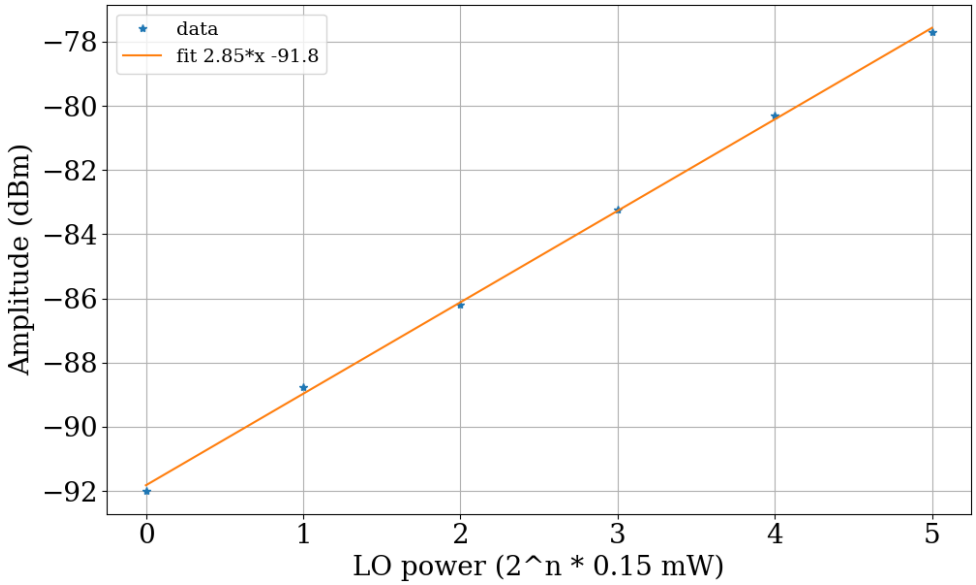

Fig. C.5 Measured spectral density integrated over a bandwidth BW of 36 MHz at central frequency 20 MHz, for each curve of figure C.4 (top) with a non-zero LO power.

C.2 Optical phase lock electronics

In this appendix, we complement the description of the optical phase lock of section 2.5 by providing the electronic schemes of the seed-pump lock and the LO-seed lock, respectively in figure C.6 and in figure C.7.

For both schemes, we demodulate the signal by mixing it with an electronic local oscillator (eLO) of frequency 60 kHz, i.e. summing the signal with a electronic signal of the shape $\propto \cos(2\pi f_{\text{mod}} t)$. Each frequency f of the signal (which is centered around 60 kHz) are then sent to the frequencies $f + f_{\text{mod}}$ and $|f - f_{\text{mod}}|$. The following low-pass filter (LPF) at 15 kHz removes the $f + f_{\text{mod}}$ component, selecting the frequency $|f - f_{\text{mod}}|$ with a bandwidth of 15 kHz: the bandwidth of the demodulation. The mixer is a ZAD-8+ mixer, allowing for all frequencies f in the range $[0.0005, 10]$ MHz.

The signal from the photodiode in figure C.6 is first filtered by a high-pass filter (HPF) of cut-off frequency 31.5 kHz to avoid saturating the filter. Indeed, as discussed in subsection 2.5.2, the measured signal is multiplied by a square-like signal at the frequency of the chopper 8 kHz. The amplitude of the frequency components of a square signal is only decreasing in $1/n$ for n a multiple of the fundamental frequency 8 kHz. If left unfiltered, these components saturate the mixer. With the 31.5 kHz HPF, the mixer functions normally. A second reason for using this HPF is to suppress the pump power fluctuations, which occur at very low frequencies (≤ 1 kHz).

On the other hand, the signal from the homodyne detection in figure C.7 is first filtered by two low-pass filters (LPF). Since the homodyne detection is very sensitive, a very high-amplitude peak is measured at 76 MHz, which corresponds to the repetition rate of the pulsed light. The amplitude is so high ($\simeq 60$ dB) that the internal filter of the mixer is not sufficient,

hence the mixer saturated. This is the purpose of both filters at cut-off frequencies 22 MHz and 100 kHz. Also note that for this lock, we used two different configurations, one using the AC channel of the homodyne detection, and another using the DC channel. For the AC configuration, a 15 dB attenuator is used to suppress electronic reflections from the amplifiers, which were introducing unwanted fluctuations in the signal measured on the scope.

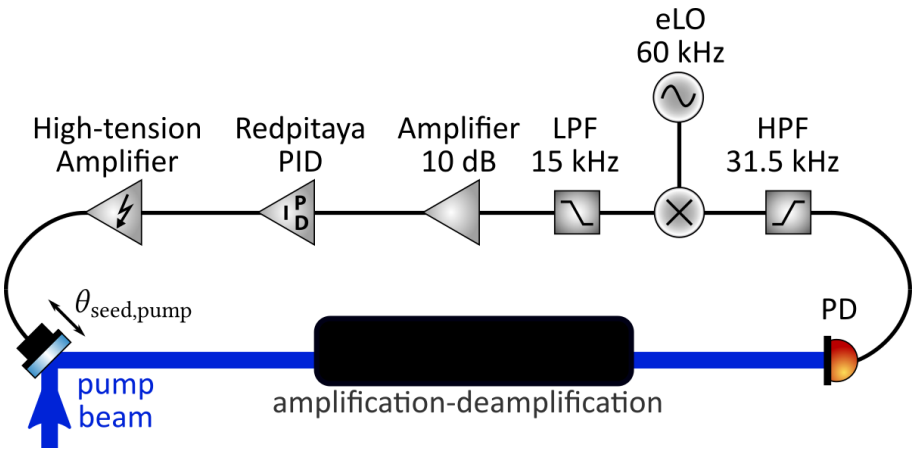

Fig. C.6 Electronic scheme of the seed-pump lock. The photodiode (PD) measure the intensity of the pump beam which depends on the seed-pump phase, due to the amplification-deamplification process occurring in the SPOPO. The electronic signal is filtered by a high-pass filter (HPF) of cut-off frequency 31.5 kHz. Then, it is demodulated, amplified and send to a PID (a redpitaya). The feedback loop is closed by driving the pump piezo with the amplified error signal from the PID. LPF: low-pass filter. eLO: electronic local oscillator.

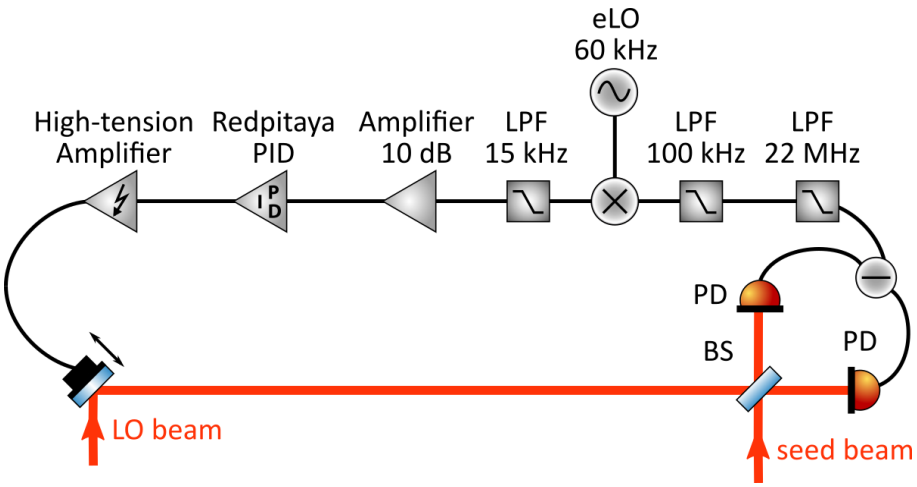

Fig. C.7 Electronic scheme of the LO-seed lock. The difference of currents from the homodyne measurement is sensible to the LO-seed phase. The electronic signal is filtered by two low-pass filters (LPF) of cut-off frequencies 22 MHz and 100 kHz. Then, it is demodulated, amplified and send to a PID (a redpitaya). The feedback loop is closed by driving the LO piezo with the amplified error signal from the PID. PD: photodiode. BS: beamsplitter. eLO: electronic local oscillator.

C.3 Double homodyne detection optical elements

In this appendix, we give some technical details on the key optical elements of our double homodyne detector. The main concern is the losses induced by the optics, which we aim at minimize for reasons explained in subsection 4.1.3.

C.3.1 Edmund Optics 780 nm Laser Line Polarizing Cube Beamsplitter #47-048

The transmission curve of the Edmund Optics 780 nm Laser Line Polarizing Cube Beamsplitter #47-048 is given in figure C.8. The curve is produced from publicly available reference data form Edmund Optics. There are no data for the reflectivity, while still featuring experimentally similar performances in terms of losses and contamination.

C.3.2 Waveplates choice and retardance flatness

In this appendix, we explicit the reasons for the choice of zero-order half-wave plates instead of achromatic ones in the double homdyne detection, see subsection 4.1.3. We compare among the best half-wave plates in each categories: the CVI Laser Optics QWPO-800-05-2-R10 one and the Edmund Optics 700-1000 nm #46-561 achromatic one.

The discussion resolves around two figures, the losses and the retardance. For the loses, the CVI plates win with 0.4% total losses (from 0.2% losses at each surfaces and two surfaces), while the Edmund ones exhibit 2.4% total losses (from 0.6% losses at each surfaces and four surfaces). As losses are critical for the experiment, we would vouch for the CVI plates, however their

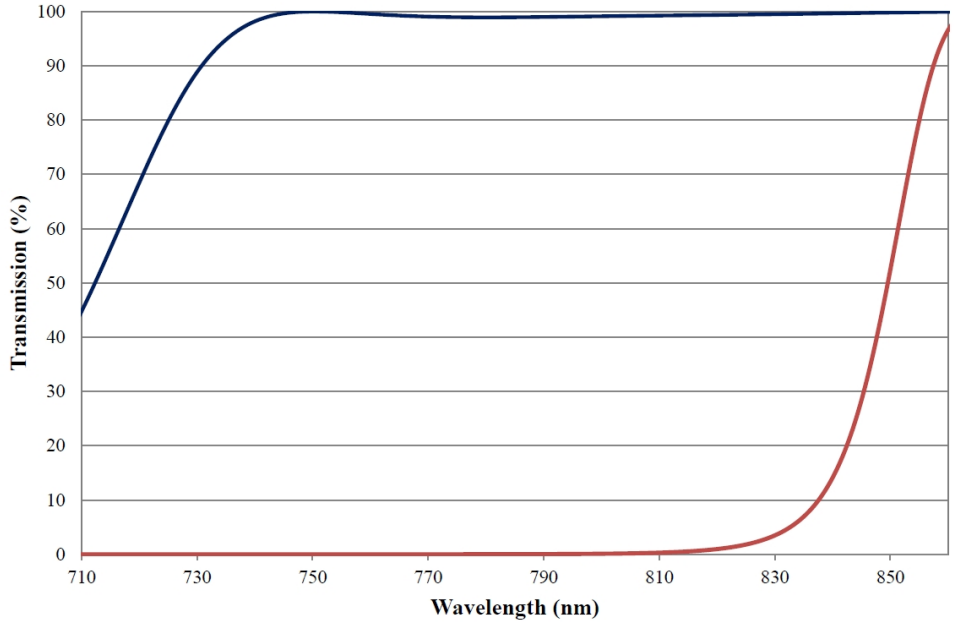

Fig. C.8 Transmission curve of a typical Edmund Optics 780 nm Laser Line Polarizing Cube Beamsplitter #47-048 . The blue curve is the transmission of horizontally polarized fields, and the red curve is the transmission of vertically polarized fields.

retardance is significanlty less flat than the Edmund ones, which is expected when comparing a zero-order half-wave plate with an achromatic one.

The retardance of both half-wave plates is given in figure C.9, graph (a). These curves are produced from publicly available reference data form CVI and Edmund Optics. One can see that while the achromatic ones feature a flat retardance around 0.505λ, the CVI ones span form 0.515λ to 0.492λ in the range $[780, 810]$ nm.

To estimate the effect of the imperfection of the retardance of these wave-plates, compared to the perfect flat 0.5λ retardance, we consider the following setup. The half-wave plate we consider is placed between two parallel polarizers, and we measure the transmittance of this ensemble at different wavelength using a linearly polarized light. After the first polarizer, the light is linearly polarized in the polarizer axis. A perfect half-wave plate with perfect retardance would then rotate this polariztion by 90°, which would then be completely absorbed by the next polarizer, as it has the same axis as the first one. Formally, one can write generally write the transimission T of this setup as

$$T = 1 - \cos^2\left(\theta_{\text{pol}}\right) \sin^2\left(\frac{\phi_{\text{ret}}}{2}\right) \tag{C.2}$$

where θ_{pol} is the angle that defines the direction of the polarizers with respect to polarization direction of the input light, and ϕ_{ret} is the optical phase induced by the retardance of the half-wave plate, i.e. $\phi_{\text{ret}} = 2\pi x_{\text{ret}}$ where x_{ret} is the retardance over lambda (i.e. 0.5 for a retardance of 0.5λ).

In practice, one would turn the polarizer until $\theta_{\text{pol}} = 0$, maximizing the transimittance. In

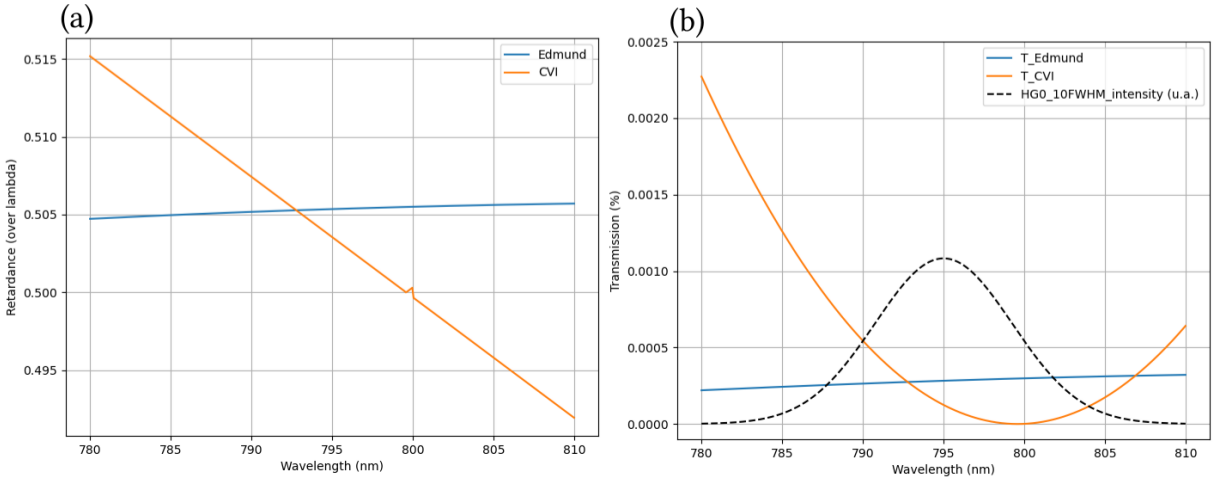

Fig. C.9 (a) Retardance (over lambda) against wavelength of a typical CVI Laser Optics QWPO-800-05-2-R10 half-wave plate (orange) and a typical Edmund Optics 700-1000 nm $\lambda/2$ #46-561 achromatic half-wave plate (blue). (b) Transmission against wavelength for the setup composed of two parallel polarizers and a half-wave plate placed between them, with the CVI one (orange) and Edmund one (blue). The dashed-dark curve represents the intensity spectral profile of the LO field, typically in a Hermite-Gaussian 0 mode with 10 nm FWHM. The unit and scale of the intensity is arbitrary, and not represented on the vertical axis.

our case we directly write

$$T = 1 - \sin^2(\pi x_{\text{ret}}) \tag{C.3}$$

where the transmission is zero for a perfect retardance $x_{\text{ret}} = 0.5$, as expected.

Using the retardance of graph C.9 (a), we compute the transmission from equation (C.3) for both wave plates, and represent them in graph C.9 (b). As expected, the transmission is zero for the CVI wave plate when its retardance crosses 0.5λ.

One can see that the transmission values are extremely low. The uniform transmission of the acrhomatic plate can be understood as losses, hence completely negligible. For the CVI one, the transmission is quadratic, hence frequency dependent. This can have a detrimental effect on the measurement, since it would deform the time-frequency mode of the LO, leading to a poorer overlap at the detection, hence losses. In graph C.9 (b), we also plot the spectral intensity of the LO in the HG0 mode. Due to the very low transmission values, the overlap of this mode before and after is very close to 1, hence negligible losses are expected. We then deduce that the retardance of the CVI half-wave plates can be considered flat in our use cases. Since they feature also low losses, we conclude this analysis by choosing the CVI half-wave plates for our experiment.

C.3.3 Choice of the mount of the half-wave plates

In this appendix, we explicit the choice of the mount for the half-wave plates we use in the double homodyne detection setup, see subsection 4.1.3.

We compare two mounts from Thorlabs, the standard RSP1D/M mount and the high-precisionPRM1/M mount. The graduations on the RSP1D/M are marked every 2°, while the graduation of the PRM1/M on its micrometer translation are marked every 0.04°, hence a factor of 50 in precision.

To estimate how this precision on the angle θ_{plate} of the wave-plate mount affects the precision on the intensity of the fields in the double homodyne detection, we consider the following setup. The half-wave plate we consider is placed before an ideal polarizing beam splitter. The PBS transmits the horizontal polarization of the linearly polarized input light. The transmission T_{H} of the setup then writes

$$T_{\text{H}} = \cos^2\left(2\theta_{\text{plate}}\right) \tag{C.4}$$

from which we deduce the transmission change per degree around $\theta_{\text{plate}} = 22.5^\circ$

$$\left.\frac{\partial T_{\text{H}}}{\partial \theta_{\text{plate}}}\right|_{\theta_{\text{plate}}=22.5^\circ} = -3.5\%/^\circ \tag{C.5}$$

In other words, we loose 3.5% of the incoming light intensity for each degree off from $\theta_{\text{plate}} = 22.5^\circ$, which corresponds to using the half-wave plate to split the input intensity evenly, with 50% of power in each arm. This configuration is used in the double homodyne detection scheme at the first PBS, to evenly split the signal field, and at the second PBSs which are used as 50:50 beamsplitters for the two homodyne detections.

We experimentally verify that the maximal accuracy we can obtain on the output power is 1% using the standard RSP1D/M mounts, using a power measurement as guide and some careful alignment time. This corresponds to a precision of 0.3° from equation (C.5), i.e. a 7th of the graduation precision of 2°. Considering the same maximal precision ratio using the high-precision PRM1/M mounts with graduation precision of 0.04°, we expect a maximal precision of 0.006°, hence a precision of 0.02% on the power.

As argued in subsection 4.1.3, for the half-wave plates used for balancing the two homodyne detections, the highest power precision the best, hence we choose the high-precision PRM1/M mounts for them.

For the half-wave plate used to evenly split the signal field, the effect of imprecision on the squeezing factor s_{dB} of the equivalent squeezing operation due to unbalancing the double homodyne detection can be computed from equation (4.29) around $T_{\text{H}} = 50\%$. We obtain

$$\left.\frac{\partial s_{\text{dB}}}{\partial T_{\text{H}}}\right|_{T_{\text{H}}=50\%} = 0.17\ \text{dB}/\% \tag{C.6}$$

which means that the squeezing factor increases by 0.17 dB for each percent off in the transmission. From the previous discussion, a percent off corresponds to 0.3° off from the position $\theta_{\text{plate}} = 22.5^\circ$.

In section 4.3, we produce simulations which suggest that such precision is enough for our use case, see in particular appendix D.2.3 for a quantitative estimation of the sensibility of the certification to the unbalancing squeezing factor. Thus, we choose the standard RSP1D/M mount. Still, in the future, we might get to regimes were finer unbalancing is required, for which choosing the the high-precision PRM1/M mount would be interesting, leading to a maximal precision of 0.004 dB on the squeezing factor.

C.4 Clipper-amplifier electronic scheme

For reference, the electronic scheme of the clipper-amplifiers used at the measurement is given in figure C.10. It basically consists in 4 stages of one amplifier and one clipper. Each clipper is a couple of parallel diodes.

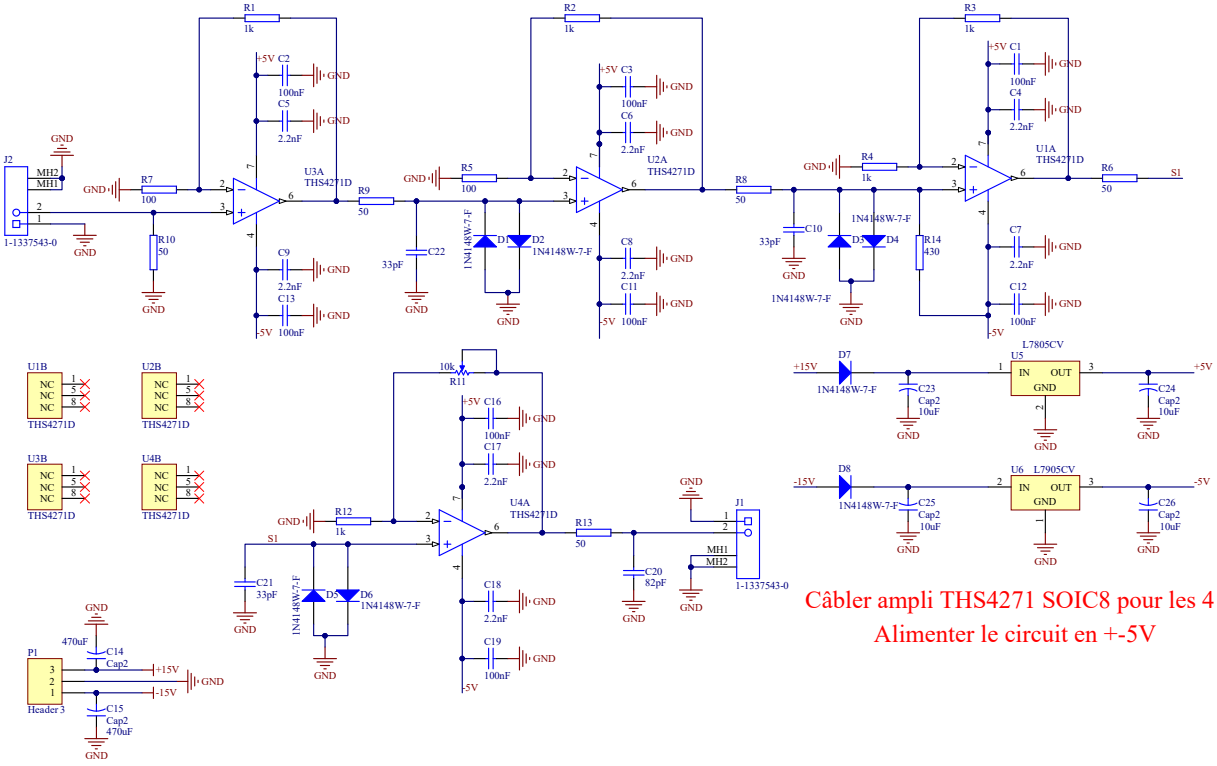

Fig. C.10 Electronic scheme of a clipper-amplifier.

Appendix D

Simulations: supplementary figures

D.1 Simulation of a single-mode OPO with output reflectivities 70% and 50%

In this appendix, we provide the results of the same simulation which produced figure 2.10 in subsection 2.3.4, changing a single parameter, the output reflectivity r_o^2. The results are given in figure D.1 for $r_o^2 = 70\%$ and in figure D.2 for $r_o^2 = 50\%$.

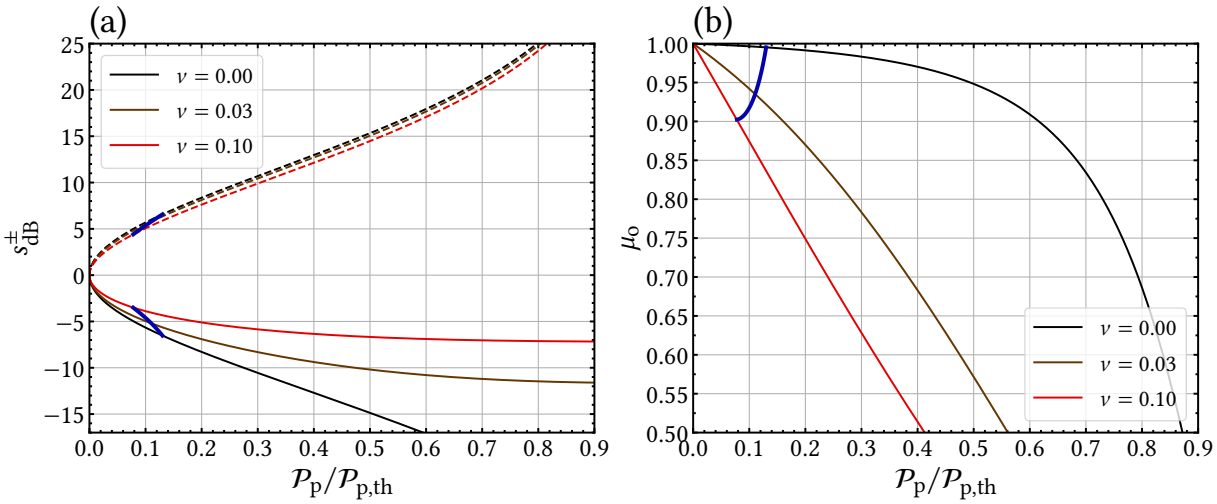

Fig. D.1 Simulation of a single-mode OPO, at $r_o^2 = 70\%$, for three intra-cavity additional loss ν values: 0% (black), 3% (black), and 10% (red). The total intra-cavity losses are $0.0015 + \nu$. (a): the squeezing factor s^-_{dB} (solid lines) and the antisqueezing factor s^+_{dB} (dashed lines) against the normalized to threshold pump power $\mathcal{P}_p/\mathcal{P}_{p,th}$. (b): the output purity μ_o against $\mathcal{P}_p/\mathcal{P}_{p,th}$. The blue bold curves corresponds to the blue curves in figure 2.11.

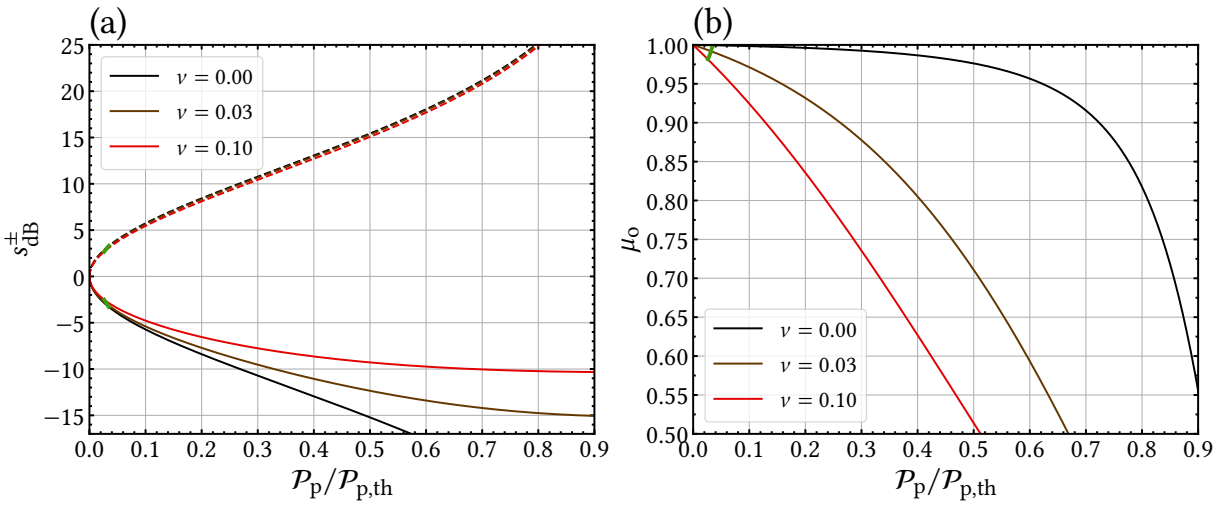

Fig. D.2 Simulation of a single-mode OPO, at $r_{\mathrm{o}}^2 = 50\%$, for three intra-cavity additional loss ν values: 0% (black), 3% (black), and 10% (red). The total intra-cavity losses are $0.0015 + \nu$. (a): the squeezing factor s^{-}_{dB} (solid lines) and the antisqueezing factor s^{+}_{dB} (dashed lines) against the normalized to threshold pump power $\mathcal{P}_{\mathrm{p}}/\mathcal{P}_{\mathrm{p,th}}$. (b): the output purity μ_{o} against $\mathcal{P}_{\mathrm{p}}/\mathcal{P}_{\mathrm{p,th}}$. The green bold curves corresponds to the green curves in figure 2.11.

D.2 Additional simulation results for the certification of single-photon subtracted squeezed vacuum states

In this appendix, we provide additional results of the simulation described in section 4.3. Appendix D.2.1 extends the simulation considering a balanced double homodyne detection, while appendix D.2.2 consider it unbalanced.

D.2.1 Using a balanced double homodyne detection

We provide the results of the same simulation which produced figure 4.6 in subsection 4.3.4, changing a single parameter, the squeezing factor s_{dB} of the squeezed vacuum state before single-photon subtraction and detection loss. The results are given in figure D.3 for $s_{\mathrm{dB}} = 2$ dB, in figure D.4 for $s_{\mathrm{dB}} = 3$ dB, in figure D.5 for $s_{\mathrm{dB}} = 4$ dB, and in figure D.6 for $s_{\mathrm{dB}} = 5$ dB. For each of these figures, we display the stellar rank 1 threshold (red horizontal line) and the Wigner negativity (at origin) witness threshold (cyan horizontal line). When the lowest point of an interval of confidence is higher than a threshold value, the property corresponding to this threshold value is certified with more than 97.5% confidence. For each purity of preparation (of the squeezed vacuum state prior to the subtraction), the simulation is performed for three values of detection losses $\eta = 1, 0.9$ and 0.8.

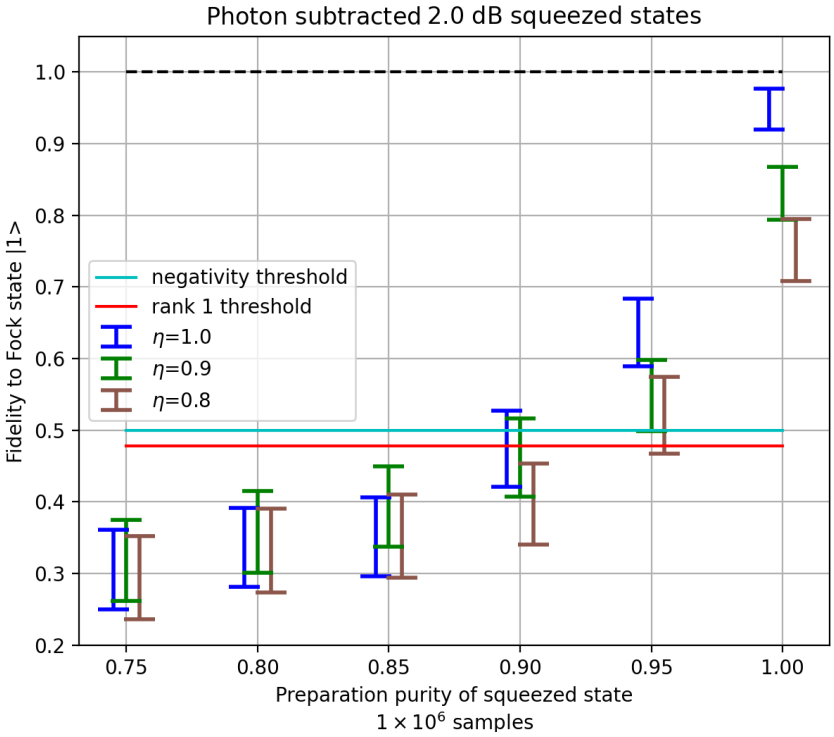

Fig. D.3 Estimates of the fidelity to Fock state $|1\rangle$ for lossy single-photon subtracted squeezed vacuum states for a squeezing factor of $s_{\mathrm{dB}} = 2\,\mathrm{dB}$.

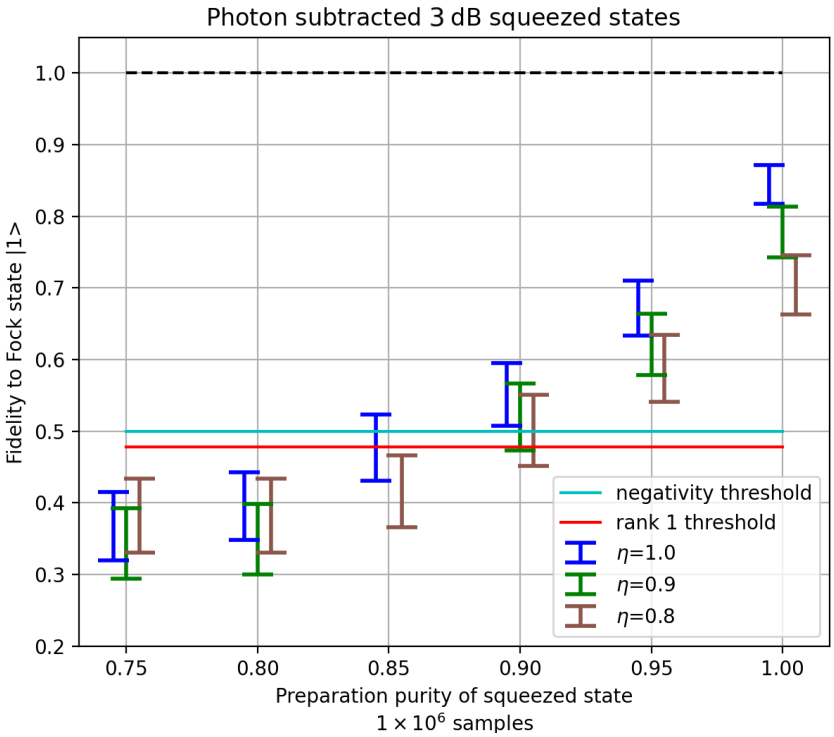

Fig. D.4 Estimates of the fidelity to Fock state $|1\rangle$ for lossy single-photon subtracted squeezed vacuum states for a squeezing factor of $s_{\mathrm{dB}} = 3\,\mathrm{dB}$.

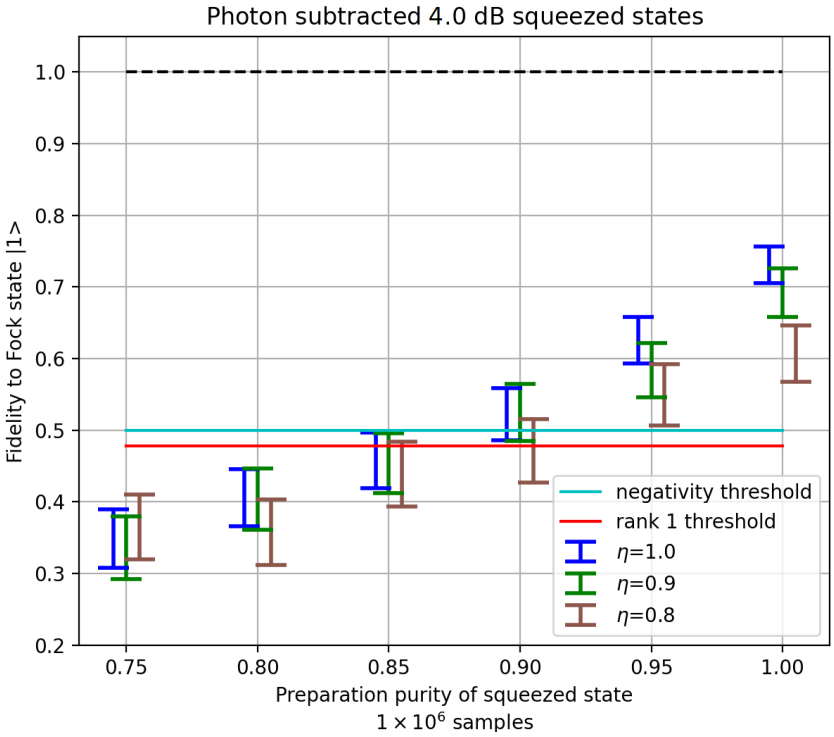

Fig. D.5 Estimates of the fidelity to Fock state $|1\rangle$ for lossy single-photon subtracted squeezed vacuum states for a squeezing factor of $s_{\mathrm{dB}} = 4\,\mathrm{dB}$.

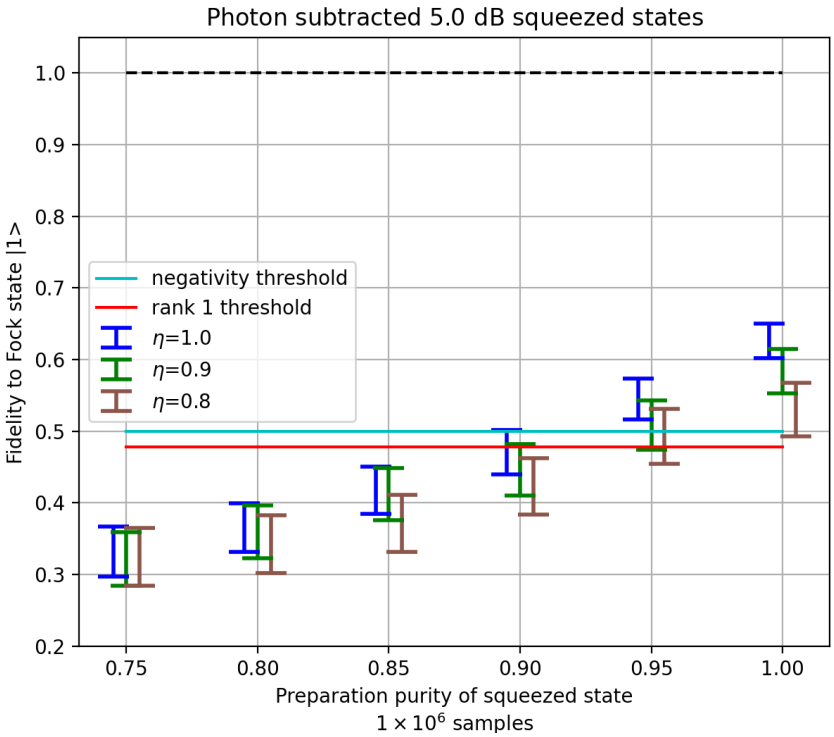

Fig. D.6 Estimates of the fidelity to Fock state $|1\rangle$ for lossy single-photon subtracted squeezed vacuum states for a squeezing factor of $s_{\mathrm{dB}} = 5\,\mathrm{dB}$.

D.2.2 Using an unbalanced double homodyne detection

We provide the results of the same simulation which produced figure 4.7 in subsection 4.3.4, changing a single parameter, the squeezing factor s_{dB} of the squeezed vacuum state before single-photon subtraction. Compared to the additional results given above in this appendix, the double homodyne detection is unbalanced, with an unbalancing which compensates exactly the squeezing factor s_{dB}. The results are given in figure D.7 for $s_{\mathrm{dB}} = 2\,\mathrm{dB}$, in figure D.8 for $s_{\mathrm{dB}} = 3\,\mathrm{dB}$, in figure D.9 for $s_{\mathrm{dB}} = 4\,\mathrm{dB}$, in figure D.10 for $s_{\mathrm{dB}} = 5\,\mathrm{dB}$. For each of these figures, we display the stellar rank 1 threshold (red horizontal line) and the Wigner negativity (at origin) witness threshold (cyan horizontal line). When the lowest point of an interval of confidence is higher than a threshold value, the property corresponding to this threshold value is certified with more than 97.5% confidence. For each purity of preparation (of the squeezed vacuum state prior to the subtraction), the simulation is performed for three values of detection losses $\eta = 1, 0.9$ and 0.8.

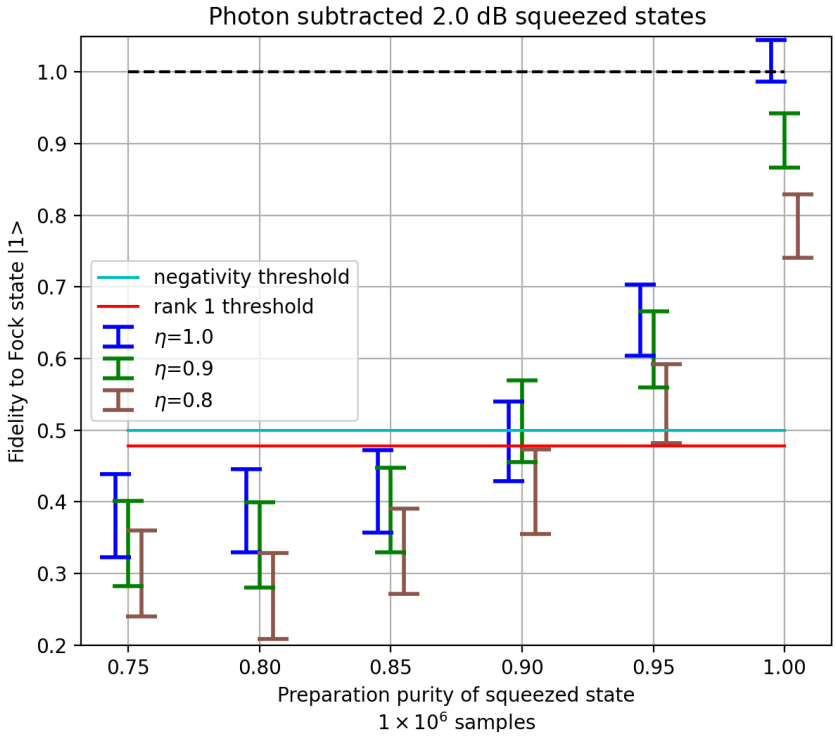

Fig. D.7 Estimates of the fidelity to Fock state $|1\rangle$ for lossy single-photon subtracted squeezed vacuum states for a squeezing factor of $s_{\mathrm{dB}} = 2\,\mathrm{dB}$, using unbalancing.

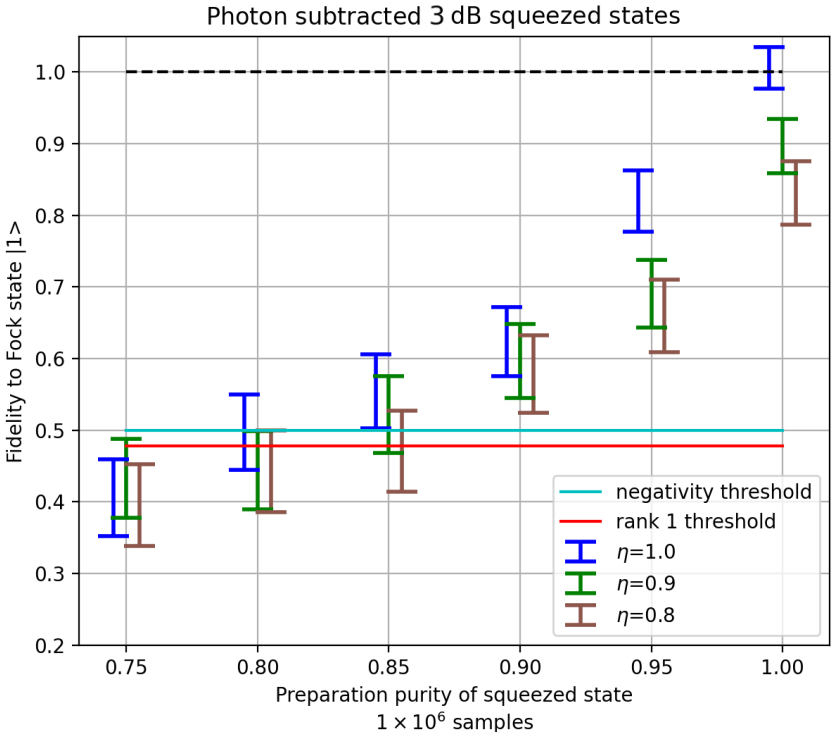

Fig. D.8 Estimates of the fidelity to Fock state $|1\rangle$ for lossy single-photon subtracted squeezed vacuum states for a squeezing factor of $s_{\mathrm{dB}} = 3\,\mathrm{dB}$, using unbalancing.

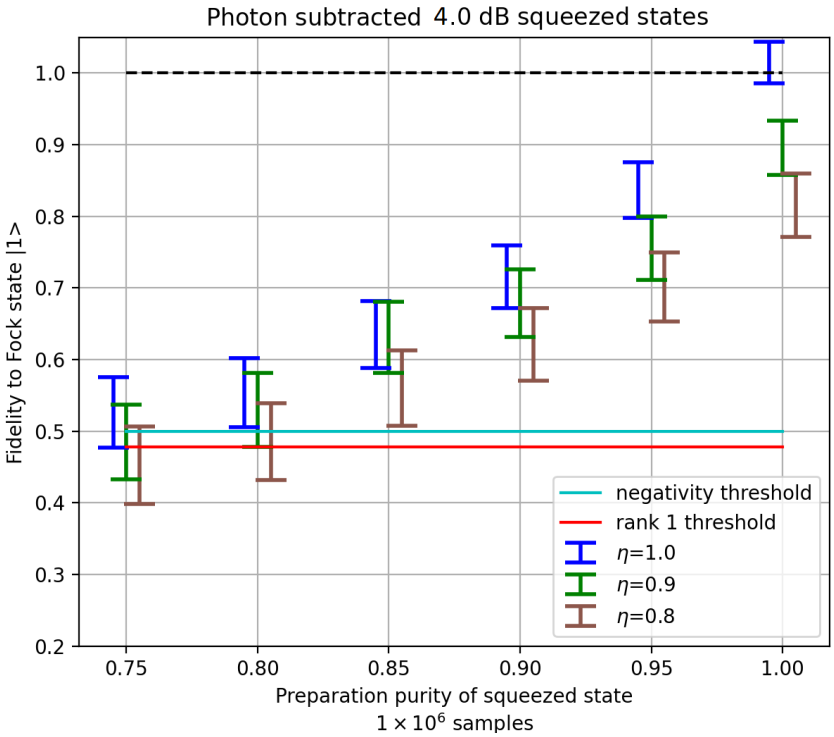

Fig. D.9 Estimates of the fidelity to Fock state $|1\rangle$ for lossy single-photon subtracted squeezed vacuum states for a squeezing factor of $s_{\mathrm{dB}} = 4\,\mathrm{dB}$, using unbalancing.

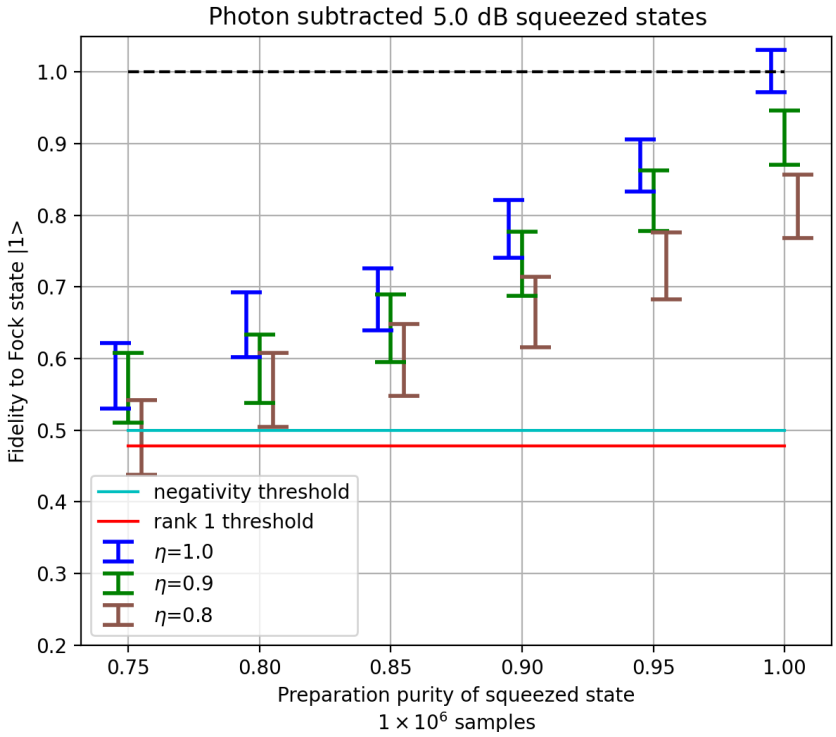

Fig. D.10 Estimates of the fidelity to Fock state $|1\rangle$ for lossy single-photon subtracted squeezed vacuum states for a squeezing factor of $s_{\mathrm{dB}} = 5\,\mathrm{dB}$, using unbalancing.

D.2.3 Unbalancing sensibility

We run the simulation for a single-photon subtracted squeezed vacuum state of initial squeezing factor $s_{\mathrm{dB}} = 3\,\mathrm{dB}$, various purity μ_{G} before subtraction, and no detection losses. Considering the double homodyne detection is balanced, this corresponds to the simulation result of figure 4.5, graph (a), which we reproduce with blue intervals of confidence in figure D.11. We then consider the double homodyne detection unbalanced for different values of unbalancing-squeezing factor u, i.e. $u = 2\,\mathrm{dB}$, $3\,\mathrm{dB}$ (perfect unbalancing) and $4\,\mathrm{dB}$, with simulation results shown in figure D.11. As one can see, the fidelity estimates are quite similar in this large range of unbalancing.

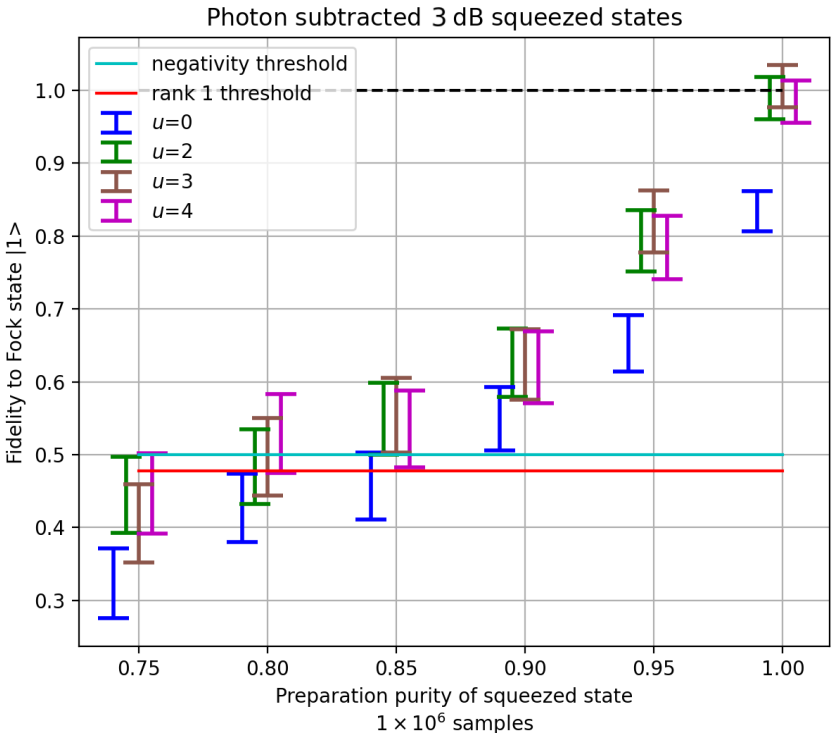

Fig. D.11 Estimates of the fidelity to Fock state $|1\rangle$ against preparation (before subtraction) purity μ_{G} for single-photon subtracted squeezed vacuum states for a squeezing factor of $s_{\mathrm{dB}} = 3\,\mathrm{dB}$. The double homodyne detection is either considered balanced (blue), or unbalanced with unbalancing squeezing factors $u = 2\,\mathrm{dB}$ (green), 3 dB (brown, perfect unbalancing) and 4 dB (magenta). We display the stellar rank 1 threshold (red horizontal line) and the Wigner negativity (at origin) witness threshold (cyan horizontal line) which, when beaten, certify the corresponding property with 97.5% confidence.

References

[Abbas 83] G. L. Abbas, V. W. S. Chan & T. K. Yee. *Local-Oscillator Excess-Noise Suppression for Homodyne and Heterodyne Detection.* Opt. Lett., OL, vol. 8, no. 8, pages 419–421, August 1983. Online URL. (Cited on page 78.)

[Adesso 14] Gerardo Adesso, Sammy Ragy & Antony R. Lee. *Continuous Variable Quantum Information: Gaussian States and Beyond.* Open Syst. Inf. Dyn., vol. 21, no. 01n02, page 1440001, June 2014. Online URL. (Cited on pages 15 and 18.)

[Appel 07] Jürgen Appel, Dallas Hoffman, Eden Figueroa & A. I. Lvovsky. *Electronic Noise in Optical Homodyne Tomography.* Phys. Rev. A, vol. 75, no. 3, page 035802, March 2007. Online URL. (Cited on page 84.)

[Arute 19] Frank Arute, Kunal Arya, Ryan Babbush, Dave Bacon, Joseph C. Bardin, Rami Barends, Rupak Biswas, Sergio Boixo, Fernando G. S. L. Brandao, David A. Buell, Brian Burkett, Yu Chen, Zijun Chen, Ben Chiaro, Roberto Collins, William Courtney, Andrew Dunsworth, Edward Farhi, Brooks Foxen, Austin Fowler, Craig Gidney, Marissa Giustina, Rob Graff, Keith Guerin, Steve Habegger, Matthew P. Harrigan, Michael J. Hartmann, Alan Ho, Markus Hoffmann, Trent Huang, Travis S. Humble, Sergei V. Isakov, Evan Jeffrey, Zhang Jiang, Dvir Kafri, Kostyantyn Kechedzhi, Julian Kelly, Paul V. Klimov, Sergey Knysh, Alexander Korotkov, Fedor Kostritsa, David Landhuis, Mike Lindmark, Erik Lucero, Dmitry Lyakh, Salvatore Mandrà, Jarrod R. McClean, Matthew McEwen, Anthony Megrant, Xiao Mi, Kristel Michielsen, Masoud Mohseni, Josh Mutus, Ofer Naaman, Matthew Neeley, Charles Neill, Murphy Yuezhen Niu, Eric Ostby, Andre Petukhov, John C. Platt, Chris Quintana, Eleanor G. Rieffel, Pedram Roushan, Nicholas C. Rubin, Daniel Sank, Kevin J. Satzinger, Vadim Smelyanskiy, Kevin J. Sung, Matthew D. Trevithick, Amit Vainsencher, Benjamin Villalonga, Theodore White, Z. Jamie Yao, Ping Yeh, Adam Zalcman, Hartmut Neven & John M. Martinis. *Quantum Supremacy Using a Programmable Superconducting Processor.* Nature, vol. 574, no. 7779, pages 505–510, October 2019. Online URL. (Cited on page 3.)

[Arzani 18] Francesco Arzani. *Measurement Based Quantum Information with Optical Frequency Combs.* PhD thesis, March 2018. Online URL. (Cited on pages 53 and 99.)

[Asavanant 19] Warit Asavanant, Yu Shiozawa, Shota Yokoyama, Baramee Charoensombutamon, Hiroki Emura, Rafael N. Alexander, Shuntaro Takeda, Junichi Yoshikawa, Nicolas C. Menicucci, Hidehiro Yonezawa & Akira Furusawa. *Generation of Time-Domain-Multiplexed Two-Dimensional Cluster State.* Science, vol. 366, no. 6463, pages 373–376, October 2019. Online URL. (Cited on page 3.)

[Aspect 82] Alain Aspect, Philippe Grangier & Gérard Roger. *Experimental Realization of Einstein-Podolsky-Rosen-Bohm Gedankenexperiment: A New Violation of Bell's Inequalities.* Phys. Rev. Lett., vol. 49, no. 2, pages 91–94, July 1982. Online URL. (Cited on page 2.)

[Aspect 15] Alain Aspect. *Closing the Door on Einstein and Bohr's Quantum Debate.* Physics, vol. 8, page 123, December 2015. Online URL. (Cited on page 2.)

[Averchenko 14] Valentin A. Averchenko, Valérian Thiel & Nicolas Treps. *Nonlinear Photon Subtraction from a Multimode Quantum Field.* Physical Review A, vol. 89, no. 6, page 063808, June 2014. Online URL. (Cited on pages 4, 102, 129, 130, and 135.)

[Averchenko 16] V Averchenko, C Jacquard, V Thiel, C Fabre & N Treps. *Multimode Theory of Single-Photon Subtraction.* New Journal of Physics, vol. 18, no. 8, page 083042, August 2016. Online URL. (Cited on pages 4, 102, 108, and 128.)

[Bartlett 02] Stephen D. Bartlett, Barry C. Sanders, Samuel L. Braunstein & Kae Nemoto. *Efficient Classical Simulation of Continuous Variable Quantum Information Processes.* Phys. Rev. Lett., vol. 88, no. 9, page 097904, February 2002. Online URL. (Cited on pages 3 and 33.)

[Bassi 03] Angelo Bassi & GianCarlo Ghirardi. *A General Scheme for Ensemble Purification.* Physics Letters A, vol. 309, no. 1, pages 24–28, March 2003. Online URL. (Cited on page 12.)

[Biagi 21] Nicola Biagi, Luca S. Costanzo, Marco Bellini & Alessandro Zavatta. *Generating Discorrelated States for Quantum Information Protocols by Coherent Multimode Photon Addition.* Advanced Quantum Technologies, vol. 4, no. 5, page 2000141, 2021. Online URL. (Cited on page 102.)

[Bloch 62] Claude Bloch & Albert Messiah. *The Canonical Form of an Antisymmetric Tensor and Its Application to the Theory of Superconductivity.* Nuclear Physics, vol. 39, pages 95–106, December 1962. Online URL. (Cited on page 27.)

[Blume-Kohout 10] Robin Blume-Kohout. *Optimal, Reliable Estimation of Quantum States.* New J. Phys., vol. 12, no. 4, page 043034, April 2010. Online URL. (Cited on page 157.)

[Bochner 33] S. Bochner. *Monotone Funktionen, Stieltjessche Integrale und harmonische Analyse.* Mathematische Annalen, vol. 108, pages 378–410, 1933. Online URL. (Cited on page 168.)

[Boeuf 00] N. Boeuf, David A. Branning, I. Chaperot, E. Dauler, S. Guerin, Gregg S. Jaeger, Antoine Muller & Alan L. Migdall. *Calculating Characteristics of Noncollinear Phase Matching in Uniaxial and Biaxial Crystals.* OE, vol. 39, no. 4, pages 1016–1024, April 2000. Online URL. (Cited on page 121.)

[Bourassa 21] J. Eli Bourassa, Rafael N. Alexander, Michael Vasmer, Ashlesha Patil, Ilan Tzitrin, Takaya Matsuura, Daiqin Su, Ben Q. Baragiola, Saikat Guha, Guillaume Dauphinais, Krishna K. Sabapathy, Nicolas C. Menicucci & Ish Dhand. *Blueprint for a Scalable Photonic Fault-Tolerant Quantum Computer.* Quantum, vol. 5, page 392, February 2021. Online URL. (Cited on pages 3 and 34.)

[Boyd 13] Robert W. Boyd. Nonlinear Optics. Academic Press, October 2013. (Cited on pages 111 and 130.)

[Brabec 92] T. Brabec, Ch Spielmann, P. F. Curley & F. Krausz. *Kerr Lens Mode Locking.* Opt. Lett., OL, vol. 17, no. 18, pages 1292–1294, September 1992. Online URL. (Cited on page 55.)

[Braunstein 05] Samuel L. Braunstein. *Squeezing as an Irreducible Resource.* Phys. Rev. A, vol. 71, no. 5, page 055801, May 2005. Online URL. (Cited on page 27.)

[Brecht 14] Benjamin Brecht. *Engineering Ultrafast Quantum Frequency Conversion.* PhD thesis, 2014. Online URL. (Cited on page 112.)

[Cahill 69a] K. E. Cahill & R. J. Glauber. *Density Operators and Quasiprobability Distributions.* Phys. Rev., vol. 177, no. 5, pages 1882–1902, January 1969. Online URL. (Cited on pages 14, 15, 16, and 17.)

[Cahill 69b] Kevin E. Cahill. *Regularization of the P Representation.* Phys. Rev., vol. 180, no. 5, pages 1244–1255, April 1969. Online URL. (Cited on page 16.)

[Cai 15] Yin Cai. *Quantum Coherent Control with an Optical Frequency Comb.* PhD thesis, Ecole normale supérieure - ENS PARIS ; East China normal university (Shanghai), October 2015. Online URL. (Cited on pages 55 and 155.)

[Cai 17] Y. Cai, J. Roslund, G. Ferrini, F. Arzani, X. Xu, C. Fabre & N. Treps. *Multimode Entanglement in Reconfigurable Graph States Using Optical Frequency Combs.* Nat Commun, vol. 8, no. 1, page 15645, August 2017. Online URL. (Cited on pages 3 and 68.)

[Caves 81] Carlton M. Caves. *Quantum-Mechanical Noise in an Interferometer*. Phys. Rev. D, vol. 23, no. 8, pages 1693–1708, April 1981. Online URL. (Cited on page 2.)

[Chabaud 17] U. Chabaud, T. Douce, D. Markham, P. van Loock, E. Kashefi & G. Ferrini. *Continuous-Variable Sampling from Photon-Added or Photon-Subtracted Squeezed States*. Phys. Rev. A, vol. 96, no. 6, page 062307, December 2017. Online URL. (Cited on page 142.)

[Chabaud 20a] Ulysse Chabaud. *Continuous Variable Quantum Advantages and Applications in Quantum Optics*. PhD thesis, Sorbonne Université, July 2020. Online URL. (Cited on pages 156 and 157.)

[Chabaud 20b] Ulysse Chabaud, Tom Douce, Frédéric Grosshans, Elham Kashefi & Damian Markham. *Building Trust for Continuous Variable Quantum States*. June 2020. Online URL. (Cited on pages 4, 140, 157, and 158.)

[Chabaud 20c] Ulysse Chabaud, Damian Markham & Frédéric Grosshans. *Stellar Representation of Non-Gaussian Quantum States*. Phys. Rev. Lett., vol. 124, no. 6, page 063605, February 2020. Online URL. (Cited on pages 4, 36, 37, 38, 39, and 40.)

[Chabaud 21a] Ulysse Chabaud, Pierre-Emmanuel Emeriau & Frédéric Grosshans. *Witnessing Wigner Negativity*. Quantum, vol. 5, page 471, June 2021. Online URL. (Cited on pages 35 and 168.)

[Chabaud 21b] Ulysse Chabaud, Giulia Ferrini, Frédéric Grosshans & Damian Markham. *Classical Simulation of Gaussian Quantum Circuits with Non-Gaussian Input States*. Phys. Rev. Research, vol. 3, no. 3, page 033018, July 2021. Online URL. (Cited on pages 44, 45, and 48.)

[Chabaud 21c] Ulysse Chabaud, Frédéric Grosshans, Elham Kashefi & Damian Markham. *Efficient Verification of Boson Sampling*. Quantum, vol. 5, page 578, November 2021. Online URL. (Cited on pages 45, 140, 157, 158, 159, and 169.)

[Chabaud 21d] Ulysse Chabaud, Ganaël Roeland, Mattia Walschaers, Frédéric Grosshans, Valentina Parigi, Damian Markham & Nicolas Treps. *Certification of Non-Gaussian States with Operational Measurements*. PRX Quantum, vol. 2, no. 2, page 020333, June 2021. Online URL. (Cited on pages 4, 6, 31, 36, 38, 41, 42, 43, 45, 140, 161, 163, 165, 169, 171, and 174.)

[Chabaud 23] Ulysse Chabaud & Mattia Walschaers. *Resources for Bosonic Quantum Computational Advantage*. Phys. Rev. Lett., vol. 130, no. 9, page 090602, March 2023. Online URL. (Cited on pages 3, 45, and 163.)

[Chalopin 10] B. Chalopin, F. Scazza, C. Fabre & N. Treps. *Multimode Nonclassical Light Generation through the Optical-Parametric-Oscillator Threshold*. Phys. Rev. A, vol. 81, no. 6, page 061804, June 2010. Online URL. (Cited on page 77.)

[Chen 14] Moran Chen, Nicolas C. Menicucci & Olivier Pfister. *Experimental Realization of Multipartite Entanglement of 60 Modes of a Quantum Optical Frequency Comb.* Phys. Rev. Lett., vol. 112, no. 12, page 120505, March 2014. Online URL. (Cited on page 3.)

[Christ 13] Andreas Christ, Benjamin Brecht, Wolfgang Mauerer & Christine Silberhorn. *Theory of Quantum Frequency Conversion and Type-II Parametric down-Conversion in the High-Gain Regime.* New J. Phys., vol. 15, no. 5, page 053038, May 2013. Online URL. (Cited on page 112.)

[Christandl 12] Matthias Christandl & Renato Renner. *Reliable Quantum State Tomography.* Phys. Rev. Lett., vol. 109, no. 12, page 120403, September 2012. Online URL. (Cited on page 157.)

[Cimini 20] Valeria Cimini, Marco Barbieri, Nicolas Treps, Mattia Walschaers & Valentina Parigi. *Neural Networks for Detecting Multimode Wigner Negativity.* Phys. Rev. Lett., vol. 125, no. 16, page 160504, October 2020. Online URL. (Cited on page 168.)

[Collett 87] M. J. Collett & R. Loudon. *Output Properties of Parametric Amplifiers in Cavities.* J. Opt. Soc. Am. B, JOSAB, vol. 4, no. 10, pages 1525–1534, October 1987. Online URL. (Cited on page 88.)

[D'Ariano 03] G. Mauro D'Ariano, Matteo G. A. Paris & Massimiliano F. Sacchi. *Quantum Tomography.* February 2003. Online URL. (Cited on page 157.)

[de Araujo 12] Renné Medeiros de Araujo. *Génération et manipulation de peignes de fréquences quantiques multimodes.* PhD thesis, Université Pierre et Marie Curie - Paris VI, November 2012. Online URL. (Cited on pages 55, 64, 67, 68, and 69.)

[de Valcárcel 06] G. J. de Valcárcel, G. Patera, N. Treps & C. Fabre. *Multimode Squeezing of Frequency Combs.* Phys. Rev. A, vol. 74, no. 6, page 061801, December 2006. Online URL. (Cited on page 4.)

[Diddams 10] Scott A. Diddams. *The Evolving Optical Frequency Comb [Invited].* J. Opt. Soc. Am. B, JOSAB, vol. 27, no. 11, pages B51–B62, November 2010. Online URL. (Cited on page 56.)

[Donley 05] E. A. Donley, T. P. Heavner, F. Levi, M. O. Tataw & S. R. Jefferts. *Double-Pass Acousto-Optic Modulator System.* Review of Scientific Instruments, vol. 76, no. 6, page 063112, June 2005. Online URL. (Cited on page 94.)

[Drever 83] R. W. P. Drever, J. L. Hall, F. V. Kowalski, J. Hough, G. M. Ford, A. J. Munley & H. Ward. *Laser Phase and Frequency Stabilization Using an Optical Resonator.* Appl. Phys. B, vol. 31, no. 2, pages 97–105, June 1983. Online URL. (Cited on page 66.)

[Dudley 10] J. M. Dudley & J. R. Taylor, editeurs. Supercontinuum Generation in Optical Fibers. Cambridge University Press, Cambridge, 2010. Online URL. (Cited on page 100.)

[Dufour 18] Adrien Dufour. *Ingénierie d'états Quantiques Multimodes Avec Des Impulsions Femtosecondes*. PhD thesis, 2018. Online URL. (Cited on pages 67, 127, 133, 135, 155, 180, and 181.)

[Duris 20] Joseph Duris, Siqi Li, Taran Driver, Elio G. Champenois, James P. MacArthur, Alberto A. Lutman, Zhen Zhang, Philipp Rosenberger, Jeff W. Aldrich, Ryan Coffee, Giacomo Coslovich, Franz-Josef Decker, James M. Glownia, Gregor Hartmann, Wolfram Helml, Andrei Kamalov, Jonas Knurr, Jacek Krzywinski, Ming-Fu Lin, Jon P. Marangos, Megan Nantel, Adi Natan, Jordan T. O'Neal, Niranjan Shivaram, Peter Walter, Anna Li Wang, James J. Welch, Thomas J. A. Wolf, Joseph Z. Xu, Matthias F. Kling, Philip H. Bucksbaum, Alexander Zholents, Zhirong Huang, James P. Cryan & Agostino Marinelli. *Tunable Isolated Attosecond X-ray Pulses with Gigawatt Peak Power from a Free-Electron Laser*. Nat. Photonics, vol. 14, no. 1, pages 30–36, January 2020. Online URL. (Cited on page 55.)

[Eckstein 12] Andreas Eckstein. *Mastering Quantum Light Pulses with Nonlinear Waveguide Interactions*. PhD thesis, Friedrich-Alexander-Universität Erlangen-Nürnberg (FAU), 2012. Online URL. (Cited on pages 67 and 204.)

[Einstein 35] A. Einstein, B. Podolsky & N. Rosen. *Can Quantum-Mechanical Description of Physical Reality Be Considered Complete?* Phys. Rev., vol. 47, no. 10, pages 777–780, May 1935. Online URL. (Cited on page 29.)

[Eisert 20] J. Eisert, D. Hangleiter, N. Walk, I. Roth, D. Markham, R. Parekh, U. Chabaud & E. Kashefi. *Quantum Certification and Benchmarking*. arXiv:1910.06343 [cond-mat, physics:quant-ph], February 2020. Online URL. (Cited on page 157.)

[Ekert 95] Artur Ekert & Peter L. Knight. *Entangled Quantum Systems and the Schmidt Decomposition*. American Journal of Physics, vol. 63, no. 5, pages 415–423, May 1995. Online URL. (Cited on page 68.)

[Fabre 20] C. Fabre & N. Treps. *Modes and States in Quantum Optics*. Rev. Mod. Phys., vol. 92, no. 3, page 035005, September 2020. Online URL. (Cited on pages 6, 8, 21, 26, and 30.)

[Faist 16] Philippe Faist & Renato Renner. *Practical and Reliable Error Bars in Quantum Tomography*. Phys. Rev. Lett., vol. 117, no. 1, page 010404, July 2016. Online URL. (Cited on page 157.)

[Fedorov 15] Ilya A. Fedorov, Aleksey K. Fedorov, Yury V. Kurochkin & A. I. Lvovsky. *Tomography of a Multimode Quantum Black Box*. New J. Phys., vol. 17, no. 4, page 043063, April 2015. Online URL. (Cited on page 135.)

[Ferraro 05] Alessandro Ferraro, Stefano Olivares & Matteo G. A. Paris. *Gaussian States in Continuous Variable Quantum Information.* arXiv:quant-ph/0503237, March 2005. Online URL. (Cited on pages 24, 29, 30, and 140.)

[Filip 11] Radim Filip & Ladislav Mišta. *Detecting Quantum States with a Positive Wigner Function beyond Mixtures of Gaussian States.* Phys. Rev. Lett., vol. 106, no. 20, page 200401, May 2011. Online URL. (Cited on page 37.)

[Fitzsimons 17] Joseph F. Fitzsimons & Elham Kashefi. *Unconditionally Verifiable Blind Quantum Computation.* Phys. Rev. A, vol. 96, no. 1, page 012303, July 2017. Online URL. (Cited on page 156.)

[Fiurášek 13] Jaromír Fiurášek & Miroslav Ježek. *Witnessing Negativity of Wigner Function by Estimating Fidelities of Catlike States from Homodyne Measurements.* Phys. Rev. A, vol. 87, no. 6, page 062115, June 2013. Online URL. (Cited on page 35.)

[Fork 84] R. L. Fork, O. E. Martinez & J. P. Gordon. *Negative Dispersion Using Pairs of Prisms.* Opt. Lett., OL, vol. 9, no. 5, pages 150–152, May 1984. Online URL. (Cited on page 55.)

[Fortier 19] Tara Fortier & Esther Baumann. *20 Years of Developments in Optical Frequency Comb Technology and Applications.* Commun Phys, vol. 2, no. 1, pages 1–16, December 2019. Online URL. (Cited on page 56.)

[Freedman 72] Stuart J. Freedman & John F. Clauser. *Experimental Test of Local Hidden-Variable Theories.* Phys. Rev. Lett., vol. 28, no. 14, pages 938–941, April 1972. Online URL. (Cited on page 2.)

[Fröhlich 77] J. Fröhlich. *Application of Commutator Theorems to the Integration of Representations of Lie Algebras and Commutation Relations.* Communications in Mathematical Physics, vol. 54, no. 2, pages 135–150, January 1977. Online URL. (Cited on page 190.)

[Furusawa 11] Akira Furusawa & Peter van Loock. Quantum Teleportation and Entanglement: A Hybrid Approach to Optical Quantum Information Processing. John Wiley & Sons, May 2011. (Cited on page 2.)

[García-Álvarez 20] Laura García-Álvarez, Cameron Calcluth, Alessandro Ferraro & Giulia Ferrini. *Efficient Simulatability of Continuous-Variable Circuits with Large Wigner Negativity.* Phys. Rev. Res., vol. 2, no. 4, page 043322, December 2020. Online URL. (Cited on page 34.)

[Genoni 07] Marco G. Genoni, Matteo G. A. Paris & Konrad Banaszek. *Measure of the Non-Gaussian Character of a Quantum State.* Phys. Rev. A, vol. 76, no. 4, page 042327, October 2007. Online URL. (Cited on page 31.)

[Genoni 08] Marco G. Genoni, Matteo G. A. Paris & Konrad Banaszek. *Quantifying the Non-Gaussian Character of a Quantum State by Quantum Relative Entropy.* Phys. Rev. A, vol. 78, no. 6, page 060303, December 2008. Online URL. (Cited on page 31.)

[Genoni 10] Marco G. Genoni & Matteo G. A. Paris. *Quantifying Non-Gaussianity for Quantum Information.* Phys. Rev. A, vol. 82, no. 5, page 052341, November 2010. Online URL. (Cited on page 31.)

[Genoni 13] Marco G. Genoni, Mattia L. Palma, Tommaso Tufarelli, Stefano Olivares, M. S. Kim & Matteo G. A. Paris. *Detecting Quantum Non-Gaussianity via the Wigner Function.* Phys. Rev. A, vol. 87, no. 6, page 062104, June 2013. Online URL. (Cited on page 36.)

[Ghotbi 04] M. Ghotbi & M. Ebrahim-Zadeh. *Optical Second Harmonic Generation Properties of BiB_3O_6.* Opt. Express, OE, vol. 12, no. 24, pages 6002–6019, November 2004. Online URL. (Cited on page 64.)

[Ghotbi 05] M. Ghotbi & M. Ebrahim-Zadeh. *990 mW Average Power, 52% Efficient, High-Repetition-Rate Picosecond-Pulse Generation in the Blue with BiB_3O_6.* Opt. Lett., OL, vol. 30, no. 24, pages 3395–3397, December 2005. Online URL. (Cited on page 64.)

[Ghotbi 06] M. Ghotbi, A. Esteban-Martin & M. Ebrahim-Zadeh. *BiB_3O_6 Femtosecond Optical Parametric Oscillator.* Opt. Lett., OL, vol. 31, no. 21, pages 3128–3130, November 2006. Online URL. (Cited on pages 64 and 66.)

[Glauber 63] Roy J. Glauber. *Coherent and Incoherent States of the Radiation Field.* Phys. Rev., vol. 131, no. 6, pages 2766–2788, September 1963. Online URL. (Cited on pages 15 and 19.)

[Gottesman 99] Daniel Gottesman & Isaac L. Chuang. *Demonstrating the Viability of Universal Quantum Computation Using Teleportation and Single-Qubit Operations.* Nature, vol. 402, no. 6760, pages 390–393, November 1999. Online URL. (Cited on page 2.)

[Gottesman 01] Daniel Gottesman, Alexei Kitaev & John Preskill. *Encoding a Qubit in an Oscillator.* Phys. Rev. A, vol. 64, no. 1, page 012310, June 2001. Online URL. (Cited on page 37.)

[Grice 01] W. P. Grice, A. B. U'Ren & I. A. Walmsley. *Eliminating Frequency and Space-Time Correlations in Multiphoton States.* Phys. Rev. A, vol. 64, no. 6, page 063815, November 2001. Online URL. (Cited on page 67.)

[Grosshans 01] F. Grosshans & P. Grangier. *Effective Quantum Efficiency in the Pulsed Homodyne Detection of a N-Photon State.* Eur. Phys. J. D, vol. 14, no. 1, pages 119–125, April 2001. Online URL. (Cited on page 83.)

[Grover 96] Lov K. Grover. *A Fast Quantum Mechanical Algorithm for Database Search.* Proceedings of the twenty-eighth annual ACM symposium on Theory of Computing, pages 212–219, July 1996. Online URL. (Cited on page 3.)

[Grynberg 10] Gilbert Grynberg, Alain Aspect & Claude Fabre. Introduction to Quantum Optics: From the Semi-classical Approach to Quantized Light. Cambridge University Press, Cambridge, 2010. Online URL. (Cited on pages 6, 8, and 105.)

[Hall 00] J.L. Hall. *Optical Frequency Measurement: 40 Years of Technology Revolutions.* IEEE Journal of Selected Topics in Quantum Electronics, vol. 6, no. 6, pages 1136–1144, November 2000. (Cited on page 56.)

[Hall 06] John L. Hall. *Nobel Lecture: Defining and Measuring Optical Frequencies.* Rev. Mod. Phys., vol. 78, no. 4, pages 1279–1295, November 2006. Online URL. (Cited on page 56.)

[Hamilton 17] Craig S. Hamilton, Regina Kruse, Linda Sansoni, Sonja Barkhofen, Christine Silberhorn & Igor Jex. *Gaussian Boson Sampling.* Phys. Rev. Lett., vol. 119, no. 17, page 170501, October 2017. Online URL. (Cited on page 34.)

[Hammer 16] J. Hammer. Spectral Wavelet Interferometry via Dispersive Fourier Transformation. 2016. (Cited on page 100.)

[Hänsch 06] Theodor W. Hänsch. *Nobel Lecture: Passion for Precision.* Rev. Mod. Phys., vol. 78, no. 4, pages 1297–1309, November 2006. Online URL. (Cited on page 56.)

[Hensen 15] B. Hensen, H. Bernien, A. E. Dréau, A. Reiserer, N. Kalb, M. S. Blok, J. Ruitenberg, R. F. L. Vermeulen, R. N. Schouten, C. Abellán, W. Amaya, V. Pruneri, M. W. Mitchell, M. Markham, D. J. Twitchen, D. Elkouss, S. Wehner, T. H. Taminiau & R. Hanson. *Loophole-Free Bell Inequality Violation Using Electron Spins Separated by 1.3 Kilometres.* Nature, vol. 526, no. 7575, pages 682–686, October 2015. Online URL. (Cited on page 2.)

[Heritage 85] J. P. Heritage, A. M. Weiner & R. N. Thurston. *Picosecond Pulse Shaping by Spectral Phase and Amplitude Manipulation.* Opt. Lett., OL, vol. 10, no. 12, pages 609–611, December 1985. Online URL. (Cited on page 61.)

[Hoeffding 63] Wassily Hoeffding. *Probability Inequalities for Sums of Bounded Random Variables.* Journal of the American Statistical Association, vol. 58, no. 301, pages 13–30, March 1963. Online URL. (Cited on page 165.)

[Hong 86] C. K. Hong & L. Mandel. *Experimental Realization of a Localized One-Photon State.* Phys. Rev. Lett., vol. 56, no. 1, pages 58–60, January 1986. Online URL. (Cited on page 32.)

[Hudson 74] R.L. Hudson. *When Is the Wigner Quasi-Probability Density Non-Negative?* Reports on Mathematical Physics, vol. 6, no. 2, pages 249–252, October 1974. Online URL. (Cited on page 34.)

[Husimi 40] Kôdi Husimi. *Some Formal Properties of the Density Matrix.* Proceedings of the Physico-Mathematical Society of Japan. 3rd Series, vol. 22, no. 4, pages 264–314, 1940. (Cited on page 16.)

[Ikramov 18] Kh. D. Ikramov. *On the Symplectic Eigenvalues of Positive Definite Matrices.* MoscowUniv.Comput.Math.Cybern., vol. 42, no. 1, pages 1–4, January 2018. Online URL. (Cited on page 28.)

[Jacquard 17] Clément Jacquard. *A Single-Photon Subtractor for Spectrally Multimode Quantum States.* PhD thesis, Université Pierre et Marie Curie - Paris VI, January 2017. Online URL. (Cited on pages 62, 127, 133, 135, and 138.)

[Jiang 12] Shifeng Jiang, Nicolas Treps & Claude Fabre. *A Time/Frequency Quantum Analysis of the Light Generated by Synchronously Pumped Optical Parametric Oscillators.* New J. Phys., vol. 14, no. 4, page 043006, April 2012. Online URL. (Cited on pages 69 and 73.)

[Joly 12] N. Joly. Contribution à l'élaboration de sources spectralement étendues par propagation d'impulsions dans les fibres microstructurées. 2012. (Cited on page 100.)

[Kalai 23] Gil Kalai, Yosef Rinott & Tomer Shoham. *Questions and Concerns About Google's Quantum Supremacy Claim.* May 2023. Online URL. (Cited on page 3.)

[Kenfack 04] Anatole Kenfack & Karol Życzkowski. *Negativity of the Wigner Function as an Indicator of Non-Classicality.* J. Opt. B: Quantum Semiclass. Opt., vol. 6, no. 10, page 396, August 2004. Online URL. (Cited on page 36.)

[Kennard 27] E. H. Kennard. *Zur Quantenmechanik einfacher Bewegungstypen.* Z. Physik, vol. 44, no. 4-5, pages 326–352, April 1927. Online URL. (Cited on page 22.)

[Kerr 75a] John Kerr. *LIV.* A New Relation between Electricity and Light: Dielectrified Media Birefringent *(Second Paper).* The London, Edinburgh, and Dublin Philosophical Magazine and Journal of Science, vol. 50, no. 333, pages 446–458, December 1875. Online URL. (Cited on page 55.)

[Kerr 75b] John Kerr. *XL.* A New Relation between Electricity and Light: Dielectrified Media Birefringent. The London, Edinburgh, and Dublin Philosophical Magazine and Journal of Science, vol. 50, no. 332, pages 337–348, November 1875. Online URL. (Cited on page 55.)

[Kim 23] Youngseok Kim, Andrew Eddins, Sajant Anand, Ken Xuan Wei, Ewout van den Berg, Sami Rosenblatt, Hasan Nayfeh, Yantao Wu, Michael Zaletel, Kristan Temme & Abhinav Kandala. *Evidence for the Utility of Quantum Computing before Fault Tolerance.* Nature, vol. 618, no. 7965, pages 500–505, June 2023. Online URL. (Cited on page 3.)

[Knill 98] Emanuel Knill, Raymond Laflamme & Wojciech H. Zurek. *Resilient Quantum Computation.* Science, vol. 279, no. 5349, pages 342–345, January 1998. Online URL. (Cited on page 3.)

[Kouadou 21] Tiphaine Kouadou. *Single-Pass Generation and Detection of Ultrafast Multimode Squeezed Light.* PhD thesis, Sorbonne Université, March 2021. Online URL. (Cited on page 206.)

[Krausz 09] Ferenc Krausz & Misha Ivanov. *Attosecond Physics.* Rev. Mod. Phys., vol. 81, no. 1, pages 163–234, February 2009. Online URL. (Cited on page 55.)

[Kumar 12] R. Kumar, E. Barrios, A. MacRae, E. Cairns, E.H. Huntington & A.I. Lvovsky. *Versatile Wideband Balanced Detector for Quantum Optical Homodyne Tomography.* Optics Communications, vol. 285, no. 24, pages 5259–5267, November 2012. Online URL. (Cited on page 85.)

[Lachman 19] Lukáš Lachman, Ivo Straka, Josef Hloušek, Miroslav Ježek & Radim Filip. *Faithful Hierarchy of Genuine n-Photon Quantum Non-Gaussian Light.* Phys. Rev. Lett., vol. 123, no. 4, page 043601, July 2019. Online URL. (Cited on page 37.)

[Larsen 19] Mikkel V. Larsen, Xueshi Guo, Casper R. Breum, Jonas S. Neergaard-Nielsen & Ulrik L. Andersen. *Deterministic Generation of a Two-Dimensional Cluster State.* Science, vol. 366, no. 6463, pages 369–372, October 2019. Online URL. (Cited on page 3.)

[Leonhardt 95] U. Leonhardt & H. Paul. *Measuring the Quantum State of Light.* Progress in Quantum Electronics, vol. 19, no. 2, pages 89–130, January 1995. Online URL. (Cited on pages 6, 13, 14, 15, 20, 22, 26, 29, 32, 145, 168, and 174.)

[Lobino 08] Mirko Lobino, Dmitry Korystov, Connor Kupchak, Eden Figueroa, Barry C. Sanders & A. I. Lvovsky. *Complete Characterization of Quantum-Optical Processes.* Science, vol. 322, no. 5901, pages 563–566, October 2008. Online URL. (Cited on page 135.)

[Loudon 00] Rodney Loudon. The Quantum Theory of Light. Oxford University Press, Oxford, New York, third edition, third edition edition, September 2000. (Cited on pages 81, 86, 88, 91, and 110.)

[Lütkenhaus 95] N. Lütkenhaus & Stephen M. Barnett. *Nonclassical Effects in Phase Space.* Phys. Rev. A, vol. 51, no. 4, pages 3340–3342, April 1995. Online URL. (Cited on page 17.)

[Lvovsky 04] A. I. Lvovsky. *Iterative Maximum-Likelihood Reconstruction in Quantum Homodyne Tomography*. J. Opt. B: Quantum Semiclass. Opt., vol. 6, no. 6, page S556, May 2004. Online URL. (Cited on pages 132 and 142.)

[Lvovsky 09] A. I. Lvovsky & M. G. Raymer. *Continuous-Variable Optical Quantum-State Tomography*. Rev. Mod. Phys., vol. 81, no. 1, pages 299–332, March 2009. Online URL. (Cited on pages 142 and 159.)

[Lvovsky 20] A. I. Lvovsky, Philippe Grangier, Alexei Ourjoumtsev, Valentina Parigi, Masahide Sasaki & Rosa Tualle-Brouri. *Production and Applications of Non-Gaussian Quantum States of Light*. June 2020. Online URL. (Cited on pages 3 and 102.)

[Lyot 33] B. Lyot. *Optical Apparatus with Wide Field Using Interference of Polarized Light*. C.R. Acad. Sci. (Paris), vol. 197, no. 1593, 1933. (Cited on page 55.)

[Maiman 60] T. H. Maiman. *Stimulated Optical Radiation in Ruby*. Nature, vol. 187, no. 4736, pages 493–494, August 1960. Online URL. (Cited on page 2.)

[Mandel 95] Leonard Mandel & Emil Wolf. Optical coherence and quantum optics. Cambridge University Press, Cambridge, 1995. Online URL. (Cited on pages 16 and 17.)

[Mari 11] A. Mari, K. Kieling, B. Melholt Nielsen, E. S. Polzik & J. Eisert. *Directly Estimating Non-Classicality*. Phys. Rev. Lett., vol. 106, no. 1, page 010403, January 2011. Online URL. (Cited on pages 35 and 168.)

[Mari 12] A. Mari & J. Eisert. *Positive Wigner Functions Render Classical Simulation of Quantum Computation Efficient*. Phys. Rev. Lett., vol. 109, no. 23, page 230503, December 2012. Online URL. (Cited on pages 3 and 34.)

[Menicucci 06] Nicolas C. Menicucci, Peter van Loock, Mile Gu, Christian Weedbrook, Timothy C. Ralph & Michael A. Nielsen. *Universal Quantum Computation with Continuous-Variable Cluster States*. Phys. Rev. Lett., vol. 97, no. 11, page 110501, September 2006. Online URL. (Cited on page 2.)

[Michel 21] Thibault Michel. *Optimisation of the Pump Spectral Shape in a Parametric down Conversion Process to Generate Multimode Entangled States*. These en préparation, Sorbonne université, 2021. Online URL. (Cited on pages 18, 25, 53, 60, 62, 63, 64, 66, 68, 70, 73, 74, 96, 99, and 155.)

[Monmayrant 05] Antoine Monmayrant. *Façonnage et Caractérisation d'impulsions Ultracourtes : Contrôle Cohérent de Systèmes Simples*. These de doctorat, Toulouse 3, January 2005. Online URL. (Cited on page 61.)

[Monmayrant 10] Antoine Monmayrant, Sébastien Weber & Béatrice Chatel. *A Newcomer's Guide to Ultrashort Pulse Shaping and Characterization*. J. Phys. B: At. Mol. Opt. Phys., vol. 43, no. 10, page 103001, May 2010. Online URL. (Cited on page 61.)

[Morin 13a] Olivier Morin. *Non-Gaussian States and Measurements for Quantum Information.* PhD thesis, Université Pierre et Marie Curie - Paris VI, December 2013. Online URL. (Cited on pages 13 and 180.)

[Morin 13b] Olivier Morin, Claude Fabre & Julien Laurat. *Experimentally Accessing the Optimal Temporal Mode of Traveling Quantum Light States.* Phys. Rev. Lett., vol. 111, no. 21, page 213602, November 2013. Online URL. (Cited on page 180.)

[Morvan 23] A. Morvan, B. Villalonga, X. Mi, S. Mandrà, A. Bengtsson, P. V. Klimov, Z. Chen, S. Hong, C. Erickson, I. K. Drozdov, J. Chau, G. Laun, R. Movassagh, A. Asfaw, L. T. A. N. Brandão, R. Peralta, D. Abanin, R. Acharya, R. Allen, T. I. Andersen, K. Anderson, M. Ansmann, F. Arute, K. Arya, J. Atalaya, J. C. Bardin, A. Bilmes, G. Bortoli, A. Bourassa, J. Bovaird, L. Brill, M. Broughton, B. B. Buckley, D. A. Buell, T. Burger, B. Burkett, N. Bushnell, J. Campero, H. S. Chang, B. Chiaro, D. Chik, C. Chou, J. Cogan, R. Collins, P. Conner, W. Courtney, A. L. Crook, B. Curtin, D. M. Debroy, A. Del Toro Barba, S. Demura, A. Di Paolo, A. Dunsworth, L. Faoro, E. Farhi, R. Fatemi, V. S. Ferreira, L. Flores Burgos, E. Forati, A. G. Fowler, B. Foxen, G. Garcia, E. Genois, W. Giang, C. Gidney, D. Gilboa, M. Giustina, R. Gosula, A. Grajales Dau, J. A. Gross, S. Habegger, M. C. Hamilton, M. Hansen, M. P. Harrigan, S. D. Harrington, P. Heu, M. R. Hoffmann, T. Huang, A. Huff, W. J. Huggins, L. B. Ioffe, S. V. Isakov, J. Iveland, E. Jeffrey, Z. Jiang, C. Jones, P. Juhas, D. Kafri, T. Khattar, M. Khezri, M. Kieferová, S. Kim, A. Kitaev, A. R. Klots, A. N. Korotkov, F. Kostritsa, J. M. Kreikebaum, D. Landhuis, P. Laptev, K.-M. Lau, L. Laws, J. Lee, K. W. Lee, Y. D. Lensky, B. J. Lester, A. T. Lill, W. Liu, A. Locharla, F. D. Malone, O. Martin, S. Martin, J. R. McClean, M. McEwen, K. C. Miao, A. Mieszala, S. Montazeri, W. Mruczkiewicz, O. Naaman, M. Neeley, C. Neill, A. Nersisyan, M. Newman, J. H. Ng, A. Nguyen, M. Nguyen, M. Yuezhen Niu, T. E. O'Brien, S. Omonije, A. Opremcak, A. Petukhov, R. Potter, L. P. Pryadko, C. Quintana, D. M. Rhodes, C. Rocque, P. Roushan, N. C. Rubin, N. Saei, D. Sank, K. Sankaragomathi, K. J. Satzinger, H. F. Schurkus, C. Schuster, M. J. Shearn, A. Shorter, N. Shutty, V. Shvarts, V. Sivak, J. Skruzny, W. C. Smith, R. D. Somma, G. Sterling, D. Strain, M. Szalay, D. Thor, A. Torres, G. Vidal, C. Vollgraff Heidweiller, T. White, B. W. K. Woo, C. Xing, Z. J. Yao, P. Yeh, J. Yoo, G. Young, A. Zalcman, Y. Zhang, N. Zhu, N. Zobrist, E. G. Rieffel, R. Biswas, R. Babbush, D. Bacon, J. Hilton, E. Lucero, H. Neven, A. Megrant, J. Kelly, I. Aleiner, V. Smelyanskiy, K. Kechedzhi, Y. Chen & S. Boixo. *Phase Transition in Random Circuit Sampling.* April 2023. Online URL. (Cited on page 3.)

[Mosley 08] Peter J. Mosley, Jeff S. Lundeen, Brian J. Smith, Piotr Wasylczyk, Alfred B. U'Ren, Christine Silberhorn & Ian A. Walmsley. *Heralded Generation of*

Ultrafast Single Photons in Pure Quantum States. Phys. Rev. Lett., vol. 100, no. 13, page 133601, April 2008. Online URL. (Cited on pages 67 and 114.)

[Nielsen 00] Michael A. Nielsen & Isaac L. Chuang. Quantum computation and quantum information. Cambridge University Press, Cambridge ; New York, 2000. (Cited on pages 11, 29, and 79.)

[Nielsen 07] Anne E. B. Nielsen & Klaus Mølmer. *Single-Photon-State Generation from a Continuous-Wave Nondegenerate Optical Parametric Oscillator.* Phys. Rev. A, vol. 75, no. 2, page 023806, February 2007. Online URL. (Cited on page 180.)

[Nieto 97] Michael Martin Nieto & D. Rodney Truax. *Holstein-Primakoff/Bogoliubov Transformations and the Multiboson System.* Fortschritte der Physik/Progress of Physics, vol. 45, no. 2, pages 145–156, 1997. Online URL. (Cited on page 146.)

[Ourjoumtsev 06] Alexei Ourjoumtsev, Rosa Tualle-Brouri, Julien Laurat & Philippe Grangier. *Generating Optical Schrödinger Kittens for Quantum Information Processing.* Science, vol. 312, no. 5770, pages 83–86, April 2006. Online URL. (Cited on pages 3 and 102.)

[Parigi 07a] V. Parigi, A. Zavatta & M. Bellini. *Manipulating Thermal Light States by the Controlled Addition and Subtraction of Single Photons.* Laser Phys. Lett., vol. 5, no. 3, page 246, November 2007. Online URL. (Cited on page 105.)

[Parigi 07b] V. Parigi, A. Zavatta, M. Kim & M. Bellini. *Probing Quantum Commutation Rules by Addition and Subtraction of Single Photons to/from a Light Field.* Science, vol. 317, no. 5846, pages 1890–1893, September 2007. Online URL. (Cited on page 3.)

[Paris 96] Matteo G. A. Paris. *Quantum State Measurement by Realistic Heterodyne Detection.* Phys. Rev. A, vol. 53, no. 4, pages 2658–2663, April 1996. Online URL. (Cited on page 157.)

[Patera 08] Giuseppe Patera. *Quantum Properties of Ultra-Short Pulses Generated by SPOPOs: Multi-Mode Squeezing and Entanglement.* PhD thesis, Université Pierre et Marie Curie - Paris VI, November 2008. Online URL. (Cited on page 68.)

[Patera 10] G. Patera, N. Treps, C. Fabre & G. J. de Valcárcel. *Quantum Theory of Synchronously Pumped Type I Optical Parametric Oscillators: Characterization of the Squeezed Supermodes.* Eur. Phys. J. D, vol. 56, no. 1, pages 123–140, January 2010. Online URL. (Cited on page 69.)

[Peres 96] Asher Peres. *Separability Criterion for Density Matrices.* Phys. Rev. Lett., vol. 77, no. 8, pages 1413–1415, August 1996. Online URL. (Cited on page 30.)

[Pinel 10] Olivier Pinel. *Optique quantique multimode avec des peignes de fréquence.* PhD thesis, Université Pierre et Marie Curie - Paris VI, December 2010. Online URL. (Cited on pages 55 and 60.)

[Polzik 92] E. S. Polzik, J. Carri & H. J. Kimble. *Spectroscopy with Squeezed Light.* Phys. Rev. Lett., vol. 68, no. 20, pages 3020–3023, May 1992. Online URL. (Cited on page 2.)

[Ra 17] Young-Sik Ra, Clément Jacquard, Adrien Dufour, Claude Fabre & Nicolas Treps. *Tomography of a Mode-Tunable Coherent Single-Photon Subtractor.* Physical Review X, vol. 7, no. 3, page 031012, July 2017. Online URL. (Cited on pages 4, 102, 133, 135, 136, and 137.)

[Ra 20] Young-Sik Ra, Adrien Dufour, Mattia Walschaers, Clément Jacquard, Thibault Michel, Claude Fabre & Nicolas Treps. *Non-Gaussian Quantum States of a Multimode Light Field.* Nat. Phys., vol. 16, no. 2, pages 144–147, February 2020. Online URL. (Cited on pages 3, 4, 102, 132, 133, 173, 174, and 180.)

[Rahimi-Keshari 16] Saleh Rahimi-Keshari, Timothy C. Ralph & Carlton M. Caves. *Sufficient Conditions for Efficient Classical Simulation of Quantum Optics.* Phys. Rev. X, vol. 6, no. 2, page 021039, June 2016. Online URL. (Cited on page 34.)

[Raussendorf 01] Robert Raussendorf & Hans J. Briegel. *A One-Way Quantum Computer.* Phys. Rev. Lett., vol. 86, no. 22, pages 5188–5191, May 2001. Online URL. (Cited on page 2.)

[Renault 22] Paul Renault. *Non Markovian Behavior and Spectral Density Measurement in Optical Quantum Networks.* PhD thesis, Sorbonne Université, April 2022. Online URL. (Cited on pages 54, 63, 66, and 100.)

[Reynaud 97] S. Reynaud, E. Giacobino & J. Zinn-Justin. Fluctuations Quantiques / Quantum Fluctuations: Les Houches Session LXIII, June 27 - July 28, 1995. January 1997. Online URL. (Cited on page 84.)

[Roeland 22] Ganaël Roeland, Srinivasan Kaali, Victor Roman Rodriguez, Nicolas Treps & Valentina Parigi. *Mode-Selective Single-Photon Addition to a Multimode Quantum Field.* New J. Phys., vol. 24, no. 4, page 043031, April 2022. Online URL. (Cited on pages 4, 102, and 127.)

[Roslund 14] Jonathan Roslund, Renné Medeiros de Araújo, Shifeng Jiang, Claude Fabre & Nicolas Treps. *Wavelength-Multiplexed Quantum Networks with Ultrafast Frequency Combs.* Nature Photon, vol. 8, no. 2, pages 109–112, February 2014. Online URL. (Cited on pages 3 and 4.)

[Royer 77] Antoine Royer. *Wigner Function as the Expectation Value of a Parity Operator.* Phys. Rev. A, vol. 15, no. 2, pages 449–450, February 1977. Online URL. (Cited on page 13.)

[Schrödinger 26] E. Schrödinger. *Der stetige Übergang von der Mikro- zur Makromechanik.* Naturwissenschaften, vol. 14, no. 28, pages 664–666, July 1926. Online URL. (Cited on page 19.)

[Serikawa 18] Takahiro Serikawa, Jun-ichi Yoshikawa, Shuntaro Takeda, Hidehiro Yonezawa, Timothy C. Ralph, Elanor H. Huntington & Akira Furusawa. *Generation of a Cat State in an Optical Sideband.* Phys. Rev. Lett., vol. 121, no. 14, page 143602, October 2018. Online URL. (Cited on page 3.)

[Shor 94] P.W. Shor. *Algorithms for Quantum Computation: Discrete Logarithms and Factoring.* Proceedings 35th Annual Symposium on Foundations of Computer Science, pages 124–134, November 1994. (Cited on page 3.)

[Shor 96] P.W. Shor. *Fault-Tolerant Quantum Computation.* Proceedings of 37th Conference on Foundations of Computer Science, pages 56–65, October 1996. (Cited on page 3.)

[Silva 17] G. B. Silva, S. Glancy & H. M. Vasconcelos. *Investigating Bias in Maximum-Likelihood Quantum-State Tomography.* Phys. Rev. A, vol. 95, no. 2, page 022107, February 2017. Online URL. (Cited on page 157.)

[Simon 88] R. Simon, E. C. G. Sudarshan & N. Mukunda. *Gaussian Pure States in Quantum Mechanics and the Symplectic Group.* Phys. Rev. A, vol. 37, no. 8, pages 3028–3038, April 1988. Online URL. (Cited on page 25.)

[Slusher 85] R. E. Slusher, L. W. Hollberg, B. Yurke, J. C. Mertz & J. F. Valley. *Observation of Squeezed States Generated by Four-Wave Mixing in an Optical Cavity.* Phys. Rev. Lett., vol. 55, no. 22, pages 2409–2412, November 1985. Online URL. (Cited on page 2.)

[Soto 83] Francisco Soto & Pierre Claverie. *When Is the Wigner Function of Multidimensional Systems Nonnegative?* Journal of Mathematical Physics, vol. 24, no. 1, pages 97–100, January 1983. Online URL. (Cited on pages 34 and 44.)

[Straka 14] Ivo Straka, Ana Predojević, Tobias Huber, Lukáš Lachman, Lorenz Butschek, Martina Miková, Michal Mičuda, Glenn S. Solomon, Gregor Weihs, Miroslav Ježek & Radim Filip. *Quantum Non-Gaussian Depth of Single-Photon States.* Phys. Rev. Lett., vol. 113, no. 22, page 223603, November 2014. Online URL. (Cited on page 37.)

[Straka 18] Ivo Straka, Lukáš Lachman, Josef Hloušek, Martina Miková, Michal Mičuda, Miroslav Ježek & Radim Filip. *Quantum Non-Gaussian Multiphoton Light.* npj Quantum Inf, vol. 4, no. 1, pages 1–5, January 2018. Online URL. (Cited on page 37.)

[Su 07] Xiaolong Su, Aihong Tan, Xiaojun Jia, Jing Zhang, Changde Xie & Kunchi Peng. *Experimental Preparation of Quadripartite Cluster and Greenberger-Horne-Zeilinger Entangled States for Continuous Variables*. Phys. Rev. Lett., vol. 98, no. 7, page 070502, February 2007. Online URL. (Cited on page 3.)

[Sudarshan 63] E C G Sudarshan. *Equivalence of Semiclassical and Quantum Mechanical Descriptions of Statistical Light Beams*. PHYSICAL REVIEW LETTERS, page 3, 1963. (Cited on pages 15 and 19.)

[Takeda 13] Shuntaro Takeda, Takahiro Mizuta, Maria Fuwa, Peter van Loock & Akira Furusawa. *Deterministic Quantum Teleportation of Photonic Quantum Bits by a Hybrid Technique*. Nature, vol. 500, no. 7462, pages 315–318, August 2013. Online URL. (Cited on page 3.)

[Temme 17] Kristan Temme, Sergey Bravyi & Jay M. Gambetta. *Error Mitigation for Short-Depth Quantum Circuits*. Phys. Rev. Lett., vol. 119, no. 18, page 180509, November 2017. Online URL. (Cited on page 3.)

[Thiel 15] Valérian Thiel. *Modal Analysis of an Ultrafast Frequency Comb : From Classical to Quantum Spectral Correlations*. PhD thesis, October 2015. Online URL. (Cited on pages 56, 58, and 89.)

[Treps 05] N. Treps, V. Delaubert, A. Maître, J. M. Courty & C. Fabre. *Quantum Noise in Multipixel Image Processing*. Phys. Rev. A, vol. 71, no. 1, page 013820, January 2005. Online URL. (Cited on page 21.)

[Tse 19] M. Tse, Haocun Yu, N. Kijbunchoo, A. Fernandez-Galiana, P. Dupej, L. Barsotti, C. D. Blair, D. D. Brown, S. E. Dwyer, A. Effler, M. Evans, P. Fritschel, V. V. Frolov, A. C. Green, G. L. Mansell, F. Matichard, N. Mavalvala, D. E. McClelland, L. McCuller, T. McRae, J. Miller, A. Mullavey, E. Oelker, I. Y. Phinney, D. Sigg, B. J. J. Slagmolen, T. Vo, R. L. Ward, C. Whittle, R. Abbott, C. Adams, R. X. Adhikari, A. Ananyeva, S. Appert, K. Arai, J. S. Areeda, Y. Asali, S. M. Aston, C. Austin, A. M. Baer, M. Ball, S. W. Ballmer, S. Banagiri, D. Barker, J. Bartlett, B. K. Berger, J. Betzwieser, D. Bhattacharjee, G. Billingsley, S. Biscans, R. M. Blair, N. Bode, P. Booker, R. Bork, A. Bramley, A. F. Brooks, A. Buikema, C. Cahillane, K. C. Cannon, X. Chen, A. A. Ciobanu, F. Clara, S. J. Cooper, K. R. Corley, S. T. Countryman, P. B. Covas, D. C. Coyne, L. E. H. Datrier, D. Davis, C. Di Fronzo, J. C. Driggers, T. Etzel, T. M. Evans, J. Feicht, P. Fulda, M. Fyffe, J. A. Giaime, K. D. Giardina, P. Godwin, E. Goetz, S. Gras, C. Gray, R. Gray, Anchal Gupta, E. K. Gustafson, R. Gustafson, J. Hanks, J. Hanson, T. Hardwick, R. K. Hasskew, M. C. Heintze, A. F. Helmling-Cornell, N. A. Holland, J. D. Jones, S. Kandhasamy, S. Karki, M. Kasprzack, K. Kawabe, P. J. King, J. S. Kissel, Rahul Kumar, M. Landry, B. B. Lane, B. Lantz, M. Laxen, Y. K. Lecoeuche, J. Leviton, J. Liu, M. Lormand, A. P. Lundgren, R. Macas, M. MacInnis, D. M. Macleod, S. Márka, Z. Márka,

D. V. Martynov, K. Mason, T. J. Massinger, R. McCarthy, S. McCormick, J. McIver, G. Mendell, K. Merfeld, E. L. Merilh, F. Meylahn, T. Mistry, R. Mittleman, G. Moreno, C. M. Mow-Lowry, S. Mozzon, T. J. N. Nelson, P. Nguyen, L. K. Nuttall, J. Oberling, R. J. Oram, B. O'Reilly, C. Osthelder, D. J. Ottaway, H. Overmier, J. R. Palamos, W. Parker, E. Payne, A. Pele, C. J. Perez, M. Pirello, H. Radkins, K. E. Ramirez, J. W. Richardson, K. Riles, N. A. Robertson, J. G. Rollins, C. L. Romel, J. H. Romie, M. P. Ross, K. Ryan, T. Sadecki, E. J. Sanchez, L. E. Sanchez, T. R. Saravanan, R. L. Savage, D. Schaetzl, R. Schnabel, R. M. S. Schofield, E. Schwartz, D. Sellers, T. J. Shaffer, J. R. Smith, S. Soni, B. Sorazu, A. P. Spencer, K. A. Strain, L. Sun, M. J. Szczepańczyk, M. Thomas, P. Thomas, K. A. Thorne, K. Toland, C. I. Torrie, G. Traylor, A. L. Urban, G. Vajente, G. Valdes, D. C. Vander-Hyde, P. J. Veitch, K. Venkateswara, G. Venugopalan, A. D. Viets, C. Vorvick, M. Wade, J. Warner, B. Weaver, R. Weiss, B. Willke, C. C. Wipf, L. Xiao, H. Yamamoto, M. J. Yap, Hang Yu, L. Zhang, M. E. Zucker & J. Zweizig. *Quantum-Enhanced Advanced LIGO Detectors in the Era of Gravitational-Wave Astronomy*. Phys. Rev. Lett., vol. 123, no. 23, page 231107, December 2019. Online URL. (Cited on pages 2 and 22.)

[Tyc 04] Tomáš Tyc & Barry C. Sanders. *Operational Formulation of Homodyne Detection*. J. Phys. A: Math. Gen., vol. 37, no. 29, page 7341, July 2004. Online URL. (Cited on page 80.)

[Tzitrin 21] Ilan Tzitrin, Takaya Matsuura, Rafael N. Alexander, Guillaume Dauphinais, J. Eli Bourassa, Krishna K. Sabapathy, Nicolas C. Menicucci & Ish Dhand. *Fault-Tolerant Quantum Computation with Static Linear Optics*. PRX Quantum, vol. 2, no. 4, page 040353, December 2021. Online URL. (Cited on page 34.)

[Udem 02] Th Udem, R. Holzwarth & T. W. Hänsch. *Optical Frequency Metrology*. Nature, vol. 416, no. 6877, pages 233–237, March 2002. Online URL. (Cited on page 56.)

[U'Ren 03] A. B. U'Ren, K. Banaszek & I. A. Walmsley. *Photon Engineering for Quantum Information Processing*. May 2003. Online URL. (Cited on page 122.)

[Usha Devi 13] A. R. Usha Devi, A. K. Rajagopal, Sudha, H. S. Karthik & J. Prabhu Tej. *Equivalence of Classicality and Separability Based on P Phase–Space Representation of Symmetric Multiqubit States*. Quantum Inf Process, vol. 12, no. 12, pages 3717–3723, December 2013. Online URL. (Cited on page 16.)

[Vahlbruch 16] Henning Vahlbruch, Moritz Mehmet, Karsten Danzmann & Roman Schnabel. *Detection of 15 dB Squeezed States of Light and Their Application for the Absolute Calibration of Photoelectric Quantum Efficiency*. Phys. Rev. Lett., vol. 117, no. 11, page 110801, September 2016. Online URL. (Cited on page 71.)

[Vaughan 05] Joshua C. Vaughan, Thomas Hornung, T. Feurer & Keith A. Nelson. *Diffraction-Based Femtosecond Pulse Shaping with a Two-Dimensional Spatial Light Modulator.* Opt. Lett., OL, vol. 30, no. 3, pages 323–325, February 2005. Online URL. (Cited on page 62.)

[Veitch 13] Victor Veitch, Nathan Wiebe, Christopher Ferrie & Joseph Emerson. *Efficient Simulation Scheme for a Class of Quantum Optics Experiments with Non-Negative Wigner Representation.* New J. Phys., vol. 15, no. 1, page 013037, January 2013. Online URL. (Cited on page 34.)

[Vogel 06] Werner Vogel & Dirk-Gunnar Welsch. Quantum Optics. Wiley, 1 edition, May 2006. Online URL. (Cited on pages 6 and 14.)

[VonNeumann 32] John VonNeumann, Robert T. Beyer & Nicholas A. Wheeler. Mathematical foundations of quantum mechanics. 1932. (Cited on page 11.)

[Wai Leong 86] Kin Wai Leong & Jeffrey H. Shapiro. *Phase and Amplitude Uncertainties in Multimode Heterodyning.* Optics Communications, vol. 58, no. 2, pages 73–77, May 1986. Online URL. (Cited on page 17.)

[Walschaers 17a] Mattia Walschaers, Claude Fabre, Valentina Parigi & Nicolas Treps. *Entanglement and Wigner Function Negativity of Multimode Non-Gaussian States.* Physical Review Letters, vol. 119, no. 18, page 183601, October 2017. Online URL. (Cited on pages 30, 47, 131, 170, and 176.)

[Walschaers 17b] Mattia Walschaers, Claude Fabre, Valentina Parigi & Nicolas Treps. *Statistical Signatures of Multimode Single-Photon-Added and -Subtracted States of Light.* Phys. Rev. A, vol. 96, no. 5, page 053835, November 2017. Online URL. (Cited on pages 47, 131, 170, and 176.)

[Walschaers 18] Mattia Walschaers, Supratik Sarkar, Valentina Parigi & Nicolas Treps. *Tailoring Non-Gaussian Continuous-Variable Graph States.* Phys. Rev. Lett., vol. 121, no. 22, page 220501, November 2018. Online URL. (Cited on page 133.)

[Walschaers 19] Mattia Walschaers, Young-Sik Ra & Nicolas Treps. *Mode-Dependent-Loss Model for Multimode Photon-Subtracted States.* Phys. Rev. A, vol. 100, no. 2, page 023828, August 2019. Online URL. (Cited on page 132.)

[Walschaers 21] Mattia Walschaers. *Non-Gaussian Quantum States and Where to Find Them.* PRX Quantum, vol. 2, no. 3, page 030204, September 2021. Online URL. (Cited on pages 3, 31, and 36.)

[Weedbrook 12] Christian Weedbrook, Stefano Pirandola, Raúl García-Patrón, Nicolas J. Cerf, Timothy C. Ralph, Jeffrey H. Shapiro & Seth Lloyd. *Gaussian Quantum Information.* Rev. Mod. Phys., vol. 84, no. 2, pages 621–669, May 2012. Online URL. (Cited on pages 18, 19, 25, and 26.)

[Weihs 98] Gregor Weihs, Thomas Jennewein, Christoph Simon, Harald Weinfurter & Anton Zeilinger. *Violation of Bell's Inequality under Strict Einstein Locality Conditions.* Phys. Rev. Lett., vol. 81, no. 23, pages 5039–5043, December 1998. Online URL. (Cited on page 2.)

[Weiner 88] A. M. Weiner, J. P. Heritage & E. M. Kirschner. *High-Resolution Femtosecond Pulse Shaping.* J. Opt. Soc. Am. B, JOSAB, vol. 5, no. 8, pages 1563–1572, August 1988. Online URL. (Cited on page 61.)

[Weiner 11a] Andrew Weiner. Ultrafast Optics. Wiley, 1st edition edition, September 2011. (Cited on page 56.)

[Weiner 11b] Andrew M. Weiner. *Ultrafast Optical Pulse Shaping: A Tutorial Review.* Optics Communications, vol. 284, no. 15, pages 3669–3692, July 2011. Online URL. (Cited on page 61.)

[Wenger 04] Jérôme Wenger, Rosa Tualle-Brouri & Philippe Grangier. *Non-Gaussian Statistics from Individual Pulses of Squeezed Light.* Phys. Rev. Lett., vol. 92, no. 15, page 153601, April 2004. Online URL. (Cited on page 3.)

[Wigner 32] E. Wigner. *On the Quantum Correction For Thermodynamic Equilibrium.* Phys. Rev., vol. 40, no. 5, pages 749–759, June 1932. Online URL. (Cited on page 12.)

[Williamson 36] John Williamson. *On the Algebraic Problem Concerning the Normal Forms of Linear Dynamical Systems.* American Journal of Mathematics, vol. 58, no. 1, pages 141–163, 1936. Online URL. (Cited on page 28.)

[Wolfgang 01] P. Schleich Wolfgang. Quantum Optics in Phase Space. February 2001. Online URL. (Cited on page 13.)

[Yang 21] Zijiao Yang, Mandana Jahanbozorgi, Dongin Jeong, Shuman Sun, Olivier Pfister, Hansuek Lee & Xu Yi. *A Squeezed Quantum Microcomb on a Chip.* Nat Commun, vol. 12, no. 1, page 4781, August 2021. Online URL. (Cited on page 3.)

[Yuen 83] Horace P. Yuen & Vincent W. S. Chan. *Noise in Homodyne and Heterodyne Detection.* Opt. Lett., OL, vol. 8, no. 3, pages 177–179, March 1983. Online URL. (Cited on page 78.)

[Yukawa 08] Mitsuyoshi Yukawa, Ryuji Ukai, Peter van Loock & Akira Furusawa. *Experimental Generation of Four-Mode Continuous-Variable Cluster States.* Phys. Rev. A, vol. 78, no. 1, page 012301, July 2008. Online URL. (Cited on page 3.)

[Yurke 86] B. Yurke & D. Stoler. *Generating Quantum Mechanical Superpositions of Macroscopically Distinguishable States via Amplitude Dispersion.* Phys. Rev. Lett., vol. 57, no. 1, pages 13–16, July 1986. Online URL. (Cited on page 37.)

[Zavatta 07] Alessandro Zavatta, Valentina Parigi & Marco Bellini. *Experimental Nonclassicality of Single-Photon-Added Thermal Light States*. Phys. Rev. A, vol. 75, no. 5, page 052106, May 2007. Online URL. (Cited on page 104.)

[Zhong 20] Han-Sen Zhong, Hui Wang, Yu-Hao Deng, Ming-Cheng Chen, Li-Chao Peng, Yi-Han Luo, Jian Qin, Dian Wu, Xing Ding, Yi Hu, Peng Hu, Xiao-Yan Yang, Wei-Jun Zhang, Hao Li, Yuxuan Li, Xiao Jiang, Lin Gan, Guangwen Yang, Lixing You, Zhen Wang, Li Li, Nai-Le Liu, Chao-Yang Lu & Jian-Wei Pan. *Quantum Computational Advantage Using Photons*. Science, vol. 370, no. 6523, pages 1460–1463, December 2020. Online URL. (Cited on page 3.)